frontiers | Research Topics

Planning, operation and control of modern power system with large-scale renewable energy generations, volume II

Edited by
Youbo Liu, Hao Xiao, Xia Lei, Yaser Qudaih and Xin Zhang

Published in
Frontiers in Energy Research

ISSN 1664-8714
ISBN 978-2-8325-5312-1
DOI 10.3389/978-2-8325-5312-1

About Frontiers

Frontiers is more than just an open access publisher of scholarly articles: it is a pioneering approach to the world of academia, radically improving the way scholarly research is managed. The grand vision of Frontiers is a world where all people have an equal opportunity to seek, share and generate knowledge. Frontiers provides immediate and permanent online open access to all its publications, but this alone is not enough to realize our grand goals.

Frontiers journal series

The Frontiers journal series is a multi-tier and interdisciplinary set of open-access, online journals, promising a paradigm shift from the current review, selection and dissemination processes in academic publishing. All Frontiers journals are driven by researchers for researchers; therefore, they constitute a service to the scholarly community. At the same time, the *Frontiers journal series* operates on a revolutionary invention, the tiered publishing system, initially addressing specific communities of scholars, and gradually climbing up to broader public understanding, thus serving the interests of the lay society, too.

Dedication to quality

Each Frontiers article is a landmark of the highest quality, thanks to genuinely collaborative interactions between authors and review editors, who include some of the world's best academicians. Research must be certified by peers before entering a stream of knowledge that may eventually reach the public - and shape society; therefore, Frontiers only applies the most rigorous and unbiased reviews. Frontiers revolutionizes research publishing by freely delivering the most outstanding research, evaluated with no bias from both the academic and social point of view. By applying the most advanced information technologies, Frontiers is catapulting scholarly publishing into a new generation.

What are Frontiers Research Topics?

Frontiers Research Topics are very popular trademarks of the *Frontiers journals series*: they are collections of at least ten articles, all centered on a particular subject. With their unique mix of varied contributions from Original Research to Review Articles, Frontiers Research Topics unify the most influential researchers, the latest key findings and historical advances in a hot research area.

Find out more on how to host your own Frontiers Research Topic or contribute to one as an author by contacting the Frontiers editorial office: frontiersin.org/about/contact

Planning, operation and control of modern power system with large-scale renewable energy generations, volume II

Topic editors

Youbo Liu — Sichuan University, China

Hao Xiao — Institute of Electrical Engineering, Chinese Academy of Sciences (CAS), China

Xia Lei — Xihua University, China

Yaser Qudaih — Higher Colleges of Technology, United Arab Emirates

Xin Zhang — Brunel University London, United Kingdom

Citation

Liu, Y., Xiao, H., Lei, X., Qudaih, Y., Zhang, X., eds. (2024). *Planning, operation and control of modern power system with large-scale renewable energy generations, volume II*. Lausanne: Frontiers Media SA. doi: 10.3389/978-2-8325-5312-1

Table of contents

frontiers | Frontiers in Energy Research

TYPE Original Research
PUBLISHED 10 August 2023
DOI 10.3389/fenrg.2023.1240542

OPEN ACCESS

EDITED BY
Xia Lei,
Xihua University, China

REVIEWED BY
Flah Aymen,
École Nationale d'Ingénieurs de Gabès, Tunisia
Hanlin Zhang,
Qingdao University, China

*CORRESPONDENCE
Dou An,
douan2017@xjtu.edu.cn

RECEIVED 15 June 2023
ACCEPTED 01 August 2023
PUBLISHED 10 August 2023

CITATION
Cui F, An D and Zhang G (2023), A game strategy for demand response based on load monitoring in smart grid.
Front. Energy Res. 11:1240542.
doi: 10.3389/fenrg.2023.1240542

A game strategy for demand response based on load monitoring in smart grid

Feifei Cui, Dou An* and Gongyan Zhang

School of Automation Science and Engineering, Faculty of Electronics and Information Engineering, Xi'an Jiaotong University, Xi'an, Shaanxi, China

Demand response technologies can achieve the objective of optimizing resource allocation and ensuring efficient operation of the smart grid by motivating the energy users to change their power usage behavior. However, the increasing uncertainty of smart grid environment brings great challenges to the development of demand response technique. In this study, we build a long short-term memory (LSTM) network as a load forecasting model to predict user load data in order to obtain accurate consumption behavior of energy users. Then, we utilize a Stackelberg game model based on the load forecasting model to dynamically optimize the electricity prices set by power suppliers at different times, enhancing the efficiency of demand response between users and suppliers. Extensive simulation experiments demonstrate that the LSTM-based load forecasting model achieves an accuracy of up to 96.37% in predicting user load demand. And the game model reduces the overall expenditure of users by 30% compared with the general pricing model.

KEYWORDS

demand response, game theory, load monitoring, smart grid, load forecasting

1 Introduction

The concept of the smart grid stems from the idea of Advanced Metering Infrastructure (AMI). Its goal is to enhance demand-side management and energy efficiency and to construct a self-healing, reliable grid protection system capable of withstanding severe human-induced disruptions and potential natural disasters (Mahela et al., 2022). However, the rapid advancement of information technology has led the power industry and research institutions to reconsider and expand the initial vision of the smart grid, enabling the full utilization of information technology within smart grids (Orlando et al., 2022). Recently, the smart grid has evolved into a typical cyber-physical system (CPS), integrating electric power, information transmission, network security communication, and intelligent computing. It has established a clean, secure, efficient, and sustainable advanced energy delivery network (Gao et al., 2023). For instance, to reduce peak demand and smooth load curves, power suppliers can use the high-speed communication network of a smart grid to encourage specific users to reduce their load during peak periods using real-time pricing signals. This not only incentivizes users to participate in the grid regulation but also smooths the load curve, thereby improving the overall energy utilization rate (Trujillo and García Torres, 2022).

The smart grid with distributed power supply model greatly enhances the reliability and self-healing capabilities of power system, reducing the scope of power outages through self-healing responses (Jasim et al., 2023). In terms of economic benefits, the cost-to-benefit

ratio of a smart grid is approximately 4:1–5:1 (Gellings et al., 2004). In addition to bringing substantial direct economic benefits to power companies, this saves a significant amount of energy, contributing to environmental protection and sustainable development in society. To achieve the aforementioned benefits and generate greater economic gains, it is necessary to invest more research effort in areas such as demand response and load supervision (Khan et al., 2023).

Load monitoring (LM) technology allows power suppliers to make predictions about user's load usage and to learn about load usage patterns, which can be divided into intrusive and non-intrusive types based on the monitoring approach. Intrusive load monitoring requires the installation of measuring devices on each load, which leads to higher overall costs and lower usage frequency (Wang et al., 2020). Non-intrusive load monitoring, on the other hand, does not require installing measuring devices in each user's home. Instead, the devices are installed at the power entry points of various centralized units to collect aggregated data. Subsequently, the aggregated energy loads are decomposed into individual energy loads, enabling a simple and effective way to forecast load operations and energy consumption (Abubakar et al., 2017).

In order to effectively encourage the participation of users in the electricity trading process, power suppliers often utilize demand response techniques to motivate the power users changing their inherent power consumption behavior by adopting certain incentives. The research efforts of demand response techniques can be divided into price-based and incentive-based. Price-based demand response techniques help power suppliers to learn autonomous pricing strategies to arrange loads of energy users (Liu et al., 2017). Tang et al. (2019) and Cheng et al. (2022) modelled the interaction strategies between power grid and energy users as a Stackelberg game model, in which the grid optimizes the price to maximize its net profit and reduce demand fluctuation, and individual energy user optimizes the hourly power demand to minimize electricity bill and effects of demand alternation from the baseline. Sofana Reka and Ramesh (2016) utilized a generalized tit for tat dominant game-based energy scheduler to shift the peak average ratio of the smart grid. While, incentive-based demand response techniques enable power suppliers to learn an economic compensation mechanism to encourage energy users reducing their peak-periods loads (Zheng et al., 2022). For instance, Mansouri et al. (2023) proposes a three-layer risk-averse game theoretic-based strategy to coordinate smart buildings and EV fleets with microgrids scheduling. In the first layer of above strategy, a demand response program is designed for smart buildings where dynamic incentive tariffs are calculated based on the consumption pattern of subscribers.

Although demand response techniques have been widely deployed in addressing the resource allocation problem of smart grid (Sivasankarareddy et al., 2021; Panda et al., 2022). However, there remaining some obstacles that prevent above methods from implementing in realistic scenarios. 1) The increasing uncertainty of users loads brings great challenges to the establishment of accurate optimization model, resulting in the inefficiency of demand response strategies. 2) Existing game model-based demand response strategies lack the theoretical analysis of Nash equilibrium. Differently, this paper investigates a demand response model integrates load monitoring technology. In this demand response model, the interaction between power suppliers and users is modeled using game theory. Each power supplier dynamically adjusts its price signal based on the user's demand, while users passively respond to the price signal by submitting their demand signals, ultimately maximizing the utility of user and profit of power supplier. The main contributions are as follows:

- This paper employs LSTM networks as the load forecasting model to predict user load data based on the load forecasting model and demand response theory. The LSTM network, with its memory units, can effectively capture historical load data and learn the periodic patterns in user load data.
- This paper designs a demand response model based on Stackelberg game theory, utilizing the load prediction results from the load forecasting model. This model accurately represents the complex demand response interaction between users and power suppliers in the smart grid. Mathematical derivations demonstrate that the entire interaction process can reach a Nash equilibrium, which can maximize the utility of both parties.
- This paper presents extensive simulation experiments to demonstrate the effectiveness of both the load forecasting model and demand response model. Simulation results prove that the LSTM-based load forecasting model can achieve up to 96.37% accuracy in load demand prediction for users. And the proposed game model can significantly reduce users' electricity expenses.

The main notations utilized in this paper are summarized in Table 1.

TABLE 1 Main notations.

Notation	Explanation
$\mathcal{N}$	Number of energy users
$\mathcal{K}$	Number of power suppliers
l_i^h	Load consumption of user i at time h
$d_{n,k}$	Amount of electricity purchased by user n from power supplier k
U_n	Utility of energy user n
γ_n, β_n	Constant coefficients
p_k	Unit power price provided by power supplier k
B_n	Maximum electricity expenditure that user n can afford
G_k	Maximum production capacity of power provider k
$\mathcal{S}_{\mathcal{K}}$	Strategy sets of power suppliers
$\mathcal{S}_{\mathcal{N}}$	Strategy sets of energy users
p_k^*	Price signal of power supplier k at Nash equilibrium

2 Related work

2.1 Research status of load monitoring models in smart grids

Load supervision is a key technology that predicts future energy demand based on historical load data, temperature data, and weather

data. The prediction of future demand from load supervision is a critical parameter for the operation and planning of a power system. Errors between the predictive model and the actual parameters can lead to increased operational costs and later increased costs for power suppliers. Hence, many load supervision models have been proposed to achieve more precise load demand prediction. Current research on load supervision models by scholars worldwide can be classified into two categories: models based on probability and statistics and models based on artificial intelligence.

Regarding probabilistic-statistical models (Huang and Shih, 2003), presents a variety of statistical models. These include the autoregressive model (AR), moving average model (MA), autoregressive moving average model (ARMA), and autoregressive integrated moving average model (ARIMA), with detailed explanations of each model's mathematical expression and prediction methods. Hermias et al. (2017) uses an ARIMA model to predict future air-conditioning load based on seasonal component compensation. Alhmoud and Nawafleh (2021) used ARMA method and two neural network-based methods to predict the load data. Through simulation, it was demonstrated that the neural network approach could effectively improve the prediction accuracy. Among artificial intelligence-based load supervision models, Walther et al. (2019) proposed a very short-term load data predictor based on machine learning. It simply used a single-step delay, taking only the current value and time load data of the single-step delay as input to predict future load data. Mocanu et al. (2016) aimed to improve the design of power infrastructure and the effective deployment of distributed and renewable energy sources by predicting the electricity consumption patterns in power systems through a deep learning network, thereby enhancing the electricity efficiency of the entire power system. The authors creatively proposed the conditional restricted Boltzmann machine (CRBM) and factor conditional restricted Boltzmann machine (FCRBM) models to predict data and validated their accuracy through simulation experiments. Afrasiabi et al. (2020) mainly proposed a hybrid predictive model based on convolution neural networks to predict residential power load curves. By predicting the loads of individual users, the power supply system can better monitor electricity usage habits, thus achieving better load scheduling.

2.2 Research status of demand response technology in smart grids

Compared with traditional power grids, the advantage of smart grids is that they can significantly improve the reliability of the entire power system and the responsiveness of users and can encourage users to participate more actively in energy trading decisions. Therefore, all scheduling and incentives on the demand side, including overall demand response management, are integral parts of the smart grid. Current demand response mechanisms can be divided into two categories: one is based on user incentive mechanisms, and the other is based on power pricing mechanisms.

Gyamfi et al. (2013) studied different demand response mechanisms, such as time-of-use (TOU) pricing, peak pricing, and real-time pricing, and applied them to users in different countries and regions to measure their response rates to these mechanisms. This laid a solid foundation for later research on demand response theories. The results showed that a large portion of households did not respond to price changes, possibly because they did not understand the pricing system and therefore did not react immediately to price changes. Zhang et al. (2023) proposed a demand response algorithm based on bidding incentives. This algorithm used Vickrey-Clarke-Groves mechanism to optimize the choice of energy policies to find the strategy that maximizes the total profit of the energy service provider while satisfying the user's minimum load power requirements. Trujillo and García Torres (2022) proposed a multi-stage control system to manage the electric vehicle users' demand, automatically adjust the load, and optimize the entire system using a stochastic optimization algorithm. This study provided the best demand response solutions for users by comparing various strategies based on pricing mechanism and incentive mechanism. Bokkisam et al. (2022) proposed a peer-to-peer demand transactive system. In this algorithm, the smart grid was divided into three agents: users, auctioneer, and utility. To consider the balance of user benefits, load demand, and energy supply, the third-party agent demonstrated method and blockchain-based method were tested. The optimal real-time demand allocation results was obtained through simulation experiments.

In summary, based on the current research status worldwide, the problem of demand response models based on load supervision in smart grids is a frontier issue that crosses multiple fields. Although many theories and results have been obtained in various fields, better integrating load supervision methods with demand response models to ensure the stability of overall system operation while achieving satisfactory returns between users and power suppliers is a subject that urgently needs to be studied.

3 Preliminaries

3.1 System model

The model of the game demand response strategy based on load demand forecasting studied in this paper includes two main entities: the power supplier and the users. Within the energy management unit, there are multiple power suppliers, each with varying capacities due to their different scales. However, each power supplier can independently supply electric power to users. Compared to the centralized power supply of traditional grids, this distributed power supply from multiple suppliers greatly enhances the stability and robustness of the entire power system. Each power supplier, constrained by its capacity and costs, sets real-time prices at each moment, resulting in different prices among suppliers. Users can choose to purchase electric power from the supplier that maximizes their own utility based on their load usage habits.

In the demand response strategy, the power suppliers first use the trained load demand prediction model to forecast the future load demand of each user. They then issue an initial electricity price signal to the users based on the predicted load demand. During this process, the prices set by each supplier differ based on the users' load demand and the suppliers' capacities and costs. Upon

receiving the price signal, users calculate the optimal energy demand from different suppliers based on their maximum energy cost expenditure and a utility optimization function. They then send the demand signals to the respective suppliers. Each supplier receives the energy demand purchased by users, and being rational and self-interested, adjusts its electricity price information to maximize its own revenue. This forms a non-cooperative game model among the power suppliers. This entire demand response process continues until the system reaches a Nash equilibrium. At equilibrium, no power supplier can increase its revenue by unilaterally changing its price information.

3.2 Game theory approach

Game theory is a formal analytical framework that studies complex interactions among independent rational players using specific mathematical representations and derives the optimal strategies of the players based on individual rational behavior. Over the decades, game theory has been widely applied in various disciplines, ranging from economics and political science to psychology, achieving significant progress across different fields. In today's large-scale smart grid systems and various cyber-physical systems (CPSs), complex interactions often exist among multiple intelligent nodes. To achieve better interactions between power suppliers and users, the framework of game theory has become an important theoretical analysis tool and has been widely applied in practical optimization scenarios (Cheng and Yu, 2019). Game models typically consist of three elements: players $\mathcal{N}$, decision sets $(\mathcal{A}_i)_{i\in\mathcal{N}}$, and utility functions $(U_i)_{i\in\mathcal{N}}$. In the entire non-cooperative static game process, each decision maker i aims to select a decision process $a_i \in \mathcal{A}_i$ from their decision set $\mathcal{A}_i$ to maximize their own utility function $U_i(a_i, a-i)$. However, the utility function of a user depends not only on their own decision a_i but also on the decisions a_{-i} of participants other than user i. As each user seeks to maximize their own utility, a game model is formed accordingly.

The aforementioned game model can be applied to demand response management in smart grids. A smart grid system has $\mathcal{N}$ users and multiple power suppliers. In a given period h, the total load consumption of all users in the system can be represented as $L_h = \sum_{i\in N} l_i^h$, where l_i^h represents the load consumption of user i at time h. When users consume electricity, power suppliers bear costs associated with electricity production and transmission. The overall costs can be represented by a cost function $C_h = \Sigma_{i\in N} C_h(L_h)$, where the cost function is a strictly increasing convex function with the user's load consumption as the independent variable. When the load consumption of users at a certain time is higher, the value of the cost function also increases. Therefore, power suppliers determine the electricity price at time h based on the magnitude of the cost function. A larger cost function indicates higher costs, resulting in a higher electricity price being set, and *vice versa*. The size of the cost function mainly depends on the consumption L_h at that time. When a user participating in scheduling changes their load consumption, it affects the current consumption L_h, which in turn influences the power supplier's setting of the electricity price through C_h. In other words, in each period, users can influence the electricity price of the entire system by scheduling their own loads. The less load consumption in the system, the lower the power supplier will set the electricity price, and the more load consumption in the system, the higher the power supplier will set the electricity price. If each user wants a lower electricity price when using their load, a game model arises. The participants are all the users N involved in scheduling, the decision set is the load consumption l_h of each user at a certain time, and the utility function represents each user's desire to maximize their own utility through the scheduling of their load. When the entire game model reaches a Nash equilibrium, no user in the system can improve their own utility simply by changing their load consumption decision, resulting in an equilibrium state for the entire system.

4 Load supervision method based on an LSTM network

In recent years, the rapid development of information technology has led to the widespread application of smart grids. In a smart grid, the integration of various renewable energy supply nodes, electric vehicle nodes, and user access nodes significantly increases the complexity and instability of the entire system. Undoubtedly, compared to the centralized energy supply in traditional grids, the access of various distributed nodes in smart grids poses unprecedented challenges to system stability. To address this issue, load supervision technology has been widely applied in practical projects. Through load supervision technology, it is possible to assist in demand response and achieve the transfer of peak demand, thereby improving the overall stability of the system. In the field of load supervision, deep learning techniques have begun to be widely used. Deep learning utilizes multilayer neural connections to extract features from input data. Compared to traditional machine learning algorithms, deep learning greatly improves the accuracy of models and enhances prediction accuracy through stacking layers and increasing the number of neurons.

4.1 LSTM network

Although classical feedforward fully connected neural networks work well for traditional data classification and regression problems, they face challenges when dealing with continuous sequential data such as time series load data and speech data. This is because sequential data have inherent order dependencies, and it is not straightforward to split these time series data into independent training samples to train a traditional feedforward neural network. Therefore, to consider the sequential nature of the data during training, adjustments need to be made to the structure of the traditional feedforward neural network by introducing memory units, giving rise to RNNs. Long short-term memory (LSTM) networks are a type of neural network architecture proposed to address the issue of vanishing gradients in RNNs (Cai et al., 2022). Compared to traditional RNN architectures, LSTM incorporates dedicated memory modules to retain previous information. In terms of the update mechanism, LSTM does not directly overwrite the information in the memory unit with the sequence information obtained at the previous time step. Instead, it accumulates information over time, ensuring the retention of information from

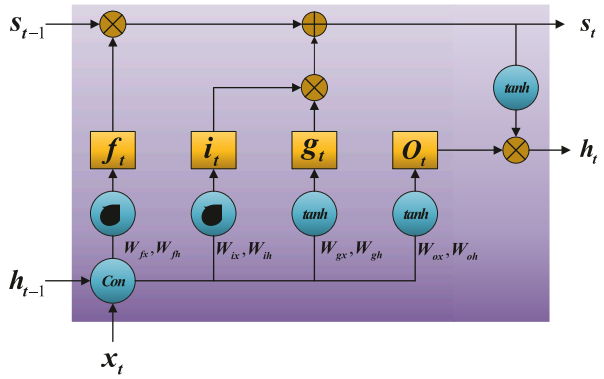

FIGURE 1
LSTM network unit structure.

much earlier sequences. Figure 1 represents a basic LSTM unit, which includes three crucial gate structures: the input gate, the output gate, and the forget gate. The input gate determines whether the current information $\boldsymbol{x}_t$ should be stored in memory cell $\boldsymbol{s}_t$. The output gate determines whether the current information in memory cell $\boldsymbol{s}_t$ should be output as the current output $\boldsymbol{h}_t$. The forget gate controls how much information from the previous memory cell $\boldsymbol{s}_{t-1}$ should be stored in the current memory cell $\boldsymbol{s}_t$.

4.2 Construction of a load monitoring model based on an LSTM network

4.2.1 Load data analysis

After obtaining the load consumption data, the first step is to perform data cleaning, which includes handling outliers and missing values in the data. Then, the correlation between different features needs to be examined. Since the dataset in this study has many features, using all of them as training data would result in an excessively high dimensionality of the training dataset. Moreover, for time series data, when constructing the supervised model data, a certain time step delay is applied, which further increases the number of features, leading to a significant computational burden and prolonged training time. Therefore, to address this issue, it is necessary to eliminate some highly correlated feature attributes through correlation analysis, aiming to improve training speed without compromising model accuracy.

Through correlation analysis, it is found that there is a strong correlation between various features. In this study, temperature and humidity are selected as the training data features (Chen et al., 2021). Additionally, since user load consumption is often related to user behavior patterns, with lower consumption during weekdays and higher consumption during weekends, this study uses an additional feature to represent whether the current date is a weekend in training the model.

4.2.2 Load supervision model framework

The load supervision model is primarily built using LSTM networks and trained with the historical load data obtained in the previous section.

The construction steps of the entire model are as follows:

1) Encode the vector data $\boldsymbol{W}$ indicating whether it is a working day, where 1 represents a working day and 0 represents a weekend.

2) Normalize the load data $\boldsymbol{L}$, temperature data $\boldsymbol{T}$, and humidity data $\boldsymbol{H}$, and then concatenate these vectors to form the input matrix $\boldsymbol{X} = \{\boldsymbol{T}, \boldsymbol{H}, \boldsymbol{W}, \boldsymbol{L}\}$.

3) Transform the preprocessed time series data $\boldsymbol{X}$ into data suitable for supervised learning based on the designated time step K. By using a sliding window approach, the input matrix $\boldsymbol{X}$ is shifted with a step size.

4) Input the matrix $\boldsymbol{X}$ into the LSTM network for model training.

The framework of the entire model is shown in Figure 2.

5 Demand response methods based on game theory

In traditional demand response models, due to the complex interaction between users and the power supply side, the optimization process often only considers one side of the demand response. For instance, when considering the maximization of user welfare, the maximization of the power supply side's benefits is not included. To model the complex interaction process between multiple users and multiple power suppliers in the demand response, this section studies a model based on a Stackelberg game as shown in Figure 3. First, each power supplier predicts the future load demand of users using the load demand prediction model proposed in the previous section and determines the initial electricity price based on the current load demand and its own power supply. Then, each user compares the price signals provided by all power suppliers to maximize their own benefits, purchases electricity from different power suppliers according to their own electricity usage habits, and synchronizes the demand information in real time to the designated power supplier. Finally, the power supplier updates its price signal based on the user's purchased demand and the price signals of the other power suppliers.

In the entire demand response model, $\mathcal{N} = \{1, 2, \ldots, N\}$ represents the number of users, and $\mathcal{K} = \{1, 2, \ldots, K\}$ represents the number of power suppliers. The entire system model is shown in Figure 3. The power supply side of this model includes the connection of various renewable and non-renewable energy suppliers. Non-renewable energy includes various fossil fuels, which produce relatively stable electricity and can continuously output electricity. However, due to the pollution caused by the combustion of such fuels and their non-renewable nature, an increasing amount of renewable clean energy is connected to the grid. On the user side, various types of users, such as residential users, industrial users, and commercial users, are distinguished by their set load demand limits. When modeling power suppliers and users, users express the utility value obtained after consuming electricity through a utility function, and power suppliers express the profit obtained after selling electricity through a profit function. The communication between the two parties is carried out through the two-way communication network, where each power supplier sends its price signal to the users in real time, and the users respond to the demand signal of the power supplier considering the maximization of their own utility after receiving different price signals.

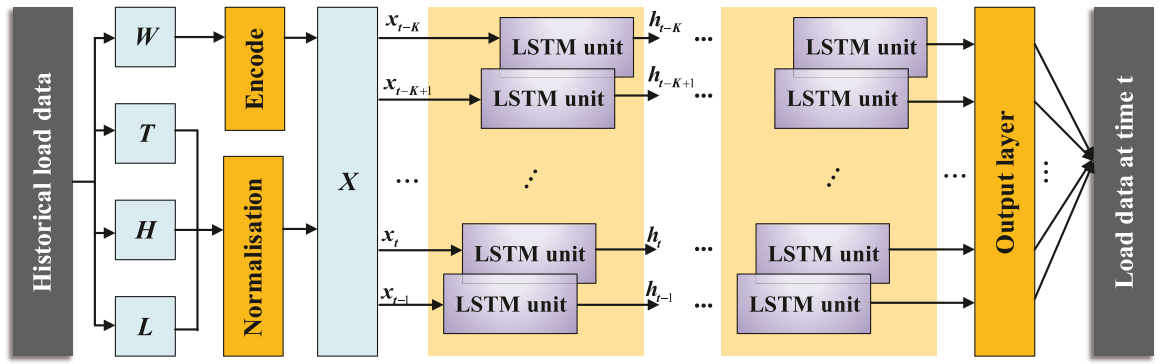

FIGURE 2
Load supervision model framework.

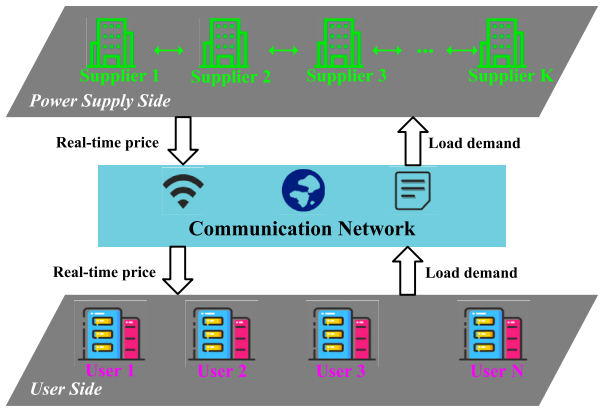

FIGURE 3
Demand response system model.

The entire interaction process of the demand response model constitutes a Stackelberg game. In this game process, the power supplier, as a leader, sends the real-time price signal to the followers first, while the user, as a follower, optimizes their load demand allocation according to the price signal issued by the leader. Therefore, the entire game process can be seen as a game of electricity prices among various power suppliers. The power suppliers set their own electricity prices according to the amount of user loads and the price levels of other power suppliers, while the users passively respond, maximizing their own utility functions through the real-time price signals issued by the power suppliers.

5.1 User-side mathematical model

The entire system architecture involves multiple users and multiple power suppliers, where each user $n \in \mathcal{N}$ selects the amount of electricity purchased $d_{n,k} \geq 0$ according to the price signal released by each power supplier $k \in \mathcal{K}$ at each unit time. The unit time is set to 30 min, and the user's energy demand purchase volume maximizes the utility function under the premise of satisfying its own cost budget. In this article, the utility functions of users at the unit time can be represented as:

$$U_n(\boldsymbol{d_n}) = \gamma_n \sum_{k \in \mathcal{K}} \ln(\beta_n + d_{n,k}) \tag{1}$$

where $\gamma_n > 0$ and $\beta_n \geq 1$ are both constant coefficients. These coefficients ensure that when the user does not purchase electricity from any power supplier, that is, when $\boldsymbol{d}_n = 0$, the value of the formula $\sum_{k \in \mathcal{K}} \ln(d_{n,k})$ will not reach $-\infty$. In Eq. 1, the user's utility is modeled through a logarithmic function (Wang et al., 2021).

The user's goal is to maximize their utility function while first satisfying their own budget by determining their electricity demand purchases based on their own electricity consumption habits and the prices of different power suppliers. The optimization function can be expressed as:

$$\begin{aligned} &\max_{\boldsymbol{d}_n} \quad U_n(\boldsymbol{d}_n) \\ &s.t. \quad \begin{cases} \sum_{k \in \mathcal{K}} p_k d_{n,k} \leq B_n \\ d_{n,k} \geq 0, \quad \forall k \in \mathcal{K} \end{cases} \end{aligned} \tag{2}$$

where p_k represents the real-time unit power price provided by power supplier k and B_n represents the maximum electricity expenditure that user n can afford. The optimization process on the user side does not involve a game between users; they only passively accept the price signals provided by the power supplier to maximize their utility functions. Each user's decision can be considered as being made independently.

To understand the energy demand optimization process on the user side more clearly, this article first assumes a general situation: there are only N users and three power suppliers in the demand response management system. After careful analysis of the general situation, the conclusion is extended to $\mathcal{K}$ power suppliers. When there are only three power suppliers in the system, the optimization problem can be expressed as:

$$\begin{aligned} &\max_{d_{n,1}, d_{n,2}, dn,3} \quad \gamma_n \sum_{k=1}^{3} \ln(\beta_n + d_{n,k}) \\ &s.t. \quad \begin{cases} p_1 d_{n,1} + p_2 d_{n,2} + p_3 d_{n,3} \leq B_n \\ d_{n,1}, d_{n,2}, d_{n,3} \geq 0 \end{cases} \end{aligned} \tag{3}$$

Introducing the Lagrange multipliers $\lambda_{n,1},\lambda_{n,2},\lambda_{n,3},\lambda_{n,4}$, the optimization problem with inequality constraints is represented by a Lagrange function as follows:

$$\mathcal{L}_n = \gamma_n \sum_{k=1}^{3} \ln(\beta_n + d_{n,k}) - \lambda_{n,1}\left(\sum_{k=1}^{3} p_k d_{n,k} - B_n\right) + \lambda_{n,2} d_{n,1} + \lambda_{n,3} d_{n,2} + \lambda_{n,4} d_{n,3} \tag{4}$$

The KKT conditions are:

$$\lambda_{n,1}\left(\sum_{k=1}^{3} p_k d_{n,k} - B_n\right) = 0 \tag{5}$$

$$\lambda_{n,2} d_{n,1} = 0 \tag{6}$$

$$\lambda_{n,3} d_{n,2} = 0 \tag{7}$$

$$\lambda_{n,4} d_{n,3} = 0 \tag{8}$$

$$\lambda_{n,1} > 0 \tag{9}$$

$$\lambda_{n,2},\lambda_{n,3},\lambda_{n,4} \geq 0 \tag{10}$$

$$x_{n,1}, x_{n,2} \geq 0 \tag{11}$$

When the utility function is maximized, the first derivative of Eq. 4 needs to be zero; that is, $\nabla \mathcal{L}_n(\boldsymbol{d}_n^*) = 0$. The partial derivative of Eq. 4 can be obtained as:

$$\begin{cases} \dfrac{\gamma_n}{\beta_n + d_{n,1}} - \lambda_{n,1} p_1 + \lambda_{n,2} = 0 \\ \dfrac{\gamma_n}{\beta_n + d_{n,2}} - \lambda_{n,1} p_2 + \lambda_{n,3} = 0 \\ \dfrac{\gamma_n}{\beta_n + d_{n,3}} - \lambda_{n,1} p_3 + \lambda_{n,4} = 0 \end{cases} \tag{12}$$

To determine the optimal amount of energy for each user to purchase from each power supplier at this time, the amount of electrical energy purchased by users from each power supplier needs to be considered in categories:

1) When $d_{n,1} > 0, d_{n,2} > 0, d_{n,3} > 0$:

Through Eqs 6–8, we can derive $\lambda_{n,2} = \lambda_{n,3} = \lambda_{n,4} = 0$. Substituting $\lambda_{n,2}$, $\lambda_{n,3}$, and $\lambda_{n,4}$ into Eq. 12, we obtain:

$$d_{n,k} = \frac{\gamma_n}{\lambda_{n,1} p_k} - \beta_n \quad \forall n \in \mathcal{N}, \quad k = 1,2,3. \tag{13}$$

Substituting Eq. 13 into Eq. 5, we can solve for:

$$\lambda_{n,1} = \frac{3\gamma_n}{B_n + \sum_{k=1}^{3} p_k \beta_n} \tag{14}$$

Finally, by substituting Eq. 14 into Eq. 13, we can solve for the amount of electricity each user purchases from each power supplier:

$$d_{n,k} = \frac{B_n + \sum_{k=1}^{3} p_k \beta_n}{3\, p_k} - \beta_n \quad k = 1,2,3. \tag{15}$$

2) When $d_{n,1} > 0, d_{n,2} = 0, d_{n,3} = 0$:

Through Eq. 6, we can obtain $\lambda_{n,2} = 0$. Substituting $\lambda_{n,2} = 0$ into Eq. 12, we obtain:

$$d_{n,1} = \frac{\gamma_n}{\lambda_{n,1} p_1} - \beta_n \tag{16}$$

Substituting Eq. 16 into Eq. 5, we can obtain:

$$\lambda_{n,1}\left(\frac{\gamma_n}{\lambda_{n,1}} - \beta_n p_1 - B_n\right) = 0 \tag{17}$$

According to $\lambda_{n,1} > 0$ in the KKT condition, $(\gamma_n/\lambda_{n,1}) - \beta_n p_1 - B_n = 0$ can be obtained. Therefore, the solved $\lambda_{n,1}$ can be brought into Eq. 16 to obtain:

$$\begin{aligned} d_{n,1} &= \frac{\beta_n p_1 + B_n}{p_1} - \beta_n \\ &= \frac{B_n}{p_1} = \frac{B_n + \beta_n(p_1 + p_2 + p_3)}{3\, p_1} + \frac{2B_n - \beta_n(p_1 + p_2 + p_3)}{3\, p_1} \end{aligned} \tag{18}$$

From $d_{n,2} = d_{n,3} = 0$, we can obtain $B_n = \beta_n(2p_3 - p_1 - p_2) = \beta_n(2p_2 - p_1 - p_3)$. Substituting this into Eq. 18, we can finally obtain:

$$\begin{aligned} d_{n,1} &= \frac{B_n + \beta_n(p_1 + p_2 + p_3)}{3\, p_1} + \frac{2B_n - \beta_n(p_1 + p_2 + p_3)}{3\, p_1} \\ &= \frac{B_n + \beta_n(p_1 + p_2 + p_3)}{3\, p_1} - \beta_n \end{aligned} \tag{19}$$

3) When $d_{n,1} = 0, d_{n,2} > 0, d_{n,3} = 0$:

Similarly, we can solve to obtain:

$$d_{n,2} = \frac{B_n}{p_2} = \frac{B_n + \beta_n(p_1 + p_2 + p_3)}{3\, p_2} - \beta_n \tag{20}$$

4) When $d_{n,1} = 0, d_{n,2} = 0, d_{n,3} > 0$:

The solution for $d_{n,3}$ is:

$$d_{n,3} = \frac{B_n}{p_3} = \frac{B_n + \beta_n(p_1 + p_2 + p_3)}{3\, p_3} - \beta_n \tag{21}$$

5) When $d_{n,1} = 0, d_{n,2} = 0, d_{n,3} = 0$:

In this scenario, users do not purchase electricity from any power provider. From Equation 5, we can deduce that $B_n = 0$, meaning that the user's electricity expenditure budget is 0. This situation is not within the scope of this paper.

Therefore, using Eqs 15, 19–21, the user's demand for each power provider can be generalized to scenarios where there are $\mathcal{K}$ power providers. The optimal demand for each power provider is:

$$d_{n,k}^* = \frac{B_n + \sum_{k=1}^{\mathcal{K}} p_k \beta_n}{K\, p_k} - \beta_n \quad k = 1,2,\ldots,\mathcal{K}. \tag{22}$$

From Eq. 22, we can see that the amount of electricity $d_{n,k}$ that user n purchases from a specific power provider k is to maximize their own utility function depends on the real-time electricity price p_k currently offered by power provider k, as well as the electricity prices offered by other power providers $\sum_{k=1}^{\mathcal{K}} p_k$. Having obtained the expression for the amount of electricity that each user purchases from each power provider, we introduce E_n^{min} to represent the amount of electricity each user needs to meet their basic daily needs, which needs to satisfy:

$$\sum_{k \in \mathcal{K}} d_{n,k} \geq E_n^{min} \tag{23}$$

Substituting Eq. 22 into Eq. 23, we find that each user's electricity expenditure needs to satisfy:

$$B_n \geq E_n^{min} K \sum_{k=1}^{\mathcal{K}} p_k + K p_k \beta_n - \beta_n \sum_{k=1}^{\mathcal{K}} p_k \tag{24}$$

where Eq. 24 represents that the user's electricity expenditure is related to the price set by each power provider and the user's minimum energy demand. Above value can be used as a baseline to test whether the user's expenditure will decrease after the demand response.

5.2 Power-supply-side mathematical model

In the game-based model considered in this paper, the price setting of a power provider is related not only to the electricity expenditure set by each user but also to the prices set by other power providers. The utility function of a power provider is expressed as:

$$U_k(p_k, \boldsymbol{p}_{-k}) = p_k \sum_{n \in \mathcal{N}} d_{n,k} \tag{25}$$

where $\boldsymbol{p}_{-k}$ represents the electricity prices set by power providers other than k.

The goal of each power provider is to maximize its profit after selling electricity under the constraint of its own production capacity. Therefore, the optimization function for each power provider can be expressed as:

$$\begin{aligned} \max_{p_k} \quad & U_k(p_k, \boldsymbol{p}_{-k}) \\ s.t. \quad & \begin{cases} \sum_{n \in \mathcal{N}} d_{n,k} \leq G_k \\ p_k \geq 0, \quad \forall k \in \mathcal{K} \end{cases} \end{aligned} \tag{26}$$

where G_k represents the maximum production capacity of each power provider. The energy demand provided for all users cannot exceed this value. In the process of selling electricity, the more electricity the power provider sells, the more profit it will obtain. Therefore, the constraint on energy sales can be converted to the equation $\sum_{n \in \mathcal{N}} d_{n,k} = G_k$. At this time, the power provider's profit is maximized. We construct the Lagrange function as:

$$\mathcal{L}_k = p_k \sum_{n \in \mathcal{N}} d_{n,k} - \lambda_k \left(\sum_{n \in \mathcal{N}} d_{n,k} - G_k \right) \tag{27}$$

When the power provider obtains the optimal price setting, $\partial \mathcal{L}_k / \partial p_k = 0$. Since $d_{n,k}$ is a function containing the variable p_k, after substituting Eq. 22 into Eq. 27, the derivative can be obtained as:

$$(K-1) \sum_{n \in \mathcal{N}} \beta_n p_k^2 - \lambda_k \times \left(\sum_{n \in \mathcal{N}} \beta_n \left(p_k - \sum_{k \in \mathcal{K}} p_k \right) + \sum_{n \in \mathcal{N}} B_n \right) = 0 \tag{28}$$

$$(K-1) Z p_k^2 - \lambda_k \left[B + Z \left(\sum_{u \in \mathcal{K}, u \neq k} p_u \right) \right] = 0 \tag{29}$$

where Eq. 29 is a simplified form of Eq. 28. $Z = \sum_{n \in \mathcal{N}} \beta_n$ and $B = \sum_{n \in \mathcal{N}} B_n$.

For each power provider, Eq. 29 provides a constraint equation. Combined with $\sum_{n \in \mathcal{N}} d_{n,k} = G_k$, we can obtain:

$$p_k = \frac{B + Z\left(\sum_{u \in \mathcal{K}, u \neq k} p_u \right)}{Z(K-1) + K G_k} \tag{30}$$

From Eq. 30, we can deduce that the real-time price of each power supplier depends both on its own capacity G_k and the electricity prices set by other power suppliers. When there is only one power supplier in the entire demand response system, i.e., $K = 1$, there is no game between power suppliers, and the optimal price set by the power supplier is $p_1 = B/G_1$, which only depends on the users' electricity expenditure budget and the supplier's own capacity. Therefore, this article considers the case of $K \geq 2$; that is, there is a price game between each power supplier, and every user sets real-time electricity prices to maximize their own profit. However, the main problem in the process of solving Eq. 30 is that the solution of p_k is related to the prices of other power suppliers, and the calculation of the prices of other power suppliers depends on p_k. The entire price calculation process falls into a vicious cycle. To solve this problem, we can substitute the price of each power supplier into Eq. 30, thus converting the calculation of the supplier's price into a function of the capacities of each power supplier:

$$p_k = \frac{B}{G_k + Z} \left(\frac{1}{K - \sum_{k \in \mathcal{K}} \frac{Z}{G_k + Z}} \right) \tag{31}$$

In the previous subsection, the optimal demand quantity for each user to purchase from each power supplier was obtained from Eq. 22. To satisfy the requirement that the electricity purchase quantity is $d_{n,k} \geq 0$ from any user $n \in \mathcal{N}$ to any power supplier $k \in \mathcal{K}$ in the system, the following equation must be satisfied:

$$B_n + \beta_n \sum_{k=1}^{\mathcal{K}} p_k \geq K \, p_k \, \beta_n \tag{32}$$

When the demand for each power supplier from the user meets $d_{n,k} \geq 0$, the price of the power supplier also needs to meet:

$$p_k \leq \frac{B_n + \beta_n \left(\sum_{u \in \mathcal{K}, u \neq k} p_u \right)}{(K-1)\beta_n} \tag{33}$$

Therefore, when the power supplier sets its own real-time electricity price, to ensure that the demand of each user from each power supplier meets $d_{n,k} \geq 0$, each power supplier must first satisfy Eq. 33 when setting the real-time price. The solution obtained through the Lagrange function in the previous section, Eq. 30, can be proven to meet this condition.

The following will prove that each power supplier's real-time electricity price, obtained through Eq. 30, can maximize each supplier's utility function and is the best response to each user.

Proof: First, assume that p_k is the power price set by supplier k obtained through Eq. 30. Then, if supplier k increases or decreases this price, it can obtain $p_k' = p_k + \epsilon_k$, while the prices of the other suppliers are not adjusted.

Then, the amount of electric energy each user buys from supplier k becomes:

$$d'_{n,k} = \frac{B_n + \beta_n \left(\sum_{u \in \mathcal{K}, u \neq k} p_u + p_k' \right)}{K \, p_k'} - \beta_n \tag{34}$$

Compared with the case when the price of supplier k is not adjusted, the difference in the amount of electricity each user buys from supplier k is:

$$d'_{n,k} - d_{n,k} = \frac{\left(p_k - p'_k\right)\left[B_n + \beta_n\left(\sum_{u\in\mathcal{K},u\neq k} p_u\right)\right]}{K\, p_k\, p'_k} \tag{35}$$

According to Eq. 35, when the electricity price set by supplier k rises, that is, $p_k - p'_k < 0$, we have $d'_{n,k} - d_{n,k} < 0$. This shows that when the price rises, the user's demand for electricity from the supplier decreases. When the electricity price set by supplier k drops, we have $d'_{n,k} - d_{n,k} > 0$, and the user's demand for electricity from the supplier increases.

After the supplier's price adjustment, the difference in the utility function compared to when it is not adjusted is:

$$\begin{aligned} U'_k - U_k &= p'_k \sum_{n\in\mathcal{N}} d'_{n,k} - p_k \sum_{n\in\mathcal{N}} d_{n,k} \\ &= \epsilon_k \frac{Z - ZK}{K} \end{aligned} \tag{36}$$

According to Eq. 36, when the supplier's price rises, that is, $\epsilon_k > 0$, and $Z - ZK < 0$, we have $U'_k - U_k < 0$. This shows that when the supplier raises its price, the profit obtained will not increase but will be less than the profit obtained at the previously set price. When the supplier's price drops, that is, $\epsilon_k < 0$, although $U'_k - U_k > 0$ at this time, due to the limit of the supplier's capacity G_k, it is impossible for the supplier to sell sufficient electricity to make a profit after lowering the price.

Therefore, it can ultimately be proven that the electricity price $p^\star_k$ set by the supplier through Eq. 30 can not only maximize its own profit function but is also the best response to user demand.

5.3 Power-supply-side game model

In the demand response model, the profits of each power supplier mainly come from the electricity expenditures of all users. The total budget for electricity consumption among all users is fixed; i.e., $\sum_{n\in\mathcal{N}} B_n$. The profit obtained by each power supplier k depends on the volume of its electricity sales and the setting of the electricity price. If the electricity price is set reasonably, the profit obtained will account for a larger proportion of the total user expenditure, and *vice versa*. Therefore, when power supplier k changes its electricity price settings, it may increase or decrease the proportion of total user expenditures it has, thus initiating a non-cooperative game among power suppliers regarding price settings.

For the Stackelberg game model, the overall process is shown in Figure 4. First, the power suppliers compete to determine the price signals most advantageous to themselves. They then distribute these price signals to each user. The users, in turn, calculate their optimal demands for each power supplier based on these price signals and then publish these demand quantities to the designated power suppliers. Finally, the users update the prices based on these demand quantities until the price competition among power suppliers reaches a Nash equilibrium.

Let $\mathcal{S}_\mathcal{K}$ and $\mathcal{S}_\mathcal{N}$ represent the strategy sets of power suppliers and users, respectively. For power suppliers, their strategy set mainly includes each power supplier's price choice strategy, i.e., $\mathcal{S}_\mathcal{K} = \mathcal{S}_1 \times \mathcal{S}_2 \times \mathcal{S}_3 \times \cdots \mathcal{S}_K$. The users, being followers, have a strategy set that primarily passively responds to the price signals of power suppliers, i.e., $\mathcal{S}_\mathcal{N} = \mathcal{S}_1 \times \mathcal{S}_2 \times \mathcal{S}_3 \times \cdots \mathcal{S}_N$. Therefore, when the price competition among power suppliers reaches a Nash equilibrium, each power supplier's price signal $p^\star_k$ satisfies:

$$U_k\left(p^\star_k, p^\star_{-k}, d(\boldsymbol{p}^\star)\right) \geq U_k\left(p_k, p_{-k}, d(\boldsymbol{p})\right) \tag{37}$$

where $d(\boldsymbol{p}^\star)$ represents the users' best response to the power suppliers' prices. As users are only responding passively, there exists a unique best response to the price signals of power suppliers; i.e., the users' optimal response signals are calculated through Eq. 22.

Thus, it only needs to be proven that a unique equilibrium point exists in the price competition among power suppliers. When

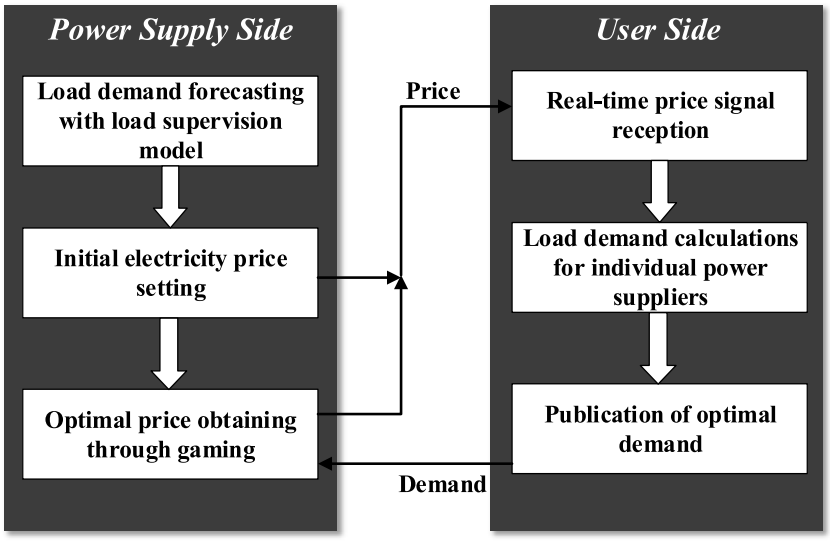

FIGURE 4
Game model.

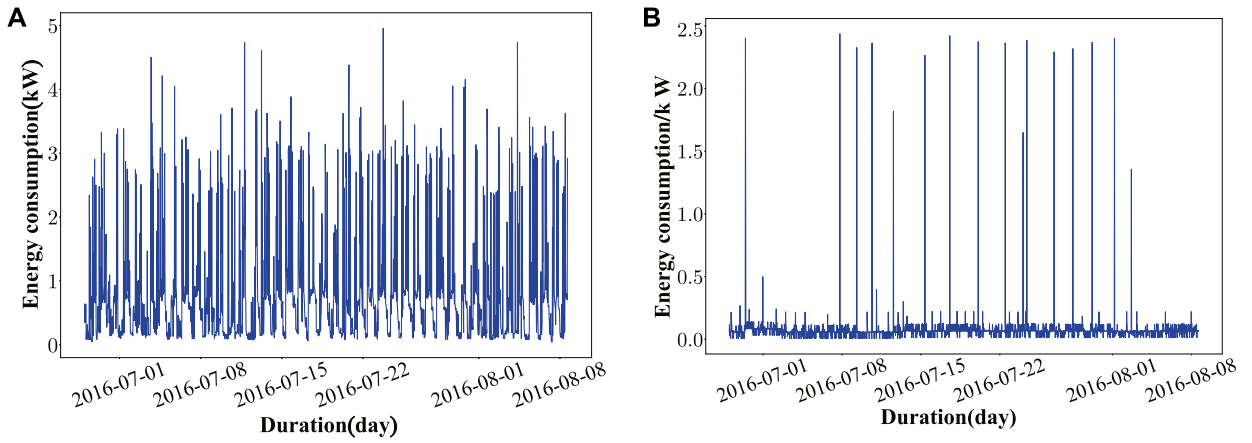

FIGURE 5
Load data for users: **(A)** user 1; **(B)** user 2.

power suppliers compete in price, they mainly consider their utility function $U_k(p_k)$, which is a continuous concave function for any power supplier. This utility function, within a specified range, necessarily satisfies $\partial^2 U_k/\partial p_k^2 < 0$. When $\partial U_k/\partial p_k = 0$, the obtained price signal can ensure that the power supplier's utility function has a unique maximum point within the specified range, and this signal satisfies $p_k^* \in \mathcal{S}_K = \mathcal{S}_1 \times \mathcal{S}_2 \times \mathcal{S}_3 \times \cdots \mathcal{S}_K$. Therefore, this proves the uniqueness of the Nash equilibrium in the price competition among power suppliers.

6 Simulations

6.1 Experiment of user load data prediction

6.1.1 Dataset

The data used for training the load supervision model come from a publicly available load dataset provided by MIT. This dataset captures the household load data of multiple users from 10 July 2014 to 31 December 2016. The data were collected through smart meter devices, with samples taken every 15 min, and include twelve features, such as temperature, humidity, pressure, wind speed, and perceived temperature of the environment, as well as the current load consumption data of multiple users. The load data of the users are shown in Figure 5.

6.1.2 Simulation of load supervision model parameters

In deep learning networks, it is challenging to determine the number of hidden layers and the number of neurons in each layer. There is no strict theoretical way of determining the optimal numbers of hidden layers and neurons in a network structure. Before determining the number of hidden layers, it should be understood that the role of the hidden layers is mainly to increase the non-linear fitting ability of the model. If the input data are linearly separable, then hidden layers are not necessary. However, for more complex sequential and speech data, it may be necessary to add more hidden layers to improve the model's learning capability. Once the number of hidden layers has been determined, the most important issue is how to determine the number of neurons in each layer. If there are too few neurons in the hidden layer, it will cause underfitting. If there are too many neurons, it may lead to overfitting. Therefore, selecting an appropriate number of neurons is extremely important.

This paper determines the relationship between the prediction accuracy and training time of the model with different numbers of layers and neurons through experiments, as shown in Figure 6.

Figure 6 show that when using a three-layer neural network, the average prediction accuracy is the highest, and the average training time of the model is relatively low. When a four-layer neural network is used, the model enters a state of overfitting, results in the low overall prediction accuracy and the long training time. Besides, we can also observe from Figure 6 that the best prediction accuracy can be achieved when the numbers of neurons in each layer are (300, 150, 50).

6.1.3 Prediction results of user load

To speed up the model's training time, the dataset is sampled every 30 min, reducing the scale of the training data. The overall flow of the training algorithm is to first divide the dataset that has not yet been trained into training, validation, and testing sets. Then, we set the number of layers and the number of neurons in each layer in the LSTM network of the load supervision model based on the model parameters from the previous subsection. Meanwhile, a dropout layer is added between each pair of layers to prevent overfitting. Finally, we specify the loss function for model training. Time series data delay steps of 1, 3, 5, 7, 10, and 15 days were selected for the load data prediction of user 1 and user 2. The delay step length refers to how many days of data are used to predict future load data. The longer the delay step length of the time series data, the more features will be obtained in the training data, allowing the model to better learn user behavior patterns. The results of user load data prediction are shown in Table 2.

For user 1, the highest prediction accuracy was achieved with a 10-day time series step delay, reaching 91.54%, higher than the 91.11% accuracy obtained with a 15-day time series step delay. The

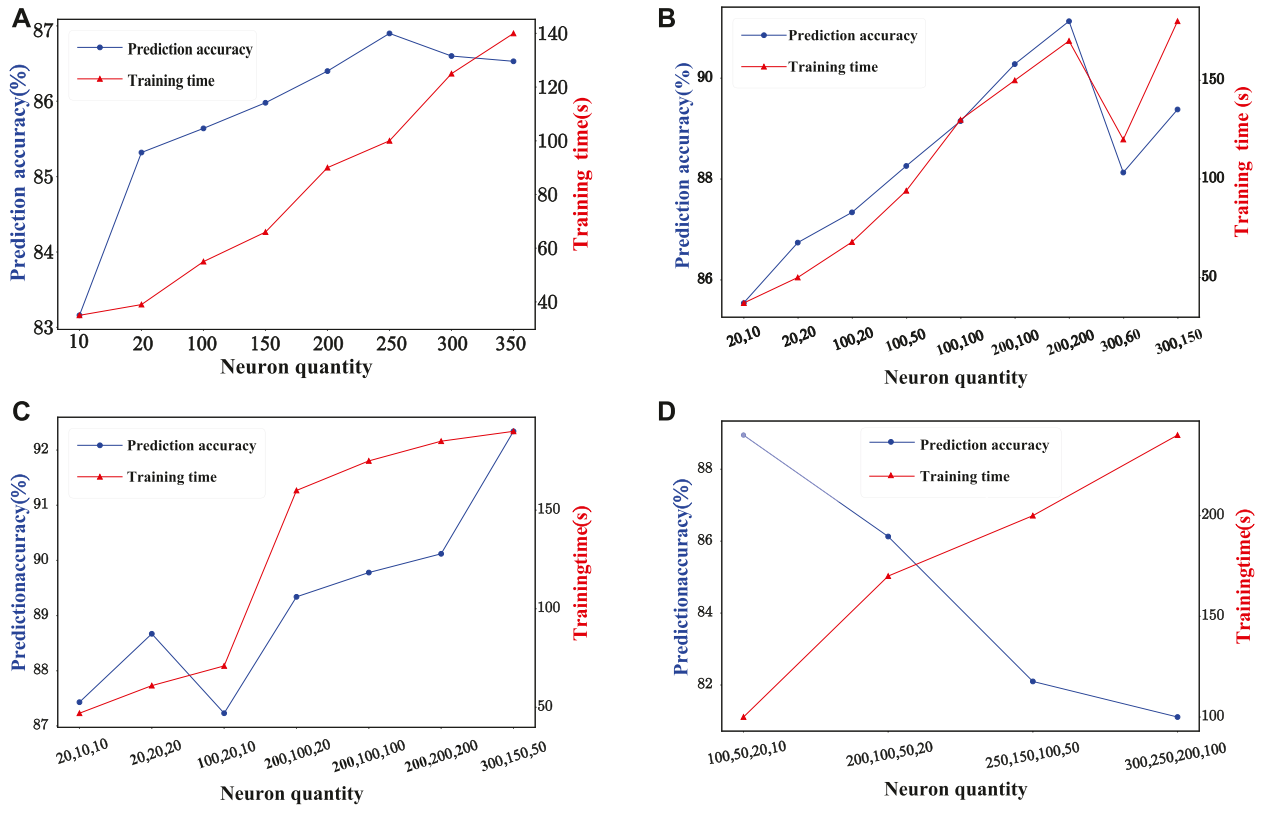

FIGURE 6
Impact of neuron quantity on prediction accuracy: **(A)** single-layer neural network; **(B)** two-layer neural network; **(C)** three-layer neural network; **(D)** four-layer neural network.

TABLE 2 User forecast accuracy.

Model	User	Accuracy (%)	MSE (%)	Training time/s
LSTM/1 step	1	90.18	9.8	68
LSTM/3 steps	1	91.05	8.9	277
LSTM/5 steps	1	91.20	8.7	506
LSTM/7 steps	1	90.78	9.2	757
LSTM/10 steps	1	91.54	8.4	1,101
LSTM/15 steps	1	91.11	8.9	1,929
LSTM/1 step	2	92.75	7.2	67
LSTM/3 steps	2	94.15	5.8	276
LSTM/5 steps	2	95.24	4.8	500
LSTM/7 steps	2	94.56	5.4	727
LSTM/10 steps	2	95.74	4.3	1,122
LSTM/15 steps	2	96.37	3.6	1,834

analysis shows that when training the model with a 15-day time series step delay, the number of features is significantly higher than that with a 10-day time series step delay. The trained prediction model should have a higher accuracy, but possibly because there are too many features, overfitting occurs, thus reducing the prediction accuracy on the test set. This can be prevented by setting the coefficient of the dropout layer, thereby improving the prediction accuracy of the model. For user 2, the highest prediction accuracy was achieved with a 15-day time series step delay, reaching 96.37%, and a lower prediction accuracy of 94.56% was achieved with a 7-day time series step delay. This indicates a significant difference in the power usage habits of user 2 on weekdays and weekends, resulting in a surge in load demand on the weekend and many jump points, thereby reducing the overall prediction accuracy. Generally, the LSTM-based load supervision model can achieve good prediction accuracy for future load demand.

6.2 Simulation and analysis of the demand response model

The optimization effect of the entire game model is studied by changing the user's own electricity budget. In the experiment, the constant coefficients in the utility functions of all users are initially set to $\gamma_n = 5, \beta_n = 5$. Then, 10 users and 4 suppliers are considered in the demand response model, with the electricity budgets for the users are set as $B_1 = 10$, $B_2 = 15$, $B_3 = 18$, $B_4 = 20$, $B_5 = 25$, $B_6 = 28$, $B_7 = 35$, $B_8 = 40$, $B_9 = 45$, $B_{10} = 50$. The capacities of the suppliers at each moment are set as $G_1 = 10, G_2 = 15, G_3 = 20, G_4 = 30$. After predicting the future load demand of each user based on the load supervision

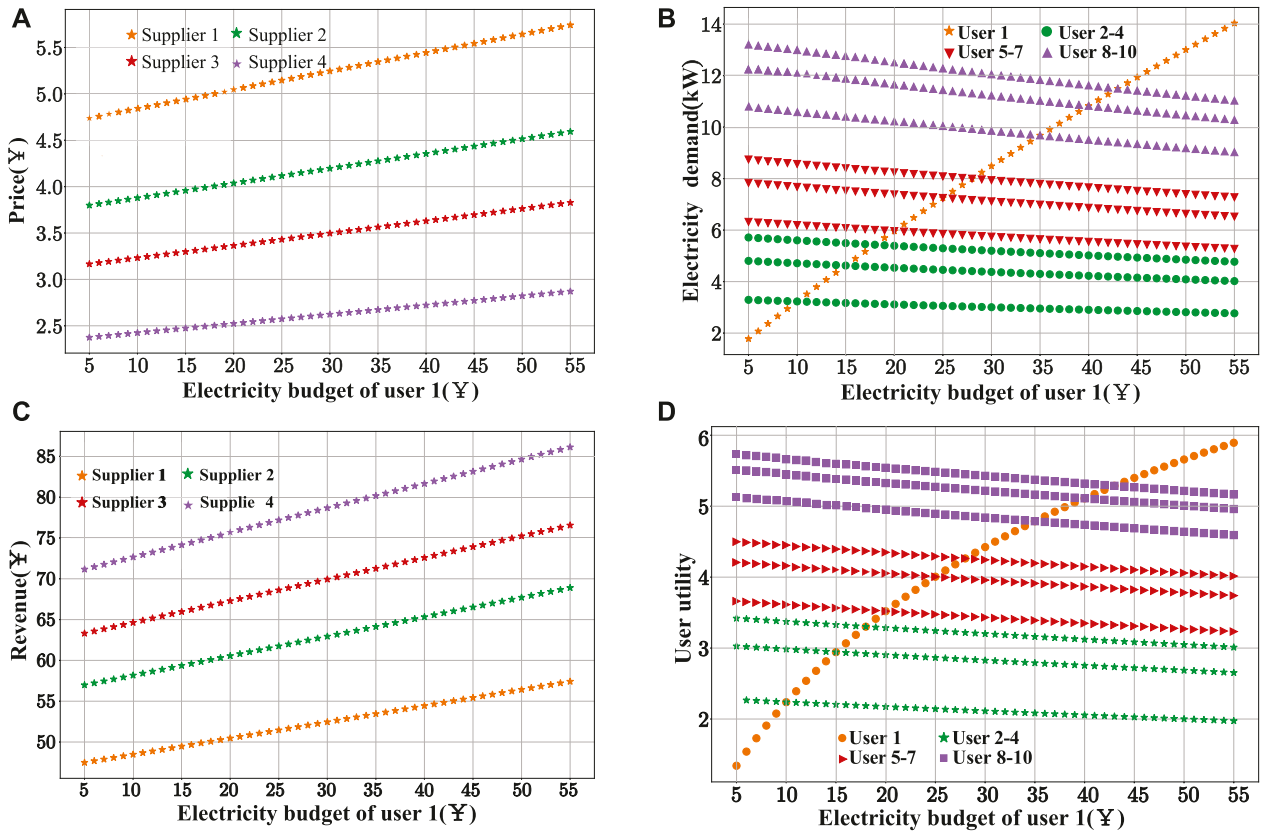

FIGURE 7
Optimization results of the game model: **(A)** power supplier price; **(B)** user demand; **(C)** power supplier revenue; **(D)** user utility.

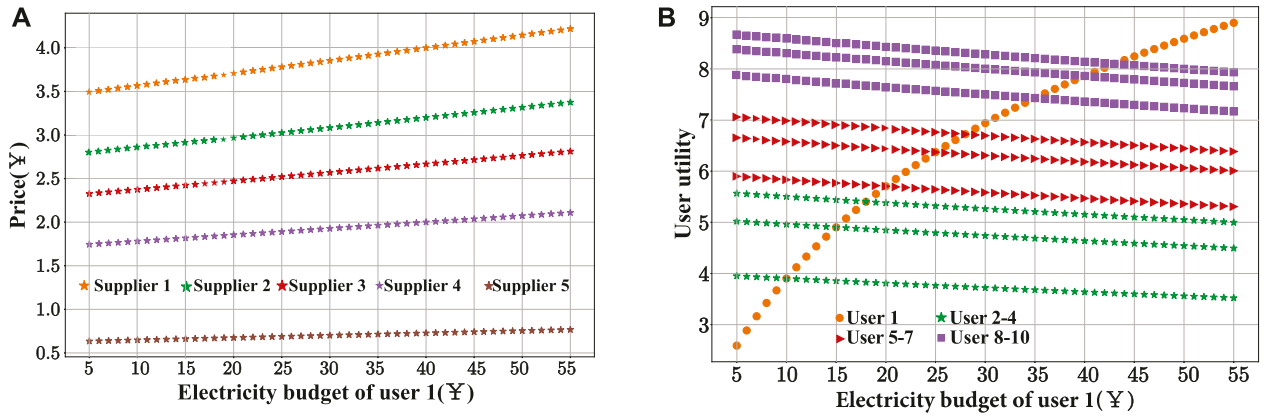

FIGURE 8
Optimization results of the game model after adding power supplier 5: **(A)** power supplier price; **(B)** user utility.

model, the initial electricity prices of the suppliers are set as $p_1 = 1.5, p_2 = 2.2, p_3 = 2.5, p_4 = 2.0$.

Figure 7A represents the optimal electricity prices set by each power supplier after the game as user 1's electricity budget continues to increase. As the user's budget increases, the electricity prices set by each power supplier also increase. Because Power Supplier 1 has the least capacity, the real-time electricity price it sets is the highest. Figure 7B represents the demand curves for electricity for each user. As user 1's electricity budget continues to increase, the purchased electricity also increases. Since the production capacity

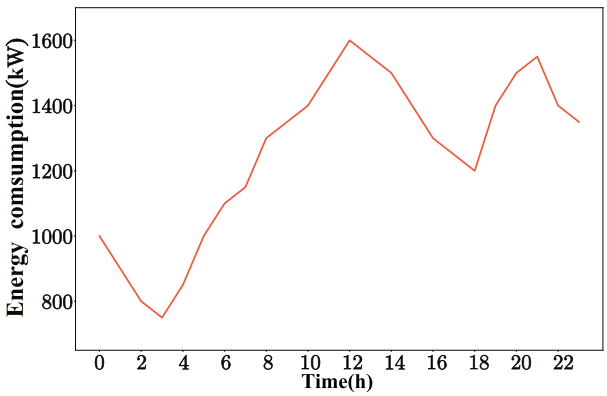

FIGURE 9
Energy consumption curves.

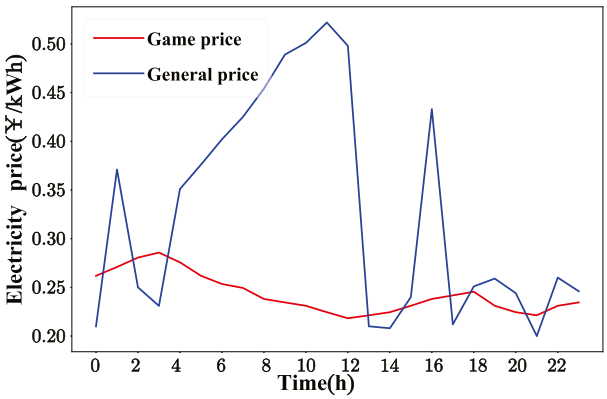

FIGURE 10
Real-time electricity price curves.

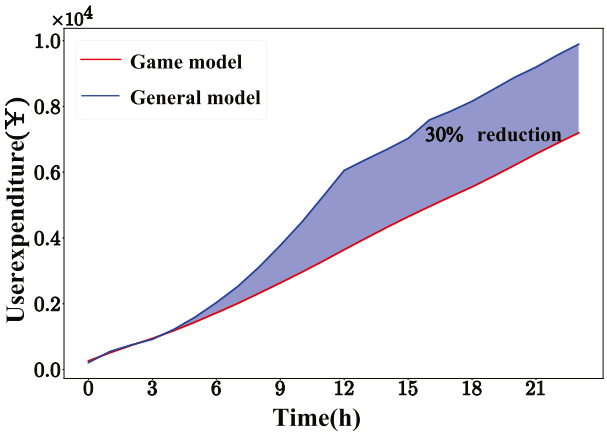

FIGURE 11
User expenditure curves.

of all suppliers is fixed at any moment, this leads to a decrease in the energy demand of other users, manifested as a declining trend in their demand curves. Figure 7C shows the profit curve of each power supplier. From this figure, it can be seen that the income of the power suppliers does not show a positive correlation with the real-time set electricity price. In the electricity price curve, the price set by Power Supplier 1 is the highest, but its profit is the lowest among all suppliers. In contrast, Power Supplier 4, which sets the lowest price, obtains the highest profit due to its larger capacity. Figure 7D represents the utility function curves of users. Since user 1 purchased a large amount of electricity, their utility curve gradually increases, causing the utility curves of other users to decrease, which conforms to real-life scenarios.

To verify whether the introduction of a large-capacity power supplier will affect the utility of users, Power Supplier 5 was added to the original experiment, and its power supply capacity was set as $G_5 = 100$. Comparing Figure 8B and Figure 7D, it can be seen that when Power Supplier 5 is added, the utility of the users increases, indicating that the addition of Power Supplier 5 does not reduce the utility of the users. As shown in Figure 8A, it is almost impossible for a power supplier in the proposed game model to control prices by significantly increasing capacity; this will only lead to an overall excess capacity in the system, causing a decrease in the prices set by all power suppliers. Therefore, in the entire system model, the more capacity a power supplier has, the more the users' utility will increase.

Finally, to further verify the application of the model in actual production, an analysis of user load data revealed that the load demand curves of all users exhibit a distinct regularity, reaching a peak at noon, followed by reduced consumption and an increase again in the evening. Therefore, we extracted a day's energy consumption data and real-time electricity price information from the U.S. National Energy website. The dataset includes 2,000 users and 5 power suppliers. The energy consumption data of these users are used to verify whether the model can improve the utility of users. Figure 9 represents the energy consumption data of users at different times of the day. Figure 10 represents the prices set by the power suppliers after the game and the normal electricity prices set daily. Figure 11 shows that after adopting the real-time electricity prices calculated based on the game model, the overall expenditure of users decreases by 30{%} compared with traditional pricing model, indicating that when all power suppliers adopt real-time electricity prices calculated based on the game model, every user in the demand response model will gain substantial benefits.

7 Conclusion

In this paper, we employ a long short-term memory (LSTM) network as a load forecasting model to predict user load data in a smart grid and utilize a Stackelberg game model based on the load forecasting model to reduce the overall expenditure of energy users. The main contribution of this paper can be summarized as follows:

1) This paper employs an LSTM network as a load supervision model to forecast users' load data. The LSTM network integrates gate structures and memory units internally, enabling it to memorize

historical data effectively and predict users' cyclical demand behaviors.

2) Based on the load supervision model, this paper built a Stackelberg game model to optimize the optimal power prices set by the power supplier in real time at each moment, making the demand response between users and the power supplier more efficient. Specifically, the power supplier first sets the initial power prices according to the forecasted user demand and then adjusts its power prices in real time in response to user reactions and price competition with other power suppliers, achieving its maximum profit.

3) This paper compares the prediction accuracy of forecasting models with different layers and numbers of neurons through simulation experiments and obtains optimal model parameters. Results of comparing actual user data and the prediction output demonstrate that LSTM-based load forecasting model achieves an accuracy of up to 96.37%. Additionally, the game model reduces the overall expenditure of users by 30% compared with the general pricing model.

Data availability statement

The original contributions presented in the study are included in the article/Supplementary Material, further inquiries can be directed to the corresponding author.

Author contributions

FC contributed to the conception, performed the experiment and wrote the manuscript. DA contributed to the manuscript correction and foundation support. GZ helped perform the analysis with constructive discussions. All authors contributed to the article and approved the submitted version.

Funding

This work was supported in part by the National Natural Science Foundation of China under Grant Nos. 62173268, 61803295, 61973247, and 61673315; in part by the Major Research Plan of the National Natural Science Foundation of China under Grant 61833015; in part by the National Postdoctoral Innovative Talents Support Program of China under Grant BX20200272; in part the National Key Research and Development Program of China under Grant 2019YFB1704103; and in part by the China Postdoctoral Science Foundation under Grant 2018M643659.

Conflict of interest

The authors declare that the research was conducted in the absence of any commercial or financial relationships that could be construed as a potential conflict of interest.

Publisher's note

All claims expressed in this article are solely those of the authors and do not necessarily represent those of their affiliated organizations, or those of the publisher, the editors and the reviewers. Any product that may be evaluated in this article, or claim that may be made by its manufacturer, is not guaranteed or endorsed by the publisher.

References

Abubakar, I., Khalid, S., Mustafa, M., Shareef, H., and Mustapha, M. (2017). Application of load monitoring in appliances' energy management–a review. *Renew. Sustain. Energy Rev.* 67, 235–245. doi:10.1016/j.rser.2016.09.064

Afrasiabi, M., Mohammadi, M., Rastegar, M., Stankovic, L., Afrasiabi, S., and Khazaei, M. (2020). Deep-based conditional probability density function forecasting of residential loads. *IEEE Trans. Smart Grid* 11, 3646–3657. doi:10.1109/tsg.2020.2972513

Alhmoud, L., and Nawafleh, Q. (2021). Short-term load forecasting for Jordan power system based on narx-elman neural network and arma model. *IEEE Can. J. Electr. Comput. Eng.* 44, 356–363. doi:10.1109/icjece.2021.3076124

Bokkisam, H. R., Singh, S., Acharya, R. M., and Selvan, M. P. (2022). Blockchain-based peer-to-peer transactive energy system for community microgrid with demand response management. *CSEE J. Power Energy Syst.* 8, 198–211. doi:10.17775/CSEEJPES.2020.06660

Cai, T., Wu, C., and Zhang, J. (2022). "A bagging long short-term memory network for financial transmission rights forecasting," in *2022 7th IEEE workshop on the electronic grid (eGRID)* (IEEE), 1–5.

Chen, C., Lu, N., Jiang, B., Xing, Y., and Zhu, Z. H. (2021). Prediction interval estimation of aeroengine remaining useful life based on bidirectional long short-term memory network. *IEEE Trans. Instrum. Meas.* 70, 1–13. doi:10.1109/tim.2021.3126006

Cheng, L., Chen, Y., and Liu, G. (2022). 2pns-eg: a general two-population n-strategy evolutionary game for strategic long-term bidding in a deregulated market under different market clearing mechanisms. *Int. J. Electr. Power Energy Syst.* 142, 108182. doi:10.1016/j.ijepes.2022.108182

Cheng, L., and Yu, T. (2019). Game-theoretic approaches applied to transactions in the open and ever-growing electricity markets from the perspective of power demand response: an overview. *IEEE Access* 7, 25727–25762. doi:10.1109/access.2019.2900356

Gao, Y., Ma, J., Wang, J., and Wu, Y. (2023). Event-triggered adaptive fixed-time secure control for nonlinear cyber-physical system with false data-injection attacks. *IEEE Trans. Circuits Syst. II Express Briefs* 70, 316–320. doi:10.1109/tcsii.2022.3217823

Gellings, C. W., Samotyj, M., and Howe, B. (2004). The future's smart delivery system [electric power supply]. *IEEE Power Energy Mag.* 2, 40–48. doi:10.1109/mpae.2004.1338121

Gyamfi, S., Krumdieck, S., and Urmee, T. (2013). Residential peak electricity demand response—Highlights of some behavioural issues. *Renew. Sustain. Energy Rev.* 25, 71–77. doi:10.1016/j.rser.2013.04.006

Hermias, J. P., Teknomo, K., and Monje, J. C. N. (2017). "Short-term stochastic load forecasting using autoregressive integrated moving average models and hidden markov model," in *2017 international conference on information and communication technologies (ICICT)* (IEEE), 131–137.)

Huang, S.-J., and Shih, K.-R. (2003). Short-term load forecasting via arma model identification including non-Gaussian process considerations. *IEEE Trans. power Syst.* 18, 673–679. doi:10.1109/tpwrs.2003.811010

Jasim, A. M., Jasim, B. H., Flah, A., Bolshev, V., and Mihet-Popa, L. (2023). A new optimized demand management system for smart grid-based residential buildings adopting renewable and storage energies. *Energy Rep.* 9, 4018–4035. doi:10.1016/j.egyr.2023.03.038

Khan, M. A., Saleh, A. M., Waseem, M., and Sajjad, I. A. (2023). Artificial intelligence enabled demand response: prospects and challenges in smart grid environment. *IEEE Access* 11, 1477–1505. doi:10.1109/access.2022.3231444

Liu, N., Yu, X., Wang, C., Li, C., Ma, L., and Lei, J. (2017). Energy-sharing model with price-based demand response for microgrids of peer-to-peer prosumers. *IEEE Trans. Power Syst.* 32, 3569–3583. doi:10.1109/tpwrs.2017.2649558

Mahela, O. P., Khosravy, M., Gupta, N., Khan, B., Alhelou, H. H., Mahla, R., et al. (2022). Comprehensive overview of multi-agent systems for controlling smart grids. *CSEE J. Power Energy Syst.* 8, 115–131. doi:10.17775/CSEEJPES.2020.03390

Mansouri, S. A., Paredes, Ángel, González, J. M., and Aguado, J. A. (2023). A three-layer game theoretic-based strategy for optimal scheduling of microgrids by leveraging a dynamic demand response program designer to unlock the potential of smart buildings and electric vehicle fleets. *Appl. Energy* 347, 121440. doi:10.1016/j.apenergy.2023.121440

Mocanu, E., Nguyen, P. H., Gibescu, M., and Kling, W. L. (2016). Deep learning for estimating building energy consumption. *Sustain. Energy, Grids Netw.* 6, 91–99. doi:10.1016/j.segan.2016.02.005

Orlando, M., Estebsari, A., Pons, E., Pau, M., Quer, S., Poncino, M., et al. (2022). A smart meter infrastructure for smart grid iot applications. *IEEE Internet Things J.* 9, 12529–12541. doi:10.1109/jiot.2021.3137596

Panda, S., Mohanty, S., Rout, P. K., Sahu, B. K., Parida, S. M., Kotb, H., et al. (2022). An insight into the integration of distributed energy resources and energy storage systems with smart distribution networks using demand-side management. *Appl. Sci.* 12, 8914. doi:10.3390/app12178914

Sivasankarareddy, V., Sundari, G., Rami Reddy, C., Aymen, F., and Bortoni, E. C. (2021). Grid-based routing model for energy efficient and secure data transmission in wsn for smart building applications. *Appl. Sci.* 11, 10517. doi:10.3390/app112210517

Sofana Reka, S., and Ramesh, V. (2016). A demand response modeling for residential consumers in smart grid environment using game theory based energy scheduling algorithm. *Ain Shams Eng. J.* 7, 835–845. doi:10.1016/j.asej.2015.12.004

Tang, R., Wang, S., and Li, H. (2019). Game theory based interactive demand side management responding to dynamic pricing in price-based demand response of smart grids. *Appl. Energy* 250, 118–130. doi:10.1016/j.apenergy.2019.04.177

Trujillo, D., and García Torres, E. M. (2022). Demand response due to the penetration of electric vehicles in a microgrid through stochastic optimization. *IEEE Lat. Am. Trans.* 20, 651–658. doi:10.1109/tla.2022.9675471

Walther, J., Spanier, D., Panten, N., and Abele, E. (2019). Very short-term load forecasting on factory level–a machine learning approach. *Procedia CIRP* 80, 705–710. doi:10.1016/j.procir.2019.01.060

Wang, L., Hou, C., Ye, B., Wang, X., Yin, C., and Cong, H. (2021). Optimal operation analysis of integrated community energy system considering the uncertainty of demand response. *IEEE Trans. Power Syst.* 36, 3681–3691. doi:10.1109/tpwrs.2021.3051720

Wang, L., Jones, D., Chapman, G. J., Siddle, H. J., Russell, D. A., Alazmani, A., et al. (2020). A review of wearable sensor systems to monitor plantar loading in the assessment of diabetic foot ulcers. *IEEE Trans. Biomed. Eng.* 67, 1989–2004. doi:10.1109/tbme.2019.2953630

Zhang, Z., Huang, Y., Chen, Z., and Lee, W.-J. (2023). Integrated demand response for microgrids with incentive compatible bidding mechanism. *IEEE Trans. Industry Appl.* 59, 118–127. doi:10.1109/tia.2022.3204626

Zheng, S., Sun, Y., Qi, B., and Li, B. (2022). Incentive-based integrated demand response considering S&C effect in demand side with incomplete information. *IEEE Trans. Smart Grid* 13, 4465–4482. doi:10.1109/tsg.2022.3149959

frontiers | Frontiers in Energy Research

TYPE Methods
PUBLISHED 16 October 2023
DOI 10.3389/fenrg.2023.1242968

OPEN ACCESS

EDITED BY
Yaser Qudaih,
Higher Colleges of Technology, United Arab Emirates

REVIEWED BY
Abdrabbi Bourezg,
Higher Colleges of Technology, United Arab Emirates
Hassan Migdadi,
Higher Colleges of Technology, United Arab Emirates

*CORRESPONDENCE
Qingshu Wang,
15172082126@163.com

RECEIVED 20 June 2023
ACCEPTED 02 October 2023
PUBLISHED 16 October 2023

CITATION
Ke Y, Wang Q, Xiao H, Luo Z and Li J (2023), Hydropower unit health assessment based on a combination weighting and improved fuzzy comprehensive evaluation method. *Front. Energy Res.* 11:1242968. doi: 10.3389/fenrg.2023.1242968

Hydropower unit health assessment based on a combination weighting and improved fuzzy comprehensive evaluation method

Yangyang Ke[1], Qingshu Wang[1]*, Huaizhi Xiao[2], Zhangping Luo[1] and Jueqing Li[1]

[1]School of Electrical and Electronic Engineering, Hubei University of Technology, Wuhan, China, [2]School of Power and Machinery, Wuhan University, Wuhan, China

The health state of hydroelectric power generation units is of great significance to ensure the stability and economy of safe operation of the power grid. In order to address the challenges in existing assessment methods of the insufficient reliability of the evaluation of multi-complex systems and the inability to reflect anomalies of a single index. A state evaluation model based on combination weighting and improved fuzzy comprehensive evaluation method is accordingly proposed. First, a hierarchical analysis system is constructed based on actual monitoring indicator data from the hydropower unit. Optimal comprehensive and indicator weights are subsequently obtained for each indicator level using a combination of the improved hierarchical analysis and CRICIT method through game theory. Next, the industry guidelines and regulations are difficult to effectively determine the limit values of each index of the unit, and they do not fully take into account the actual situation of the unit itself and the huge amount of accumulated historical health data. To address this issue. The Gaussian threshold method was proposed to determine the limit values of the monitoring data for each indicator, which more accurately determines the indicator thresholds as well as their standard values. The degradation degree of the hydroelectric unit can be calculated by comparing the real-time monitoring data with these limits. Finally, the combined weights of dynamic change and the fuzzy evaluation matrix are used to obtain the state evaluation matrix reflecting the condition of the turbine. The proposed approach is validated using the actual monitoring data and operating conditions for case study hydroelectric station, The results show that the improved evaluation method has an optimal evaluation effect.

KEYWORDS

health assessment, hydropower unit, game theory, fuzzy hierarchical analysis, combination weighting, CRITIC method, theory of variation

1 Introduction

Hydroelectric power generation is the most common renewable energy source and a critical means to reduce CO_2 emission (Awan et al., 2023). With the adjustment of China's energy structure, hydropower generation has become an indispensable method for generating power, due to its excellent stability. Therefore, it is critical to fully utilize the

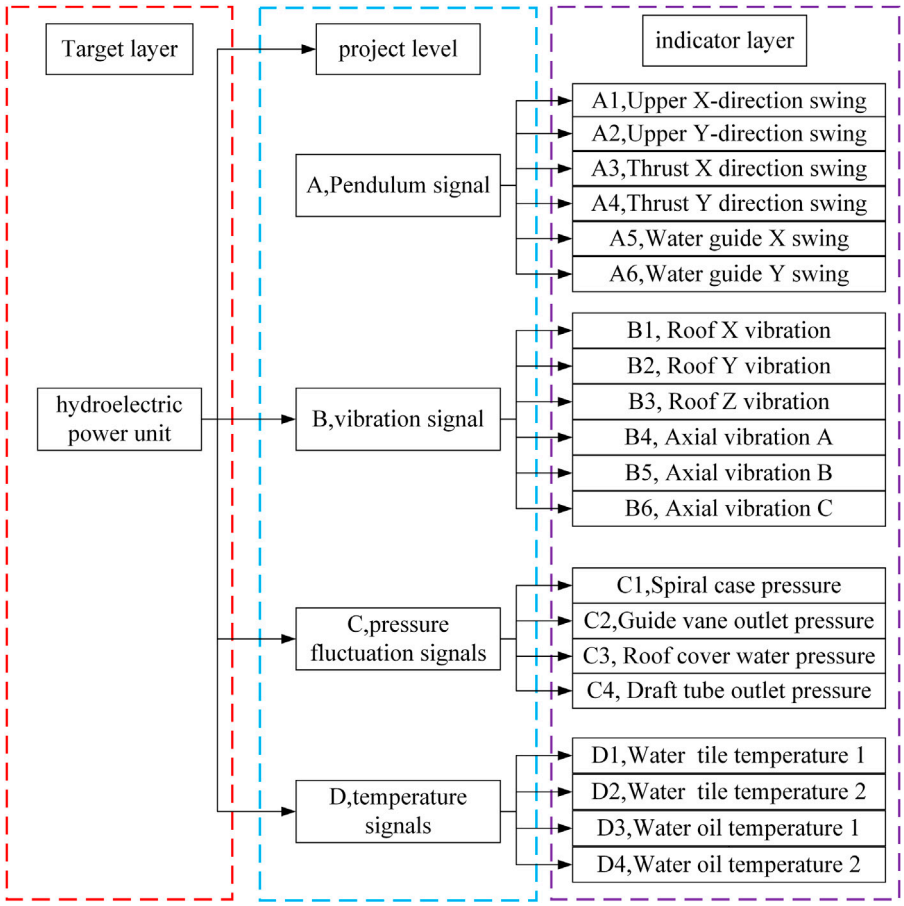

FIGURE 1
Hydraulic turbine system hierarchy system.

power generation functionality of hydraulic turbine sets to ensure the safe and stable operation of the power grid. This requires highly reliable hydroelectric generator sets, which can be ensured by evaluating the health state of hydropower units through monitoring and analyzing their parameters to assess whether there is any anomaly or potential risk of unit failure. This allows unit faults to be discovered in a timely manner and appropriate repair and maintenance procedures to be implemented, improving dependability and stability while extending service life. Thus, the steady operation of the power system and the quality of the power supply can be ensured (Zeng et al., 2023).

The main elements of the comprehensive condition assessment of hydropower units combine the structural system of the equipment with the distribution of measurement points, Extracting and constructing correlation indicators that reflect the operational health state, and integrating the performance indicators to make a holistic and global evaluation of the system health state. In recent years, as the concept of condition maintenance continues to advance, The power industry has successively established comprehensive condition detection systems, A wealth of measurement point information provides data support for the overall evaluation of the health state of the equipment, Condition assessment theory and techniques have also developed considerably, Commonly used condition evaluation methods include hierarchical analysis (Ge et al., 2020), cluster analysis (Hu et al., 2019), fuzzy comprehensive evaluation (Fang et al., 2016), grey system theory (Huang et al., 2022), etc.

In terms of calculating the weights, hierarchical analysis, as a classic system analysis method, is widely used in risk assessment, resource allocation, equipment evaluation and other fields due to its clear structure, hierarchical nature and adaptability to complex systems (Zhang H. et al., 2020; Liu et al., 2022; Cai et al., 2023; Zhu et al., 2023). Yucesan and Kahraman (2019) use hierarchical analysis for risk assessment of hydropower plants to help ensure grid security and prevent economic losses. Zeng et al. (2023) used hierarchical analysis and fuzzy integrated evaluation method to assess water resources pollution and proposed risk level evaluation, A hierarchical analysis is a traditional analysis method comprising a simple hierarchical structure (Ma et al., 2020). However, this method has several drawbacks: 1) It is extremely difficult to test the consistency of judgement matrices 2) the assignment of indicators relies too much on the experience of experts and is not objective enough. The fuzzy hierarchical analysis method (Doz et al., 2023) used in this paper not only retains the advantages of hierarchical analysis, but also adds a fuzzy consistency matrix, which ensures the consistency of the judgement matrix and solves the problem of the difficulty of checking whether the judgement matrix is

TABLE 1 Meaning of affiliation values used to compare indicators on a scale of 0.1–0.9.

Scale	Description
0.5 Equally important	Equally important
0.6 Slightly important	One element is slightly more important than the other
0.7 Significantly important	One element is significantly more important than the other
0.8 Much more important	One element is much more important than the other
0.9 Extremely important	One element is more extremely important than the other
0.1, 0.2, 0.3, 0.4	Compare element a_i with element a_j to obtain the judgment r_{ij}, then obtain the judgment as $r_{ji} = 1 - r_{ij}$

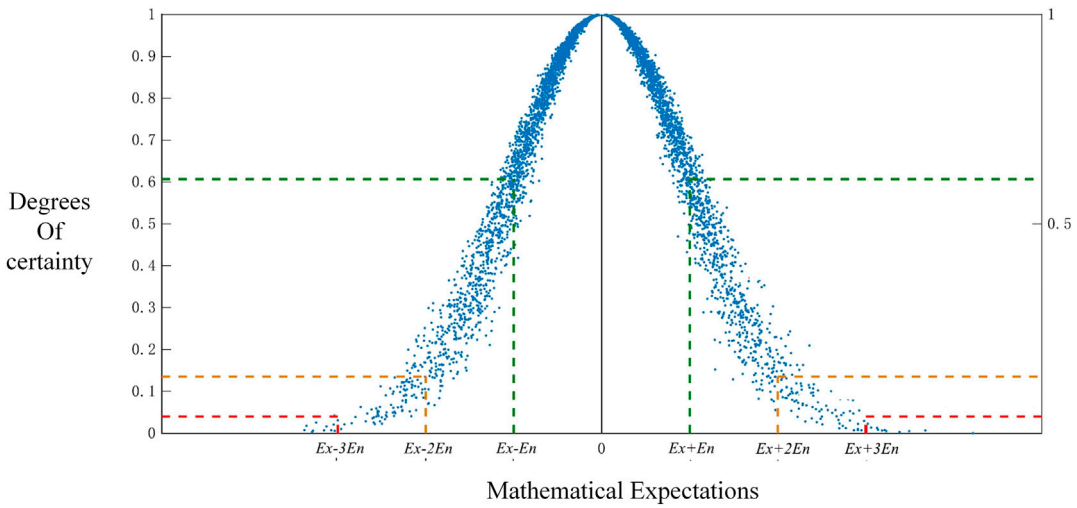

FIGURE 2
Normal distribution chart.

consistent. Also, due to its lack of objectivity, this paper applies the CRITIC method (Krishnan et al., 2021; Wen et al., 2022) to calculate its objective weights through historical health samples. However, subjective weights or objective weights cannot fully represent the weights of the indicator, in order to allocate the rationality of the weights, the method of game theory (Li H. et al., 2022; Li et al., 2023) is introduced to calculate the optimal weights, so as to make its weight allocation more reasonable.

Although fuzzy theory has made many advances in equipment condition evaluation, there are still some limitations in its research and application in the field of hydropower units: 1) It is difficult to determine the indicator limit value, and when using the affiliation function, it is necessary to calculate the indicator degradation degree according to the indicator limit value. 2) It fails to consider the influence of the unit's own operating conditions well. Hydropower units in different operating conditions, some state parameters such as pendulum, temperature, etc., there will be a big difference, the general use of uniform regulations to calculate the state of deterioration degree lack of reasonableness: 3) indicators of deterioration degree of different intervals and affiliation function of the mapping of the different evaluation state of the relationship between the lack of effective explanation. Geng and Liang (2022) proposed the degradation degree of hydropower units and applied the principle of maximum affiliation to determine the condition of the units, providing scientific guidance for the evaluation of the health of hydropower generators. Li C. et al. (2022) constructed a hierarchical index system for transmission lines and combined it with the triangular-semi-trapezoidal affiliation function in fuzzy theory, Second, the mapping relationship between the different degradation degree intervals and evaluation states of the affiliation function lacks effective and reasonable explanation. Therefore, to evaluate the unit health state more accurately, the Gaussian threshold method (Zhang et al., 2022; Paialung et al., 2023) can be used to determine the indicator limit value. This study accordingly proposed an improved adaptive fuzzy comprehensive evaluation model for hydropower units that combines the Gaussian threshold method with the fuzzy comprehensive evaluation method to achieve a more effective and reliable evaluation of unit status.

To address to the shortcomings of current hydropower unit evaluation research, an adaptive fuzzy evaluation model that integrates the game theory-based combination of assignment with an improved fuzzy comprehensive evaluation is proposed in this paper. Based on the structure of the research object and the distribution of measurement points, the fuzzy hierarchical analysis method is used to construct the unit hierarchy system (Tian et al., 2020; Xia et al., 2020) and calculate the subjective

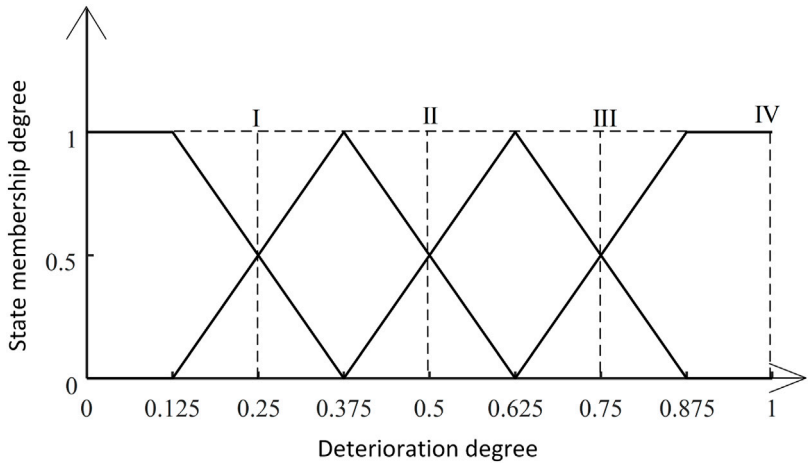

FIGURE 3
Improved triangle-semi-trapezoid affiliation function graph.

TABLE 2 Hydroelectric unit condition evaluation table.

Evaluated state	Status description
Good	The monitoring values of each parameter are far from the thresholds or within the standard values, the maintenance cycle can be extended appropriately
Qualified	Monitoring data for each parameter is within the permissible range and not as far from the threshold as in good condition
Attention	Monitoring data deviate from the normal operating value, the trend is close to the standard limit, but does not exceed the standard limit
Abnormal	Monitoring data seriously exceeds the standard limit, should immediately arrange for shutdown maintenance

weights for indicator parameters. The objective weights of each indicator are calculated by the CRITIC method based on historical monitoring data, and the corresponding optimal objective and subjective weights are subsequently calculated using game theory. Then, the state affiliation of each indicator is determined according to the improved comprehensive evaluation model to determine the unit state. In the final results, it is found that in the hydropower unit indicator evaluation system, the influence of the weight of the bottom indicator on the overall evaluation results is weakened with the increase of the number of transmission layers, which is similar to the phenomenon of the disappearance of the gradient of the neural network. Therefore, this paper proposes a variable weighting algorithm (Fu et al., 2017) with a penalty factor that can adaptively adjust the weight of the indicator according to the operating state of the indicator, and applies it through the case study and verifies its optimal evaluation effect by comparing the improved method with other methods without improvement.

2 Safety evaluation system for hydropower units

Due to the complex structure of hydropower units, the need to monitor many parts, the need to monitor many parts, and the differences in the types of measurement points between different power plants and unit models, a hydropower unit evaluation system can be constructed using division by components or division according to monitoring signals. The latter approach was applied in this study. The monitoring signals for a hydraulic turbine system can be divided into pendulum, vibration type, pressure pulsation, and temperature type signals. In order to reflect the real operation of the unit and determine the reliability of the evaluation method, this study constructed a hierarchical analysis system according to the type of monitoring signals (Zhang et al., 2023), taking Unit 4 of a power plant as an example. This hydropower unit was divided into the three layers shown in Figure 1.

A goal layer, project layer, and indicator layer. The project layer consists of the four monitoring signal types: pendulum, vibration, pressure pulsation, and temperature. The indicator layer comprises the different measurement points under each of the four signals, comprehensively reflecting the operation status of the hydropower unit.

3 Combinatorial empowerment via game theory

How to scientifically and reasonably determine the weights of indicators for the evaluation of hydropower units has a significant impact on the evaluation structure. Currently, the commonly used evaluation methods include subjective and fuzzy methods. If the calculation process is complicated and inaccurate, no traditional evaluation method will lead to acceptable solution. In such cases, need for improvement of the capacity of the single assessment

TABLE 3 Correspondence between indicator boundary values and unit states.

State	Boundary values				
	μ	$\mu + \sigma$	$\mu + 2\sigma$	$\mu + 3\sigma$	$\mu + 4\sigma$
Good	100%	50%	0	0	0
Qualified	0	50%	50%	0	0
Attention	0	0	50%	50%	0
Abnormal	0	0	0	50%	100%
Degradation	0	0.25	0.5	0.75	1

methodology to address practical problems. Therefore, this study combined a game theory weight determination method with the subjective weights of the fuzzy hierarchical analysis method and the objective weights of the CRITIC method to obtain the two optimal weight vectors through game aggregation.

3.1 Fuzzy hierarchical analysis method

The fuzzy hierarchical analysis method has been widely used as a basis for quantifying evaluation indicators and selecting an optimal solution. It combines a fuzzy consistency matrix with a hierarchical analysis, retaining the advantages of the latter while overcoming its fuzziness in the judgment matrix to ensure consistency and functionality more to imitate the human decision-making.

The fuzzy complementary matrix of hydropower unit evaluation indicators can be established by comparing the evaluation indicators r_i and r_j to determine and quantitatively express the importance of one factor over the other. The fuzzy relationship affiliation degree

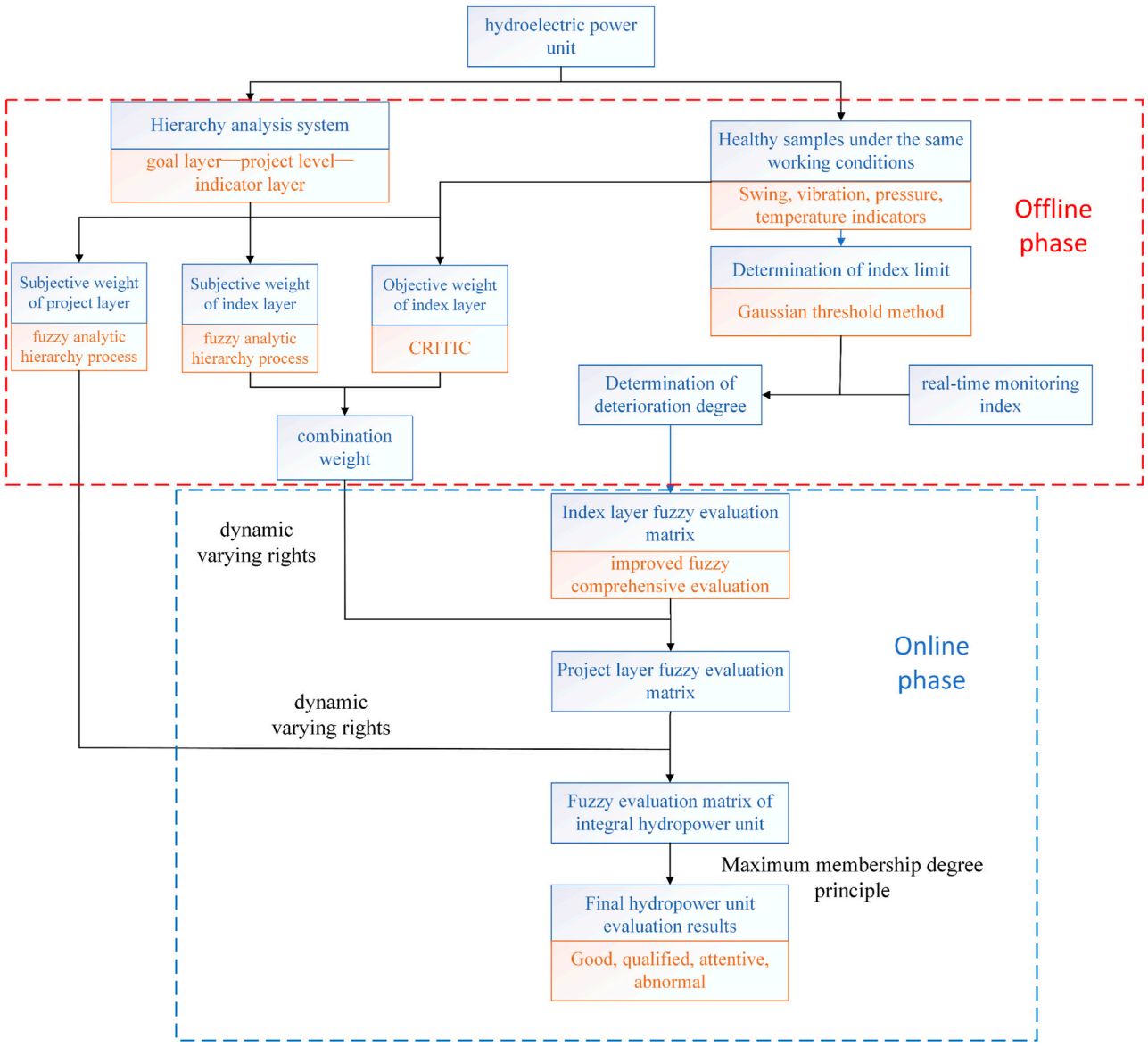

FIGURE 4
Flowchart of the health model algorithm for hydropower units.

TABLE 4 Project layer weighting table.

Indicator	Subjective weights	Objective weights	Portfolio empowerment
Pendulum	(1/6,1/6,1/6,1/6,1/6,1/6)	(0.156,0.163,0.142,0.165,0.217,0.157)	(0.161,0.165,0.154,0.166,0.192,0.162)
Vibration	(1/6,1/6,1/6,1/6,1/6,1/6)	(0.172,0.108,0.111,0.209,0.211,0.189)	(0.169,0.137,0.140,0.189,0.187,0.178)
Pressure	(0.30,0.30,0.233,0.167)	(0.274,0.231,0.192,0.312)	(0.287,0.266,0.213,0.234)
Temperature	(0.283,0.283,0.217,0.217)	(0.267,0.293,0.202,0.238)	(0.273,0.289,0.208,0.230)

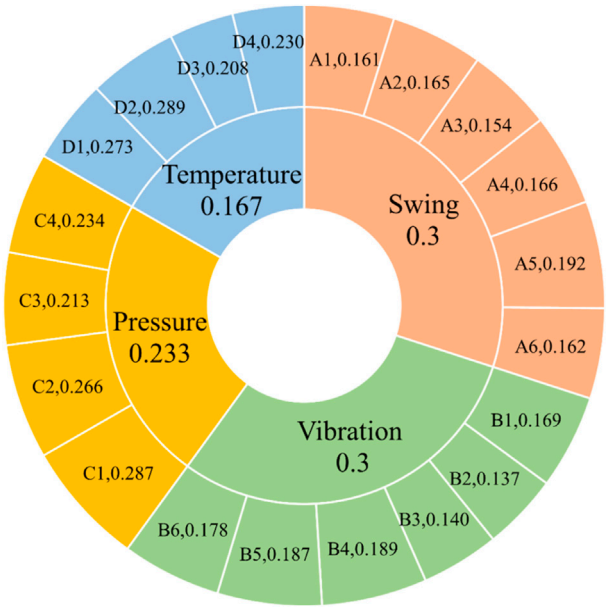

FIGURE 5
Combined weight assignment diagram.

between these two indicators, a_{ij}, is quantitatively described on a scale of 0.1–0.9, with the meaning of each interval in this range expressed in Table 1. Thus, the fuzzy complementary judgment matrix of the evaluation indicators for hydropower units is expressed as A = $(a_{ij})_{n\times n}$ which satisfies $0 \le a_{ij} \le 1$ and $a_{ij} + a_{ji} = 1$, where:

$$a_{ii} = 0.5\,(i = 1, 2, \ldots, n)$$
$$a_{ij} + a_{ji} = 1\ (i, j = 1, 2, \cdots, n);$$

As shown in Table 1, $a_{ii} = 0.5$ indicates that each factor is equally important; $a_{ij} \in [0.1,0.5)$ indicates that factor x_j is more important than x_i; and $a_{ij} \in [0.5,0.9]$ indicates that factor x_i is more important than x_j. For the last case, the fuzzy consistency matrix performs a summation operation for each row of the fuzzy judgment matrix as follows:

$$r_i = \sum_{j=1}^{n} a_{ij} \tag{1}$$

The matrix transformation conducted according to Eq. 1 yields the fuzzy judgment matrix E = $(e_{ij})_{n\times n}$, which is consistent, as follows.

$$e_{ij} = \frac{r_i - r_j}{2n} + 0.5 \tag{2}$$

where e_{ij} is the consistency-processed value of a_{ij} in the i th row and j th column of matrix E and r_i is the value from the fuzzy complementary matrix A = $(a_{ij})_{n\times n}$. The value of the row-by-row summation of the weight of each indicator $i, w_i = (w_1, w_2, w_3, \ldots, w_n)$ is subsequently obtained from the matrix E = $(e_{ij})_{n\times n}$ as follows:

$$w_i = \frac{2\sum_{j=1}^{n} e_{ij} - 1}{n(n-1)} \tag{3}$$

3.2 CRITIC method

The CRITIC method is an objective weighting method that uses the quantity of information for each indicator to calculate the value of its weight. This represents a superior method compared to entropy weighting or the coefficient of variation when the information describing each indicator to be evaluated is provided by varying intensities and conflicts with that describing other indicators. Indeed, the CRITIC method determines the weights not only by taking the variability of the indicator information as a premise, but also by combining the correlation between indicators, thereby preventing subjective factors from having an outsized effect and causing the results to deviate from objective reality.

Indicator dissimilarity is generally expressed as a standard value that represents the volatility of the indicator; the greater the volatility, the greater the indicator dissimilarity. Conflict between two different indicators is expressed in terms of correlation; the greater the conflict, the smaller the correlation.

Generally, CRITIC method modeling is conducted using the following steps.

(1) Dimensionless processing

Considering the inconsistency in the scale of the data for each indicator, dimensionless processing is first conducted on each indicator to remove the influence of such inconsistency on the evaluation results. When there are many objects to be evaluated, standardization can be used for this task as follows:

$$y_i = (x_i - x_0)/s \tag{4}$$

where x_i is the sample mean for each indicator, x_0 is the actual variable value, and s is the standard value.

(2) Calculate indicator dissimilarity

TABLE 5 Indicator limits and monitoring values at considered moments.

Indicator	Lower limit value	Upper limit value	Monitoring values					
			Base value	Moment A	Moment B	Moment C	Moment D	Moment E
A1 (μm)	99.29	131.95	115.62	111.65	118.33	119.17	108.23	103.87
A2 (μm)	96.94	128.00	112.47	120.40	117.53	118.24	116.58	117.92
A3 (μm)	516.60	697.10	606.08	568.18	570.37	561.27	566.79	550.59
A4 (μm)	473.21	637.14	555.17	541.10	538.85	521.13	567.13	555.95
A5 (μm)	170.77	278.47	224.62	200.05	228.11	287.72	331.47	316.27
A6 (μm)	138.96	253.2	196.08	178.98	164.58	172.05	233.46	232.77
B1 (μm)	20.84	31.53	26.18	27.51	22.54	24.50	28.682	20.84
B2 (μm)	21.41	30.93	26.17	25.64	28.58	27.53	30.76	25.26
B3 (μm)	0.56	2.18	1.37	1.645	0.684	1.347	0.973	1.304
B4 (μm)	97.82	161.01	129.41	132.45	248.05	298.32	417.65	471.01
B5 (μm)	81.82	153.36	117.59	104.05	197.60	246.99	372.00	413.36
B6 (μm)	79.61	158.44	119.02	105.58	207.60	270.31	381.94	458.43
C1 (kPa)	0.56	1	0.78	0.69	0.65	0.596	0.557	0.549
C2 (kPa)	0.20	0.21	0.205	0.206	0.203	0.205	0.203	0.203
C3 (kPa)	0.34	0.35	0.345	0.345	0.345	0.345	0.345	0.345
C4 (kPa)	0.136	0.265	0.20	0.194	0.182	0.174	0.172	0.212
D1 (°C)	44.49	63.234	53.87	52.58	52.64	50.77	59.19	57.234
D2 (°C)	46.326	64.932	55.62	51.43	53.21	51.32	57.33	58.32
D3 (°C)	41.03	59.56	50.30	49.00	49.15	50.17	59.92	59.56
D4 (°C)	40.13	59.66	49.90	48.32	48.46	51.22	58.35	59.32

The CRITIC method uses the standard deviation to express the variability between indicators as follows:

$$S_j = \sqrt{\frac{\sum_{i=1}^{n}(x_{ij} - \tilde{x_j})^2}{n-1}} \tag{5}$$

where $\tilde{x_j}$ is the mean value of each indicator. The larger the standard deviation, the greater the difference between the indicator values, the more information is provided among them, and the greater their assessment strength, suggesting that they should be given higher weights.

(3) Calculate indicator conflict

Indicator conflict is expressed in terms of the correlation coefficient as follows:

$$E_j = \sum_{i=1}^{n}(1 - r_{ij}) \tag{6}$$

where r_{ij} denotes the Pearson correlation coefficient (Edelmann et al., 2021) between indicators i and j

(4) Calculate quantity of information

The quantity of information is determined by:

$$V_j = S_j \times E_j \tag{7}$$

(5) Calculate the objective weights

The objective weight of the j indicator W_j is given by

$$W_j = \frac{V_j}{\sum_{j=1}^{n} V_j} \tag{8}$$

and $W = (W_1, W_2, \cdots, W_n)^T$ is the indicator objective weight vector.

3.3 Portfolio empowerment based on game theory

Game theory provide a mathematical method for investigating how to make decisions and maximize benefits when there are multiple struggling or competing individuals in a group. When used in subjective–objective combination weight calculations, game theory can apply weighting to the combinations between indictors and determine weights that deviate the least from each basic value,

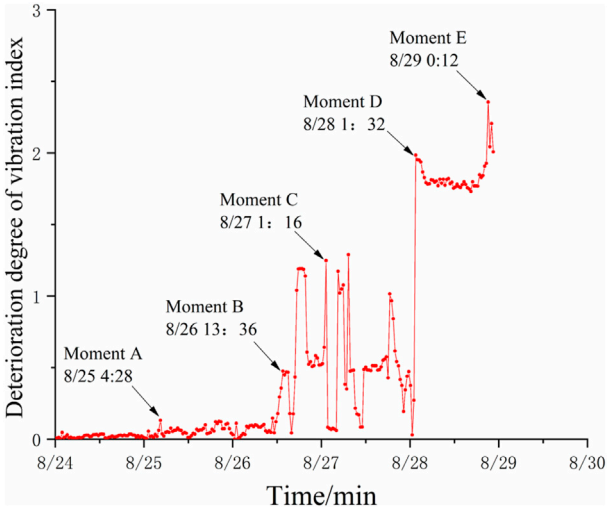

FIGURE 6
Trend of deterioration in axial vibration indicator.

thereby ensuring that the calculated values match the actual situation. This "portfolio empowerment" method is conducted as follows.

(1) Employ the game theory concept of outlier minimization to find the optimal weights w_k^* as follows:

$$\boldsymbol{w_k^* = \min\left\|\sum_{k=1}^{n} a_k w_k^T\right\|_2} \tag{9}$$

where k represents the number of approaches (thus, the number of weights obtained) and w_i is the matrix of the weights obtained for each approach.

(2) Normalize the obtained $(\alpha_1, \alpha_2, \ldots\ldots, \alpha_q)$ to derive α_k^* as follows:

$$\begin{pmatrix} w_1 w_1^T & \cdots & w_1 w_k^T \\ \vdots & \ddots & \vdots \\ w_k w_1^T & \cdots & w_k w_k^T \end{pmatrix} \begin{pmatrix} \alpha_1 \\ \vdots \\ \alpha_k \end{pmatrix} = \begin{pmatrix} w_1 w_1^T \\ \vdots \\ w_k w_k^T \end{pmatrix} \tag{10}$$

$$a_k^* = \frac{a_k}{\sum_{k=1}^{n} a_k} \tag{11}$$

(3) Assign a combination of weights to obtain the combined weight of the evaluation indicators as w^*:

$$w^* = \sum_{k=1}^{n} a_k^* w_k^T \tag{12}$$

and the combined weight vector is $w = (w_1, w_2, \ldots w_n)$.

4 Improved fuzzy comprehensive evaluation method

The indicator monitoring volume limits determined using regulation guidelines are not clear and do not consider the actual operating conditions of the hydropower unit. However, the indicator thresholds obtained from historical indicator monitoring data can accurately reflect the unit status. Therefore, to evaluate the health state of the hydropower unit more accurately, the indicator limits are determined from these data using the Gaussian threshold method.

4.1 Determination of the indicator limits using Gaussian thresholds

The indicator data from a hydropower unit include random measurement errors and exhibit obvious normal distribution characteristics (Zheng et al., 2017; Zhang S. et al., 2020), as shown in Figure 2. For normally distributed unit monitoring indicators $V_i = \{V_i(1), V_i(2), \ldots, V_i(t) \ldots, V_i(m)\}$, the probability that an indicator value falls in the range $[\mu - 3\sigma, \mu + 3\sigma]$, where μ is the optimal value of the indicator, is 99.74% and the probability it falls outside this range is 0.26%. Thus, the interval $[\mu - 3\sigma, \mu + 3\sigma]$ can be considered the normal operation limit of an indicator and the interval $[\mu - 4\sigma, \mu + 4\sigma]$ can be considered its overall, where:

$$\boldsymbol{u = mean(V_i) = \frac{1}{m}\sum_{i=1}^{m} V_i(t)} \tag{13}$$

$$\boldsymbol{\sigma = \sqrt{\frac{1}{m}\sum_{i=1}^{m}(V_i(t) - \mu)^2}} \tag{14}$$

4.2 Determination of degradation

The degradation degree when using indicators for which larger values are better is expressed as:

$$\boldsymbol{g = \begin{cases} 1 & x_i < a \\ \dfrac{\beta - x_i}{\beta - a} & a < x_i < \beta \\ 0 & x_i > \beta \end{cases}} \tag{15}$$

where g is the degradation degree, x_i is the measured value of the indicator, β is the optimal value of the indicator, a is the lower limit of the indicator, and $a < \beta$.

The degradation degree when using indicators for which smaller values are better is given by:

$$\boldsymbol{g = \begin{cases} 0 & x_i < a \\ \dfrac{x_i - \beta}{\beta - a} & a < x_i < \beta \\ 1 & x_i > \beta \end{cases}} \tag{16}$$

where $\beta < a$.

4.3 Improved fuzzy comprehensive evaluation method

When establishing the safety evaluation model for a hydropower unit in use, most of the risk evaluation indicators have randomness, fuzziness, and other uncertainties. The fuzzy comprehensive evaluation method has unique advantages for solving such problems. Fuzzy comprehensive evaluation is based on fuzzy

TABLE 6 Fuzzy evaluation matrix of hydropower station system at each moment.

Moment	Indicator	Evaluation matrix at the indicator level	Result	Target level evaluation matrix after weighting change	Result
A	Pendulum	$(0.760,0.240,0,0)^T$	Good	$(0.576,0.424,0,0)^T$	Good
	Vibration	$(0.673,0.327,0,0)^T$	Good		
	Pressure	$(0.781,0.219,0,0)^T$	Good		
	Temperature	$(0.594,0.406,0,0)^T$	Good		
B	Pendulum	$(0.081,0.531,0.231,0.243)^T$	Qualified	$(0.190,0.266,0.331,0.213)^T$	Attention
	Vibration	$(0.121,0.138,0.452,0.289)^T$	Attention		
	Pressure	$(0.521,0.260,0.219,0)^T$	Good		
	Temperature	$(0.494,0.306,0.2,0)^T$	Good		
C	Pendulum	$(0.150,0.201,0.449,0.200)^T$	Attention	$(0.051,0.042,0.410,0.497)^T$	Abnormal
	Vibration	$(0.006,0.045,0.284,0.712)^T$	Abnormal		
	Pressure	$(0.721,0.279,0,0)^T$	Good		
	Temperature	$(0.199,0.801,0,0)^T$	Qualified		
D	Pendulum	$(0.063,0.024,0.282,0.626)^T$	Abnormal	$(0.020,0.067,0.353,0.560)^T$	Abnormal
	Vibration	$(0.008,0.036,0.087,0.901)^T$	Abnormal		
	Pressure	$(0.572,0.427,0,0)^T$	Good		
	Temperature	$(0.258,0.418,0.324,0)^T$	Qualified		
E	Pendulum	$(0.081,0.031,0.472,0.424)^T$	Attention	$(0.050,0.086,0.243,0.621)^T$	Abnormal
	Vibration	$(0.005,0.006,0.034,0.954)^T$	Abnormal		
	Pressure	$(0.412,0.288,0.123,0.177)^T$	Good		
	Temperature	$(0.187,0.432,0.211,0.170)^T$	Qualified		

TABLE 7 Turbine system monitoring limits.

Monitoring volume	Lower value	Upper value
A1、A2 (um)	0	150
A3、A4 (um)	0	600
A5、A6 (um)	0	200
B1、B2、B3 (um)	0	70
B4、B5、B6 (um)	0	450
C1、C2、C3、C4 (kpa)	0	4
D1、D2、D3、D4 (°C)	25	75

mathematics and uses fuzzy relationship synthesis to quantify factors with unknown boundaries that are not easy to quantify, then comprehensively evaluate the system considering multiple factors. This approach is based on correlation theory, which converts a qualitative evaluation into a quantitative evaluation. This study accordingly adopted the fuzzy comprehensive evaluation method to evaluate and analyze the state of hydropower units.

The triangular/semi-trapezoidal membership function has been widely used in fuzzy comprehensive assessments due to its simple distribution, and it provides results comparable to other more complex membership functions used in risk assessments and equipment evaluations. However, as the degradation values used in the traditional triangular/semi-trapezoidal affiliation function for equipment evaluation depend on expert experience, and the correspondence among different levels lacks explanation. To explain the rationality of the relationships corresponding to different evaluation levels, an improved triangular/semi-trapezoidal affiliation function was proposed for use in this study as shown in the diagram in Figure 3.

The diagram shows that the hydropower unit can be classified into four states: I, II, III, and IV, representing good, qualified, attention, and abnormal conditions, respectively, corresponding to degradation degrees of 0.25, 0.50, 0.75, and 1, respectively. These four conditions can intuitively express hydropower unit health as defined in Table 2.

Since the hydropower unit indicators exhibit normal distribution characteristics, as shown in Figure 2, the hydropower unit states in Table 2 were defined using the four indicator value intervals shown in Table 3. These intervals are defined as $[\mu, \mu+2\sigma]$, $[\mu+\sigma, \mu+2\sigma]$, $[\mu+2\sigma, \mu+3\sigma]$, and $[\mu+3\sigma, \mu+4\sigma]$, where $[\mu]$, $[\mu+\sigma]$, $[\mu+2\sigma]$, $[\mu+3\sigma]$, and $[\mu+4\sigma]$ are zone boundary values corresponding to degradation degrees of 0, 0.25, 0.5, 0.75, 0.1, respectively, $[\mu, \mu+3\sigma]$

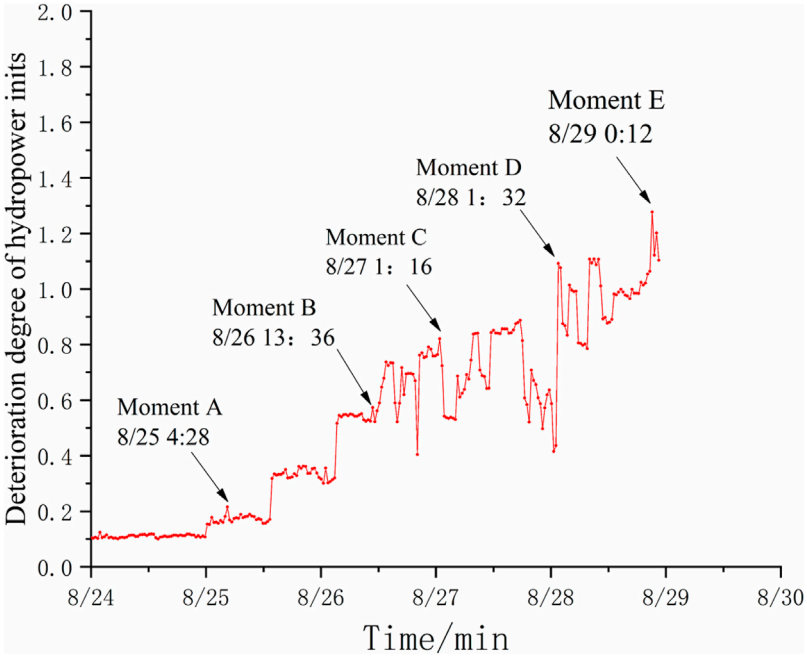

FIGURE 7
Comprehensive deterioration trend for the case study hydropower unit.

denotes the standard limits, and $[\mu, \mu + 4\sigma]$ denotes the overall limits.

According to the intervals defined in Table 3 and based on the triangular/semi-trapezoidal affiliation function in Figure 3, the expressions for the affiliation function were constructed as follows:

$$f_1 = \begin{cases} 1 & g < 0.125 \\ -4g + 1.5 & 0.125 < g < 0.375 \\ 0 & g > 0.375 \end{cases} \quad (17)$$

$$f_2 = \begin{cases} 0 & g < 0.125 \\ 4g - 0.5 & 0.125 < g < 0.375 \\ -4g + 2.5 & 0.375 < g < 0.625 \\ 0 & g > 0.625 \end{cases} \quad (18)$$

$$f_3 = \begin{cases} 0 & g < 0.375 \\ 4g - 1.5 & 0.375 < g < 0.625 \\ -4g + 3.5 & 0.625 < g < 0.875 \\ 0 & g > 0.875 \end{cases} \quad (19)$$

$$f_4 = \begin{cases} 0 & g < 0.625 \\ 4g - 2.5 & 0.625 < g < 0.875 \\ 1 & g > 0.875 \end{cases} \quad (20)$$

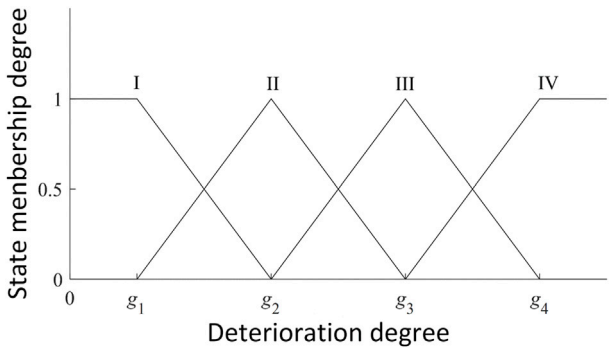

FIGURE 8
Distribution of traditional affiliation functions.

5 Case study example

5.1 Hydropower unit health assessment process

The following sequence was used to conduct the hydropower unit case study in this example (a flow chart of this process is provided in Figure 4).

1) According to the actual situation of the case study hydropower plant unit structure and the arrangement of measurement points, a hierarchical analysis system was constructed by dividing the unit into a target layer, project layer, and indicator layer. Historical health data describing the oscillation, vibration, pressure, and temperature indicators—included in the project layer—were obtained under the same working conditions used in the example calculation.
2) Next, a fuzzy hierarchical analysis was employed to determine the subjective weights of the items in the project and indicator layers. The historical health data were inserted into the CRITIC method to determine the objective weights for the items in the indicator layer, and the optimal comprehensive weights were

TABLE 8 Evaluation results of the state of each moment based on the traditional fuzzy evaluation method.

Moment	Indicator	Evaluation matrix at the indicator level	Result	Evaluation matrix under traditional fuzzy evaluation	Result
A	Pendulum	$(0.693,0.307,0,0)^T$	Good	$(0.91,0.09,0,0)^T$	Good
	Vibration	$(1,0,0,0)^T$	Good		
	Pressure	$(0.99,0.01,0,0)^T$	Good		
	Temperature	$(0.95,0.05,0,0)^T$	Good		
B	Pendulum	$(0.42,0.58,0,0)^T$	Qualified	$(0.60,0.26,0.10,0.04)^T$	Good
	Vibration	$(0.32,0.16,0.37,0.15)^T$	Attention		
	Pressure	$(0.99,0.01,0,0)^T$	Good		
	Temperature	$(0.70,0.30,0.,0)^T$	Good		
C	Pendulum	$(0.2,0.22,0.38,0.20)^T$	Attention	$(0.30,0.40,0.12,0.18)^T$	Qualified
	Vibration	$(0.17,0.16,0.24,0.42)^T$	Abnormal		
	Pressure	$(0.56,0.44,0,0)^T$	Good		
	Temperature	$(0.23,0.77,0,0)^T$	Qualified		
D	Pendulum	$(0.28,0.18,0.38,0.16)^T$	Attention	$(0.02,0.15,0.56,0.27)^T$	Attention
	Vibration	$(0.01,0.11,0.38,0.50)^T$	Abnormal		
	Pressure	$(0.57,0.43,0,0)^T$	Good		
	Temperature	$(0.26,0.42,0.32,0)^T$	Qualified		
E	Pendulum	$(0,0.1,0.47,0.43)^T$	Attention	$(0.16,0.23,0.35,0.26)^T$	Attention
	Vibration	$(0.005,0.006,0.034,0.954)^T$	Abnormal		
	Pressure	$(0.54,0.30,0.16,0)^T$	Good		
	Temperature	$(0.20,0.45,0.20,0.05)^T$	Qualified		

determined based on game theory principle by combining the subjective and objective weights.

3) The upper limit, lower limit, and benchmark value for each indicator were obtained using the Gaussian threshold method and the corresponding historical data based on the indicator operating limits and real-time monitoring values.
4) Using the improved adaptive fuzzy comprehensive evaluation method as the health evaluation model, the indicators were divided into four intervals corresponding to good, qualified, attention, and abnormal states. The degradation degree for each indicator was substituted into Eqs 17–20 to obtain the state affiliation for each indicator corresponding to the oscillation, vibration, pressure, and temperature, thereby obtaining the indicator layer fuzzy evaluation matrix.
5) The variable weight theory was subsequently applied to adjust the weight for each indicator, and the fuzzy evaluation matrix was weighted and calculated to obtain the fuzzy evaluation matrix for the project level of the hierarchy structure.
6) The fuzzy evaluation matrix for the entire hydropower unit system was derived using variable weight theory, and the final hydropower unit evaluation result was obtained according to the principle of maximum subordination.

5.2 Calculation of portfolio weights

The subjective project level weights included vibration, oscillation, pressure pulsation, and temperature indicators. The hierarchical analysis method was used to determine the weight of each indicator type. As the vibration, oscillation, and pressure pulsation indicators changed faster and were more sensitive to the state of the unit, the indictor importance was defined as vibration fault = oscillation fault > pressure pulsation fault > temperature fault. According to the 0.1–0.9 scale, the fuzzy judgment matrix for the project level was determined as follows:

$$\boldsymbol{C} = (\boldsymbol{C}_{ij}) = \begin{bmatrix} \mathbf{0.5} & \mathbf{0.5} & \mathbf{0.7} & \mathbf{0.9} \\ \mathbf{0.5} & \mathbf{0.5} & \mathbf{0.7} & \mathbf{0.9} \\ \mathbf{0.3} & \mathbf{0.3} & \mathbf{0.5} & \mathbf{0.7} \\ \mathbf{0.1} & \mathbf{0.1} & \mathbf{0.3} & \mathbf{0.5} \end{bmatrix}$$

And the fuzzy consistency matrix was obtained as

$$(\boldsymbol{E}_{ij}) = \begin{bmatrix} \mathbf{0.5} & \mathbf{0.5} & \mathbf{0.6} & \mathbf{0.7} \\ \mathbf{0.5} & \mathbf{0.5} & \mathbf{0.6} & \mathbf{0.7} \\ \mathbf{0.4} & \mathbf{0.4} & \mathbf{0.5} & \mathbf{0.6} \\ \mathbf{0.3} & \mathbf{0.3} & \mathbf{0.4} & \mathbf{0.5} \end{bmatrix}$$

and subjective weights at the project level were (0.3, 0.3, 0.233, 0.167).

TABLE 9 Evaluation results of the state of each moment under constant weights.

Moment	Indicator	Evaluation matrix at the indicator level	Result	Target level evaluation matrix with unchanged weights	Result
A	Pendulum	$(0.63,0.30,0.07,0)^T$	Good	$(0.676,0.324,0,0)^T$	Good
	Vibration	$(0.53,0.47,0,0)^T$	Good		
	Pressure	$(0.98,0.02,0,0)^T$	Good		
	Temperature	$(0.51,0.49,0,0)^T$	Good		
B	Pendulum	$(0.28,0.701,0.02,0)^T$	Qualified	$(0.26,0.53,0.16,0.05)^T$	Qualified
	Vibration	$(0.09,0.33,0.50,0.1)^T$	Attention		
	Pressure	$(1,0,0,0)^T$	Good		
	Temperature	$(0.52,0.48,0.2,0)^T$	Good		
C	Pendulum	$(0.150,0.201,0.449,0.200)^T$	Attention	$(0.20,0.29,0.25,0.26)^T$	Qualified
	Vibration	$(0.006,0.045,0.284,0.712)^T$	Abnormal		
	Pressure	$(0.61,0.39,0,0)^T$	Good		
	Temperature	$(0.39,0.50,0.11,0)^T$	Qualified		
D	Pendulum	$(0.063,0.024,0.282,0.626)^T$	Abnormal	$(0.20,0.16,0.15,0.46)^T$	Abnormal
	Vibration	$(0.008,0.036,0.087,0.901)^T$	Abnormal		
	Pressure	$(0.572,0.427,0,0)^T$	Good		
	Temperature	$(0.258,0.418,0.324,0)^T$	Qualified		
E	Pendulum	$(0.08,0.43,0.37,0.12)^T$	Qualified	$(0.21,0.09,0.23,0.47)^T$	Abnormal
	Vibration	$(0.07,0.11,0.22,0.70)^T$	Abnormal		
	Pressure	$(1,0,0,0)^T$	Good		
	Temperature	$(0.20,0.52,0.18,0.10)^T$	Qualified		

The objective and subjective weights at the indicator level and the combination weights were subsequently obtained as shown in Table 4.

5.3 Determination of indicator limits

According to the case study unit model and its parameters, including operating head and rated speed, and other parameters, the oscillation, vibration, pressure pulsation, and temperature indicator limits were obtained by consulting international industry regulations, as well as power station regulations and guidelines. Then, the historical health indicator data and Gaussian threshold method has been applied to obtain the final weights of the oscillation, vibration, and pressure pulsation, and temperature indicators as shown in Figure 5.

5.4 Determination of degradation degree

As shown in Table 5, the axial vibration class indicators exhibited the largest variation. Therefore, the axial vibration class degradation graph was obtained as shown in Figure 6, which identifies five moments representing the degradation trend over time. Note that all monitoring indicators considered in this example were minimum optimal (smaller is better) type indicators.

5.5 Unit condition assessment

During the evaluation of hydropower units, the serious deviation of a certain indicator or indicator type from its normal value often means that the feature of this indicator is abnormal and must be paid careful attention, or the system should be shut down for maintenance (Xu et al., 2016; Lin et al., 2020). However, as the weight value of a problematic indicator could be quite small in practice, the state of the response may not be reflected in the results for the entire hydropower unit. Therefore, an adaptive penalty factor algorithm was introduced to adjust the weight of each indicator according to its operating state as follows:

$$w_i = \frac{\partial_k w_i}{\sum_{j=1}^{n} \partial_k w_i} \tag{21}$$

where $\partial_k = \{1,2,3,4\}$ is the penalty, defined according to the principle of maximum affiliation and the dynamics of the indicator state assessment results. In state 1, $\partial_k = \partial_1 = 1$, in state 2, $\partial_k = \partial_2 = 2$, etc. The project layer fuzzy evaluation matrix was constructed according

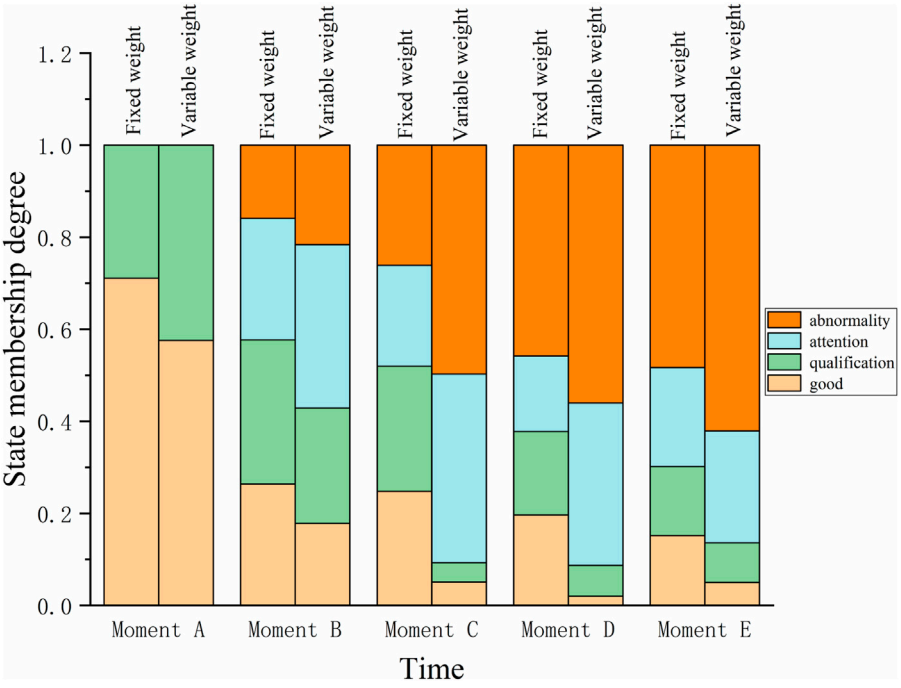

FIGURE 9
Comparison of the unit's operational condition assessment using variable and fixed weights.

to the variable weight theory and combined with the subjective weights of the project layer to obtain the overall fuzzy evaluation matrix.

The values of the indicators in Table 5 were substituted into Eq. 16 to obtain the deterioration degree for each indicator. These deterioration degrees were substituted into Eqs 17–20 to obtain the fuzzy evaluation matrix for each item level indicator as follows:

$$M_B = \begin{bmatrix} 0.623 & 0.377 & 0 & 0 \\ 0.588 & 0.412 & 0 & 0 \\ 0.313 & 0.687 & 0 & 0 \\ 0 & 0 & 0.548 & 0.452 \\ 0 & 0 & 0.652 & 0.348 \\ 0 & 0 & 0.631 & 0.369 \end{bmatrix}$$

As shown above, the weight of each indicator was reallocated using the variable weight theory. According to the principle of maximum subordination, the top vibrations in the X- and Y-directions are in state 1 (corresponding to penalty factor ∂_1), the top vibration in the Z-direction is in state 2 (corresponding to penalty factor ∂_2), and the axial vibrations A, B, and C are in state 3 (corresponding to penalty factor ∂_3). The vibration class indicator weights were combined into w_B and substituted into Eq. 4 to obtain the new vibration class weight vector as follows:

$$w' = (0.075, 0.061, 0.124, 0.252, 0.250, 0.238)$$

The vibration class fuzzy evaluation matrix was subsequently obtained based on the new vibration indicator weight vector as follows:

$$W_B = w_B' \cdot M_B = (0.121, 0.138, 0.451, 0.289)$$

The fuzzy evaluation matrices for the other indicator types have been obtained similarly, then the project level fuzzy evaluation matrix has been determined as follows:

$$M = \begin{bmatrix} 0.081 & 0.531 & 0.231 & 0.243 \\ 0.121 & 0.138 & 0.451 & 0.289 \\ 0.521 & 0.260 & 0.219 & 0 \\ 0.494 & 0.306 & 0.2 & 0 \end{bmatrix}$$

The new project layer weight vector has been obtained after the subjective weights of the project layer were weighted as w' =(0.316.0.474,0.123,0.087), and the final fuzzy evaluation matrix was given by $w' \cdot M$ =(0.190,0.266,0.331,0.213).

According to the calculated fuzzy evaluation matrix, the weights of each indicator were reallocated using variable weight theory, giving the results shown in Table 6.

Furthermore, the comprehensive deterioration degree of the hydropower unit is plotted in Figure 7, which shows that the deterioration of the hydroelectric unit increased obviously from August 26, with abnormalities at C, D, and E. At the end of August, the vibration of the case study unit was reported to have been quite violent. After an accident probe of the site personnel, it was determined that the runner chamber steel plate fell off during this time period, leading to a hydraulic imbalance that would obviously change the vibration pendulum signal. Thus, the calculated deterioration degree is consistent with the reported reality.

6 Comparison of methods

In order to further validate the advantages of the proposed method for the health assessment of hydropower units, two sets of controlled experiments are designed in this section: fuzzy assessment based on traditional monitoring quantities and

regulatory guidelines, fuzzy assessment based on constant-weighted Gaussian thresholds (You et al., 2022).

6.1 Comparison with traditional guideline protocol-fuzzy evaluation methods

This method is compared with the fuzzy evaluation method for hydropower units, which is based on traditional monitoring quantities and regulations. According to the unit type, working head, rated speed and other parameters, the upper and lower limit values of each measurement point of the hydraulic turbine system under steady state operation are determined by consulting the national standards and regulations and the guidelines of power plant regulations, as shown in Table 7.

It can be seen that all the monitored quantities are of the smaller and better type, therefore the degree of deterioration is calculated according to Eq. 16, as shown in the traditional plot of the membership function in Figure 8:

Where g_1,g_2,g_3,g_4, correspond to (0.2, 0.4, 0.6, 0.8), respectively, as a comparison to evaluate the operating status of the turbine system A-E at each moment, corresponding to the actual monitoring values shown in Table 5, According to Table 5, the final state evaluation table under the traditional fuzzy evaluation method can be obtained as shown in Table 8:

Table 8 shows that the turbine system status and vibration indexes at C, D, and E time are still assessed as qualified or attention, but at this time, through the comprehensive deterioration diagram of the unit, it is obvious to see that there are abnormalities in the unit, and the evaluation results obviously cannot reflect the real state of the unit, in contrast, the evaluation results based on the combination of the assignment and the Gaussian threshold method of the state of the unit are more in line with the actual situation, and can be more real and effective. Reflecting the actual operating status of the unit.

6.2 Comparison with unweighted methods

According to the real-time evaluation status of each component in the unit hierarchical analysis system, the penalty factor is introduced to dynamically adjust the original weights of each component, so as to propose an adaptive variable weighting method. Compare it with the evaluation method using fixed constant weights to verify the advantages of introducing the variable weight theory. When using constant weights, the penalty factors in Eq. 21 are all 1, and the results are shown in Table 9.

Under the constant weighting mode, the evaluation status of the turbine system of the unit is qualified at two moments B and C. At this time, as shown in Figure 5, the vibration deterioration increases significantly and the evaluation results of vibration indexes at the two moments in Table 7 are attention and abnormality, respectively. In the case of a single category of indicators abnormal, but still the overall evaluation of the system as a qualified obviously does not match the actual situation. Figure 9 shows the difference between the evaluation results of the two methods more intuitively, and it can be seen that, Compared with the fixed constant weights, and conventional weights can not objectively reflect the serious deviation of indicators from the normal situation, so the introduction of variable weights theory can be based on the actual state of the unit to dynamically change the ratio of each component, highlighting the hidden equipment, variable weights mode of the unit's condition assessment results and the actual operating state of the unit is more in line with the actual operating state of the unit.

7 Conclusion

This study proposed a fuzzy comprehensive evaluation model using a combination of game theory assignment and the Gaussian threshold method to address difficulties associated with determining the indicator limits, the lack of reasonable correspondence between the degradation degree and the affiliation function, and the fact that indicator abnormality cannot be effectively reflected in the overall condition of the hydropower unit. The proposed model was confirmed to effectively and accurately reflect the operation of the case study example of unit 4 of a power station. The following conclusions were obtained by this study.

(1) The use of fuzzy comprehensive hierarchical analysis overcomes the lack of consistency in the traditional fuzzy hierarchical analysis by using historical health monitoring data to determine the objective weights via the CRITIC method. This results in more reasonable objective weights that can be analyzed using game theory to obtain the optimal values.
(2) Analysis of historical and real-time monitoring health indicator data can determine indicator limits using the Gaussian threshold method. When combined with the fuzzy comprehensive evaluation method, this results in a more accurate evaluation of the overall hydropower unit.
(3) Since the indicator weights for the bottom layer of the hierarchy will continue to decay in the overall evaluation results as the number of transmission layers increases, the serious deviation of a certain indicator from its normal value may go unnoticed as it accounts for a relatively small portion of the overall unit state. The use of a variable weight algorithm effectively solves the problem of individual indicator anomalies.

Data availability statement

The raw data supporting the conclusion of this article will be made available by the authors, without undue reservation.

Author contributions

YK: Conceptualization, Methodology, Software, Writing-Original Draft, Writing-Review and Editing, Investigation QW: Revision and viewing of papers HX: Discontinuation of data supply has been thesis revision ZL: Assisted completion JL: Check the papers. All authors contributed to the article and approved the submitted version.

Conflict of interest

The authors declare that the research was conducted in the absence of any commercial or financial relationships that could be construed as a potential conflict of interest.

Publisher's note

References

Awan, A., Kocoglu, M., Bandyopadhyay, A., Rej, S., and Altuntaş, M. (2023). Household fuel choices and consumption intensity in Pakistan: evidence from HIES data 2001-2019. *Environ. Model. Assess.*, 2023, 1–16. doi:10.1007/s11356-023-27227-3

Cai, F., Hu, Z., Jiang, B., Ruan, W., Cai, S., and Zou, H. (2023). Ecological health assessment with the combination weight method for the river reach after the retirement and renovation of small hydropower stations. . *Water* 15 (2), 355. doi:10.3390/w15020355

Doz, D., Felda, D., and Cotič, M. (2023). Demographic factors affecting fuzzy grading: a hierarchical linear regression analysis. *Mathematics* 11 (6), 1488. doi:10.3390/math11061488

Edelmann, D., Móri, T. F., and Székely, G. J. (2021). On relationships between the Pearson and the distance correlation coefficients. *Statistics Probab. Lett.* 169, 108960. doi:10.1016/j.spl.2020.108960

Fang, R., Wu, M., and Jiang, S. (2016). On-line status assessment of wind turbines based on improved fuzzy comprehensive evaluation method. *J. Intelligent Fuzzy Syst.* 31 (6), 2813–2819. doi:10.3233/jifs-169163

Fu, L., Wei, Y., Fang, S., Zhou, X., and Lou, J. (2017). Condition monitoring for roller bearings of wind turbines based on health evaluation under variable operating states. *Energies* 10 (10), 1564. doi:10.3390/en10101564

Ge, L., Li, Y., Zhu, X., Zhou, Y., Wang, T., and Yan, J. (2020). An evaluation system for HVDC protection systems by a novel indicator framework and a self-learning combination method. *IEEE Access* 8, 152053–152070. doi:10.1109/access.2020.3017502

Geng, Q., and Liang, C. (2022). Turbine health evaluation based on degradation degree. *Energy Rep.* 8, 435–444. doi:10.1016/j.egyr.2022.01.214

Hu, A., Xie, N., and Zheng, M. (2019). Air quality evaluation based on grey clustering method: a case study of 74 cities in China. *J. Grey Syst.* 31 (2).

Huang, X., Wang, Z., and Liu, S. (2022). Health status evaluation method of CNC machine tools based on grey clustering analysis and fuzzy comprehensive evaluation. *J. Intelligent Fuzzy Syst.* 42 (4), 4065–4082. doi:10.3233/jifs-212406

Krishnan, A. R., Kasim, M. M., Hamid, R., and Ghazali, M. F. (2021). A modified CRITIC method to estimate the objective weights of decision criteria. *Symmetry* 13 (6), 973. doi:10.3390/sym13060973

Li, C., Chen, X., Li, Z., Zhang, Y., Yue, K., Ma, J., et al. (2022b). Comprehensive evaluation method of transmission line operating status based on improved combination weighting evaluation model. *Energy Rep.* 8, 387–397. doi:10.1016/j.egyr.2022.01.207

Li, H., Chen, L., Tian, F., Zhao, L., and Tian, S. (2022a). Comprehensive evaluation model of coal mine safety under the combination of game theory and TOPSIS. *Math. Problems Eng.* 2022, 1–15. doi:10.1155/2022/5623282

Li, X., Wang, J., and Sun, C. (2023). Safety evaluation of steel temporary beam service status based on the combination weighting-fuzzy model of game theory. *Math. Problems Eng.* 2023. doi:10.1155/2023/6271946

Lin, K., Chen, H., Xu, C. Y., Yan, P., Lan, T., Liu, Z., et al. (2020). Assessment of flash flood risk based on improved analytic hierarchy process method and integrated maximum likelihood clustering algorithm. *J. Hydrology* 584, 124696. doi:10.1016/j.jhydrol.2020.124696

Liu, G., Zhang, C., Zhu, Z., and Wang, X. (2022). Power quality assessment based on rough AHP and extension analysis. *Energy Eng.* 119 (3), 929–946. doi:10.32604/ee.2022.014816

Ma, Y., Wei, J., Li, C., Liang, C., and Liu, G. (2020). Fuzzy comprehensive performance evaluation method of rolling linear guide based on improved analytic hierarchy process. *J. Mech. Sci. Technol.* 34, 2923–2932. doi:10.1007/s12206-020-0624-3

Paialunga, P., and Corcoran, J. (2023). Damage detection in guided wave structural health monitoring using Gaussian process regression. *Struct. Health Monit.*, 1, 147592172311593. doi:10.1177/14759217231159399

Tian, D., Wang, Y., and Yu, T. (2020). Fuzzy risk assessment based on interval numbers and assessment distributions. *Int. J. Fuzzy Syst.* 22, 1142–1157. doi:10.1007/s40815-020-00837-6

Wen, X., Nie, Y., Du, Z., and Huang, L. (2022). Operational safety assessment of straddle-type monorail vehicle system based on cloud model and improved CRITIC method. *Eng. Fail. Anal.* 139, 106463. doi:10.1016/j.engfailanal.2022.106463

Xia, P., Hu, X., Wu, S., Ying, C., and Liu, C. (2020). Slope stability analysis based on group decision theory and fuzzy comprehensive evaluation. *J. Earth Sci.* 31, 1121–1132. doi:10.1007/s12583-020-1101-8

Xu, X., Niu, D., Qiu, J., Wu, M., Wang, P., Qian, W., et al. (2016). Comprehensive evaluation of coordination development for regional power grid and renewable energy power supply based on improved matter element extension and TOPSIS method for sustainability. *Sustainability* 8 (2), 143. doi:10.3390/su8020143

You, P., Liu, S., and Guo, S. (2022). A hybrid novel fuzzy MCDM method for comprehensive performance evaluation of pumped storage power station in China. *Mathematics* 10 (1), 71. doi:10.3390/math10010071

Yucesan, M., and Kahraman, G. (2019). Risk evaluation and prevention in hydropower plant operations: a model based on Pythagorean fuzzy AHP. . *Energy policy* 126, 343–351. doi:10.1016/j.enpol.2018.11.039

Zeng, B., He, C., Mao, C., and Wu, Y. (2023). Forecasting China's hydropower generation capacity using a novel grey combination optimization model. *Energy* 262, 125341. doi:10.1016/j.energy.2022.125341

Zhang, B., Yan, X., Liu, G., and Fan, K. (2022). Multi-source fault diagnosis of chiller plant sensors based on an improved ensemble empirical mode decomposition Gaussian mixture model. *Energy Rep.* 8, 2831–2842. doi:10.1016/j.egyr.2022.01.179

Zhang, H., Li, W., Miao, P., Sun, B., and Kong, F. (2020a). Risk grade assessment of sudden water pollution based on analytic hierarchy process and fuzzy comprehensive evaluation. *Environ. Sci. Pollut. Res.* 27, 469–481. doi:10.1007/s11356-019-06517-9

Zhang, H., Xiu, B., Jiang, D., Zhuang, G., Zhang, Y., and Li, B. (2023). An evaluation method of health condition for wind turbine based on asymmetric proximity. *Front. Energy Res.* 11, 1111355. doi:10.3389/fenrg.2023.1111355

Zhang, S., Xiang, M., Xu, Z., Wang, L., and Zhang, C. (2020b). Evaluation of water cycle health status based on a cloud model. *J. Clean. Prod.* 245, 118850. doi:10.1016/j.jclepro.2019.118850

Zheng, K., Han, L., Guo, S., Wang, Z., Zhang, X., and Dong, X. (2017). Fuzzy synthetic condition assessment of wind turbine based on combination weighting and cloud model. *J. Intelligent Fuzzy Syst.* 32 (6), 4563–4572. doi:10.3233/jifs-169220

Zhu, L., Wu, Z., and Huang, S. (2023). Assessment method of distribution network health level based on multivariate information. *Front. Energy Res.* 11, 1178631. doi:10.3389/fenrg.2023.1178631

frontiers | Frontiers in Energy Research

TYPE Original Research
PUBLISHED 25 October 2023
DOI 10.3389/fenrg.2023.1275232

OPEN ACCESS

EDITED BY
Youbo Liu,
Sichuan University, China

REVIEWED BY
Gang Lei,
University of Technology Sydney, Australia
Chuan He,
Sichuan University, China
Siguang An,
China Jiliang University, China

*CORRESPONDENCE
Shiyou Yang,
eesyyang@zju.edu.cn

RECEIVED 09 August 2023
ACCEPTED 05 October 2023
PUBLISHED 25 October 2023

CITATION
Zhou H, Lu L, Shen L, Zhang P, Wen Y, Jiang H and Yang S (2023), Two-stage robust optimal capacity configuration of a wind, photovoltaic, hydropower, and pumped storage hybrid energy system. *Front. Energy Res.* 11:1275232. doi: 10.3389/fenrg.2023.1275232

Two-stage robust optimal capacity configuration of a wind, photovoltaic, hydropower, and pumped storage hybrid energy system

Hong Zhou[1], Liang Lu[1], Li Shen[1], Peng Zhang[1], YiYu Wen[1], Hongyu Jiang[2] and Shiyou Yang[2]*

[1]Development Planning Department, Southwest Branch of SGCC, Chengdu, China, [2]College of Electrical Engineering, Zhejiang University, Hangzhou, China

The hybrid energy system of hydro-powers, pumped storages and renewable energies has become a new topic direction in modern power system developments. Consequently, it is essential to realize a rational and efficient allocation of different energy source capacities. Nevertheless, there is still a gap between the available studies and the requirement for further hybrid energy system development. This paper focuses on the optimal capacity configuration of a wind, photovoltaic, hydropower, and pumped storage power system. In this direction, a bi-level programming model for the optimal capacity configuration of wind, photovoltaic, hydropower, pumped storage power system is derived. To model the operating mode of a pumped storage power station, two 0-1 variables are introduced. To handle the nonlinear and nonconvex lower level programing problem caused by the two 0-1 variables, it is proposed that the 0-1 variables are treated as some uncertain parameters. Also, by treating the 0-1 variables as some uncertain parameters, a two-stage robust optimization problem to decompose the original bi-level programing one into a master problem and a subproblem is finally introduced. The Karush-Kuhn-Tucker (KKT) conditions are then applied to simplify and linearize the min-max problem and nonlinear terms in the master problem. This results in both the master problem and the subproblem being formulated as mixed integer linear programming (MILP) problems. By utilizing the powerful Column-and-Constraint Generation (C&CG) algorithm, the two-stage robust optimization model is decomposed into an iterative procedure of solving the master problem and the subproblem sequentially. This approach eliminates the need for intricate optimization algorithms as commonly used in existing bi-level planning problems in hybrid energy systems. Finally, the effectiveness and advantages of the proposed model is verified by the numerical results on a case study.

KEYWORDS

hybrid energy system, two-stage robust optimization, C&CG algorithm, capacity configuration, pumped storage station

1 Introduction

Developing sustainable energies, particularly promoting the integration of clean energy sources into grid, is a crucial means to address the environmental pollution, the climate change, and the scarcity of fossil fuels (Huang et al., 2009). Consequently, in response to the global energy transition and the increasing prominence of environmental issues, the green energy sources such as photovoltaic and wind powers are receiving more and more attentions. For example, the wind power and photovoltaic installations in China have, respectively, reached 280 GW and 250 GW in year 2020 (Li et al., 2018). However, the intermittent and the fluctuating nature of the renewable energy sources, together with their high degree of uncertainty, lead to a deviation between the renewable energy generation capacity and the energy demand (Bao et al., 2021; Aien et al., 2014; Y et al., 2021). This intermittency, volatility, and anti-peak-shaving characteristics of the renewable energy sources can adversely affect the safe operation of the grid (Pothiya et al., 2008).

Pumped storage power plants, as energy storage facilities, operating on pumping and discharging modes, can be employed to effectively regulate the anti-peak-shaving characteristics of renewable energy sources, thus achieving de-peaking and valley-compensating functions (Zou et al., 2015; Liu et al., 2017). Moreover, hydropower plants possess flexible regulation capabilities (Wen et al., 2021). Obviously, both pumped storage power and hydropower plants are beneficial for mitigating the uncertainty of the renewable energy generation and facilitating the consumption of the renewable energy sources (Abdeltawab and Mohamed, 2017). Consequently, the hybrid energy system of hydropower, pumped storage, and renewable energy has become a new topic direction in modern power system developments.

In order to achieve a maximum economic benefit of the hybrid energy system throughout the duty cycle and ensure its competitiveness in the electricity market, it is essential to realize a rational and efficient allocation of different energy source capacities (Xu et al., 2020). In this direction, numerous efforts have been devoted to the operation and capacity allocation of hybrid energy systems incorporating pumped storage power stations. In the studies of (Baniasad and Ameri, 2012; Wang and Cui, 2014; Zhang et al., 2020), the authors have primarily focused on the economic and environmental issues of the hybrid energy system. The goal of these studies is to minimize the wind power curtailment, the generation cost, the penalties associated with pollutant emissions, and the penalties resulting from renewable energy power curtailments. The models for optimizing the schedule of hybrid energy systems incorporating pumped storage power plants are developed therein. In (Zhang et al., 2020), the authors have considered the integration of wind, photovoltaic, hydropower, thermal power, and other energy sources at a system level for the purpose of optimization their scheduling. In (Wang and Cui, 2014), the authors have investigated the optimal operation of pumped storage power plants in the context of photovoltaic integrations. In (Baniasad and Ameri, 2012), the authors have proposed a joint operation strategy for wind, photovoltaic and pumped storage hydro energy, taking into account the multiple performance benefits. However, a common limitation of these studies is that the capacity allocation of the energy storage systems, and the optimization of their operation and scheduling are considered relatively independently, without establishing a coupling between the two procedures and achieving their coordination.

To address the aforementioned deficiencies of the previously mentioned methodologies in hybrid energy system studies, in recent years, the bi-level programming has been widely applied in system optimizations involving the new energy system optimization. In (Zhao et al., 2014), the authors have used the upper-level procedure to minimize the annual total cost, while the lower-level to minimize the scenario-based distribution network operation cost. The upper-level procedure is used for planning, while the lower-level one performs optimization and simulation based on the upper-level planning. In (Zeng et al., 2017), the authors have employed the upper-level optimization to minimize the total investment cost, and the lower-level one to minimize the operating input. Particle swarm optimization algorithm and the interior point method are respectively used to solve the upper and lower-level optimization problems. Subsequently, most of the solution methodologies for such studies involve the use of complex optimization algorithms to separately solve the upper and lower level optimization problems. In (Luo et al., 2020), the authors have chosen a heuristic algorithm for the upper-level system planning problem, while a sequential quadratic programming algorithm for the lower-level one. In (Chen et al., 2021), the authors have improved a grey wolf algorithm based on tent mapping chaos optimization to solve the optimal capacity configuration of hybrid energy systems.

It should be pointed out that the aforementioned studies have mainly concentrated on a hybrid energy system where the thermal power occupies a large proportion of the system. As explained previously, with the global energy transformation and the concerns on environmental issues, the proportion of the thermal power in a hybrid energy system will be gradually decreased, and a zero-carbon hybrid energy system without any thermal power will emerge. Moreover, the solution approaches for the bi-level model of hybrid energy systems have predominantly been constrained to the application of intricate optimization algorithms for optimizations of the upper and lower-level functions. To bridge the gap between the available studies and the requirement for further hybrid energy system, this paper focuses on the optimal capacity configuration of wind, photovoltaic, hydropower, and pumped storage power system. In this direction, a bi-level programming model for the optimal capacity configuration of wind, photovoltaic, hydropower, and pumped storage power system is derived. To model the operating mode of a pumped storage power station, two 0-1 variables are introduced. To handle the nonconvex lower level programing problem caused by the two 0-1 variables, it is proposed that the 0-1 variables are treated as some uncertain parameters. Also, by treating the 0-1 variables as some uncertain parameters, a two-stage robust optimization procedure to decompose the original problem into a master problem and a subproblem is finally proposed. Moreover, by transforming the min-max form of the master problem using KKT conditions, both the master problem and the subproblem become MILP problems, and can be solved efficiently. Finally, the effectiveness and advantages of the proposed model is verified by solving a case study using the C&CG algorithm.

2 Bi-level model of the proposed hybrid energy systems

The hybrid energy system studied in this paper is consisted of pumped storages, hydro-powers, wind and photovoltaic powers. It

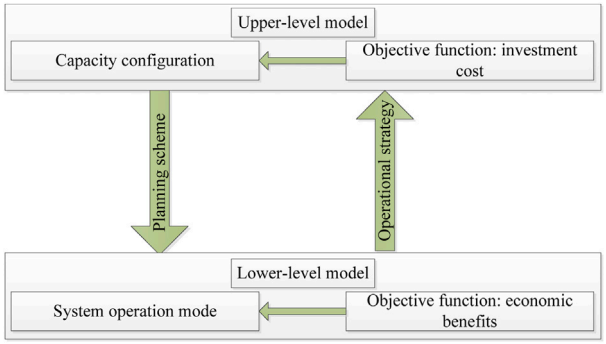

FIGURE 1
Schematic diagram of a bi-level programming.

uses the flexible regulation capabilities of hydropower and the energy storage capabilities of the pumped storage to mitigate the uncertainty of the renewable energy generation and to facilitate the consumption of the renewable energy sources. To optimize the capacity allocation of hydropower, pumped storage, and renewable energy of a hybrid energy system considering the coupling of different energy sources, a bi-level two-stage robust mathematical programming model is developed.

A bi-level programming, also known as a dual-layer optimization problem, is different from a conventional optimization one in its characteristics of hierarchy, independence, conflict, priority, and autonomy. It is typically mathematically expressed as:

$$\begin{cases} \min\limits_{x} F(x,y)\ s.t.\ \{f_1(x,y)\le 0,\cdots,f_n(x,y)\le 0\} \\ \min\limits_{y} G(x,y)\ s.t.\ \{g_1(x,y)\le 0,\cdots,g_n(x,y)\le 0\} \end{cases} \tag{1}$$

where, x and y represent the decision variables in the upper and lower-level respectively, $F(x, y)$ and $G(x, y)$ are the objective functions in the upper and lower-level optimizations respectively, f_n and g_n are the corresponding constraint conditions.

In the proposed bi-level optimization model, the upper-level minimizes the investment, while the lower-level optimize the operational plan based on optimized results in the upper-level, in order to achieve maximum economic benefits of the hybrid energy system. The upper-level allocates the capacity to the lower level under the condition that its own constraints are satisfied, and the lower-level designs the optimal power distribution under this capacity and transmits the results to the upper level, thereby influencing the upper level's decision-making (Boloukat and Foroud, 2018). It can be seen that there is a game relationship between the capacity, the power distribution, and the operation mode in the entire hybrid energy system; and this paper attempts to find a balance between the capacity and the power distribution in order to obtain the maximum economic benefits. The schematic diagram of the proposed bi-level programming model is shown in Figure 1.

2.1 Upper-level optimization model

2.1.1 The objective function

The goal of the upper-level optimization is to minimize the total investment of the whole hybrid energy system by determining the capacity allocation of the pumped storage and the small hydropower in the system. The total investment is composed of three parts: the construction investment, the operation and maintenance investment, and the replacement investment. Consequently, the mathematical expression of the upper-level model is given as:

$$\min(NPC) = \min\left(NPC_{\text{pump}} + NPC_{HS}\right) \tag{2}$$

where, NPC represents the total investment cost, NPC_{pump} represents the total cost of the pumped storage, and NPC_{HS} represents the total cost of the small hydropower. The formulas for calculating these costs are:

$$NPC_{pump} = C_{pump}P_{pump\_\max} + \sum_{n=1}^{T_a}\frac{C_{OP}P_{pump\_\max}}{(1+r)^n} + \frac{C_{rep\_pump}P_{pump\_\max}}{(1+r)^{T_{rep\_pump}}} \tag{3}$$

where, $P_{pump\_\max}$ represents the planned installed capacity of the pumped storage unit, C_{pump} refers to the unit price of the installed capacity per kilowatt, C_{OP} represents the operation and maintenance costs of the reversible pumped storage unit, T_a signifies the whole duty cycle, r denotes the discount rate, C_{rep_pump} represents the replacement cost of the pumped storage unit, T_{rep_pump} represents the lifespan of the pumped storage unit,

$$NPC_{\text{HS}} = C_{HS}P_{HS\_\max} + \sum_{n=1}^{T_a}\frac{C_{OH}P_{HS\_\max}}{(1+r)^n} + \frac{C_{rep\_HS}P_{HS\_\max}}{(1+r)^{T_{rep\_\text{HS}}}} \tag{4}$$

where, $P_{HS\_\max}$ represents the planned installed capacity of the hydropower unit, C_{HS} refers to the unit price of the installed capacity per kilowatt, C_{OH} represents the operating and maintenance costs of the hydropower unit, C_{rep_HS} represents the replacement cost of the hydropower unit, T_{rep_HS} represents the lifespan of the hydropower unit.

2.1.2 The constraints

1) Pumped storage unit constraint

The capacity of a pumped storage unit needs to satisfy the following constraint condition:

$$0 \le P_{pump\_\max} \le P_{pump\_power\max} \tag{5}$$

where $P_{pump\_power\max}$ represents the maximum value of the installed capacity of the reversible pumped storage unit.

2) Hydropower unit constraint

The capacity of the hydropower unit needs to satisfy the following constraint condition:

$$0 \le P_{HS\_\max} \le P_{HS\_power\max} \tag{6}$$

where $P_{HS\_power\max}$ represents the maximum value of the installed capacity of the hydropower unit.

3) Minimum power constraint

In the entire hybrid energy system, stabilizing the uncertainty of new energy outputs is proposed to be jointly accomplished by the pumped

storage and the small hydropower regulations. In addition, there is no any thermal power generation in the system to bear the base load. Consequently, the sum of the installed capacities of the aforementioned two power plants should be not less than the total of the curtailed wind and photovoltaic power at any given time instant. Moreover, the total energy production should also satisfy the load demand with an enough surplus. Therefore, the minimum power constraints on the two energy productions should satisfy the following constrains:

$$P_{HS\_\max} + P_{pump\_\max} \geq 2\max\left\{P_{w\text{-}q}(t) + P_{pv\text{-}q}(t), L(t) - P_W(t) - P_{PV}(t)\right\} \tag{7}$$

where, $P_{w\text{-}q}$ (t) represents the curtailed wind power, $P_{pv\text{-}q}$ (t) represents the curtailed photovoltaic power, L (t) represents the load, P_W (t) represents the wind power output, and P_{PV} (t) represents the photovoltaic power output, at time t.

2.2 Lower-level optimization model

2.2.1 The objective function

The goal in the proposed lower-level programing is to maximize the economic benefits of the hybrid energy system by optimizing its operational mode, given the capacity allocation from the upper-level procedure. Mathematically, the lower-level problem is formulated as:

$$\max(I) = \max\left\{\sum_{t=1}^{T} EP(t) \cdot \left[P_{PV}(t) + P_W(t) + P_{HS}(t) + P_{pump}(t)\right]\right\} \tag{8}$$

where, EP (t) represents the time-of-use electricity price, $P_{HS}(t)$ represents the electricity sold by a small hydropower power plant at time t, P_{pump} (t) represents the electricity sold by a pumped storage power station at time t, T represents the number of time periods, I represents the total revenue obtained from optimizing the operation.

The electricity sold by a pumped storage power station is calculated from:

$$P_{pump}(t) = \begin{cases} -1.1 \times \dfrac{P_{ch}(t)}{\eta_{ch}} \\ \eta_{dis} P_{dis}(t) \end{cases} \tag{9}$$

where, P_{ch} (t) represents the power consumed when the pumped storage power station operates in the pumping mode, so the electricity sold is negative as it requires purchasing electricity; P_{dis} (t) represents the power generated when the pumped storage power station operates in the discharging mode, so the electricity sold is positive. η_{ch} and η_{dis} represent the efficiencies of the pumping and discharging processes, respectively.

2.2.2 The constraints

1) Operation constraints of the pumped storage power station

In the operation of a pumped storage power station, different factors such as the maximum power of the units and the upstream reservoir capacity should be considered. Consequently, the following constraints are applied.

(a) Power constraint

The constraints applied to the power include:

$$\begin{cases} 0 \leq P_{dis}(t) \leq \min\left(P_{pump\_\max}, E_{pump\_\max}/h\right) \\ 0 \leq P_{ch}(t) \leq \min\left(P_{pump\_\max}, E_{pump\_\max}/h\right) \end{cases} \tag{10}$$

where, $E_{pump\_\max}$ represents the electricity generation corresponding to the maximum capacity of the upstream reservoir of the pumped storage power plant. It limits the maximum power in the operation of the pumped storage plant to be smaller than the minimum value between the maximum installed capacity of the units and the maximum electricity generation capacity based on the reservoir storage capacity.

(b) Reservoir capacity constraint

The constrains applied to the reservoir capacity are:

$$0 \leq \sum_{t=1}^{N_k} P_{pump}(t) \cdot \Delta t + 0.5 E_{pump\_\max} \leq E_{pump\_\max} \tag{11}$$

This constraint assumes that the initial reservoir capacity of the upstream reservoir is half of its maximum capacity. N_k represents the kth time period, Δt represents the length of the time periods, ensuring that the upstream reservoir capacity at each time is not smaller than zero and does not exceed its maximum capacity.

(c) Water inflow and outflow constraint

The constraint for the water inflow and the outflow is:

$$\sum_{t=1}^{T} P_{pump}(t) \cdot \Delta t = 0 \tag{12}$$

This constraint is used to ensure that the consumed electricity and generated electricity of the pumped storage power station remain consistent within a day, guaranteeing that the proposed model can still be applicable after 1 day.

2) Operation constraints of the small hydropower station

Similar to a pumped storage power station, a small hydropower station also needs to meet the following three constraints in operation.

(a) Power constraint

$$0 \leq P_{HS}(t) \leq \min\left(P_{HS\_\max}, E_{HS\_\max}/h\right) \tag{13}$$

where $E_{HS\_\max}$ represents the electricity generation corresponding to the maximum capacity of the upstream reservoir of the hydropower plant.

(b) Reservoir capacity constraint

$$0 \leq \sum_{t=1}^{N_k} P_{HS}(t) \cdot \Delta t + 0.5 E_{HS\_\max} \leq E_{HS\_\max} \tag{14}$$

(c) Water inflow and outflow constraint

$$\sum_{t=1}^{T} \left[P_{HSK}(t) \cdot \Delta t - P_{HS}(t) \cdot \Delta t\right] = 0 \tag{15}$$

where $P_{HSK}(t)$ represents the corresponding electricity generation capacity for the inflow volume of the water from the upstream at time t.

10.3389/fenrg.2023.1275232

3 Linearization and solution strategy

3.1 0-1 Variables and a two-stage robust optimization model

A pumped storage power station can not work simultaneously on the pumping and discharging modes. To model this phenomena, two 0-1 variables are introduced in Eq. 10. The two variables respectively indicate that the unit operates on pumping or discharging mode. Moreover, 0 represents that the unit does not operate in the mode in question, while 1 represents that the unit operates in the mode in question. By introducing these two 0-1 variables, the summation of the two variables at a time instant t should not exceed 1 to prevent the occurrence of the two working states simultaneously. Moreover,

$$\begin{cases} 0 \le P_{dis}(t) \le Z_{dis}(t) \cdot \min\left(P_{pump\_\max}, E_{pump\_\max}/h\right) \\ 0 \le P_{ch}(t) \le Z_{ch}(t) \cdot \min\left(P_{pump\_\max}, E_{pump\_\max}/h\right) \\ Z_{dis}(t) + Z_{ch}(t) \le 1 \; Z_{dis}(t), Z_{ch}(t) \in \{0,1\} \end{cases} \tag{16}$$

After the introduction of the aforementioned two 0-1 variables, the corresponding lower lever optimization problem becomes a nonlinear and nonconvex one, giving rise to difficulties in developing an efficient and accurate solution methodology. On the other hand, the minimization of the investment cost is only related to the capacities of the pumped storage power station and the small hydropower station, and is independent of the two 0-1 variables. In this point of view, the capacity planning and operation optimizing can be solved separately, and implemented in two consecutive phases. More specially, in the first phase, the decision on the capacity allocation is made, and are then transferred to the second phase. To transform the nonconvex lower level problem to a convex one, it is proposed that the 0-1 variables are treated as some uncertain parameters related to the second-stage decision variables, and are characterized by an uncertain set. As a result, a two-stage robust optimization problem is developed for the lower–level programming, and mathematically formulated as (Zeng and Zhao, 2013):

$$\begin{cases} \min\limits_{y} c^T y + \max\limits_{z \in Z} \max\limits_{x \in F(y,z)} b^T x \\ s.t. \quad Ay \ge d, Gx \ge h - Ey - Mz \end{cases} \tag{17}$$

where, x represents the decision variables for the optimal operation of the pumped storage and the small hydropower; y represents the decision variables for the capacity allocation; c, b, d, h, A, G, E, *and* M represent the deterministic parameters related to the decision variables; z represents the 0-1 variables, and the uncertain set composed of all possible values of z is denoted by Z; $F(y,z)$ represents the feasible domain of the inner level in the second stage, where the first stage decision variables y and uncertain parameter z are both fixed values at this phase. The corresponding robust "max max" problem in Eq. 17 is readily to be solved by any existing technique. Moreover, in Eq. 17, $c^T y$ corresponds to the upper-level model in Eq. 2, while $b^T x$ corresponds to the lower-level model in Eq. 8; z represents the 0-1 variables mentioned in Eq. 16. The constraints here include all the constraints of Eqs 5–7; Eqs 10–15.

After the aforementioned manipulations, the proposed optimization model is no longer a nonconvex optimization problem with 0-1 variables, but rather transformed into a convex two-stage robust optimization problem. It is readily to solve the corresponding problem by using a robust optimizer.

3.2 C&CG algorithm

To simplify the solution methodologies, the C&CG algorithm is used to solve the proposed two-stage robust optimization problems and its fundamental procedure is explained as: initially, only the decision variables and constraints of the first stage are considered, which is equivalent to taking a relaxed version of the original problem. The optimized decision variables of the first stage are then fixed, and the corresponding subproblem of the second stage is solved to find a possible worst-case scenario. The decision variables and constraints corresponding to this scenario are added to the master problem. As the number of variables and constraints in the main problem increases, the objective function values obtained from solving the master problem and subproblem gradually approaches each other until the algorithm converges.

The general form of the master problem is:

$$\begin{cases} \min\limits_{y} c^T y + \eta \\ s.t. \; Ay \ge d, Gx^l \ge h - Ey - Mz^l \\ \eta \ge b^T x^l \end{cases} \tag{18}$$

where, η represents the objective function of the second stage, x^l and u^l denote the decision variables and uncertain parameter values identified under the recognized scenario l.

The general form of the subproblem is:

$$\begin{cases} \max\limits_{z \in Z, x \in F(z,y)} b^T x \\ s.t. \; Gx \ge h - Ey - Mz \end{cases} \tag{19}$$

The lower bound of this subproblem determined by solving the master problem, while the solution of the subproblem provides an upper bound for the original problem. The upper and lower bounds are continuously updated by iterations, and their expressions are as follows:

$$\begin{cases} LB = \max\{c^T y_k^* + \eta_k^*, LB\} \\ UB = \min\{b^T x_k^*, UB\} \end{cases} \tag{20}$$

where, $y^* k$ represents the value of the decision variables in the first stage in the kth iteration, $x^* k$ represents the value of the decision variables in the second stage in the kth iteration, $\eta^* k$ represents the objective value in the second stage in the kth iteration, UB and LB represent the upper and lower bound. When the condition $|UB\text{-}LB| \le \varepsilon$ is satisfied, the iteration is stopped. To facilitate the numerical implementations of the proposed methodology, its flowchart is intuitively shown in Figure 2.

3.3 KKT equivalence

The Karush-Kuhn-Tucker (KKT) condition is usually used to simplify and linearize the double-layer structure and nonlinear terms existing in optimization models.

When solving the master problem, there exists a min-max problem that cannot be solved directly. However, for the inner level function in the second stage, the decision variables and uncertain parameters in the first stage are fixed, so the subproblem becomes a continuous linear optimization problem. KKT conditions can be used for reasonable equivalence (Korani and Eydi, 2021), that is, the lower-level objective function and constraint conditions are equivalent to KKT conditions, and then these KKT conditions are

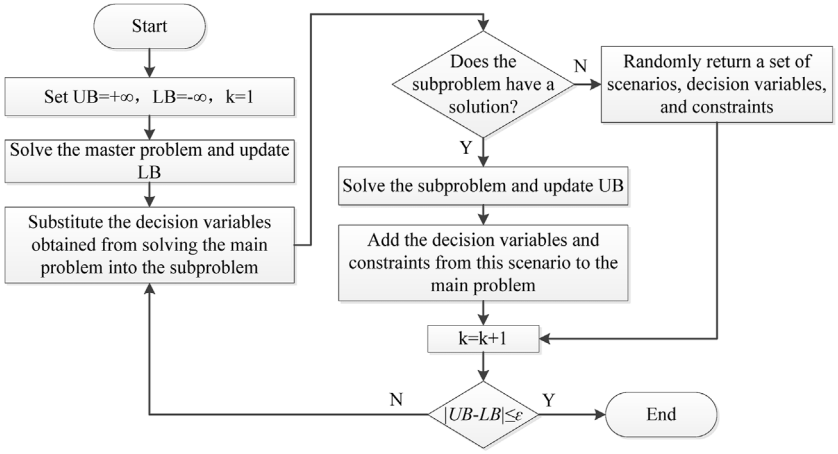

FIGURE 2
Flow chart of C&CG algorithm.

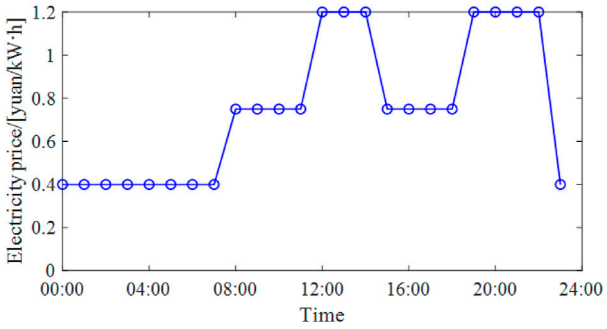

FIGURE 3
Electricity price variation in 1 day.

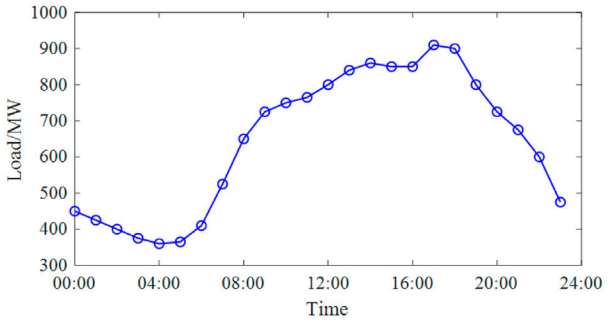

FIGURE 4
Typical daily load variations.

added to the upper-level model to form a complementary mathematical programming problem.

4 Case study

To validate the effectiveness and the applicability of the proposed model and methodology for the optimal capacity allocation of a hybrid energy system, the numerical results on a case study are given.

4.1 Prototype hybrid energy system

A typical daily scene in the southwestern part of China is selected as the scenario for optimizing and scheduling the hybrid energy system. The system is equipped with a total installed capacity of 207.5 MW wind power units, a total installed capacity of 1000 MW photovoltaic units, and a yet-to-be-optimized installed capacity of small hydropower and pumped storage.

In this study, the time-of-use electricity prices from an industrial park electricity trading in China are used for the system operation optimization in the lower-level planning model (Huang et al., 2022). The fluctuation trend of electricity prices is shown in Figure 3, indicating the presence of peak-valley fluctuations. Prices are higher during periods of higher electricity load, such as from 11:00 to 14:00 and 18:00 to 22:00, and lower during the night when electricity load is lower. This reflects that electricity prices are determined by the market.

The predicted loads, photovoltaic, and wind power outputs from an industrial park for the typical day in summer are shown in Figures 4–6, respectively. The technical and economic parameters of pumped storage and small hydropower units are given in Table 1, 2. From Figures 4–6, it can be observed that the typical daily loads exhibit two peaks before and after 13:00 and 18:00, with low wind power output and high photovoltaic output. However, the photovoltaic output shows significant fluctuations. The photovoltaic output roughly corresponds to the typical daily loads and demonstrates strong load tracking capabilities with peak-shaving characteristics.

4.2 Numerical results

In the numerical implementations of the proposed methodology, the optimization period for the typical day is T = 24 h, with a time

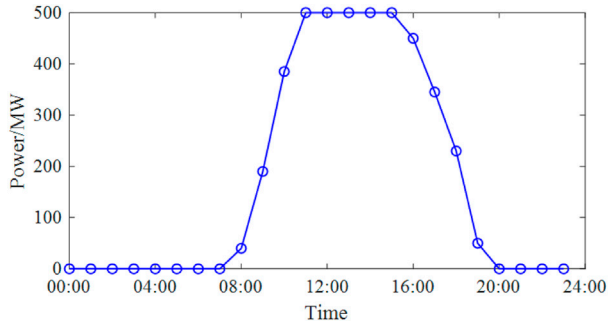

FIGURE 5
Typical daily photovoltaic output characteristics.

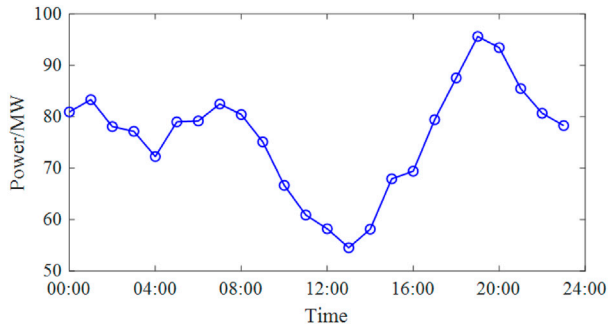

FIGURE 6
Typical daily wind power output characteristics.

TABLE 1 Technical and economic parameters of the pumped storage units.

Parameters	Value
Investment cost of pumped storage units/(yuan/kW)	2,100
Operation and maintenance cost/[yuan/(kW/year)]	21
Replacement cost/(yuan/kW)	2,100
Discount rate/%	4
Lifespan of the pumped storage unit/year	15
Project cycle/year	15
Water head/m	100
Maximum value of installed capacity/MW	1,000
Maximum capacity of upstream reservoir/MW·h	1,200
Efficiency of the pumping processes/%	80
Efficiency of the discharging processes/%	90

scale of Δt = 1 h. In order to analyse the impact of different energy storage modes in a hybrid energy system on the operational strategies of various power stations and the economic benefits throughout the duty cycle, and to verify the feasibility of optimizing the capacity

TABLE 2 Technical and economic parameters of the small hydro units.

Parameters	Value
Investment cost of small hydro units/(yuan/kW)	3,120
Operation and maintenance cost/[yuan/(kW/year)]	60
Replacement cost/(yuan/kW)	6,000
Discount rate/%	4
Lifespan of the pumped storage unit/year	15
Duty cycle/year	15
Water head/m	60
Maximum value of installed capacity/MW	1,000
Maximum capacity of upstream reservoir/MW·h	500
Efficiency of the units/%	85

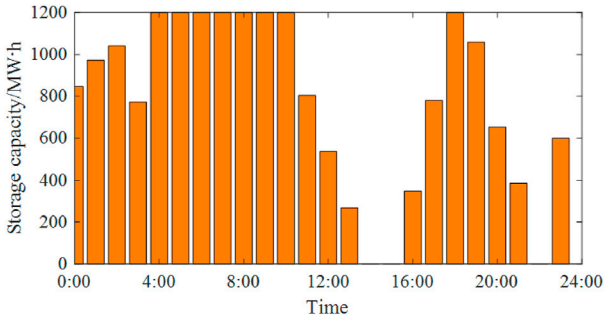

FIGURE 7
Optimized operation results of the hydropower station in the system with electricity storages.

allocation of the hybrid energy system using the proposed bi-level planning model, two different cases, the hybrid energy systems with and without electricity storages, are considered.

Using the model parameters and cost parameters set in Section 4.1, the planning model proposed in the paper is solved by the C&CG algorithm. According to the typical daily loads and renewable energy output, it is determined that the total installed capacity of the small hydropower and pumped storage needs to reach 1200 MW. The optimized capacity allocation scheme for the hybrid energy system with an energy storage is 500 MW for a pumped storage and 700 MW for a small hydropower. On the other hand, without any energy storage, the installed capacity of hydropower is 1200 MW. Obviously, with and without an electricity storage in the hybrid energy system will significantly affect the capacity allocation of the power plants and therefore influence the economic efficiency of the capacity allocation scheme over the entire duty cycle, as detailed in the proceeding sections. The model parameters and constraints can be abstracted from Table 1, 2.

The following will investigate the optimal capacity configuration of the system obtained through the planning model from the perspectives of the operation mode and the economic benefits of the hybrid energy system. This analysis aims to verify the

TABLE 3 Comparison of operation results of the hybrid energy system with/without electricity storages.

Parameters	With electricity storage	Without electricity storage
Load reduction/MW·h	2,334	2,892
renewable energy curtailments/MW·h	0	0
Photovoltaic benefits/(million yuan/day)	3.84	3.84
Wind power benefits/(million yuan/day)	1.356	1.356
Hydropower benefits/(million yuan/day)	7.99	6.669
Pumped storage benefits/(million yuan/day)	0.625	-
System benefits/(million yuan/day)	13.811	11.865
Recoup investment span/year	1.945	3.213

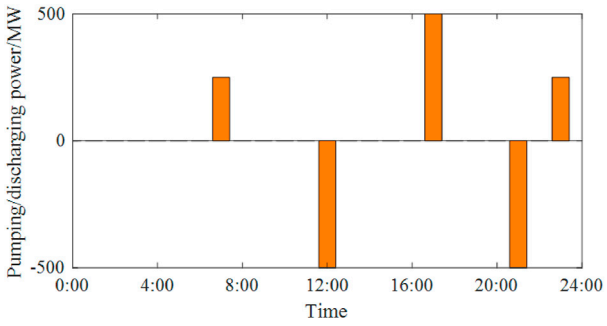

FIGURE 8
Optimized operation results of the pumped storage power station in the system with electricity storages.

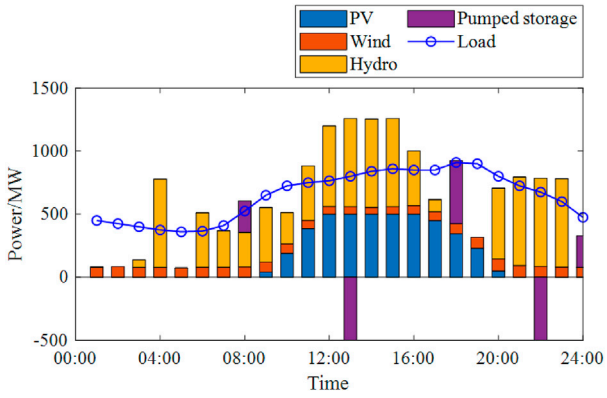

FIGURE 9
Optimized operation results of the hybrid energy system.

effectiveness of the planning model in solving the capacity optimization configuration problem of the hybrid energy system.

4.2.1 Operation mode of the system

The optimal operation results of the small hydropower plant with electricity storages is shown in Figure 7 (regardless of the dead water level). From the figure, it can be observed that the small hydropower plant adopts the following operational strategies based on the market electricity price: during the highest electricity price periods 11:00–14:00 and 18:00–22:00, the plant releases waters to generate electricity to maximize economic benefits while meeting all operational constraints. During the lowest electricity price period from 4:00 to 7:00 and the relatively lower electricity price period from 16:00 to 18:00, the water is stored by upstream inflow into the reservoir, so as to have sufficient water volumes for power generations during a high electricity price period.

In a system without any electricity storage, the operation results of the small hydropower plant is to continuously release waters through water turbine to generate electricity and sell it to the grid based on the natural flow rate. In this mode, only a small portion of the water flow exceeding the planned turbine capacity can be stored and sold in the peak electricity price periods. As a result, the annual revenue from electricity sales is relatively low, which is also reflected in Table 3.

The hourly pumping and discharge volumes of the reversible pump-turbine in the hybrid energy system with electricity storages are shown in Figure 8. In the lower-level planning model optimization operation mode, the pumped storage power station can receive powers generated by other power plants during the off-peak period (22:00 to 7:00), as well as purchase power from the grid. In the high electricity price periods (12:00 and 21:00), the power station releases water to generate electricity, thus ensuring profitable power sales for the system. By incorporating pumped storage power stations, the hybrid energy system enriches the power supply options and greatly affects the increase in the annual revenue from electricity sales.

4.2.2 Economic benefits of the system

The optimal operation results of the hybrid energy system are shown in Figure 9, and the comparisons of the operational outcomes with and without electricity storages according to various parameters are tabulated in Table 3.

The recoup investment span for the hybrid energy system with an electricity storage is 1.945 years, compared to 3.213 years in the system without any electricity storage. This indicates that, under the precondition of meeting the optimized operational mode of the hybrid energy system, the system with an energy storage has a higher

recoup investment rate compared to that of the system without any energy storage, other thing being equal.

Furthermore, the hybrid energy system with an electricity storage also reduces load reduction to a certain extent.

In addition to the recoup investment span of the hybrid energy system, the benefits obtained during its operation are also important indicators to measure the economy of the system. As shown in Table 3, the hybrid energy system with an energy storage generates a daily revenue of 13.811 million Chinese yuan from electricity sales, which is 1.16 times higher than that in the system without any energy storage.

The above results indicate that the hybrid energy system with an electricity storage can bring significant economic benefits throughout the project cycle, playing a crucial role in the development and investment of renewable energy generation companies.

5 Conclusion

This paper explores the capacity configuration and operational scheduling optimization of the pumped storage and small hydropower plants for a hybrid energy system of wind power, photovoltaic, small hydropower, and pumped storage power plants. In this respect, a two-stage robust optimization model and the corresponding solution methodology are proposed. The numerical results on a case study have demonstrated that integrating the energy storage in hybrid energy systems enhances the consumption capability of renewable energy while ensuring economic benefits, validating that the presented work effectively achieves the coordinated development between the energy storage and the new energy sources.

Data availability statement

The raw data supporting the conclusion of this article will be made available by the authors, without undue reservation.

Author contributions

HZ: Supervision, Conceptualization, Project administration, Resources, Writing–review and editing. LL: Writing–original draft, Investigation, Conceptualization. LS: Writing–original draft, Formal Analysis, Software, Resources. PZ: Data curation, Resources, Validation, Writing–review and editing. YW: Methodology, Conceptualization, Investigation, Writing–original draft. HJ: Methodology, Investigation, Validation, Writing–review and editing, Writing–original draft, Software. SY: Investigation, Writing–review and editing, Supervision, Funding acquisition.

Funding

The author(s) declare that no financial support was received for the research, authorship, and/or publication of this article.

Conflict of interest

Authors HZ, LL, LS, PZ and YW were employed by Southwest Branch of SGCC.

The remaining authors declare that the research was conducted in the absence of any commercial or financial relationships that could be construed as a potential conflict of interest.

The author(s) declared that they were an editorial board member of Frontiers, at the time of submission. This had no impact on the peer review process and the final decision.

Publisher's note

References

Abdeltawab, H. H., and Mohamed, A. R. I. (2017). Mobile energy storage scheduling and operation in active distribution systems. *IEEE Trans. Industrial Electron.* 64 (9), 6828–6840. doi:10.1109/tie.2017.2682779

Aien, M., Fotuhi-firuzabad, M., and Rashidinejad, M. (2014). Probabilistic optimal power flow in correlated hybrid wind-photovoltaic power systems. *IEEE Trans. Smart Grid* 5 (1), 130–138. doi:10.1109/tsg.2013.2293352

Baniasad, A. I., and Ameri, M. (2012). Techno-economic feasibility analysis of stand-alone renewable energy systems (PV/bat, wind/bat and hybrid PV/wind/bat) in Kerman, Iran. *Energy Sources Part B Econ. Plan. Policy* 7 (1), 45–60. doi:10.1080/15567240903330384

Bao, Y., Zhang, J., Xu, T., et al. (2021). Online transient stability risk assessment method considering the uncertainty of wind power output. *South. Power Syst. Technol.* 15 (11), 42–48. doi:10.13648/j.cnki.issn1674-0629.2021.11.005

Boloukat, M. H. S., and Foroud, A. A. (2018). Multiperiod planning of distribution networks under competitive electricity market with penetration of several microgrids part-I: modeling and solution methodology. *IEEE Trans. Industrial Inf.* 4 (11), 4884–4894. doi:10.1109/tii.2018.2807396

Chen, M., Tang, Y., Shang, W., et al. (2021). Optimal capacity configuration of pumped-storage power station in wind-pv-fire-pump storage system. *Electr. Power Constr.* 42 (11), 72–81. doi:10.12204/j.issn.1000-7229.2021.11.008

Huang, C., Liu, H., Ma, B., et al. (2022). Research on optimal operation of shared energy-storage power station applying nash negotiation. *Electr. Power Constr.* 43 (02), 1–9.

Huang, D., Shu, Y., Ruan, J., and Yi Hu, (2009). Ultra high voltage transmission in China: developments, current status and future prospects. *Proc. IEEE* 97 (3), 555–583. doi:10.1109/jproc.2009.2013613

Korani, E., and Eydi, A. (2021). Bi-level programming model and KKT penalty function solution approach for reliable hub location problem. *Expert Syst. Appl.* 184, 115505. doi:10.1016/j.eswa.2021.115505

Li, J., Liu, G., and Zhang, S. (2018). Smoothing ramp events in wind farm based on dynamic programming in energy internet. *Front. Energy* 12 (4), 550–559. doi:10.1007/s11708-018-0593-8

Liu, Y., Tan, S., and Jiang, C. (2017). Interval optimal scheduling of hydro-PV-wind hybrid system considering firm generation coordination. *IET Renew. Power Gener.* 11 (1), 63–72. doi:10.1049/iet-rpg.2016.0152

Luo, S., Hu, W., Huang, Q., et al. (2020). Optimization of photovoltaic/small hydropower/pumped storage power station system sizing under the market mechanism. *Trans. China Electrotech. Soc.* 35 (13), 2792–2804. doi:10.19595/j.cnki.1000-6753.tces.191843

Pothiya, S., Ngamroo, I., and Kongprawechnon, W. (2008). Application of multiple tabu search algorithm to solve dynamic economic dispatch considering generator constraints. *Energy Convers. Manage* 49 (4), 506–516. doi:10.1016/j.enconman.2007.08.012

Wang, H., and Cui, J. (2014). Optimal operation of pumped hydro energy storage in power system with large integration of photovoltaic generation. *Power Syst. Technol.* 38 (8), 2095–2101. doi:10.13335/j.1000-3673.pst.2014.08.012

Wen, J., Liu, J., Wen, Z., et al. (2021). Capacity allocation method for wind-solar-hydro-storage complementary system considering time and spatial transfer characteristics of load. *Electr. Power* 54 (02), 66–77+97. doi:10.11930/j.issn.1004-9649.202002151

Xu, X., Hu, W., Cao, D., Huang, Q., Chen, C., and Chen, Z. (2020). Optimized sizing of a standalone PV-wind-hydropower station with pumped-storage installation hybrid energy system. *Renew. Energy* 147, 1418–1431. doi:10.1016/j.renene.2019.09.099

Yang, X., Ding, L., Li, Y., et al. (2021). Study on optimal allocation of hybrid energy storage system considering wind power uncertainty. *Power Dsm* 23 (06), 69–74. doi:10.3969/j.issn.1009-1831.2021.06.014

Zeng, B., and Zhao, L. (2013). Solving two-stage robust optimization problems using a column-and-constraint generation method. *Operations Res. Lett.* 41 (5), 457–461. doi:10.1016/j.orl.2013.05.003

Zeng, Q., Zhang, B., Fang, J., and Chen, Z. (2017). A bi-level programming for multistage co-expansion planning of the integrated gas and electricity system. *Appl. Energy* 200, 192–203. doi:10.1016/j.apenergy.2017.05.022

Zhang, G., Chen, Y., Zhang, J., et al. (2020). Research on optimization of day-ahead dispatching of wind power-photovoltaic-hydropower-thermal power-pumped storage combined power generation system. *Acta Energiae Solaris Sin.* 41 (8), 79–85. doi:10.19912/j.0254-0096.2020.08.011

Zhao, Y., An, Y., and Ai, Q. (2014). Research on size and location of distributed generation with vulnerable node identification in the active distribution network. *Transm. Distribution* 8 (11), 1801–1809. doi:10.1049/iet-gtd.2013.0887

Zou, J., Lai, X., and Wang, N. (2015). Mitigation of wind curtailment by coordinating with pumped storage. *Proc. CSEE* 39 (9), 2472–2477. doi:10.13335/j.1000-3673.pst.2015.09.015

frontiers | Frontiers in Energy Research

TYPE Original Research
PUBLISHED 15 November 2023
DOI 10.3389/fenrg.2023.1240553

OPEN ACCESS

EDITED BY
Xin Zhang,
Brunel University London,
United Kingdom

REVIEWED BY
Xiangyu Kong,
Tianjin University, China
Nagesh Prabhu,
Nitte University, India

*CORRESPONDENCE
Xuebo Sun,
boxue_sg@163.com

RECEIVED 15 June 2023
ACCEPTED 31 October 2023
PUBLISHED 15 November 2023

CITATION
Wei Z, Sun X, Chen W and Shi J (2023), Identification of dominant propagation paths based on sub-synchronous oscillation using branch oscillation energy distribution coefficient. *Front. Energy Res.* 11:1240553. doi: 10.3389/fenrg.2023.1240553

Identification of dominant propagation paths based on sub-synchronous oscillation using branch oscillation energy distribution coefficient

Zhanhong Wei[1], Xuebo Sun[1,2]*, Wei Chen[1] and Jinhui Shi[1]

[1]College of Electrical and Information Engineering, Lanzhou University of Technology, Lanzhou, China, [2]Wuwei Power Supply Company of State Grid Gansu Provincial Electric Power Company, Wuwei, China

The large-scale integration of wind power into the power grid can cause a new type of sub-synchronous power oscillation, different from traditional thermal power generation. The oscillation energy will spread extensively in the grid, causing power oscillation and even grid-cascading events. To address this issue, this article proposes a method for quantitatively analyzing the propagation characteristics of oscillation energy based on branch oscillation energy. Firstly, analyzing the oscillation energy shared by different branches in the network based on transient energy function. Next, a method is proposed to identify the dominant propagation path of sub-synchronous oscillation by defining the oscillation energy of branches under the dominant oscillation mode and the oscillation energy distribution coefficient of each branch. The oscillation partition set formed by the dominant propagation path can be used to locate the high-risk oscillation area of the system. Finally, the effectiveness of the method proposed in this paper for studying the wide-area propagation characteristics of sub-synchronous oscillations was verified through time-domain simulation analysis.

KEYWORDS

sub-synchronous oscillations, branch oscillation energy, energy distribution factor, oscillation propagation path, high-risk oscillation area

1 Introduction

Currently, series compensation devices are widely used in the transmission lines of large-scale wind power grid-connected systems in China. However, in recent years, sub-synchronous oscillations caused by large-scale wind power being connected to the grid through series compensation have occurred multiple times (Li and Peng, 2016; Xie et al., 2017; Zhao et al., 2019), seriously affecting the large-scale transmission of new energy wind power and the safe and stable operation of the power grid (Chen et al., 2018). Multiple accidents have occurred globally where power transmission through series-compensated transmission lines from wind farms has caused sub-synchronous oscillations. In 2009, the Double Fed Wind Power Plant in Texas, United States, experienced sub-synchronous power oscillations due to the series-compensated transmission lines. The detection revealed sub-synchronous components of 20 Hz in the wind farm output current, leading to many wind turbines tripping and causing damage to the crowbar circuit (Adams et al., 2012). In 2011, Ontario, Canada also experienced sub-synchronous power oscillations of 9–13 Hz due to a

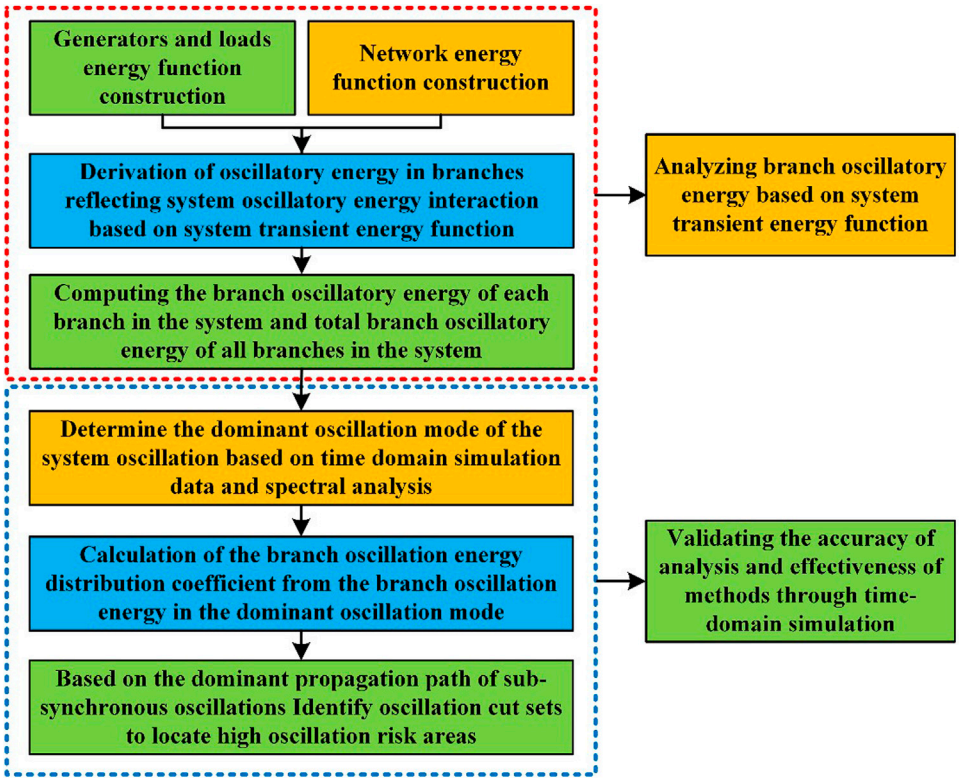

FIGURE 1
Block diagram of the research process.

double-fed wind power system connected through series compensation (Narendra et al., 2011). In 2012, the Guyuan Wind Farm in Hebei, China also experienced sub-synchronous oscillations of 6–8 Hz multiple times, resulting in a large number of wind turbines tripping and seriously affecting the safe operation of power grid equipment (Li et al., 2017). In 2015, a wind farm in Hami, Xinjiang, China experienced sub-synchronous oscillations of 20–40Hz, leading to the tripping of the generator rotor protection of a thermal power plant located 300 km away due to torsional vibration, causing it to be disconnected from the grid and shut down (Wang et al., 2015; Xie et al., 2016; Liu et al., 2017). These oscillation incident reports indicate that compared to direct-drive permanent magnet generator units, double-fed units are more susceptible to sub-synchronous oscillations incidents when series-compensated capacitors are present in the transmission line.

This type of sub-synchronous oscillation issue is typically believed to be caused by the sub-synchronous control interaction between the power electronic converter of the double-fed wind turbine generator and the series-compensated capacitor in the power system (Ostadi et al., 2009). Sub-synchronous oscillations caused by large-scale wind power grid integration typically involve multiple regions, units, and equipment. The sub-synchronous oscillation energy permeates from the wind farm side to the remote power system and spreads widely across multiple levels of the power system. Preliminary research results indicate that sub-synchronous oscillation energy has the characteristic of wide-area propagation in the power system (Ma et al., 2020).

Currently, research on disturbance energy propagation leading to system oscillations mainly focuses on the scope of electromechanical transients in power systems. In reference (Thorp et al., 1998), a mathematical model was established for the propagation of electromechanical disturbance energy. The concept of electromechanical waves was used to describe the evolution process of disturbance energy in the system. Reference (Ma and Wang, 2016) studied the dynamic characteristics of electromechanical wave reflection and transmission in a continuum model and explained from an energy perspective that the oscillation nature of power systems is the dynamic superposition of different frequency electromechanical waves during their propagation. The research in reference (Wang et al., 2017) showed that the dynamic characteristics of disturbance energy during its propagation are greatly influenced by the oscillation frequency. However, it remains to be further verified and explored whether the existing theory on electromechanical wave disturbances propagation applies to the wide-area propagation of sub-synchronous oscillations caused by large-scale wind power integration. Although phasor measurement units (PMUs) can provide wide-area measurement information, in practice, the PMUs only collect fundamental electrical quantities, and the electrical quantities of sub-synchronous frequency and various harmonic and inter harmonic components are filtered out by the filters. The traditional power frequency measurement method of PMUs is difficult to accurately measure the oscillating electrical quantities (Xie et al., 2019).

In reference (Ren et al., 2018), the transient energy flow method was applied to the study of sub-synchronous oscillations, and its physical meaning was discussed in depth, explaining the relationship between transient energy flow in oscillations and the power and damping in the system. However, the study was limited to sub-synchronous oscillations involving the generator shaft system. In reference (Cao et al., 2020), the transient energy flow method was used for oscillation source localization, and the transient energy flow of a doubly-fed wind turbine was derived. The direction of the energy flow during system oscillations was determined by the energy flow power index, and thus the forced oscillation source of the system was located. However, there was no research on the influence of the control parameters of the system inverter on the transient energy flow. Reference (Maslennikov et al., 2017) proposed a dissipation energy flow method to locate weakly-damped oscillation sources in the system using measured PMU data. However, network losses and load characteristics can affect the accuracy of the dissipation energy flow method, and further verification is needed to determine whether this method can be used for studying oscillation propagation characteristics. Reference (Ma et al., 2022) proposed an analysis method that combines the dissipation energy flow method with signal processing to locate and identify sub-synchronous oscillation sources. However, it is not possible to determine the diffusion and propagation path of oscillation energy in the system based solely on the branch dissipation energy flow.

Reference (Wen et al., 2019) proposed a sub-synchronous oscillation propagation factor that characterizes the propagating characteristics of sub-synchronous oscillations based on frequency domain methods. This factor is obtained from the transfer function matrix of the system, but no analysis was performed on the factors that affect the propagation factor during the study. Reference (Zhang et al., 2017) proposed a branching coefficient method to locate the propagation path of sub-synchronous oscillations caused by wind power integration into weak grids. However, this method did not consider the effect of oscillation power and can only characterize the propagation path of sub-synchronous currents in the system. In addition, the branching coefficients depend on the frequency characteristics and network structure of the system. Reference (Xie et al., 2020) proposed criteria and a framework for identifying sub-synchronous and super-synchronous oscillation sources based on measurements but did not provide a clear explanation of the specific form of oscillation power. Reference (Yang et al., 2021) analyzed the spreading characteristics of sub-synchronous oscillation power in different branches of the network through the proposed branching coefficient. However, it is difficult to determine the propagation strength of oscillation power at each node through quantitative analysis. Reference (Gong et al., 2019) studied the propagation characteristics of oscillating current along a weakly damped path based on an RLC circuit model under the condition of a single oscillation frequency. However, it did not consider the situation where different frequency components coexist and the propagation mechanism in complex networks. In the study presented in reference (Yang et al., 2019), a propagation factor was proposed to quantify the amplitude of oscillations propagated from one point to other points through a multi-input multi-output transfer function. However, it cannot identify the critical nodes and branches for the propagation of oscillation power in the network. Reference (Zhan et al., 2019) used frequency-domain modal analysis to identify the stability and propagation paths of oscillation modes in renewable energy-integrated systems. However, there was no specific quantitative analysis of the propagation paths of oscillation power at specific oscillation frequencies.

Exploring the evolution path of sub-synchronous oscillations can provide early warning of critical equipment and lines, and effectively interrupt the propagation path of sub-synchronous oscillations by adding damping control devices at weak nodes in the power grid, thereby mitigating its further development in the power grid. Currently, the wide-area propagation mechanism of sub-synchronous oscillation is still unclear, and its wide-area propagation characteristics need to be further explored from different perspectives.

In summary, studying the wide-area propagation characteristics of sub-synchronous oscillations, and tracking and locating the propagation path of sub-synchronous oscillations are the basis for effectively suppressing and blocking the development and evolution of sub-synchronous oscillations. Obtaining the propagation characteristics of oscillation power caused by large-scale wind power integration can deepen our understanding of the oscillation propagation mechanism, provide the basis for the location of oscillation propagation paths and regions, and ensure the warning, control, monitoring, and suppression of oscillations, ensuring the safe, stable, and economic operation of the “double high” power system for efficient export and integration of large-scale renewable energy power in China. This study will provide the foundation for enhancing the stability of new-generation high-penetration renewable energy power systems. Therefore, studying the wide-area propagation characteristics of sub-synchronous oscillations in the power grid has profound research significance.

The main contribution of this paper is to address the challenge of quantitatively analyzing the propagation characteristics of sub-synchronous oscillations generated by large-scale wind farms during grid integration. A quantitative analysis method is proposed based on branch oscillation energy to identify the dominant propagation paths of sub-synchronous oscillations. This method aims to determine the propagation and distribution patterns of oscillation energy within the system after oscillation occurrence. The research provides a foundation for the subsequent real-time monitoring, control, and wide-area warning and suppression of sub-synchronous oscillations. The specifc research process of the paper is shown in Figure 1.

2 Construction of system transient energy function

The method based on energy function construction is used to derive and construct the system’s transient energy function. Assuming there are N nodes in a certain power system, according to Kirchhoff’s current law in circuit theory, the system node voltage equation can be written as:

$$\boldsymbol{Y}\dot{\boldsymbol{U}} - \dot{\boldsymbol{I}}_{\mathrm{G}} + \dot{\boldsymbol{I}}_{\mathrm{L}} = 0 \tag{1}$$

Where $\dot{\boldsymbol{U}}$, $\dot{\boldsymbol{I}}_{\mathrm{G}}$, and $\dot{\boldsymbol{I}}_{\mathrm{L}}$ are n-dimensional complex vectors representing the system node voltage, generator output current, and current flowing into the load, respectively, and $\boldsymbol{Y}$ is the node admittance matrix of the system. At any moment, the system operation satisfies Equation 1 of the node voltage equation. From this, we can obtain:

10.3389/fenrg.2023.1240553

$$\left[\left(\boldsymbol{Y}\dot{\boldsymbol{U}}-\dot{\boldsymbol{I}}_{\mathrm{G}}+\dot{\boldsymbol{I}}_{\mathrm{L}}\right)^{*}\right]^{\mathrm{T}}\mathrm{d}\dot{\boldsymbol{U}}=0 \tag{2}$$

Taking the imaginary part of the above Equation 2 and integrating it, we can get:

$$\begin{aligned}&\int \mathrm{Im}\left\{\left[\left(\boldsymbol{Y}\dot{\boldsymbol{U}}-\dot{\boldsymbol{I}}_{\mathrm{G}}+\dot{\boldsymbol{I}}_{\mathrm{L}}\right)^{*}\right]^{\mathrm{T}}\mathrm{d}\boldsymbol{U}\right\}\\&=\int \mathrm{Im}\left[\sum_{i=1}^{n}\left(\sum_{j=1}^{n}\boldsymbol{Y}_{ij}^{*}\dot{\boldsymbol{U}}_{j}^{*}\right)\mathrm{d}\dot{\boldsymbol{U}}_{i}-\sum_{i\in i_{\mathrm{G}}}\dot{\boldsymbol{I}}_{\mathrm{G}i}^{*}\mathrm{d}\dot{\boldsymbol{U}}_{i}+\sum_{i\in i_{\mathrm{L}}}\dot{\boldsymbol{I}}_{\mathrm{L}i}^{*}\mathrm{d}\dot{\boldsymbol{U}}_{i}\right]\end{aligned} \tag{3}$$

In the equation, $\dot{\boldsymbol{I}}_{Gi}^{*}$and $\dot{\boldsymbol{I}}_{Li}^{*}$represent:

$$\dot{\boldsymbol{I}}_{\mathrm{G}i}^{*}=\frac{P_{\mathrm{G}i}+\mathrm{j}Q_{\mathrm{G}i}}{\dot{\boldsymbol{U}}_{i}}=\frac{P_{\mathrm{G}i}+\mathrm{j}Q_{\mathrm{G}i}}{U_{i}}\mathrm{e}^{-\mathrm{j}\theta_{i}} \tag{4}$$

$$\dot{\boldsymbol{I}}_{\mathrm{L}i}^{*}=\frac{P_{\mathrm{L}i}+\mathrm{j}Q_{\mathrm{L}i}}{\dot{\boldsymbol{U}}_{\boldsymbol{i}}}=\frac{P_{\mathrm{L}i}+\mathrm{j}Q_{\mathrm{L}i}}{U_{i}}\mathrm{e}^{-\mathrm{j}\theta_{i}} \tag{5}$$

Here, $\dot{\boldsymbol{U}}_{i}=U_{i}\mathrm{e}^{\mathrm{j}\theta_{i}}$, $\mathrm{d}\dot{\boldsymbol{U}}_{i}=\mathrm{e}^{\mathrm{j}\theta_{i}}\mathrm{d}U_{i}+\mathrm{j}U_{i}\mathrm{e}^{\mathrm{j}\theta_{i}}\mathrm{d}\theta_{i}$, $\boldsymbol{Y}=[G_{ij}+\mathrm{j}B_{ij}]$, and U_{i} is the amplitude of node i's voltage $\dot{\boldsymbol{U}}_{\boldsymbol{i}}$, and θ_{i} is the phase angle of node i's voltage $\dot{\boldsymbol{U}}_{\boldsymbol{i}}$.

2.1 Energy function of a generator

When a generator adopts a classical second-order model, its state equation is:

$$\begin{cases}\dfrac{\mathrm{d}\delta_{i}}{\mathrm{d}t}=\omega_{i}\\[2ex] M_{i}\dfrac{\mathrm{d}\omega_{i}}{\mathrm{d}t}=P_{mi}-P_{ei}-D_{i}\omega_{i}\end{cases} \tag{6}$$

In the equation, the unit of δ_{i} is radian, which represents the rotor angle of the generator, the unit of ω_{i} is rad/s, which represents the difference between synchronous speed and rotor angular speed, D_{i} is the damping coefficient, M_{i} is the inertia constant, P_{ei} and P_{mi} are the per-unit values of the electromagnetic power and mechanical power, respectively. Taking the imaginary part of the above equation and integrating it yields:

$$\begin{aligned}\int \mathrm{Im}\left(-\dot{\boldsymbol{I}}_{\mathrm{G}i}^{*}\mathrm{d}\dot{\boldsymbol{U}}_{i}\right)&=\int\left(-I_{xi}\mathrm{d}U_{yi}+I_{yi}\mathrm{d}U_{xi}\right)\\&=\int\left[-I_{xi}\mathrm{d}\left(U_{i}\sin\delta_{i}\right)+I_{yi}\mathrm{d}\left(U_{i}\cos\delta_{i}\right)\right]\\&=\int\left[-\left(I_{xi}U_{xi}+I_{yi}U_{yi}\right)\mathrm{d}\delta_{i}\right]=\int\left(-P_{ei}\mathrm{d}\delta_{i}\right)\\&=\int\left[-\left(P_{mi}-D_{i}\omega_{i}-M_{i}\frac{\mathrm{d}\omega_{i}}{\mathrm{d}t}\right)\mathrm{d}\delta_{i}\right]\\&=\int\left(-P_{mi}\mathrm{d}\delta_{i}+D_{i}\omega_{i}^{2}\mathrm{d}t+M_{i}\omega_{i}\mathrm{d}\omega_{i}\right)\\&=\sum_{i\in i_{\mathrm{G}}}\left(\tfrac{1}{2}M_{i}\omega_{i}^{2}-P_{mi}\delta_{i}\right)\Big|_{x_{0}}^{x}+\int D_{i}\omega_{i}^{2}\mathrm{d}t\end{aligned} \tag{7}$$

Equation 7 above is the energy function corresponding to the generator.

2.2 Energy function of the load

Usually, the changes in active and reactive power of a load with frequency and voltage variations can be described by algebraic equations using the static model of the load. When a constant power static load model is used for the load model, the following relationship is established:

$$\begin{aligned}\mathrm{Im}\left(\dot{\boldsymbol{I}}_{\mathrm{L}i}^{*}\mathrm{d}\dot{\boldsymbol{U}}_{i}\right)&=\mathrm{Im}\left[\frac{P_{\mathrm{L}i}+\mathrm{j}Q_{\mathrm{L}i}}{U_{i}\mathrm{e}^{\mathrm{j}\theta_{i}}}\left(\mathrm{e}^{\mathrm{j}\theta_{i}}\mathrm{d}U_{i}+\mathrm{j}U_{i}\mathrm{e}^{\mathrm{j}\theta_{i}}\mathrm{d}\theta_{i}\right)\right]\\&=\frac{Q_{\mathrm{L}i}}{U_{i}}\mathrm{d}U_{i}+P_{\mathrm{L}i}\mathrm{d}\theta_{i}\end{aligned} \tag{8}$$

Integrating the above equation gives the energy function of the load:

$$\int \mathrm{Im}\left(\dot{\boldsymbol{I}}_{\mathrm{L}i}^{*}\mathrm{d}\dot{\boldsymbol{U}}_{i}\right)=\sum_{i\in i_{\mathrm{L}}}\left(Q_{\mathrm{L}i}\ln U_{i}\,|_{U_{0}}^{U}+P_{\mathrm{L}i}\theta_{i}\,|_{\theta_{0}}^{\theta}\right) \tag{9}$$

2.3 Energy function of the network

The node's admittance matrix of the system is $\boldsymbol{Y}_{ij}=G_{ij}+\mathrm{j}B_{ij}$, assuming that the system is a lossless network, and the conductance G_{ij} is approximately zero, then there is the following relationship:

$$\begin{aligned}\mathrm{Im}\left[\sum_{i=1}^{n}\left(\sum_{j=1}^{n}\boldsymbol{Y}_{ij}^{*}\dot{\boldsymbol{U}}_{j}^{*}\right)\mathrm{d}\dot{\boldsymbol{U}}_{i}\right]&=\mathrm{Im}\left(\sum_{i=1}^{n}\left(\sum_{j=1}^{n}\left(-\mathrm{j}B_{ij}\right)U_{j}\mathrm{e}^{-\mathrm{j}\theta_{j}}\right)\left(\mathrm{e}^{\mathrm{j}\theta i}\mathrm{d}U_{i}+\mathrm{j}U_{i}\mathrm{e}^{\mathrm{j}\theta i}\mathrm{d}\theta_{i}\right)\right)\\&=-\sum_{i=1}^{n}\sum_{j=1}^{n}\left(B_{ij}U_{j}\cos\theta_{ij}\mathrm{d}U_{i}-B_{ij}U_{i}U_{j}\sin\theta_{ij}\mathrm{d}\theta_{i}\right)\end{aligned} \tag{10}$$

Sorting out the terms $i=j$ and the terms $i\neq j$ in Equation 10 above yields:

$$\mathrm{Im}\left[\sum_{i=1}^{n}\left(\sum_{j=1}^{n}\boldsymbol{Y}_{ij}^{*}\dot{\boldsymbol{U}}_{j}^{*}\right)\mathrm{d}\dot{\boldsymbol{U}}_{i}\right]=-\sum_{i=1}^{n}B_{ii}U_{i}\mathrm{d}U_{i}-\sum_{i=1}^{n-1}\sum_{j=i+1}^{n}B_{ij}\mathrm{d}\left(U_{i}U_{j}\cos\theta_{ij}\right) \tag{11}$$

Integrating the Equation 11 further gives:

$$\int \mathrm{Im}\left[\sum_{i=1}^{n}\left(\sum_{j=1}^{n}\boldsymbol{Y}_{ij}^{*}\dot{\boldsymbol{U}}_{j}^{*}\right)\mathrm{d}\dot{\boldsymbol{U}}_{i}\right]=\left(-\frac{1}{2}\sum_{i=1}^{n}B_{ii}U_{i}^{2}-\sum_{i=1}^{n-1}\sum_{j=i+1}^{n}B_{ij}U_{i}U_{j}\cos\theta_{ij}\right)\Bigg|_{(U_{0},\theta_{0})}^{(U,\theta)} \tag{12}$$

Equation 12 is also commonly referred to as transient electromagnetic potential energy in a network.

2.4 Transient energy function of the system

When the generator is modeled as a classical model and the load is modeled as a constant power model, assuming that the system is a lossless network and neglecting the system's damping, let W be:

$$\begin{aligned}W=&\sum_{i\in i_{\mathrm{G}}}\left(\tfrac{1}{2}M_{i}\omega_{i}^{2}-P_{mi}\delta_{i}\right)\Big|_{x_{0}}^{x}+\sum_{i\in i_{\mathrm{L}}}\left(Q_{\mathrm{L}i}\ln U_{i}\,|_{U_{0}}^{U}+P_{\mathrm{L}i}\theta_{i}\,|_{\theta_{0}}^{\theta}\right)\\&+\left(-\frac{1}{2}\sum_{i=1}^{n}B_{ii}U_{i}^{2}-\sum_{i=1}^{n-1}\sum_{j=i+1}^{n}B_{ij}U_{i}U_{j}\cos\theta_{ij}\right)\Bigg|_{(U_{0},\theta_{0})}^{(U,\theta)}\end{aligned} \tag{13}$$

Differentiating the sum of equations (7) and (9), and (12) yields:

$$\frac{\mathrm{d}W}{\mathrm{d}t}+\sum_{i\in I_{\mathrm{G}}}D_{i}\omega_{i}^{2}=\mathrm{Im}\left\{\left[\left(\boldsymbol{Y}\dot{\boldsymbol{U}}-\dot{\boldsymbol{I}}_{\mathrm{G}}+\dot{\boldsymbol{I}}_{\mathrm{L}}\right)^{*}\right]^{\mathrm{T}}\mathrm{d}\dot{\boldsymbol{U}}\right\}=0 \tag{14}$$

W in the above equations is the transient energy function of the entire system.

3 Analysis and quantification of branch oscillation energy

During sub-synchronous oscillations, branches can often reflect a lot of information about oscillation energy propagation and diffusion in the network. The oscillation energy of branch oscillations at the time of oscillation occurrence is analyzed according to the system energy function, and the dominant oscillation branches of the oscillation system are identified and located.

3.1 System energy function during oscillation

According to Kirchhoff's current law, it follows from $Y\dot{U} = \dot{I}_{ij}$ and Equation 2 that:

$$\sum_{i=1}^{n}\left(\sum_{j=1}^{n}\boldsymbol{Y}_{ij}^{*}\dot{\boldsymbol{U}}_{j}^{*}\right)-\sum_{i\in i_{\mathrm{G}}}\dot{\boldsymbol{I}}_{\mathrm{G}i}^{*}+\sum_{i\in i_{\mathrm{L}}}\dot{\boldsymbol{I}}_{\mathrm{L}i}^{*}=\sum_{i=1}^{n}\left(\sum_{j=1}^{n}\dot{\boldsymbol{I}}_{ij}^{*}\right)-\sum_{i\in i_{\mathrm{G}}}\dot{\boldsymbol{I}}_{\mathrm{G}i}^{*}+\sum_{i\in i_{\mathrm{L}}}\dot{\boldsymbol{I}}_{\mathrm{L}i}^{*}=0 \tag{15}$$

In Equation 15, the current flowing from node i to node j is $\dot{\boldsymbol{I}}_{ij}$, the current flowing out of the generator is $\dot{\boldsymbol{I}}_{\mathrm{G}i}$, the current injected into the load is $\dot{\boldsymbol{I}}_{\mathrm{L}i}$, all of which are n-dimensional complex vectors. Furthermore, Equation 15 can be derived as follows:

$$\left[\left(\sum_{i=1}^{n}\left(\sum_{j=1}^{n}\boldsymbol{Y}_{ij}^{*}\dot{\boldsymbol{U}}_{j}^{*}\right)-\sum_{i\in i_{\mathrm{G}}}\dot{\boldsymbol{I}}_{\mathrm{G}i}^{*}+\sum_{i\in i_{\mathrm{L}}}\dot{\boldsymbol{I}}_{\mathrm{L}i}^{*}\right)^{*}\right]^{\mathrm{T}}\mathrm{d}\dot{\boldsymbol{U}}_{i}=0 \tag{16}$$

When sub-synchronous oscillations occur in the system, the oscillation energy also appears accordingly. The total oscillation energy of the entire system during oscillation can be obtained by Equation 3 based on the above equation.

$$\begin{aligned}E_{s}&=\int\mathrm{Im}\left\{\left[\left(\sum_{i=1}^{n}\left(\sum_{j=1}^{n}\dot{\boldsymbol{I}}_{ij}^{*}\right)-\sum_{i\in i_{\mathrm{G}}}\dot{\boldsymbol{I}}_{\mathrm{G}i}^{*}+\sum_{i\in i_{\mathrm{L}}}\dot{\boldsymbol{I}}_{\mathrm{L}i}^{*}\right)^{*}\right]^{\mathrm{T}}\mathrm{d}\dot{\boldsymbol{U}}_{i}\right\}\\&=\int\mathrm{Im}\left[\sum_{i=1}^{n}\left(\sum_{j=1}^{n}\dot{\boldsymbol{I}}_{ij}^{*}\right)\mathrm{d}\dot{\boldsymbol{U}}_{i}-\sum_{i\in i_{\mathrm{G}}}\dot{\boldsymbol{I}}_{\mathrm{G}i}^{*}\mathrm{d}\dot{\boldsymbol{U}}_{i}+\sum_{i\in i_{\mathrm{L}}}\dot{\boldsymbol{I}}_{\mathrm{L}i}^{*}\mathrm{d}\dot{\boldsymbol{U}}_{i}\right]\end{aligned} \tag{17}$$

In the above equation, E_s represents the total oscillation energy in the system after oscillation occurs. During the oscillation process, the oscillation energy in the system interacts with each other between the sending and receiving ends of the transmission line. However, the total oscillation energy in the system is conserved, namely, the total oscillation energy in the system is a constant, denoted as $E_s = C$.

3.2 Energy function of branch oscillation

The transmission lines in the entire power network serve as the medium for the interaction and propagation of oscillation energy in the system. The electrical quantities and oscillation energy in the transmission lines reflect the oscillation characteristics and specific conditions of the whole system after oscillation occurs. At this point, the total oscillation energy of all transmission lines in the power network is defined as E_{B}:

$$\begin{aligned}E_{\mathrm{B}}&=C-\int\mathrm{Im}\left[\sum_{i\in i_{\mathrm{G}}}\dot{\boldsymbol{I}}_{\mathrm{G}i}^{*}\mathrm{d}\dot{\boldsymbol{U}}_{i}+\sum_{i\in i_{\mathrm{L}}}\dot{\boldsymbol{I}}_{\mathrm{L}i}^{*}\mathrm{d}\dot{\boldsymbol{U}}_{i}\right]\\&=\int\mathrm{Im}\left[\sum_{i=1}^{n}\left(\sum_{j=1}^{n}\dot{\boldsymbol{I}}_{ij}^{*}\right)\mathrm{d}\dot{\boldsymbol{U}}_{i}\right]\end{aligned} \tag{18}$$

For any branch in the network, the oscillation energy will be injected into the branch from one of its terminals. Therefore, the oscillation energy of branch $i-j$ is defined as:

$$\begin{aligned}E_{ij}&=\int\mathrm{Im}\left[\dot{\boldsymbol{I}}_{ij}^{*}\,\mathrm{d}\dot{\boldsymbol{U}}_{i}+\dot{\boldsymbol{I}}_{ji}^{*}\,\mathrm{d}\dot{\boldsymbol{U}}_{j}\right]\\&=\int\mathrm{Im}\left[\begin{array}{l}\dfrac{P_{ij}+\mathrm{j}Q_{ij}}{\dot{U}_{i}\mathrm{e}^{\mathrm{j}\theta_{i}}}\left(\mathrm{e}^{\mathrm{j}\theta_{i}}\mathrm{d}U_{i}+\mathrm{j}U_{i}\mathrm{e}^{\mathrm{j}\theta_{i}}\mathrm{d}\theta_{i}\right)\\+\dfrac{P_{ji}+\mathrm{j}Q_{ji}}{\dot{U}_{j}\mathrm{e}^{\mathrm{j}\theta_{j}}}\left(\mathrm{e}^{\mathrm{j}\theta_{j}}\mathrm{d}U_{j}+\mathrm{j}U_{j}\mathrm{e}^{\mathrm{j}\theta_{j}}\mathrm{d}\theta_{j}\right)\end{array}\right]\\&=\int\left(P_{ij}\mathrm{d}\theta_{i}+P_{ji}\mathrm{d}\theta_{j}+Q_{ij}\mathrm{d}\ln U_{i}+Q_{ji}\mathrm{d}\ln U_{j}\right)\end{aligned} \tag{19}$$

In the equation, P_{ij} is the active power flowing from node i to node j on the branch $i-j$, P_{ji} is the active power flowing from node j to node i on the branch $i-j$, and similarly, Q_{ij} and Q_{ji} are the reactive powers flowing from node i to node j and from node j to node i, respectively, on the branch $i-j$.

3.3 Branch mode oscillation energy

The total oscillation energy of all branches in the entire system is shared by each branch, and the difference in oscillation energy shared by each branch can reflect the distribution of oscillation energy in the whole system after oscillation occurs, indirectly reflecting the wide-area propagation characteristics of the oscillation energy. In practical engineering, when sub-synchronous oscillations occur in the system, the oscillation mode is often not unique, and there are oscillation characteristics with multiple sub-synchronous frequencies overlaid. Therefore, based on the derivation of branch oscillation energy and the existence of different oscillation modes during oscillation, research on the oscillation distribution of the entire system under different oscillation modes is conducted.

During system oscillation, various electrical quantities are composed of the steady-state component of power frequency and the sub-synchronous oscillation component of different frequencies. The active power of a branch during system oscillation is defined as:

$$\begin{cases}P_{\mathrm{b}}=P_{1}+P_{\mathrm{s}}\\P_{\mathrm{s}}=P_{\lambda1}+\cdots+P_{\lambda\mathrm{k}}\end{cases} \tag{20}$$

In the equation, P_{b} is the active power of the branch during oscillation, P_1 is the steady-state active power component of the branch during oscillation, P_{s} is the sub-synchronous frequency oscillation component of the active power of the branch during oscillation, and $P_{\lambda1},\cdots,P_{\lambda\mathrm{k}}$ is the sub-synchronous frequency oscillation component of the active power of different oscillation modes in the system. Similarly, other electrical quantities have a

similar compositional form as in Equation 20. At this point, the branch oscillation energy can be expressed as:

$$E_{ij} = \int \begin{bmatrix} \left(P_{ij-1} + P_{ij-s}\right)\mathrm{d}\left(\theta_{i-1} + \theta_{i-s}\right) + \left(P_{ji-1} + P_{ji-s}\right)\mathrm{d}\left(\theta_{j-1} + \theta_{j-s}\right) \\ + \left(Q_{ij-1} + Q_{ij-s}\right)\mathrm{d}\left(\ln U_{i-1} + \ln U_{i-s}\right) \\ + \left(Q_{ji-1} + Q_{ji-s}\right)\mathrm{d}\left(\ln U_{j-1} + \ln U_{j-s}\right) \end{bmatrix} = \int \begin{bmatrix} \left(P_{ij-1} + P_{ij,\lambda1} + \cdots + P_{ij,\lambda k}\right)\mathrm{d}\left(\theta_{i-1} + \theta_{i,\lambda1} + \cdots + \theta_{i,\lambda k}\right) \\ + \left(P_{ji-1} + P_{ji,\lambda1} + \cdots + P_{ji,\lambda k}\right)\mathrm{d}\left(\theta_{j-1} + \theta_{j,\lambda1} + \cdots + \theta_{j,\lambda k}\right) \\ + \left(Q_{ij-1} + Q_{ij,\lambda1} + \cdots + Q_{ij,\lambda k}\right)\mathrm{d}\left(\ln U_{i-1} + \ln U_{i,\lambda1} + \cdots + \ln U_{i,\lambda k}\right) \\ + \left(Q_{ji-1} + Q_{ji,\lambda1} + \cdots + Q_{ji,\lambda k}\right)\mathrm{d}\left(\ln U_{j-1} + \ln U_{j,\lambda1} + \cdots + \ln U_{j,\lambda k}\right) \end{bmatrix} \tag{21}$$

Although there are multiple oscillation modes during system oscillation, there are usually a few dominant oscillation modes that have much larger oscillation energy than other oscillator modes. Additionally, the steady-state component of power frequency is much larger than the sub-synchronous frequency oscillation component during oscillation. Assuming that the dominant oscillation modes in the oscillating system are modes $\lambda1$ and $\lambda2$, and only consider active power, which is represented by the first term in Equation 21, the following relationship exists:

$$\left\{\int P_{ij-1}\mathrm{d}\theta_{i,\lambda1}、\ \int P_{ij-1}\mathrm{d}\theta_{i,\lambda2}\right\} \gg \left\{\begin{matrix} \int P_{ij,\lambda1}\mathrm{d}\theta_{i,\lambda1}、\ \int P_{ij,\lambda1}\mathrm{d}\theta_{i,\lambda2}、 \\ \int P_{ij,\lambda2}\mathrm{d}\theta_{i,\lambda1}、\ \int P_{ij,\lambda2}\mathrm{d}\theta_{i,\lambda2}、 \end{matrix}\right\} \tag{22}$$

$$\int P_{ij-1}\mathrm{d}\theta_{i-1} = \int P_{ij,\lambda1}\mathrm{d}\theta_{i-1} = \int P_{ij,\lambda2}\mathrm{d}\theta_{i-1} = 0 \tag{23}$$

The following relationship can be obtained in this case:

$$\begin{aligned} \int\left[\left(P_{ij-1} + P_{ij-s}\right)\mathrm{d}\left(\theta_{i-1} + \theta_{i-s}\right)\right] &\approx \int P_{ij-1}\mathrm{d}\theta_{i,\lambda1} + \int P_{ij-1}\mathrm{d}\theta_{i,\lambda2} \\ &\approx P_{ij-1}\cdot\theta_{i,\lambda1} + P_{ij-1}\cdot\theta_{i,\lambda2} + C_1 + C_2 \end{aligned} \tag{24}$$

Similar to the derivation process above, simplifying all terms in Equation 21 yields:

$$\begin{aligned} E_{\mathrm{b}ij} &\approx \left(P_{ij-1}\cdot\theta_{i,\lambda1} + P_{ji-1}\cdot\theta_{j,\lambda1}\right) + \left(P_{ij-1}\cdot\theta_{i,\lambda2} + P_{ji-1}\cdot\theta_{j,\lambda2}\right) \\ &\quad + \left(Q_{ij-1}\cdot\ln U_{i,\lambda1} + Q_{ji-1}\cdot\ln U_{j,\lambda1}\right) \\ &\quad + \left(Q_{ij-1}\cdot\ln U_{i,\lambda2} + Q_{ji-1}\cdot\ln U_{j,\lambda2}\right) + C_3 \\ &= E_{\mathrm{b}ij,\lambda1} + E_{\mathrm{b}ij,\lambda2} + C_3 \end{aligned} \tag{25}$$

The above equation represents the branch mode oscillation energy under the dominant oscillation mode. In this equation, A represents the branch mode oscillation energy under oscillation mode B, while C represents the branch mode oscillation energy under oscillation mode D. The specific relationship they satisfy is shown in Equation 26:

$$\begin{cases} E_{\mathrm{b}ij,\lambda1} = \left(P_{ij-1}\cdot\theta_{i,\lambda1} + P_{ji-1}\cdot\theta_{j,\lambda1}\right) + \left(Q_{ij-1}\cdot\ln U_{i,\lambda1} + Q_{ji-1}\cdot\ln U_{j,\lambda1}\right) \\ \qquad = E_{\mathrm{b}ij,\lambda1-\mathrm{P}} + E_{\mathrm{b}ij,\lambda1-\mathrm{Q}} \\ E_{\mathrm{b}ij,\lambda2} = \left(P_{ij-1}\cdot\theta_{i,\lambda2} + P_{ji-1}\cdot\theta_{j,\lambda2}\right) + \left(Q_{ij-1}\cdot\ln U_{i,\lambda2} + Q_{ji-1}\cdot\ln U_{j,\lambda2}\right) \\ \qquad = E_{\mathrm{b}ij,\lambda2-\mathrm{P}} + E_{\mathrm{b}ij,\lambda2-\mathrm{Q}} \end{cases} \tag{26}$$

3.4 Identification of dominant paths for oscillation propagation

Based on the derived oscillation energy of the branch mode defined in the previous section, this section defines the oscillation energy distribution coefficient of the branch and proposes a method for identifying the dominant propagation path of sub-synchronous oscillation based on the oscillation energy distribution coefficient of the branch. The dominant propagation path of sub-synchronous oscillation can be identified by the difference in the oscillation energy distribution coefficients of different branches. The branches with higher oscillation energy distribution coefficients are also the most fragile branches that share the most oscillation energy in the system. These fragile branches together form the oscillation cut set of the system. The oscillation cut set can be used to locate the areas of high oscillation risk in the system after oscillation occurs. Therefore, the identification of the dominant propagation path of the system oscillation can be completed by locating the area of dominant oscillation in the system.

The oscillation energy distribution coefficient (OEDC) of the branch $i-j$ under the dominant oscillation mode λk in the power network is specifically defined as:

$$OEDC = \alpha = \frac{E_{\mathrm{b}ij,\lambda\mathrm{k}}}{E_{\mathrm{B}}} = \frac{E_{\mathrm{b}ij,\lambda\mathrm{k}}}{\sum_{i=1}^{n}\sum_{j=1}^{n} E_{\mathrm{b}ij,\lambda\mathrm{k}}} \tag{27}$$

In the equation, E_{B} represents the total oscillation energy of all branches in the entire power network under oscillation mode λk, $E_{\mathrm{b}ij,\lambda\mathrm{k}}$ represents the oscillation energy of branch $i-j$ under oscillation mode λk, and n represents the number of nodes in the system.

The main steps of the method are as follows:

(1) Using the time-domain simulation platform built for the doubly fed wind farm connected to the grid system with series capacitor compensation, set the relevant parameters in the simulation model to excite sub-synchronous oscillation phenomena in the system. After the system generates oscillations, calculate the oscillation energy $E_{\mathrm{b}ij}$ of all branches in the network and the total oscillation energy E_{B} of all branches in the system using Equation 19 based on the time-domain simulation data of various electrical quantities in the system.

(2) Obtain the dominant oscillation mode λk of the system through spectrum analysis, and then obtain the oscillation energy of the branch mode under the dominant oscillation mode and the total oscillation energy of all branch modes under the dominant oscillation mode, and then calculate the oscillation energy distribution coefficient of the oscillation mode according to the definition.

(3) The size of the oscillation energy distribution coefficient of all branches in the system is used to determine and identify the dominant paths of oscillation propagation. These dominant paths of oscillation propagation are often fragile branches with lower damping in the system. Therefore, after identifying the dominant paths of oscillation propagation, these fragile branches are defined as the oscillation cut set of the system, and the oscillation energy distribution coefficients of the branches included in the oscillation cut set are compared under the dominant oscillation mode. Based on the size of the oscillation energy shared by the oscillation cut set, the high oscillation risk area of the system can be further located.

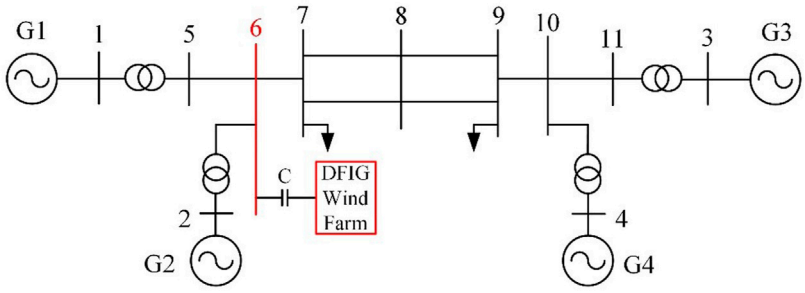

FIGURE 2
The equivalent model of the four-machine two-area system with the doubly fed wind farm connected to it through a series compensating line.

4 Case analysis

To verify the accuracy of the theoretical analysis and the effectiveness of the proposed research method in this paper, a simulation system model of sub-synchronous oscillation is constructed based on the PSCAD/EMTDC simulation platform. The simulation models include a doubly fed wind power plant with series compensating lines connected to a four-machine two-area system and an IEEE 10-machine 39-bus system, and are subjected to time-domain simulation analysis and verification.

4.1 Single oscillation source case study of four-machine two-area system

The time-domain simulation verification of the series capacitor compensated line connected to the four-machine two-area small system is carried out by connecting the doubly fed wind power plant with series capacitor compensated lines to Node 6. The doubly-fed wind power plant connected to Node 6 is equivalent to 40 doubly-fed wind turbines with the same parameters of the rated power of 5MW, which operate under the same control parameters and at their rated states. The system frequency is 60 Hz. The doubly fed wind power plant is stepped up through a 0.69kV/35 kV transformer before being connected to the busbar, then stepped up again through a 35kV/230 kV transformer before being connected to the series capacitor compensated line, and finally connected to Node 6 of the four-machine two-area system through the series capacitor compensated line, as shown in Figure 2.

40 doubly fed wind turbines are integrated into the system for steady-state operation. At 1s of the system operation, series compensating capacitors are put into operation and the series compensation degree is set to 30%, which excites the occurrence of sub-synchronous oscillation phenomenon. Data is recorded continuously for 4 s from 1 s before the onset of oscillation. The current output and its frequency spectrum analysis of the wind farm are shown in Figure 3, while the measured output power and its frequency spectrum analysis of one phase of the wind farm are shown in Figure 4.

From Figure 3, it can be observed that in the steady-state stage before introducing the series compensating line, the system frequency is only at the steady-state power frequency. When the series compensating capacitor is introduced at 1 s, the wind farm output current quickly diverges. By the time it reaches 2 s, the wind farm output current tends to a state of equal amplitude oscillation. During the equal amplitude sub-synchronous oscillation stage, the current waveform contains not only the steady-state power frequency component of 928A and 59 Hz, but also sub-synchronous components with an amplitude of 1.69 kA and frequency of 13.5 Hz, as well as an amplitude of 136A and frequency of 32 Hz (small enough to be ignored). During the rapid divergence stage of the oscillation, in addition to containing the steady-state power frequency component of 683A and 59 Hz, there are also sub-synchronous components with an amplitude of 958A and frequency of 28.3 Hz, as well as an amplitude of 740A and frequency of 13.7 Hz. From Figure 4, it can be seen that in the power waveform after exciting the sub-synchronous oscillation, there are sub-synchronous components with an amplitude of 18.7 MW and frequency of 31.25 Hz, as well as an amplitude of 40.1 MW and frequency of 45.5 Hz.

It can be inferred from this that after the system is excited into sub-synchronous oscillation, the system exhibits sub-synchronous oscillation characteristics in which the sub-synchronous frequency of the oscillating current and the sub-synchronous frequency of the oscillating power complement each other, that is, the sum of the sub-synchronous oscillation current frequency and the sub-synchronous oscillation power frequency is the steady-state power frequency of the system at 60 Hz.

At this point, the oscillation power and its spectrum of the four generator outlet branches in the system are obtained, as shown in Figure 5. It can be seen that the oscillation amplitudes in the outlet branches of generators G1 and G2 in the sending end area are the largest, and the oscillations are the most obvious among all. The amplitude corresponding to the sub-synchronous oscillation frequency is also the largest. It can be inferred that the oscillation energy shared by the branches around these sending-end generators is also relatively large.

At the same time, the dominant sub-synchronous oscillation mode of the system is the sub-synchronous oscillation mode with an equal wind farm output amplitude of 18.7 MW and frequency of 31.25 Hz, and amplitude of 40.1 MW and frequency of 45.5 Hz. The sub-synchronous oscillation component with a frequency of 31.25 Hz is defined as system oscillation mode one, and the sub-synchronous oscillation component with a frequency of 45.5 Hz is defined as system oscillation mode two. Based on the quantified index of the oscillation energy of the defined branch mode and the

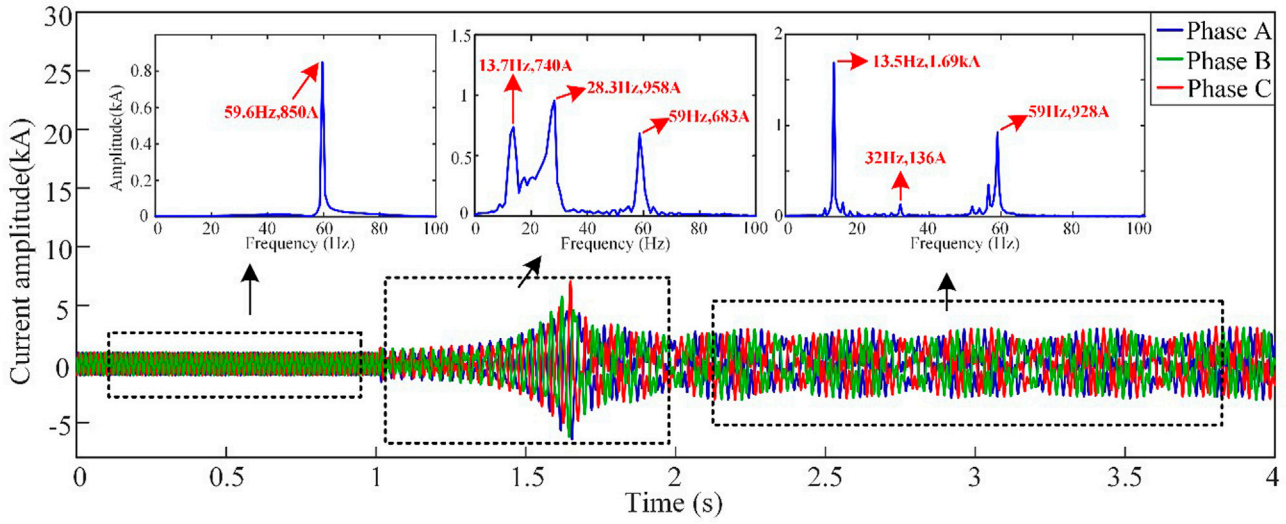

FIGURE 3
Wind farm output current and frequency spectrum in different time periods.

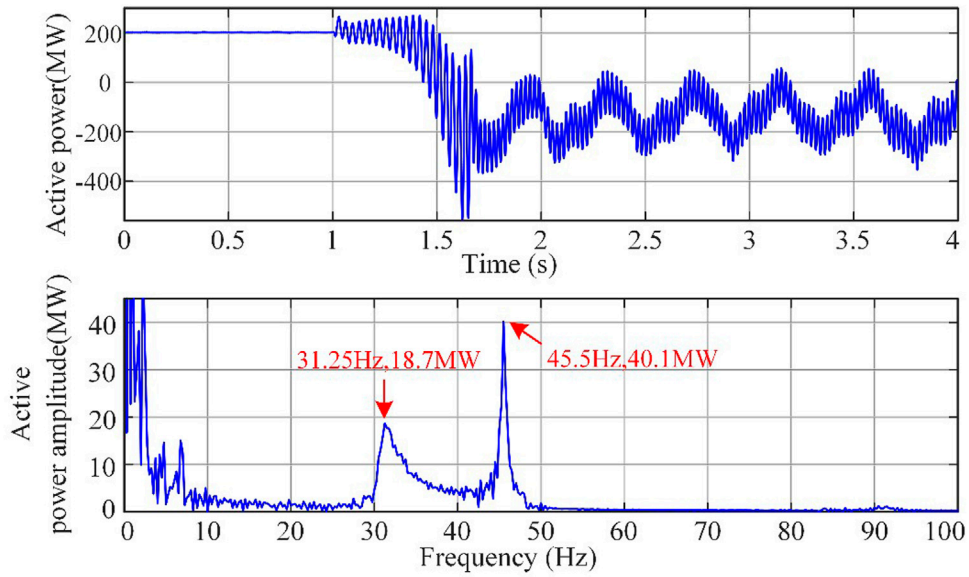

FIGURE 4
Wind farm output power and its spectral analysis.

oscillation energy distribution system, the oscillation energy of each branch of the system is analyzed and calculated, and the oscillation energy distribution coefficients of each branch are obtained for the two oscillation modes of the system, as shown in Figure 6. It can be observed from the figure that the oscillation energy distribution coefficients of branches 1–5, 2–6, 5-6, and 6-7 are relatively large, and the oscillation energy distribution coefficients of the branches far from the oscillation source are relatively small. Branch 9–10 is located at the sending end of area 2 in the four-machine system, so the oscillation energy distribution coefficient on this branch increases. Furthermore, in the branches after node 6 where the oscillation source is connected, the oscillation energy distribution coefficient of mode one with a frequency of 31.25 Hz is greater than that of mode two with a frequency of 45.5 Hz, starting from branch 6–7.

From this, it can be inferred that oscillation modes with higher frequencies generally have less effect on distant areas of the system, while oscillation modes with lower frequencies have a wider range of energy propagation and a greater impact on distant areas of the system. Therefore, in the power grid, oscillation components with lower frequencies contain more energy than those with higher frequencies, and are less likely to be dissipated in the grid.

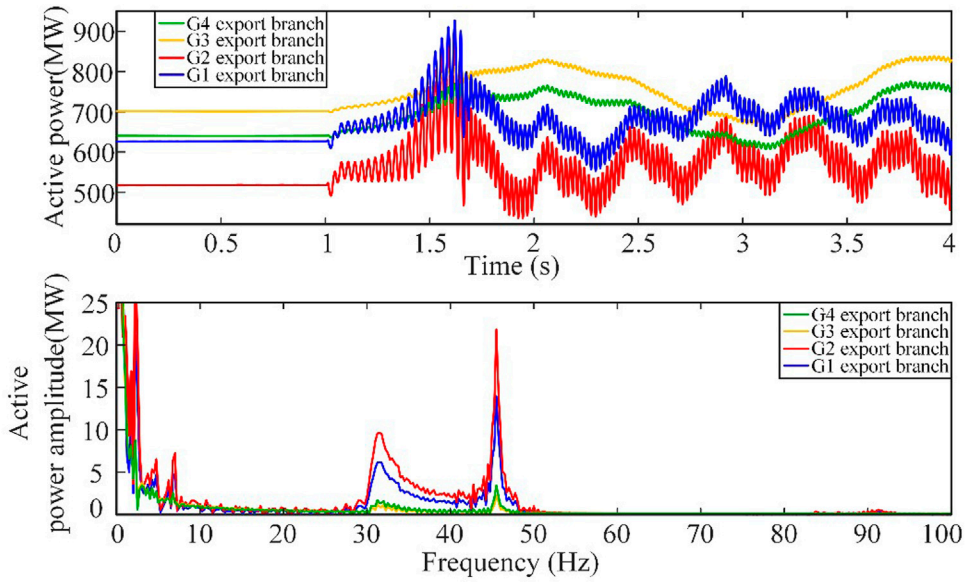

FIGURE 5
Oscillating power and spectrum of generator export branches.

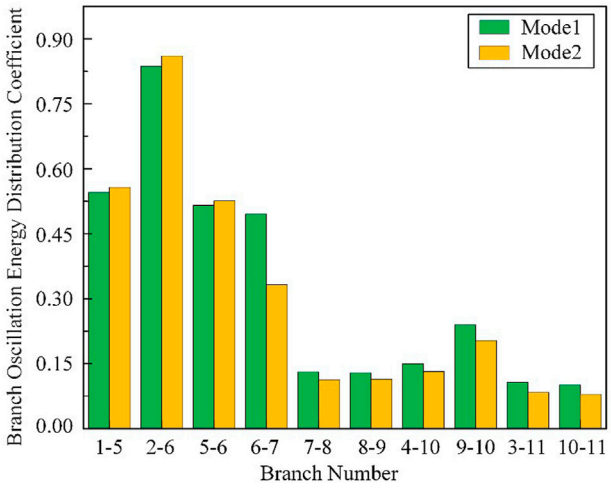

FIGURE 6
Oscillation energy distribution coefficient of each branch in the system.

Consequently, the sub-synchronous oscillation components with lower frequencies propagate to farther areas in the grid and have a greater impact on the oscillation range.

Based on the calculation and analysis of the oscillation energy distribution coefficients of each branch in the system, the dominant paths of oscillation propagation can be identified, and the fragile branches that bear larger oscillation energy can be located. These fragile branches form the oscillation-cut set of the system, as shown in the blue dashed line in Figure 7 for the four-machine two-area system. The oscillation high-risk areas in the studied system can be further located based on these oscillation-cut sets. In the subsequent research, with the real-time data of measuring devices on the high-risk areas of oscillation and the dominant paths of oscillation propagation, the oscillation can be accurately warned and monitored, and the sub-synchronous oscillation of the system can be further controlled and suppressed, improving the safety and stability of the system's operation.

4.2 Case of multiple oscillation sources in the 10-machine 39-node system

The previous section considered the possibility that research results on the mechanism and distribution characteristics of sub-synchronous oscillation propagation in a four-machine two-area small system might be affected by system structural parameters. It also considered the limitations of sub-synchronous oscillation in a system caused by a single oscillation source. In this section, we continue to investigate the propagation mechanism and distribution characteristics of sub-synchronous oscillation energy in the IEEE 10-machine 39-bus system, while also considering the universality of the research conclusions.

The IEEE 10-machine 39-bus system is shown in Figure 8. The difference between the constructed research system in the previous example and the simulation case is that two equivalent doubly-fed wind farm oscillation sources are simultaneously connected at different locations in the system. The specific system parameter settings are as follows:

The system steady-state frequency is set to 50 Hz, and the two doubly-fed wind farms are connected to the system at nodes 9 and 10 via series compensating lines. Doubly-fed wind farm 1 consists of 20 identical 5 MW doubly-fed induction wind turbines, with each turbine having the same control parameters and running at the rated state. It is connected to node 9 via a series compensating line with a compensator rating of 9%. Doubly-fed wind farm 2 consists of 30 identical 5.5 MW doubly-fed induction wind turbines and is

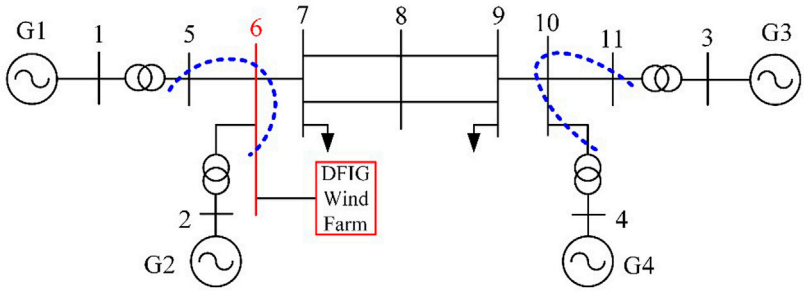

FIGURE 7
System high oscillation risk area identification.

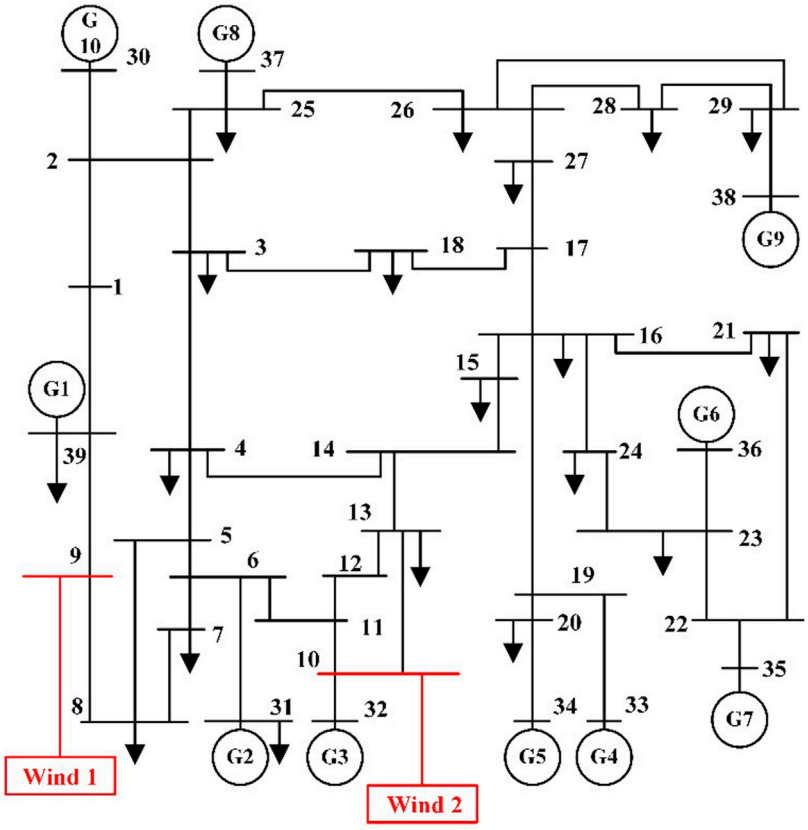

FIGURE 8
Two doubly-fed wind farms connected to IEEE 10 machine 39 node system.

connected to node 10 via a series compensating line with a compensator rating of 20%. Both wind farms are stepped up via 0.69kV/35 kV transformers and connected to the main bus after being stepped up to 35kV/345 kV. Then they are connected to series capacitor compensating lines. Both series capacitor compensating lines are 100 km long and their line parameters correspond to typical transmission line parameters.

The simulation system for the IEEE 10-machine 39-node system with the above system parameters for the two wind farms is shown in Figure 8. After 1 s of steady-state operation of the system, the series capacitor compensating lines in the output lines of the two wind farms are simultaneously put into operation, which will excite the phenomenon of sub-synchronous oscillation in the system.

Measurements were made on the output current and power of doubly-fed wind farm 1 connected to node 9 and doubly-fed wind farm 2 connected to node 10. The system was set to operate continuously for 2 s, and when it reached the first second, the series capacitor compensator was put into operation, immediately exciting the same amplitude of the sub-synchronous oscillation phenomenon in the system. The waveforms and spectral analysis

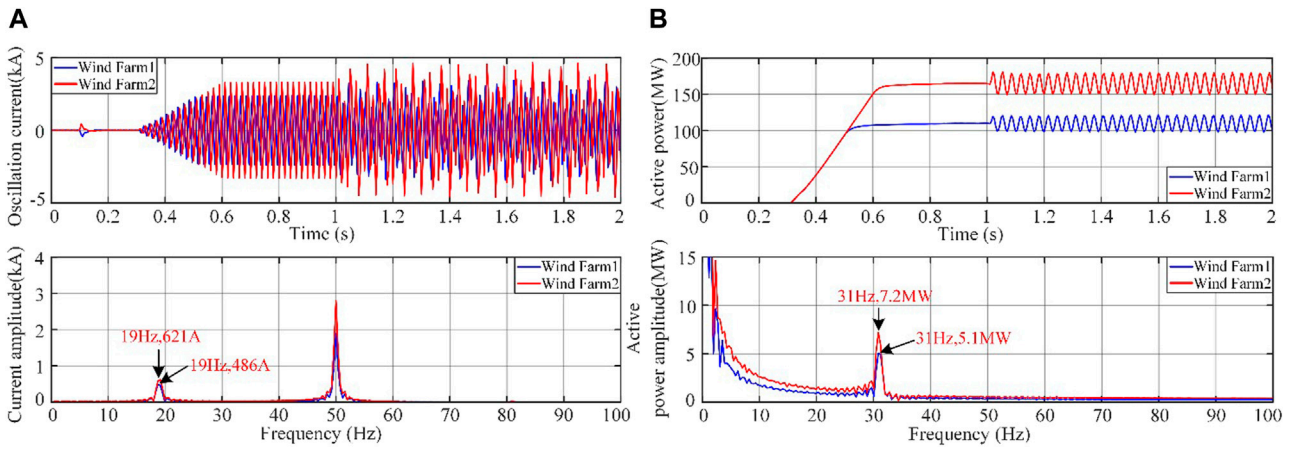

FIGURE 9
Frequency spectrum analysis. **(A)** Oscillation current and its frequency spectrum from two wind farms' outputs. **(B)** Oscillation power and its frequency spectrum from two wind farms' outputs.

TABLE 1 Corresponding numbers for each branch of the IEEE 10 machine 39 node system.

Branch	No.	Branch	No.	Branch	No.	Branch	No.	Branch	No.	Branch	No.
1–2	1	1–39	2	2–3	3	2–25	4	2–30	5	3–4	6
3–18	7	4–5	8	4–14	9	5–6	10	5–8	11	6–7	12
6–11	13	6–31	14	7–8	15	8–9	16	9–39	17	10–11	18
10–13	19	10–32	20	11–12	21	12–13	22	13–14	23	14–15	24
15–16	25	16–17	26	16–19	27	16–21	28	16–24	29	17–18	30
17–27	31	19–20	32	19–33	33	20–34	34	21–22	35	22–23	36
22–35	37	23–24	38	23–36	39	25–26	40	25–37	41	26–27	42
26–28	43	26–29	44	28–29	45	29–38	46	—	—	—	—

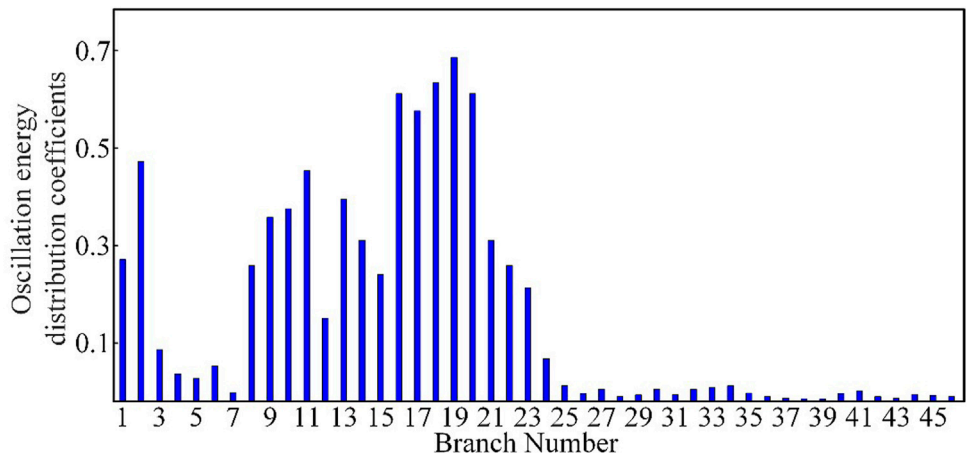

FIGURE 10
Oscillation energy distribution coefficient for each branch of the system.

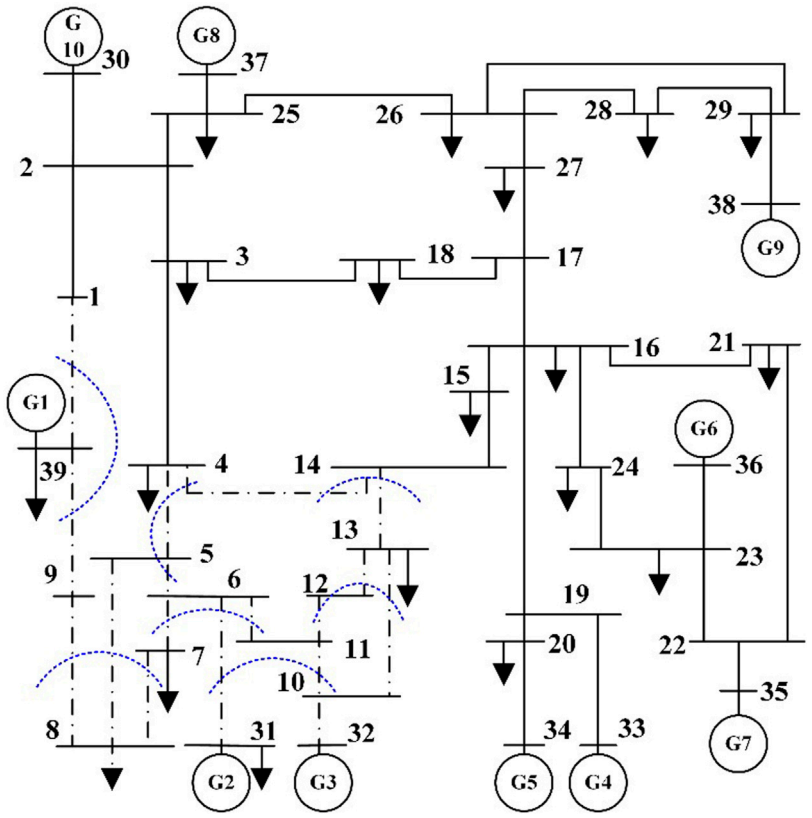

FIGURE 11
Systematic oscillation cut sets and location of oscillation high-risk areas.

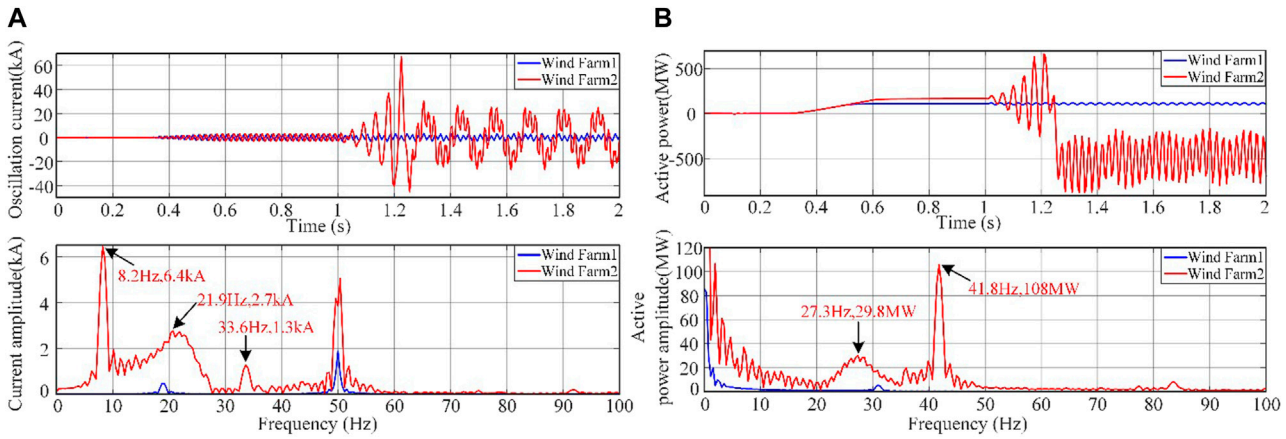

FIGURE 12
Frequency spectrum analysis. **(A)** Oscillatory current and its spectrum after changing the series compensation of wind farm 2. **(B)** Oscillation power and its spectrum after changing the series compensation of wind farm 2.

of the output current and power of the two wind farms are shown in (a) and (b) of Figure 9, respectively.

From the figure, it can be seen that there is a sub-synchronous oscillation component of 19 Hz in the oscillating current and a sub-synchronous oscillation component of 31 Hz (dominant oscillation mode) in the oscillating power. Specifically, the amplitudes of sub-synchronous frequency components of the oscillating current and power of doubly-fed wind farm 1 at sub-synchronous frequency are 486A and 5.1 MW, respectively; the amplitudes of sub-synchronous frequency components of the oscillating current and power of doubly-fed wind farm 2 at sub-synchronous frequency are 621A and 7.2 MW, respectively. Their oscillation characteristics also

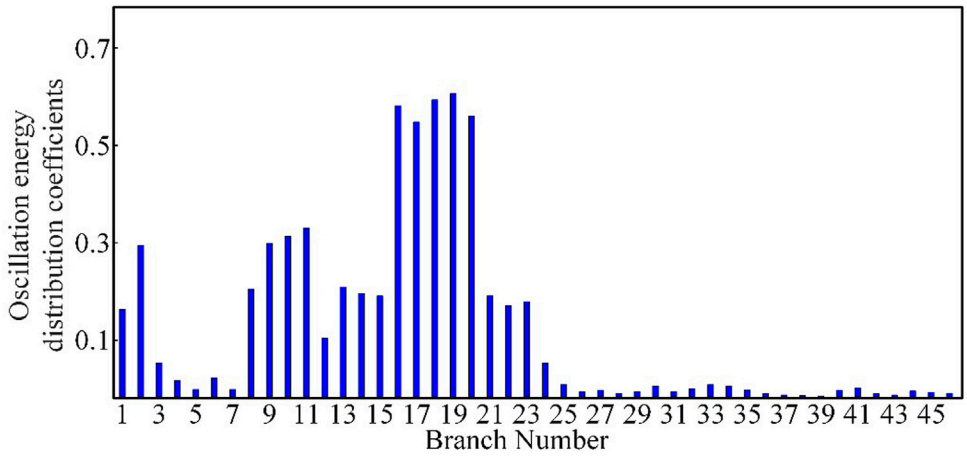

FIGURE 13
Sub-synchronous oscillation energy distribution coefficients of each branch after changing the series compensation of wind farm 2.

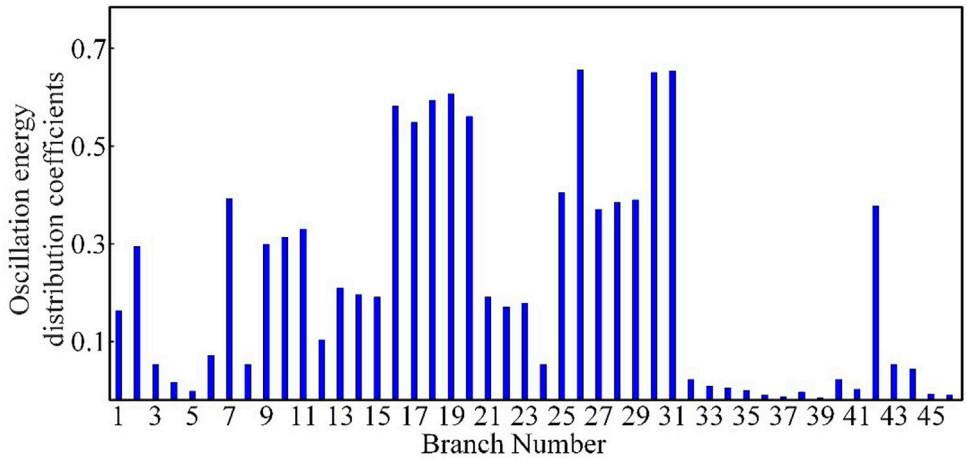

FIGURE 14
Sub-synchronous oscillation energy distribution coefficients of each branch after changing the location of wind farm 2.

satisfy the complementary relationship between the sub-synchronous oscillation frequencies of the oscillating power and current.

The branches of the IEEE 10-machine 39-node system are numbered, and the specific number corresponding to each branch is shown in Table 1. There are a total of 46 branches and 39 nodes in the entire system, of which 10 nodes are traditional generator-sending end nodes.

Through simulation data and calculations, it was found that the oscillation at the exits of the 31st, 32nd, and 39th generator nodes closest to the two doubly-fed wind farm oscillation sources is the most significant, and the oscillation energy around these branches is also the largest. Based on theoretical derivations, the oscillation energy in the system and the branch oscillation energy of each branch under the condition of equal-amplitude oscillation mode were calculated. The oscillation energy distribution coefficients of each branch under the dominant oscillation mode were then obtained, as shown in Figure 10.

By calculating the oscillation energy distribution coefficients of each branch in the system under the dominant 31 Hz oscillation mode, the dominant path for the propagation of sub-synchronous oscillation in the entire network can be located. From the magnitudes of the branch oscillation energy distribution coefficients in Figure 10, it can be seen that after the sub-synchronous oscillation is excited in the network by the two doubly-fed wind farms connected through series capacitor compensator, the areas near the oscillation source are most significantly affected by the oscillation. After being excited by the two wind farms, the oscillation diffuses and spreads to the downstream circuits and surrounding tie lines connected to nodes 9 and 10, which are where the wind farms are integrated. According to the results of the branch oscillation energy distribution coefficients, the largest share of branch oscillation energy occurs on the branches 9–8, 9–39, 10–11, 10–13, and 10–32, i.e., branches with numbers 16, 17, 18, 19, and 20. The oscillation gradually spreads to the downstream

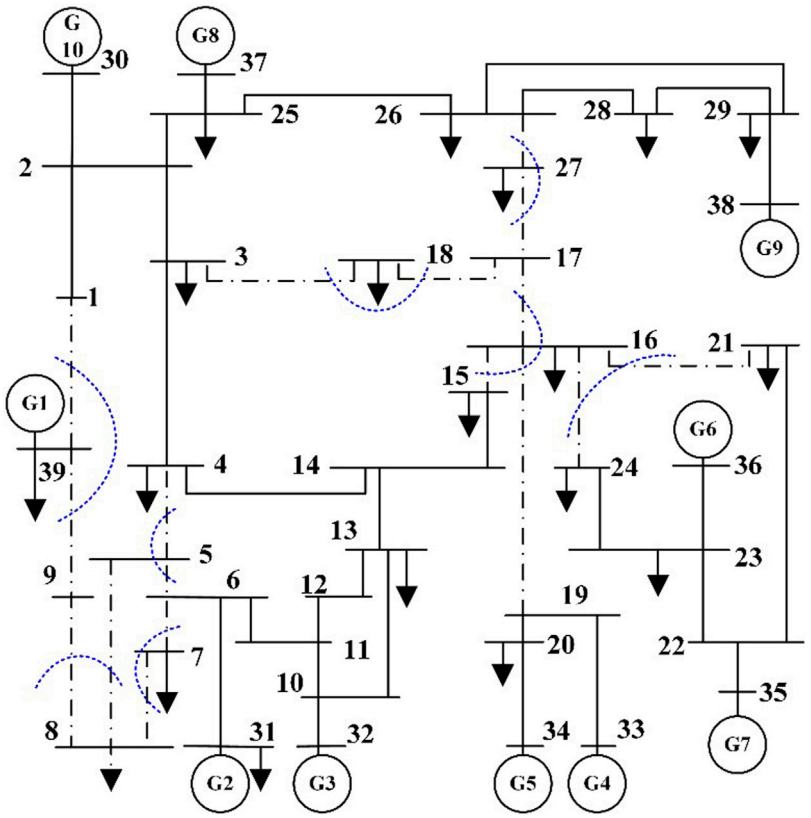

FIGURE 15
Locating oscillation cut-sets and high-risk areas of sub-synchronous oscillation after changing the location of wind farm 2.

branches and adjacent lines connected to these five branches, and the distribution coefficients of branch oscillation energy also gradually decrease. The branches with the maximum impact from the oscillation and the largest distribution coefficients are all near the power sources G1, G2, and G3, indicating that the propagation and diffusion of oscillation are most significant in the power-sending end area near the oscillation sources in the system. The oscillation energy on the lines and other power-sending end branches far away from the sending end area near the oscillation source is almost negligible, and their oscillation energy distribution coefficients are much smaller than those of the oscillation energy distribution coefficients of the dominant path of oscillation propagation.

Furthermore, the oscillation cut set can be determined to locate the high-risk oscillation areas of the system. The system's oscillation cut set determined by the branch oscillation energy distribution coefficients is shown in Figure 11. The black dashed line in the figure represents the high-oscillation-risk area of the system when the oscillation sources are connected to nodes 9 and 10.

Keeping the series compensation level of 9% of the series capacitor compensation line of doubly-fed wind farm 1 unchanged, the series compensation level of the series capacitor compensation line of doubly-fed wind farm 2 connected to node 10 is increased to 40%. After 1 s of system operation, the series compensation line is energized, causing sub-synchronous oscillation in the system. The waveforms and spectra of the oscillating current and power output of the two doubly-fed wind farms are compared in (a) and (b) of Figure 12.

From the figure, it can be observed that after the doubly-fed wind farm 2 is connected with series compensation line, its output current and power diverge rapidly, and approximately 0.25 s later, its output current and power remain in an equal-amplitude oscillation state. During the phase where its output current and power diverge rapidly, the oscillating current output by Doubly Fed Wind Farm 2 comprises oscillation frequencies and amplitudes of 21.9 Hz and 2.7 kA, as well as 33.6 Hz and 1.3 kA. The oscillating power output by Doubly Fed Wind Farm 2 comprises oscillation frequencies and amplitudes of 27.3 Hz and 29.8 MW, as well as 16.4 Hz and 11.9 MW. During the equal-amplitude oscillation phase of its output current and power, the frequencies and amplitudes of the oscillating current and power are 8.2 Hz and 6.4 kA, and 41.8 Hz and 105.6 MW, respectively. Its oscillation characteristics still satisfy the complementary relationship between the sub-synchronous oscillation frequency of the oscillating power and the oscillating current. At this time, the oscillation energy distribution coefficients of each branch were calculated under the equal-amplitude oscillation phase, i.e., the dominant oscillation mode with a frequency of 41.8 Hz, as shown in Figure 13. The oscillation cutting set and high-risk areas determined by this method are similar to those shown in Figure 11.

Keeping the series compensation degree of 9% for the capacitor of Doubly Fed Wind Farm 1's series compensation line unchanged

and the connection position unchanged, the connection position of Doubly Fed Wind Farm 2 was changed to busbar 17, and its series compensation degree of the series compensation capacitor line was increased to 40%. After one second of system operation, the series compensation line was put into operation, causing sub-synchronous oscillation in the system. At this time, the oscillation energy distribution coefficients of each branch were calculated based on the simulation data of the system, as shown in Figure 14.

After changing the position of Wind Farm 2 to connect to node 17, the results of the calculation of the branch oscillation energy distribution coefficients showed that the branches 17–16, 17–18, and 17–27 had a greater share of the oscillation energy, specifically, branches 26, 30, and 31. The oscillations propagated to the downstream lines connected to these three branches, and the oscillation energy distribution coefficients of the branches gradually decreased. Besides, except for the oscillation energy distribution coefficients of branches near node 9 remaining relatively large, the oscillation did not have much influence on the branches in the power supply area far away from node 17. When the oscillation source is connected to the system's busbar, the oscillation energy will radiate from the connection point to the surrounding lines, making it difficult to propagate to the nearby power supply areas. It only affects some branches of the contact lines without power support nearby and the receiving end area.

Based on this, the dominant propagation path of the system oscillation was identified, and further determination of the oscillation cutting set was made to locate the high-risk area of the system oscillation as shown in Figure 15. The black dotted line in the figure represents the high-risk oscillation area of the system when the oscillation source is connected to nodes 9 and 17.

The analysis and calculation results of the simulation example above show that when the oscillation source is connected near the power supply area, the oscillation energy has a significant impact on the power supply area, and the distribution of oscillation energy will change with the flow of active power in the system. However, the impact of oscillation energy on remote power supply areas far from the oscillation source is minimal, and it is difficult for oscillation energy to propagate to the remote power supply areas of the system through transmission lines. When the oscillation source is connected to the system busbar, the oscillation energy will radiate from the connection point to the surrounding lines, making it difficult to propagate to nearby power supply areas. It only affects the contact lines without power support nearby and the system receiving end area lines, thereby affecting the nearby electrical equipment and loads. Therefore, it can be concluded that the propagation and diffusion characteristics of system sub-synchronous oscillation energy are influenced by multiple factors such as network source-load structure, system active power flow, and the location of the oscillation source connection.

5 Conclusion

Based on the theoretical foundation of system transient energy function, this article analyzes the oscillation energy shared by different branches in the power grid and quantitatively analyzes the degree of different branches participating in the sub-synchronous oscillation. Based on the distribution and evolution of oscillation disturbance energy in the branches of the power network after oscillation occurs, the dominant paths of oscillation energy distribution can be identified and quantified by defining a coefficient based on the oscillation energy in the branches under the dominant oscillation mode. If these dominant paths carry a large amount of oscillation energy under the dominant oscillation mode, they are more fragile in the system. These fragile branches are defined as oscillation cut-sets, which are used to further locate high-risk areas of sub-synchronous oscillation in the system. The proposed quantitative analysis method for oscillation energy propagation characteristics can rapidly and accurately compute the distribution of oscillation energy in the power system after oscillations occur in large-scale wind power integration systems. This method identifies the dominant propagation paths of oscillation energy and high oscillation risk areas within the system. The effectiveness of the proposed research method was verified through time-domain simulation, and the conclusion is as follows:

(1) In the power supply end area near the oscillation source in the system, the branches that share the oscillation energy after oscillation occurs carry a large amount of energy, and the propagation and diffusion of the oscillation are the most significant in these branches.
(2) The sub-synchronous oscillation modes with higher frequencies have less impact on the areas that are far away from the oscillation source in the system, while the oscillation energy under the sub-synchronous oscillation modes with lower frequencies can propagate and diffuse to a wider range, and have a greater impact on the distant areas of the system.
(3) The system network structure, the distribution of active power flow, and the connection position of the oscillation source can affect the propagation and distribution characteristics of sub-synchronous oscillation energy in the system. When the oscillation source is connected to the system's tie bus, the oscillation energy will radiate from the connection point to the surrounding lines, making it difficult to propagate to nearby power supply end areas. It will only affect the tie lines without power support nearby and some branches in the receiving end area.

Data availability statement

The original contributions presented in the study are included in the article/Supplementary Material, further inquiries can be directed to the corresponding author.

Author contributions

ZW: resources and investigation. XS: methodology, software implementation, and writing. WC: review and editing. JS: supervision. All authors contributed to the article and approved the submitted version.

Funding

This work was supported in part by the National Natural Science Foundation of China (Nos. 51767017 and 51867015), the Basic Research and Innovation Group Project of Gansu (No. 18JR3RA133), and the Gansu Provincial Natural Science Foundation of China (No. 21JR7RA255).

Conflict of interest

Author XS was employed by Wuwei Power Supply Company of State Grid Gansu Provincial Electric Power Company.

The remaining authors declare that the research was conducted in the absence of any commercial or financial relationships that could be construed as a potential conflict of interest.

Publisher's note

All claims expressed in this article are solely those of the authors and do not necessarily represent those of their affiliated organizations, or those of the publisher, the editors and the reviewers. Any product that may be evaluated in this article, or claim that may be made by its manufacturer, is not guaranteed or endorsed by the publisher.

References

Adams, J., Carter, C., and Huang, S.-H. (2012). "ERCOT experience with sub-synchronous control interaction and proposed remediation," in Proceedings of the IEEE PES Transmiss. Distrib. Conf. Expo., Orlando, FL, USA, May 2012, 1–5.

Cao, N., Zhao, X., and Yu, Q. (2020). Forced oscillation source location of doubly-fed wind turbine based on transient energy flow. *Power Syst. Autom.* 44 (10), 103–110.

Chen, W., Xie, X., Wang, D., Liu, H., and Liu, H. (2018). Probabilistic stability analysis of sub-synchronous resonance for series-compensated DFIG-based wind farms. *IEEE Trans. Sustain. Energy* 9 (1), 400–409. doi:10.1109/tste.2017.2737599

Gong, Y., Huang, Q., Li, J., and Cai, D. (2019). "Analysis on oscillation propagation characteristics based on impedance model," in Proceedings of the 2019 IEEE Innovative Smart Grid Technologies - Asia (ISGT Asia), Chengdu, China, May 2019, 1226–1229.

Li, J., and Ping, X. (2016). Impact of increased wind power generation on sub synchronous resonance of turbine-generator units. *J. Mod. Power Syst. Clean. Energy*. 4 (2), 219–228. doi:10.1007/s40565-016-0192-9

Li, M., Yu, Z., Xu, T., He, J., Wang, C., Xie, X., et al. (2017). Study of complex oscillation caused by renewable energy integration and its solution. *Power Syst. Technol.* 41 (4), 1035–1042. doi:10.13335/j.1000-3673.pst.2016.3049

Liu, H., Xie, X., He, J., Xu, T., Yu, Z., Wang, C., et al. (2017). Sub-synchronous interaction between Direct-drive PMSG based wind farms and weak AC networks. *IEEE Trans. Power Syst.* 32 (6), 4708–4720. doi:10.1109/tpwrs.2017.2682197

Ma, N., and Wang, D. (2016). Study on dispersion phenomena of electromechanical disturbance propagation in power systems. *Int. Trans. Elect. Energy Syst.* 26 (12), 2657–2671. doi:10.1002/etep.2226

Ma, N., Xie, X., He, J., and Wang, H. (2020). Review and discussion of wide-band oscillation in renewable and power electronics highly integrated power systems. *Proc. CSEE* 40 (15), 4720–4732. doi:10.13334/j.0258-8013.pcsee.191968

Ma, Y., Huang, Q., Gooi, H. B., Zhang, Z., Yang, X., and Wang, Y. (2022). Sub-synchronous oscillation analysis using multisynchrosqueezing transform and dissipating energy flow method. *IEEE Trans. Ind. Appl.* 58 (3), 3134–3141. doi:10.1109/tia.2022.3149684

Maslennikov, S., Wang, B., and Litvinov, E. (2017). Dissipating energy flow method for locating the source of sustained oscillations. *Int. J. Elect. Power Energy Syst.* 88, 55–62. doi:10.1016/j.ijepes.2016.12.010

Narendra, K., Fedirchuk, D., Midence, R., Zhang, N., Mulawarman, A., Mysore, P., et al. (2011). "New microprocessor based relay to monitor and protect power systems against sub-harmonics," in Proceedings of the 2011 IEEE Electrical Power and Energy Conference, Winnipeg, MB, Canada, October 2011, 438–443.

Ostadi, A., Yazdani, A., and Varma, R. K. (2009). Modeling and stability analysis of a DFIG-based wind-power generator interfaced with a series-compensated line. *IEEE Trans. Power Del* 24 (3), 1504–1514. doi:10.1109/tpwrd.2009.2013667

Ren, Y., Chen, L., Min, Y., Li, Y., and Li, W. (2018). Relationship between transient energy flow, electric power and damping torque in sub-synchronous oscillation. *Power Syst. Autom.* 42 (22), 52–58.

Thorp, J. S., Seyler, C. E., and Phadke, A. G. (1998). Electromechanical wave propagation in large electric power systems. *IEEE Trans. Circuits Syst. I* 45 (6), 614–622. doi:10.1109/81.678472

Wang, D., Ma, N., and Guo, C. (2017). Characteristics of electromechanical disturbance propagation in non-uniform power systems. *IET Gener. Transm. Distrib.* 11 (8), 1919–1925. doi:10.1049/iet-gtd.2016.1126

Wang, L., Xie, X., Jiang, Q., Liu, H., Li, Y., and Liu, H. (2015). Investigation of SSR in practical DFIG-based wind farms connected to a series-compensated power system. *IEEE Trans. Power Syst.* 30 (5), 2772–2779. doi:10.1109/tpwrs.2014.2365197

Wen, Z., Peng, S., Yang, J., Deng, J., He, H., and Wang, T. (2019). Analysis of the propagation characteristic of sub-synchronous oscillation in wind integrated power system. *Energies* 12 (6), 1081. doi:10.3390/en12061081

Xie, X., Liu, H., He, J., Zhang, C., and Qiao, Y. (2016). Mechanism and characteristics of sub-synchronous oscillation caused by the interaction between full-converter wind turbines and AC systems. *Proc. CSEE* 36 (9), 2366–2372. doi:10.13334/j.0258-8013.pcsee.2016.09.007

Xie, X., Zhan, Y., Liu, H., Li, W., and Wu, C. (2019). Wide-area monitoring and early-warning of sub-synchronous oscillation in power systems with high-penetration of renewables. *Int. J. Elect. Power Energy Syst.* 108, 31–39. doi:10.1016/j.ijepes.2018.12.036

Xie, X., Zhan, Y., Shair, J., Ka, Z., and Chang, X. (2020). Identifying the source of sub-synchronous control interaction via wide-area monitoring of sub/super-synchronous power flows. *IEEE Trans. Power Del.* 35 (5), 2177–2185. doi:10.1109/tpwrd.2019.2963336

Xie, X., Zhang, X., Liu, H., Li, Y., and Zhang, C. (2017). Characteristic analysis of sub-synchronous resonance in practical wind farms connected to series-compensated transmissions. *IEEE Trans. Energy Conv.* 32 (3), 1117–1126. doi:10.1109/tec.2017.2676024

Yang, J., Wang, T., and Wang, Z. (2019). "Analysis of sub-synchronous oscillation propagation characteristics caused by interharmonics in wind integrated power system," in Proceedings of the 2019 IEEE Power & Energy Society General Meeting (PESGM), Atlanta, GA, USA, August 2019, 1–5.

Yang, N., Ma, W., Wang, X., Xie, D., Gu, C., Zhao, D., et al. (2021). Defining SSO power and characterizing SSO propagation in power system with wind farms integration. *IEEE Trans. Power Syst.* 36 (4), 3531–3540. doi:10.1109/tpwrs.2020.3044993

Zhan, Y., Xie, X., Liu, H., Liu, H., and Li, Y. (2019). Frequency-domain modal analysis of the oscillatory stability of power systems with high-penetration renewables. *IEEE Trans. Sustain. Energy* 10 (3), 1534–1543. doi:10.1109/tste.2019.2900348

Zhang, P., Xu, P., and Bi, T. (2017). Analysis of sub-synchronous current propagation path of sub-synchronous oscillation induced by renewable energy integrated to the power grid. *J. Eng.* 2017 (13), 2449–2454. doi:10.1049/joe.2017.0769

Zhao, S., Wang, N., Li, R., Gao, B., Shao, B., and Song, S. (2019). Sub-synchronous control interaction between direct-drive PMSG-based wind farms and compensated grids. *Int. J. Electr. Power Energy Syst.* 109, 609–617. doi:10.1016/j.ijepes.2019.02.021

Nomenclature

D_i	the damping coefficient
E_s	the total oscillation energy
E_B	the total oscillation energy of all transmission lines
E_{ij}	the oscillation energy of branch $i-j$
$E_{bij,\lambda k}$	the oscillation energy of branch $i-j$ under oscillation mode λk
$\dot{I}_G$	generator output current
$\dot{I}_L$	current flowing into the load
$\dot{I}_{ij}$	the current flowing from node i to node j
$\dot{I}_{Gi}$	the current flowing out of the generator
$\dot{I}_{Li}$	the current injected into the load
M_i	the inertia constant
n	the number of nodes in the system
P_{ei}	per-unit values of the electromagnetic power
P_{mi}	per-unit values of the mechanical power
P_{ij}	the active power flowing from node i to node j on the branch $i-j$
P_{ji}	the active power flowing from node j to node i on the branch $i-j$
P_b	the active power of the branch during oscillation
P_1	the steady-state active power component of the branch during oscillation
P_s	the sub-synchronous frequency oscillation component of the active power of the branch during oscillation
$P_{\lambda 1},\cdots,P_{\lambda k}$	the sub-synchronous frequency oscillation component of the active power of different oscillation modes in the system
Q_{ij}	the reactive powers flowing from node i to node j on the branch $i-j$
Q_{ji}	the reactive powers flowing from node j to node i on the branch $i-j$
U_i	the amplitude of node i's voltage $\dot{U}_i$
$\dot{U}$	the system node voltage
W	the transient energy function of the entire system
Y	node admittance matrix of the system
θ_i	the phase angle of node i's voltage $\dot{U}_i$
δ_i	the rotor angle of the generator
ω_i	the difference between synchronous speed and rotor angular speed
DFIG	Doubly Fed Induction Generator
OEDC	The oscillation energy distribution coefficient
RLC	Resistor-Inductor-Capacitor

frontiers | Frontiers in Energy Research

TYPE Original Research
PUBLISHED 16 November 2023
DOI 10.3389/fenrg.2023.1261268

OPEN ACCESS

EDITED BY
Youbo Liu,
Sichuan University, China

REVIEWED BY
Zhaoxi Liu,
South China University of Technology, China
Zao Tang,
Hangzhou Dianzi University, China
Xi Zhang,
Southwest Petroleum University, China
Yuxiong Huang,
Xi'an Jiaotong University, China

*CORRESPONDENCE
Qihe Lou,
ZHX361725487@outlook.com

RECEIVED 19 July 2023
ACCEPTED 07 September 2023
PUBLISHED 16 November 2023

CITATION
Lou Q and Li Y (2023), Techno-economic model for long-term revenue prediction in distribution grids incorporating distributed energy resources.
Front. Energy Res. 11:1261268.
doi: 10.3389/fenrg.2023.1261268

Techno-economic model for long-term revenue prediction in distribution grids incorporating distributed energy resources

Qihe Lou[1,2]* and Yanbin Li[1]

[1]School of Economics and Management, North China Electric Power University, Beijing, China, [2]State Grid Corporation of China, Beijing, China

Distributed energy resources (DER) is a prevalent technology in distribution grids. However, it poses challenges for distribution network operators to make optimal decisions, estimate total investment returns, and forecast future grid operation performance to achieve investment development objectives. Conventional methods mostly rely on current data to conduct a static analysis of distribution network investment, and fail to account for the impact of dynamic variations in relevant factors on a long-term scale on distribution network operation and investment revenue. Therefore, this paper proposes a techno-economic approach to distribution networks considering distributed generation. First, the analysis method of the relationship between each investment subject and distribution network benefit is established by using the system dynamics model, and the indicator system for distribution network investment benefit analysis is constructed. Next, the distribution network operation technology model based on the dist flow approach is employed. This model takes into account various network constraints and facilitates the comprehensive analysis of distribution network operation under dynamic changes in multiple factors. Consequently, the technical index parameters are updated to reflect these changes. This updated information is then integrated into the system dynamics model to establish an interactive simulation of the techno-economic model. Through rigorous verification using practical examples, the proposed method is able to obtain the multiple benefits of different investment strategies and be able to select the better solution. This can provide reference value for future power grid planning.

KEYWORDS

distribution network, distributed energy resources, techno-economic model, system dynamics, dist flow model

1 Introduction

Distributed energy resources (DER) is widely regarded as one of the important renewable energy generation modes in the distribution network (International Energy Agency, 2022). The distribution network characterized by accepting large-scale renewable energy has become the main trend and direction of the future development of the distribution network. DG has changed the energy flow mode of the traditional distribution network, which brings great challenges to the economy, reliability and power quality of the distribution network

(Dhivya and Arul, 2021). DER integration challenges distribution investment optimization and return estimation. Uncertain DER generation output complicates infrastructure planning. Bidirectional power flows from DERs require investments to manage voltage, loading, and protection. DERs cause voltage fluctuations potentially exceeding regulations, needing voltage regulation equipment. Varying DER loading causes asset under/over-utilization. Long planning horizons with rapidly adopting DERs make forecasting difficult. Therefore, effective and reasonable distribution network investment planning is the necessary condition to solve the above problems (Yi et al., 2021). How to fully consider the influence of DG on the distribution network and make reasonable investment decisions is one of the core tasks of distribution network planning under the condition of limited investment (Maheshwari et al., 2020).

Academics endeavor to address the challenges presented by the integration of distributed renewable resources into the distribution network through the interactive operation of generators, networks, and energy storage systems. Literature (Ehsan and Yang, 2019) evaluates uncertainty modeling techniques within the framework of active distribution network planning and discusses their additional challenges and solutions. Literature (Adefarati and Bansal, 2019) evaluates the reliability, environmental, and economic impacts of several case studies using the fmincon optimization tool in MATLAB. Literature (Panigrahi et al., 2020) introduces control methods for small photovoltaic power stations and several aspects of grid-connected photovoltaic systems, ranging from various standards to emergency operations. Literature (Luo et al., 2020) proposes a RES management approach applicable to different RES distribution networks and attempts to find the optimal energy management of grid-connected distribution networks using an improved bat algorithm (MBA). Literature (Cui et al., 2019) aims to improve the revenue of distributed wind power generation (DWPG) and reduce grid upgrade costs by establishing a model considering the collaborative planning of distributed wind power generation and distribution networks.

The above literature mainly focuses on planning distribution networks that maximize the economic benefits while considering the uncertainty of renewable energy, grid constraints, and the integration of distributed energy resources. These methods can only provide investment in the current form of the distribution network on a certain investment basis. In reality, the investment in the distribution network is interrelated and is dynamically affected by various factors such as load growth, DER growth, and GDP over a long period (Thang, 2021). Traditional optimization methods cannot represent the long-term effects of multiple dynamic external factors on the demand of distribution networks. Moreover, it cannot analyze the long-term overview of distribution networks and consider the investment return expectations of these factors.

System dynamics is an ideal method for solving long-term forecasting problems involving multiple factors and complex feedback. Moreover, it has been widely applied in power systems (Teufel et al., 2013). For instance (Song et al., 2021), constructed a system dynamics model for a multi-market coupled trading system to study the coupling effects of multiple factors on renewable energy sources (RES) evolution (Li et al., 2022). developed a system dynamics model to predict long-term loads considering carbon neutrality targets (Tang et al., 2021). used system dynamics to predict power generation combinations on the rolling horizon and employed it as a forecasting method considering multiple factors. Furthermore, system dynamics can be employed to analyze the impact of certain variables on the system (Ying et al., 2020). used system dynamics to study demand-side incentives under renewable energy portfolio standards. Similarly (Chi et al., 2022), applied system dynamics to analyze carbon emissions under electricity market reform, which indicates that future market electricity prices will show advantages in efficiency and liquidity.

However, there exist multiple short-term operational constraints in distribution networks. System dynamics is a long-term simulation tool, and many constraints cannot be calculated, leading to invalid or even incorrect results. In this case, some scholars propose using integrated models with system dynamics to address its limitations (Tang et al., 2021). combined rolling horizon optimization with a system dynamics model to predict the evolution of power generation combinations. Although the article proposed a calculation model that integrates system dynamics with other methods, the problem of limited computation remains unsolved. The dynamic correlation among a large number of complex factors in long-term models and the operational constraints in short-term models cannot be reconciled and need further research (Ying et al., 2020).

This paper presents a simulation method of distribution network planning investment based on dual time scale fusion. The system dynamics is used as the long-term simulation, and the optimal power flow calculation model of the distribution network is used as the short-term simulation. First, based on the demand of economic and social development for regional distribution network planning, the main influencing factors of distribution network planning investment are screened out, and the multi-factor complex system is modeled through system dynamics. Secondly, the optimal power flow calculation is introduced, and some key parameters of the system dynamics are introduced and solved. The short-term simulation verifies the operation constraints of the distribution network in the long-term evolution, and obtains the profit value of various investments. The results can be returned to the system dynamics model to obtain more valuable long-term inference conclusions. The proposed techno-economic approach provides an advanced, adaptive framework for long-term distribution investment analysis, overcoming limitations of conventional techniques. It uses system dynamics modeling to capture long-term trends rather than static optimization. It incorporates complex interdependent impacts on investments over time that conventional methods miss. Integration of the dist flow model represents network constraints lacking in traditional approaches. Closed loop updating of system dynamics with the dist flow method enables adaptive decisions, improving on conventional inflexibility.

The main contributions of this paper are summarized as follows:

1. Traditional optimization models are unable to capture the dynamic impacts of various factors on the long-term investment returns of distribution networks. In this paper, a long-term simulation model is designed that utilizes system dynamics to model the long-term trends of relevant factors. The resulting

outcomes can more effectively infer the long-term evolution trend of the distribution network over a longer time scale.
2. There are multiple constraints in the operation of distribution networks, and traditional system dynamics cannot perform constraint calculations. In this paper, a dual-time-scale simulation model is designed. System dynamics is used for long-term simulation, while key parameters related to power system constraints are calculated through optimal power flow constraint for short-term simulation. This can address the limitations of system dynamics.
3. A comprehensive investment return evaluation index system is constructed in this paper. The evaluation indexes are calculated based on the results of short-term simulations, while the changes in these indexes' impact on the long-term evolution of the distribution network are characterized through long-term simulation. This method is only applicable to dual-time-scale simulation models and can provide decision-makers with intuitive investment return references.

2 System dynamics model

Distribution network investment decision is a multi-objective decision problem, which is also a multi-stage planning problem in a long time scale. The entity responsible for the distribution network investments being modeled and analyzed in this study can be the distribution system operator or utility company that owns and operates the network assets. The model outputs aim to inform their long-term planning and investment decisions. The decision goals are of various types. Some indicators are as large as possible, such as the user power supply reliability rate, voltage compliance rate, and some are neither larger nor smaller, such as power supply per unit variable capacity. To transform the multi-attribute decision problem into a single attribute decision problem can effectively improve the efficiency and accuracy of the solution. The core idea is to unify the evaluation indicators of different dimensions into the same dimension by normalization and weighting.

The investment in regional distribution network is often affected by demand. The greater the demand for a certain benefit, the greater the investment necessity and the greater the investment scale for relevant measures. However, restricted by the actual investment of the power network, the investment limit cannot be exceeded. In addition, since the distribution network requires balanced development to some extent, each benefit of the distribution network should complete its basic distribution network planning objectives, and some benefits of the distribution network should not be ignored in order to improve the comprehensive benefits of the distribution network, which is also an important constraint for investment decisions. The investment demand, investment capacity and basic planning objectives of each benefit of distribution network are considered comprehensively.

In this paper, system dynamics is used to construct a long-term simulation model for the evolution of distribution network. The construction process is:

1. Defined boundaries and assumptions;
2. Construct the causal loop diagram;
3. Define sub-systems and construct the stock flow chart.

2.1 Model boundary and assumptions

The first step to construct a functional SD model is to define the boundaries and assumptions of the model. The research object of this paper is grid distribution network. It refers to the distribution network divided by geographical and administrative units within a certain area. Due to regional development, natural conditions, grid company assessment and other factors, the distribution network conditions are different. By subdividing a large area into a grid distribution network, the difficulty of analysis can be reduced by subdividing analysis objects. Grid distribution network has the following characteristics:

1. The power supply mode of the distribution network changes from single source to multi-source, and the average load rate and the distribution transformer capacity load ratio of the distribution network change. The transmission power along the feeder decreases, and the voltage at each node increases. The change depends on the volume and location of DG.
2. The uncertainty of DG output leads to voltage fluctuations in the distribution network, and energy storage and other devices need to be added to suppress fluctuations;
3. DG is generally incorporated into the power grid through the inverter, which will produce a large number of harmonic components. This will change the voltage and current waveform of the distribution network, causing harmonic pollution, need to add a filtering device;
4. Two-way transmission of distribution network, traditional protection devices are difficult to identify and troubleshoot faults, which increases the investment demand of secondary system of distribution network.

Based on the above features, the model boundary and assumptions in this paper are as follows:

1. This paper mainly studies the distribution network with distributed power supply. The proposed model is not suitable for the distribution network without DG.
2. For the verification of grid fees for distributed energy, it is necessary to comprehensively consider the grid assets, voltage levels, and electrical distances occupied by both parties in the market-oriented transaction of distributed generation under the market-oriented trading of electricity. At present, however, Chinese electric power market is not completely popular. In this case, most distributed power sources do not participate in the electricity market, so they ignore the impact of the electricity market.
3. Electric vehicles and distributed energy storage are not included in the model.
4. Assume that the type of equipment invested in the distribution network is fixed and the investment cost is unchanged.

2.2 Casual loop diagram

The casual loop diagram of the model is shown in the Figure 1. Based on the casual loop diagram, the model can be divided into three subsystems.

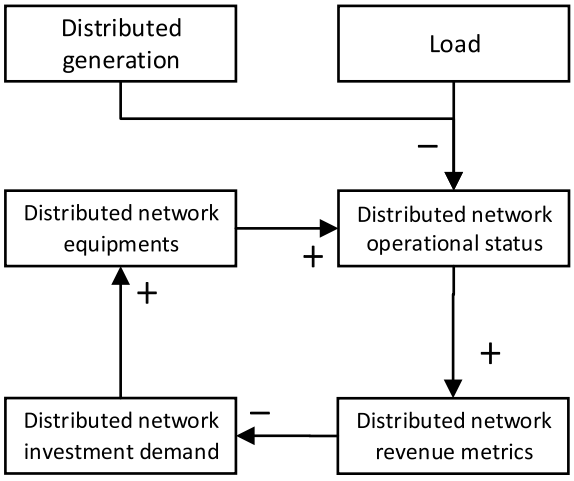

FIGURE 1
Casual loop diagram.

1. Distribution network investment subsystem. This module simulates the growth of various types of equipment in the distribution network. Key elements include: distributed energy storage, static var compensator, transformer, line capacity.
2. End user subsystem. This module simulates distribution network user demand and DER growth. Key elements include: DER, peak load, electricity demand, GDP growth.
3. Revenue calculation subsystem. This module simulates the growth of distribution network revenue. Among them, the short-term simulation model is included, that is, the optimal power flow calculation model. Key elements include: power quality, power self-supply rate, RES consumption rate, line load rate, and network loss rate.

2.3 Stack-flow model

In the SD model, the quantitative relationship between variables are characterized by a stack flow model. This section details the above three sub-system formulations, as shown in Figure 2.

2.3.1 Distribution network investment subsystem

There are five types of distribution network investment objects in this paper. They are DESS, SVC, CRC, transformer and transmission line. The type of DESS in this paper is electrochemical energy storage such as lithium-ion and flow batteries, which are common distribution-level storage technologies. State of charge constraints limit usable capacity. Storage decision variables are charge/discharge amounts, State-of-Charge, and charging/discharging status. For each investment object, it is represented by the corresponding stock variable, which is an integral function based on the growth variable.

$$CAP_i(t) = CAP_i(t-1) \times (1 + IV_i), i \in ESS, SVC, CRC, T, L \quad (1)$$

$$IV_i = \frac{RF}{IVF_i}, i \in ESS, SVC, CRC, T, L \quad (2)$$

where, IV is the investment index defined as the ratio of current capacity.

Investment decisions should be based on economic indicators of investment profitability. In this paper, the investment decision is made through the revenue index RF whose calculation process is similar to net profit value (NPV) (Petitet et al., 2017).

$$RF = \sum_{t=0}^{n} \frac{R_i - C_i}{(1+dis)^t} - IVF_i, i \in ESS, SVC, CRC, T, L \quad (3)$$

where dis is a discount factor of 5%, n is the time period which is 20 years in this paper, R_i is presented in Eq. 18.

The growth of DER is influenced not only by cost and technological factors but also by operational indicators of the distribution network. Among these indicators, energy self-sufficiency and the integration rate of renewable energy are the two most important ones. The relationship between these indicators is as follows:

$$CAP_{DER}(t) = CAP_{DER}(t-1) \times (1 + r_{DER}) \quad (4)$$

$$r_{DER} = \alpha_1 \times (1 + (1 - \eta_s) + \alpha_2 \times \eta_D ER) \quad (5)$$

2.3.2 Revenue calculation subsystem

This module focuses on income calculation. First, various operating parameters of the distribution network are calculated through short-term simulation, and then the parameters are converted into income-related coefficients. The short-term simulation model refers to Section 3. This section focuses on the modeling of profitability parameters.

Power quality:

The power supply quality index of distribution network is similar to that of distribution network, which reflects the average power quality of distribution network. In this paper, the power quality indexes of load access nodes and grid-connected nodes of distribution network are averaged in time and space to reflect the characteristics of power supply quality in statistical time of distribution network. For example, the formula for calculating the mean value of voltage deviation degree and three-phase voltage unbalance degree is respectively

$$ND = \sum_{t=1}^{T} \sum_{n=1}^{N} \left| \delta U_n(t)(\%) \right| / (N \times T) \quad (6)$$

$$\eta_U = \frac{U_m - U_N}{U_N} \times 100\% \quad (7)$$

Self-supply rate:

The self-smoothness of energy represents the self-sufficiency capacity of the distribution network, which is expressed by the ratio of the self-consumed electricity of the distribution network to the total load power supply within the statistical time, and the calculation formula is

$$\eta_s = \int_{i=1}^{t} \left(1 - \frac{E_i^{PCC}}{E_i^{Load}}\right) di/t \times 100\% \quad (8)$$

Reliability benefit:

Average percentage of power supply shortage of users. The ratio of average power failure to power failure of users represents the

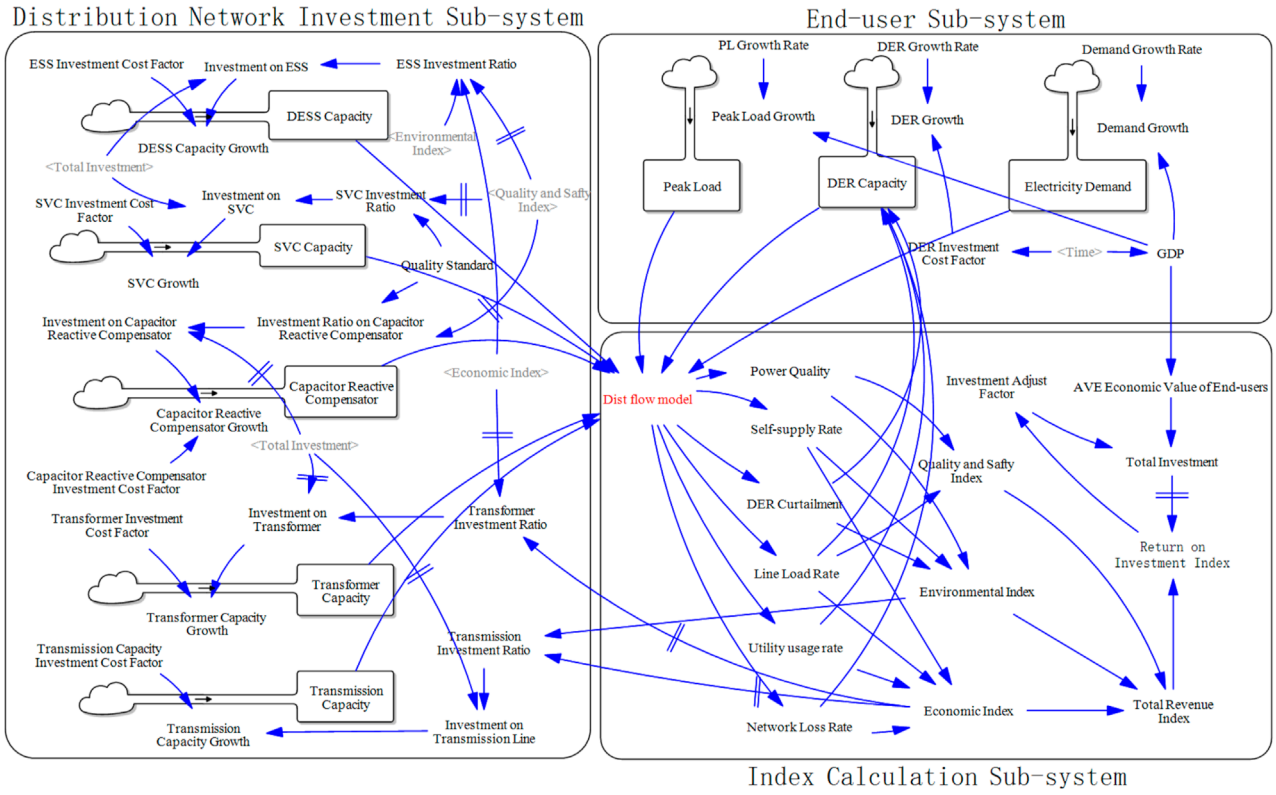

FIGURE 2
Stack-flow model.

power failure of users, and is expressed by the ratio of total power failure to power failure within the statistical period and the expected power failure within the statistical period, where the expected power failure is the sum of actual power supply and power failure, and the statistical period is 1 year.

$$\eta_r = c_l * LOLE \tag{9}$$

where c_l is the cost index of non-served energy; LOLE is loss of load expectation;

The benefit-cost ratio η of distributed energy access to the grid is defined as the ratio of the annual power outage loss cost change value Δ Closs to the annual investment cost C_{invest}.

$$\eta = \Delta C_{loss} / C_{invest} \tag{10}$$

It is used to quantify the improvement benefits of various access methods to the distribution network reliability index, sort and compare the benefit-cost ratio, and obtain the best benefit measures.

Line load rate:

Line load factor is the ratio of actual load to rated capacity. It evaluates line performance, guides planning, improves energy efficiency, and aids in operational management in power systems.

$$\eta_a = \frac{S_a}{S_0} \times 100\% \tag{11}$$

where η_a is the distribution network load rate level of the system; S_a is the average load capacity of the distribution network; S_0 is the rated load capacity of the distribution network.

Utility usage rate:

Equipment utilization is an index that can reflect the working status and production efficiency of the equipment in the system, and has important evaluation significance. Equipment utilization refers to the ratio of the actual working time of the equipment to the planned working time within a certain period of time. The value of this value is directly related to the project benefit. The specific expression is:

$$\eta_e = \left(\sum_{n=1}^{N} T_n \right) (NT_O) \tag{12}$$

where η_e is the equipment utilization rate of the system; T_O is the unit planned working hours; T_n is the actual working hours of the first device in a unit time; N is the number of energy link equipment in the system.

DER curtailment:

The power abandonment rate of clean energy refers to the ratio of the product of the running time of each DG year (unit: h) and its installed capacity (unit: kW) in the distribution network to the rated power generation of each DG year due to the unstable wind power output. The calculation formula is

$$R_{DER} = 1 - E_{DER} / E_{DER\_F} \tag{13}$$

$$\eta_{DER} = \int_{i=1}^{t} \left(1 - \frac{E_i^{DER}}{E_i^{DER\_F;}} \right) di / t \times 100\% \tag{14}$$

where R_{DER} is the curtailment rate of DER; E_{DER} is the actual grid-connected power generation; E_{DER_F} is the power generation.

Quality and safty index:

$$RF_Q = 1 - (1 - \eta_U) + \eta_r/\beta_1 \tag{15}$$

Economic index:

$$RF_{ECO} = (1 - \eta_s) + \eta_r/\beta_2 \tag{16}$$

Environment index:

$$RF_{EN} = (1 - \eta_s) + (\eta_a/\beta_3) + (1 - \eta_e) - (1 - \eta_{DER}) \tag{17}$$

Total revenue index: In the indicator system of this paper, weights are added to the three indicators respectively, expressed as

$$RF = \alpha_1 \times RF_Q + \alpha_2 \times RF_{ECO} + \alpha_3 \times RF_{EN} \tag{18}$$

where α_1, α_2, and α_3 are weight factors.

2.3.3 End user subsystem

This module is mainly based on external variables. Including electricity demand, peak load, DER capacity. Among them, DER capacity is affected by other module variables, while power demand and peak load are purely external input variables.

$$ED(t) = ED(t-1) \times (1 + r_{ED}) \tag{19}$$

$$r_{ED} = e_1 \star Ln(e_2 \times (Time - 2020)) \tag{20}$$

where ED is the electricity demand; r_{ED} and r_{PL} represents the growth rate of electricity demand and peak load, respectively. Note that e_1 and e_2 are 0.05 and −0.03427 in this paper, which are calculated by fitting historical data from the past 20 years.

The peak load variable is critical in the system dynamics model, directly affecting distribution network infrastructure sizing and operation simulated by the dist flow model. Larger peak load requires increased capacity components and equipment ratings to handle maximum flows. Peak demand drives asset utilization and overloading risk analysis in the dist flow. It also dictates voltage regulation needs, as bigger peaks cause larger voltage drops. Furthermore, peak load determines nodal demands and network flows in the dist flow. The annual peak load is influenced by various factors, which can be divided into two categories: trend changes and random fluctuations. Trend changes are influenced by policies and economic development, while random fluctuations are affected by load fluctuations and major events. Considering that the annual peak load exhibits a relatively stable trend growth, it can be viewed as a random variation, with random factors superimposed on the relatively stable trend changes, resulting in fluctuating randomness. As a result, the increase in load is uncertain, and the extent of variation is unpredictable.

$$P_T = \frac{1}{\sqrt{2\pi}\sigma} \exp\left(-\frac{(x - (1 + a))^2}{2\sigma^2}\right) \tag{21}$$

where, a represents the growth rate of the long-term trend change, x denotes the growth rate of the current year, and the scale parameter is represented by σ.

3 Dist flow method

The utilization of an economic model within the system dynamics framework allows for the simulation of diverse investment growth scenarios. However, the accurate calculation of indicators necessitates a thorough analysis of operational data from the distribution network. In this context, the employment of an optimization model, integrated with engineering constraints, becomes imperative. It is worth noting that the system dynamics model cannot be effectively solved through constrained optimization techniques alone. Consequently, this paper introduces a novel linear power flow calculation model for multi-scenario distribution networks.

3.1 Dist flow model

The dist flow model, also known as the linear power flow calculation model, plays a crucial role in analyzing and optimizing the operation of distribution networks. This model provides significant benefits for power flow analysis in distribution networks compared to other methods. This model is employed to estimate the power flow and voltage profiles within the network, considering various constraints and operational conditions, as well as the impacts of DER such as solar panels, wind turbines, and energy storage systems. The dist flow model utilizes a linear approximation of the power flow equations, enabling efficient and computationally tractable solutions. It considers the voltage magnitudes and angles at different network nodes, reactive power flows, and real power losses. By solving this model, researchers and engineers can obtain valuable insights into network performance, voltage regulation, power losses, and the integration of renewable energy sources. Moreover, the distribution flow model serves as a fundamental tool for various applications, including network planning, voltage control, optimal DER placement, and analysis of fault conditions. Its integration with optimization algorithms allows for the identification of optimal operating strategies and the evaluation of investment decisions, considering factors such as cost, reliability, and environmental impact. This makes dist flow method low a versatile tool for applications in planning, voltage regulation, DER integration, and more.

3.1.1 Objective function

The objective function including the optimal power flow problem of DER distribution network generally includes the minimum loss of distribution network, the minimum node voltage deviation and the minimum DER operating cost. It can be expressed in the general form shown in Eq. 1.

$$\min \sum_{i=0}^{n} C_i(P_{i,t}, Q_{i,t}, U_{i,t}) = C_{\text{loss}} + C_{\text{U}} + C_{\text{res}} + C_{\text{ess}} \tag{22}$$

where C_{loss} is the total loss. $P_{i,t}$ and $Q_{i,t}$ are respectively the active power and reactive power of injection at node i at time t; $U_{i,t}$ is the voltage amplitude of node i at time t; $C_i(\cdot)$ is the cost function of node i, n is the total number of nodes.

The cost function contains 4 parts: distribution network loss, node voltage deviation, penalty cost for RES reduction, energy storage charge and discharge cost.

Distribution network loss:

$$C_{\text{loss}} = \sum_{i=0}^{n} P_{i,t} \tag{23}$$

That is, the distribution network loss is equal to the sum of the active power injections of all nodes including the root node.

Node voltage deviation:

$$C_{\text{U}} = \sum_{i=1}^{n} c_{\text{U}} \left(U_{i,t} - U_{\text{base}}\right)^2 \tag{24}$$

where c_U is the node voltage amplitude deviation penalty coefficient; U_{base} is the voltage reference value, which can be taken as the voltage value of the root node.

Penalty cost of RES reduction:

Taking the photovoltaic power supply as an example, it is shown in formula 40.

$$C_{\text{res}} = c_{\text{res}} \left(P_{i,t,\max} - P_{i,t}\right) \tag{25}$$

where C_{res} is the light abandonment penalty coefficient; $P_{i,t,\max}$ is the maximum active power of photovoltaic determined by the maximum power tracking technology at time t; $i \in N_{\text{res}}$, N_{res} is the set of renewable energy grid-connected nodes.

Energy storage charge and discharge cost:

$$C_{\text{ess}} = c_{\text{ess}} P_{i,t}^2 \tag{26}$$

where C_{ess} is the energy storage charge and discharge cost coefficient;$i \in N_{\text{ess}}$, N_{ess} is the set of energy storage grid-connected nodes.

3.1.2 Power flow constraint

$$\sum_{j=1}^{N^i} \left[U_i U_j \left(G_{ij} \cos\theta_{ij} + B_{ij} \sin\theta_{ij} \right) \right] = P_i \tag{27}$$

$$\sum_{j=1}^{N^i} \left[U_i U_j \left(G_{ij} \sin\theta_{ij} - B_{ij} \cos\theta_{ij} \right) \right] = Q_i \tag{28}$$

$$P_i = P_i^{\text{line}} + P_i^{\text{dis}} - P_i^{\text{Load}} Q_i = Q_i^{\text{line}} + Q_i^{\text{dis}} - Q_i^{\text{Load}} \tag{29}$$

where P_i^{line} and Q_i^{line} are the active and reactive power rates injected by the active power, distributed energy storage and reactive power compensation device connected to node *i*; P_i^{Load} and Q_i^{Load} are active and reactive loads of node *i*.

3.1.3 DER power generation

$$\left(P_{\text{pv}}\right)^2 + \left(Q_{\text{pv}}\right)^2 \le \left(S_{\text{pv}}^{\max}\right)^2 \tag{30}$$

$$Q_{\text{pv}}^{\min} \le Q_{\text{pv}} \le Q_{\text{pv}}^{\max} \tag{31}$$

where Q_{pv} is reactive power output of distributed photovoltaic power station; $S_{\text{pv}}^{\max}$ is the capacity of distributed photovoltaic power station inverter; $Q_{\text{pv}}^{\min}$, $Q_{\text{pv}}^{\max}$ are minimum and maximum reactive power values of distributed photovoltaic power station. In this paper, distributed photovoltaic tracking maximum power point output active power, inverter operation power.

3.1.4 Communication line constraints of superior power grid

$$P_{0,\min} \leqslant P_{0,t} \leqslant P_{0,\max} \tag{32}$$

where $P_{0,t}$ is the injection active power of node 0 (root node) at time *t*.

3.1.5 Line current constraint

$$I_{i,t} \leqslant I_{i,\max} \tag{33}$$

where, $I_{i,t}$ is the current amplitude of the i circuit at time *t*; $I_{i,\max}$ is the maximum allowable current of line *i*; $i \in N_{\text{line}}$, where N_{line} is a set of distribution network lines.

3.1.6 Node voltage constraint

$$U_{\min} \leqslant U_{i,t} \leqslant U_{\max} \tag{34}$$

where, $U_{\max}$ and $U_{\min}$ are the upper and lower limits of allowable node voltage amplitude for safe operation of distribution network, respectively; $i \in N$.

3.1.7 Energy storage system constraints

$$-P_{\text{dis}}^{\max} \le P_{\text{ess}} \le P_{\text{clh}}^{\max} \tag{35}$$

$$SOC_{\text{ess},t+1} = SOC_{\text{ess},t} + \frac{P_{\text{ess},t}\eta_{\text{ch}}\Delta t}{E_{\text{ess}}}, \quad P_{\text{ess},t} > 0 \tag{36}$$

$$SOC_{\text{ess}}^{\min} \le SOC_{\text{ess}} \le SOC_{\text{ess}}^{\max} \tag{37}$$

$$\left(P_{\text{ess}}\right)^2 + \left(Q_{\text{ess}}\right)^2 \le \left(S_{\text{ess}}^{\max}\right)^2 \tag{38}$$

$$Q_{\text{ess}}^{\min} \le Q_{\text{ess}} \le Q_{\text{ess}}^{\max} \tag{39}$$

where $P_{\text{ess},t}$ is the active power at time t of the energy storage system; $P_{\text{ch}}^{\max}$ is the maximum charging power of the energy storage system; $P_{\text{dis}}^{\max}$ is the maximum discharge power; η_{ch} for energy storage system charging efficiency; η_{dis} is discharge efficiency, and both charging and discharging efficiency is 0.9; E_{ess} is the capacity of energy storage system; $SOC_{\text{ess},t}$ indicates the state of charge; $SOC_{\text{ess}}^{\min} SOC_{\text{ess}}^{\max}$ is the lowest and highest state of charge allowed by the energy storage system; Q_{ess} is the reactive power output of the energy storage system; $S_{\text{ess}}^{\max}$ is the capacity of energy storage system inverter; $Q_{\text{ess}}^{\min}$, $Q_{\text{ess}}^{\max}$ are the minimum and maximum reactive power rates of the energy storage system.

3.1.8 Capacitor reactive compensator constraint

$$Q_{\text{CB}} = k_{\text{CB}} Q_{\text{CB}}^1 \tag{40}$$

$$0 \le k_{\text{CB}} \le k_{\text{CB}}^{\max} \tag{41}$$

where, Q_{CRC}^1 is a group of reactive power compensation of capacitance compensator; k_{CRC} is the gear input of capacitor compensator; $k_{\text{CRC}}^{\max}$ is the maximum gear of capacitor reactive compensator;

3.1.9 Static reactive compensator constraint

$$Q_{\text{SVC}}^{\min} \le Q_{\text{SVC}} \le Q_{\text{SVC}}^{\max} \tag{42}$$

where, $Q_{\text{SVC}}^{\max}$ and $Q_{\text{SVC}}^{\min}$ are the upper and lower limits of power compensation for static reactive compensator.

3.1.10 Transformer capacity constraint

$$P_{i,\min}^T \le P_{i,t}^T \le P_{i,\max}^T \tag{43}$$

where $P_{0,t}^T$ is the load of node i at time *t*.

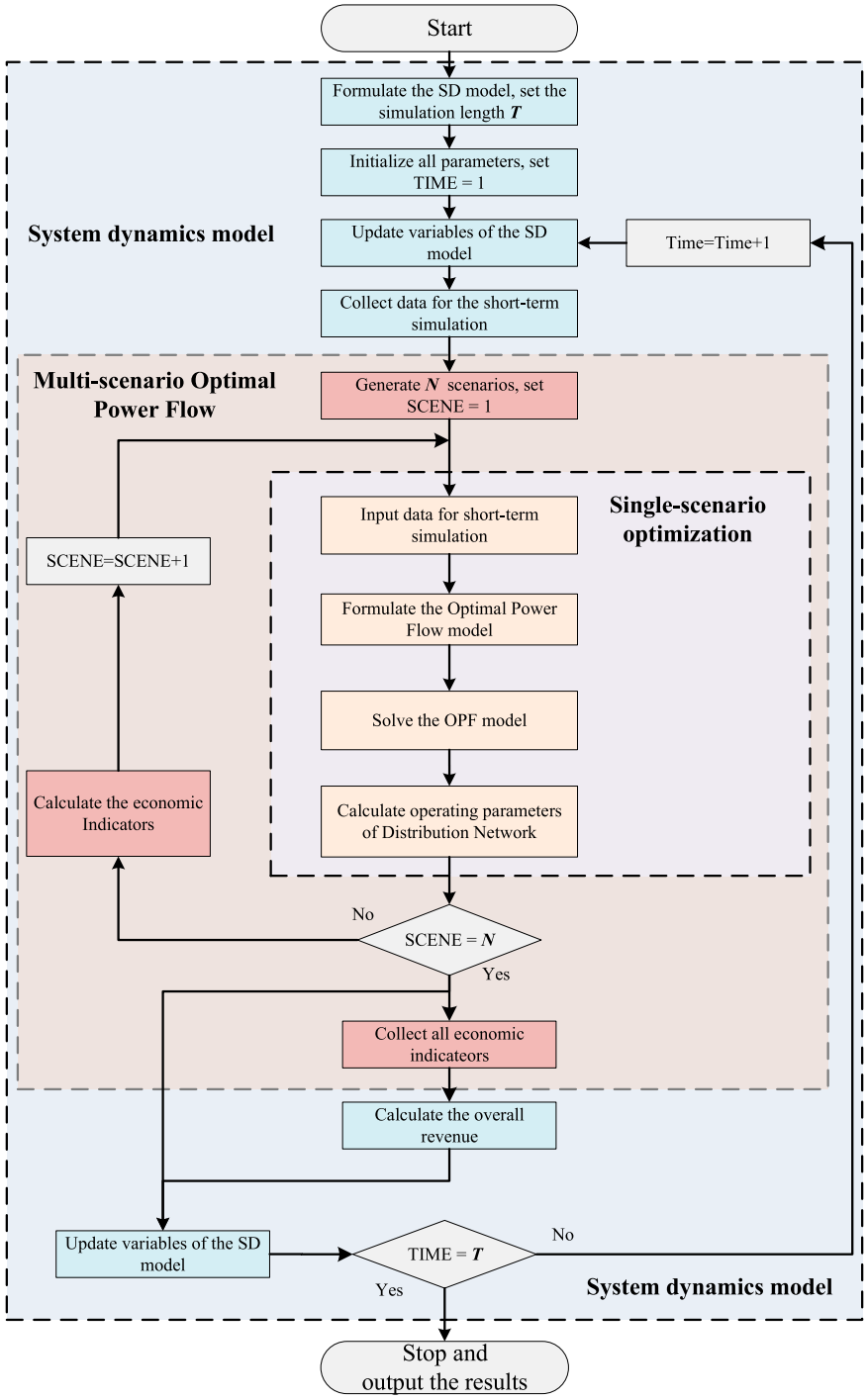

FIGURE 3
Flow chart of the proposed method.

3.2 The general simulation model

In this study, we propose a dual-timescale kinetic model integrating long-term and short-term simulations. Long-term simulations utilize system dynamics (SD) models to analyze complex and multivariate dynamic relationships and simulate distribution network investment trends. On the other hand, hourly short-term simulations are performed using the Dist flow model to calculate the fundamental parameters of market liquidation.

The SD model passes the current values of certain variables as input parameters to the Dist flow model at each time step to do multi-scenario simulations. The results of these simulations

are then incorporated back into the SD model to update the parameters for each investment. The overall process is shown in the Figure 3.

4 Case study

4.1 Scenario setting

In this paper, the IEEE 39-bus system is used for testing. In order to facilitate the calculation of system dynamics model, we set the total load of the IEEE 33-bus system to 600MW, and use the default load of 3.75MW as the benchmark to scale up all load and line parameters in proportion. In the long-term SD simulation, DER increases by a percentage every year, while in the short-term simulation, the newly added capacity of DER is allocated to each node immediately. This paper divides different types of distribution networks to subdivide their respective characteristics and development trends. Combined with the needs of economic and social development for regional distribution network planning, the typical regional characteristics of distribution networks are classified according to the load growth rate and distributed power growth rate, as shown in Table 1.

The time period of simulation is 2021–2040 and the time step is 1 year. The parameter setting of exogenous variables are presented in Table 2 where all data are cited from power exchange center (gzp, 2022). It is worth to mention that, since this model only models a certain area, DER Capacity and DESS Capacity from (gzp, 2022) are approximated to meet the needs of this paper.

TABLE 1 Different scenarios of the system.

Scenario	Characteristic
I	High DER and high load growth rate, base index
II	High DER and low load growth rate, base index
III	Low DER and high load growth rate, base index
IV	Low DER and low load growth rate, base index
V	High DER and high load growth rate, modified index
VI	High DER and high load growth rate, modified index

TABLE 2 Parameter setting of the system dynamics model.

Term	Value	Unit	Source
Initial investment	1×10^7	yuan	(gzp, 2022)
Peak load	6×10^5	kW	(gzp, 2022)
Electricity demand	1×10^9	kW· h	(gzp, 2022)
DER Capacity	3.32×10^4	kW	(gzp, 2022)
DESS Capacity	8×10^3	kW· h	(gzp, 2022)
Peakload growth rate	8×10^3	kW· h	(gzp, 2022)
Investment cost of 10KV line	7.5×10^4	yuan/km	(gzp, 2022)
investment cost of Energy storage	1.1×10^3	yuan/kW· h	(gzp, 2022)
investment cost of SVC	6.2×10^2	yuan/kVar	(gzp, 2022)

4.2 DER trend

First, the long-term trend of DER penetration is shown in the Figure 4. Affected by various factors such as economic conditions, power grid form, and environmental conditions, the four scenarios show great differences. Moreover, a feedback mechanism has been added to the end user sub-model, and the investment in the distribution network has affected the growth of DER, and its trend has reference value. In S1, due to the rapid growth of DER capacity, its power generation also increases rapidly. Therefore, DESS also increases with DER capacity. However, the load growth rate is very high, resulting in a limited increase in the proportion of DER and DESS. In the second scenario, the load does not increase rapidly but the DER increases rapidly, so the electric energy self-sufficiency rate increases significantly. S3 is the opposite, DER grows slowly and load grows fast, resulting in the slowest growth of electric energy self-sufficiency rate. But still reach the 25% level by around 2037. In S4, the load and DER increase slowly, and the electricity self-sufficiency rate is close to Scenario 1. Under the four scenarios, the power self-sufficiency rate is close to S1. The power supply rate at the end of the simulation is between 25%–45%, which highlights the trend of the future distribution network to develop towards a high self-sufficiency rate.

4.3 Investment analysis

To analyze and maintain various operational indicators within the distribution network under different scenarios, we present the trends of total investment increase and final indicator values in Figure 5. The scenarios demonstrate the varying degrees to which DERs can alleviate the investment pressure on the distribution network, underscoring the significance of strategic DER deployment and planning in achieving a balanced and cost-effective network operation.

Observing Figure 5, it is evident that the total investment in the distribution network exhibits an initial prominent growth trend in S1, followed by a gradual deceleration. This pattern arises due to the substantial increase in load demand necessitating the rapid upgrade of distribution network equipment. Despite the partial offsetting effect of DER on net load, the limited initial DER capacity restricts the potential reduction in investment. Over time, as the cumulative DER capacity reaches a certain threshold, the investment pressure on the distribution network begins to alleviate. In S2, after a slight early-stage increase, the total investment experiences a downward trend, eventually falling below the initial investment amount. This indicates that the rapid growth of DERs has significantly alleviated the operating burden on the distribution network. Conversely, in S3, The rapid growth of load imposes a severe burden on the network, while the scarcity of distributed energy sources reduces the network's balancing ability. To ensure the stable operation of the system, the investment level of distribution lines and transformers will increase rapidly. Lastly, S4 depicts a slow growth in both load and DERs, resulting in the total investment remaining relatively stable at the initial level, as there's no urgent need for balancing sources and loads.

According to the growth trend of distributed energy, distribution network investment will also undergo major changes. In S1, the load

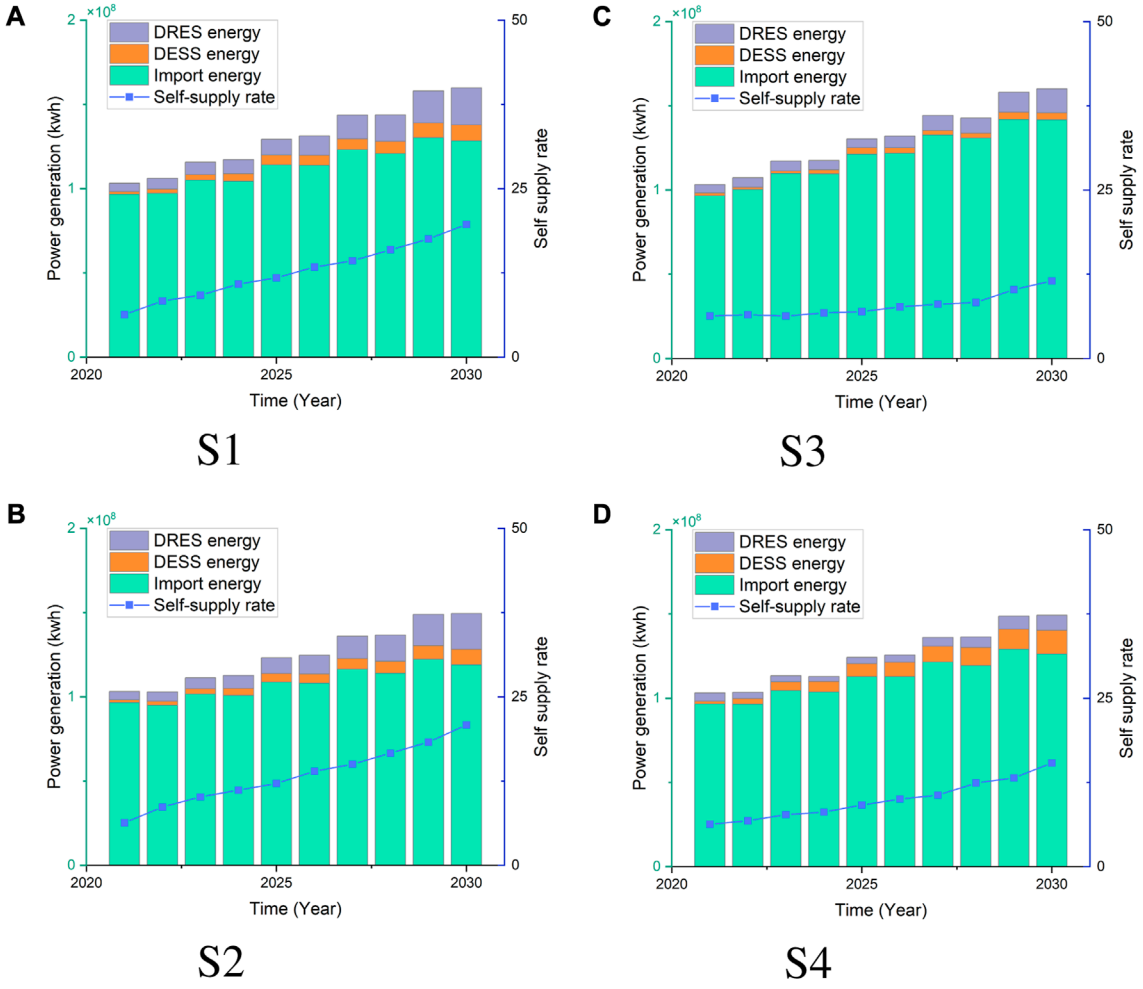

FIGURE 4
Long-term trend of DER penetration.

growth rate is relatively fast, but the proportion of investment in lines and transformers is also gradually increasing. This is because the new power flow of the distribution network brought about by the load growth requires new investment in lines and transformers. Among them, the rapid growth of DESS balances the fluctuation of new energy in the distribution network. In addition, DESS partially replaces the reactive power compensation of SVC and CRC. In S2, investment in line, SVC, and CRC declines, and the proportion of DESS increases rapidly. It shows that the rapid growth of DER requires a large amount of flexible resources, while the rapid growth of DESS partially replaces the role of other investments in the distribution network. Due to the strong volatility and uncertainty of distributed energy sources, which are mostly new energy sources such as wind and solar power, a large amount of DESS is required to cooperate with them to achieve maximum consumption and maintain the safety and stability of the power grid. S3 is the opposite. The small increase of DER leads to the slow growth of DESS, while the increase of load strengthens the demand for lines and other equipment in the distribution network. In S4, due to the small increase in distributed energy and load, the investment ratio is similar to S1, and the investment is concentrated in conventional lines and transformers. Meanwhile, the investment ratios of CRC and SVC are also decreasing year by year. This is because the slow growth of load side and DER does not have high requirements for grid auxiliary services.

4.4 Index structure

This study proposes three distinct types of returns, and their respective proportions in long-term simulations under different scenarios are illustrated in Figure 6. These technical index parameters reflect the real-time performance of the distribution network under different operating conditions and investment scenarios. They are fed as dynamic inputs into the long-term system dynamics model, allowing the investment decisions and revenue forecasts to adapt based on the latest values of these technical parameters. The distribution of benefit types exhibits significant variations among the scenarios. In S1, the higher presence of DER leads to greater environmental benefits. Furthermore, the

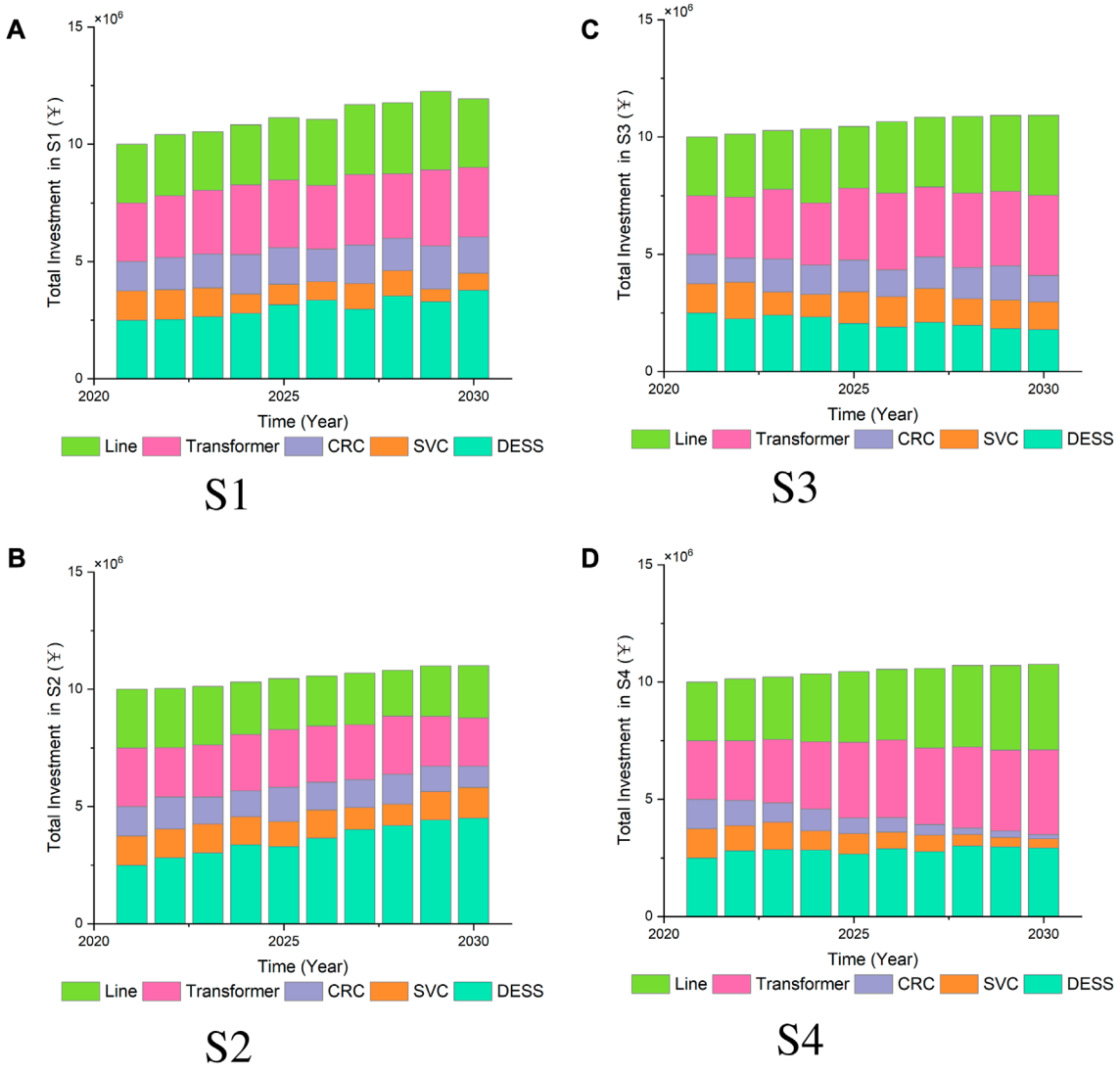

FIGURE 5
Investment ratio adjustment under different scenarios.

power quality benefits display an upward trend during long-term operation. This trend can be attributed to the steady growth of DESS investments and loads, which partially enhance the efficacy of reactive power compensation equipment, resulting in increased revenue. In S2, the proportion of direct economic benefits is the highest. This is primarily due to the substantial increase in DER, which leads to a rapid rise in the share of self-supplied power within the distribution network, subsequently driving up revenue from electricity sales. However, as DER enables a significant amount of power consumption within the node, reducing the load on the grid, the demand for reactive power compensation equipment is diminished, thereby reducing its revenue. S3 exhibits the lowest proportion of electricity sales benefits, while power quality and overall benefits are relatively high. This can be attributed to the slower growth of DER, coupled with higher average electricity prices, resulting in lower income from electricity sales. In S4, both DER and DESS experience gradual growth, leading to a more balanced distribution of various benefits across the board.

4.5 Application of RES and ESS

The utilization of RES and ESS is depicted in Figure 7. In scenarios S1, S2, and S4, curtailment rate of RES is obviously higher. Moreover, the overall curtailment rate of S2 is higher because DER is growing much faster compared to the load, and various adjustment methods cannot achieve real-time power balance, so it can only be partially abandoned for RES. On the contrary, lower loads and DER growth rates reduce system operational risks, improve the matching between the two, and result in a lower curve for S4. In scenarios S1, S2, and S3, the substantial reduction in renewable energy generation results in a high number of hours of energy storage requirement. Conversely, in S4, the

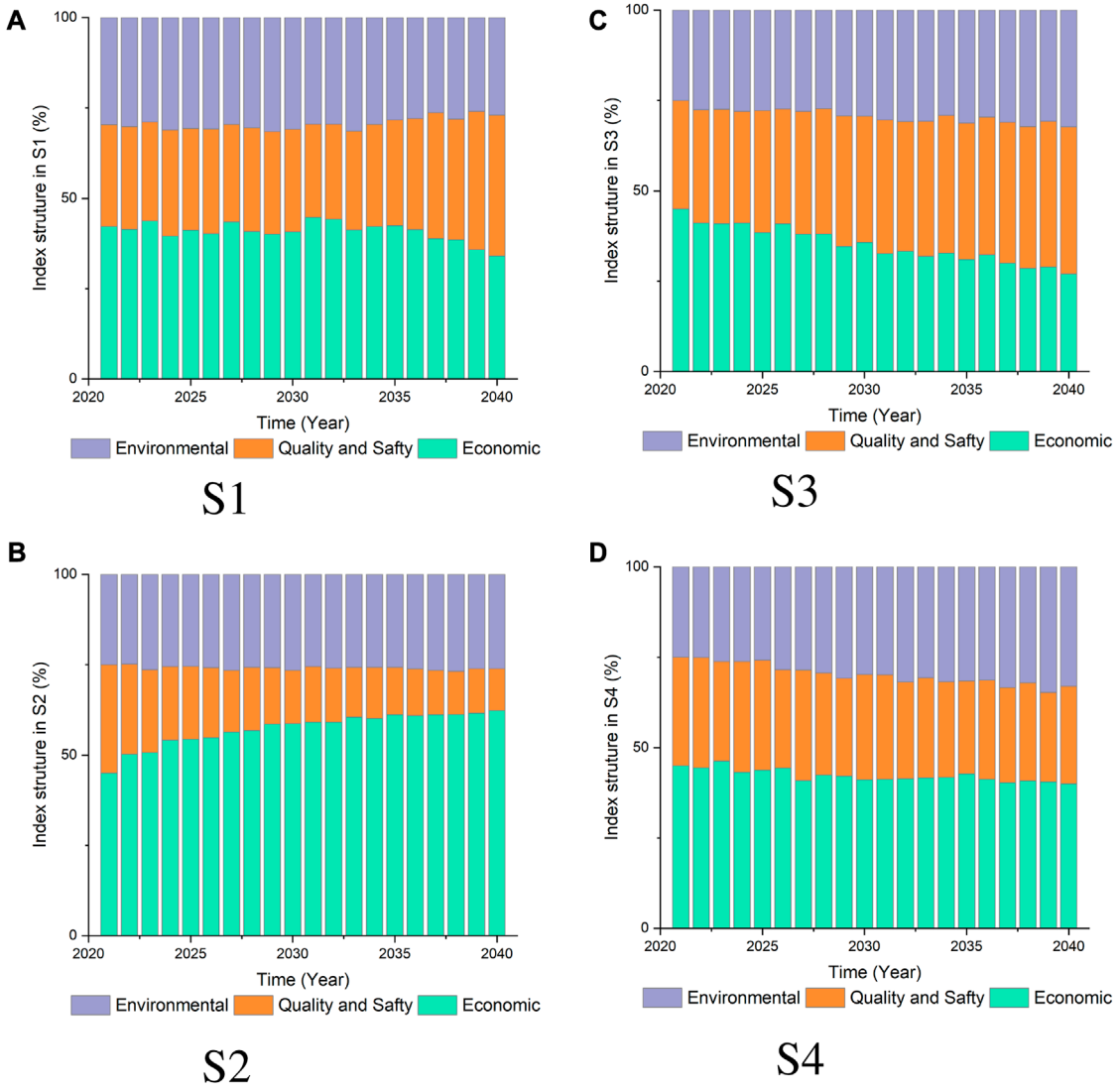

FIGURE 6
Index structure in different scenarios.

slower growth of both load and renewable energy generation leads to a significant increase in the renewable energy penetration rate. Consequently, the demand for energy storage diminishes accordingly.

4.6 The impact of adjusting parameter weights on investment strategy and demand

In this section, a sensitivity analysis is conducted to examine the influence of the adjusted income parameter weight on the model results. S1 will serve as the benchmark case, while new scenarios, S5 and S6, will be designed for comparison. In S5, the weightings assigned to the quality and safety index, environmental index, and economic index are 0.3, 0.3, and 0.4, respectively. Conversely, in S6, the weightings assigned to the quality and safety index, environmental index, and economic index are 0.2, 0.4, and 0.4, respectively. The results are shown in Figure 8; Figure 9.

It is evident that both environmental indicators, namely, energy self-sufficiency and the integration rate of renewable energy, exhibit substantial proportions in both S5 and S6. Conversely, the proportions of quality and safety indicators display a decreasing trend. This trend can be attributed to the significant environmental benefits brought about by the expansion of DER, which consequently yields a relatively higher return on investment in this aspect. In contrast, the growing installed capacity of DERs ensures the power supply capacity and reliability of the distribution network, leading to relatively lower investment benefits in terms of quality and safety indicators. Meanwhile, the total investment shows a rapid growth trend in both S5 and S6. This is partly due to the decline of the economic index, which makes the investor tend to invest more funds to achieve the construction of distributed energy system. Meanwhile, in S6, it can be noticed that growth rate

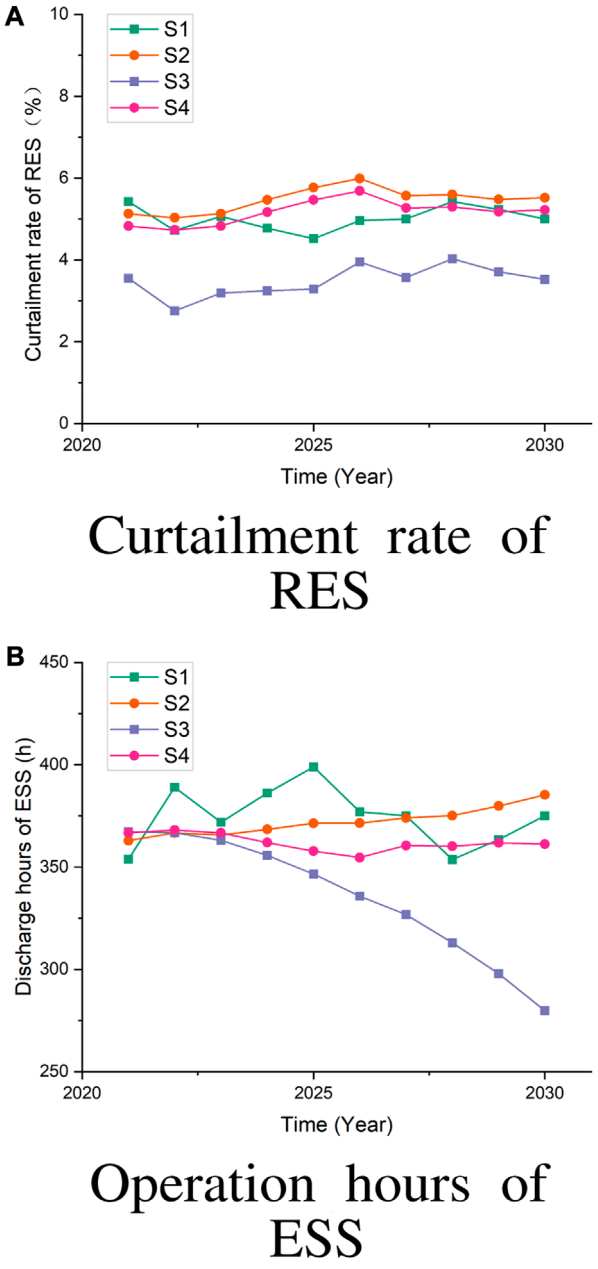

FIGURE 7
Status of RES and ESS in different scenarios.

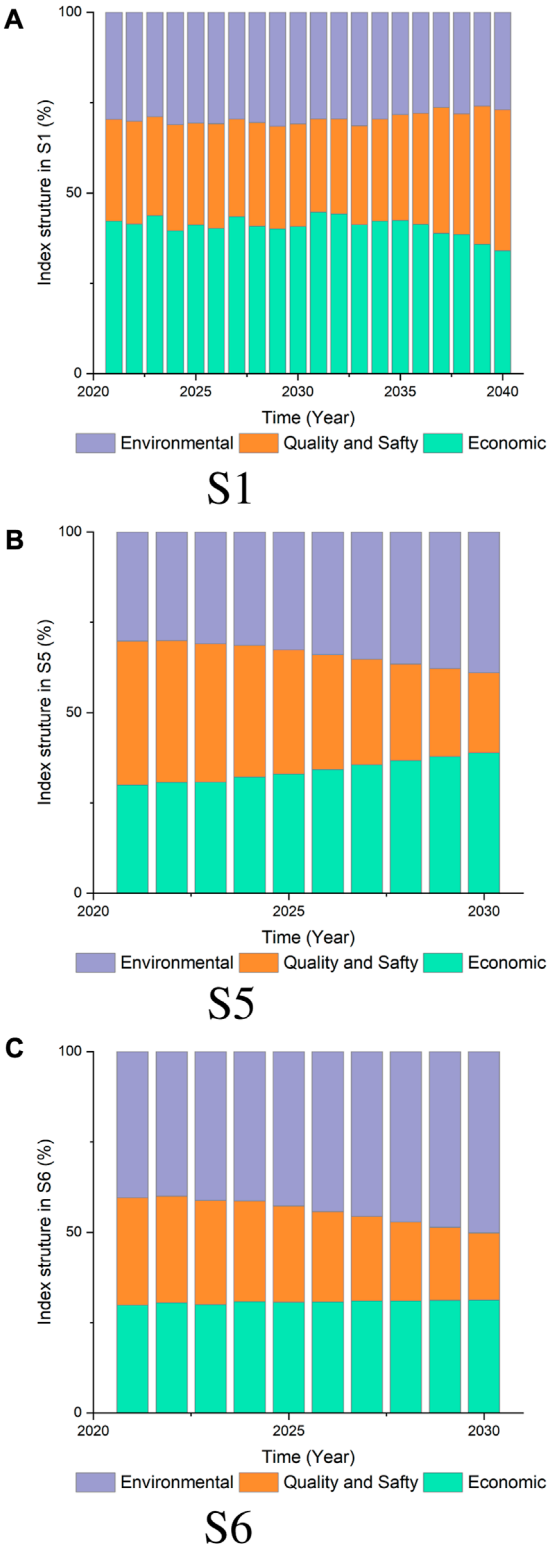

FIGURE 8
Index structure in different scenarios.

of investment in DESS is significantly faster, while its transmission line investment is relatively slow. This may be caused by its high environmental index and low safety index.

4.7 Sensitivity analysis of DER capacity

A sensitivity analysis is conducted to examine the influence of Total Investment, Peak Load Growth Rate and Demand Growth Rate on DER capacity. The result is shown in Figure 10. Figure 10B shows that peak load growth rate has little impact on DER capacity. This is because DER is mostly made of new energy sources such as wind and solar, which itself has great volatility and uncertainty, making it difficult to effectively support peak load demand. Therefore, there is little coupling between DER capacity and peak load growth rate.

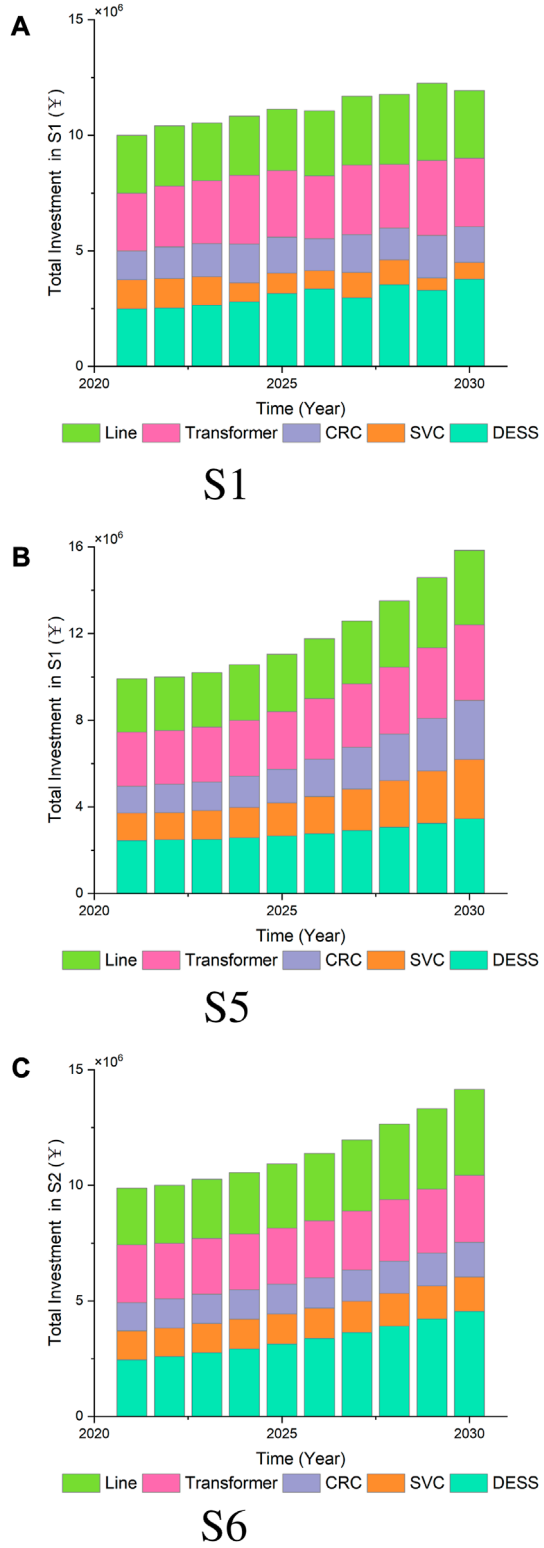

FIGURE 9
Investment adjustment in different scenarios.

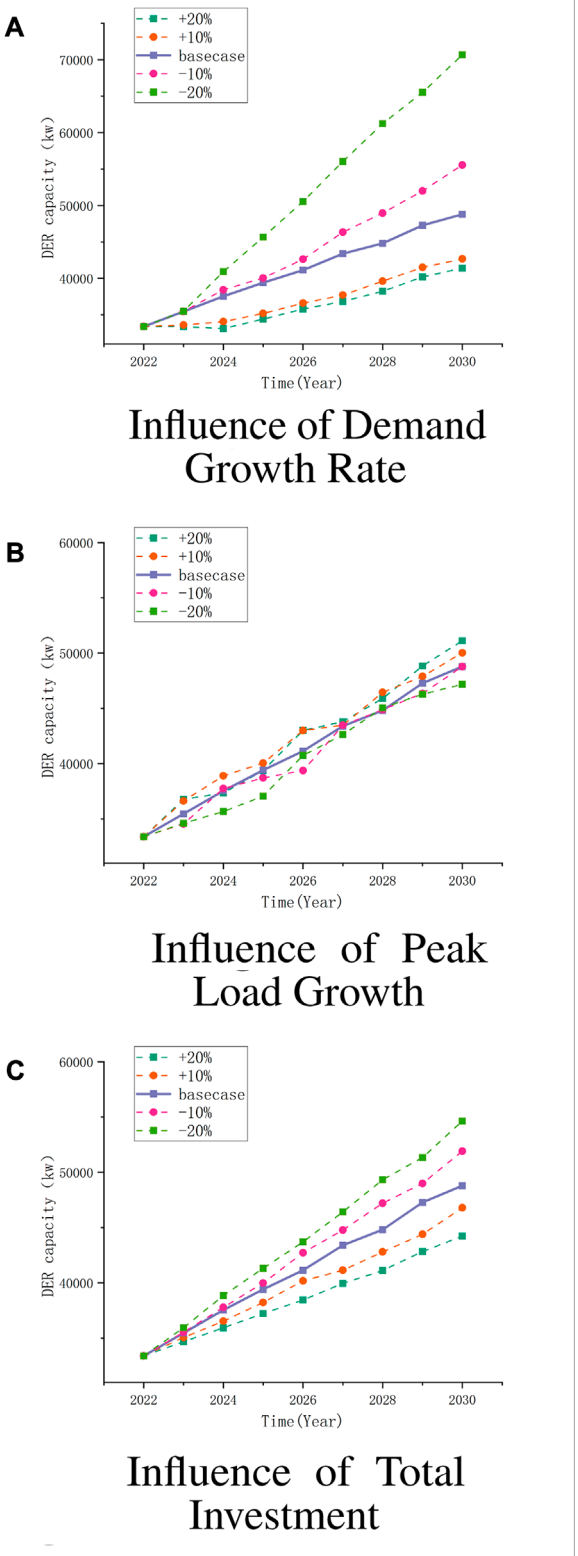

FIGURE 10
Sensitivity analysis of DER capacity.

On the contrary, changes in aggregate demand will significantly affect the development of DER capacity, as shown in the Figure 10A. This is because in the future, DER will be one of the important energy sources and play a decisive role in the total load demand. Therefore, the acceleration of load growth rate will significantly stimulate the development of DER. The impact of total investment on DER capacity is less than that of demand growth, as shown in Figure 10C. This is because the investment amount needs to increase

exponentially if it wishes to achieve higher investment benefits in some other investment areas of the power system, such as grid capacity transformation and transformer capacity transformation, leaving Not much for DER.

5 Conclusion

The growth of distributed generation brings new challenges to distribution network planning. Traditional planning methods fail to effectively divide the indicators for the multi-objective characteristics of distribution network investment. And it is unable to take into account the changes of other related elements under the long-term scale to realize the shortcoming of dynamic adjustment. This paper integrates simulations of system dynamics and optimal power flow models at two different time scales. In the long-term simulation, a multi-objective and multi-element complex system is constructed, and in the short-term simulation, the basic constraints of the distribution network are verified. The obtained simulation results are more convincing. The results show that in the distribution network with different development conditions, the income of each investment is different, and the distribution of investment should also be adjusted according to the characteristics of the distribution network. Overall, in the high DER and low load growth rate scenario, investment demand for various aspects of the power grid will increase synchronously, and the most important indicator of the power grid will gradually become the quality and safety of the grid. This is also the most likely situation that China may face. In this scenario, it is very important to coordinate and plan investment projects for the healthy, safe, and stable operation of the power grid.

The long-term simulation model studied in this paper does not consider the impact of the electricity market. In the future, distributed energy will enter the wholesale power market through aggregation, or end-user peer-to-peer transactions will become the mainstream trend. The short-term simulation only studies the optimal power flow problem, focusing on the scheduling of conventional scenarios, while ignoring some extreme scenarios and fault analysis. And the model does not accurately model some parameters with uncertainties in the distribution network operation. In the future, starting from these three points, we will further analyze the impact of the power market, fault scenarios and uncertainties on the simulation.

Data availability statement

The original contributions presented in the study are included in the article/Supplementary Material, further inquiries can be directed to the corresponding author.

Author contributions

QL: Conceptualization, Data curation, Funding acquisition, Methodology, Project administration, Resources, Software, Visualization, Writing–original draft, Writing–review and editing. YL: Data curation, Funding acquisition, Investigation, Methodology, Software, Software, Writing–review and editing.

Funding

The author(s) declare that no financial support was received for the research, authorship, and/or publication of this article. This work was supported in part by the State Grid Hubei Electric Power Company under Grant 22H0455. The funder was not involved in the study design, collection, analysis, interpretation of data, the writing of this article, or the decision to submit it for publication.

Conflict of interest

Author QL was empolyed by State Grid Corporation of China.

The authors declare that this study received funding from State Grid Hubei Electric Power Company. The funder was not involved in the study design, collection, analysis, interpretation of data, the writing of this article, or the decision to submit it for publication.

Publisher's note

References

Adefarati, T., and Bansal, R. C. (2019). Reliability, economic and environmental analysis of a microgrid system in the presence of renewable energy resources. *Appl. energy* 236, 1089–1114. doi:10.1016/j.apenergy.2018.12.050

Chi, Y.-y., Zhao, H., Hu, Y., Yuan, Y.-k., and Pang, Y.-x. (2022). The impact of allocation methods on carbon emission trading under electricity marketization reform in China: A system dynamics analysis. *Energy* 259, 125034. doi:10.1016/j.energy.2022.125034

Cui, Q., Bai, X., and Dong, W. (2019). Collaborative planning of distributed wind power generation and distribution network with large-scale heat pumps. *CSEE J. Power Energy Syst.* 5, 335–347. doi:10.17775/CSEEJPES.2019.00140

Dhivya, S., and Arul, R. (2021). Demand side management studies on distributed energy resources: A survey. *Trans. Energy Syst. Eng. Appl.* 2, 17–31. doi:10.32397/tesea.vol2.n1.2

Ehsan, A., and Yang, Q. (2019). State-of-the-art techniques for modelling of uncertainties in active distribution network planning: A review. *Appl. energy* 239, 1509–1523. doi:10.1016/j.apenergy.2019.01.211

Guangzhou Power Exchange Center (2022). Available at: https://www.gzpec.cn/main/index.do.

International Energy Agency (2022). *Unlocking the potential of distributed energy resources*. Paris: International Energy Agency.

Li, J., Luo, Y., and Wei, S. (2022). Long-term electricity consumption forecasting method based on system dynamics under the carbon-neutral target. *Energy* 244, 122572. doi:10.1016/j.energy.2021.122572

Luo, L., Abdulkareem, S. S., Rezvani, A., Miveh, M. R., Samad, S., Aljojo, N., et al. (2020). Optimal scheduling of a renewable based microgrid considering photovoltaic

system and battery energy storage under uncertainty. *J. Energy Storage* 28, 101306. doi:10.1016/j.est.2020.101306

Maheshwari, A., Heleno, M., and Ludkovski, M. (2020). The effect of rate design on power distribution reliability considering adoption of distributed energy resources. *Appl. energy* 268, 114964. doi:10.1016/j.apenergy.2020.114964

Panigrahi, R., Mishra, S. K., Srivastava, S. C., Srivastava, A. K., and Schulz, N. N. (2020). Grid integration of small-scale photovoltaic systems in secondary distribution network—A review. *IEEE Trans. Industry Appl.* 56, 3178–3195. doi:10.1109/tia.2020.2979789

Song, X.-h., Han, J.-j., Zhang, L., Zhao, C.-p., Wang, P., Liu, X.-y., et al. (2021). Impacts of renewable portfolio standards on multi-market coupling trading of renewable energy in China: A scenario-based system dynamics model. *Energy Policy* 159, 112647. doi:10.1016/j.enpol.2021.112647

Tang, L., Guo, J., Zhao, B., Wang, X., Shao, C., and Wang, Y. (2021). Power generation mix evolution based on rolling horizon optimal approach: A system dynamics analysis. *Energy* 224, 120075. doi:10.1016/j.energy.2021.120075

Teufel, F., Miller, M., Genoese, M., and Fichtner, W. (2013). *Review of system dynamics models for electricity market simulations*.

Thang, V. (2021). Optimal sizing of distributed energy resources and battery energy storage system in planning of islanded micro-grids based on life cycle cost. *Energy Syst.* 12, 637–656. doi:10.1007/s12667-020-00384-x

Yi, Z., Xu, Y., Gu, W., Yang, L., and Sun, H. (2021). Aggregate operation model for numerous small-capacity distributed energy resources considering uncertainty. *IEEE Trans. Smart Grid* 12, 4208–4224. doi:10.1109/tsg.2021.3085885

Ying, Z., Xin-gang, Z., and Zhen, W. (2020). Demand side incentive under renewable portfolio standards: A system dynamics analysis. *Energy Policy* 144, 111652. doi:10.1016/j.enpol.2020.111652

frontiers | Frontiers in Energy Research

TYPE Original Research
PUBLISHED 06 December 2023
DOI 10.3389/fenrg.2023.1294832

OPEN ACCESS

EDITED BY
Youbo Liu,
Sichuan University, China

REVIEWED BY
Hui Liu,
Guangxi University, China
Bing Sun,
Tianjin University, China
Pupu Chao,
Dalian University of Technology, China
Wuhui Chen,
Taiyuan University of Technology, China

*CORRESPONDENCE
Yupeng Wang,
20172753@neepu.edu.cn

RECEIVED 15 September 2023
ACCEPTED 20 November 2023
PUBLISHED 06 December 2023

CITATION
Yan G, Wang Y, Yang C and Yue L (2023), Analysis of sub-synchronous oscillation characteristics of PMSGs based on transient energy.
Front. Energy Res. 11:1294832.
doi: 10.3389/fenrg.2023.1294832

Analysis of sub-synchronous oscillation characteristics of PMSGs based on transient energy

Gangui Yan[1,2], Yupeng Wang[1,2]*, Cheng Yang[2] and Lin Yue[2]

[1]Key Laboratory of Modern Power System Simulation and Control and Renewable Energy Technology, Ministry of Education (Northeast Electric Power University), Jilin, China, [2]School of Electrical Engineering, Northeast Electric Power University, Jilin, China

Faced with the problem of sub-synchronous oscillation (SSO) caused by the interaction between permanent magnetic synchronous generator (PMSG)-based wind farms and weak AC grids, we construct a transient energy function model that follows the structure of a PMSG. The transient energy composition of a PMSG is analyzed, and the dissipation energy expression that can intuitively reflect the development trend of SSO is derived, reflecting the damping level of a grid-connected wind power system. Furthermore, in response to the problem of mutual coupling between the control links of the PMSG during the SSO process, which hinders oscillation characteristic assessment, a method based on oscillation energy is proposed to analyze the oscillation characteristics. Considering the dynamic changes in the output of the phase-locked loop during sub-synchronous oscillation, the transient energy dominated by various control links is derived, and the effects of the phase-locked loop, current inner loop, and voltage outer loop on transient energy and oscillation characteristics are analyzed. The simulation verifies the effectiveness of the analysis of the transient energy model.

KEYWORDS

permanent magnet synchronous generator, sub-synchronous oscillation, characteristic analysis, transient energy, dissipation energy

1 Introduction

With the rapid development of new energy represented by wind power, permanent magnet synchronous generators (PMSGs) have been widely used because of their high efficiency and low failure rate. A PMSG employs the power electronic converter as the interface for the power grid, which makes its power generation dynamic characteristics disparate from a traditional synchronous generator. When the converter interacts with the power grid, it can induce resonance or oscillation issues that potentially trigger unit tripping, cause equipment damage, and compromise the safe and stable operation of the power grid (Yuan et al., 2016; Zhou et al., 2018; Xie et al., 2021). In Xinjiang's Hami region of China, sub-synchronous oscillation (SSO) frequently occurs since 2015 among wind turbine generator clusters, manifesting at frequencies of 20–40 Hz. The sub-synchronous power flows into the power grid with multiple voltage levels of 35, 110, 220, 500, and 750 kV. Furthermore, it even excites torsional vibration of the turbine generators, resulting in tripping of a thermal power unit steam turbine 300 km away and sudden power drops in HVDC transmission systems (Chen et al., 2017a; Li et al., 2017).

Several techniques have been currently employed for analyzing SSO in wind power grid-connected systems, including eigenvalue analysis, complex torque coefficient analysis,

impedance analysis, and time-domain simulation, and henceforth, certain results are obtained. Some references use the eigenvalue analysis to study sub-synchronous oscillation, which investigates the system's dynamic response by solving the eigenvalue of a linearized model for small disturbances (Wu et al., 2016; Chen et al., 2017b). This method can yield insights into the oscillation mode, damping characteristics, participation factor, and sensitivity. However, it can only be used for dynamic characteristic analysis of isolated modes. Some studies apply the complex torque coefficient analysis method to determine the risk of SSO in the system under torsional vibration frequency (Fan and Miao, 2012; Xie et al., 2016). This method involves the scanning and numerical analysis of the equivalent elastic coefficient and damping coefficient. However, it is only suitable for analyzing single-input single-output systems and cannot study complex systems with multiple variable interactions. Some studies use the impedance analysis to establish positive- and negative-sequence impedance models in the abc stationary coordinate system and frequency-domain impedance models in the dq synchronous rotating coordinate system (Dong et al., 2015; Gao et al., 2015). This is a recently globally adopted theoretical method to determine the stability of the system by establishing the small-signal frequency-domain impedance model for power electronic devices and using the (generalized) Nyquist criterion, though it is difficult to analyze the coupling effect between the control links. The time-domain simulation analysis method, as applied in the work of Xie et al. (2016), involves solving the differential equations governing the system's dynamic characteristics through numerical integration to obtain its time-domain response curve. Although this method can capture the system's nonlinear behavior, it may not offer adequate information for analyzing the mechanism characteristics of SSO.

SSO in power systems occurs when there is an energy exchange between the oscillating units and the system at a frequency that is lower than the synchronous frequency, which is manifested as power oscillation. Recently, low-frequency oscillations and SSO based on the transient energy method have been studied (Min and Chen, 2007; Chen et al., 2013a; Li et al., 2013a; Chen et al., 2013b). A method for constructing the transient energy function of a power system based on Kirchhoff's current law was proposed by Min and Chen (2007), where the transient energy function for an induction motor model is derived. Some references propose the concept of energy flow and quantitatively deduce the correlation between the real part of eigenvalue and energy dissipation (Chen et al., 2013a; Chen et al., 2013b). Furthermore, the transient energy is also applied to the identification of oscillation source units (Yu et al., 2010; Li et al., 2013a; Li et al., 2013b) and the classification of low-frequency oscillation types (Mi et al., 2018). In the work of Chen et al. (2016), the transient energy flow method has been expanded to analyze SSO, and an expression for the transient energy during SSO is proposed. The source of sub-synchronous forced oscillation in a single-machine infinite bus system with a steam turbine generator unit has been successfully identified using this method, thus demonstrating its suitability for studying SSO. The above energy methods are mostly traditional synchronous generators, with little involvement in the direct drive wind turbines, and the impact of different time scale control links of PMSGs are not discussed.

We have analyzed the SSO of a PMSG by employing the transient energy flow method, and the contributions of different time scale control links to the SSO process have been examined. On the grounds of the relevant mathematical model, the transient energy flow calculation formula applicable to a PMSG is derived in Section 3. In Section 4, the transient energy properties of different control links are analyzed. The simulations are given in Section 5, whereas the conclusions and prospects of future studies are presented in Section 6.

2 Model construction of the PMSG

2.1 PMSG model

The machine-side converter of a PMSG is decoupled from the grid, and the time scale of wind speed change is far greater than the time scale of converter control. The influence of the grid-side converter (GSC) of a PMSG should be emphatically considered while analyzing SSO in grid-connected wind power systems (Xie et al., 2013; Xie et al., 2016). Figure 1 illustrates the configuration of PMSG GSC connected to the grid. $\dot{E}$ is the internal voltage of the GSC, $\dot{U}_t$ is the terminal voltage of the converter, and L_f is the filter inductance of the converter. The coordinate space position and phase relationship of the relevant phasors are shown in Figure 2. The phase-locked dq coordinate system is a coordinate system rotating at speed ω_p. When the phase-locked loop is fully tracked, the phase-locked dq coordinate system rotates at synchronous angular frequency ω_0.

The GSC of a PMSG includes a DC capacitor and an AC inductor, which are two energy storage components to realize energy exchange with the grid. To maintain the stability of the state variable of the DC capacitor and AC inductor, DC voltage control and AC current control are designed for the GSC (Wang et al., 2022).

The GSC utilizes the phase-locked loop (PLL) to sense the phase of point of interconnection voltage $\dot{U}_t$. This generates a reference coordinate system for the GSC's vector control. Figure 3 shows a three-phase synchronous PLL control block diagram based on dq synchronous coordinate transformation.

2.2 Multiple time scale characteristics of the PMSG

Owing to the different energy storage capacities of the DC capacitor and AC inductor, the bandwidths of control loops designed according to their state variable are also different. When disturbances occur in the power grid, both the DC capacitor voltage and AC inductance current of the converter change and drive each controller to act. Since the bandwidths of both the DC voltage and AC current controllers differ, the speed and sequence of their response to grid disturbances are also different; i.e., the PMSG control system shows the characteristics of sequential action.

Owing to the sequential action of the controller, the response process of the PMSG to different time scale disturbances is different; i.e., the PMSG exhibits multiple time scale dynamic response characteristics to the power grid. According to the characteristics of energy storage elements and the response speed of their

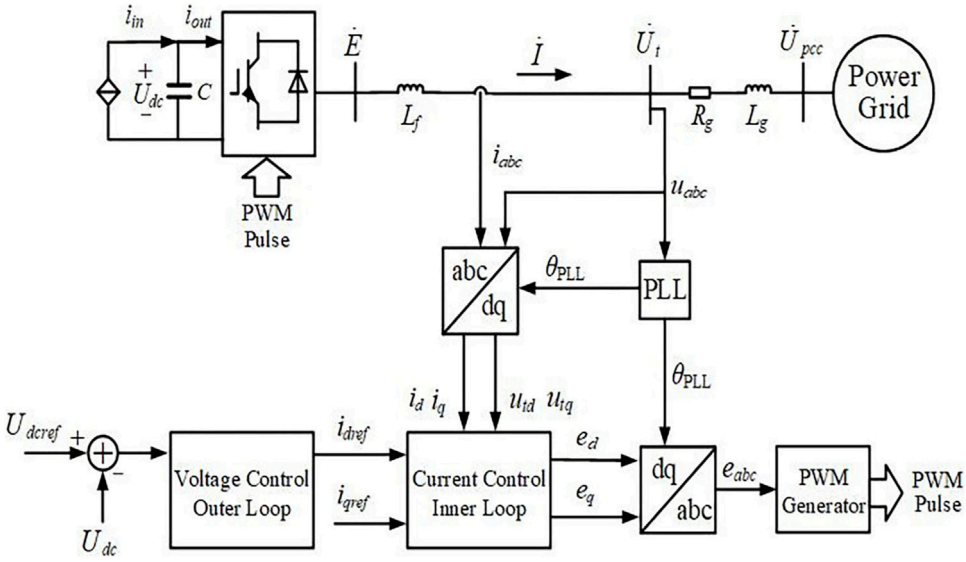

FIGURE 1
Configuration of the PMSG's GSC connected to the grid.

corresponding controllers, Yuan et al. (2016) roughly divided the multi-scale control dynamics of the grid-connected converter into an AC current control scale (about 0.01s) and a DC voltage control scale (about 0.1 s). Generally, the current inner loop control bandwidth in the new energy systems is around 100 Hz, whereas the control bandwidths for the DC voltage loop and terminal voltage loop are designed to be approximately 1/10 of the current inner loop bandwidth (about 10 Hz). Therefore, the dynamics of the PMSG can be divided into different categories according to the time scale, as shown in Figure 4.

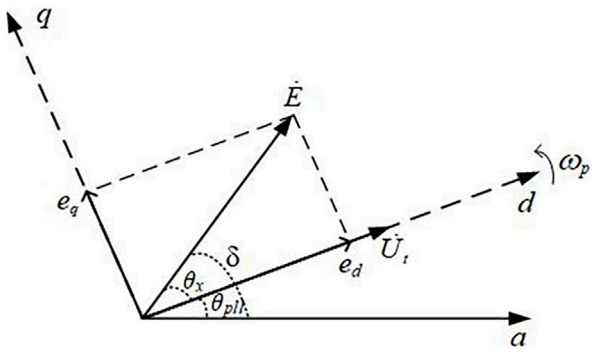

FIGURE 2
Spatial position and phase relationship of the coordinate system.

3 Construction of the transient energy function of the PMSG under sub-synchronous frequency

3.1 Node current equation-based transient energy modeling

The essence of oscillation is the accumulation and consumption of disturbance energy between devices. The energy function construction is based on the pure mathematical definition, but the potential energy and dissipated energy contained in the energy function have the same expression as the energy in the real physical process. In the work of Moon et al. (1999), a method has been introduced to derive the system's transient energy function from the nodal current equations. The transient energy of the system can be obtained by integrating the branch circuit and node information.

$$\boldsymbol{W}=\int \mathrm{Im}\left(\left(\left(\boldsymbol{Y}\boldsymbol{U}_{\boldsymbol{B}}-\boldsymbol{I}_{\boldsymbol{G}}+\boldsymbol{I}_{\boldsymbol{L}}\right)^{*}\right)^{T}\boldsymbol{dU}_{\boldsymbol{B}}\right), \tag{1}$$

where Y denotes the admittance matrix of the system, U_B is the column vector of node voltages, and I_G and I_L are the column vectors of injected current at the generator node and load node, respectively. Im (*) indicates the imaginary component of a complex number.

We expand Eq. (1) as

$$\begin{aligned} W_{net} &= \int \mathrm{Im}\left[\sum_{i=1}^{n}\left(\sum_{j=1}^{n} Y_{ij}^{*}U_j^{*}\right)dU_i\right], \\ &= \left(-\frac{1}{2}{}^{*}\sum_{i=1}^{n} B_{ii}U_i^2 - \sum_{i=1}^{n-1}\sum_{j=i+1}^{n} B_{ij}U_iU_j\cos\theta_{ij}\right)\Bigg|_{(U_0,\theta_0)}^{(U,\theta)}, \\ W_{gen} &= \int \mathrm{Im}\left(\sum_{i\in i_G} I_{Gi}^{*}dU_i\right) = \left(\frac{1}{2}M_i\omega_i^2 - P_{mi}\delta_i\right)\Bigg|_{x_0}^{x} + \int D_i\omega_i^2 dt, \\ W_{load} &= \int \mathrm{Im}\left(\sum_{i\in i_L} I_{Li}^{*}dU_i\right) = Q_{Li}\,ln U_i\Big|_{U_0}^{U} + P_{Li}\theta\Big|_{\theta_0}^{\theta}, \end{aligned} \tag{2}$$

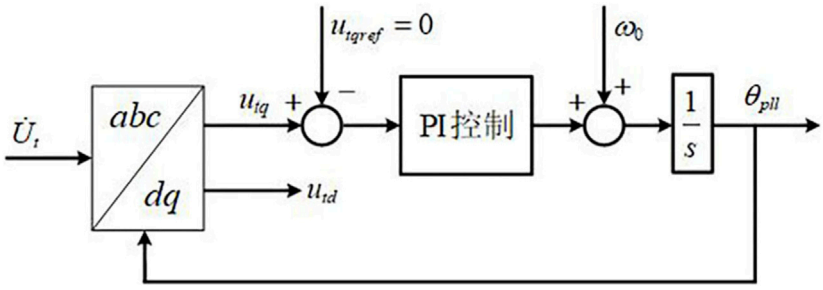

FIGURE 3
Structure of the PLL.

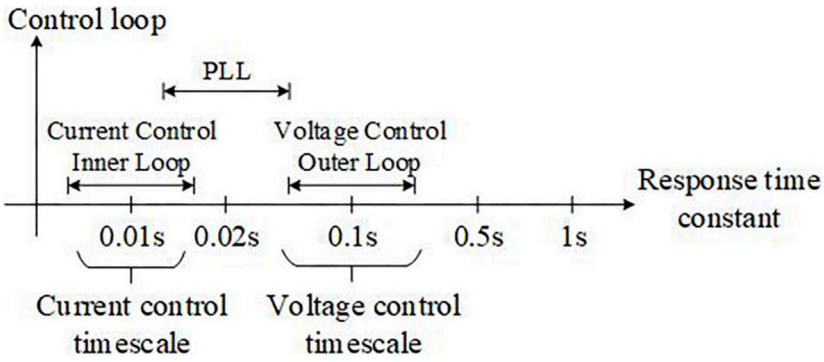

FIGURE 4
Dynamic time scale division of inverter control.

where W_{gen} represents the transient energy of the generator, W_{net} is the transient energy of the system, and W_{load} is the transient energy of the load.

Equation (2) is consistent with the transient energy function obtained by the first integral method in the power system structure-preserving model (Min and Chen, 2007). Therefore, this method can be employed to analyze the transient energy of the system, and it only requires the information of voltage and current or the information of active power, reactive power, and voltage. Thus, the construction process of the energy function is simple.

In Eq. (2), W_{gen} is a general expression for the transient energy of the generator port, which can be employed for both traditional generators and direct-drive wind turbines. The generator's transient energy model has been introduced and used to derive the transient energy function of a direct-drive wind turbine. We equate the output current of the grid side of the generator's PMSG to the generator current and substitute it into the transient energy expression. Instantaneous values are used for analysis since it is not appropriate to use power frequency phasors in sub-synchronous oscillation scenarios. The abc coordinate system values of different physical quantities have been transformed into the dq-axis coordinate system using coordinate transformation. The transformation relationship is given as

$$\begin{bmatrix} x_d \\ x_q \end{bmatrix} = P(\theta_{pll}) \begin{bmatrix} x_a \\ x_b \\ x_c \end{bmatrix}, \tag{3}$$

where the instantaneous value of the voltage or current is represented as $x_a/x_b/x_c$, the d and q components of voltage or current are represented as x_d/x_q, $P(\theta_{pll}) = \frac{2}{3}\begin{bmatrix} \cos\theta_{pll} & \cos\left(\theta_{pll} - \frac{2}{3}\pi\right) & \cos\left(\theta_{pll} + \frac{2}{3}\pi\right) \\ -\sin\theta_{pll} & -\sin\left(\theta_{pll} - \frac{2}{3}\pi\right) & -\sin\left(\theta_{pll} + \frac{2}{3}\pi\right) \end{bmatrix}$, and θ_{pll} represents the output angle of the PLL.

The transient energy of the PMSG in the dq-axis coordinate system is given as

$$\boldsymbol{W_{TE}} = \int \boldsymbol{Im}[(\boldsymbol{i_d} - \boldsymbol{ji_q})\boldsymbol{d}(\boldsymbol{e_d} + \boldsymbol{je_q})]. \tag{4}$$

According to Figure 2, the phase angle of the internal voltage $\dot{E}$ of the GSC of the PMSG is δ, and Eq. (4) can be further expanded as

$$\begin{aligned} W_{TE} &= \int (i_d de_d - i_q de_q) + \int (i_d e_d + i_q e_q) d\delta, \\ &= W_{TE1} + W_{TE2}, \end{aligned} \tag{5}$$

including

$$\begin{aligned} W_{TE1} &= \int (i_d de_d - i_q de_q), \\ W_{TE2} &= \int (i_d e_d + i_q e_q) d\delta = \int P_{out} d\delta, \end{aligned} \tag{6}$$

where W_{TE1} refers to the transient energy component that is dependent on the internal potential and output current of the PMSG. W_{TE2} corresponds to the transient energy component

that is influenced by the PLL and the output active power (δ is mainly composed of the PLL output phase angle θ_{pll}).

3.2 Relationship between sub-synchronous transient energy and electric power of the PMSG

By measuring the power, voltage, and current information of the PMSG, the transient energy and its variation trend of the PMSG can be calculated.

The transient energy of the electrical device obtained through integration cannot be distinguished between potential and kinetic energy. The transient energy of a component consists of two parts. One is a conservative term that is independent of the path, corresponding to the periodic variables, which reflects the periodic change of the transient energy of the electrical device, i.e., kinetic and potential energy over time. The other part is a non-conservative term related to the path, corresponding to the non-periodic variables, which reflects the transient energy consumed by the electrical device, which corresponds to damping. This part of energy is defined as the dissipated energy.

The integration-based approach for obtaining the transient energy of an electrical device cannot differentiate between potential energy and kinetic energy, which is not conducive to analyzing the characteristics of the electrical device. Dissipated energy corresponds to damping in a physical sense. When SSO occurs, the change in dissipated energy determines the damping level of SSO, which is the main basis for analyzing the SSO. In actual calculations, each variable can be represented by its deviation from the steady-state value.

Assuming that there is a symmetrical sub-synchronous sinusoidal disturbance current in the three-phase current output by the GSC of the PMSG, the phase current and voltage can be described as

$$\begin{cases} i_a = i_{0a} + i_{sa} = i_0 \sin(\omega_0 t + \varphi_{i0}) + i_s \sin(\omega_s t + \varphi_{is}) \\ e_a = e_{0a} + e_{sa} = e_0 \sin(\omega_0 t + \varphi_{u0}) + e_s \sin(\omega_s t + \varphi_{us}) \end{cases}, \quad (7)$$

where i_a and e_a are the A phase current and voltage of the GSC after disturbance, respectively. Furthermore, i_0 and e_0 are the current and voltage amplitude of the GSC in steady state, respectively, ω_0 is the grid angular frequency in steady state, and φ_{i0} and φ_{u0} are the current and voltage initial phase in steady state, respectively. Furthermore, i_s and e_s are the disturbance current and voltage amplitude of the GSC, respectively. ω_s is the sub-synchronous disturbance angular frequency, and φ_{is} and φ_{us} are the disturbance current and voltage initial phase, respectively.

To obtain the PMSG's transient energy, we first convert the voltage and current values of the PMSG from the static abc coordinate system to the rotating dq-axis coordinate system. Considering the PLL response, the voltage and current converted to the rotating dq-axis coordinate system are as follows:

$$\begin{bmatrix} i_d \\ i_q \end{bmatrix} = P(\theta_{pll}) \begin{bmatrix} i_a \\ i_b \\ i_c \end{bmatrix} = \begin{bmatrix} i_0 \cos(\varphi_{u0} - \varphi_{i0}) + i_s[\cos(\omega_0 - \omega_s)t + \varphi_{us} - \varphi_{is}] \\ -i_0 \sin(\varphi_{u0} - \varphi_{i0}) - i_s[\sin(\omega_0 - \omega_s)t + \varphi_{us} - \varphi_{is}] \end{bmatrix}, \quad (8)$$

$$\begin{bmatrix} e_d \\ e_q \end{bmatrix} = P(\theta_{pll}) \begin{bmatrix} e_a \\ e_b \\ e_c \end{bmatrix} = \begin{bmatrix} e_0 + e_s[\cos(\omega_0 - \omega_s)t + \varphi_{u0} - \varphi_{us}] \\ -e_s[\sin(\omega_0 - \omega_s)t + \varphi_{u0} - \varphi_{us}] \end{bmatrix}. \quad (9)$$

The dissipated energy is the integral of the non-periodic component in the transient energy expression. We calculate the derivatives e_d'/e_q' of e_d/e_q using Eq. (9). Substituting the calculated e_d', e_q', and Eq. (8) into the W_{TE1} of Eq. (6), and preserving the non-periodic term in the integral, we obtain the expression for the dissipated energy W_{DE1} in the W_{TE1} as

$$W_{DE1} = -(\omega_0 - \omega_s) e_s i_s \cos(\varphi_{us} - \varphi_{is}) \cdot t. \quad (10)$$

Substituting Eqs (8), (9) into the W_{TE2} of Eq. (6), and retaining the non-periodic term in the expression W_{TE2}, we obtain the expression for the dissipated energy W_{DE2} in the W_{TE2} as

$$\boldsymbol{W_{DE2} = \omega_0 e_s i_s \cos(\varphi_{us} - \varphi_{is}) \cdot t}. \quad (11)$$

Therefore, the dissipated energy at the GSC of the PMSG is given as

$$W_{DE} = W_{DE1} + W_{DE2} = \omega_s e_s i_s \cos(\varphi_{us} - \varphi_{is}) \cdot t. \quad (12)$$

Equation (12) illustrates the relationship between the transient energy of the GSC of the PMSG and the actual electrical power in the SSO, i.e., the dissipated energy rate in the SSO is proportional to the sub-synchronous power of the PMSG, thus reflecting the damping behavior of the PMSG. Its magnitude depends on the sub-synchronous voltage and current amplitudes, whereas its sign depends on the phase difference of the sub-synchronous voltage and current. When $W_{DE}>0$, the PMSG continuously generates the dissipated energy during SSO, which exhibits negative damping characteristics for the oscillation. The transient energy flowing from the PMSG into the power grid continuously increases, thus inducing the instability of oscillation divergence. When $W_{DE}<0$, the PMSG absorbs the dissipated energy in the process of SSO and shows positive damping characteristics for the oscillation. The transient energy of the PMSG flowing from the PMSG into the power grid gradually decreases, and the oscillation finally converges. When $W_{DE} = 0$, the PMSG neither generates nor absorbs the dissipated energy, and the system oscillates with equal amplitude under ideal conditions.

4 Analysis of transient energy properties of the PMSG

During the process of sub-synchronous oscillation, the interdependence of each control link of the GSC complicates the analysis of oscillation characteristics. Here, the dynamic effects of the phase-locked loop, current inner loop, and DC voltage outer loop control are considered, and the influence of different time scale control links on transient energy and oscillation characteristics is studied.

4.1 Influence of the dynamic PLL process

According to Eq. (6), calculating the transient energy expression of the PMSG requires obtaining the phase angle δ of the internal voltage of the GSC. According to Figure 2,

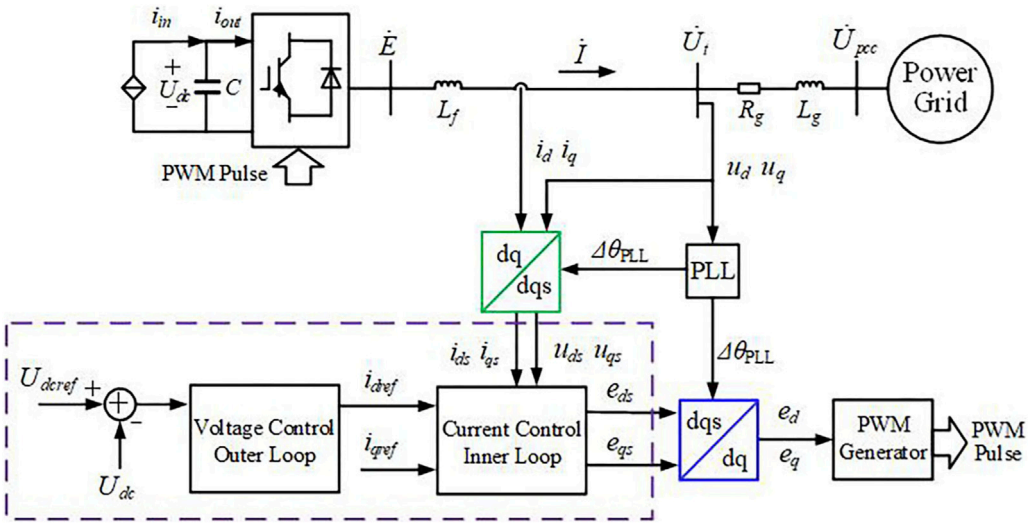

FIGURE 5
Equivalent control system diagram of the GSC of the PMSG.

$$\delta = \theta_{pll} + \theta_x, \tag{13}$$

where θ_{pll} is the output phase angle of the PLL and θ_x is the phase angle difference caused by the filtering inductance.

While SSO occurs, the PLL phase angle is not equal to the steady-state voltage phase angle at the measuring point. This induces a misalignment between the dq-axis coordinate system in the control system and that of the power grid, and the included angle is the variation of the phase-locked angle $\Delta\theta_{pll}$. The variation of the phase-locked angle $\Delta\theta_{pll}$ is primarily affected by the control parameters of the PLL and the q-axis component of the terminal voltage of the PMSG. Based on the three-phase synchronous phase-locked control structure (Yang et al., 2018), the variation of the phase-locked angle $\Delta\theta_{pll}$ can be derived as

$$\Delta\theta_{pll} = -\int\left(k_{p\theta} + \frac{k_{i\theta}}{s}\right)u_{sq}dt. \tag{14}$$

The transformation relationship between the voltage or current in the dq-axis coordinate system of the control system and the voltage or current in the dq-axis coordinate system of the power grid is

$$\begin{bmatrix} x_{ds} \\ x_{qs} \end{bmatrix} = A\begin{bmatrix} x_d \\ x_q \end{bmatrix}, \tag{15}$$

where $A = \begin{bmatrix} cos(\Delta\theta_{pll}) & sin(\Delta\theta_{pll}) \\ -sin(\Delta\theta_{pll}) & cos(\Delta\theta_{pll}) \end{bmatrix}$, x represents voltage or current, and ds and qs represent the coordinate axes of the control system.

4.2 Influence of each control link of the GSC on transient energy

Simultaneous Eqs 6, 13 can give

$$W_{TE2} = \int P_{out}d(\theta_{pll} + \theta_x).$$

Since θ_x is affected by SSO only slightly, it can approximately be unchanging.

$$W_{TE2} = \int P_{out}\omega_0 dt + \int P_{out}d\Delta\theta_{pll}. \tag{16}$$

W_{TE2} consists of two parts. The first part is the transient energy $\int P_{out}\omega_0 dt$, which is the steady-state output part of the transient energy of the PMSG that is primarily affected by the operating conditions and unrelated to wind turbine control. The second part of the transient energy, $\int P_{out}d\Delta\theta_{pll}$, is affected by the variation of the phase-locked angle.

To calculate W_{TE1}, it is necessary to obtain the current i_d/i_q and internal voltage differential value de_d/de_q in the dq-axis coordinate system of the power grid. Owing to the inability to directly obtain de_d/de_q, the mathematical model and control structure of the GSC of the PMSG have been used for analysis. Considering the influence of the dynamic process of the PLL and using the coordinate transformation relationship as shown in Eq. (15), the equivalent control system of the GSC of the PMSG can be obtained (Figure 5). The coordinate system used in the control system is the dq-axis, denoted as dqs.

In the dqs-axis coordinate system of the control system, which is obtained from the current inner loop control equation,

$$\begin{bmatrix} e_{ds} \\ e_{qs} \end{bmatrix} = \left(k_{pi} + \frac{k_{ii}}{s}\right)\begin{bmatrix} i_{dref} - i_{ds} \\ i_{qref} - i_{qs} \end{bmatrix} + \omega_0 L_f \begin{bmatrix} -i_{qs} \\ i_{ds} \end{bmatrix} + \begin{bmatrix} u_{ds} \\ u_{qs} \end{bmatrix}, \tag{17}$$

where the proportional and integral coefficients of the current inner loop PI controller are given by k_{pi} and k_{ii}, respectively, whereas i_{dref} and i_{qref} indicate the reference values of the d-axis and q-axis currents, respectively.

Simultaneously, Eqs (15), (17) give the expression of the internal voltage of the GSC as

$$\begin{bmatrix} e_d \\ e_q \end{bmatrix} = A^{-1}\left(\left(k_{pi}+\frac{k_{ii}}{s}\right)\left(\begin{bmatrix} i_{dref} \\ i_{qref} \end{bmatrix} - A\cdot\begin{bmatrix} i_d \\ i_q \end{bmatrix}\right) + \omega_0 L_f A\cdot\begin{bmatrix} i_d \\ i_q \end{bmatrix} + A\cdot\begin{bmatrix} u_d \\ u_q \end{bmatrix}\right). \tag{18}$$

Since $\Delta\theta_{pll}$ is very small, $A \approx \begin{bmatrix} 1 & \Delta\theta_{pll} \\ -\Delta\theta_{pll} & 1 \end{bmatrix}$; therefore,

$$\begin{bmatrix} e_d \\ e_q \end{bmatrix} = \left(k_{pi}+\frac{k_{ii}}{s}\right)\begin{bmatrix} 1 & -\Delta\theta_{pll} \\ \Delta\theta_{pll} & 1 \end{bmatrix}\begin{bmatrix} i_{dref} \\ i_{qref} \end{bmatrix} - \left(k_{pi}+\frac{k_{ii}}{s}\right)\begin{bmatrix} i_d \\ i_q \end{bmatrix} + \omega_0 L_f \begin{bmatrix} & -1 \\ 1 & \end{bmatrix}\begin{bmatrix} i_d \\ i_q \end{bmatrix} + \begin{bmatrix} u_d \\ u_q \end{bmatrix}. \tag{19}$$

Then,

$$\begin{bmatrix} de_d \\ de_q \end{bmatrix} = k_{pi}\begin{bmatrix} di_{dref} - di_d \\ di_{qref} - di_q \end{bmatrix} + k_{ii}\begin{bmatrix} i_{dref} - i_d \\ i_{qref} - i_q \end{bmatrix}dt + \omega_0 L_f \begin{bmatrix} -di_q \\ di_d \end{bmatrix} + \begin{bmatrix} du_d \\ du_q \end{bmatrix} + d\left(k_{pi}\Delta\theta_{pll}\begin{bmatrix} -i_{qref} \\ i_{dref} \end{bmatrix}\right) + k_{ii}\Delta\theta_{pll}\begin{bmatrix} -i_{qref} \\ i_{dref} \end{bmatrix}dt. \tag{20}$$

According to Eq. (20), the differential value of d/q-axis internal voltage of the GSC is related to the differential value of d/q-axis terminal voltage and current derived from the measurement terminal, besides being affected by the filter reactance L_f, the variation of the phase-locked angle $\Delta\theta_{pll}$, and the reference value of d/q-axis current.

In engineering, the control bandwidth of the current loop is usually about twice that of the PLL and 10 times that of the voltage outer loop control (Yuan et al., 2017). Therefore, while calculating the differentiation of the related terms coupled with the current loop control, it can be considered that the output values $\Delta\theta_{pll}$, i_{dref}, and i_{qref} of the PLL and the voltage outer loop control remain unchanged. Therefore,

$$\begin{bmatrix} de_d \\ de_q \end{bmatrix} = \begin{bmatrix} -k_{pi} & -\omega_0 L_f \\ \omega_0 L_f & -k_{pi} \end{bmatrix}\begin{bmatrix} di_d \\ di_q \end{bmatrix} + k_{ii}\begin{bmatrix} i_{dref} - i_d \\ i_{qref} - i_q \end{bmatrix}dt + \begin{bmatrix} du_d \\ du_q \end{bmatrix} + k_{ii}\Delta\theta_{pll}\begin{bmatrix} -i_{qref} \\ i_{dref} \end{bmatrix}dt. \tag{21}$$

Furthermore, calculating the differential of the relevant terms coupled with the PLL control, it is considered that i_{dref} and i_{qref} are unchanged. Therefore,

$$dk_{pi}\left(\Delta\theta_{pll}\begin{bmatrix} -i_{qref} \\ i_{dref} \end{bmatrix}\right) = k_{pi}\begin{bmatrix} -i_{qref} \\ i_{dref} \end{bmatrix}d\Delta\theta_{pll}. \tag{22}$$

It is assumed that the current loop and PLL control have achieved steady state when calculating the differential of the voltage outer loop control output, which yields the expression

$$k_{pi}\begin{bmatrix} di_{dref} \\ di_{qref} \end{bmatrix} = k_{pi}\begin{bmatrix} -k_{pdc}du_{dc} + k_{idc}\left(u_{dcref} - u_{dc}\right)dt \\ 0 \end{bmatrix}, \tag{23}$$

where k_{pdc} and k_{idc} represent the proportion and integral gains of the voltage outer loop PI controller, respectively, and u_{dcref} denotes the reference value of DC voltage, generally the fixed value, $du_{dcref} = 0$. The control objective for the q-axis current of the GSC grid side converter in the PMSG is the unity power factor control, and the reference value can be assumed to remain constant during the transient process, thus leading to $di_{qref} = 0$.

From the simultaneous Eqs 6, 21–23, we obtain

$$\begin{aligned} W_{TE1} = {} & \omega_0 L_f \int\left(i_d di_d + i_q di_q\right) + \int\left(i_d de_q - i_q de_d\right) \\ & - k_{pi}\int\left(i_d di_q - i_q di_d\right) + k_{ii}\int\left(i_d i_{qref} - i_q i_{dref}\right)dt \\ & + k_{pi}\int\left(i_{dref} i_d + i_{qref} i_q\right)d\Delta\theta_{pll} + k_{ii}\int\Delta\theta_{pll}\left(i_{dref} i_d + i_{qref} i_q\right)dt \\ & + k_{pi}k_{pdc}\int i_q du_{dc} - k_{pi}k_{idc}\int i_q\left(u_{dcref} - u_{dc}\right)dt. \end{aligned} \tag{24}$$

Here, $\omega_0 L_f \int\left(i_d di_d + i_q di_q\right)$ in the first item of Eq. (24) represents the transient energy related to the filtering inductance, which is less affected by control. $\int\left(i_d de_q - i_q de_d\right)$ in the first item represents the transient energy value of the measurement port, which is mainly determined by the operating conditions of the PMSG. The transient energy values of these two parts change periodically in the SSO.

The other items are the transient energy items that are directly affected by the control link. The second item of the expression is the transient energy dominated by the current loop control. The third item is the transient energy controlled by the PLL, and the fourth item is the transient energy controlled by the DC voltage outer loop.

The third item is the transient energy dominated by the PLL control, whose positive and negative values mainly depend on the PLL link, though the magnitude of the transient energy is still affected by the current loop. The GSC of the PMSG uses a decoupling control technique for the active and reactive power, which causes the d-axis current to govern the output of active power and the q-axis current to govern the output of reactive power: $i_d \gg i_q$ and $i_{qref} \approx 0$. Therefore, $\int\left(i_d i_{qref} - i_q i_{dref}\right)dt < 0$, and the transient energy provided by the current loop is negative, which can be understood as the consumption of transient energy. The fourth item is the transient energy dominated by the voltage outer loop. Since the proportion coefficient of the current loop is generally below one, the order of magnitude of transient energy of this item is negligible.

By combining Eq. 16 and removing the transient energy components $\int P_{out}\omega_0 dt$, $\omega_0 L_f \int\left(i_d di_d + i_q di_q\right)$, and $\int\left(i_d de_q - i_q de_d\right)$ dominated by the operating conditions, the transient energy expression determined by the GSC control system can be obtained as

$$\begin{aligned} W_C = {} & -k_{pi}\int\left(i_d di_q - i_q di_d\right) + k_{ii}\int\left(i_d i_{qref} - i_q i_{dref}\right)dt + k_{pi}\int\left(i_{dref} i_d + i_{qref} i_q\right)d\Delta\theta_{pll} + k_{ii}\int\Delta\theta_{pll}\left(i_{dref} i_d + i_{qref} i_q\right)dt + \int P_{out}d\Delta\theta_{pll} \\ & + k_{pi}k_{pdc}\int i_q du_{dc} - k_{pi}k_{idc}\int i_q\left(u_{dcref} - u_{dc}\right)dt. \end{aligned} \tag{25}$$

Therefore, the influence of the controls of the PLL, current loop, and DC voltage outer loop of the GSC on the transient energy characteristics of the PMSG is obtained. In the case of the transient energy W_C contributed by the control link being positive, the transient energy input from the PMSG to the system continuously increases during the transient process, which exacerbates the SSO divergence. If the oscillation energy W_C contributed by the control link is negative, the transient energy input from the PMSG to the system gradually converges during the transient process, which suppresses the development of SSO.

TABLE 1 Parameters of the GSC of the PMSG.

Symbol	Quantity	Values
S_{base}	Rated output power of the wind turbine	1.5 MW
V_{base}	Rated voltage of the wind turbine	0.69 kV
f_{base}	Rated frequency	50 Hz
U_{dcref}	DC voltage control reference value	1.15 kV
C_{dc}	DC capacitor	0.09 F
(k_{pdc} and k_{idc})	DC voltage outer loop control parameters of the PMSG	(10, 1,000)
(k_{ppll} and k_{ipll})	Phase-locked loop control parameters	(2, 50)
(k_{pi} and k_{ii})	AC current loop control parameters	(0.2, 50)

5 Verification

In PSCAD/EMTDC, a simulation example system is built to demonstrate the integration of a direct drive wind farm with a weak AC power grid. The wind farm's overall generating capacity is 900 MW (1.5 MW*600), and the terminal voltage of the PMSG is 0.69 kV. Furthermore, the power grid is connected after the voltage rise (0.69 kV/220 kV). We set different operating conditions to measure the transient energy and dissipated energy of the PMSG and check the reliability of the PMSG's transient energy model. Parameters of the GSC of the PMSG are shown in Table 1.

5.1 Understanding the SSO characteristics of the grid-connected wind power system through transient energy

We set different oscillation types, *viz.*, SSO divergence and SSO convergence, to ascertain the accuracy and feasibility of the transient energy model of the PMSG.

(1) Sub-synchronous divergence oscillation occurs in the grid-connected wind power system

At an operational condition of 4 m/s, the AC grid's equivalent impedance changes, where the grid strength is reduced from SCR = 3.4 to 1.5 at t = 5s, thus causing divergent SSO in the example system. The transient and dissipated energy of the PMSG are measured.

The upper half of Figure 6 indicates that the grid-connected wind power system undergoes divergent SSO, and after reaching the power limit, the PMSG's output power exhibits equal amplitude SSO. By calculating the transient and dissipated energy of the port of the PMSG, the lower half of Figure 6 illustrates that the dissipated energy of the PMSG increases as the power divergence progresses. After the power reaches the limit, the dissipated energy increases uniformly. Therefore, when SSO occurs in the grid-connected wind power system, the total dissipated energy of the PMSG increases continuously, and the PMSG provides energy for the SSO, thus showing a negative damping characteristic.

(2) Sub-synchronous convergence oscillation occurs in the grid-connected wind power system

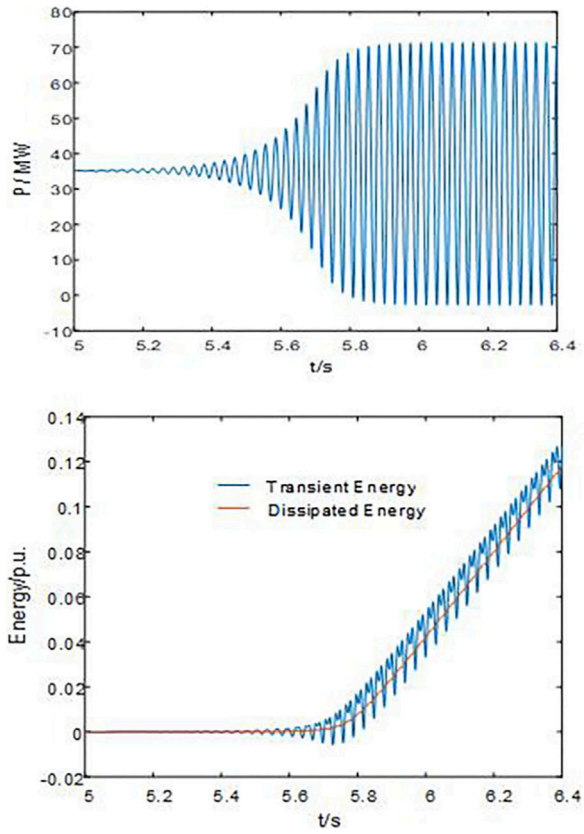

FIGURE 6
Power waveform, transient energy, and dissipated energy waveform of the PMSG under the divergent SSO in the system.

At an operational condition of 7 m/s, the AC grid's equivalent impedance changes, where the grid strength is reduced from SCR = 3.4 to 1.5 at t = 5s, thus causing convergent SSO in the example system. The transient and dissipated energy of the PMSG are measured.

The upper half of Figure 7 shows that the grid-connected wind power system undergoes SSO, and the output power of the PMSG oscillates and converges. By calculating the dissipated energy of the port of the PMSG, the lower half of Figure 7

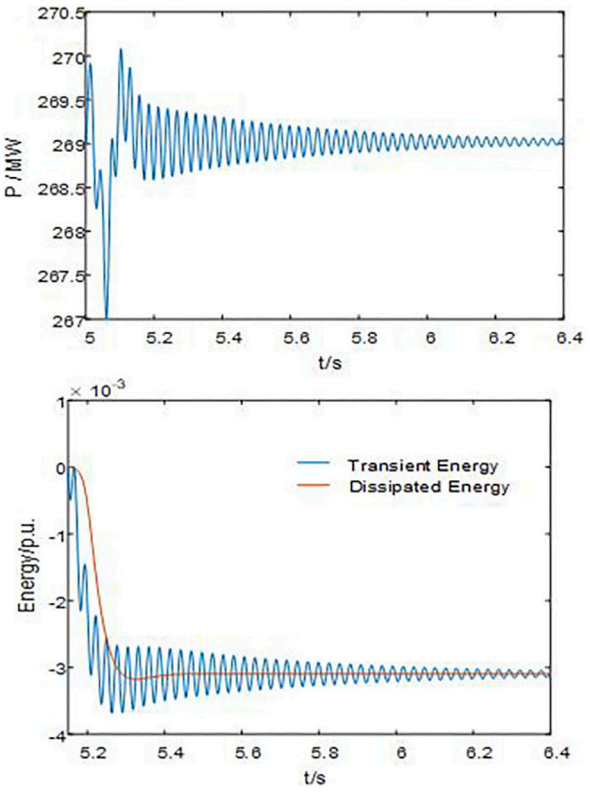

FIGURE 7
Power waveform, transient energy, and dissipated energy waveform of the PMSG for the sub-synchronous convergence oscillation in the system.

illustrates that the dissipated energy of the PMSG is negative; hence, the PMSG absorbs the energy of SSO, which results in a positive damping effect on the SSO, which is consistent with the result of gradual convergence of power oscillation, as shown in the upper half of Figure 7.

As mentioned above, the dissipated energy of the PMSG can be employed to gauge the damping level of the grid-connected wind power system besides understanding the sub-synchronous oscillation characteristics.

5.2 Understanding the impact of each PMSG under different operating conditions on the SSO characteristics of the system via transient energy analysis

The direct drive wind farm connected to the weak power grid faces SSO risk. Since there are differences in the operating conditions of each sub-wind farm, their influence on the SSO characteristics can also vary. Here, it is assumed that the operating conditions of the PMSGs in each sub-wind farm are identical.

We divide the 600 PMSGs in the example system into two sub-wind farms, each with 300 PMSGs. The operating condition of sub-wind farm 1 is 4 m/s, and the operating condition of sub-wind farm 2 is 7 m/s. The transient energy and dissipated energy of the PMSGs of two sub-wind farms are measured.

According to Figure 8, the direct drive wind farm with two sub-wind farms with different operating conditions undergoes SSO. The output power of both the sub-wind farms oscillates and diverges, and the role of the two sub-wind farms in the process of SSO cannot be analyzed through the power oscillation curve.

According to Figure 9, the PMSG of sub-wind farm 1 generates dissipated energy, whereas the PMSG of sub-wind farm 2 absorbs dissipated energy. The two sub-wind farms play different roles in the process of SSO. The PMSG in sub-wind farm 1 generates more dissipated energy than the PMSG in sub-wind farm 2 can absorb. This leads to a net positive dissipated energy and a continuous increase in the transient energy that ultimately results in system instability.

Therefore, the corresponding manifestation mode of SSO is power oscillation, which primarily depends on the energy exchange between the wind farm and the power grid.

5.3 Influence of each control link of the GSC of the PMSG on transient energy

The GSC parameters of the PMSG are provided in Table 1, including the current inner loop's proportional and integral coefficients k_{pi} and k_{ii}, set at 0.2 and 50, respectively. The PMSG operates at 4 m/s and experiences divergent SSO when the equivalent impedance of the power grid changes from SCR = 3.4 to 1.5 at t = 5s. The influence of each control link of the GSC of the PMSG on transient energy is calculated and shown in Figure 10. The power curve of the PMSG is shown in Figure 6.

According to Figure 10, the transient energy provided by the current loop of the GSC of the PMSG is negative, thus exhibiting the characteristic of reducing the transient energy of the PMSG, which is beneficial for system stability. The transient energy provided by the PLL control is positive, which shows the characteristics of generating the transient energy and having a negative damping effect on the SSO. Furthermore, its energy size exceeds the negative transient energy provided by the current loop, which results in the total transient energy exceeding zero, the transient energy output of the PMSG increasing continuously, and the grid-connected wind power system losing stability. The DC voltage outer loop control provides negligible transient energy; hence, it has negligible impact on the transient energy of the PMSG.

(1) The impact of the proportional coefficient of the current inner loop on transient energy

We change the proportion coefficient (k_{pi} = 0.2 increased to 0.23) and observe the changes in the transient energy caused by each control link of the GSC, as shown in the lower half of Figure 11. The power curve of the PMSG is detailed in the upper half of Figure 11.

According to Figure 11 and Figure 6, the simulation example system undergoes sub-synchronous convergence oscillation under the same disturbance. Increasing the proportion coefficient is beneficial for system stability. According to Figure 11, the transient energy provided by the current loop of the GSC exceeds the transient energy provided by the PLL control in this case, thus resulting in the total transient energy being below zero and the power system ultimately remaining stable.

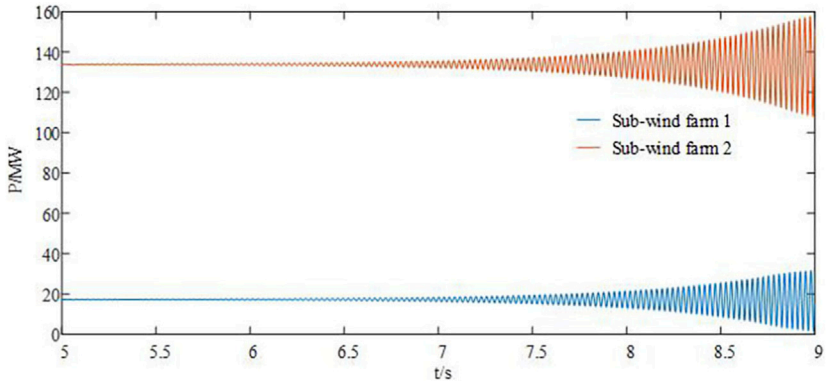

FIGURE 8
Power waveform of sub-wind farm 1 and sub-wind farm 2.

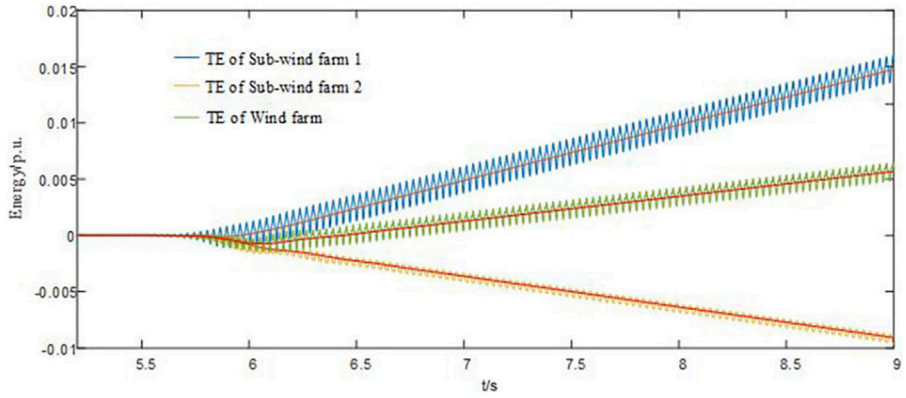

FIGURE 9
Transient energy curve of sub-wind farm 1 and sub-wind farm 2.

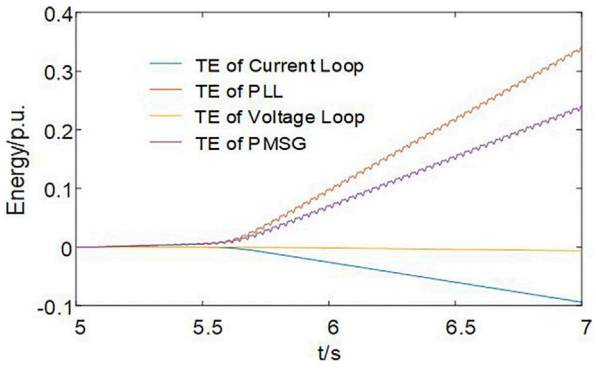

FIGURE 10
Transient energy of each control link of the PMSG.

(2) The influence of the integral coefficient of the current inner loop on transient energy

We change the integral coefficient (k_{ii} = 50 decreased to 40) and observe the changes in the transient energy caused by each control link of the GSC, as shown in the lower half of Figure 12. The output power curve of the PMSG is detailed in the upper half of Figure 12.

Comparing Figure 12 and Figure 6, the simulation example system still undergoes sub-synchronous divergence oscillation under the same disturbance, though the divergence speed slows down. Decreasing the integral coefficient is beneficial for system stability. According to Figure 12 and Figure 10, although the total transient energy exceeds zero after decreasing the integral coefficient, the absolute value of transient energy provided by the current loop and PLL decreases, and the total oscillation energy decreases, besides the damping level of the power system being enhanced.

Thus, the participation of the PMSG in the SSO is primarily associated with the control of the GSC. The transient energy dominated by each control link of the GSC is derived with the support of simulation results.

In the process of SSO, the transient energy contributed by the PLL is positive, which increases the transient energy of the PMSG and easily leads to oscillation divergence. The transient energy contributed by the current loop is negative, which decreases the transient energy of the PMSG and is beneficial to the oscillation convergence.

Both the order of magnitude of the transient energy contributed by the voltage outer loop and its effect on SSO are negligible.

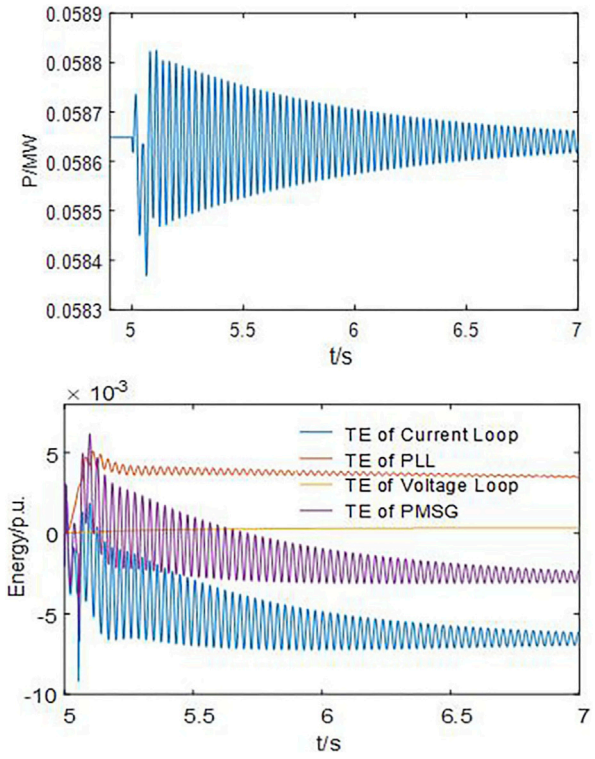

FIGURE 11
Power waveform of the PMSG and transient energy of each link of the PMSG when k_{pi} = 0.23.

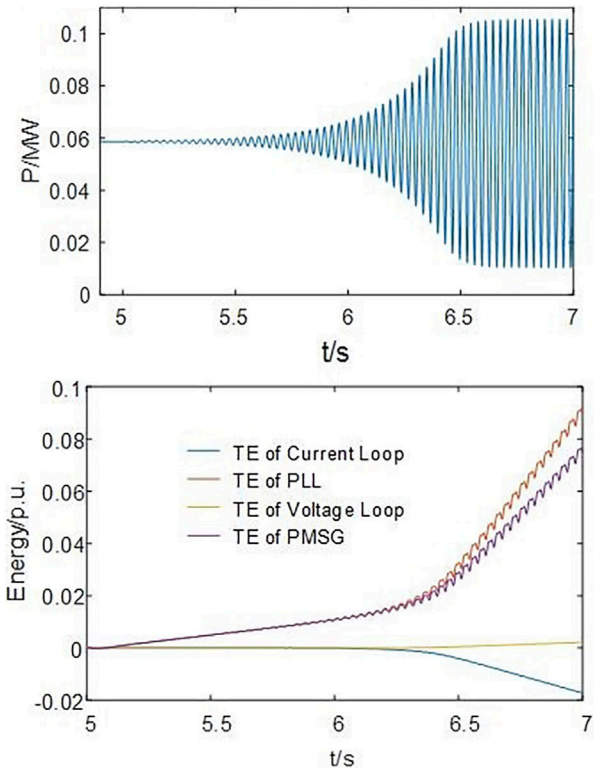

FIGURE 12
Power waveform of the PMSG and transient energy of each link of the PMSG when k_{ii} = 40.

For the GSC's current loop parameters of the PMSG, increasing the proportional coefficient and decreasing the integral coefficient can reduce transient energy, which is beneficial for suppressing oscillations.

6 Conclusion

Starting from the physical essence, this article describes the dynamic development process of SSO by employing the transient energy and, based on that, constructs a method for analyzing SSO. Focusing on the coupling effects between control links at different time scales, the transient energy dominated by various control links is derived, and the effects of the PLL, current inner loop, and voltage outer loop on transient energy and oscillation characteristics are analyzed. The results of the simulation demonstrate that the transient energy analysis can provide valuable insights into the SSO characteristics of the grid-connected wind power system, and the impact of each PMSG under different operating conditions on the sub-synchronous oscillation characteristics of the system can be understood. In the control link of the GSC, the transient energy contributed by the PLL and current loop plays a dominant role in the transient energy characteristics, determining the characteristics of SSO.

A striking number of PMSGs are typically present in a direct drive wind farm, and there is mutual influence between PMSGs during the process of SSO. The transient energy characteristic analysis of the PMSG by considering the coupling relationship is the focus of our future work.

Data availability statement

The original contributions presented in the study are included in the article/Supplementary Material; further inquiries can be directed to the corresponding author.

Author contributions

GY: writing–review and editing. YW: writing–original draft and writing–review and editing. CY: writing–review and editing. LY: writing–review and editing.

Funding

The authors declare financial support was received for the research, authorship, and/or publication of this article. This work was supported by the National Natural Science Foundation of China (No. U1866601).

Conflict of interest

The authors declare that the research was conducted in the absence of any commercial or financial relationships that could be construed as a potential conflict of interest.

Publisher's note

References

Chen, G., Li, M., Xu, T., and Liu, M. (2017a). Study on technical bottleneck of new energy development. *Proc. Chin. Soc. Electr. Eng.* 37 (1), 20–26. doi:10.13334/j.0258-8013.pcsee.161892

Chen, L., Chen, Y., Min, Y., Hu, W., and Zhang, K. (2013b). Low frequency oscillation analysis and oscillation source location based on oscillation energy: Part two method for oscillation source location and case studies. *Autom. Electr. Power Syst.* 36 (4), 1–5+27. doi:10.3969/j.issn.1000-1026.2012.04.001

Chen, L., Min, Y., and Hu, W. (2013a). Low frequency oscillation analysis and oscillation source location based on oscillation energy: Part one mathematical foundation and energy flow computation. *Autom. Electr. Power Syst.* 36 (3), 22–27+86. doi:10.3969/j.issn.1000-1026.2012.03.004

Chen, L., Wang, W., Wang, M., Min, Y., Xie, X., and Xu, F. (2016). Disturbance source location of subsynchronous forced oscillation and damping evaluation using transient energy flow. *Autom. Electr. Power Syst.* 40 (19), 1–8. doi:10.7500/AEPS20160503007

Chen, W., Wang, D., Xie, X., Ma, J., and Bi, T. (2017b). Identification of modeling boundaries for SSR studies in series compensated power networks. *IEEE T Power Syst.* 32 (6), 4851–4860. doi:10.1109/TPWRS.2017.2669402

Dong, X., Xie, X., Han, Y., and Li, J. (2015). Mechanism study of DFIG-related SSR based on separate stator and rotor torque analysis. *Proc. Chin. Soc. Electr. Eng.* 35 (19), 4861–4869. doi:10.13334/j.0258-8013.pcsee.2015.19.003

Fan, L., and Miao, Z. (2012). Nyquist-stability-criterion-based SSR explanation for type-3 wind generators. *IEEE T Energy Conver* 27 (3), 807–809. doi:10.1109/TEC.2012.2193491

Gao, B., Li, R., Yang, D., Song, R., Zhao, S., Liu, J., et al. (2015). Damping characteristics and countermeasures of DFIG subsynchronous oscillation. *Electr. Power Autom. Equip.* 35 (12), 11–21. doi:10.16081/j.issn.1006-6047.2015.12.002

Li, M., Yu, Z., Xu, T., He, J., Wang, C., Xie, X., et al. (2017). Study of complex oscillation caused by renewable energy integration and its solution. *Power Syst. Technol.* 41 (4), 1035–1042. doi:10.13335/j.1000-3673.pst.2016.3049

Li, W., Guo, J., Li, Y., Zhou, X., Chen, L., Bu, G., et al. (2013a). Power system oscillation analysis and oscillation source location based on WAMS: Part 1 method of cutset energy. *Proc. Chin. Soc. Electr. Eng.* 33 (25), 41–46. doi:10.13334/j.0258-8013.pcsee.2013.25.013

Li, W., Li, Y., Zhou, X., Guo, J., Bu, G., Tao, X., et al. (2013b). Power system oscillation analysis and oscillation source location based on WAMS: Part 2 method of torques decomposition. *Proc. Chin. Soc. Electr. Eng.* 33 (25), 47–53. doi:10.3897/zookeys.326.5970

Mi, X., Wang, J., and Wang, R. (2018). Frequency analysis of low frequency oscillation in multi-machine system based on energy function and incomplete elliptic integral. *High. Volt. Engg* 44 (1), 321–328. doi:10.13336/j.1003-6520.hve.20171227039

Min, Y., and Chen, L. (2007). A transient energy function for power systems including the induction motor model. *Sci. China Ser. E Technol. Sci.* 50 (5), 575–584. doi:10.1007/s11431-007-0077-2

Moon, Y. H., Cho, B. H., Lee, Y. H., and Hong, H. S. (1999). "Energy conservation law and its application for the direct energy method of power system stability," in Proceedings of the Paper presented at IEEE Power Engineering Society. 1999 Winter Meeting, New York, NY, USA, February 1999. doi:10.1109/PESW.1999.747540

Wang, Y., Yan, G., Mu, G., and Yang, C. (2022). Research on aggregation modeling of grid connected VSC under AC current control scale. *Proc. Chin. Soc. Electr. Eng.* 42 (8), 2900–2909. doi:10.13334/j.0258-8013.pcsee.220294

Wu, M., Xie, L., Cheng, L., and Sun, R. (2016). A study on the impact of wind farm spatial distribution on power system sub-synchronous oscillations. *IEEE T Power Syst.* 31 (3), 2154–2162. doi:10.1109/TPWRS.2015.2455873

Xie, X., He, J., Mao, H., and Li, H. (2021). New issues and classification of power system stability with high shares of renewables and power electronics. *Proc. Chin. Soc. Electr. Eng.* 42 (2), 461–474. doi:10.13334/j.0258-8013.pcsee.201405

Xie, X., Liu, H., He, J., Zhang, C., and Qian, Y. (2016). Mechanism and characteristics of subsynchronous oscillation caused by the interaction between full-converter wind turbines and AC systems. *Proc. Chin. Soc. Electr. Eng.* 36 (9), 2366–2372. doi:10.13334/j.0258-8013.pcsee.2016.09.007

Xie, X., Liu, H., He, J., Zhang, C., and Qiao, Y. (2013). Mechanism and characteristics of subsynchronous oscillation caused by the interaction between full-converter wind turbines and AC systems. *Proc. Chin. Soc. Electr. Eng.* 36 (9), 2366–2372. doi:10.13334/j.0258-8013.pcsee.2016.09.007

Yang, L., Chen, Y., Zhou, L., Chen, Z., Zhou, X., Wu, W., et al. (2018). Effect of phase locked loop on the small-signal perturbation modeling and stability analysis for three-phase LCL-type grid-connected inverter in weak grid. *Proc. Chin. Soc. Electr. Eng.* 38 (13), 3792–3804. doi:10.13334/j.0258-8013.pcsee.171652

Yu, Y., Min, Y., Chen, L., and Zhang, Y. (2010). Gains by a space-time-code based signaling scheme for multiple-antenna RFID tags. *Autom. Electr. Power Syst.* 34 (5), 1–6. doi:10.1109/CCECE.2010.5575154

Yuan, H., Yuan, X., and Hu, J. (2017). Modeling of grid-connected VSCs for power system small-signal stability analysis in DC-link voltage control timescale. *IEEE T Power Syst.* 32 (5), 3981–3991. doi:10.1109/TPWRS.2017.2653939

Yuan, X., Cheng, S., and Hu, J. (2016). Multi-time scale voltage and power angle dynamics in power electronics dominated large power systems. *Proc. Chin. Soc. Electr. Eng.* 36 (19), 5145–5154. doi:10.13334/j.0258-8013.pcsee.161247

Zhou, X., Chen, S., Lu, Z., Huang, Y., Ma, S., and Zhao, Q. (2018). Technology features of the new generation power system in China. *Proc. Chin. Soc. Electr. Eng.* 38 (7), 1893–1904. doi:10.13334/j.0258-8013.pcsee.180067

frontiers | Frontiers in Energy Research

TYPE Original Research
PUBLISHED 08 January 2024
DOI 10.3389/fenrg.2023.1335683

OPEN ACCESS

EDITED BY
Youbo Liu,
Sichuan University, China

REVIEWED BY
Jun Wang,
Henan University of Technology, China
Guozhou Zhang,
Southwest University, China
Bi Liu,
Sichuan Agricultural University, China

*CORRESPONDENCE
Yiyu Wen,
1917043834@qq.com

RECEIVED 09 November 2023
ACCEPTED 21 December 2023
PUBLISHED 08 January 2024

CITATION
Shen L, Wen Y, Wang Q and Zhang P (2024), Enhanced bi-layer scheduling strategies for the cascade hydropower-photovoltaic complementary system using a novel meta-heuristic algorithm.
Front. Energy Res. 11:1335683.
doi: 10.3389/fenrg.2023.1335683

Enhanced bi-layer scheduling strategies for the cascade hydropower-photovoltaic complementary system using a novel meta-heuristic algorithm

Li Shen, Yiyu Wen*, Qing Wang and Peng Zhang

State Grid Southwest Branch Corporation, State Grid Corporation of China, Chengdu, China

Improving energy efficiency is crucial for China's power industry to meet global energy conservation and emission reduction goals. The rapid development of photovoltaic (PV) and hydropower has greatly assisted in the construction of China's novel power system. The stochastic characteristics of PV power generation pose significant challenges to the reliable and economical scheduling of power systems. In fact, the cascade hydropower station can effectively address the issue. To fully utilize the advantages of hydropower, this paper proposes a bi-layer scheduling optimization model for the cascade hydro-PV complementary system considering power market. The upper-layer model simultaneously maximizes the benefit and minimizes the output volatility of the complementary system. The lower-layer model carries out market clearing with the objective of social cost. Besides, PV uncertainty and market price volatility are considered in the decision-making process for power market transactions. To solve the bi-layer model, a novel meta-heuristic algorithm (geometric mean optimizer) is applied, demonstrating excellent performance compared to similar methods. For the complementary system, the results show that its total power output can be improved, and its output volatility can be effectively alleviated.

KEYWORDS

cascaded hydropower station, hydropower-PV system, bi-layer scheduling strategy, meta-heuristic algorithm, power market

1 Introduction

In recent years, due to climate change and the goal of building novel power systems, the development of renewable energy represented by photovoltaics has been excessive (Ming et al., 2018; Yin et al., 2019). However, the strong uncertainty in solar resources and large-scale access will increase the power fluctuation of the grid, thus threatening the safe and stable operation of the grid (Zhu et al., 2018). By utilizing the flexibility of hydropower and natural resource complementarity, renewable energy consumption can be effectively promoted. (Xu et al., 2019; Chen et al.,2016; Huang et al., 2021). Hydropower-PV complementary system is a vital operation mode to promote grid-connected PV consumption. The key to smoothing the variability of PV is to utilize the regulation ability of hydropower stations, allowing PV to support the power grid effectively.

Research on optimizing multi-energy complementarity of renewable sources like hydropower and PV is focused on planning, design, and operation scheduling. (Li and

Qiu, 2016; Zhang et al., 2019; Yang et al., 2021). Ming et al. (2019) established the connection between short-term and long-term scheduling models based on the PV loss function. They proposed a self-adaptive operation rule for the hydro-PV complementary system. An et al. (2015) established a computational model of hydropower/PV complementary operation based on the Longyangxia project, showing that hydropower can improve the power quality of PV in short-term dispatch, and hydropower shortage can make up for PV in medium- and long-term dispatch. Kougias et al. (2016) quantitatively analyzed the water-PV complementary performance, and their research results are of great significance to the joint scheduling of multiple power stations. Wang et al. (2019a) and Wang et al. (2018) discussed the principle of complementary operation of multi-energy power generation systems and the coordinated operation modes and strategies to maximize the new energy consumption and promote carbon emission reduction. Tan et al. (2021) considered the hydraulic coupling between the upstream and downstream of the stepped hydropower plant, optimized the stepped hydropower power generation plan to maximize the total day-ahead power generation, and constructed an intraday hydropower regulation method considering the risk of the hydropower plant due to the stepped hydropower providing regulation for PV. Lu et al. (2021) used kernel density estimation to simulate the probability distribution of PV output by generating a large number of PV output scenarios and a representative uncertainty set of PV through K-means clustering. It is helpful to study the stochastic optimal scheduling method of hydro-wind-solar complementation to maximize the revenue of the co-generation system. Liu et al. (2020) constructed a chance constraint model based on PV probability distribution for hydro-wind-solar complementary operation. None of the above literature considers the decision-making behavior of the hydro-PV complementary system in the power market transaction, which is not conducive to the long-term economic and stable development of hydropower plants.

The types of objective functions in the optimization model of water-PV complementary systems mainly include maximizing power generation output and benefit, minimizing output fluctuation, and improving energy efficiency. The generation output type models include maximizing the generation capacity of the complementary system and PV output (Wang et al., 2018; Wang et al., 2019b). On the other hand, (Ming et al., 2019), proposed an energy-efficient model by maximizing hydropower storage or minimizing the abandoned power. (Zhang et al., 2017; Lu et al., 2021). presented an efficiency-optimal model to maximize the power generation revenue and reduce the system operation cost. Based on the above research, this paper combines these four types to establish a decision optimization model for the cascade hydro-PV complementary system in the power market. The model is a bi-layer model. In the upper layer, a multi-objective function model is proposed to maximize the return and minimize the volatility of the complementary system. In the lower layer, the power market clearing model is presented. The bi-layer model fully considers the reservoir capacity constraints, water flow constraints, and power constraints of the cascade hydropower, PV, and other units. The mixed-integer linear programming is usually used to solve this type problem (Yuan et al., 2021). To solve the problem, the bi-layer model should be converted into a single-layer model and the nonlinear terms of the lower-layer model should be linearized. This significantly increases the algorithm's complexity. This work utilizes a combination of linear programming and intelligent optimization algorithms to solve this bi-layer model. The upper-level model is solved by using a linear programming approach and the lower level is solved by an intelligent optimization algorithm. During the solving process, the upper layer model needs to pass the market decision of the solved complementary system to the lower-layer model. The lower-layer model solves on the basis of the upper layer model and passes the solved market clearing result back to the upper layer. Convergence is achieved by iterating through this cycle to produce the final result. The lower layer model is solved by the geometric mean optimizer (GMO) (Rezaei et al., 2023), which does not require pre-set parameter values and has a strong ability to detach from the local solution during the solving process. The algorithm is used to solve the lower layer model. The rationality of the model and the feasibility of GMOs are verified by a case study. The main contributions of this paper are as follows.

(1) A multi-objective model is proposed for a hydro-PV cascade system. The model takes into account market demand and price fluctuations to optimize scheduling decisions for maximum economic efficiency and minimum volatility.
(2) GMO and linear programming methods are used to solve a bi-layer optimization model with considering nonlinear elements.
(3) Based on the cascade hydropower-PV complementary system model, the benefits of hydropower plants in the Southwest China region are evaluated.

The rest of this paper is organized as follows: Section 2 introduces the output model for each unit participating in the market transaction. Section 3 introduces the bi-layer model and the constraints; Section 4 introduces the solution methodology and the solution steps.; Section 5 illustrates the case study and discusses the results; Section 6 concludes this paper and suggests future work.

2 Power generation models of the units

2.1 PV power generation model

PV output has a strong uncertainty, positively correlated with the light intensity and the surrounding temperature in different scenarios. The PV power output is:

$$P_{\mathrm{PV},t} = P_{\mathrm{PV}}^{\mathrm{m}} \sum_{s}^{S} \left(\lambda_t^s L_{\mathrm{AC},t}^s\right) \left[1 + K_{\mathrm{T}} \left(T_{\mathrm{c},t} - T_{\mathrm{r}}\right) / L_{\mathrm{stc}}\right] \tag{1}$$

where $L_{\mathrm{AC},t}^s$ is the light intensity of the PV power station at time t in scene s. λ_t^s is the corresponding scene probability. $P_{\mathrm{PV}}^{\mathrm{m}}$ is the maximum power of the PV panel in the standard test environment. K_{T} is the power temperature coefficient. $T_{\mathrm{c},t}$ is the ambient temperature of the PV power station. T_{r} is the reference temperature, set as 25°C. L_{stc} is the light intensity in the standard test environment, set as 1000 W/m^2. S is the number of scenarios.

The power output constraint of PV is as follows

$$0 \le P_{\mathrm{PV},t} \le P_{\mathrm{PV},t}^{\mathrm{pre}} \tag{2}$$

where $P_{\mathrm{PV},t}^{\mathrm{pre}}$ is the predicted output of the PV plant at moment t.

2.2 Cascade hydropower power generation model

The cascade hydropower plant needs to consider the power generation flow relationship between the upper and lower levels of the plant, the time lag relationship of the water flow, the natural water inflow, and the constraints of the reservoir level. The water resources available for hydropower plants in the entire cascade basin are limited, so the scheduling of hydropower plants is interrelated at various times. The scheduling plan of the higher-level hydropower plant affects the available water resources of its lower-level hydropower plant and affects the whole scheduling plan. The output of hydropower plants is generally modelled as follows:

$$P_{\mathrm{h},i,t} = \eta_i \bullet g \bullet q_{\mathrm{h},i,t} \bullet H_{i,t} = \theta_i q_{\mathrm{h},i,t} \tag{3}$$

where g is a constant. This paper takes the value of 9.8. η_i is the power generation efficiency coefficient of hydropower station i. $q_{\mathrm{h},i,t}$ is the power generation flow of hydropower station i in t time. $H_{i,t}$ is the reservoir head of hydropower station i in t time. θ_i is the conversion coefficient between water flow and power generation of hydropower station i.

Hydropower plant capacity constraint is bounded. The equation of the constraint is as follows:

$$V_{\mathrm{h},i,t}^{\min} \le V_{\mathrm{h},i,t} \le V_{\mathrm{h},i,t}^{\max} \tag{4}$$

where $V_{\mathrm{h},i,t}^{\min}$ and $V_{\mathrm{h},i,t}^{\max}$ are the minimum and maximum values of hydropower plant i at time t, respectively.

The constraint of water flow in cascade hydropower generation is as follows:

$$q_{\mathrm{h},i,t}^{\min} \le q_{\mathrm{h},i,t} \le q_{\mathrm{h},i,t}^{\max} \tag{5}$$

where $q_{\mathrm{h},i,t}^{\min}$ and $q_{\mathrm{h},i,t}^{\max}$ are the minimum and maximum flow rates allowed for hydropower plant i in time t, respectively.

The power generation output constraint of the cascade hydropower plant is as follows:

$$P_{\mathrm{h},i,t}^{\min} \le P_{\mathrm{h},i,t} \le P_{\mathrm{h},i,t}^{\max} \tag{6}$$

where $P_{\mathrm{h},i,t}^{\min}$ and $P_{\mathrm{h},i,t}^{\max}$ are the minimum and maximum outputs of hydropower plant i, respectively.

Water balance constraint for cascade hydropower plants is as follows:

$$V_{\mathrm{h},i,t} = V_{\mathrm{h},i,t-1} + Q_{\mathrm{h},i,t} - q_{\mathrm{h},i,t} + \sum_{j \in \Omega_i} q_{\mathrm{h},j,t-\tau_j} \tag{7}$$

where $V_{\mathrm{h},i,t}$ and $Q_{\mathrm{h},i,t}$ are the reservoir volume and natural inflow of hydropower station i at time t, respectively. $V_{\mathrm{h},i,t-1}$ is the reservoir volume of hydropower station i at time t-1. $q_{\mathrm{h},j,t-\tau_j}$ is the power generation flow of upstream power station j before the τ_j th hour.

2.3 Thermal power generation model

In the process of power generation, the main costs of thermal power units are fixed costs and fuel costs. Therefore, the cost function of thermal power units can be written in the form of a quadratic function, as shown in the following formula (8). The marginal cost of thermal power units is shown in formula (9).

$$C_{th,j} = c_{th,j} + b_{th,j} P_{th,j} + 0.5 a_{th,j} P_{th,j}^2 \tag{8}$$

$$\lambda_{th,j} = b_{th,j} + a_{th,j} P_{th,j} \tag{9}$$

where $P_{th,j}$ is the thermal power unit j generation output. $c_{th,j}$ is the fixed cost coefficient of the unit j. $b_{th,j}$ and $a_{th,j}$ are the variable cost coefficient of the unit j. $\lambda_{th,j}$ and $C_{th,j}$ are the marginal cost and the generation cost of thermal power unit j.

The generation constraints of thermal power units are as follows:

$$P_{th,j}^{\min} \le P_{th,j} \le P_{th,j}^{\max} \tag{10}$$

where $P_{th,j}^{\min}$ and $P_{th,j}^{\max}$ are the upper limit and lower limit of output of thermal power unit j.

3 Cascade hydro—photovoltaic complementary optimal scheduling model

This paper proposes a model for optimizing the scheduling of cascaded hydropower and PV, using a bi-layer approach. The cascade hydro-photovoltaic complementary system is shown in Figure 1. The upper layer of the model is the decision trading model for the cascaded hydropower and PV, with the objective of maximizing income while minimizing fluctuations in power generation to ensure the stability and security of the power grid transmission. The upper layer constitutes a multi-objective function. The lower model, on the other hand, is the market clearing model, aimed at maximizing social welfare and minimizing social transaction costs. The relationship between the upper and lower models is illustrated in Figure 2.

3.1 The upper model: market trading decisions of the cascade hydropower-photovoltaic complementary system

The cascade hydropower-PV complementary system can inhibit the fluctuation of PV with the advantage of strong adjustability of hydropower station and improve the usage rate of renewable energy. Therefore, in order to guarantee the reliable and economic operation of the system, this paper comprehensively considers the economy of system operation and the fluctuation of water-PV output, and proposes the optimal scheduling of multi-objective function. Formula (11) is the objective function. Formula (12) represents the output of the complementary system. The benefits of complementary systems is shown in formula (13).

$$f_1 = \max E \tag{11}$$

$$P_{\mathrm{h},t} = \sum_{i=1}^{I} P_{\mathrm{h},i,t} + P_{\mathrm{PV},t} \tag{12}$$

$$\begin{aligned} E &= \sum_{t=1}^{T} \pi_t P_{\mathrm{h},t} \\ &= P_{\mathrm{PV}}^{\mathrm{m}} \sum_{t=1}^{T} \sum_{s=1}^{S} \sum_{i=1}^{I} \left\{ P_{\mathrm{h},i,t} + \pi_t \left(\lambda_t^s L_{\mathrm{AC},t}^s \right) \left[1 + K_{\mathrm{T}} \left(T_{\mathrm{c},t} - T_{\mathrm{r}} \right) / L_{\mathrm{stc}} \right] \right\} \end{aligned} \tag{13}$$

where f_1 is the objective function to maximize the economy of this system. E is benefits of the cascade hydropower-PV complementary system. $P_{\mathrm{h},t}$ is the total output of this system at time t. π_t is the price of

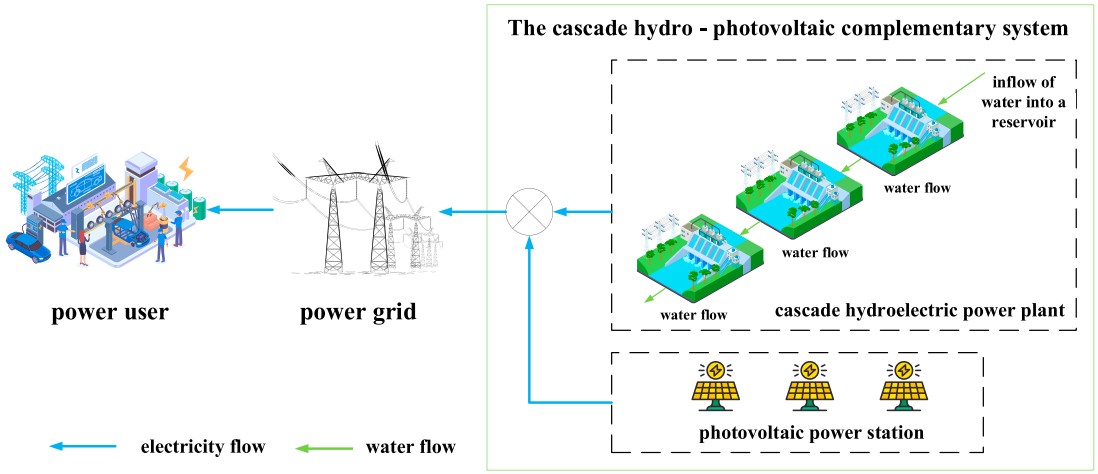

FIGURE 1
The cascade hydropower-PV complementary system.

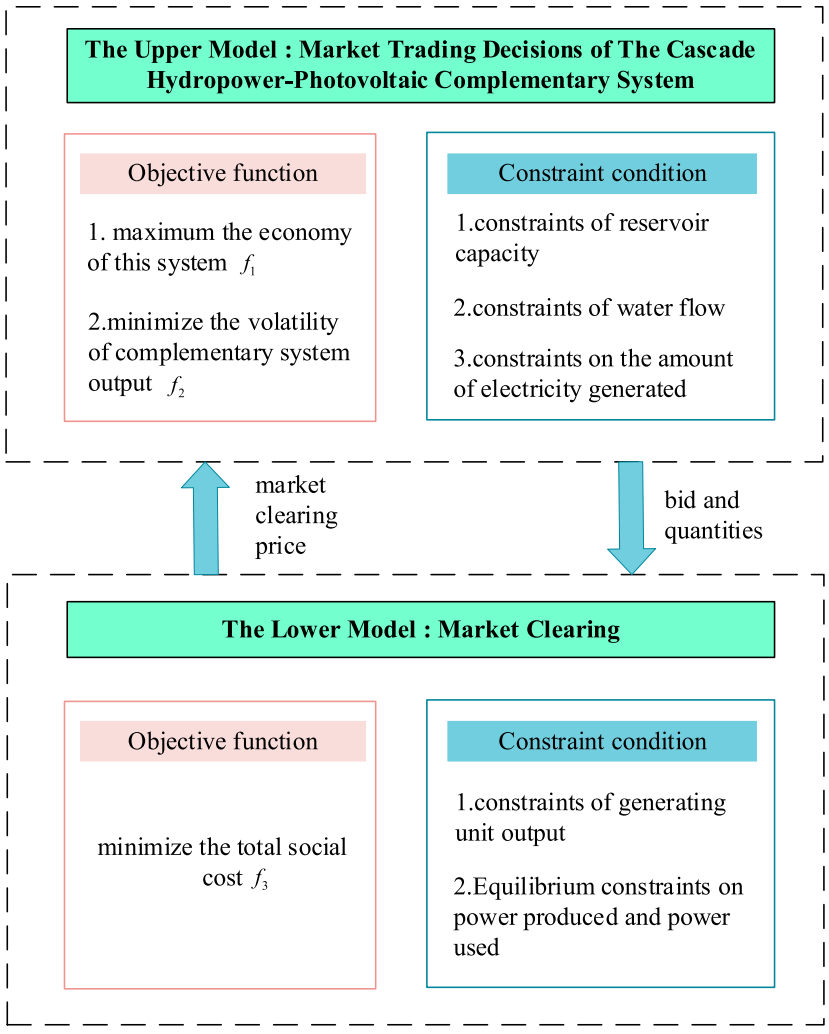

FIGURE 2
The relationship between the upper and lower models.

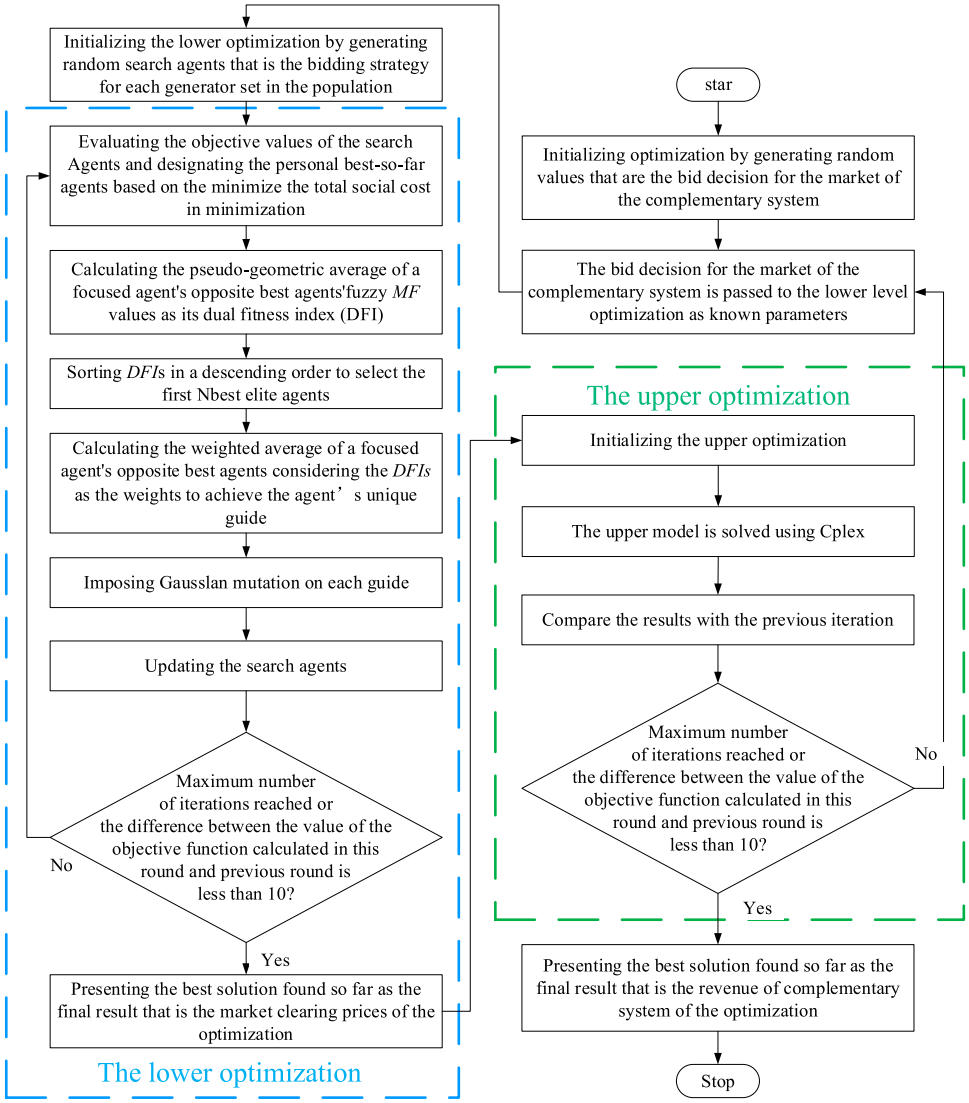

FIGURE 3
Flowchart of the bi-layer optimization model solution.

electricity sold in the electricity spot market at time *t*. *I* is the number of hydroelectric power stations.

The function that aims to minimum volatility is:

$$f_2 = \min F \tag{14}$$

$$F = \sqrt{\frac{1}{T}\sum_{t=1}^{T}(P_t - \bar{P})^2} \tag{15}$$

where F is the volatility of the system's output. $\bar{P}$ is the average output of the system.

The constraints of the upper model are formula (5) to formula (7).

3.2 The lower model: market clearing

This paper discusses the process of generator bidding in the market. The generator is required to provide the quotation and quantity of each unit. The trading center then collects the price of each unit in descending order and clears them. As a price taker, the user only quotes the quantity and not the price during the day-ahead market transaction. The daily market clearing model is then optimized to minimize the total social cost using the following formulas.

$$f_3 = \max C \tag{16}$$

$$C = \sum_{t=1}^{T}\sum_{j}^{N_{th}}\left(\lambda_{\mathrm{h},t}P_{\mathrm{h},t} + \lambda_{th,j,t}P_{th,j,t}\right) \tag{17}$$

$$\lambda_{\mathrm{h},t} = \max\left(\delta_{\mathrm{h}}, \gamma_{\mathrm{PV}}\right)P_{\mathrm{h},t} \tag{18}$$

where f_3 is the function with the objective of minimize the total social cost. C is the total social cost. N_{th} is total number of thermal power units. $\lambda_{\mathrm{h},t}$ and $\lambda_{th,j,t}$ are the quotations of complementary system and thermal power unit j at time t respectively. $P_{\mathrm{h},t}$ and $P_{th,j,t}$ are the quantities of the complementary system and thermal power unit j at time t,

10.3389/fenrg.2023.1335683

TABLE 1 The initial data of three cascade hydropower stations.

Parameters	$P_{h,t}^{min}$/MW	$P_{h,t}^{max}$/MW	θ_i/(MWh/10^{6}m^3)	$q_{h,t}^{min}$/(10^6 m^3/h)	$q_{h,t}^{max}$/(10^6 m^3/h)	$V_{h,t}^{min}$/(10^{6}m^3)	$V_{h,t}^{max}$/(10^{6}m^3)	V_0/(10^{6}m^3)
Station 1	80	800	16	5	50	100	220	160
Station 2	42	120	14	3	40	80	180	120
Station 3	24	60	12	2	30	60	140	100

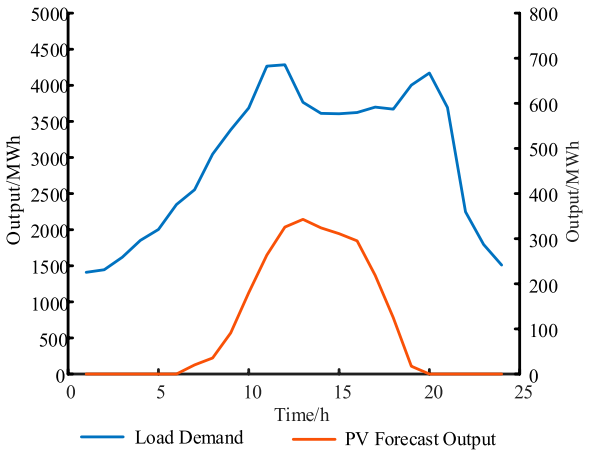

FIGURE 4
The PV generation data and electrical load data.

respectively. δ_h and γ_{PV} are the variable cost coefficient of the cascade hydropower and PV, respectively.

The constraints of the lower model are as follows:

$$\sum_{t=1}^{T}\left(P_{h,t}+P_{th,j,t}\right)=\sum_{t=1}^{T}D_t \tag{19}$$

where D_t is the users' electricity demand at time t.

The other constraints are formula (6) and formula (10).

4 Model solution

4.1 Uncertainty analysis of PV output

PV power generation is highly uncertain. Therefore, describing uncertainty through probabilistic forecasting is better suited for decision-making in uncertain environments. In this paper, PV power generation is treated as obeying a normal distribution as $P_{PV} \sim N(\mu, \sigma^2)$, and the probability density function is:

$$f(P_{PV})=\frac{1}{\sqrt{2\pi}\sigma}\exp\left[\frac{-(P_{PV}-\mu)^2}{2\sigma^2}\right] \tag{20}$$

where μ is the mean, and $\mu = 0$. σ^2 is the variance, and $\sigma^2 = 10$.

In this paper, PV scenarios are generated using the Monte Carlo method, which is a random simulation technique. If the probability distribution of the data is known, random samples can be obtained by sampling, and the characteristics can be analyzed. PV has certain regularity, and PV scenarios are similar. In order to ensure operational speed, simulation accuracy, and scenario typicality, initial scenarios should be classified. According to the law that the prediction error of PV output follows normal distribution, 100 scenarios are initially generated by Monte Carlo method. The array formed by the predicted values of illumination and other days is normalized as a whole, and the reduction method considering Kantorovich distance is used for scenario processing, and finally 10 typical scenarios are obtained.

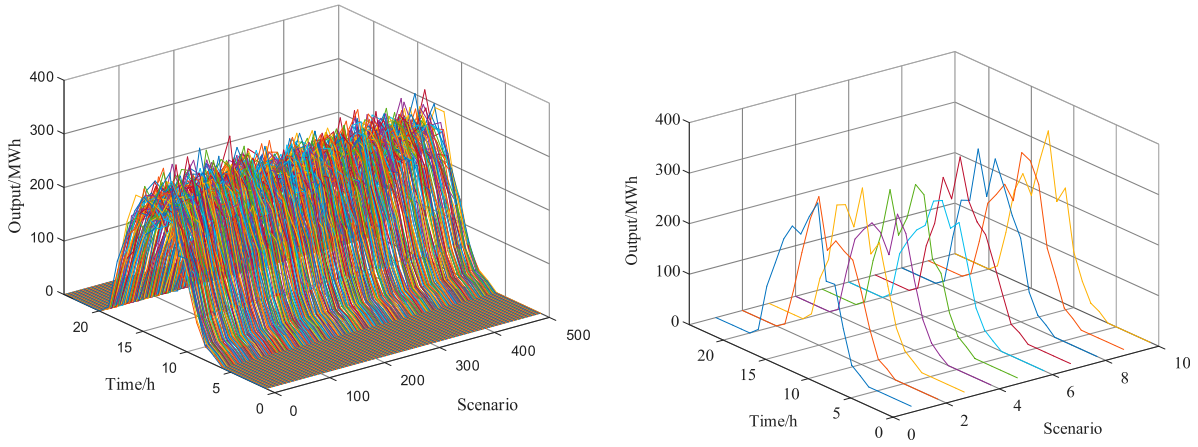

FIGURE 5
Scenario generation and scenario reduction for PV generation.

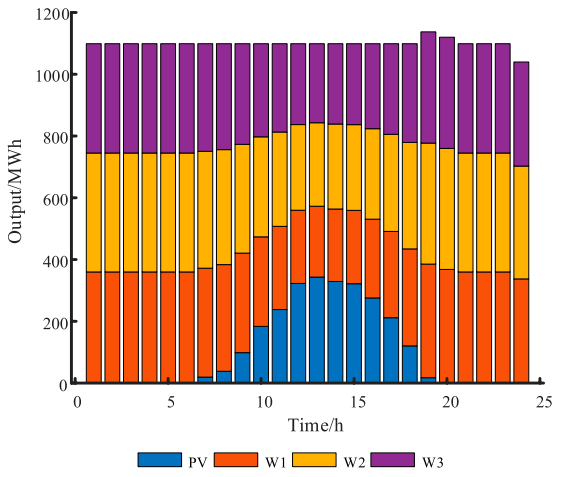

FIGURE 6
The output of each unit in the cascade hydropower-PV complementary system.

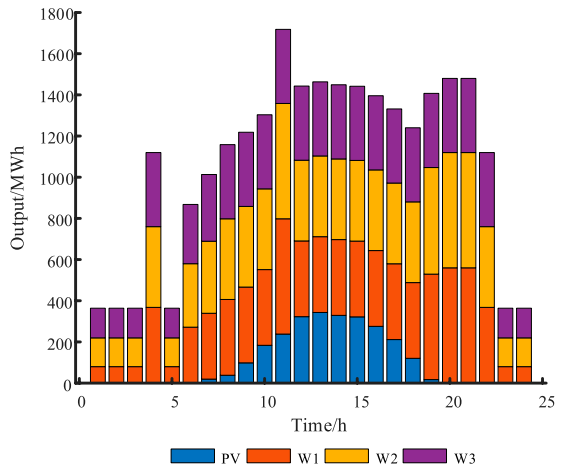

FIGURE 7
Electricity traded in electricity markets by cascade hydro-PV complementary systems without considering volatility.

4.2 Multi-objective function solution analysis

In this paper, we adopt the adaptive variable weighting method to transform the two objective functions into a single objective function, and adaptively adjust the weight coefficients of the two sub-objectives according to the operation of the cascade hydropower-PV complementary system. Due to the different magnitudes of the two sub-objective functions, they need to be normalized. The objective function is shown in formula (21). Formula (22) and formula (23) are represented as normalising formula (11) and formula (14), respectively.

$$f = \min\left[\alpha f_1^* + (1-\alpha) f_2^*\right] \tag{21}$$

$$f_1^* = \frac{f_1^{\max} - f_1}{f_1^{\max} - f_1^{\min}} \tag{22}$$

$$f_2^* = \frac{f_2 - f_2^{\min}}{f_2^{\max} - f_2^{\min}} \tag{23}$$

where α is the adaptive weight coefficient. When the objective function f_1 changes, the relationship between f_1^* and the weight coefficient can be dynamically adjusted. When the comprehensive operating cost of the system is higher, the weight coefficient of the objective will be increased appropriately. f_1^* and f_2^* are the value after the normalization of the two objective functions. $f_1^{\max}$ and $f_1^{\min}$ are the maximum and minimum values of f_1, respectively. $f_2^{\max}$ and $f_2^{\min}$ are the maximum and minimum values of f_2, respectively.

4.3 The method of solving Bi-Level model

In this paper, the upper model obtains the biding amount of the combined power generation by calculating the value of the multiple objective functions, and passes it to the lower model. The lower model determines the market clearing price by

TABLE 2 System failure rates corresponding to different impact indicators in a specific region.

a	0.1	0.3	0.5	0.7	0.9
Max/MWh	1718.330768	1,480	1,463.392147	1,442.757536	1,137.320986
Min/MWh	364	364	364	364	1,039.732709
Average/MWh	1,076.517898	1,085.976329	1,096.360761	1,099.017898	1,099.017898
F	445.9381366	400.26495	351.8940968	216.186045	15.03067535
Revenue/¥	8,853,812.55	8,835,948.65	8761316.334	8652440.068	8586751.584

TABLE 3 Results from ten iterations of PSO and GMO.

Number of iterations	1	2	3	4	5	6	7	8	9	10
PSO/¥	1,182,872	1,190,344	1,056,545	1,019,599	1,033,513	1,019,598	1,060,111	1,031,231	1,019,598	1,019,598
GMO/¥	1,019,598	1,019,598	1,019,598	1,019,598	1,019,598	1,019,598	1,019,598	1,019,598	1,019,598	1,019,598

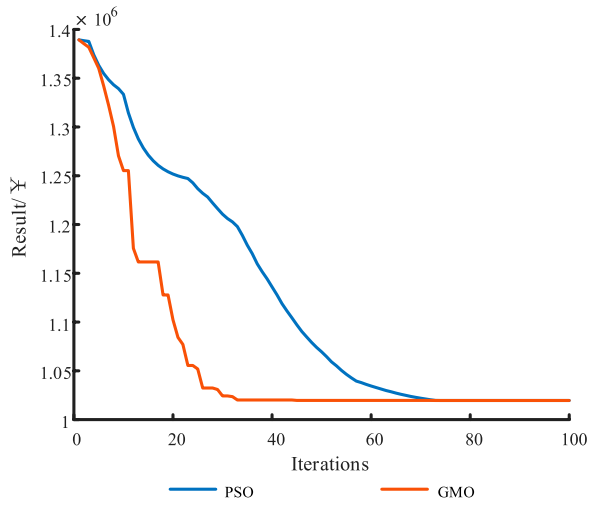

FIGURE 8
Comparison of PSO and GMO operating results.

calculating the objective function and passes it to the upper model. The upper model changes its strategy according to the market clearing price. In this way, the optimal solution can be obtained. Considering that the upper model is linear and the lower model has a nonlinear part, the objective function is solved using the solver Cplex for the upper model and GMO for the lower model.

GMO is a new meta-heuristic algorithm. It simulates the unique properties of geometric average operators in mathematics. The operator can simultaneously evaluate the fitness and diversity of search individuals in the search space. In GMO, when solving an optimization problem, the geometric mean of the scale target values of an individual's opposite is assigned as its weight, representing its overall qualification to guide other individuals in the search process. Therefore, the algorithm does not need to set parameters according to the form of the objective function, which greatly improves the universality and calculation speed of the algorithm. The results were published in *Soft computing* in 2023 by scholars such as Farshad Rezaei. The flow chart of solving the bi-level model is shown in Figure 3.

5 Case study

In this paper, the bi-level optimization model established above is validated and analyzed using GMO and Cplex with a cascade hydro–PV complementary system in a basin in Southwest China as an arithmetic example.

5.1 Data

According to statistics, The PV generation data and electrical load data for a typical day are shown in Figure 4. The data of cascade hydropower stations is shown in Table 1, and all three hydropower stations have daily regulation capacity. Both the initial population number and the maximum number of iterations for GMO are set to 100.

5.2 Results analysis

Due to the strong randomness of natural resources such as light, this paper reduces the error of scheduling results by selecting typical PV power scenarios. Figure 5 shows the scenario reduction results of PV output in 24 h.

Figure 6 shows the results of the joint participation of the cascade hydro-PV in electricity market trading. Figure 7 shows the results of the complementary system participating in electricity market trading when volatility is not considered. Therefore, Figure 7 is the results of the separate participation of the cascade hydro-PV in electricity market trading.

In Figure 6, the total power generation of the complementary system of the cascade hydro-PV after participating in the market trading is 28,896 MWh. Among them, the power generation of terraced hydropower units 1, 2 and 3 is 7,680, 8,400 and 7,776 MWh respectively, which accounts for 26.58%, 29.07% and 26.91% of the total power generation, respectively. Photovoltaic power generation amounted to 2,520 MWh, accounting for 8.72% of the total power generation.

The total benefit of the complementary system is 9,554,994 yuan and the volatility of output is 15.03, of which 8,586,751 yuan is generated by the cascading hydropower. However, the total return from the separate market participation of the cascade hydro-PV is 9,739,344 yuan and the volatility of the output is 445.94, of which 8,835,948 yuan for the cascade hydropower. Comparison of Figures 6, 7 shows that the return of the complementary system is reduced, but its volatility is much higher. For the cascade hydropower, the return is reduced by 2.8%, but the volatility is much lower, which greatly improves the stability of the unit's output. The low volatility is more favorable, both from the point of view of the security of grid operation and from the point of view of the lifetime of the unit generation. At the same time, the revenue of the PV units in the complementary system was increased by 64,846 yuan, reducing the abandonment rate and volatility costs.

Therefore, the complementary system improves the stability of the system power generation and the stability of the grid power supply while reducing the part of the revenue of the cascade hydropower. Such measures can be taken when there is a high demand for power supply stability in some areas.

Table 2 shows the maximum generation, minimum generation, average generation, volatility, and returns per hour when the complementary system participates in the market under different a. From the data in the table, it can be seen that as *a* gets larger, the average generation of the complementary system is more, but the willingness to pay and the volatility are less. With the same amount of incoming water, more average generation means less water abandonment and higher resource utilization. With the shortage of renewable resources, the high utilization of water resources is more in line with the current concept of energy utilization.

5.3 Comparative analysis of GMO and PSO

In this paper, GMO is used to solve the objective function. In order to show the advantage of GMO, PSO is additionally used to solve the objective function in this paper as a comparison. The initialization program sets the PSO parameters w to 0.8, c1 to 1.5, and c2 to 1.5. The results show that PSO has fewer steps in the time scale of the solution, so the solution time will be shorter. PSO and GMO run for 1.04877 and 1.38686 s, respectively. However, PSO needs to set the values of parameters w, c1 and c2 in advance, and it consumes a lot of time to adjust them with the results of the computation. GMO does not need to set the parameters and adapts automatically with the solved function. In the final calculation result, GMO and PSO have about the same data. However, in this paper, the number of particles that need to be solved is large, which causes PSO to often fall into localized solutions when solving, while GMO does not. As can be seen from Table 3, when the number of calculations is 10 times, PSO has a 60% probability of falling into a localized solution, while GMO does not appear to fall into a localized solution. When the number of populations increases, the PSO's trapped local solutions decrease, but the running time increases. The results of one of the best PSO and GMO runs were selected for comparison, as shown in Figure 8. The results show that GMO is able to converge in a very short number of iterations, while PSO takes longer to find the correct result. It can be concluded that GMO has better algorithmic accuracy.

6 Conclusion and future work

The proportion of installed capacity of renewable energy sources, such as PV, will continue to rise in China's efforts to build a new power system. Hydropower, with the largest adjustable clean power capacity in China, must fulfill the dual purpose of supporting grid power supply and regulating new energy. Based on this, a scheduling decision-making model is constructed for optimizing the cascade hydropower-PV complementary system. This model provides decision support for safe and economic operation. The bi-layer model consists of two layers, with the upper layer optimizing multiple objectives that include maximizing returns and minimizing volatility for the complementary system. The lower layer deals with the clearing of various types of generating units to facilitate market transactions. A bi-level GMO is used to solve the model. The results show that the volatility of complementary systems is much lower than that of systems without joint market participation. Moreover, the revenue of PV in the complementary system is increased, and the resource curtailment rate of the cascade hydro-PV is reduced, which greatly improves the utilization of renewable energy. Low generation volatility is more favorable for the safe and stable operation of the grid. It has been verified that utilizing GMO as the solution algorithm for solving the bi-level optimization model is simpler and more stable compared to PSO.

The paper focuses on the participation of thermal units and complementary units in electricity market trading. However, the impact of other units on market trading and the participation of thermal units in carbon market trading are not considered. Additionally, the impact of the difference in PV output and incoming water during the rainy and dry seasons on the complementary system is also not considered. Future work will investigate the impact of the participation of complementary systems in market transactions during different seasons and the impact of carbon market development on power market clearing.

Data availability statement

The original contributions presented in the study are included in the article/Supplementary material, further inquiries can be directed to the corresponding author.

Author contributions

LS: Writing–original draft. YW: Writing–original draft. QW: Writing–review and editing, Writing–original draft. PZ: Writing–review and editing, Writing–original draft.

Funding

The author(s) declare financial support was received for the research, authorship, and/or publication of this article. This work was supported by the Southwest Branch of State Grid Corporation of China (SGSW0000FGJS2310063). The funder was not involved in the study design, collection, analysis, interpretation of data, the writing of this article, or the decision to submit it for publication.

Conflict of interest

Authors LS, YW, QW, and PZ were employed by State Grid Corporation of China.

Publisher's note

References

An, Y., Fang, W., Ming, B., and Huang, Q. (2015). Theories and methodology of complementary hydro/photovoltaic operation: applications to short-term scheduling. *J. Renew. Sustain. Energy* 7, 063133. doi:10.1063/1.4939056

Chen, Y., Wei, W., Liu, F., and Mei, S. (2016). Distributionally robust hydro-thermal-wind economic dispatch. *Appl. Energy* 173, 511–519. doi:10.1016/j.apenergy.2016.04.060

Huang, K., Liu, P., Ming, B., Kim, J., and Gong, Y. (2021). Economic operation of a wind-solar-hydro complementary system considering risks of output shortage, power curtailment and spilled water. *Appl. Energy* 290, 116805. doi:10.1016/j.apenergy.2021.116805

Kougias, I., Szabo, S., Monforti-Ferrario, F., Huld, T., and Bodis, K. (2016). A methodology for optimization of the complementarity between small-hydropower plants and solar PV systems. *Renew. Energy* 87, 1023–1030. doi:10.1016/j.renene.2015.09.073

Li, F., and Qiu, J. (2016). Multi-objective optimization for integrated hydro-photovoltaic power system. *Appl. Energy* 167, 377–384. doi:10.1016/j.apenergy.2015.09.018

Liu, B., Lund, J., Liao, S., Jin, X., Liu, L., and Cheng, C. (2020). Optimal power peak shaving using hydropower to complement wind and solar power uncertainty. *Energy Convers. Manag.* 209, 112628. doi:10.1016/j.enconman.2020.112628

Lu, L., Yuan, W., Su, C., Wang, P., Cheng, C., Yan, D., et al. (2021). Optimization model for the short-term joint operation of a grid-connected wind-photovoltaic-hydro hybrid energy system with cascade hydropower plants. *Energy Convers. Manag.* 236, 114055. doi:10.1016/j.enconman.2021.114055

Ming, B., Liu, P., Cheng, L., Zhou, Y., and Wang, X. (2018). Optimal daily generation scheduling of large hydro–photovoltaic hybrid power plants. *Energy Convers. Manag.* 171, 528–540. doi:10.1016/j.enconman.2018.06.001

Ming, B., Liu, P., Guo, S., Cheng, L., and Zhang, J. (2019). Hydropower reservoir reoperation to adapt to large-scale photovoltaic power generation. *Energy* 179, 268–279. doi:10.1016/j.energy.2019.04.209

Rezaei, F., Safavi, H., Abd Elaziz, M., and Mirjalili, S. (2023). GMO: geometric mean optimizer for solving engineering problems. *Soft Comput.* 27, 10571–10606. doi:10.1007/s00500-023-08202-z

Tan, Q., Wen, X., Sun, Y., Lei, X., Wang, Z., and Qin, G. (2021). Evaluation of the risk and benefit of the complementary operation of the large wind-photovoltaic-hydropower system considering forecast uncertainty. *Appl. Energy* 285, 116442. doi:10.1016/j.apenergy.2021.116442

Wang, X., Chang, J., Meng, X., and Wang, Y. (2018). Short-term hydro-thermal-wind-photovoltaic complementary operation of interconnected power systems. *Appl. Energy* 229, 945–962. doi:10.1016/j.apenergy.2018.08.034

Wang, X., Virguez, E., Kern, J., Chen, L., Mei, Y., Patino-Echeverri, D., et al. (2019b). Integrating wind, photovoltaic, and large hydropower during the reservoir refilling period. *Energy Convers. Manag.* 198, 111778. doi:10.1016/j.enconman.2019.111778

Wang, Y., Zhao, M., Chang, J., Wang, X., and Tian, Y. (2019a). Study on the combined operation of a hydro-thermal-wind hybrid power system based on hydro-wind power compensating principles. *Energy Convers. Manag.* 194, 94–111. doi:10.1016/j.enconman.2019.04.040

Xu, B., Zhu, F., Zhong, P., Chen, J., Liu, W., Ma, Y., et al. (2019). Identifying long-term effects of using hydropower to complement wind power uncertainty through stochastic programming. *Appl. Energy* 253, 113535. doi:10.1016/j.apenergy.2019.113535

Yang, Z., Liu, P., Cheng, L., Liu, D., Ming, B., Li, H., et al. (2021). Sizing utility-scale photovoltaic power generation for integration into A hydropower plant considering the effects of climate change: a case study in the Longyangxia of China. *Energy* 236, 121519. doi:10.1016/j.energy.2021.121519

Yin, Y., Liu, T., and He, C. (2019). Day-ahead stochastic coordinated scheduling for thermal-hydro-wind-photovoltaic systems. *Energy* 187, 115944. doi:10.1016/j.energy.2019.115944

Yuan, W., Wang, X., Su, C., Cheng, C., Liu, Z., and Wu, Z. (2021). Stochastic optimization model for the short-term joint operation of photovoltaic power and hydropower plants based on chance-constrained programming. *Energy* 222, 119996. doi:10.1016/j.energy.2021.119996

Zhang, Q., Wang, X., Yang, T., and Liang, J. (2017). Research on scheduling optimisation for an integrated system of wind-photovoltaic-hydro-pumped storage. *J. Eng.* 13, 1210–1214. doi:10.1049/joe.2017.0521

Zhang, Y., Ma, C., Lian, J., Pang, X., Qiao, Y., and Chaima, E. (2019). Optimal photovoltaic capacity of large-scale hydro-photovoltaic complementary systems considering electricity delivery demand and reservoir characteristics. *Energy Convers. Manag.* 195, 597–608. doi:10.1016/j.enconman.2019.05.036

Zhu, Y., Chen, S., Huang, W., Wang, L., and Ma, G. (2018). Complementary operational research for A hydro-wind-solar hybrid power system on the upper jinsha river. *J. Renew. Sustain. Energy* 10, 043309. doi:10.1063/1.5027758

frontiers | Frontiers in Energy Research

TYPE Original Research
PUBLISHED 15 January 2024
DOI 10.3389/fenrg.2023.1295043

OPEN ACCESS

EDITED BY
ZhaoYang Dong,
Nanyang Technological University, Singapore

REVIEWED BY
John Fredy Franco,
São Paulo State University, Brazil
Hassan Migdadi,
Higher Colleges of Technology, United Arab Emirates

*CORRESPONDENCE
Wang Shangbing,
stec@ncepu.edu

RECEIVED 15 September 2023
ACCEPTED 29 December 2023
PUBLISHED 15 January 2024

CITATION
Linjuan Z, Han F, Zhiheng Z, Shangbing W and Jinbin Z (2024), Site selection and capacity determination of charging stations considering the uncertainty of users' dynamic charging demands.
Front. Energy Res. 11:1295043.
doi: 10.3389/fenrg.2023.1295043

Site selection and capacity determination of charging stations considering the uncertainty of users' dynamic charging demands

Zhang Linjuan[1], Fu Han[2], Zhou Zhiheng[1], Wang Shangbing[3,4]* and Zhang Jinbin[5]

[1]Economics and Technology Research Institute of State Grid Henan Electric Power Company, Zhengzhou, Henan, China, [2]Henan Society of Electrical Engineering, Zhengzhou, Henan, China, [3]Department of Automation, North China Electric Power University, Baoding, Hebei, China, [4]Baoding Key Laboratory of State Detection and Optimization Regulation for Integrated Energy System, Baoding, China, [5]Beijing Qunling Energy Technology Co., Ltd., Beijing, China

Aiming at the problems of high investment and low efficiency in the planning and construction of electric vehicle (EV) charging stations in cities, an optimization model for site selection and capacity determination of charging stations considering the uncertainty of users' dynamic charging demands is proposed. Firstly, based on the travel chain theory and the Origin-Destination (OD) matrix, the travel characteristics of EVs are studied, and the spatial and temporal distribution prediction model of EV charging load is established through the dynamic Dijkstra algorithm combined with the Monte Carlo method. Secondly, a site selection model for the charging station is established which takes the minimum annualized cost of the charging station operator and the annualized economic loss of the EV users as the goal. At the same time, the weighted Voronoi diagram and Adaptive Simulated Annealing Particle Swarm Optimization algorithm (ASPSO) are adopted to determine the optimal number/site selection and service scope of charging stations. Finally, an uncertain scenario set is introduced into the capacity determination model to describe the uncertainty of the users' dynamic charging demands, and the robust optimization theory is utilized to solve the capacity of the charging station. A case study is carried out for the EV charging station planning problem in some urban areas of a northern city, and the validity of the model is verified.

KEYWORDS

charging stations, site selection, capacity determination, robust optimization, weighted voronoi diagram, adaptive simulated annealing particle swarm algorithm

1 Introduction

To achieve the goals set by China in the Paris Agreement, which include peaking carbon emissions by 2030 and achieving carbon neutrality by 2060, the vigorous development of electric vehicles in the transportation sector, characterized by low pollution and noise, has become an inevitable trend (Zhang et al., 2019a). As a public infrastructure providing charging services for EV users, the optimal planning of charging stations in terms of site selection and capacity directly affects their service efficiency and cost. Rational planning of charging station locations and

TABLE 1 Summary of charging station planning methods.

References	Issuing time	Site selection and capacity determination method	Optimization target and constraints	Limitations
Li et al. (2018)	2018	Site selection planning based on human assumptions	Minimize the annualized total time-consuming cost of EV users; EV charging station distance constraint, voltage limits constraint, etc.	Charging demand readings based on artificial simulation deviate from real charging demand
Zhao et al. (2016)	2016	Analysis method for location and capacity determination of electric vehicle charging stations based on a two-step search	Minimize the sum of the charging station construction cost, the driving cost of the EV owner, and the cost of waiting in line at the charging station; The queue waiting time constraint, etc.	The energy state of the electric vehicle when it arrives at the charging station is not considered
Xin et al. (2018)	2018	Chaos simulated annealing particle swarm optimization algorithm	Minimize the annualized total social cost; The queue waiting time constraint, the voltage limits constraint, etc.	The planning of EV charging stations lacks comprehensive consideration of road network topology, actual traffic conditions, and capacity constraints of the power distribution network
Gan et al. (2020)	2020	Genetic Algorithm	Maximize charging station profitability and enhance user convenience in charging; The total demands constraint, charging pile number constraints, etc.	Without considering the uncertainty of users' charging demands, only fast charging stations are considered
Ge et al. (2016)	2016	Quantum Genetic Algorithm	Minimize the sum of the annual cost of taxi charging operation and the annual cost of charging station construction and operation; The total demands constraint, charging pile number constraints, etc.	The impact of actual traffic conditions on vehicles is not considered, and only fast charging stations are considered
Xiao and Gao (2022)	2022	Simulated annealing algorithm and Dijkstra algorithm	Minimize the sum of the annualized total cost of charging stations and the annual economic loss of EV users; EV charging station distance constraint, charging power constraints, etc.	The impact of actual traffic conditions on vehicles is not considered, and only fast charging stations are considered
Yan et al. (2021a)	2021	Improved Particle Swarm Optimization	Minimize the sum of the annualized total cost of charging stations and the annual economic loss of EV users; The queue waiting time constraint, etc.	Without considering the uncertainty of users' charging demands
Dong et al. (2016)	2016	Shared Neighbor Algorithm	Minimize waiting costs and charging costs of EV users; The queue waiting time constraints, etc.	Multi-stage planning without considering dynamic demands, and the planning scenario limited to a circular highway
Cao et al. (2022)	2016	Particle Swarm Optimization	Maximize the sum of social benefits of fast charging station revenue and electric taxi operating revenue; The total demands constraint, charging pile number constraints, etc.	Without considering the uncertainty in capacity planning and only focusing on the planning of fast-charging stations
Zhao et al. (2021)	2022	Data-driven distributed robust optimization	Minimize the annual average lifecycle cost of charging stations; The queue waiting time constraint, charging pile number constraints, etc.	Without considering the uncertainty in capacity planning and with the planning scenario limited to a circular highway
Luo et al. (2018)	2018	Two-step equivalence and second-order conic relaxation	Minimize the annualized total social cost. System power flow constraints, the voltage limits constraint, etc.	Without considering the obligatory path selection decisions of EV users and with relatively high complexity in the solution algorithm
Khardenavis et al. (2021)	2021	Robust optimization	Minimize lifecycle cost of charging stations; Recharging demand constraint, capacity constraint, etc.	Without considering the dynamic charging demand influenced by traffic

capacities, to meet the capacity constraints of the distribution network while considering the interests of station operators and EV users, is an urgent problem to be solved for the large-scale development of electric vehicles. It is of great significance in achieving the dual carbon goals.

In recent years, a large amount of research has been conducted by international scholars on charging station planning problems. However, a mature and comprehensive theoretical basis has not yet been established. Li et al. (2018) considers the feeder layout of charging stations connected to the power distribution network and establishes an annual total travel time cost model for EV users based on road network traffic flow and users' travel characteristics, using a discrete

binary particle swarm optimization algorithm to solve the problem. Zhao et al. (2016) introduces the EV charging convenience factor, combines urban road information and EV driving range, and uses queuing theory to determine the station capacity. Xin et al. (2018) considers the comprehensive interests of charging station operators, EV users, and power grid companies, and uses a chaotic simulated annealing particle swarm optimization algorithm and Voronoi diagram to solve the site selection and capacity determination model. Gan et al. (2020) proposed a partition planning model based on candidate points. Ge et al. (2016) establishes a probability selection function for taxi drivers to choose charging stations based on utility functions and uses an improved quantum genetic algorithm to solve the site selection and capacity determination for electric taxi charging stations. Xiao and Gao (2022) establishes an upper-level model to minimize the sum of the users' annual loss cost and the charging station's annual total cost, and a lower-level model to minimize the users' travel distance to the station, using a simulated annealing algorithm and Dijkstra algorithm to solve the problem. Yan et al. (2021a) proposes an improved particle swarm optimization algorithm based on single-dimensional search volume probability mutation for charging station planning optimization. Dong et al. (2016) clusters charging demands, and determines station locations and capacities using the shared neighbor algorithm and queuing theory. Cao et al. (2022) proposes a fast charging station capacity allocation model based on EV path simulation results under a dynamic traffic network model and solves it using a particle swarm optimization algorithm. Zhao et al. (2021) proposes a two-stage site selection and capacity determination method for solar-battery-charging stations based on data-driven distributed robust optimization. Luo et al. (2018) establishes an optimization model for electric vehicle charging stations with multiple types of charging piles, performs equivalent treatment and second-order cone relaxation, and solves it as a mixed-integer second-order cone programming problem. Khardenavis et al. (2021) proposes a robust model for urban charging infrastructure planning based on dynamic charging demands. Ge et al. (2021) considers the deep interaction between the power system and the transportation system, as well as the transfer of users between charging stations, and proposes a city fast charging station planning method that considers network transfer performance. Fakhrmoosavi et al. (2021) considers the dynamic charging demands under traffic and weather influences, to minimize the total investment cost of charging stations, EV users' charging, and waiting costs and solves it using a simulated annealing algorithm. In recent years, scholars have commonly utilized charging station planning models, and the characteristics of different references are summarized in Table 1 as follows.

Based on the reviewed literature, it is evident that existing research on charging station planning predominantly focuses on static charging demands. These studies consider factors such as construction costs, maintenance costs, and other relevant aspects of EV charging stations. They establish corresponding models for site selection and capacity determination. However, there are still limitations that need to be addressed.

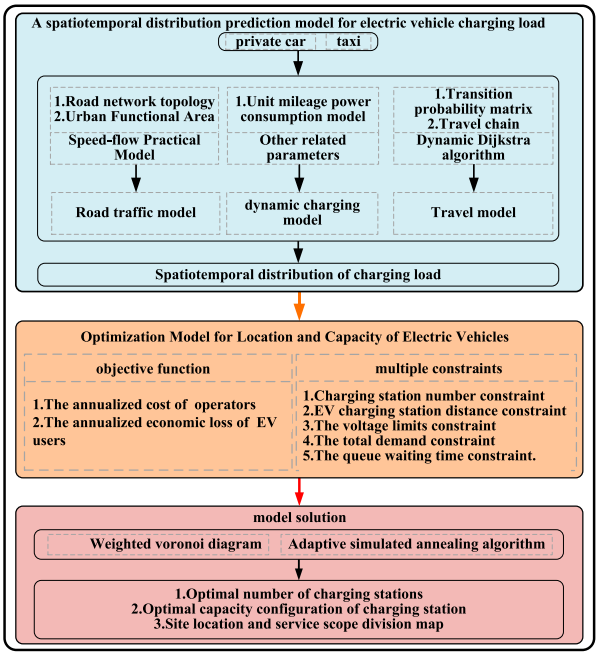

FIGURE 1
Technology roadmap of the paper.

1) Lack of comprehensive consideration of road network topology, actual traffic conditions, and capacity constraints of the distribution network in the planning of EV charging stations.
2) The site selection planning for charging stations in urban areas is partly based on artificial assumptions or random generation, without analyzing the dynamic charging demands of different EV users. As a result, the obtained predictions of charging load information are biased.
3) Some existing research is based on the typical daily charging demands of users, without considering the uncertainty of charging demands. This omission has resulted in weak robustness of the planned charging station capacity and ambiguity in defining the service areas for charging stations.

To address the above issues, this paper proposes a charging station site selection and capacity determination model that considers the uncertainty of dynamic charging demands. Based on users' travel characteristics, the users' travel process is simulated using trip chain theory, OD matrix, and an improved Dijkstra algorithm to obtain the spatiotemporal distribution of EV charging load through dynamic Monte Carlo simulation. Considering constraints such as charging station distance and queue waiting time, an objective function is established to minimize the annual operational cost for station operators and the annual economic loss for EV users. The model is solved using an adaptive simulated annealing particle swarm optimization algorithm. The proposed model aims to achieve an optimal allocation of charging stations in terms of site selection and capacity, taking into account the dynamic nature of charging demands and the constraints of the transportation and power distribution networks.

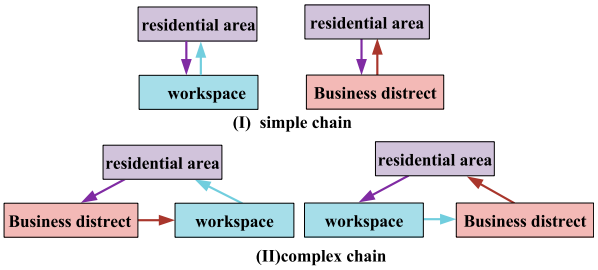

FIGURE 2
Schematic diagram of typical simple chain and complex chain.

2 Optimized model of the proposed system

Based on the electric vehicle charging load spatiotemporal distribution prediction model, the electric vehicle site selection and capacity optimization model, and the model solution algorithm, a research framework for charging station location and capacity considering the uncertainty of users' dynamic charging demands is proposed. The technology roadmap is shown in Figure 1.

2.1 EV travel characteristics and urban functional area division

Based on the travel chain theory and OD matrix, we study the travel characteristics of EVs, consider the attributes of urban functional areas, road topology, and other factors, set different charging trigger requirements in the dynamic charging demand model according to EV types, and use the dynamic Dijkstra algorithm combined with the Monte Carlo method. Establish a prediction model for the temporal and spatial distribution of EV charging load.

Studying the travel characteristics and charging demands of EVs is the basis for selecting the site and capacity of charging stations. Currently, to better describe EV travel destinations, the planning area is divided into three types of urban functional areas: residential areas, commercial areas, and work areas based on urban functional area attributes and load types. EVs are usually divided into four functional types: urban function vehicles, buses, electric private cars, and electric taxis (Zuo et al., 2022). Since the charging locations of the first two types of vehicles are relatively fixed, only the spatial and temporal distribution of charging loads of electric private cars and electric taxis are analyzed.

The EV travel chain is a special Markov chain. The Markov chain is used to describe a random process with no aftereffects: if each state transition is only related to the state of the previous moment and has nothing to do with the past state (Chen, 2018). It can be described as: at a certain moment, the EV sets off from the current parking location, and the destination of this trip is only related to the destination of the previous trip, forming a travel chain based on the location at different times. The four travel chains composed of electric private cars are shown in Figure 2. It is assumed that the probabilities of the four travel chains are 50%, 15%, 10%, and 10%, respectively.

Statistically analyze the travel chain data of electric private cars, and fit the statistical data of the first trip time and length of stay in residential areas, work areas, and commercial areas. Logarithmic distribution is used to fit the first trip time. The Weibull distribution is used to fit the length of stay in residential areas, work areas, and commercial areas. The former is fitted with Weibull distribution, and the latter two are fitted with generalized extreme value distribution. The corresponding values are found in the literature (Zhao et al., 2017). The state of charge at the time of the first trip follows the normal distribution N (0.6, 0.1). The initial locations of electric private cars and electric taxis are evenly distributed at various points in residential areas and on roads respectively.

Since the taxi travel pattern has strong uncertainty and randomness, the (Origin-Destination, OD) analysis method is used to describe the taxi travel characteristics. Through traffic survey statistics, the distribution pattern of taxi travel starting and ending points can be determined, thus obtaining The OD probability matrix of urban road network nodes in each period (Zhu et al., 2023), the corresponding values are shown in Tables 2–4.

2.2 Speed-flow practical model

EV driving speed directly affects the power consumption per unit mileage, which in turn affects its charging demands (Zhang et al., 2022). Since the EV driving process is simulated in the urban transportation system, it is necessary to accurately analyze the impact of vehicle speed at different times on road capacity and traffic flow (Shao et al., 2017). Therefore, this paper introduces the speed-flow practical model. The speed V_{ij}(t) of the vehicle traveling on the road segment R (i,j) at time t can be expressed as

$$V_{ij}(t) = \frac{V_{ij-f}}{1 + \left(\frac{q_{ij}(t)}{C_{ij}}\right)^{\beta}} \tag{1}$$

$$\beta = a + b\left(\frac{q_{ij}(t)}{C_{ij}}\right)^{n} \tag{2}$$

In Eqs 1, 2, a, b, and n are the adaptive coefficients under different road grades. $V_{ij\text{-}f}$ represents the zero flow speed of road segment $R(i,j)$; the ratio of traffic volume $q_{ij}(t)$ of road segment $R(i,j)$ at time t to the traffic capacity C_{ij} of road $R(i,j)$ is called t Moment road saturation. This paper mainly considers main roads (I) and secondary roads (II), and the corresponding values of a, b, and n refer to (Shao et al., 2017).

$$\Delta T_{ij}(t) = l_{ij}V_{ij}(t)^{-1}\left(i, j = 1, 2, \ldots, N_R \text{且} i \neq j\right) \tag{3}$$

Equation 3 defines N_R as the total number of road nodes in the traffic network and l_{ij} as the length of the road section $R(i,j)$ in the traffic network. If there is no road connecting two nodes, the value of l_{ij} is infinity.

2.3 Simulating EV travel routes based on dynamic Dijkstra algorithm

They are considering urban road network information, which mainly includes attributes of urban functional zones and road

TABLE 2 Taxi OD probability matrix 06:00–18:00.

Urban functional area	Residential area	Business district	Workspace
Residential area	0.15	0.2	0.65
Business district	0.15	0.15	0.7
Workspace	0.2	0.4	0.4

TABLE 3 Taxi OD probability matrix 18:00–21:00.

Urban functional area	Residential area	Business district	Workspace
Residential area	0.15	0.2	0.65
Business district	0.15	0.15	0.7
Workspace	0.2	0.4	0.4

TABLE 4 Taxi OD probability matrix 21:00–06:00.

Urban functional area	Residential area	Business district	Workspace
Residential area	0.3	0.4	0.3
Business district	0.3	0.3	0.4
Workspace	0.4	0.3	0.3

topology, graph theory methods can be used to describe the topological structure of the road network. After using the Monte Carlo method to randomly select the origin and destination points for EV users, users typically choose the travel path with the shortest travel time from a set of candidate shortest paths. Based on the travel characteristics of EVs, the traditional Dijkstra algorithm can be improved to find the EV travel path with the minimum travel time.

This article is based on the dynamic Dijkstra algorithm. The first step is to establish a road adjacency matrix, where the starting and ending points of roads within the planning area, as well as intersections, are considered as nodes. The algorithm aims to find the M shortest candidate paths with the shortest distance from a given starting point to the destination node for an EV. Additionally, the speed-flow utility model described in Section 2.2 is utilized to minimize the travel time. The solution process is outlined as follows:

(1) Determine the road adjacency matrix D, the starting and destination nodes, and the number of paths M;
(2) Apply Dijkstra algorithm to find the i-th shortest path and its corresponding set of road segments;
(3) Remove the last road segment from the first i shortest paths and obtain m subgraphs by sequentially removing other road segments;
(4) Use the Dijkstra algorithm to find the shortest path set R_s from the starting node to the destination node for each subgraph;
(5) Remove duplicate paths from the candidate set, sort them based on path length, and select the shortest path as the (i+1)-the shortest path;
(6) Repeat steps 3, 4, and 5 until $i = m$, obtaining the top M shortest paths. Then, use the speed-flow utility model to determine the travel path L with the minimum travel time.

2.4 EV charging load spatiotemporal distribution prediction model

The vehicles requiring charging on the road can be integrated into the road nodes, considering the traffic nodes as charging demand points (Xin et al., 2018). Using the dynamic Dijkstra algorithm, the travel path with the minimum travel time is determined. The unit mileage consumption model is used to dynamically update parameters such as the remaining battery level for EVs, establishing an individual EV dynamic charging demand model. When an EV triggers a charging demand, the dynamic Dijkstra algorithm is employed to calculate the route with the minimum travel time from the charging demand point to the charging station. In actual road travel, users do not always choose the shortest travel time path due to their reasons. Considering the diversity of users' path choices, the shortest travel time path is defined as the path that users are most likely to choose, and the probability of choosing other paths is the same and uniformly distributed. If there are s ($s > 1$) sets of paths for users from the origin to the destination, the probability of choosing the shortest travel time path is P_s, and the probability of choosing other paths is $(1\text{-}P_s)/(s\text{-}1)$. This paper takes $P_s = 0.9$.

According to reference (Song, 2014), based on actual road travel data and considering the actual traffic congestion and vehicle conditions, a unit mileage consumption model for EVs is

established for different road levels. Therefore, the expression for the unit mileage consumption model E_{ij} for two-level roads is:

$$E_{ij} = \begin{cases} -0.179 + 0.004V_{ij} + \dfrac{5.492}{V_{ij}}, \text{main road (I)} \\ 0.21 - 0.001V_{ij} + \dfrac{1.531}{V_{ij}}, \text{Secondary road (II)} \end{cases} \quad (4)$$

In Eq. 4, E_{ij} is the EV power consumption per unit mileage of the main road (I) and the secondary road (II).

Based on the travel characteristics of EVs, when analyzing dynamic charging demand information, it is necessary to set different charging trigger requirements in the dynamic charging demand model according to the type of EV.

Electric private cars: The travel chain structure of electric private cars is relatively fixed (Zhu et al., 2023), and it is necessary to determine whether the remaining power of the EV meets the power requirements for the next trip before the next trip. When the remaining power $Cap_t(i)$ cannot be satisfied, the charging requirement is triggered.

$$Cap_t(i) \le \sum_{(i,j)\in R_s} l_{ij}E_{ij} \quad (5)$$

In Eq. 5, E_{ij} is the electric energy consumption per unit kilometer of the road segment $R(i,j)$ at time t of EV.

Taxi: Considering the mileage anxiety constraint of taxi users, set the capacity of the electric taxi battery to be lower than $0.3Cap_i$. In Eq. 6, Cap_i is the capacity of the i-th electric taxi battery. When $Cap_t(i)$ is lower than the set threshold power, charging demand is triggered.

$$Cap_t(i) \le 0.3Cap_i \quad (6)$$

This paper considers the dynamic charging demands of electric private cars and electric taxi users and uses the dynamic Dijkstra algorithm combined with the Monte Carlo method to establish a spatiotemporal distribution prediction model of EV charging load. The specific process is shown in Supplementary Appendix Figure SA1.

3 EV charging station site selection and capacity optimization model

When establishing EV charging stations, it is crucial to consider not only the annualized cost of operators but also the satisfaction of the users during the charging process. The satisfaction of EV users primarily depends on the time loss incurred while driving to the charging station, the cost of energy loss during the travel from the charging demand point to the charging station, and the users' queuing time cost. A compromise between the interests of the charging station and the users is inevitable. On the one hand, to enhance user satisfaction, it is necessary to construct more charging stations, which inevitably leads to increased costs for the charging station operators. On the other hand, to save costs, the operators would prefer to minimize the number of charging stations, but this may adversely affect the interests of the users. In this study, we assume that the interests of both the charging stations and the users are equally important, and the objective function of our model is to minimize the annualized total economic cost. Therefore, the establishment of EV charging stations involves striking a balance between the interests of the charging station operators and the users. The goal is to minimize the annualized total economic cost while ensuring satisfactory charging experiences for EV users.

3.1 EV charging station site selection model

The objective function of the EV charging station site selection model is shown in Eqs 7–10.

$$\min F = F_1 + F_2 \quad (7)$$

$$F_1 = \sum_{k\in K} (C_a + C_b) \quad (8)$$

$$C_a = \frac{r_0(1+r_0)^m}{(1+r_0)^m - 1}\left(N_k^{\text{high}}C_{\text{ch}}^{\text{high}} + N_k^{\text{low}}C_{\text{ch}}^{\text{low}} + G_k\right) \quad (9)$$

$$C_b = \alpha T_{\text{ch}} T_{\text{year}}\left(N_k^{\text{high}}C_{\text{ch}}^{\text{high}} + N_k^{\text{low}}C_{\text{ch}}^{\text{low}}\right) \quad (10)$$

Equation 7 breaks down the annualized total economic cost: F, into two parts: F_1, the annualized cost of operators, and F_2, the annualized economic loss of EV users. The cost of F_1 for operators is made up of three main components: the annual cost of constructing EV charging station infrastructure, the cost of purchasing charging piles, and the average annual cost of operation and maintenance.

In Eq. 8, C_a is the average annual construction investment cost of EV charging stations; C_b is the average annual operation and maintenance cost of EV charging stations; $k\in K = \{1,2, \ldots k_{\max}\}$, K is the set of EV charging stations, and $k_{\max}$ is the total number of charging stations. In Eq. 9, m is the design operating life of the charging station; r_0 is the discount rate; Nhigh $k$and$N$low k are respectively the number of high-power/low-power charging piles configured at charging station k, Chigh chand Clow chares the high-power/low-power charging piles respectively. The unit price of low-power charging pile; G_k is the infrastructure cost of charging station k; in Eq. 10, α is the conversion rate of annual operation and maintenance cost according to the annual operating capacity of charging station k; T_{ch} is the average effective charging time of charging station per day; T_{year} is the number of days in a year.

The annualized economic loss F_2 of EV users mainly takes into account the travel time cost, power loss cost, and queuing time cost of the EV users' journey to the charging station. The expression of F_2 calculated using Eq. 11 is as follows:

$$F_2 = T_{\text{year}}\left(C_{wk} + C_{gk} + C_{mk}\right) \quad (11)$$

The travel time cost C_{wk} for EV users to travel from charging demand point j to the k-th charging station can be expressed as

$$C_{wk} = C_{\text{evu}} \sum_{k=1}^{k_{\max}} \sum_{j=1}^{j_{\max}} N_j \Delta T_{jk} \quad (12)$$

The expression (Eq. 12) states that C_{evu} represents the unit time equivalent economic loss for EV users during their travel. N_j represents the number of EVs charging at charging demand point j and heading to the k-th charging station. $j_{\max}$ is the total number of charging demand points, and ΔT_{jk} represents the travel time for an EV from charging demand point j to the k-th charging station.

The cost of energy loss during the travel from charging demand point j to the k-th charging station for EV users denoted as C_{gk} can be expressed as:

$$C_{gk} = C_{ch} \sum_{k=1}^{k_{max}} \sum_{j=1}^{j_{max}} f N_j L_{jk} \tag{13}$$

In Eq. 13, C_{ch} represents the unit price of charging for EVs, f is the conversion coefficient between EV travel distance and energy consumption, and L_{jk} represents the total length of the road segments for EVs traveling from charging demand point j to charging station k.

3.2 Fixed capacity model of EV charging station

For users, the number of charging piles configured determines the queuing time. How to rationally allocate the number of high-power/low-power charging piles, which not only takes into account the interests of both charging station operators and users but also improves charging pile service efficiency and reduces charging station costs, is an issue that needs to be considered in charging station capacity determination. Therefore, the M/M/c queuing theory method is used to calculate the queuing waiting time of EV users. It is assumed that the number of EVs arriving at the charging station per hour obeys the Poisson distribution with parameter λ (Liu et al., 2016). Then the service intensity ρ and the average waiting time W_k of EV users are

$$\rho = \frac{\lambda}{\mu N_k^{cs}} \tag{14}$$

$$W_k = \frac{\left(N_k^{cs}\rho\right)^{N_k^{cs}}\rho}{N_k^{cs}!\left(1-\rho\right)^2\lambda} P_0 \tag{15}$$

$$P_0 = \left[\sum_{i=0}^{N_k^{cs}-1} \frac{1}{i!}\left(\frac{\lambda}{\mu}\right)^i + \frac{1}{N_k^{cs}!\left(1-\rho\right)}\left(\frac{\lambda}{\mu}\right)^{N_k^{cs}}\right]^{-1} \tag{16}$$

In Eq. 14, $Ncs\ k$ is the number of charging piles configured in the k-th charging station, and μ is the number of vehicles that each charging pile completes service per hour.

Equation 15 uses λ to represent the number of electric vehicles that receive services at charging stations within an hour. For Eq. 15 to be accurate, the condition $\rho < 1$ must be met. Equation 16 defines P_0 as the probability of all charging piles being idle.

In Eq. 17, the average captain L_k per unit time is

$$L_k = \frac{\left(N_k^{cs}\rho\right)^{N_k^{cs}}\rho}{N_k^{cs}!\left(1-\rho\right)^2} P_0 + \frac{\lambda}{\mu} \tag{17}$$

In Eq. 18, to simplify the calculations and consider different charging durations for q EVs, the average number of vehicles served per hour, denoted as $\bar{\mu}$, for each charging station can be calculated using the following formula:

$$\bar{\mu} = \frac{\frac{1}{t_1} + \frac{1}{t_2} + \cdots + \frac{1}{t_q}}{q} \tag{18}$$

Assuming that the number of vehicles receiving charging services at time i in charging station k is λ_i, then the EV users' queuing time cost C_{mk} is

$$C_{mk} = C_{evu} \sum_{k=1}^{k_{max}} \sum_{i=1}^{24} W_{ki}\lambda_i \tag{19}$$

In Eq. 19, W_{ki} represents the average queueing time at charging station k during the period i.

Due to the holiday and random nature of EV charging loads, the robustness of charging station capacity results obtained based on typical days of charging demand is weak (Zhu et al., 2019). To address the uncertainty in users' dynamic charging demands, robust optimization theory is utilized. It involves incorporating an uncertain scenario set to capture the uncertainty in users' demands and adjusting the size of the set through an uncertain budget. This approach enables the optimization of the number of high-power/low-power charging stations within the charging station to meet the diverse needs of decision-makers while considering the uncertainties in users' demands.

Let the number of EVs that need to be charged at the charging demand point j be x_j, x_j represents the lower bound of the uncertainty parameter $\tilde{x_j}$ (j = 1, 2, 3...j_{max}), and d_j represents the length of the interval. Therefore $x_j \in [x_j, x_j + d_j]$, In Eq. 20, ξ_j is used to describe the deviation degree x_j from the worst-case scenario, and the expression is given by:

$$\xi_j = \frac{\tilde{x_j} - x_j}{d_j} \tag{20}$$

Furthermore, to constrain the sum of relative deviation degrees of uncertain parameters, let the sum of relative deviation degrees of uncertain parameters not exceed the uncertain budget Γ_k. In Eq. 21, A larger Γ_k value indicates a broader range of the uncertain scenario set and reflects a higher degree of risk preference by the decision maker. The expression is as follows:

$$\sum_{j=1}^{j_{max}} \xi_j \le \Gamma_k, k = 1, 2, 3...k_{max} \tag{21}$$

3.3 Multiple constraints

The inequality constraints for the integration of EV charging stations into the distribution network primarily consider the capacity constraints of the distribution network (Ge et al., 2013).

3.3.1 Charging station number constraints

$$N_{min} \le N \le N_{max} \tag{22}$$

In Eq. 22, N_{min} and N_{max} are respectively the minimum and maximum number of charging stations to be built in the planned area.

3.3.2 EV charging station distance constraint

$$R_k \le d_{ef} \le 2R_k \; e \in K, f \in K, e \ne f \tag{23}$$

Equation 23 represents the distance constraint from neighboring charging station e to charging station f. R_k represents the service radius of the charging station.

3.3.3 The voltage limits constraint for distribution network node *j*

$$V_j^{\min} \le V_j \le V_j^{\max} \qquad j \in N_d \tag{24}$$

In Eq. 24: $V\max j$ and $V\min j$ are the upper and lower voltage limits of node j respectively; N_d is the number of nodes in the distribution network in the planning area.

3.3.4 The total demands constraint

$$\sum_{k=1}^{k_{\max}} T_{ch}\left(P_{high}N_k^{high} + P_{low}N_k^{low}\right) \ge P_D \tag{25}$$

In Eq. 25, P_{high} represents the power of high-power charging equipment, P_{low} represents the power of low-power charging equipment, and P_D represents the total daily demands of EV users in the planning area.

3.3.5 The queue waiting time constraint

$$W_h \le W_{h\_max} \tag{26}$$

In Eq. 26, W_{h_max} represents the maximum value for the queue waiting time of users.

4 Optimized model construction algorithm

Because the Voronoi diagram has the nearest neighbor property, it was early applied to the substation planning and site selection problem (Ge et al., 2007). In the planning and site selection of similar charging stations, site selection layout, and service scope division need to be carried out according to load demands. Therefore, a weighted Voronoi diagram is introduced to divide the service range of charging stations. In recent years, heuristic algorithms have been widely used in EV charging station site selection and capacity determination problems (Kong et al., 2019). Such as genetic algorithm (Genetic Algorithm, GA) (Li et al., 2018) simulated annealing algorithm (Fakhrmoosavi et al., 2021), whale optimization algorithm (Zhang et al., 2019b), etc. Among these heuristic algorithms, Particle Swarm Optimization (PSO) has been widely used due to its simple structure and fast convergence speed. However, as the number of iterations increases in the later stage of the algorithm, the population diversity is lost. As a result, It is often easy to fall into the local optimal solution (Kennedy and Eberhart, 1995). Therefore, to apply the algorithm to charging station site selection planning, it is necessary to improve the algorithm to avoid the group falling into local optimality prematurely.

4.1 Weighted voronoi diagram

The weighted Voronoi diagram, introduced in the text, is defined as follows:

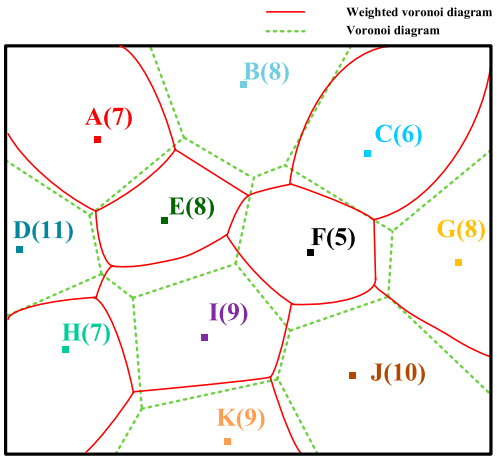

FIGURE 3
Comparison between weighted voronoi diagram and voronoi diagram.

Let $P = \{P_1, P_2, ..., P_n\}$ $(3 \le n \le \infty)$ be a set of control points in the plane, and τ_i $(i = 1, 2, ..., n)$ is the given n positive real numbers, The weighted Voronoi diagram for any point is defined as:

$$V(P_i, \tau_i) = \left\{ x \in V(P_i, \tau_i) \middle| \frac{d(x, P_i)}{\tau_i} \le \frac{d\left(x, P_j\right)}{\tau_j}, \; j = 1, 2 \cdots, n, j \ne i \right\} \tag{27}$$

In Eq. 27, $d(x, P_i)$ is the Euclidean distance between any point x and P_i on the plane; τ_i is the weight of the vertex P_i. As shown in Figure 3, there are a total of eleven vertices A...K, and the value in parentheses in the figure represents the weight of the vertex.

It can be seen that the weighted Voronoi diagram also has the function of dividing the space. The weighted distance from any point in a V-curved shape of the weighted Voronoi diagram to the growing element of the curved shape is smaller than the distance from the point to other curved-shaped growing elements weighted distance. For situations where the weights of each vertex are significantly different, the weighted Voronoi diagram has a more accurate reflection ability in spatial segmentation than the ordinary Voronoi diagram. This feature can be exploited to adjust the respective service range with the weight of charging stations.

In the iterative process of automatic division and alternation of EV charging station site selection and service scope, EV charging stations with a large number of charging piles and a large reference capacity in the planned partition are given a greater initial weight. When the EV charging demands in some planned partitions are too large or too small, unreasonable partition weights need to be fine-tuned during the iterative process. If the reference capacity of the charging station in the planned area is close to the capacity margin of the distribution network node to which it is connected, the weight of the charging station needs to be adjusted to narrow the service scope. The weight of each planning partition can be calculated by Eq. 29.

$$\omega_i = \sqrt{\frac{Q_r}{Q_i}}, \quad i = 1, 2, \cdots N \tag{28}$$

In Eq. 28, i is the number of planned partitions, Q_i is the EV charging demands of planned partition i, and Q_r is the charging station reference capacity of the planned partition.

4.2 Adaptive simulated annealing particle swarm algorithm

This paper proposes an adaptive simulated annealing particle swarm optimization algorithm (ASAPSO). The PSO algorithm introduces a simulated annealing operation and uses the Metropolis criterion to guide the population to accept differential solutions with a certain probability, which improves the algorithm's ability to jump out of the local optimal solution (Yan et al., 2021b). And adaptively adjust the inertial weight, self-cognition, and social cognition parts.

The optimization process of the particle swarm algorithm is completed by the flight of particles in the search space. The expressions for each iterative update of particle speed and position are:

$$v_i(h+1) = \omega v_i(h) + c_1 r_1 \left(P_{\text{best},i}(h) - x_i(h)\right) + c_2 r_2 \left(G_{\text{best}} - x_i(h)\right) \tag{29}$$

$$x_i(h+1) = x_i(h) + v_i(h+1) \tag{30}$$

In Eq. 29, The PSO algorithm involves several parameters, including the inertia weight coefficient (ω), cognitive acceleration coefficient (c_1), and social acceleration coefficient (c_2). These parameters play a crucial role in shaping the behavior of the algorithm and can significantly impact its performance.

The inertia weight coefficient controls the trade-off between global exploration and local exploitation. A high ω value allows particles to maintain their momentum and explore the search space more extensively, enhancing global search capabilities. On the other hand, a low ω value reduces the particle's inertia, leading to more local exploitation and fine-tuning of solutions. Selecting an appropriate ω value is crucial to balancing exploration and exploitation.

$P_{\text{best},i}$ and G_{best} are the individual optimal position of the i-th particle and the global optimal position of the population respectively. c_1, and c_2 determine $P_{\text{best},\ i}$ and G_{best} on each movement, c_1 controls the particle's tendency to move towards its personal best, while c_2 determines the attraction towards the global best position. These coefficients regulate the balance between exploiting the particle's own experiences and leveraging information from other particles in the swarm.

r_1 and r_2 are random numbers between 0 and 1, in Eq. 30, $x_i(h)$ and $v_i(h)$ are the position and velocity of the i-th particle at the h-th iteration, respectively, and h is the current number of iterations. ω gives particles sufficient time to conduct a large-scale global search in the early stage of the search, and its decline rate is slow; in the middle stage, it strengthens local search and decreases approximately linearly; in the later stage, it focuses on detailed local search, and the rate of change decreases again. Non-linear changes are used to control c_1 and c_2, and the learning factors c_1 and c_2 adopt non-linear inverse cosine acceleration. Multiple expressions are:

$$\omega = \frac{(\omega_{\max} + \omega_{\min})}{2} + \frac{(\omega_{\max} - \omega_{\min})}{2} \tanh\left(-4 + 8\frac{h_{\max} - h}{h_{\max}}\right) \tag{31}$$

$$c_1 = c_{1\_e} + (c_{1\_s} - c_{1\_e})\left(1 - \frac{\arccos\left(-\frac{2h}{h_{\max}} + 1\right)}{\pi}\right) \tag{32}$$

$$c_2 = c_{2\_e} + (c_{2\_s} - c_{2\_e})\left(1 - \frac{\arccos\left(-\frac{2h}{h_{\max}} + 1\right)}{\pi}\right) \tag{33}$$

In Eq. 31, $\omega_{\max}$ and $\omega_{\min}$ are the maximum and minimum values of ω, and $h_{\max}$ is the maximum number of iterations.

In Eq. 32, c_{1_s} and c_{1_e} are the iterative initial value and terminal value of the self-learning factor respectively; in Eq. 33, c_{2_s} and c_{2_e} are the iterated initial value and terminal value of the social learning factor, respectively.

By setting a higher initial temperature, the ASAPSO algorithm can significantly increase the possibility of searching for the global optimal solution. The formula is as follows:

$$T(h) = \begin{cases} -\frac{Q_{\text{best}}}{\ln(0.2)}, & h = 1 \\ \mu T(h-1), & h > 1 \end{cases} \tag{34}$$

$T(h)$ is the current temperature, Q_{best} is the optimal value in the initial particle population, and μ is the cooling coefficient.

When each particle moves to a new position, its fitness is calculated. If the fitness value is better than the previous fitness value, the particle is updated and moved to the new position; otherwise, according to the Metropolis criterion, the fitness difference ΔE is calculated (ΔE is The difference between the current fitness value and the previous fitness value), if $p(h) = \exp[-\Delta E/T(h)] > rand$ (*rand* is any random number between 0 and 1), then accept it with a certain probability The current solution is the new solution and the particles move to the new position.

4.3 Solution process

The solution process is as follows.

Step 1: Initial data processing. In Eqs 35, 36, process the EV charging demands for each hour at the demand points in the planning area to obtain the total EV charging demands (Q_{eva}). Estimate the maximum number of charging stations ($N_{\max}$) and the minimum number of charging stations ($N_{\min}$) based on the capacity constraints of a single charging station. Within the range of Nmin to Nmax, set the number of charging station constructions as a loop variable N. Initialize N=$N_{\min}$ and start the iteration. Increase N by 1 after each iteration.

$$N_{\max} = \text{ceil}\left(\frac{Q_{\text{eva}}}{Q_{\min}}\right) \tag{35}$$

$$N_{\min} = \text{ceil}\left(\frac{Q_{\text{eva}}}{Q_{\max}}\right) \tag{36}$$

Step 2: Algorithm parameter initialization. Set the coordinates of N charging stations as a solving dimension. Randomly generate initial velocities (v_0) and positions (X_0) for all particles in this dimension. Set the parameters of the ASAPSO algorithm: swarm size (N_{size}), maximum number of iterations ($Iter_{\max}$), maximum inertia weight ($\omega_{\max}$), minimum inertia weight ($\omega_{\min}$), cognitive coefficients (c_{1_s}

and c_{1_e}), social coefficients (c_{2_s} and c_{2_e}), and mutation probability (μ).

Step 3: Use a weighted Voronoi diagram to divide the service range of charging stations.

Step 4: Calculate the queue waiting time for each charging station and determine the corresponding quantities of high-power and low-power charging equipment.

Step 5: Update the velocities and positions of the particles.

Step 6: Update the individuals based on the fitness function and calculate the global best value (G_{best}).

Step 7: Calculate the acceptance probability [$p(h)$] for accepting new solutions.

Step 8: Use the Metropolis criterion to compare $p(h)$ with a random number (*rand*) and determine whether the new solution replaces the global best solution. Update the temperature according to Eq. 34.

Step 9: Check if the maximum number of iterations ($Iter_{max}$) has been reached. If the condition is satisfied, stop the search and output the optimization result. Otherwise, return to Step 5.

Step 10: Check if the maximum number of charging stations (N_{max}) has been reached. If the condition is satisfied, stop the loop. This will yield N_{max}-N_{min}+1 site selection and capacity determination solutions. Sort them based on the annual total economic cost and select the optimal solution. Otherwise, return to Step 2.

5 Results and discussions

5.1 Parameter scene setting

This study focuses on the site selection and capacity optimization of EV charging stations in a specific region of a northern city. The planning area of this region is approximately 58 km^2, with an east-west span of about 7.56 km and a north-south span of about 8.62 km. The total population in this area reaches 250,000. The first step is to divide the transportation road network within this region. There are 48 road nodes and 82 road segments. Within the planning area, there are 3,000 electric private vehicles and 1,100 electric taxis. For simplicity, it is assumed that each electric vehicle has an average capacity of 50 kWh.The coverage of nodes for each functional zone within this area can be found in Supplementary Appendix Table SA1, and the schematic diagram of the road network structure is provided in Supplementary Appendix Figure SA2.

In the given example, the parameters for the particle swarm optimization algorithm are set as follows:

- Swarm size (N_{size} = 100)
- Maximum number of iterations ($Iter_{max}$ = 100)
- Maximum inertia weight (ω_{max} = 0.95)

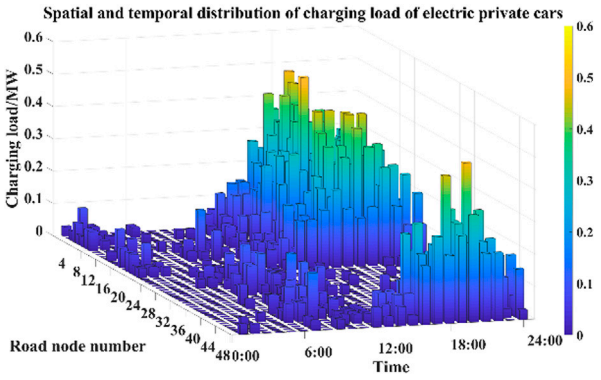

FIGURE 4
Spatial and temporal distribution of charging load of electric private cars.

- Minimum inertia weight (ω_{min} = 0.45)
- Cognitive coefficient (c_{1_s} = 2.50)
- Cognitive coefficient (c_{1_e} = 1.25)
- Social coefficient (c_{2_s} = 1.25)
- Social coefficient (c_{2_e} = 2.50)
- Mutation probability (μ = 0.95)
- Γ_k = 1

The parameters related to the charging stations are as follows:

- High-power charging station power (P_{high} = 80 kW)
- Cost of purchasing a high-power charging station: 20,000 yuan per unit
- Low-power charging station power: (P_{low} = 30 kW)
- Cost of purchasing a low-power charging station: 8,000 yuan per unit
- Minimum number of charging stations to be built (N_{min} = 5)
- Maximum number of charging stations to be built: (N_{max} = 12)
- Service radius (R_k = 1.5 km)
- Maximum waiting time for charging (W_{h_max} = 20 min)

Other charging station planning parameter values can be found in Supplementary Appendix Table SA2.

5.2 Spatiotemporal distribution prediction results

Using the load forecasting method proposed in Section 2, which takes into account the dynamic charging demands of users, the spatial and temporal distribution of charging load for electric private vehicles and electric taxis is obtained. The specific results are shown in Figure and Figure 5.

Analysis of Figures 4, 5 reveals that the spatial and temporal distribution of charging load at each node is closely related to the functional zones of the respective cities. The nighttime peak charging demand areas are predominantly concentrated in residential areas, while the daytime peak charging demand areas are primarily concentrated in working and commercial zones. For electric private vehicles, the peak charging demands during the

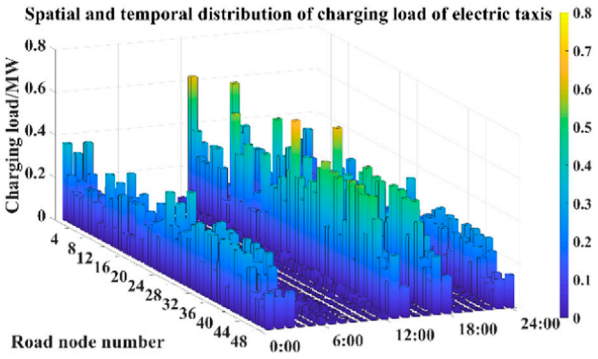

FIGURE 5
Spatial and temporal distribution of charging load of electric taxis.

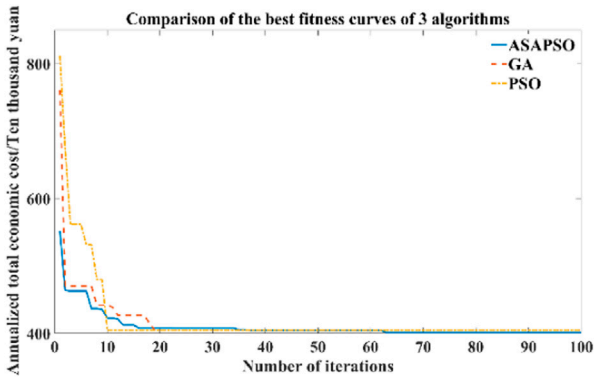

FIGURE 6
Comparison of optimal fitness curves of three algorithms.

nighttime are mainly concentrated between 19:00 and 03:00. This is because most electric private vehicle owners prefer to charge their vehicles slowly during the night. The peak charging load in residential areas occurs around 19:00 when most electric private vehicle users return home.

For taxis, the charging load reaches its peak between 12:00 and 14:00, with another peak occurring between 17:00 and 18:00. During the first period, taxi drivers take a break and have lunch, so they prefer fast charging to quickly replenish their vehicle's battery. The second period is 1 h before the evening rush hour when they need to quickly recharge to cope with the upcoming peak demand. In different functional zones, significant charging demands for electric private vehicles are observed at nodes 1–9, 16–21, 46–48, etc. After work or commercial activities, most electric private vehicle users return to residential areas. If their remaining battery level is insufficient for the next trip, charging demands arise. For taxis, nodes 8–10, 22–24, and 38–42 represent the road nodes with the highest number of charging stations in each functional zone. These nodes primarily serve as transportation hubs connecting residential and commercial areas and are linked to main roads. From a spatial perspective, the charging load for taxis is significantly influenced by the attributes of the functional zones. On one hand, users concentrate along the main roads connecting residential areas to commercial areas, which are the main destinations and passenger pick-up areas for taxis, resulting in higher charging demands. On the other hand, main roads in the urban transportation system provide advantages such as wider roads and easier travel, making drivers more likely to choose them, thereby increasing the charging demands.

5.3 Algorithm verification

To verify the superiority of the proposed algorithm, we chose to run it on the same computer and used the ASAPSO algorithm, Particle Swarm Optimization (PSO), and Genetic Algorithm (GA) mentioned in the article to solve the example, respectively, the optimal fitness curves of the three algorithms are obtained, as shown in Figure 6. Comparing the three curves in the figure, we can see that the PSO algorithm has the fastest convergence speed in the early iterations and converges quickly with a smaller number of iterations. The GA algorithm has the slowest convergence speed. Compared with other algorithms, ASAPSO has better convergence speed and accuracy in the early iterations, and after 60 iterations, when the other two algorithms have fallen into local optimal solutions, the ASAPSO algorithm can still continuously update the global optimal value, still maintaining good population diversity in the middle and late stages of iteration. It can be seen that ASAPSO has certain advantages in both convergence speed and accuracy, and the comprehensive optimization results are better than the other two algorithms.

TABLE 5 Annualized total economic cost of each planning scheme.

N	C_a	C_b	C_{wk}	C_{gk}	C_{mk}	F
5	78.71	88.16	125.79	90.04	80.03	462.73
6	87.59	100.73	101.17	79.16	70.89	439.54
7	94.36	110.72	83.98	60.48	50.47	400.01
8	107.23	123.08	78.74	54.53	48.53	412.11
9	121.49	143.68	73.74	50.10	43.10	432.11
10	133.18	150.67	69.68	49.33	40.33	443.19
11	150.13	183.25	64.98	47.39	38.39	484.14
12	164.13	192.50	62.73	46.93	36.93	503.22

5.4 Result of charging station site selection and capacity determination

Based on the prediction of the spatial and temporal distribution of charging demands, the planning process is solved according to Section 4.3, and the annualized total economic cost of each planning scheme is obtained, as shown in Table 5 and Figure 7.

Table 5 shows that for EV charging station operators, the number of charging stations has a linear relationship with the annual average fixed construction costs and annual average operational and maintenance costs. For EV users, an increase in the number of charging stations reduces costs associated with travel

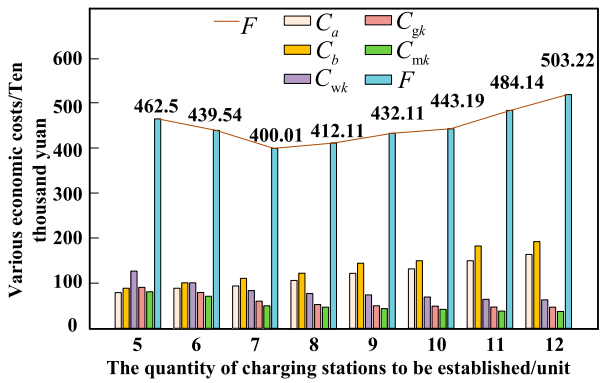

FIGURE 7
Annualized total economic cost comparison chart.

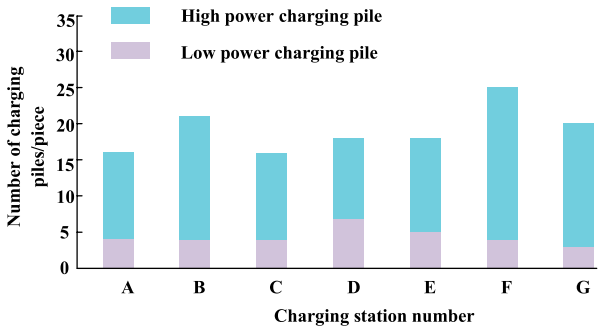

FIGURE 8
The number of high-power/low-power electric piles configured in each charging station.

TABLE 6 The site selection of the EV charging station and the number of charging piles.

Charging station number	*x*/km	*y*/km	The total amount of charging piles	Road network node number
A	1.84	8.40	16	1, 2, 3, 7, 8, 9
B	6.97	7.13	21	4–6, 10–12, 13–15
C	1.43	5.10	16	17–20, 29, 30
D	4.99	4.62	18	16, 21, 22, 27, 28
E	7.93	3.79	18	24, 25, 26, 36
F	1.88	1.53	25	31–33, 37–39, 43–45
G	6.94	1.34	20	34, 35, 40–42, 46–48

distance, time, and waiting queues. When constructing 5 to 7 charging stations, the total annual economic cost decreases as the number of EV charging stations increases. However, when constructing 7 to 12 stations, the total annual economic cost increases with the number of stations. The optimal planning solution is achieved when there are 7 charging stations, resulting in the minimum total annual economic cost of 4,000,100 yuan.

For the planning solution with seven charging stations, the objective is to minimize the sum of EV users' annual economic losses and charging station operators' annual costs. The optimal number and locations of charging stations are determined using the risk-value theory to solve the robust capacity model. The weighted Voronoi diagram is employed to divide the service range of the charging stations. The coordinates of the charging station sites and the number of charging piles for each station are shown in Table 6. The configuration of high-power and low-power charging piles is illustrated in Figure 8, and the layout and service range division of the charging stations are presented in Figure 8. The layout and service coverage of the charging stations are depicted in Figure 9, with the numbering of the 7 charging stations as A, B, C, D, E, F, and G.

From the results in Table 6 combined with Figure 8, it can be seen that the number of charging piles in different charging stations is related to the charging load of the coverage area. According to the analysis of the EV charging load demand prediction results in Section 5.2, it can be seen that EVs generally replenish electric energy quickly in a short time in commercial areas. Charging times are relatively long in work areas and residential areas. Road node numbers with large charging load requirements are 5, 11, 33, 38, 41, 44, etc.; charging stations covering these nodes, such as charging stations B, F, and G are equipped with a larger number of charging piles. Charging stations A, C, and D exhibit comparatively lower charging demand within their respective coverage areas, leading to a noticeably reduced number of charging points allocated correspondingly. It can be seen from Figure 8 that for charging stations with a larger total number of charging piles, the proportion of high-power charging piles is greater than that of low-power charging piles, and most of these charging stations are distributed in areas with high charging demands, such as charging stations B and F. It is not only close to the business district but also located in the heart of the residential area or work area. Charging stations with a high proportion of low-power charging piles mean that there are less demands for fast charging in the coverage area. As long as it can meet normal charging, the corresponding total charging demands are relatively low, such as charging stations A, C, and D.

Based on the aforementioned results, it can be concluded that the proposed optimization strategy for configuring high-power and low-power charging stations effectively addresses the charging demand in different planning areas. This approach expands the range of options available to EV users. Compared to methods that only consider the deployment of high-power charging stations, this strategy demonstrates superiority in practical capacity-based applications of charging stations.

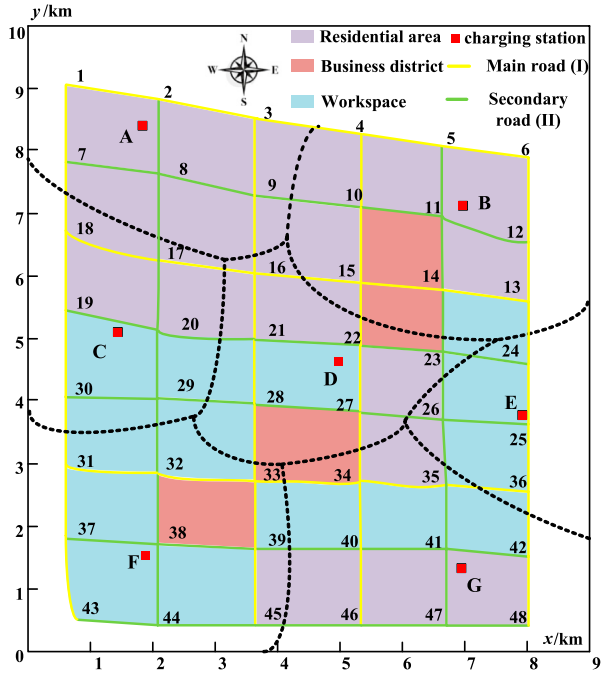

FIGURE 9
Site selection and service scope division map.

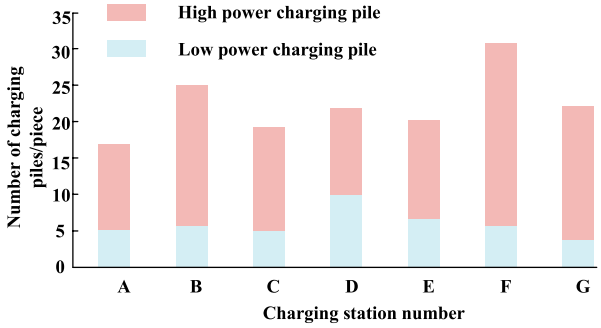

FIGURE 10
The number of electric piles in each charging station in Scenario 2 when the demands increase by 20%.

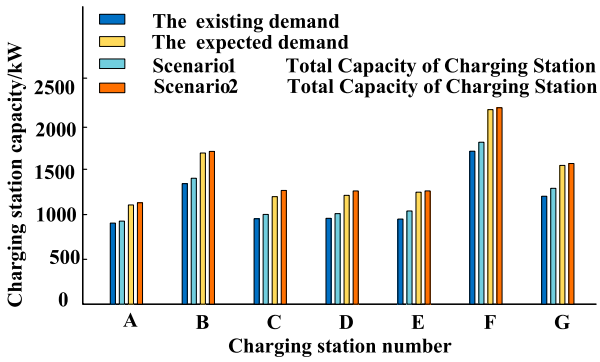

FIGURE 11
Comparison of the total capacity of charging stations in Scenario 1 and Scenario 2.

In addition, due to the increasing demand from EV users in recent years, to further highlight the advantages of the robust optimization model, deterministic Scenario 1 and uncertain Scenario 2 were designed in this section for analysis and comparison.

Scenario 1: Under the deterministic condition of EV user charging demand, the number, location, and capacity of charging stations are determined using the charging station optimization model established in Section 3.

Scenario 2: Under the uncertain condition of EV user charging demand, without adding new charging station locations, the capacity of existing charging stations is adjusted using the capacity-based robust model.

To compare the resilience of the two scenarios against risks, the existing demand at each charging point was increased by 20% to represent the expected demand. Figure 10 illustrates the quantities of charging points configured when the demand is increased by 20%.

Based on Figure 11, it can be observed that the charging station capacity in Scenario 1 almost perfectly meets the current existing users' charging demands. However, when the users' anticipated charging demand increases by 20%, the daily service capacity of the previously optimized seven charging stations is unable to meet the users' requirements. This would significantly diminish the charging experience for EV users. Without considering the addition of new charging station locations, and only taking into account the uncertainty of demand, a robust capacity planning model adjusts the capacity of the existing charging stations. Comparing the capacity planning results, it is evident that Scenario 2, in contrast to Scenario 1, not only effectively satisfies the current users' charging demands but also leaves room for expansion. Even with a 20% increase in the anticipated charging demand, the capacity planning results in Scenario 2 still meet the users' expected requirements. This indicates that the capacity adjustment in Scenario 2, implemented through a robust capacity planning model that considers demand uncertainty without the need for additional charging station locations, proves capable of meeting the users' anticipated demands. Moreover, it demonstrates that Scenario 2 charging station capacity is more than sufficient to accommodate the increased demand, ensuring a satisfactory charging experience for EV users.

6 Conclusion

The paper proposes a capacity determination method for siting charging stations considering the uncertainty of users' dynamic charging demands. Through a case study analyzing a specific city's urban area in the northern region, the main conclusions obtained are as follows:

1) The proposed charging station planning model, which aims to minimize the annual total economic cost, provides reasonable charging station locations and the configuration of high-power/low-power charging piles. It aligns well with the

actual situation. The annual costs of EV charging station operators and the annual economic losses of users are relatively low, balancing the interests of both parties.

2) The ASAPSO algorithm, introduced in the study, incorporates a simulated annealing mechanism and adaptively adjusts the self-cognition and social cognition components, improving algorithm performance. This leads to more accurate siting planning results for charging stations. The introduced weighted Voronoi diagram effectively delineates the service range of charging stations.
3) The proposed capacity-constrained robust model, which considers the configuration of high-power/low-power charging piles, enables effective optimization of these piles' quantities. It provides a reference for addressing the uncertainty of charging demands in charging station planning.

Data availability statement

The original contributions presented in the study are included in the article/Supplementary Material, further inquiries can be directed to the corresponding author.

Author contributions

ZL: Conceptualization, Data curation, Formal Analysis, Writing–original draft, Writing–review and editing. FH: Conceptualization, Software, Writing–original draft. ZZ: Conceptualization, Writing–review and editing. WS: Writing–original draft, Writing–review and editing.

Funding

The authors declare financial support was received for the research, authorship, and/or publication of this article. This paper is supported by the Science and Technology Project of State Grid Henan Electric Power Company (5217L0220001).

Acknowledgments

The authors are grateful to the editor and reviewers for their work.

Conflict of interest

Authors ZL and ZZ were employed by Economics and Technology Research Institute of State Grid Henan Electric Power Company. Author ZJ was employed by Beijing Qunling Energy Technology Co., Ltd.

The remaining authors declare that the research was conducted in the absence of any commercial or financial relationships that could be construed as a potential conflict of interest.

Publisher's note

Supplementary material

The Supplementary Material for this article can be found online at: https://www.frontiersin.org/articles/10.3389/fenrg.2023.1295043/full#supplementary-material

References

Cao, F., Hu, J., Luo, J., and Zheng, J. (2022). Capacity con-figuration of EV path simulation based on road network dynamic model. *Electr. Power Autom. Equip.* 42 (10), 107–115. doi:10.16081/j.epae.202205003

Chen, L. (2018). *Research on the impact of extensive access to electric vehicles on the power grid and its regulation strategy*. China: South China University of Technology.

Dong, X., Mu, Y., Jia, H., Wu, J., and Yu, X. (2016). Planning of fast EV charging stations on a round freeway. *IEEE Trans. Sustain. Energy* 7 (4), 1452–1461. doi:10.1109/tste.2016.2547891

Fakhrmoosavi, F., Kavianipour, M. R., Shojaei, M. H. S., Zockaie, A., Ghamami, M., Wang, J., et al. (2021). Electric vehicle charger placement optimization in Michigan considering monthly traffic demand and battery performance variations[J]. *Transp. Res. Rec.* 2675 (5), 13–29. doi:10.1177/0361198120981958

Gan, X., Zhang, H., Hang, G., Qin, Z., and Jin, H. (2020). Fast-charging station deployment considering elastic demand. *IEEE Trans. Transp. Electrification* 6 (1), 158–169. doi:10.1109/tte.2020.2964141

Ge, S., Hui, L. I., and Liu, H. (2007). Optimal planning of substation based on weighted Voronoi diagram. *Automation Electr. Power Syst.* 3 1 (3), 29–34. doi:10.3321/j.issn:1000-1026.)2007.03.007

Ge, S., Liang, FENG, Liu, H., et al. (2013). Charging station planning considering traffic flow information and distribution network capacity constraints. *Power Syst. Technol.* 37 (03), 582–589. doi:10.13335/j.1000-36.73.pst.2013.03.018

Ge, S., Rong, L. I., Han, J., et al. (2016). Charging station planning considering stochastic probabilistic behavior characteristics of electric taxi. *Automation Electr. Power Syst.* (4), 50–58. doi:10.7500/AEPS20150513014

Ge, S., Shen, K., Liu, H., et al. (2021). Urban fast charging network planning considering network transfer performance. *Power Syst. Technol.* 45 (09), 3553–3564. doi:10.13335/j.1000-3673

Kennedy, J., and Eberhart, R. (1995). *Particle swarm optimization [C]//proceeding of the IEEE international conference on neural networks*. Piscataway: IEEE, Press, 1942–1948.

Khardenavis, A., Hewage, K., Perera, P., Shotorbani, A. M., and Sadiq, R. (2021). Mobile energy hub planning for complex urban networks: a robust optimization approach[J]. *Energy*. doi:10.1016/j.energy.2021.121424

Kong, W., Luo, Y., Feng, G., et al. (2019). Optimal location planning method of a fast charging station for electric vehicles considering operators, drivers, vehicles, traffic flow, and power grid. *Energy* 186 (Nov. 1), 11–115826.

Li, H., Qiang, W., and Gao, Y., etc. Charging station planning considering users' travel characteristics and available margin of distribution network lines. *Electr. Power Syst. Autom.*, 2018, 42(23): 48–56.

Liu, H., Rong, L. I., Ge, S., et al. Multi-objective planning of charging stations considering random behavior characteristics of taxis and reliability of road network travel time. *Power Syst. Technol.*, 2016,40(02):433–441. doi:10.13335/j.1000-3673.pst.2016.02.015

Luo, L. Z., Gu, W., Zhou, S. Y., Huang, H., Gao, S., Han, J., et al. (2018). Optimal planning of electric vehicle charging stations comprising multi-types of charging facilities. *Appl. Energy* 226, 1087–1099. doi:10.1016/j.apenergy.2018.06.014

Shao, Y., Mu, Y., and Yu, X. (2017). Spatial and temporal prediction of electric vehicle charging load under vehicle-road-network mode and its influence on power flow in distribution network. *Proc. CSEE* 37 (18), 52–5219. doi:10.13334/j.0258-8013.pcsee.161470

Song, Y. (2014). *Research on energy consumption modeling and driving range estimation of pure electric vehicles based on driving conditions*. Beijing: Beijing Jiaotong University.

Xiao, B., and Gao, F. (2022). Location and capacity optimization method for electric vehicle charging station with different capacity charging piles. *Electr. Power Autom. Equip.* 42 (10), 157–166. doi:10.16081/j.epae.202207001

Xin, A. I., Li, Y., Wang, K., et al. (2018). Site selection and capacity determination of electric vehicle charging station based on chaotic simulated annealing particle swarm optimization algorithm. *Electr. Power Autom. Equip.* 38 (9), 9–14. doi:10.16081/j.issn.1006-6047.2018.09.002

Yan, G., Liu, H., and Han, N. (2021a). Calculation and optimization method of charging station site selection and fixed capacity for electric vehicle space-time distribution status. *Chin. J. Electr. Eng.* 41 (18), 6271–6284. doi:10.13334/j.0258-8013.pcsee.202001

Yan, Q., Ma, R., Ma, Y., et al. (2021b). An adaptive simulated annealing particle swarm optimization algorithm. *J. Xidian Univ.* 48 (04), 120–127. doi:10.19665/j.issn1001-2400.2021.04.016

Zhang, H., Tang, L., Yang, C., and Lan, S. (2019b). Locating electric vehicle charging stations with service capacity using the improved whale optimization algorithm. *Adv. Eng. Inf.* 41 (AUG), 100901–101100. doi:10.1016/j.aei.2019.02.006

Zhang, Y., Zhang, Q., Farnoosh, A., Chen, S., and Li, Y. (2019a). GIS-Based Multi-Objective Particle Swarm Optimization of charging stations for electric vehicles. *Energy* 169, 844–853. doi:10.1016/j.energy.2018.12.062

Zhang, M., Sun, Q., and Yang, X. (2022). Electric vehicle charging load prediction considering real-time interaction of multi-source information and users' regret. *Power Syst. Technol.* 46 (02), 632–645. doi:10.13335/j.1000-3673.pst.2021.0273

Zhao, F., Li, J., and Gao, F. (2021). Considering uncertainty, the location and capacity setting of highway photovoltaic storage charging station. *Electr. Power Autom. Equip.* 41 (08), 111–117. doi:10.16081/j.epae.202105007

Zhao, S., Li, Z., and Dang, L. (2016). Optimal site selection and capacity setting of electric vehicle charging station based on urban trans-portation network information. *Electr. Power Autom. Equip.* 36 (10), 8–15. doi:10.16081/j.issn.1006-6047.2016.10.002

Zhao, S., Zhou, J., Li, Z., et al. (2017). *Electr. Power Autom. Equip.* 37 (08), 105–112. doi:10.16081/j.issn.1006-6047.2017.08.014

Zhu, S., Yu, S., Wang, Ge, et al. (2019). Planning of electric vehicle charging station based on conditional value at risk[J/OL]. *Electr. Meas. Instrum.* 10, 1. [2023-05-19].

Zhu, Y., Yang, Z., Ding, T., et al. (2023). Planning of electric vehicle charging station considering users' dynamic charging demand. *J. Zhengzhou Univ. Sci.* 44 (02), 82–90. doi:10.13705/j.issn.1671-6833.2023.02.001

Zuo, Y., Li, W., and Yang, W. (2022). Planning of EV charging station considering the spatiotemporal distribution characteristics of charging lo-ad[J/OL]. *Electr. Meas. Instrum.* 10, 1. [2023-04-05].

frontiers | Frontiers in Energy Research

TYPE Original Research
PUBLISHED 23 January 2024
DOI 10.3389/fenrg.2023.1267303

OPEN ACCESS

EDITED BY
Hao Xiao,
Chinese Academy of Sciences (CAS), China

REVIEWED BY
Shaobo He,
Central South University, China
Feixiong Chen,
Fuzhou University, China

*CORRESPONDENCE
Zhenbo Niu,
niuzhenbo_epri@163.com

RECEIVED 26 July 2023
ACCEPTED 19 December 2023
PUBLISHED 23 January 2024

CITATION
Niu Z, Zheng C, Lv S, Shan Y and Ni F (2024), Transient angle stability analysis of maximum Lyapunov exponent based on the key branch response information.
Front. Energy Res. 11:1267303.
doi: 10.3389/fenrg.2023.1267303

Transient angle stability analysis of maximum Lyapunov exponent based on the key branch response information

Zhenbo Niu*, Chao Zheng, Sizhuo Lv, Yunjing Shan and Fengyi Ni

China Electric Power Research Institute Co., Ltd., Beijing, China

Based on real-time access to response information on wide-area tributaries, in order to assess the system stability more quickly, this paper combines the simplified branch transient transmission capability (sBTTC) index and the largest Lyapunov exponent (MLE). An online identification method for transient power angle stability is proposed. Firstly, the method is based on a two-machine system to study the consistency of the power angle difference between the two ends of the critical branch and the change of the phase difference of the fleet. Secondly, the transient power angle stability problem is transformed into the MLE analysis problem according to the change rule of sBTTC index of the key branch. Then, by combining the characteristics of MLE curve and sBTTC index curve, the transient power angle stability criterion is given. Finally, the proposed method is verified and analysed by simulation examples. The method has strong industrial applicability because it does not need system model, the information source is easy to measure, it has strong anti-noise ability, and it overcomes the defect of the traditional method that needs to set a fixed symbolic observation window.

KEYWORDS

maximum Lyapunov exponent, transient branch transmission capacity index, transient angle stability, the key branch, wide-area measurement system

1 Introduction

Transient angle stability assessment constitutes a crucial research aspect for ensuring the secure and stable operation of power systems (Wang and Wu, 1991; Sun et al., 2006; Chen et al., 2017). In recent years, the introduction of new energy sources and power electronic devices into the power grid, alongside the implementation of extra-high voltage direct current transmission projects, has significantly altered the stability profile of the power grid. (Kundur et al., 2004; Liu T et al., 2023; Andersson et al., 2005). Therefore, accurate identification of power system stability patterns is an important prerequisite for effective emergency control.

At present, for the system generator rotor angle stability problem has been carried out by scholars a lot of research. In terms of the out-of-step criterion based on generating unit information, the most ahead and lagging unit pairs are captured, and the equal area criterion is applied to quickly discriminate the stability (Paudyal S et al., 2010). Stability criterion is constructed based on single machine energy function and group pair energy function (Mu et al., 1993; Gou Jing et al., 2015; Gou J. et al., 2015) devises a transient stability discrimination index set based on the energy function of generator pairs and utilizes this index set for stability discrimination. Additionally, (Xie et al., 2006), leverages the concavity

and convexity characteristics of the phase trajectory of equivalent units to accomplish stability discrimination through unit grouping. System stability is assessed based on the distance of the state point from the boundary of the dynamic security domain (Zeng et al., 2018; Liu et al., 2018).

The above method of stability determination based on unit response information needs to involve the whole network units and the required information is difficult to measure. The stability judgement relies on the generator grouping result, which is difficult to apply to the new type of power system. (Xue et al., 1989; Xue and Xue, 1999).

Based on the measurement information provided by wide area measurement system (WAMS) (Qin et al., 2008), the mode of "real-time decision-making, real-time control" can accurately and efficiently identify the system stability, effectively reduce the chain reaction caused by large disturbances, and have important significance for the safe and stable operation of the power grid (Liu et al., 2013; Tang, 2014; Lin et al., 2016). The research methods based on the network response information include transient energy function method, phase trajectory characteristic analysis method, artificial intelligence method (Tian and Zhao, 2023) and so on. Among them, the Maximum Lyapunov Exponential analysis method based on chaos theory has become research hotspot (Ravikumar and Khaparde, 2018). The concept of MLE was firstly applied to the power system transient stability discrimination, and the positive and negative signs of MLE were used to predict whether the power system was destabilized or not (Liu C W et al., 1994). A method for calculating the MLE and then determining the transient stability of the system based on the system model is proposed (Yan et al., 2011). Combining the mathematical model of the system with the definition of MLE, the stability of the system is monitored by calculating the Lyapunov exponential spectrum (Wadduwage D P et al., 2013). The above methods for calculating MLE have many disadvantages, such as being dependent on the system model, requiring high-dimensional phase space reconstruction, being extremely computationally complex, and being unfavorable for online engineering applications. The transient angle stability of the system is monitored by solving the MLE for a time series window of relative angles of all generators of the system. The algorithm requires only simple arithmetic calculations and is computationally fast (Dasgupta et al., 2013). By presetting the time observation window of MLE symbols, an MLE calculation method without system model is proposed (Dasgupta et al., 2015). However, the fixed time observation window cannot adapt to the variable fault disturbances, and it is necessary to observe the generating units of the whole network, which involves a huge amount of information. For this reason, a transient stability monitoring method based on the dynamic characteristics of the trajectory MLE of the key unit pair is proposed by finding the key unit pair, but the generator angle information is difficult to be measured directly (Huang et al., 2020). By analyzing the machine-end voltage information that can be measured directly, the least squares method is used to improve the calculation method of MLE, and the system instability criterion is given by combining the characteristics of the MLE curve (Shaopan et al., 2017). However, relying only on any one-dimensional end-voltage response sequence as the analysis data lacks reliability, and it is difficult to locate the key information sources.

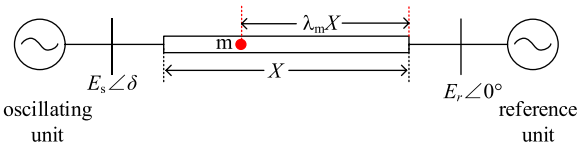

FIGURE 1
Typical model for angle stability analysis.

Building upon prior research, this paper introduces a Maximum Lyapunov Exponent (MLE) transient stability analysis method based on the key branch response information. The approach involves several key steps. Firstly, this paper analyzes the characteristics of network node phase with clustering attribution in unstable system. The angle difference between the nodes at both ends of the key branch is consistent with the change of the angle difference between the leading and lagging clusters. Secondly, in this paper, the transient angle stabilization problem is transformed into a problem of MLE curve trajectory analysis of sBTTC exponential curves. In both stable and unstable forms, this paper analyses the MLE key properties of the sBTTC exponential response time series using the MLE solution mechanism. Combining the crucial attributes of sBTTC and MLE, by optimizing the initial time window and the maximum observation time window of the MLE method, this paper proposes a new transient stability judgement method based on the disturbed response information of the key branch. Finally, for a typical 39-node system and a real AC-DC hybrid grid, this paper verifies the validity of the criterion by simulation.

2 Unit-branch association characterization

In the typical model of a single machine infinity system shown in Figure 1, *Es* and δ represent the terminal voltage and angle of the oscillating unit. *Er* denotes the terminal voltage of the reference unit. *X* signifies the total reactance between the oscillating unit and the reference unit.

Point "m" represents an any measurement node associated with the position factor λm. The branch current and voltage vectors at node "m" are denoted by Eq. 1 and Eq. 2 respectively.

$$\dot{I} = \frac{\dot{E}_s - E_r}{jX} \tag{1}$$

$$\dot{U}_m = E_r + j\lambda_m X\dot{I} \tag{2}$$

Substituting Eq. 1 into Eq. 2 yields Eq. 3, as follows

$$\begin{aligned}\dot{U}_m &= E_r + j\lambda_m X\frac{\dot{E}_s - E_r}{jX} \\ &= [(1-\lambda_m)E_r + \lambda_m E_s\cos\delta] + j\lambda_m E_s\sin\delta\end{aligned} \tag{3}$$

Consequently, the angle information at point "m" is expressed in Eq. 4.

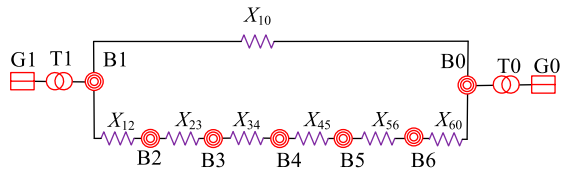

FIGURE 2
The single machine infinity system model.

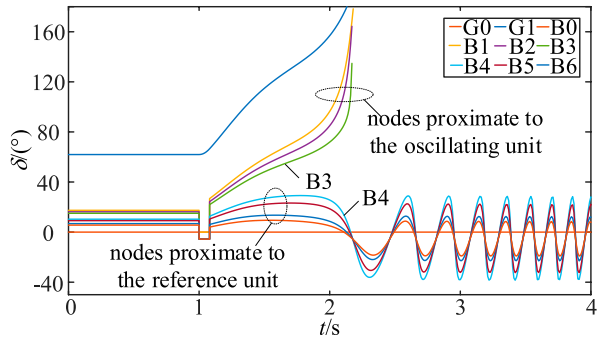

FIGURE 3
The curve of generator angle and phase change of each node.

$$\theta_m = \arctan\frac{\lambda_m E_s \sin\delta}{(1-\lambda_m)E_r + \lambda_m E_s \cos\delta} \tag{4}$$

Based on Eq. 4, it is evident that the phase θ_m of the node "m" relies on the position factor λ_m and the angle δ. To delve deeper into the correlation between θ_m, λ_m, and δ, the single machine infinity system model shown is established in Figure 2. X_{10} = 0.04pu, X_{12} = X_{60} = X_{45} = 0.004pu, X_{34} = X_{56} = 0.008pu, X_{23} = 0.012pu. The actual active power output of generator G1 is 100pu. The position factor λ_2-λ_6 of nodes B2-B6 correspond to [0.9, 0.6, 0.3, 0.1] respectively.

At 1 s, a three-phase ground short-circuit fault occurs on the front side of the B1-B0 branch. In the case of system transient stability and transient instability, the fault clearing time is set to 0.06 s and 0.08 s respectively. In the example of system instability, the curve of generator angle and phase change of each node is shown in Figure 3.

As depicted in Figure 3, when angle instability occurs in the system, depending on the electrical distance to the reference unit, the phase of each node will be characterized by subgroup attribution. Using the electrical midpoint as a dividing line, Nodal phases close to the oscillating unit will tend to be close to the angle of the oscillating unit, while nodal phases close to the reference unit will be attributed to the angle of the reference unit. Therefore, the nodes in the network are consistent with the angle variation characteristics of the ahead and behind generator group. They all have the property of subgroup attribution. Within the B3-B4 branch comprising two nodes, the phase of the B3 node follows the same trend as that of the swing unit, and the phase of the B4 node follows the same trend as that of the reference unit. The phase difference between the B3-B4 branch and the angle of the unit always shows the trend of increasing in the same direction. Therefore, the B3-B4 branch is the key branch of the system, which can characterize the angle stability level of the system.

3 The simplified branch transient transmission capability index method and the maximum Lyapunov exponent method

3.1 The sBTTC index method based on network information

3.1.1 Principle of sBTTC method

(Zheng et al., 2021a) defines an sBTTC index that monotonically represents the system stability condition based on wide-area branch response information. Based on this, Eq. 5 represents the simplified sBTTC index. The deterioration of system stability is reflected by setting a stability threshold.

$$\text{sBTTC} = U_{im}U_{in}\cos^2\frac{\Delta\theta}{2} \tag{5}$$

Where: U_{im} and U_{in} represent the node voltage amplitude at the two ends of the i branch, respectively. $\Delta\theta$ signifies the difference in the mode value of the node voltage vector at the two ends of the i branch.

In the destabilized system, the phase difference between the nodes at the two ends of the key branch shows a continuous increase and tends to be unbounded, while the voltage product keeps decreasing. This characteristic is reflected in Eq. 5, which shows that the phase difference between the two ends of the branch is 180° when the sBTTC index drops to 0, indicating system instability. During the initial descent phase of the sBTTC index, the sBTTC index values of all observed branches in the network are ordered from smallest to largest. According to Eq. 6, the key branch k has the smallest index value, and the candidate the key branch clusters have the next smallest index value. Additionally, the branch droop voltage coefficient ξ_v is introduced and combined with the branch droop voltage coefficient located within the interval [1,2] to distinguish the key branches (Zheng et al., 2021b; Zheng et al., 2022). Meanwhile, in order to improve the accuracy of discriminating the key branch, the branch droop voltage coefficient ξ_v is introduced and combined with the branch droop voltage coefficient located in the interval [1,2] for discrimination (Zheng et al., 2021a; Zheng et al., 2022).

$$k = \underset{i\in\{1,2,\cdots N\}}{\text{argmin}}\{\text{sBTTC}_i\} \tag{6}$$

$$1 \le \xi_v \le 2 \tag{7}$$

3.1.2 Transient characteristics of the key branch sBTTC indices

When a system generator destabilisation occurs, at least one branch exists in the network. The phase difference between the nodes at the ends of this branch is consistent with the change in the power angle difference between the overrun and lagging units, and the centre of oscillation is located here. Among the AC lines in the whole network, the key branches have the weakest stability

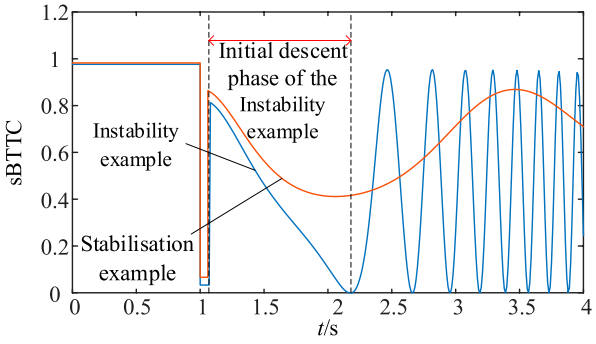

FIGURE 4
sBTTC curve for branch B3-B4.

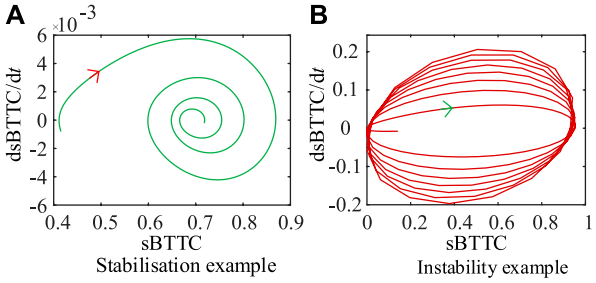

FIGURE 5
sBTTC-d (sBTTC)/d*t* curves for branch B3-B4.

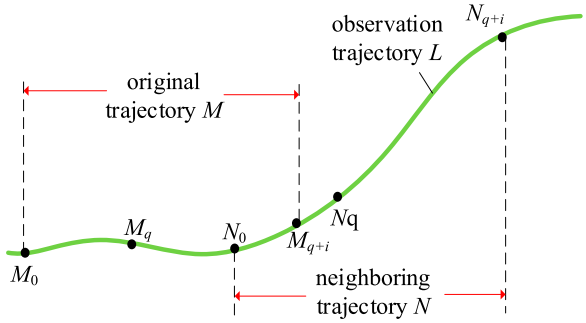

FIGURE 6
Observation trajectory.

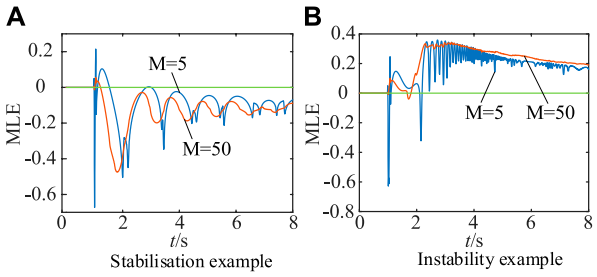

FIGURE 7
MLE-*t* curves for different initial time windows.

performance. The dynamic response process of sBTTC index of the key branch can directly reflect the transient angle stability of the whole system.

The sBTTC exponential variation curves for the key branch B3-B4 are illustrated in Figure 4 for the single machine infinity system in Section 2 under both the instability and stability cases.

The sBTTC exponential curve of branch B3-B4 is transformed to the sBTTC-d (sBTTC)/d*t* plane as shown in Figure 5. Calculate d (sBTTC)/d*t* as in Eq. 8:

$$\left.\frac{\mathrm{d}(\mathrm{sBTTC})}{\mathrm{d}t}\right|_{m\Delta t,i} = \frac{\mathrm{sBTTC}_{m\Delta t,i} - \mathrm{sBTTC}_{(m-1)\Delta t,i}}{\Delta t} \tag{8}$$

where d (sBTTC)/d*t* and $\mathrm{sBTTC}_{(m-1)\Delta t,i}$ represent the sBTTC index values of branch *i* at time instances $m\Delta t$ and (m−1) Δt, respectively.

As can be seen from Figure 5A, if the system transient angle is stability, the trajectory of sBTTC-d (sBTTC)/d*t* curve will gradually converge to a stable point, at which time the value of sBTTC-d (sBTTC)/d*t* is close to zero; from Figure 5B if the system transient angle is instability, the curve of sBTTC-d (sBTTC)/d*t* will be diverging around the zero axis, and cannot be converted to a stability equilibrium point. Therefore, the system angle stability analysis problem can be transformed into the problem of whether the sBTTC exponential curve can converge to a certain point. With the help of MLE, it can be used to determine the motion behavior of the power system; a negative MLE characterizes the convergence of trajectories, which represents the stability of the power system; a positive MLE characterizes the divergence of trajectories, which represents the instability of the power system.

3.2 The MLE method based on network information

The computations of MLE can be divided into those based on a system model and those that do not based on a system model. The PMU can measure the response information of the system, which facilitates the calculation of MLE without the need for a system model.

In Figure 6, the dynamic system observation trajectory is *L*. *M* is the original trajectory. *N* is the neighboring trajectory. M_0, and N_0 the starting points of the original and neighboring trajectories, respectively. Similarly, M_q and N_q stand as the reference points for the original and neighboring trajectories, while M_{q+i} and N_{q+i} represent the *i* point after the respective reference points.

The system sampling interval is Δt. At the moment $i\Delta t$, the logarithmic Euclidean distance curve lgL between the original and neighbouring trajectories is calculated as in Eq. 9.

$$\lg L(i\Delta t) = \lg\left|N_{q+i} - M_{q+i}\right| \tag{9}$$

As shown in Eq. 10, the MLE of the system at the moment $i\Delta t$ is solved approximately using the MLE definition.

$$\mathrm{MLE}(i\Delta t) = \frac{1}{i\Delta t}\lg\left|\frac{N_{q+i} - M_{q+i}}{N_q - M_q}\right| \tag{10}$$

Eq. 10 only considers the resultant information of two points. In order to study the point-to-point transition process on the trajectory, it is necessary to use *K* data on the observation curve *L* as the initial time window. This necessitates satisfying the condition: $\varepsilon_1 < \|L_{k\Delta t} - L_{(k-1)\Delta t}\| < \varepsilon_2$, where $k = 1, 2 \ldots K$. The

parameters ε_1 and ε_2 represent the upper and lower bounds, respectively, for the deviation of the observations. Consequently, the MLE of the system at the moment $i\Delta t$ is (Dasgupta et al., 2015):

$$\mathrm{LLE}(i\Delta t) = \frac{1}{Ki\Delta t}\sum_{k=1}^{K}\lg\left|\frac{L_{(k+i)\Delta t} - L_{(k+i-1)\Delta t}}{L_{k\Delta t} - L_{(k-1)\Delta t}}\right| \tag{11}$$

3.3 Correlation analysis between the sBTTC index method and the MLE method

The MLE method is used to determine the convergence of the curves. During the angle instability of the system, since the wide-area measurement system cannot directly measure the generator angle, it is necessary to find a suitable reference machine in order to effectively analyse the generator angle change curve. Therefore, the MLE analysis using the key branch sBTTC index time series as an observation has the following advantages:

(1) The branch sBTTC index takes the wide-area branch response information as the signal source, which can be obtained directly by the synchronous phase measurement unit (PMU). Compared with the traditional method (using the rotor angle of the most advanced generator as the information source), the MLE analysis of branch sBTTC index has the advantage of easy access to the information source.
(2) The branch sBTTC index has the property of monotonically decreasing with deterioration of stability properties. However, it is not possible to determine whether the system has crossed the unstable equilibrium point. The MLE analysis of the sBTTC index curve and the joint judgement of stability with the sBTTC index can determine the stability level of the system more quickly.
(3) The MLE method must select one-dimensional time series observations for phase space reconstruction in the N-dimensional dynamic system. Based on the sBTTC method, the key branch can be accurately located, and the system can be analysed in terms of stability preservation and dimensionality reduction.
(4) The MLE method can only calculate the MLE sign at a specific moment to reflect the eigenvalue sign at infinite moments. The sBTTC method can determine the optimal observation time window for the MLE method. The time window can be adjusted adaptively and is suitable for a variety of fault situations.

4 Online identification of transient angle stability based on the key branch response information

4.1 Optimisation of MLE solution

4.1.1 Selection of the initial time window

The selection of the initial time window requires ensuring that the distance change between the original and neighboring trajectories exhibits clear dynamic characteristics. In Section 3.1.2, the sBTTC-d (sBTTC)/dt plane trajectories have obvious dynamic convergence or divergence characteristics at the beginning. Both d(sBTTC)/dt and lg$L$, as calculated by Eq. 8 and 9 respectively, closely relate to the disparity between two points along the trajectories. Therefore, the beginning stage of original and neighbouring trajectory calculation also has obvious dynamic characteristics. In this paper, the initial value of the initial time window is chosen as the initial moment of the MLE calculation.

To examine the impact of different initial time window lengths on the MLE-t curve, we conducted calculations for two scenarios: $M = 5$ and $M = 50$, focusing on the stability and destabilization cases of a two-machine system. The resulting MLE-t curves for the sBTTC indices of key branches B3-B4 are presented in Figures 7A, B.

Under the stability and instability calculations for the stand-alone system, in order to analyse the effect of the selection of the initial time window length on the MLE-t curves, the initial window length $M = 5$ as well as $M = 50$ is set for the calculation. Figure 7 demonstrates the MLE-t curves for the sBTTC index of the B3-B4 key branch.

From Figure 7, the MLE-t curve can be divided into four phases:

(i) Initial stage: marked by significant fluctuations occurring in a brief span of time.
(ii) Descending stage: wherein the MLE-t curve consistently declines.
(iii) Oscillating stage: characterized by a continuous, periodic oscillation pattern in the MLE-t curve.
(iv) Stable stage: where the MLE-t curve eventually converges towards a stable value.

In the stability and instability cases, both $M = 5$ and $M = 50$ have no effect on the final sign of the MLE-t curve. Regardless of the length of the initial time window, the MLE-t curve eventually tends to be negative in the instability case and positive in the stability case. In this paper, the initial time window length M is taken as shown in Eq. 12, which can be adapted to systems of different sizes.

$$M = 5\mathrm{int}(\lg n_{\mathrm{bus}}) \tag{12}$$

Where: n_{bus} denotes the number of system nodes, and int represents upward rounding.

4.1.2 Selection of optimal observation window

Maximum Lyapunov Exponent to discriminate the stability of the system needs to judge the final sign characteristics of the MLE. A time observation window of finite window length is usually predefined. The optimal time window depends on many factors and is difficult to determine. Theoretically, the length of the observation window tends to infinity to reflect the final MLE of the system. However, it is impossible to calculate the MLE at infinite moments due to the limitation of practical computational conditions.

If the optimal time observation window is too long, it may lead to the instability system crossing the unstable equilibrium point long time ago, and then the control action is implemented too late; if the optimal time observation window is too short, it may lead to the observation window not reflecting the final situation of the MLE-t curve, and then there is a misjudgment.

The sBTTC index can reflect the system stability level. Therefore, the initial moment of the optimal time window in this paper is set as the beginning moment of the initial decline phase of the sBTTC index, and the ending moment is the end moment of the initial decline phase of the sBTTC index. The dynamic observation time window set in this paper can be adapted to a variety of fault scenarios and can effectively discriminate the final sign of MLE.

It should be noted that, under the complex multivariable system, if the MLE sign is clear within the optimal time window, the observation of the MLE curve does not need to wait until the end of the optimal time window. On the contrary, if the MLE curve within the observation window has not entered the oscillation phase, the MLE sign cannot be determined. In this case, it is necessary to observe the value of the sBTTC index at the end of the dynamic observation window to make a determination.

4.1.3 Savitzky-Golay filtering of MLE

The aim is to reduce the effect of noise on the signal and improve the curve smoothness. This paper employs the Savitzky-Golay filtering signal processing technique to refine the calculation of the MLE.

Following the fault occurrence, the sBTTC index information of the key branch can be acquired through real-time PMU sampling. Utilizing Eq. 9, the logarithmic Euclidean variation distance of the sBTTC index generates a one-dimensional signal sequence of length N, denoted as lgL $\lg L = [\lg L_1, \lg L_2, \ldots. \mathrm{Lg}L_N]$. To apply the filter, a window of length $2d + 1$ is selected, resulting in the subsequence $\lg L\_\mathrm{w} = [\lg L_{\mathrm{n}-d}, \ldots \lg L_{\mathrm{n}}, \ldots \lg L_{\mathrm{n}+d}]$, where $\lg L_{\mathrm{n}}$ serves as the central data. The order of polynomial fitting is set as p, and the window's subsequence is represented by the fitting polynomial, as shown in Eq. 13:

$$\lg L\_w \approx \mathrm{a}_0 + a_1 X + a_2 X^2 + \ldots + a_p X^p \tag{13}$$

Where: X is the relative position within the window, i.e., $[-d, -d+1, \ldots d]$.

The objective function corresponds to the squared discrepancy between the subsequence fitting polynomial and the original signal subsequence, expressed as shown in Eq. 14.

$$\min = \sum \left[\lg L\_w - \left(\mathrm{a}_0 + a_1 X + \ldots + a_p X^p\right)\right]^2 \tag{14}$$

The fitting polynomial coefficients, denoted as $\mathrm{a}_0, \mathrm{a}_1, \ldots \mathrm{a}_p$, can be obtained by achieving an objective function min value of 0 as shown in Eq. 14. Utilizing a_0, the smoothed value of the central data can be estimated. Thereafter, employing a sliding window approach to each position of the signal, the entire signal sequence lg$L$ is comprehensively filtered. Subsequently, Eq. 11 is employed to calculate the MLE value of the sBTTC exponential trajectory.

4.2 Dynamic characterisation of MLE based on response trajectories

After the system is disturbed, the MLE curve of the sBTTC index of the key branch will show certain dynamic characteristics. This characteristic can reflect the system stability. Therefore, the MLE dynamic characteristics of this response trajectory are studied to discern the system stability in time.

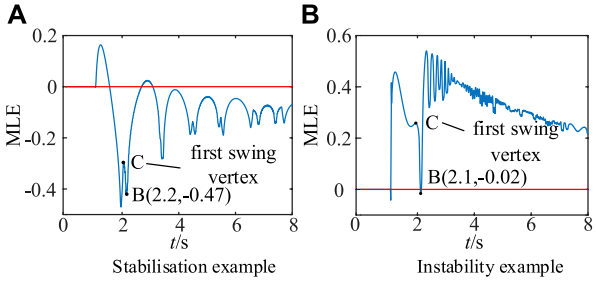

FIGURE 8
MLE-t curves of key branches in Double-machine.

In Section 2, the MLE-t curve of the response time series for the sBTTC index of the key branch B3-B4 is depicted in Figure 8, utilizing the stabilisation and instability examples of the two-machine system. The point B moment corresponds to the end moment of the initial descending phase of the sBTTC index, signifying the conclusion of the observation window.

As can be seen from Figures 8A, B, the MLE-t curves of the stabilisation and instability cases continue to decrease after an initial fluctuation phase, then oscillate and oscillate continuously, and finally equilibrate at a constant value. During the process from the beginning of the calculation to point B, the apex of the first swing of the MLE curve is less than zero in the stabilisation case, while the apex of the first swing of the MLE curve is greater than zero in the destabilisation case. Therefore, the stability of the system can be determined by observing the characteristics of the first swing vertex of the MLE-t curve.

4.3 Transient stability analysis of MLE metrics based on sBTTC exponential trajectories

The application architecture for the joint judgement of stability between the sBTTC method and the MLE method can be divided into three modules:

(1) Data preparation module: This module utilizes the wide-area measurement system to gather voltage and phase data from the nodes at both ends of the branch.
(2) Calculation module: In this module, the following steps are performed:

i) The sBTTC index of the observed branch is computed using Eq. 5, and the key branch is identified through Eq. 6 and 7. The response time series of the sBTTC index for the key branch, denoted as sBTTC = [sBTTC_1, sBTTC_2, ... , sBTTC_n], is obtained, where n represents the number of sampling points. The phase space dimension of the key branch response information is one, implying that the MLE is calculated for a single curve. ii) M initial data points are selected from the sBTTC sequence, satisfying the condition $\varepsilon_1 < \|L_{m\Delta t} - L_{(m-1)\Delta t}\| < \varepsilon_2$, where $m = 1, 2, \ldots M$, and ε_1 and ε_2 are non-zero minima. The Euclidean distance of the sBTTC index undergoes Savitzky-Golay filtering. iii) Eq. 11 is employed to calculate the MLE of

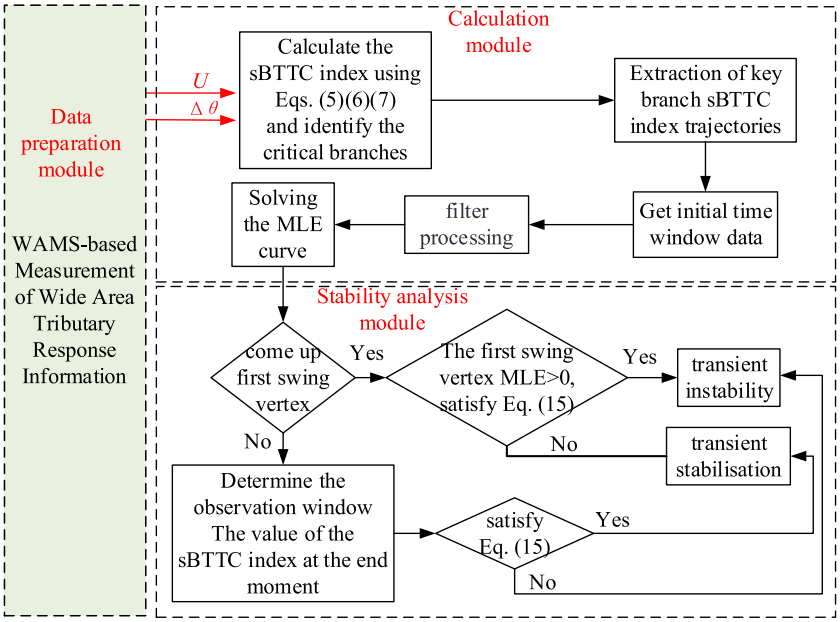

FIGURE 9
Flowchart of the framework.

the system at the moment $i\Delta t$, with the moment of fault occurrence serving as the initial point for MLE calculation.

(3) Stability analysis module: The system stability is discriminated according to the different characteristics presented by the MLE curve in the initial decline stage of the sBTTC index. Considering the timeliness of the system stability monitoring and the reduction of the false judgement rate, combined with the feature that the sBTTC index can reflect the deterioration of the system stability, the system stability level can be jointly discriminated by Eq. 15. Here, t_c denotes the moment corresponding to the first peak vertex of the MLE curve, and ε_{Lth} represents the threshold value set for the sBTTC index.

$$\mathrm{sBTTC}_{t_c \Delta t} < \varepsilon_{Lth} \tag{15}$$

The transient stability analysis framework based on the MLE index and sBTTC index trajectory is depicted in Figure 9.

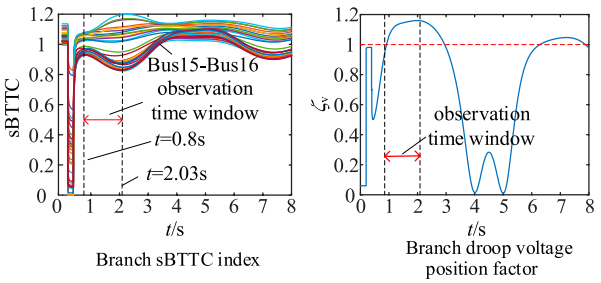

FIGURE 10
sBTTC index vs. dropout voltage position factor.

5 Simulation verification

5.1 Simulation verification of 10-machine 39-node system

The transient stability simulation calculation tool BPA is used to simulate the standard arithmetic case of a 10-machine, 39-node system. The disturbance response information is simulated as WAMS measurement data. The transient stability monitoring simulation calculation is carried out with a simulation step size of 0.01 s, for example,. sBTTC index threshold value ε_{Lth} is set to 0.8.

5.1.1 Stability example

A three-phase grounded short-circuit fault occurs on the front side of the bus16-bus17 branch at 0.2 s. The fault removal moment is set to 0.4 s. The system is transiently stable. The sBTTC index of the wide-area branch circuit based on WAMS measurement is shown in Figure 10.

In Figure 10A, it is evident that the sBTTC index experiences the initial decline phase from t = 0.8 s to t = 2.03 s, which represents the MLE observation time window. Within this window, the bus15-bus16 branch exhibits the lowest sBTTC index value. The droop voltage position coefficient of this branch is illustrated in Figure 10B, and it satisfies the conditions stated in Eq. 7, confirming its key ity.

Next, the MLE curve of the sBTTC index trajectory for the bus15-bus16 branch is determined and depicted in Figure 11. At 1.33 s, the MLE curve exhibits its first swing vertex with a negative sign, while the value of the sBTTC index at that moment is 0.88, which is greater than the threshold value of 0.8 set previously. Based on these observations, we can conclude that the system is in a state of transient stability.

5.1.2 Example of destabilisation

At 0.2 s, a three-phase grounded short-circuit fault emerges on the front side of the bus16-bus17 branch, with the fault removal

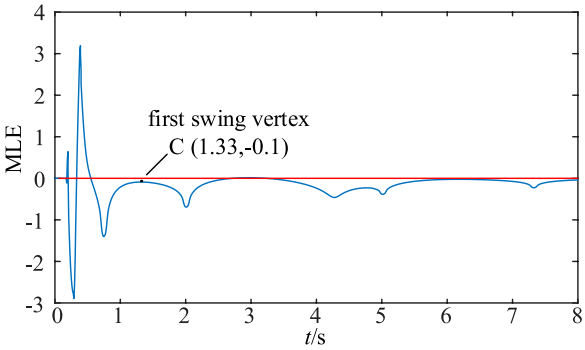

FIGURE 11
MLE-*t* curve under the destabilisation case.

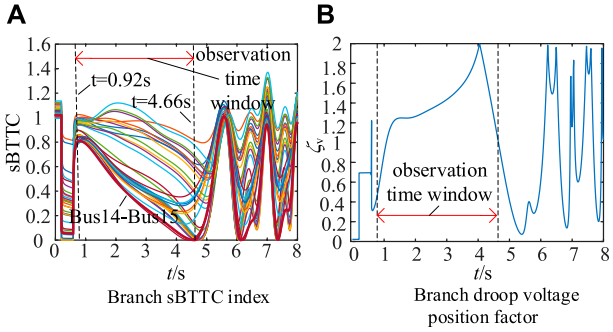

FIGURE 13
sBTTC index vs. dropout voltage position factor.

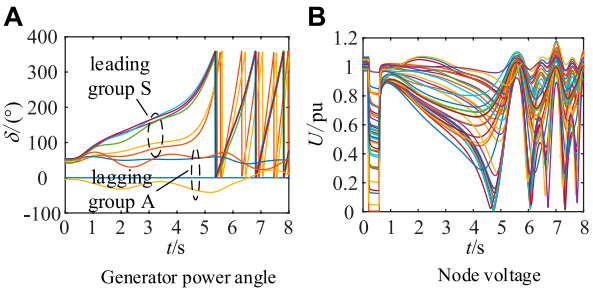

FIGURE 12
Transient response curve of 39-node system.

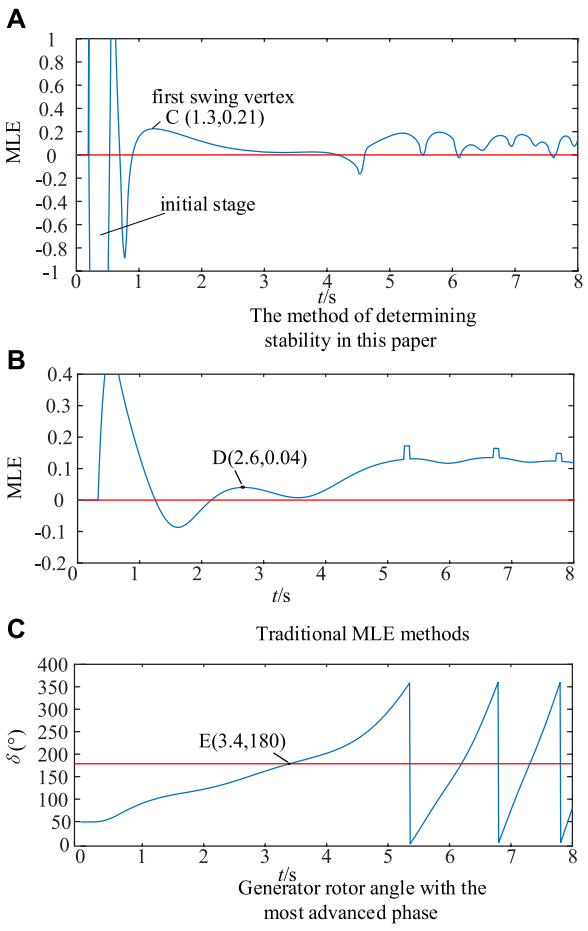

FIGURE 14
MLE-*t* curve under the destabilisation case.

scheduled for 0.6 s. Consequently, the system experiences a single-swing destabilisation. In Figure 12, we observe the response curves of the generator angle and the entire network node voltage for the node system, with G30 serving as the reference machine.

Figures 12A, B clearly indicates that the generator angle loses synchronisation after the fault, leading to a significant decline in node voltage, followed by continuous periodic oscillations. The system units divide into two groups: the leading group S, comprising 6 generators, and the lagging group A, comprising the remaining 4 generators, represented as S = {G31, G32, G33, G34, G35, G36} and A = {G30, G37, G38, G39}, respectively.

Upon calculating the sBTTC indices of the branches based on the disturbed response information and identifying the key branches, we assess whether their branch droop voltage location coefficients fall within the interval [1, 2], as depicted in Figure 13.

From Figure 13A, we can observe that within the time frame of 0.92 s–4.66 s, the branch sBTTC index consistently decreases to a value of zero. Throughout this process, the Bus14-Bus15 branch maintains the minimum sBTTC index value, and the branch footing voltage is situated atop this branch, confirming it as the key branch of the system.

Subsequently, we obtain the sBTTC index traces of the key branch and compute the MLE curve, as shown in Figure 14. Also, the MLE calculation curves for the traditional method of obtaining the most overrun unit G35 are given in Figure 14 (Dasgupta et al., 2015).

In Figure 14A, the system stability is discriminated using the method proposed in this paper. The initial phase of the MLE-t curve is not given due to the large fluctuation, and the oscillation phase has long entered in the observation window. The first swing vertex of the MLE curve can be detected quickly at point C, and the value of the first swing vertex is 0.21. The value of the sBTTC index at this moment is 0.71, which is smaller than the set threshold value of 0.8. Therefore, this paper determines that the system is unstable for 1.3 s, and the maximum relative angle difference of the generator at this time is 1.91 rad.

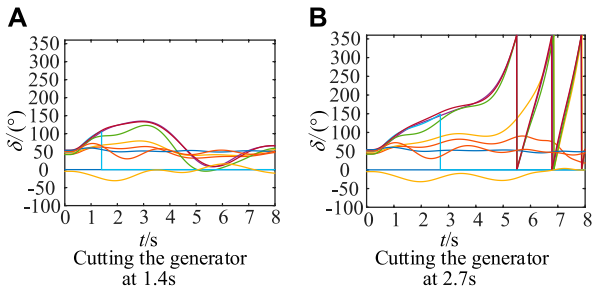

FIGURE 15
Transient response curve after emergency control measures.

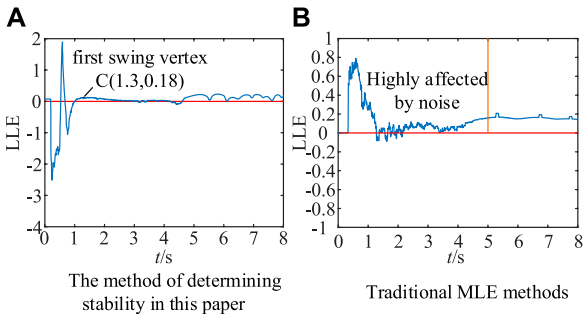

FIGURE 16
Result after adding Gaussian noise.

In Figure 14B, the traditional method is used to calculate the MLE and determine the stability of the system. If the observation window is set to 3 s, the MLE sign can be determined to be positive at 2.6 s, and then the system is judged to be unstable. If the observation window is set too short, such as 2 s, the system will be misjudged as stable.

In Figure 14C, the time required to discriminate the system stability using the traditional stability engineering criterion (generator rotor angle over 180) is 3.4 s.

In summary, the time required to judge the stability for MLE analysis based on the SBTTC exponential curve is 1.3 s, the time required to judge the stability for MLE analysis based on the generator rotor angle curve is 2.6 s, and the time required to judge the stability of the system based on the traditional engineering stability criterion is 3.4 s. Therefore, the method proposed in this paper is characterised by its rapidity in determining the stability of the system.

Considering 0.1 s communication delay, emergency control measures are implemented at 1.4 s and 2.7 s respectively. Cutting out the most overrun unit G35, the system generator angle curve is obtained as shown in Figures 15A, B. After the implementation of emergency control measures at 1.4 s, the generator group can maintain synchronous operation. After the implementation of emergency control measures in 2.7 s, the generator group loses synchronous stability and is unable to maintain system stability.

5.1.3 Noise test

The method proposed in this study incorporates the Savitzky-Golay filtering processing technique for MLE calculation, endowing it with a considerable degree of noise immunity. Typically, the signal noise ratio (SNR) of PMU measurements surpasses 100, ensuring that the measurement error remains below 1 percent (Dasgupta and Paramasivam, 2013). A Gaussian noise with a SNR of 60 dB is added to the above instability example to simulate the actual PMU measurement noise. The results of the MLE curves for both algorithms are shown in Figure 16.

From Figure 16A, in the method proposed in this paper, the addition of noise does not have a delayed effect on the time point corresponding to when the MLE curve reaches the apex of the first swingback in the discriminant. There is no effect on the time required for the stability discrimination.

From Figure 16B, in the traditional MLE method, the MLE curve is affected by noise with a larger magnitude in the first 5 s, when it is not appropriate to discriminate the MLE sign. Until the 5 s curve is slightly smooth, then the MLE symbols can be discriminated, but the discriminatory timeliness is poor.

From this, the method proposed in this paper has strong anti-noise ability.

5.1.4 Reliability validation

To further validate the reliability of the proposed method, a traversing fault test is performed at the 39-node system. So that all lines excluding the generator node have a three-phase short-circuit fault (N−1) at the moment of 0.2 s. The double return line defaults to disconnect the first return line. The fault removal moments are traversed sequentially from 0.2 to 3 s in steps of 0.2 s. Total 480 groups of faults.

In each set of tests, the key branch was quickly identified after fault removal using the method proposed in Section 4.3. The MLE curve of the sBTTC index of the key branch is analyzed to determine the system stability. Comparison is made with two judgments. These two criteria are the criterion based on the stability characteristic quantity (generator angle greater than 180°) and the criterion based on the traditional MLE calculation method. To increase the conservatism, the time window based on the traditional MLE calculation method is chosen as the end moment of the simulation. The third of these methods uses the batBPA batch program, and the first and second methods are implemented by building a Python interface to BPA. The statistical results are shown in the following table.

From Table 1, the method of this paper can successfully identify 404 sets of destabilizing samples through the traversal failure test. If based on the amount of stabilization features, the recognition rate of the destabilization samples of this paper's criterion is 100%. The stabilization misjudgment rate is 2.6%. And in the test results, the average time required to judge the system stability is within 1.4 s after failure. The first method in the above table is obviously better than the second.

5.2 AC/DC hybrid system simulation verification

In a specific reference year, the local structure of the transmission grid in the eastern region of Inner Mongolia is

TABLE 1 Comparison table.

	Based on the methods proposed in this paper	Based on the traditional MLE methods	Based on a stable characteristic
Number of instability samples identified	404	409	402
Mean value of required discrimination time	1.4s	3.1s	3.8s
Identification rate of destabilized samples	100%	100%	—
Misidentification rate of stabilized samples	2.6%	8.9%	—

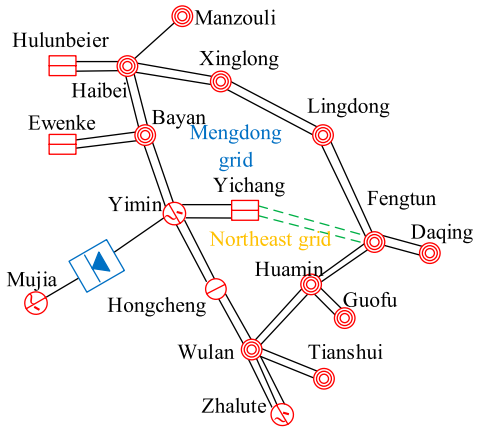

FIGURE 17
DC hybrid grid.

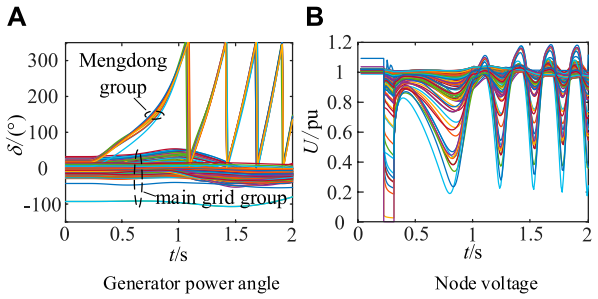

FIGURE 18
Transient response curve of DC hybrid system.

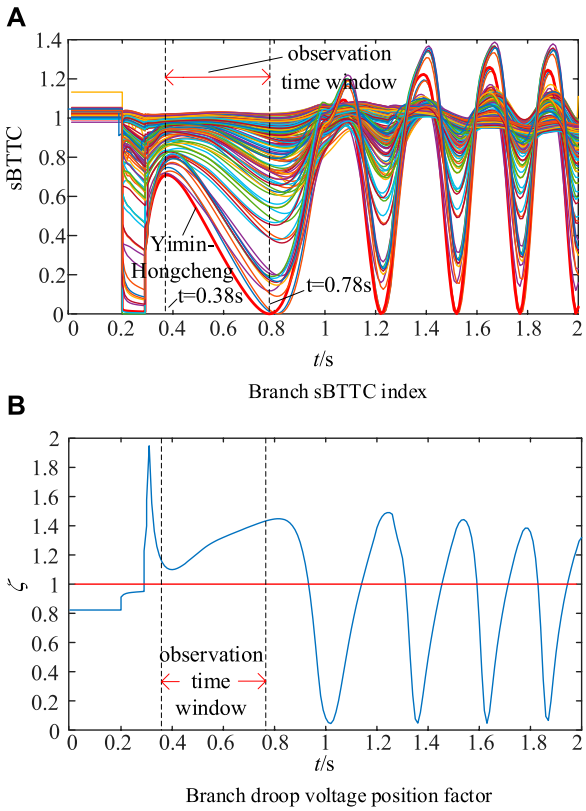

FIGURE 19
sBTTC index vs. dropout voltage position factor.

illustrated in Figure 17. The eastern Mengdong grid is interconnected with the Northeast grid through three 500 KV AC branch circuits: Xinglong-Lingdong, Yifang-Fengtun, and Yimin-Hongcheng. Additionally, the eastern Mengdong grid features a ±500 KV/3000 MW UHVDC connection in Yimin-Mujia, forming a mixed pattern of AC and DC with the AC branch circuits.

During a particular operational scenario, the Yimin-Mujia UHVDC transmits 2000 MW, while the Xinglong-Lingdong, Yifang-Fengtun, and Yimin-Hongcheng three 500 KV AC branch circuits transmit 3520 MW. The Yifang-Fengtun line plays a crucial role in the structure of the Northeastern local grid. Unfortunately, it experiences a three-phase permanent short-circuited double circuit fault at 0.2 s, leading to the isolation of the faulty line and parallel line disturbances at 0.3 s. Generator angle curve and node voltage curve as shown in Figures 18A, B can be seen, by the short-circuit impact fault, electrical connection weakening, the tide of a wide range of transfer and other factors, the angle of the Mengdong group of machines relative to the main grid group of machines out of synchronisation, the node voltage of the system to occur a large drop and show the characteristics of the cyclic oscillations, the system occurred in the transient angle destabilisation.

Concomitant with the aforementioned destabilisation process, the response curve of the sBTTC index for the 500 KV AC lines

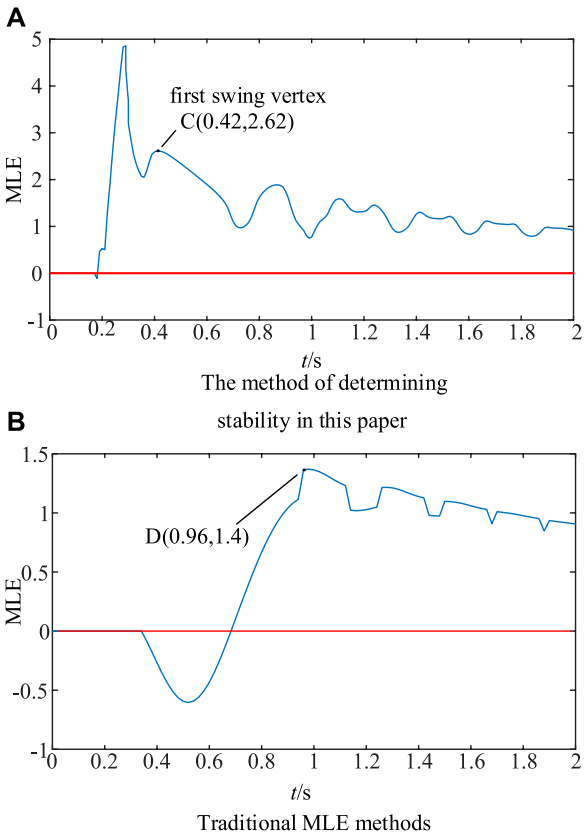

FIGURE 20
MLE-t curve under the destabilisation case.

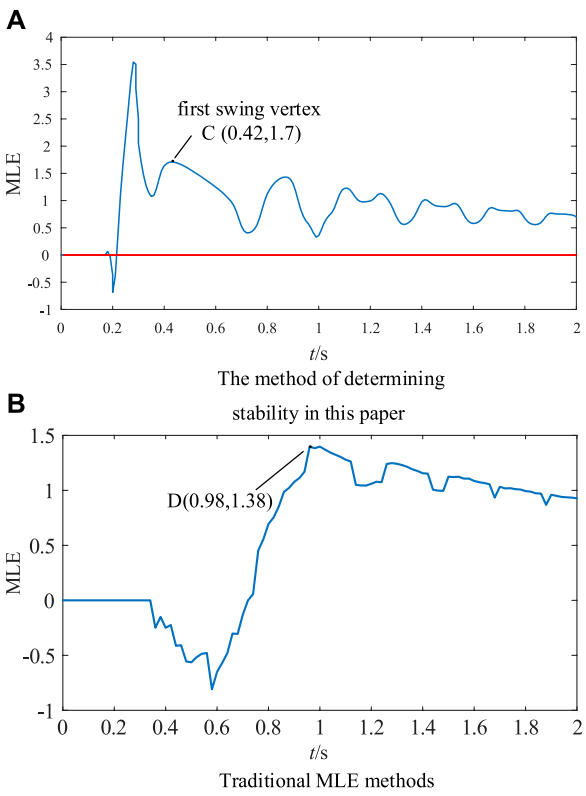

FIGURE 21
Result after adding Gaussian noise.

throughout the network is depicted in Figure 19A. Notably, the Yimin-Hongcheng branch consistently displays the smallest sBTTC index during the initial decline stage of the sBTTC index. Furthermore, the branch droop voltage coefficient $\xi_v \in [1,2]$, as illustrated in Figure 19B, reaffirms the key nature of the Yimin-Hongcheng branch within the network.

The MLE-t curve of sBTTC index of Emin-Hongcheng branch is shown in Figure 20A. Meanwhile, the MLE-t curve of the angle trajectory of the generator Ewenk, for example, is solved using the traditional method for the overrun unit Ewenk as shown in Figure 20B.

From Figure 20A, at 0.42 s, the first pendulum fixed point value of MLE curve is 2.62, which is positive, and at this time, the sBTTC index is 0.67. To judge the instability of Mengdong grid, the maximum relative angle difference of the generator at this time is 1.48 rad.

From Figure 20B, under the premise of setting the observation time window appropriately, the MLE sign can be determined to be positive only at 0.96 s. It is only at this moment that the traditional MLE calculation method can determine the instability of the Mengdong power grid. Compared with the method in this paper, the timeliness of the determined 0.96 s is poor. Moreover, if the observation time window is not set properly, it is easy to misjudge that the system is stable at 0.5 s. Therefore, the proposed method is better than the one in this paper. Therefore, the method proposed in this paper has more advantages than the traditional MLE solving method.

Similarly, considering the communication delay, the implementation of emergency control measures at 0.5 s and the removal of the Ewenke unit can restore the stability of the system. At 1.0 s, resection of Ewenke unit cannot make the system restore stability.

In order to verify the effectiveness of this paper's method in a large system, the Gaussian noise interference with SNR of 60 dB is added to the above example, and the results of the MLE curve calculated by the proposed method are shown in Figure 21A, and the results of the MLE curve calculated by the traditional method are shown in Figure 21B.

From Figure 21A, it can be seen that after adding 60 dB noise to the sampled data, the time point corresponding to the first pendulum vertex of the MLE curve obtained by the method in this paper is unchanged, and the judgement of the stability time before and after the addition of noise is 0.42 s, the judgement of the stability time is unchanged, and the curve is still smooth.

As can be seen from Figure 21B, after adding 60 dB noise to the sampled data, the judgement of stability time of the traditional method is 0.98 s, and the difference between before and after is not significant. However, the MLE curve fluctuates significantly after the addition of noise before the time node, which is not conducive to the identification of the MLE symbols, and it is very easy to lead to the occurrence of misjudgment.

The method proposed in this paper has strong noise immunity in large systems as well. And the example of Mengdong Power Grid shows that the method has better applicability in large-scale power systems. It can judge the system stability level in time and is not easily affected by noise.

6 Conclusion

After a system generator is destabilized, certain combinations of electrical quantities in the branches of the network contain information characterizing the system stability. In this paper, MLE analysis is carried out for the key branch response information, and the main conclusions of the study are as follows.

(1) Under both system stability and instability patterns, the sBTTC index trajectories in the critical branches show two typically different characteristics. The system transient stability problem can be transformed into a problem of MLE analysis of sBTTC index time series data.
(2) In this paper, the MLE stability discrimination principle is utilised to analyse the dynamic characteristics of the sBTTC exponential response trajectory. Combining the sBTTC method with the MLE method, the MLE transient stability analysis method based on the key branch response is proposed. Compared with the traditional method, the method has the following advantages: easy access to information sources, rapid discriminative stability, strong noise resistance, and strong engineering application value.
(3) On the one hand, the proposed method determines the optimal dynamic observation time window through the variation of the sBTTC index trajectories of the key branches. On the other hand, the stability discrimination is realised through the dynamic characteristics of MLE curves. The method still achieves transient power angle steady state assessment quickly and accurately under large-scale systems, and overcomes the difficulty of finding the optimal time window for MLE stability monitoring methods.

Data availability statement

The original contributions presented in the study are included in the article/Supplementary Material, further inquiries can be directed to the corresponding author.

Author contributions

ZN: Writing–original draft. CZ: Writing–review and editing. SL: Writing–original draft. YS: Writing–review and editing. FN: Validation, Writing–review and editing.

Funding

The author(s) declare financial support was received for the research, authorship, and/or publication of this article. This work is supported by National Key Research and Development Program projects “Response-driven intelligent enhancement analysis and control of large grid stability Technology” (2021YFB2400800).

Conflict of interest

Authors ZN and CZ were employed by China Electric Power Research Institute Co., Ltd.

Publisher’s note

All claims expressed in this article are solely those of the authors and do not necessarily represent those of their affiliated organizations, or those of the publisher, the editors and the reviewers. Any product that may be evaluated in this article, or claim that may be made by its manufacturer, is not guaranteed or endorsed by the publisher.

References

Andersson, G., Donalek, P., Farmer, R., Hatziargyriou, N., Kamwa, I., Kundur, P., et al. (2005). Causes of the 2003 major grid blackouts in North America and Europe, and recommended means to improve system dynamic performance. *IEEE Trans. Power Syst.* 20 (4), 1922–1928. doi:10.1109/TPWRS.2005.857942

Chen, G., Li, M., Xu, T., Zhang, J. Y., and Wang, C. (2017). Practice and challenge of renewable energy development based on interconnected power grids[j]. *Power Syst. Technol.* 41 (10), 3095–3103. doi:10.7500/AEPS2017120004

Dasgupta, S., Paramasivam, M., Vaidya, U., and Ajara, V. (2015). PMU-based model-free approach for real-time rotor angle monitoring. *IEEE Trans. Power Syst.* 30 (5), 2818–2819. doi:10.1109/TPWRS.2014.2357212

Dasgupta, S., Paramasivam, M., Vaidya, U., and Ajjarapu, V. (2013). Real-time monitoring of short-term voltage stability using PMU data. *IEEE Trans. Power Syst.* 28 (4), 3702–3711. doi:10.1109/tpwrs.2013.2258946

Dasgupta, S., Paramasivam, M., Vaidya, U., and Ajjarapu, V. (2013). Real-time monitoring of short-term voltage stability using PMU data. *IEEE Trans. Power Syst.* 28 (4), 3702–3711. doi:10.1109/TPWRS.2013.2258946

Gou, J., Liu, J., Taylor, G., et al. (2015a). Fast assessment of power system transient stability based on generator pair transient potential energy sets. *Grid Technol.* 39 (02), 464–471. doi:10.13335/j.1000-3673.pst.2015.02.026

Gou, J., Liu, J. Y., Taylor, G., et al. (2015b). Rapid assessment of power system transient stability based on generator pair transient potential energy sets. *Grid Technol.* 39 (02), 464–471. doi:10.13335/j.1000-3673

Huang, D., Sun, H., Zhou, Q., Zhang, J., Jiang, Y. L., and Zhang, Y. C. (2020). Online monitoring of transient stability based on the dynamic characteristics of maximum Lyapunov exponent of response trajectory. *Power Autom. Equip.* 40 (4), 48–55. doi:10.16081/j.epae.202004002

Kundur, P., et al. (2004). Definition and classification of power system stability IEEE/CIGRE joint task force on stability terms and definitions. *IEEE Trans. Power Syst.* 19 (3), 1387–1401. doi:10.1109/TPWRS.2004.825981

Lin, Li, Wu, C. C., and Qi, J. (2016). Analysis of emergency cutover strategies under severe faults in large-scale wind-fire hybrid feeder systems. *Power Grid Technol.* 40 (3), 882–888. doi:10.13335/j.1000-3673.pst.2016.03.032

Liu, C. W., Thorp, J. S., Lu, J., Thomas, R., and Chiang, H-D. (1994). Detection of transiently chaotic swings in power systems using real-time phasor measurements. *IEEE Trans. Power Syst.* 9 (3), 1285–1292. doi:10.1109/59.336138

Liu, D. W., et al. (2013). Response-based online quantitative assessment method for transient stabilisation potential of power grids. *Chin. J. Electr. Eng.* 33 (4), 85–95+12. doi:10.13334/j.0258-8013.pcsee.2013.04.014

Liu, R., Chen, L., Min, Y., et al. (2018). A linear approximation method for the boundary of dynamic security domain of wind-fire bundled delivery system. *Grid Technol.* 42 (10), 3211–3218. doi:10.13335/j.1000-3673

Liu, T., Tang, Z., Huang, Y., Xu, L., and Yang, Y. (2023). Online prediction and control of post-fault transient stability based on PMU measurements and multi-task learning. *Front. Energy Res.* 10, 1084295. doi:10.3389/fenrg.2022.1084295

Mu, G., Wang, Z., Han, Y., et al. (1993). Quantitative analysis of transient stability-trajectory analysis method. *Chin. J. Electr. Eng.* (03), 25–32. doi:10.13334/j.0258-8013

Paudyal, S., Ramakrishna, G., and Sachdev, M. S. (2010). Application of equal area criterion conditions in the time domain for out-of-step protection. *IEEE Power Transm. Lett.* 25 (2), 600–609. doi:10.1109/tpwrd.2009.2032326

Qin, X., Bi, T., Yang, Q., et al. (2008). Power system transient stability assessment based on WAMS dynamic trajectories. *Automation Electr. Power Syst.* 32 (23), 18–22.

Ravikumar, G., and Khaparde, S. A. (2018). Taxonomy of PMU data based catastrophic indicators for power system stability assessment. *IEEE Syst. J.* 12 (1), 452–464. doi:10.1109/JSYST.2016.2548419

Shaopan, W., Yang, M., Han, X., et al. (2017). An online identification method of transient angle stability using the MLE index of machine terminal voltage amplitude trajectory. *Chin. J. Electr. Eng.* 37 (13), 3775–3786. doi:10.13334/j.0258-8013.pcsee.162476

Sun, H., Tang, Y., and Ma, S. (2006). A commentary on definition and classification of power system stability. *Power Syst. Technol.* 30 (17), 31–35. doi:10.13335/j.1000-3673.pst.2006.17.006

Tang, C. (2014). Response-based wide-area security and stability control of power systems. *Chin. J. Electr. Eng.* 34 (29), 5041–5050. doi:10.13334/j.0258-8013.pcsee.2014.29.005

Tian, X., Zhao, L., Tong, C., Meng, X., Bo, Q., Chen, Y., et al. (2023). Optimal configuration of grid-side energy storage considering static security of power system. *Front. Energy Res.* 1. doi:10.3389/frsgr.2022.1110871

Wadduwage, D. P., Wu, C. Q., and Anakie, U. D. (2013). Power system transient stability analysis via the concept of Lyapunov Exponents. *Electr. Power Syst. Res.* 104, 183–192. doi:10.1016/j.epsr.2013.06.011

Wang, M., Wu, J., et al. (1991). *Large power grid system technology*. Beijing, China: Water Conservancy and Electric Power Press, 140.

Xie, H., Zhang, B., Yu Guang, L., et al. (2006). Identification of power system transient stability based on phase trajectory concavity. *Chin. J. Electr. Eng.* 2006 (05), 38–42. doi:10.13334/j.0258-8013.pcsee.2006.05.007

Xue, F., and Xue, Y. (1999). Stability-preserving reduced dimensional mapping of multi-rigid body disturbed trajectories. *Power Syst. Autom.* 24, 11–15.

Xue, Y., Van Custom, T., and Ribbens-Pavella, M. (1989). Extended equal area criterion justifications, generalizations, applications. *IEEE Trans. Power Syst.* 4 (1), 44–52. doi:10.1109/59.32456

Yan, J., Liu, C.-C., and Vaidya, U. (2011). PMU-based monitoring of rotor angle dynamics. *IEEE Trans. Power Syst.* 26 (4), 2125–2133. doi:10.1109/TPWRS.2011.2111465

Zeng, Y., Chang, J., Qin, C., et al. (2018). A practical dynamic safety domain construction method based on phase trajectory analysis. *Chin. J. Electr. Eng.* 38 (07), 1905–1912. doi:10.13334/j.0258-8013

Zheng, C., Sun, H., and Deng, J. (2022). Active detrainment control of angle instability based on wide-area branch response. *Chin. J. Electr. Eng.* 42 (11), 3885–3896. doi:10.13334/j.0258-8013.pcsee.211592

Zheng, C., Sun, H., and Li, H. (2021a). Response-based transient transmission capacity index and emergency control of branch circuits. *Chin. J. Electr. Eng.* 41 (02), 581–592. doi:10.13334/j.0258-8013.pcsee.200969

Zheng, C., Sun, H., Zhang, A., et al. (2021b). Angle and voltage dominant stability mode discrimination and emergency control based on wide-area branch response. *Chin. J. Electr. Eng.* 41 (18), 6148–6160. doi:10.13334/j.0258-8013.pcsee.202469

frontiers | Frontiers in Energy Research

TYPE Original Research
PUBLISHED 24 January 2024
DOI 10.3389/fenrg.2024.1343520

OPEN ACCESS

EDITED BY
Youbo Liu,
Sichuan University, China

REVIEWED BY
Xiaokang Liu,
Polytechnic University of Milan, Italy
Andrea Toscani,
University of Parma, Italy

*CORRESPONDENCE
Jinwei He,
jinwei.he@tju.edu.cn

RECEIVED 23 November 2023
ACCEPTED 05 January 2024
PUBLISHED 24 January 2024

CITATION
Feng D, Chen T, Zhang L, Meng W and He J (2024), A control method for the single-phase three-leg unified power quality conditioner without a phase-locked loop.
Front. Energy Res. 12:1343520.
doi: 10.3389/fenrg.2024.1343520

A control method for the single-phase three-leg unified power quality conditioner without a phase-locked loop

Depin Feng[1], Tao Chen[1], Liang Zhang[2], Weiqi Meng[3] and Jinwei He[3]*

[1]Linyi Power Supply Company of State Grid Shandong Electric Power Company, Linyi, China, [2]Yinan Power Supply Company of State Grid Shandong Electric Power Company, Linyi, China, [3]School of Electrical and Information Engineering, Tianjin University, Tianjin, China

The single-phase three-leg unified power quality conditioner (UPQC) can achieve the functions of voltage compensation, reactive power compensation, and harmonic compensation. However, traditional control algorithms require a phase-locked loop to obtain the real-time phase angle of the grid voltage, which undoubtedly increases algorithm complexity. To simplify the phase-locked calculation, this paper proposes a control method without the phase-locked loop for the single-phase three-leg UPQC. In the proposed scheme, the instantaneous value of the grid voltage is employed to realize the grid integration control. Then, the load voltage reference is calculated in real time using a second-order generalized integrator. Moreover, a simple algorithm for reactive power and harmonic compensation is discussed, further simplifying the control algorithm. Finally, a small-scale experimental platform is built, and the effectiveness of the proposed method is verified by the experimental results.

KEYWORDS

unified power quality conditioner, phase-locked loop, voltage fluctuation, harmonic control, power quality

1 Introduction

With the popularization of large-scale distributed renewable energy generation and the addition of disruptive and non-linear loads, the power quality of the grid side in distribution networks is facing severe challenges (Sun et al., 2013; He et al., 2015; Zhang et al., 2022a). Voltage fluctuations and harmonic problems, as the typical representatives of power quality issues, not only affect the safe and stable electricity consumption of power users but also add significant costs to power transmission and distribution (Moeini et al., 2018; He et al., 2020; Wang and Yang, 2023).

As a series-parallel hybrid power quality compensation device, the unified power quality conditioner (UPQC) is widely utilized to improve the power quality of the grid side. This equipment can address current-related power quality issues in distribution systems through its parallel compensation terminal (Lakshmi and Ganguly, 2019; Silva et al., 2020). Moreover, the voltage-related power quality issues can also be addressed through its series compensation terminal. Compared to the traditional isolated single-phase four-leg topology, the single-phase three-leg UPQC topology can eliminate the isolation transformer and reduce the number of legs for a low cost. Importantly, the lack of components does not compromise the effectiveness of power quality control. Therefore, this topology has gained widespread attention in recent years (Lu et al., 2016; Abdalaal and Ho, 2021).

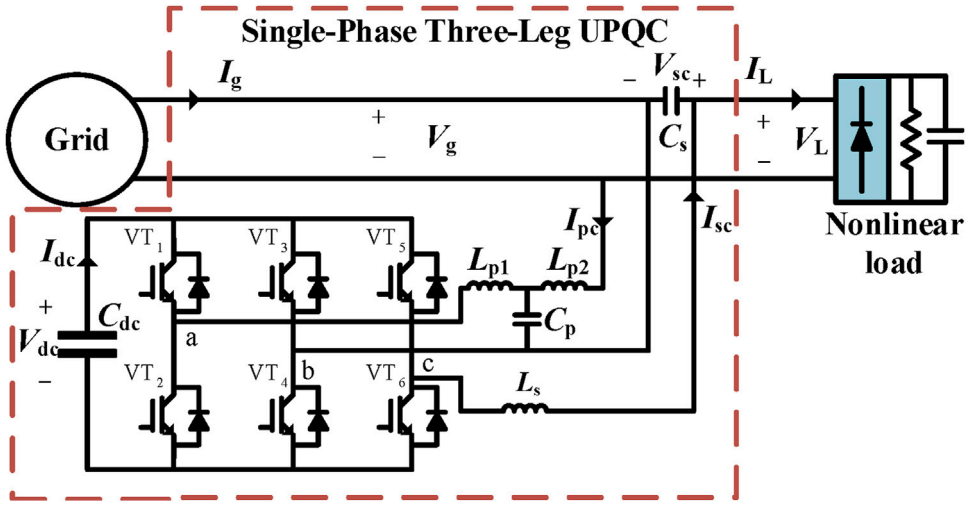

FIGURE 1
Diagram of the single-phase three-leg UPQC topology.

In traditional control methods of the UPQC, the real-time phase angle of the grid voltage needs to be obtained through a phase-locked loop (PLL). First, the parallel compensation terminal requires the real-time phase angle of the grid voltage for grid integration (Cheng and Lee, 2006; He et al., 2019). Second, the series compensation terminal needs the real-time phase angle of the grid voltage to obtain an accurate compensation voltage reference (Srinivas et al., 2019). Moreover, the extraction of reactive current and harmonic current from the system also relies on the real-time phase angle of the grid voltage (Zhang et al., 2022b; Xia et al., 2022). However, the PLL not only increases the complexity of the control algorithm but also fails to respond promptly to phase variations in the grid voltage, leading to overcurrent issues in the compensation device (Mishra and Lal, 2022; Mohammed et al., 2023).

To overcome these previously discussed disadvantages, a control method without the PLL is proposed for the single-phase three-leg UPQC in this paper. Different from the traditional method, the proposed method utilizes the instantaneous value of the grid voltage for grid integration. Then, the real-time amplitude of the grid voltage is obtained through a second-order generalized integrator and the compensation voltage reference is calculated. Additionally, the proposed method uses the load current as a reference for the parallel inverter output, eliminating the need for the extraction of reactive current and harmonic currents. Then, the compensation of the reactive and harmonic power can be realized. The subsequent sections of this article analyze the proposed control method in the frequency domain using a coordinated control system. In addition, the feasibility and effectiveness of the proposed method through experiments is validated through the experimental results.

2 The proposed control method for the single-phase three-leg UPQC

2.1 The topology structure of the single-phase three-leg UPQC

This paper begins by providing a brief introduction to the topology of the single-phase three-leg UPQC. As shown in Figure 1, the parallel compensation port consists of leg a, leg b, and parallel interface filters (L_{p1}, L_{p2}, and C_p), while the series compensation port consists of leg b, leg c, and series interface filters (L_s and C_s). When the grid voltage V_g is not equal to the rated voltage V_N, the series compensation voltage V_{sc} will be provided through the series compensation port. As a result, the load voltage V_L can reach its rated value. Additionally, the series compensation port can compensate for the harmonic components of the grid voltage. The device also compensates for the harmonic currents generated by non-linear loads by providing the parallel compensation current I_{pc} through the parallel compensation terminal. Then, the grid current I_g can be sinusoidal. In addition, the reactive power component of the load current can be compensated through this single-phase three-leg UPQC. The two converters share a DC bus capacitor C_{dc}, and the DC bus voltage V_{dc} is controlled using a parallel compensator.

2.2 Parallel compensation control method

There are three control objectives for the parallel compensation terminal, including stabilizing the DC bus voltage, compensating for the load reactive current, and compensating for the load harmonic current. Therefore, the control strategy needs to be individually formulated around these three control objectives.

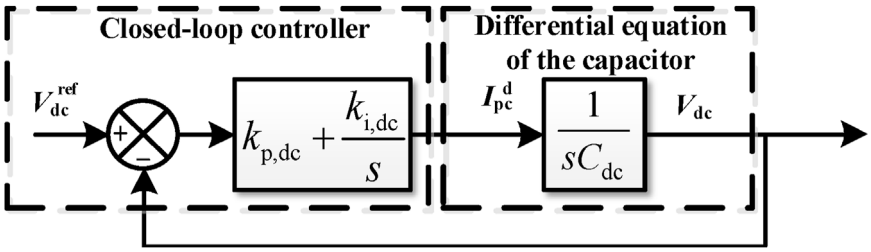

FIGURE 2
Control block diagram of the DC bus voltage system.

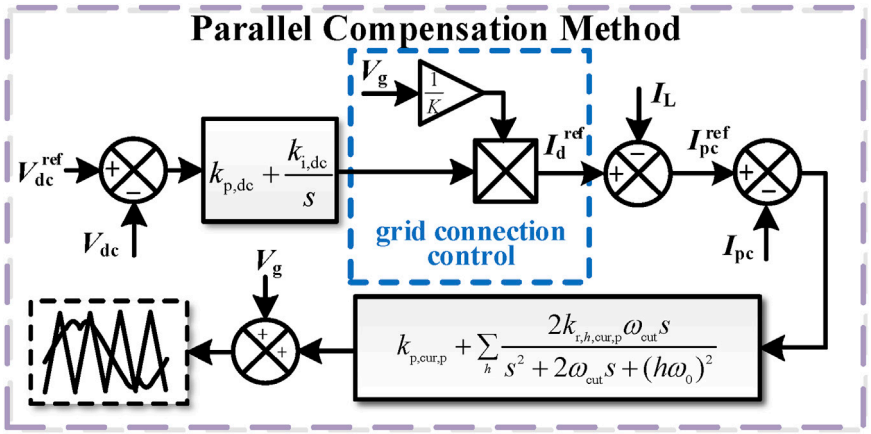

FIGURE 3
The proposed parallel compensation control strategy.

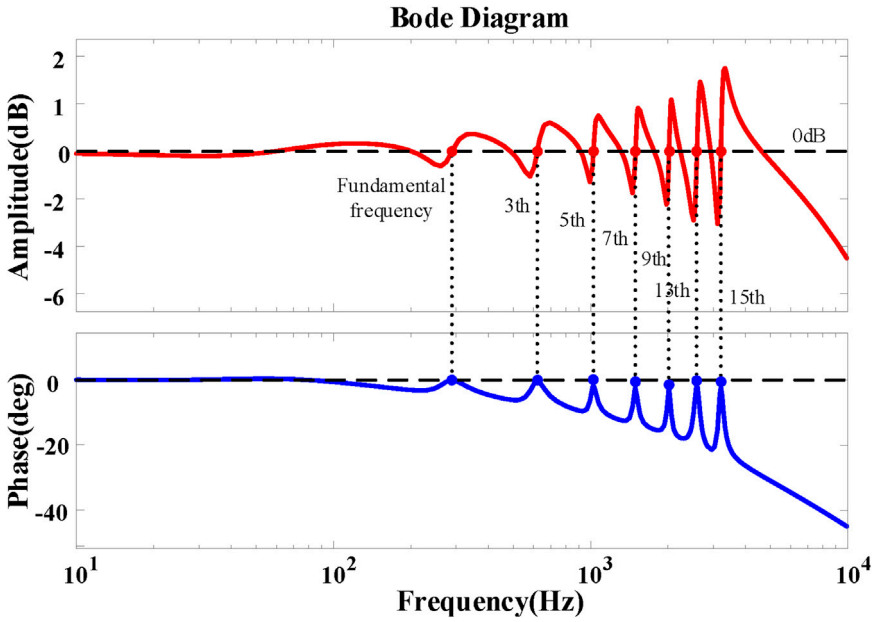

FIGURE 4
Closed-loop Bode plot of the parallel controller.

TABLE 1 Table of the relevant parameters for plotting the Bode plot of the control system.

Parameter symbol	Parameter name	Value (unit)
Parallel filter inductor 1	L_{p1}	0.4 mH
Parallel filter inductor 2	L_{p2}	0.05 mH
Parallel filter capacitor	C_p	60 μF
Series filter inductor	L_s	0.4 mH
Series filter capacitor	C_s	40 μF
DC bus capacitor	V_{dc}	650 V
PWM modulation gain	K_{PWM}	1

For the control of the DC bus voltage, first, the differential equation of the DC bus capacitor is derived as follows:

$$\boldsymbol{I}_{dc} = \boldsymbol{C}_{dc}\frac{d\boldsymbol{V}_{dc}}{\boldsymbol{dt}}, \tag{1}$$

where I_{dc} represents the current flowing into the DC bus. Therefore, the expression of the DC bus voltage can be obtained from Eq. (1)

$$\boldsymbol{V}_{dc} = \frac{\boldsymbol{1}}{\boldsymbol{sC}_{dc}}\boldsymbol{I}_{dc}. \tag{2}$$

According to Kirchhoff's current law, it can be known that $I_{dc} = I_{pc}$. However, the reactive component of I_{pc} only causes a ripple voltage at twice the frequency on the DC bus, while its active component $I_{pc,d}$ plays a role in stabilizing the DC bus voltage. By designing a controller based on Eq. (2), the stability of the DC bus capacitor voltage can be achieved by controlling the active component $I_{pc,d}$ of the parallel compensating current. The control strategy for $I_{pc,d}$ is as follows:

$$\boldsymbol{I}_{pc,d} = \left(\boldsymbol{k}_{p,dc} + \frac{\boldsymbol{k}_{i,dc}}{\boldsymbol{s}}\right)\left(\boldsymbol{V}_{dc}^{ref} - \boldsymbol{V}_{dc}\right),$$

where $k_{p,dc}$ represents the proportional coefficient of the PI controller and $k_{i,dc}$ represents the integral coefficient of the PI controller. The overall control block diagram of the entire control system is shown in Figure 2.

The load current can be decomposed into three parts as follows:

$$\boldsymbol{I}_L = \boldsymbol{I}_{L,d} + \boldsymbol{I}_{L,q} + \boldsymbol{I}_{L,h}, \tag{3}$$

where $I_{L,d}$ represents the active component of the load current, $I_{L,q}$ represents the reactive component of the load current, and $I_{L,h}$ represents the harmonic component of the load current. To achieve compensation for $I_{L,q}$ and $I_{L,h}$, it is necessary to first extract $I_{L,q}$ and $I_{L,h}$ and then control the parallel output port to output currents in the opposite direction of $I_{L,q}$ and $I_{L,h}$, which can be implemented by the current closed-loop controller. According to Kirchhoff's current law and Eq. (3), the grid current will no longer contain any reactive or harmonic components. Based on this idea, the control strategy proposed in this paper is given as follows: first, we obtain the reference value of the effective active current that is required to maintain the stability of the DC bus voltage based on the control loop of the DC bus voltage; then, it is multiplied by $1/K$ of the collected real-time grid voltage to generate the active current output

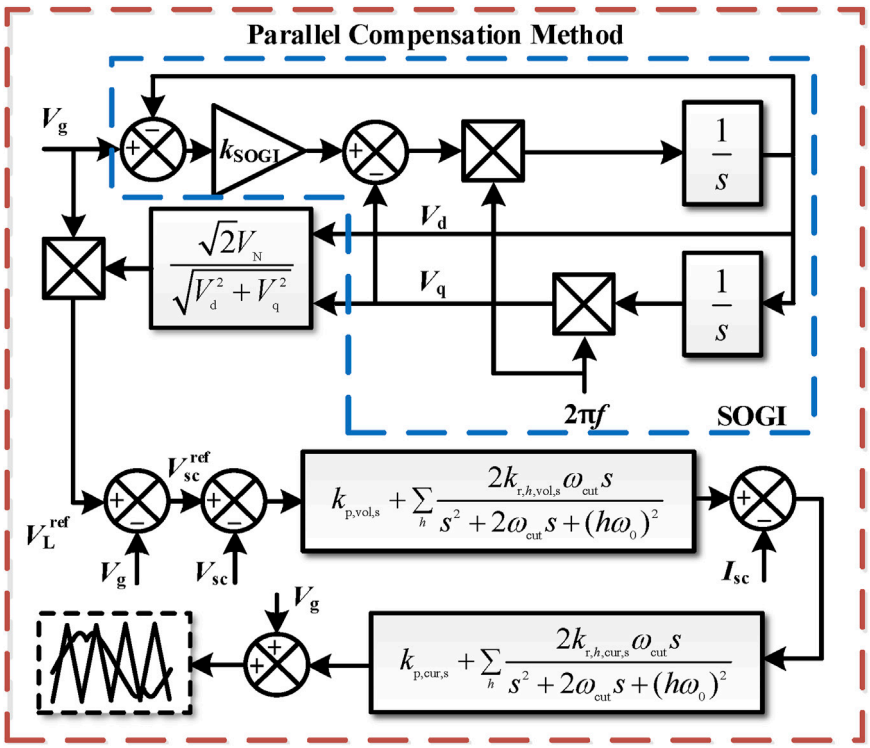

FIGURE 5
The proposed series compensation strategy.

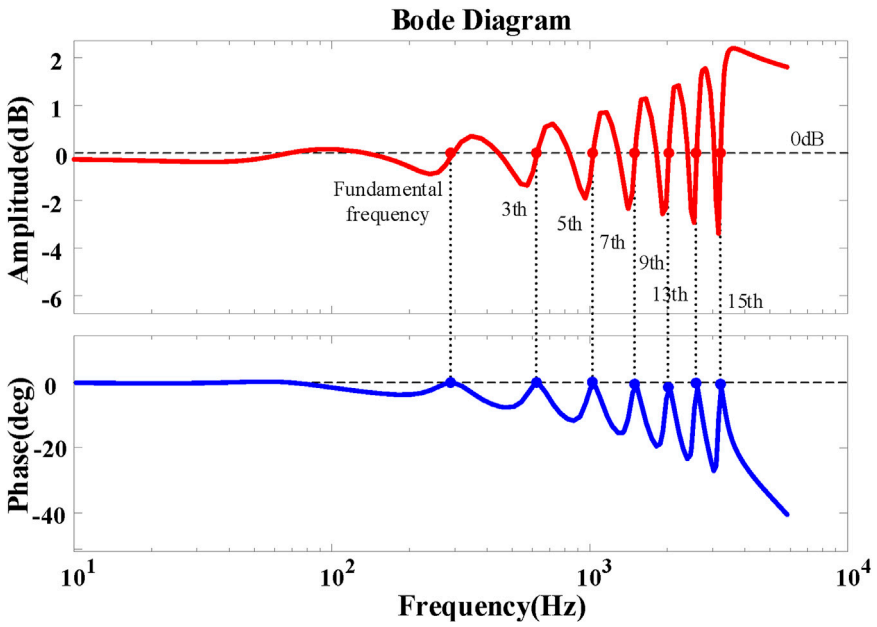

FIGURE 6
Closed-loop Bode plot of the series controller.

reference using the parallel compensator, denoted as I_d^{ref}, where K generally takes the rated grid voltage amplitude. Therefore, the reference current of the parallel compensator's output, denoted as I_{pc}^{ref}, is given as

$$\boldsymbol{I}_{pc}^{ref} = \boldsymbol{I}_{d}^{ref} - \boldsymbol{I}_{L}. \tag{4}$$

Since the active current reference for the DC bus voltage loop has been given, the active current reference for the parallel port output I_{pc}^{ref}, obtained from Eq. (4), represents the opposite current of the load reactive current $I_{L,q}$ and the load harmonic current $I_{L,h}$. Then, the output current I_{pc} of the parallel port is controlled in real time using a current closed-loop controller. The current controller adopts a proportional resonant (PR) controller, which is denoted as $G_{cur,p}$. Therefore, the expression for the drive signal of the parallel inverter is given as

$$\boldsymbol{d}_{p} = \left(\boldsymbol{k}_{p,cur,p} + \sum_{h} \frac{2\boldsymbol{k}_{r,h,cur,p}\boldsymbol{\omega}_{cut}\boldsymbol{s}}{\boldsymbol{s}^2 + 2\boldsymbol{\omega}_{cut}\boldsymbol{s} + (\boldsymbol{h}\boldsymbol{\omega}_0)^2} \right) \left(\boldsymbol{I}_{pc}^{ref} - \boldsymbol{I}_{out,p} \right), \tag{5}$$

where $k_{p,cur,p}$ represents the proportional coefficient of the PR controller, $k_{r,h,cur,p}$ represents the resonance coefficient for each frequency h, ω_{cut} is the resonant bandwidth control parameter, and ω_0 is the natural angular frequency. The detailed control strategy for the parallel compensator is shown in Figure 3. It can be seen from the figure that the grid-connected control uses the instantaneous value of V_g instead of the real-time phase angle of V_g.

The circuit structure of the parallel port and the overall control block diagram are shown in Figure 1, where L_{p1}, L_{p2}, and C_p constitute the interface filters of the parallel inverter. Therefore, the expression for the output current $I_{out,p}$ of the parallel inverter with respect to the inverter drive signal d_p is given by the following:

$$\boldsymbol{I}_{out,p} = \boldsymbol{d}_{p}\boldsymbol{G}_{i,dc}, \tag{6}$$

where $G_{i,dc}$ represents the transfer function of the inverter drive signal d_p to $I_{out,p}$, and its expression is given as follows:

$$\boldsymbol{G}_{i,dc} = \frac{\boldsymbol{V}_{dc}\left(1 + \boldsymbol{s}^2\boldsymbol{L}_{p2}\boldsymbol{C}_{p}\right)}{\boldsymbol{s}\left(\boldsymbol{L}_{p1} + \boldsymbol{L}_{p2}\right) + \boldsymbol{s}^3\boldsymbol{L}_{p1}\boldsymbol{L}_{p2}\boldsymbol{C}_{p}}. \tag{7}$$

Based on the control block diagram and the topology of the single-phase three-leg UPQC, the closed-loop transfer function Φ_p of the parallel port output current I_{pc}, with respect to the output current reference I_{pc}^{ref}, can be obtained as follows:

$$\boldsymbol{\Phi}_{p} = \frac{\boldsymbol{G}_{cur,p}\boldsymbol{K}_{PWM}\boldsymbol{G}_{i,dc}}{1 + \boldsymbol{G}_{cur,p}\boldsymbol{K}_{PWM}\boldsymbol{G}_{i,dc}}, \tag{8}$$

where K_{PWM} is the gain of PWM modulation, which represents the proportional coefficient between the controller output variable and the converter output voltage. From Eqs (6–8), the Bode plot of this closed-loop transfer function is obtained, as shown in Figure 4 and the parameters for plotting the Bode plot can be found in Table 1. From this graph, it can be observed that at odd harmonics frequencies, the magnitude response is 0 dB and the phase response is 0°. This indicates that the amplitude of the parallel port output current I_{pc} is equal to the amplitude of the output current reference I_{pc}^{ref}, and the phase of the parallel port output current I_{pc} is equal to the phase of the output current reference I_{pc}^{ref}, i.e., $I_{pc} = I_{pc}^{ref}$. Then, the control requirements can be satisfied.

2.3 Series compensation control method

The series compensation port has two control objectives. First, when the grid voltage exceeds the limits, it provides compensating voltage on the line to maintain the load voltage at the rated value. Second, it aims to reduce the harmonic components in the compensated grid voltage and increase the sinusoidal quality of the load voltage. To achieve these objectives, similar to the parallel compensation strategy, a PR controller is selected as the control function for the voltage loop and the current loop. The specific control block diagram is shown in Figure 5. The d-axis voltage V_d and the q-axis voltage V_q can be obtained through a second-order generalized integrator (SOGI), where the transfer functions of V_d and V_q relative to V_g are, respectively, as follows:

$$D(s) = \frac{V_d}{V_g} = \frac{k_{SOGI}\omega_0 s}{s^2 + k_{SOGI}\omega_0 s + \omega_0^2}, \tag{9}$$

$$Q(s) = \frac{V_q}{V_g} = \frac{k_{SOGI}\omega_0^2}{s^2 + k_{SOGI}\omega_0 s + \omega_0^2}, \tag{10}$$

where k_{SOGI} is the filter gain coefficient. It is evident from Eqs (9, 10) that when the frequency of V_g is ω_0, the amplitude gains of $D(s)$ and $Q(s)$ are both 1 and the phase angle gains are 0 and −90°, respectively. As a result, the grid voltage amplitude V_g^{amp} is as follows:

$$V_g^{amp} = \sqrt{V_d^2 + V_q^2}. \tag{11}$$

We compare V_g^{amp} from Eq. (11) with the rated grid voltage amplitude and perform some simple calculations, as shown in Figure 7, to obtain the load voltage reference, which has an effective value of V_N and the same phase as the grid voltage.

The circuit structure of the series port and the control block diagram of the overall system are shown in Figure 1, where L_s and C_s constitute the interface filter of the series inverter. The expression for the compensation voltage V_{sc} in terms of the inverter drive signal d_s is given by the following:

$$V_{sc} = d_s G_{v,dc}, \tag{12}$$

where $G_{v,dc}$ represents the gain of the inverter drive signal d_s with respect to the output voltage V_{sc}, and its expression is shown as follows:

$$G_{v,dc} = \frac{V_{dc}}{1 + s^2 L_{s1} C_f}. \tag{13}$$

Similar to the parallel port, d_s is determined by the control system. Based on the control block diagram, as shown in Figure 5, the expression for d_s can be obtained by the following:

$$d_s = \frac{G_{vol,s} G_{cur,s} K_{PWM}}{1 + G_{cur,s} G_{PWM} G_{v,i}} \left(V_{sc}^{ref} - V_{sc}\right), \tag{14}$$

where $G_{vol,s}$ represents the transfer function of the voltage controller and $G_{cur,s}$ represents the transfer function of the current controller, both of which are PR controllers. Moreover, $k_{p,vol,s}$ and $k_{r,h,vol,s}$ are the proportional coefficient and the resonance coefficient of the voltage controller for the series compensator, respectively; $k_{p,cur,s}$ and $k_{r,h,cur,s}$ are the proportional coefficient and the resonance coefficient of the current controller for the series compensator, respectively. $G_{v,i}$ represents the transfer function of the load current to the output voltage of the series inverter, and its expression is shown as follows:

$$G_{v,i} = \frac{s V_{dc} C_f}{1 + s^2 L_{s1} C_f}. \tag{15}$$

Therefore, the closed-loop transfer function Φ_s of the series port output voltage V_{sc} with respect to the output voltage reference V_{sc}^{ref} can be obtained as follows:

$$\Phi_s = \frac{G_{vol,s} G_{cur,s} K_{PWM} G_{v,dc}}{1 + G_{cur,s} K_{PWM} G_{v,i} + G_{vol,s} K_{PWM} G_{cur,s} G_{v,dc}}. \tag{16}$$

From Eq. (12–16), the Bode plot of the closed-loop transfer function Φ_s is obtained, as shown in Figure 6. The parameters for plotting the Bode plot can be found in Table 1. From the graph, it can be observed that at odd harmonic frequencies, the magnitude response is 0 dB and the phase response is 0°. This indicates that the amplitude of the series port output voltage V_{sc} is equal to the amplitude of the output voltage reference V_{sc}^{ref}, and the phase of

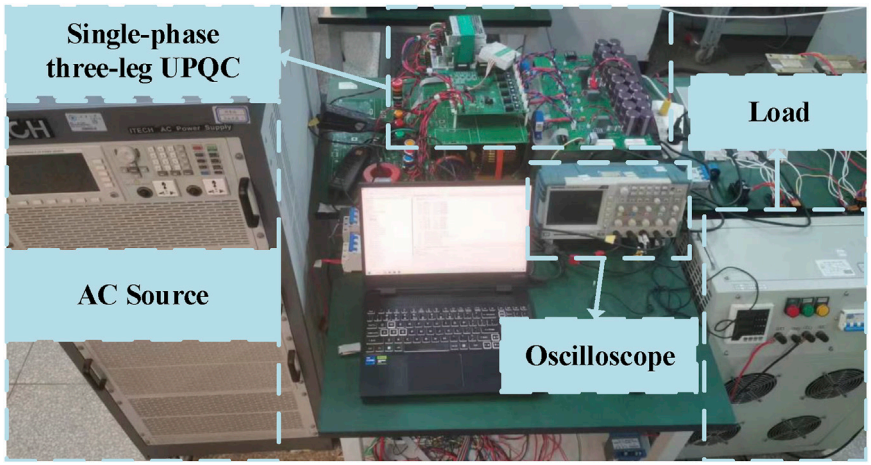

FIGURE 7
Experimental platform.

TABLE 2 Some key parameters of the experiment.

Controller name	Parameter setting
DC bus voltage controller	$k_{p,dc} = 2$; $k_{i,dc} = 5$
Current controller for the parallel compensator	$k_{p,cur,p} = 1$; $k_{r,h,cur,p} = 80$ ($h = 1$); $k_{r,h,cur,p} = 40$ ($h = 3, 5, 7$, and 9); $k_{r,h,cur,p} = 20$ ($h = 11, 13, 15$, and 17)
Voltage controller for the series compensator	$k_{p,vol,s} = 4$; $k_{r,h,vol,s} = 50$ ($h = 1$); $k_{r,h,vol,s} = 20$ ($h = 3, 5, 7$, and 9); $k_{r,h,vol,s} = 10$ ($h = 11, 13, 15$, and 17)
Current controller for the series compensator	$k_{p,cur,s} = 2$; $k_{r,h,cur,s} = 20$ ($h = 1$); $k_{r,h,cur,s} = 10$ ($h = 3, 5, 7$, and 9); $k_{r,h,cur,s} = 5$ ($h = 11, 13, 15$, and 17)

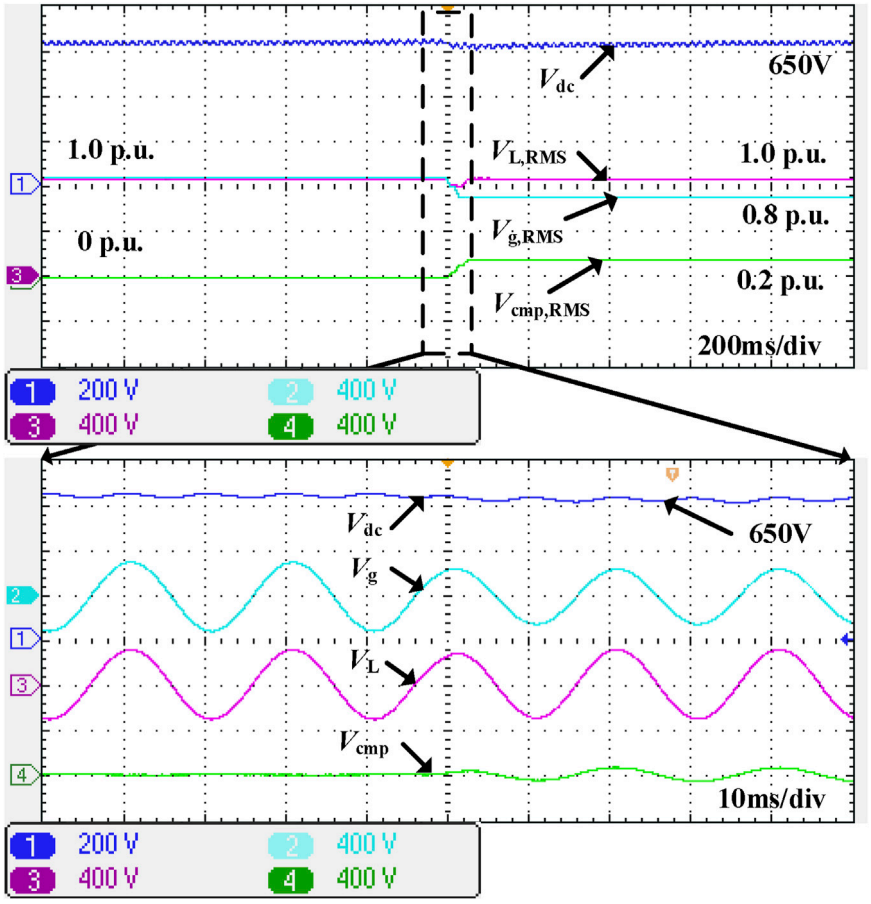

FIGURE 8
Voltage fluctuation compensation experiment.

the series port output voltage V_{sc} is equal to the phase of the output voltage reference V_{sc}^{ref}, i.e., $V_{sc} = V_{sc}^{ref}$. Then, the control requirements can be satisfied.

3 Experiment results

To verify the effectiveness of the proposed method, the experimental prototype of a single-phase three-leg UPQC is built, as shown in Figure 7. The parameters of the experimental prototype are the same as those given in Table 1. Some controller parameters are shown in Table 2. In addition, the switching frequency is 10 kHz, and the DC bus capacitance value is 2500 μF.

The first validation was carried out for the effectiveness of series port voltage regulation. The results of the first set of experiments are shown in Figure 8. The grid voltage suddenly dropped from 1.0 p. u. to 0.8 p. u. From the experimental results, it can be seen that there is a slight fluctuation in the DC bus voltage because of the direct utilization of the grid voltage in the proposed method. However, the compensated load voltage remains at 1.0 p. u., and from the detailed waveform, it can be seen that the compensated load voltage has almost no step change, meeting the expected effect.

Moreover, the effectiveness of the parallel port current compensation was verified, as shown in Figure 9. The load is a power electronic non-linear rectifier. Before compensation, the THD of the grid current is 25.67%. After compensation, the THD of the grid

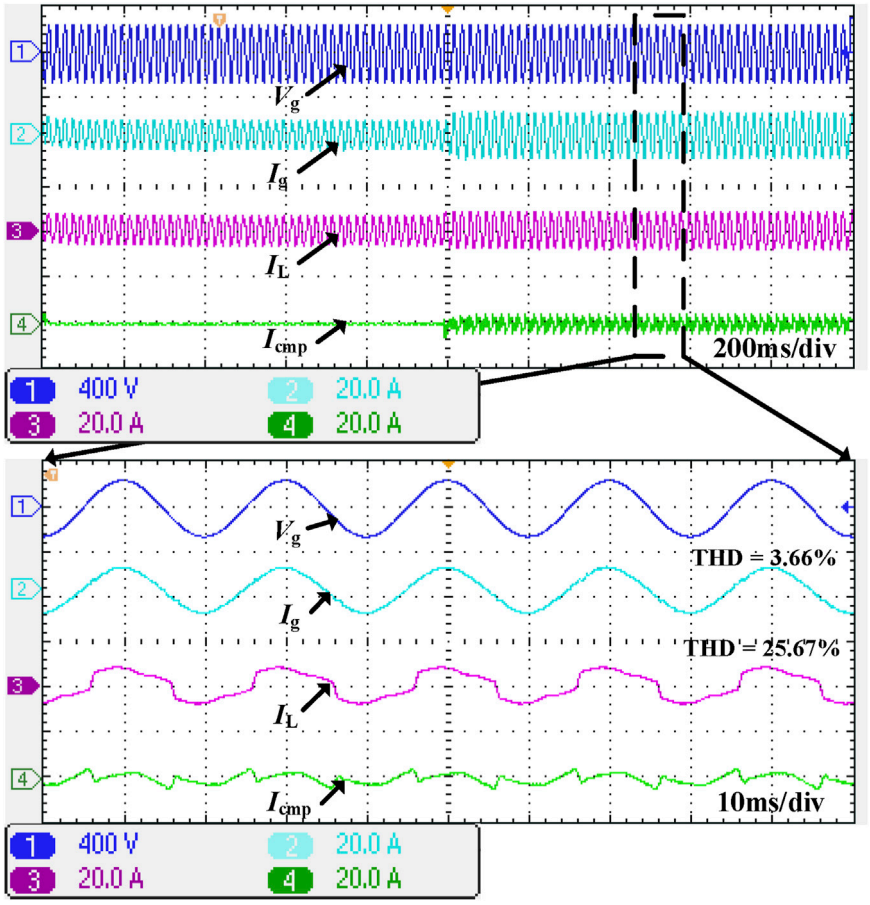

FIGURE 9
Parallel port compensation effect.

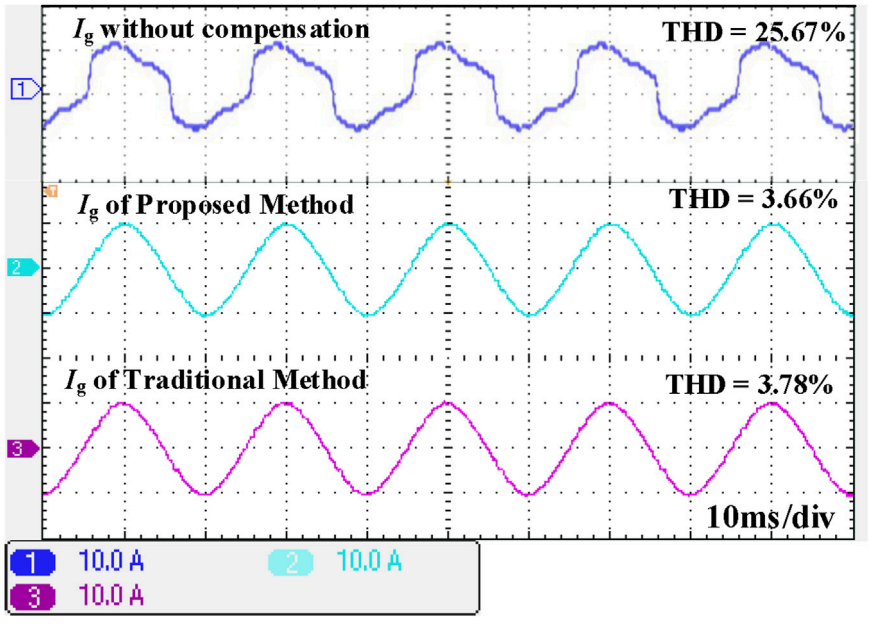

FIGURE 10
Comparison of the effects between the proposed method and the traditional method.

current is 3.66%. It can be seen that after compensation, the grid current has almost no harmonic distortion, which means that the experimental results meet the expectations.

In addition, the comparison between the traditional control method and the proposed method can be seen in Figure 10. The load of this experiment is the same as that of experiment 2. The THD of the grid current is 25.67% without any compensation. However, whether the proposed method or the traditional method is applied, the THD of the grid current is significantly improved, where the proposed method can improve to 3.66% and the traditional method can improve to 3.78%. There is no difference in this fact. However, compared to the complexity of the algorithm, the method proposed in this article is greatly simplified.

4 Conclusion

This article presents a control method without a phase-locked loop for the single-phase three-leg UPQC. The instantaneous value of the grid voltage is used for grid connection, which greatly simplifies the complexity of the control algorithm. Furthermore, a simple compensation method is proposed for reactive power current and harmonic current at the grid connection point, which eliminates the need for extracting reactive power current and harmonic current. As a result, it further simplifies the computational complexity of the control. Finally, the experimental results show that the proposed method can achieve series voltage compensation along with reactive power current and harmonic current compensation at the grid connection point. The control method, without the phase-locked loop, proposed in this article is applied for the single-phase UPQC. As for the control method without the phase-locked loop for the three-phase UPQC, it will be further studied in the follow-up work.

Data availability statement

The data analyzed in this study are subject to the following licenses/restrictions: the datasets in this article are the voltage and current values obtained during the experiment. We recorded them using an oscilloscope. The resulting voltage and current waveforms are displayed in the manuscript. Requests to access these datasets should be directed to Weiqi Meng, weiqi_meng@tju.edu.cn.

Author contributions

DF: funding acquisition, investigation, project administration, and writing–original draft. TC: resources, software, validation, and writing–original draft. LZ: formal analysis, supervision, and writing–original draft. WM: writing–review and editing. JH: conceptualization, project administration, and writing–review and editing.

Funding

The authors declare that financial support was received for the research, authorship, and/or publication of this article. This research was funded by State Grid Shandong Electric Power Company.

Conflict of interest

Authors DF and TC were employed by Linyi Power Supply Company of State Grid Shandong Electric Power Company.Author LZ was employed by Yinan Power Supply Company of State Grid Shandong Electric Power Company.

The remaining authors declare that the research was conducted in the absence of any commercial or financial relationships that could be construed as a potential conflict of interest.

Publisher's note

References

Abdalaal, R., and Ho, C. (2021). Analysis and validations of modularized distributed TL-UPQC systems with supervisory remote management system. *IEEE Trans. Smart Grid* 12 (3), 2638–2651. doi:10.1109/TSG.2020.3044992

Cheng, P. T., and Lee, T. L. (2006). Distributed active filter systems (DAFSs): a new approach to power system harmonics. *IEEE Trans. Ind. Appl.* 42 (5), 1301–1309. doi:10.1109/TIA.2006.880856

He, J., Du, L., Yuan, S., Zhang, C., and Wang, C. (2019). Supply voltage and grid current harmonics compensation using multi-port interfacing converter integrated into two-AC-bus grid. *IEEE Trans. Smart Grid* 10 (3), 3057–3070. doi:10.1109/TSG.2018.2817491

He, J., Li, Y. W., and Blaabjerg, F. (2015). An enhanced islanding microgrid reactive power, imbalance power, and harmonic power sharing scheme. *IEEE Trans. Power Electron.* 30 (6), 3389–3401. doi:10.1109/TPEL.2014.2332998

He, J., Liu, X., Lei, M., and Wang, C. (2020). A broad frequency range harmonic reduction for cascaded-power-cell-based islanded microgrid with lumped PCC filter. *IEEE Trans. Power Electron.* 35 (9), 9251–9266. doi:10.1109/TPEL.2020.2970462

Lakshmi, S., and Ganguly, S. (2019). An on-line operational optimization approach for open unified power quality conditioner for energy loss minimization of distribution networks. *IEEE Trans. Power Syst.* 34 (6), 4784–4795. doi:10.1109/TPWRS.2019.2919786

Lu, Y., Xiao, G., Wang, X., Blaabjerg, F., and Lu, D. (2016). Control strategy for single-phase transformerless three-leg unified power quality conditioner based on space vector modulation. *IEEE Trans. Power Electron.* 31 (4), 2840–2849. doi:10.1109/TPEL.2015.2449781

Mishra, M. K., and Lal, V. N. (2022). An enhanced control strategy to mitigate grid current harmonics and power ripples of grid-tied PV system without PLL under distorted grid voltages. *IEEE J. Emerg. Sel. Top. Power Electron.* 10 (4), 4587–4602. doi:10.1109/JESTPE.2021.3107869

Moeini, A., Zhao, H., and Wang, S. (2018). A current-reference-based selective harmonic current mitigation PWM technique to improve the performance of cascaded H-bridge multilevel active rectifiers. *IEEE Trans. Ind. Electron.* 65 (1), 727–737. doi:10.1109/TIE.2016.2630664

Mohammed, N., Ravanji, M. H., Zhou, W., and Bahrani, B. (2023). Enhanced frequency control for power-synchronized PLL-less grid-following inverters. *IEEE Open J. Industrial Electron. Soc.* 4, 189–204. doi:10.1109/OJIES.2023.3285010

Silva, S., Campanhol, L., Pelz, G., and Souza, V. (2020). Comparative performance Analysis involving a three-phase UPQC operating with conventional and dual/inverted power-line conditioning strategies. *IEEE Trans. Power Electron.* 35 (11), 11652–11665. doi:10.1109/TPEL.2020.2985322

Srinivas, V., Singh, B., and Mishra, S. (2019). Fault ride-through strategy for two-stage grid-connected photovoltaic system enabling load compensation capabilities. *IEEE Trans. Ind. Electron.* 66 (11), 8913–8924. doi:10.1109/TIE.2019.2899546

Sun, X., Zeng, J., and Chen, Z. (2013). Site selection strategy of single-frequency tuned R-APF for background harmonic voltage damping in power systems. *IEEE Trans. Power Electron.* 28 (1), 135–143. doi:10.1109/TPEL.2011.2179121

Wang, S., and Yang, J. (2023). Active disturbance rejection control of three-phase LCL power conversion system under non-ideal grid conditions. *Front. Energy Res.* 11. doi:10.3389/fenrg.2023.1170058

Xia, Y., Feng, Z., Chen, R., Wu, J., and Huang, Q. (2022). A harmonic suppression strategy for grid-connected inverters based on quadrature sinewave extractor. *Front. Energy Res.* 10. doi:10.3389/fenrg.2022.1020676

Zhang, F., Wang, Y., Huang, D., Lu, N., Jiang, M., Wang, Q., et al. (2022a). Integrated energy system region model with renewable energy and optimal control method. *Front. Energy Res.* 10. doi:10.3389/fenrg.2022.1067202

Zhang, S., Chen, C., Ling, B., Li, X., Lu, D., and Hu, H. (2022b). A generalized harmonic extraction algorithm based on multi-window average filter under synchronous rotating frame. *IEEE Trans. Power Electron* 38 (3), 3752–3764. doi:10.1109/TPEL.2022.3217942

frontiers | Frontiers in Energy Research

TYPE Methods
PUBLISHED 26 January 2024
DOI 10.3389/fenrg.2024.1352356

OPEN ACCESS

EDITED BY
Youbo Liu,
Sichuan University, China

REVIEWED BY
Zao Tang,
Hangzhou Dianzi University, China
Peng He,
Chongqing University of Posts and Telecommunications, China
Wei Xiao,
Chengdu University of Technology, China

*CORRESPONDENCE
Donglai Tang,
tangdonglai@sohu.com

RECEIVED 08 December 2023
ACCEPTED 08 January 2024
PUBLISHED 26 January 2024

CITATION
Tang D, Zhang Q, Ma T, Ou Y, Wu L and Tang J (2024), Aggregated demand-side response in residential distribution areas based on tiered incentive prices.
Front. Energy Res. 12:1352356.
doi: 10.3389/fenrg.2024.1352356

Aggregated demand-side response in residential distribution areas based on tiered incentive prices

Donglai Tang[1]*, Qiang Zhang[1], Tiefeng Ma[2], Yuan Ou[1], Lei Wu[1] and Jizhong Tang[1]

[1]Aostar Information Technology Co., Ltd, Chengdu, China, [2]School of Statisncs Southwestern University of Finance and Economics, Chengdu, China

The residential area refers to the power supply area from distribution transformers to the end users that contains multiple types of flexible resources, such as photovoltaics, energy storage, and power users. Focusing on the challenge of insufficient demand response incentives to multiple types of users in residential distribution areas, a tiered incentive price-based demand-side aggregated response method is proposed in this paper. Users in residential distribution areas are classified with an improved k-means clustering method for obtaining typical types of users. Thereafter, initial scores of users are calculated, and their grades are assigned based on their scores. Corresponding tiered incentive prices are designed for different grades. On this basis, a leader–follower game is proposed to obtain the demand response base price, and tiered incentives are provided to users of different grades to increase their enthusiasm for participating in demand response. In the case study, an actual urban residential distribution area is studied. The results show that the proposed user clustering method has an accuracy of 99.8% in classifying users in a residential distribution area. In addition, the proposed method has better performance in terms of improving the benefit of the load aggregator and users in the residential distribution area compared with methods such as potential game, hidden Markov, and Monte Carlo. Specifically, from the results, the benefit of load aggregators is increased by 101.96%, 76.07%, and 112.37%, and the income of the users is increased by 54.51%, 36.94%, and 64.91%.

KEYWORDS

tiered incentives, residential distribution areas, demand response, leader–follower game, adjustable load

1 Introduction

Through guiding and motivating power users to proactively optimize their energy consumption behaviors and trading strategies in markets, while exploring the response potential of demand-side flexible resources in depth, demand response (DR) can help mitigate the gap between load peak and load valley, smooth the load curve, support power grid operation and regulation, and maintain the dynamic balance of supply and demand. DR has become an important promotion to the revitalization of massive demand-side flexible resources and development of emerging power systems (Chen et al., 2022). With the widespread connection of distributed resources in residential distribution areas (RDAs) and

continuous improvement of power distribution automation levels, DR programs gradually extend from commercial buildings and industrial parks to cover controllable energy resources, such as rooftop photovoltaics and energy storage systems (Urban et al., 2019; Pan et al., 2020). However, because resources of users in RDAs are usually widely dispersed, the response potential of a single user is limited, the current market entry threshold is relatively high, direct control is not fully realized, and a large number of DR resources have not been fully exploited. Therefore, using the idea of aggregation to integrate resources in RDAs and fully exploiting the scale effect to promote DR has become the key to promote source–load interaction (Klaucke et al., 2020; Preeti et al., 2022; Tan and Zeng, 2022).

The RDA users mainly include power users, rooftop photovoltaic users, and users with energy storage. The number of these users is large. However, their individual capacities are small, and they hardly participate in the DR independently. The RDA load aggregator participates on behalf of users in the DR programs. Through guiding contracted users to proactively change their energy consumption behaviors (Wang BB. et al., 2022; Fan et al., 2022), the RDA load aggregator achieves flexible regulation of resources in the RDA, such as rooftop photovoltaics, energy storage systems, and controllable loads (Hassanniakheibari et al., 2020; Zhang et al., 2021), while maximizing the benefit. However, due to limited participation willingness of RDA users caused by lack of incentives (Duan et al., 2021), the effectiveness of DR programs is not as expected. Therefore, effective incentive mechanisms for multiple types of RDA users are urgently needed.

In recent years, incentive-based DR programs have been extensively studied. Guo et al. (2020) elaborates on the construction of an incentive-based DR model between a single load aggregator and multiple RDA users. RDA users receive incentives through the load aggregator's DR compensation. However, in Guo et al. (2020), RDA users are regarded as static price takers and their dynamic price bidding features cannot be reflected.

Qi et al. (2022); Striani et al. (2021) considered the dynamic response characteristics of RDA users and designed a method for load aggregators to guide RDA users to participate in the DR. It solves the problem of the dynamic bidding adaptability of RDA users through dynamic parameters, but this method lacks the analysis of users' willingness of participating in the DR. Wei et al. (2021); Xu et al. (2021); Sun et al. (2022) analyzed the correlation between user response willingness and RDA response potential. Then, a comprehensive DR optimization incentive strategy is designed, using a multi-period subsidy strategy to increase user enthusiasm for participating in the DR. However, this method focuses on the exploration of a single DR incentive measure, and the willingness of different types of RDA users to participate in DR varies significantly. Therefore, exploring the DR incentive mechanism for multiple types of users is of significance for promoting the DR participation of the RDA.

Designing reasonable incentives is the key to fully exploring the system's flexibility, maintaining the dynamic balance of supply and demand, and effectively motivating users to participate in DR. To this end, from the perspective of the RDA load aggregator, users in an RDA are classified and graded to different levels. On this basis, a tiered incentive price-based demand-side aggregated response method is proposed. In addition, the impacts of different incentives on multiple types of users are revealed.

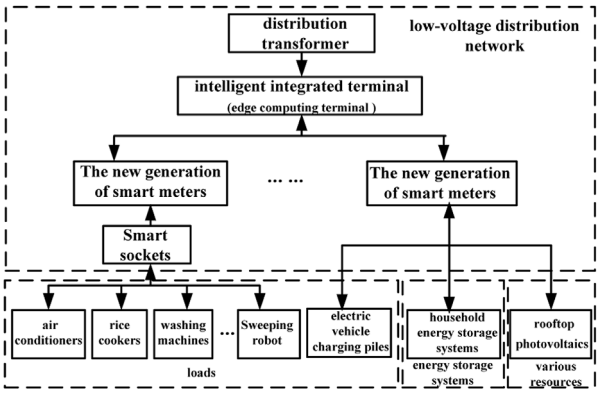

FIGURE 1
Structure of the RDA low-voltage distribution network.

The contributions of this paper are threefold:

(1) An RDA user classification method based on an improved k-means clustering algorithm that improves the accuracy of RDA user classification by dynamically adjusting the number of clusters to adapt data volume is proposed.
(2) An RDA demand response pricing model based on a leader–follower game between load aggregators and multi-type RDA users is proposed, through which the optimal benefit for all participants can be achieved.
(3) Incentive mechanisms for multiple types of RDA users are designed to increase their enthusiasm in participating in DR.

2 The structure of the RDA demand response

2.1 Physical structure

The structure of the RDA low-voltage distribution network takes edge computing as the core, forming a source–grid–load–storage collaborative and interactive system. By relying on intelligent integrated terminals, plug and play, situational awareness, intelligent interaction, and collaborative control (Sheng et al., 2021; Avordeh et al., 2022; Gharibshah and Zhu, 2022) of resources in an RDA, such as rooftop photovoltaics, electric vehicle charging piles, and household energy storage systems, can be realized. The structure is shown in Figure 1.

The intelligent integrated terminal is an edge computing terminal developed by the State Grid Company of China in 2019 and an open platform that integrates data aggregation, edge computing, and intelligent applications. It now serves as the main carrier for the RDA to participate in DR (Yang et al., 2022). Data aggregation is realized through applying AC sampling, high-speed power line carriers, micro-power wireless, and other advanced methods. Data are collected from various sources, such as loads and energy storage systems, in an RDA. In addition, edge computing and applications are deployed with the software development

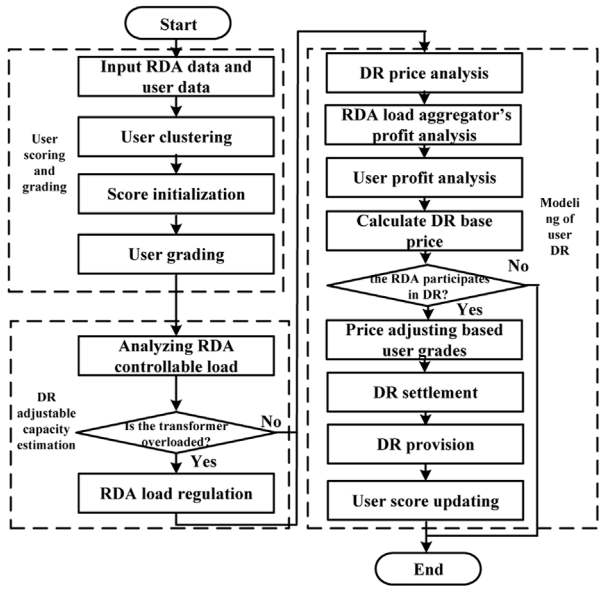

FIGURE 2
RDA demand response framework.

platform, realizing multiple types of users in the RDA being able to participate in DR.

The new generation of smart meters is an energy router developed by the State Grid Company in 2020 that integrates data collection, communication, and control functions (Rashidizadeh-kermani et al., 2020). The smart meter can accept DR control tasks sent by intelligent integrated terminals and issue energy control instructions to various resources, loads, and energy storage systems in an RDA.

Smart sockets, as a household appliance energy control device, can collect energy consumption data of household appliances, such as air conditioners, rice cookers, and washing machines, and perform intelligent control to those household appliances, such as tripping and power consumption adjustment, based on DR instructions issued by the smart meter (Zheng et al., 2022).

2.2 Theoretical analysis framework

2.2.1 Mechanism of the tiered RDA demand response

The tiered RDA DR is a user-level incentive program. After the RDA load aggregator receives the DR request from the main grid, it adjusts the power according to the capacity of the users' interruptible and adjustable loads, the generation of rooftop photovoltaics, and the stored energy of the energy storage system. The compensation price is adjusted according to the grades of the users for increasing their enthusiasm in DR participation.

2.2.2 The framework of the RDA demand response

The framework of the tiered incentive price-based demand-side aggregated response method in the RDA is shown in Figure 2.

(1) User classification and grading

First, clustering analysis is conducted based on the characteristics of RDA users and classifies user grades based on their initial credits.

(2) Measuring RDA adjustable power

The characteristics of the RDA adjustable loads are analyzed, and the adjustable power from resources, including rooftop photovoltaics, home energy storage systems, interruptible loads, and adjustable loads, is calculated. On this basis, the overload status of the distribution transformer is monitored. When overload happens, the RDA emergency program is activated and the load is regulated to reduce the power through the transformer.

(3) RDA user demand response model

The RDA aggregator conducts load aggregation and user benefit analysis based on the DR instructions sent by the main grid and determines the baseline DR strategy. Then, the RDA aggregator determines if the RDA participates in the DR. If yes, the RDA aggregator formulates a tiered DR strategy based on the number and grades of users that participate in the DR in the RDA and organizes users to follow instructions according to grades. After demand response, compensations to users are settled and the grades of users participating in DR are adjusted for increasing their enthusiasm for future participation.

3 Tiered RDA demand response model

3.1 RDA user classification and grading

3.1.1 RDA user classification

The RDA demand response program is designed to motivate RDA users to actively participate in DR, alleviate distribution line congestion, and guarantee RDA peak load supply. Different household users have different response willingness. For example, high-income household users may show lower DR willingness. Based on the characteristics shown by the daily load profiles of RDA users, Liu et al. (2020); Liu H. et al. (2022) classified them into afternoon and evening peak load, evening single peak, afternoon peak load, and evening sub-peak load and identified the degree of willingness of RDA users. In this section, RDA users are classified to explore the degrees of their willingness in participating in DR.

Since 2016, the State Grid Company has been carrying out the construction of the "Friendly Interaction between Supply and Demand" project. By upgrading the low-voltage power line high-speed carrier (HPLC) module, the energy consumption data of RDA users on a time scale of 15 min can be collected. This lays the foundation of data for RDA users interacting with the main grid (Wan and Song, 2021).

In order to improve the accuracy of RDA user classification, clustering features are selected following the typical recommendation from the Electric Power Industry Association, as shown in Table 1.

The k-means clustering method is an unsupervised iterative clustering method. This method can divide the data into k clusters. First, k users are randomly selected as initial cluster centers. Then,

TABLE 1 Clustering features of RDA users.

Feature	Comment
User load profile	Load profile (96 data points)
User imported power curve	Imported power (96 data points of a day)
User power generation curve	Power generation from rooftop photovoltaics (96 data points of a day)
User energy accommodation curve	Energy accommodation (96 data points of a day)
User exported power curve	Exported power from rooftop photovoltaics (96 data points of a day)
User energy storage charging power curve	Energy storage charging power (96 data points of a day)
User energy storage exported power curve	Energy storage exported power (96 data points of a day)
User energy storage discharging power curve	Energy storage discharging power (96 data points of a day)
User daily electricity consumption curve	Daily electricity consumption
User daily purchased electricity curve	Daily purchased electricity
User daily exported electricity curve	Daily exported electricity from rooftop photovoltaics and energy storage

each remaining user is assigned to a cluster based on the distances to the cluster centers, and thereafter the cluster centers are updated. This process is repeated until convergence (Zhao et al., 2020). The k-means clustering method has a high efficiency and a relatively high accuracy, which makes it widely used. However, the k, namely the number of clusters, needs to be determined in advance, which is difficult. To this end, in this section, the traditional K-means clustering algorithm is improved so that it can dynamically adjust the number of clusters, being adaptable to the number of users in clusters. In other words, when the number of users in a cluster is less than a certain threshold, the cluster will be merged into others. When the number of users in a certain cluster is too large, the cluster will be split into two.

The steps of the improved k-means clustering algorithms are as follows:

Step 1. Randomly select k RDA users as the initial clustering centers.

Step 2. Calculate the Euclidean distance $D_j(k)$ of each RDA user to the cluster center, as in Eq. 1, where X_j represents the values of clustering features, and assign each RDA user to the nearest cluster.

$$d_j(k) = \min\left\{\left\|X_j - Z_j(k)\right\|\right\}. \tag{1}$$

Step 3. Based on the number of clusters after Step 2, if in any cluster, the number of users is less than the threshold Δy, the cluster is removed, and all users in it are assigned to the other clusters according to their Euclidean distances.

Step 4. With the RDA users' feature values, update the cluster centers $Z_j(k)$ as in Eq. 2. In Eq. 2, F_j is the number of users in the jth cluster, and cRDA represents the feature values.

$$Z_j(k) = \frac{1}{F_j}\sum_{j=1}^{k} c_j^{\mathrm{RDA}} x_j. \tag{2}$$

Step 5. Determine whether a cluster needs to be split with Eq. 3, where $\triangle a$ represents the cluster splitting threshold. If Eq. 3 is satisfied, perform cluster splitting. In Eq. 3, $\triangle a$ is the splitting threshold.

$$k < \Delta a. \tag{3}$$

Step 6. Determine whether clusters need to be merged with Eq. 4, where $\triangle b$ represents the cluster merging threshold. If Eq. 4 is satisfied, perform cluster merging. In Eq. 4, $\triangle b$ is the merging threshold.

$$k > \Delta b. \tag{4}$$

Step 7. Calculate the squared error to check whether the convergence condition is met. The squared error of the jth cluster can be calculated as in Eq. 5.

$$\sigma = \sqrt{\frac{1}{F_j}\sum_{j=1}^{k}\left(c_j^{RDA} - Z_j(k)\right)^2}. \tag{5}$$

When the square error is less than the preset threshold over iterations, the algorithm is terminated, and RDA user classification is obtained.

3.1.2 Initial scoring and grading of RDA users

In this paper, different DR incentive prices are adopted for users with different scores. As an example, Wang L. et al. (2022) scores positive points for users consuming electricity at load valley periods and negative points at load peak periods. We adopt a 100-point system for scoring users. The incentive area is 60–100 points, within which the RDA load aggregator is rewarded on the basis of the benchmark DR price, and the penalty area is 0–59 points, within which the RDA load aggregator is punished on the basis of the benchmark DR price.

TABLE 2 Tiered demand response incentives to RDA users.

Grade	Score range	Floating price scale
A1	90 to 100	Increase △a1 from the base price
A2	80 to 89	Increase △a2 from the base price
A3	70 to 79	Increase △a3 from the base price
A4	61 to 69	Increase △a4 from the base price
A5	60	The base price
A6	50 to 59	Decrease △a6 from the base price
A7	40 to 49	Decrease △a7 from the base price
A8	30 to 39	Decrease △a8 from the base price
A9	20 to 29	Decrease △a9 from the base price
A10	0 to 19	Decrease △a10 from the base price

TABLE 3 Typical controllable loads of RDA users.

Type	Device
Interruptible load	Dehumidifier
	Dishwasher
	Sweeping robot
	Disinfection cabinet
Adjustable load	Air conditioner
	Electric vehicle charging pile
	Refrigerator
	Rice cooker
	Washing machine
	Dryer

With the user's initial score according to the features of RDA users and typical weights from the industry association as shown in Table 1, a user's standard score can be calculated as in Eq. 6.

$$d^{\mathrm{STD}} = \frac{\sum_{i=1}^{n^{\mathrm{RDA}}} \left(d_i^{\mathrm{FEA}} \times w_i\right)}{n^{\mathrm{RDA}}}. \tag{6}$$

In Eq. 6, n^{RDA} is the number of RDA users; dFEA i represents the feature values of RDA users; and w_j represents the weights corresponding to the features.

The initial score of a user can be calculated as in Eq. 7, where dR i is the industry typical value of the features of different types of RDA users and 60 is the passing score in the 100-point system.

$$d^{\mathrm{INIT}} = \frac{\sum_{i=1}^{n^{\mathrm{RDA}}} \left(d_i^{\mathrm{R}} \times w_i\right)}{d^{\mathrm{STD}}} \times 60. \tag{7}$$

The RDA aggregator designs the grades, corresponding score ranges, and floating price scales referring to the standards from the Electric Power Industry Association. Clustering results based on features in Table 1 determine the types of users, and each type has the categories as shown in Table 2.

As given in Table 2, users with different scores will be assigned to different grades and have different floating prices which are designed for providing diverse incentives.

3.2 Adjustable capacity estimation of RDA controllable resources

3.2.1 Adjustable capacity estimation of RDA loads

RDA controllable resources include, but are not limited to, residential loads, rooftop photovoltaics, and energy storage systems. Residential loads can be divided into two categories: non-controllable and controllable. The former includes lighting loads and televisions which will not participate in DR. Controllable loads can be further divided as interruptible and adjustable. Interruptible loads can be interrupted during operation, and adjustable loads can adjust the power consumption in a certain range. Typical controllable loads are shown in Table 3.

The interruptible power of RDA users, $P^{\mathrm{INT}}(t)$, can be calculated as in Eq. 8.

$$P^{\mathrm{INT}}(t) = \sum_{i=1}^{m^{\mathrm{INT}}} p_i^{\mathrm{UINT}}(t). \tag{8}$$

In Eq. 8, m^{INT} is the number of interruptible loads participating in DR in the RDA and pUNIT $i(t)$ is the interruptible power of different PRD interruptible loads in time interval t. The range of the interruptible power from RDA users is 0 to $P^{\mathrm{INT}}(t)$.

The adjustable power of RDA users, $P^{\mathrm{REG}}(t)$, can be calculated as in Eq. 9.

$$P^{\mathrm{REG}}(t) = \sum_{i=1}^{m^{\mathrm{REG}}} \left(p_i^{\mathrm{UREG}}(t) \times \lambda_i \times t_i^{\mathrm{REG}}\right). \tag{9}$$

In Eq. 9, m^{REG} is the number of adjustable loads that participate in DR; pUREG $i(t)$ is the rated power of adjustable loads of RDA users; λ_i represents the power reduction ratios of adjustable loads of different RDA users; and tREG i represents the adjustable load power ratios of different RDA users. During time interval t, the adjustable power range of RDA users is 0 to $P^{\mathrm{REG}}(t)$.

3.2.2 Estimating the power adjustable range of the distribution transformer

When the total RDA load is greater than the rated capacity of the distribution transformer, distribution transformer overload happens. A traditional dry-type transformer can only operate for 60 min, being overloaded by 20% (Liu ZH. et al., 2022). In severe cases, the distribution transformer will be burned out, resulting in a power outage. Therefore, load regulation should be conducted at the first time, when the distribution transformer is overloaded. In this paper, the overload time of the transformer is set to 1% of the typical value, namely, 0.6 min, to prevent from burning out.

When the distribution transformer is overloaded, the RDA load aggregator implements the RDA emergency load control strategy to reduce the RDA load within the normal operating range of the distribution transformer. This leads to no compensation to RDA

users. During the overload period of the distribution transformer, the reduced load $P^{\mathrm{OL}}(t)$ can be represented as in Eq. 10.

$$P^{\mathrm{OL}}(t) = P^{\mathrm{INT}}(t) + P^{\mathrm{REG}}(t) + P^{\mathrm{PV}}(t) + P^{\mathrm{ES}}(t). \tag{10}$$

In Eq. 10, $P^{\mathrm{PV}}(t)$ is the power generation that can be provided by the rooftop photovoltaics and $P^{\mathrm{ES}}(t)$ is the power from energy storage discharging.

3.3 RDA user demand response model

3.3.1 RDA load aggregator revenue model

The essence of RDA demand response is that after the RDA load aggregator receives the instructions from the main grid, it estimates the capacity of available DR and determines whether participating in DR can be profitable. If yes, it will organize users in the RDA to participate in DR. The compensation prices will be adjusted according to the user grades to increase the enthusiasm of RDA users to participate in DR.

In this paper, the load aggregators are of two levels: the transformer distribution area level and regional level. The transformer distribution area level load aggregators are responsible for integrating RDA resources within the scope of a single distribution transformer, and the regional load aggregators are responsible for further integrating the load aggregators of transformer distribution areas. Controllable loads are aggregated by aggregators to participate in DR, and RDA users of different types are incentivized as in Table 2. RDA users' photovoltaic and energy storage systems can sell electricity to load aggregators for profit.

The comprehensive income function of a regional level load aggregator, f^{AREA}, can be formulated as in Eq. 11, where m^{RDA} is the number of residential distribution areas of distribution area level load aggregator and fRDA i represents the incomes of transformer distribution area level load aggregators.

$$f^{\mathrm{AREA}} = \max\left\{\sum_{i=1}^{m^{\mathrm{RDA}}} f_i^{\mathrm{RDA}}\right\}. \tag{11}$$

The income function of a distribution area level load aggregator can be formulated as in Eq. 12.

$$f^{\mathrm{E}} = \max\{f^{\mathrm{GET}} - f^{\mathrm{BUYU}} - f^{\mathrm{BUYPE}}\}, \tag{12}$$

$$f^{\mathrm{BUYU}} = \sum_{i=1}^{m^{\mathrm{INT}}+m^{\mathrm{REG}}} p_i^{\mathrm{USER}}(t) \times v_i^{\mathrm{USER}}, \tag{13}$$

$$f^{\mathrm{BUYPE}} = \sum_{i=1}^{m^{\mathrm{PE}}} p_i^{\mathrm{PE}}(t) \times v_i^{\mathrm{PE}}. \tag{14}$$

In Eq. 12 to Eq. 14, f^{GET} is the profit of the load aggregator obtained from the main grid operator for participating in DR; f^{BUYU} is the compensation to users in the RDA for participating in the DR; f^{BUYPE} is the compensation from the load aggregator to the RDA users for using the rooftop photovoltaics and energy storage in participating in DR; pUSER $i(t)$ is the power of different RDA users during the DR period; vUSER represent the prices for different RDA users to participate in DR; m^{PE} is the number of rooftop photovoltaics and energy storage systems in the RDA; pPE $i(t)$ represents the power from the rooftop photovoltaics and the energy storage system in the DR period; and vPE i represents the price for the rooftop photovoltaic and the energy storage system for exporting power to the main grid.

The constraint of the adjustable load can be formulated as in Eq. 15, where pRPL $i(t)$ is the rated power of the RDA transformer.

$$p_i^{\mathrm{RPL}}(t) \geq p_i^{\mathrm{USER}}(t) - p_i^{\mathrm{PE}}(t). \tag{15}$$

3.3.2 RDA demand response pricing

RDA DR pricing is to set the benchmark price for RDA users in DR. When the RDA load aggregator benefits from participating in DR, it obtains the price from the equilibrium of the game considering the DR price from the main grid, energy export prices to rooftop photovoltaic generation, and energy export prices to energy storage discharging. The equilibrium will be used to derive the DR base price.

The leader–follower game is a static game model with complete information. The leader takes the lead in making decisions, and the followers make decisions based on the leader's decisions. The above process is repeated until a Nash equilibrium is reached (Huang et al., 2023) to maximize the benefits of participants. The leader–follower game is a classic game model with the advantages of high efficiency, flexibility, and reliability and has been widely used in the field of power systems. Based on the user classification results, this section uses the leader–follower game to implement the demand response pricing game between the RDA load aggregator and RDA users of different types. In the game, the RDA load aggregator is considered the leader, and different types of RDA users who participate in DR through load adjustment, rooftop photovoltaic power generation, and energy storage system discharging are considered followers. After several iterations, the game is terminated when reaching the Nash equilibrium, achieving optimal benefits for the leader and the followers.

The objective of the RDA demand response pricing game, z^{SG}, can be formulated as in Eq. 16.

$$z^{\mathrm{SG}} = \left\{ \begin{array}{c} \{l^{\mathrm{RA}} \cup l^{\mathrm{USER}} \cup l^{\mathrm{PV}} \cup l^{\mathrm{ES}}\}, \\ \{r^{\mathrm{RA}}(v^{\mathrm{INIT}}, v^{\mathrm{RAP}})\}, \\ \{r^{\mathrm{USER}}(p_i^{\mathrm{USER}}(t))\}\{r^{\mathrm{PV}}(p_i^{\mathrm{PV}}(t))\}\{r^{\mathrm{ES}}(p_i^{\mathrm{ES}}(t))\} \\ \{\mathrm{Q}^{\mathrm{RA}}\}, \{\mathrm{Q}^{\mathrm{USER}}\}, \{\mathrm{Q}^{\mathrm{PV}}\}, \{\mathrm{Q}^{\mathrm{ES}}\} \end{array} \right\}, \tag{16}$$

$$\left\{ \begin{array}{l} l^{\mathrm{USER}} = \{l_1^{\mathrm{USER}}, l_2^{\mathrm{USER}}, \ldots, l_m^{\mathrm{USER}}\} \\ l^{\mathrm{PV}} = \{l_1^{\mathrm{PV}}, l_2^{\mathrm{PV}}, \ldots, l_m^{\mathrm{PV}}\} \\ l^{\mathrm{ES}} = \{l_1^{\mathrm{ES}}, l_2^{\mathrm{ES}}, \ldots, l_m^{\mathrm{ES}}\} \end{array} \right. . \tag{17}$$

In Eq. 16 to Eq. 17, l^{RA}, l^{USER}, l^{PV}, and l^{ES} represent the RDA load aggregator, RDA users participating in DR load reduction, rooftop photovoltaic power generation, and energy storage discharging, respectively. Different types of RDA users have different capacities on load reduction, rooftop photovoltaic power generation, and energy storage discharging. {lUSER 1, lUSER 2, …, lUSER m} represent the m categories of RDA users who participate in DR load reduction; {lPV 1, lPV 2, …, lPV m} represent the m categories of RDA users who participate in rooftop photovoltaic power generation; and {lES 1, lES 2, …, lES m} represent the m categories of RDA users participating in energy storage discharging. r^{RA}, r^{USER}, r^{PV}, and r^{ES} are the price bidding strategies of the above four game participants, respectively. v^{INIT} and v^{RAP} are the DR basic price and reward/penalty incentive price for

the RDA load aggregator, respectively. In addition, pUSER $i(t)$ represents the power consumption of RDA users participating in DR load reduction; pPV $i(t)$ is the power consumption of RDA users participating in rooftop photovoltaic power generation; pEV $i(t)$ is the power consumption of RDA users participating in energy storage discharging. Q^{RA}, Q^{USER}, Q^{PV}, and Q^{ES} are the utility functions of the RDA load aggregator, RDA users participating in DR load reduction, RDA users participating in rooftop photovoltaic power generation, and RDA users participating in energy storage discharging, respectively.

In the leader–follower game, the RDA load aggregator, RDA user rooftop photovoltaics, and RDA user energy storage systems take maximizing the utility as the objective. RDA users participate in the game, taking minimizing the utility as the objective. The iterative process is repeated until the Nash equilibrium is reached and game participants stop updating their strategies. The basic price v^{BASIC} from the Nash equilibrium can be written as in Eq. 18.

$$v^{BASIC} = \text{argmax}Q^{RA}\begin{pmatrix} v^{INIT}, v^{RAP}, p_i^{LUSER}(t), \\ p_i^{LPV}(t), p_i^{LES}(t) \end{pmatrix}. \tag{18}$$

In Eq. 18, pLUSER $i(t)$ is the power consumption of RDA users in the Nash equilibrium solution; pLPV $i(t)$ is the rooftop photovoltaic power generation in the Nash equilibrium solution; and pLES $i(t)$ is the energy storage discharging power in the Nash equilibrium solution.

The power consumption of RDA users in the Nash equilibrium solution should satisfy Eq. 19.

$$p_i^{LUSER}(t) = \text{argmin}Q^{USER}\left(v^{INIT}, v^{RAP}, p_i^{USER}(t)\right). \tag{19}$$

The rooftop photovoltaic power generation pLPV should satisfy Eq. 20.

$$p_i^{LPV}(t) = \text{argmax}Q^{PV}\left(v^{INIT}, v^{RAP}, p_i^{PV}(t)\right). \tag{20}$$

The energy storage discharging power pLES i should satisfy Eq. 21.

$$p_i^{LES}(t) = \text{argmax}Q^{ES}\left(v^{INIT}, v^{RAP}, p_i^{ES}(t)\right). \tag{21}$$

With the Nash equilibrium, the RDA load aggregator, RDA users, RDA rooftop photovoltaics, and RDA energy storage systems cannot gain more profit by unilaterally changing their strategy. The solving process of the game can be referred to Huang et al. (2020), and due to the space limitation, it is not repeated in this paper.

3.3.3 Constraints

(1) Power constraint

$$\begin{cases} p_i^{DR}(t) = p_i^{USER}(t) + p_i^{PV}(t) + p_i^{EV}(t) \\ p_i^{DR}(t) \le p_i^{RPL}(t) \end{cases}. \tag{22}$$

In Eq. 22, pDR $i(t)$ is the integrated power from the RDA load aggregator.

The power from rooftop photovoltaics and energy storage discharging should satisfy Eq. 23.

$$p_i^{PV}(t) + p_i^{EV}(t) \le p_i^{RPL}(t). \tag{23}$$

(2) Price constraint

The highest compensation price paid by the RDA load aggregator to RDA users, v^{MAX}, should satisfy Eq. 24.

$$v^{MAX} \le v^{GRID}. \tag{24}$$

In Eq. 24, v^{GRID} is the price sent by the main grid to the RDA load aggregator.

3.3.4 DR process and scoring

In order to avoid the fact that an RDA user's willingness to participate in DR decreases after it already has a high score, the RDA demand response model proposed in this paper deducts scores after users enjoyed the DR incentives for realizing sustainable incentives to RDA users. The score adjustment rules, as shown in Table 4, are based on the typical settings of the power industry.

In the settlement, the RDA load aggregator updates the scores of RDA users according to Table 4 and adjusts the corresponding tiers. The adjusted scores, V_e, for RDA users can be calculated as in Eq. 25.

$$\begin{aligned} v_e = v_b + (w_a \times \Delta s_1) - (w_b \times \Delta s_2) \\ -(w_c \times \Delta s_3) - (w_d \times \Delta s_4) - (w_e \times \Delta s_5) \end{aligned}. \tag{25}$$

In Eq. 25, V_b represents the initial scores of RDA users; w_a is the provided demand response; w_b is the load growth default during DR time; w_c is the score deduction after having increased prices; w_d is the number of abnormal disconnections of rooftop photovoltaics and energy storage systems; w_e represents the power quality deviation of rooftop photovoltaic power generation and energy storage discharging. In addition, $\triangle s_1$, $\triangle s_2$, $\triangle s_3$, $\triangle s_4$, and $\triangle s_5$ are the score adjustments, as shown in Table 4.

4 Case study

With the real data from a residential distribution area in a city of China in June 2022, the proposed tiered incentive price-based demand-side aggregated response method is verified in this section. One residential distribution area corresponds to one distribution transformer. There are 18 distribution transformers in this residential area with a total capacity of 22.5 MVA. There are 6,120 residential users, including 516 users for rooftop photovoltaics, with a total capacity of 3.2 MW, and 672 users for energy storage systems. The total discharging power can reach 2.2 MW, and the total energy storage capacity is 3.6 MWh. The average solar irradiance is considered 4800 MJ/m-^{2}. Tiered demand response incentives to RDA users and RDA user score adjustment rules are shown in Tables 5, 6. The cluster splitting threshold Δa and the merging threshold Δb are both set as 2. The proposed model is compared with mainstream methods such as potential game (Hong et al., 2020), hidden Markov (Kadadha and Otrok, 2021), and Monte Carlo (Zhang et al., 2020). The numerical simulation in this paper is implemented on a server with Intel Xeon Silver 4214R CPU and Windows Server 2019.

4.1 RDA user classification result

This section classifies users based on the features shown in Table 1. The typical daily load profiles of users and the daily

TABLE 4 RDA user score adjustment rules.

Term	Score adjustment
DR power per $\triangle c_1 \times \triangle c_2$ (time duration)	$+\triangle s_1$
Load growth default during DR time (per $\triangle c_3$ kW× time duration)	$-\triangle s_2$
Score deduction after having increased prices (per $\triangle c_4$kWh)	$-\triangle s_3$
Rooftop photovoltaics and energy storage abnormal disconnection ($\triangle c_5$ times)	$-\triangle s_4$
Power quality deviation exceeds the threshold $\triangle c_6$	$-\triangle s_5$

TABLE 5 Tiered demand response incentives to RDA users in the studied case.

Grade	Score range	Floating price scale
A1	90 to 100	Increase 20% from the base price
A2	80 to 89	Increase 10% from the base price
A3	70 to 79	Increase 5% from the base price
A4	61 to 69	Increase 3% from the base price
A5	60	The base price
A6	50 to 59	Decrease 3% from the base price
A7	40 to 49	Decrease 5% from the base price
A8	30 to 39	Decrease 10% from the base price
A9	20 to 29	Decrease 15% from the base price
A10	0 to 19	Decrease 20% from the base price

TABLE 6 RDA user score adjustment rules of the studied case.

Term	Score adjustment
DR power per 1 kW × 15 min	+0.05
Load growth default during DR time (per 1 kw × 15 min)	−0.1
Score deduction after having increased prices (per 10 kWh)	−0.2
Rooftop photovoltaics and energy storage abnormal disconnection (every time)	−5
Power quality deviation exceeds 5% threshold (every time)	−1

electricity consumption curves are shown in Figure 3. The classification results are shown in Table 5.

As shown in Figure 3; Table 7, RDA users can be classified into seven categories.

(1) Stay-at-home type

As shown in Figure 3A, these users have peak power consumption from 7:30 to 9:00, 11:00 to 12:30, and 19:00 to 21:30. The power consumption in other periods is low. As shown in Figure 3B , the daily electricity consumption of this type of users fluctuates slightly. As they always stay at home, they are more sensitive to DR incentives and are willing to participate in DR.

(2) Commuter type

As shown in Figure 3A, these users have peak power consumption between 19:00 and 22:30, and the power consumption in other periods is low. As shown in Figure A1B, the user consumes less electricity on weekdays than on weekends. These users are relatively sensitive to DR incentives and are willing to participate in DR.

(3) Work-from-home type

As shown in Figure 3A, these users have peak power consumption during 9:00–12:00, 14:00–18:00, and 20:30–23:00, and their daily electricity consumption fluctuates slightly. They are highly sensitive to DR incentives and are willing to participate in DR.

(4) Idle on weekends type

For this type of users, the statistical period is weekdays. As shown in Figure 3A, the peak electricity consumption hours are 7:00–8:00 and 18:00–22:00. As shown in Figure A1B, the electricity consumption of this type of users on weekdays is several times of that on weekends. The economic conditions of these users are good, and the DR participation willingness is not high.

(5) Idle on weekdays type

For this type of users, the statistical period is weekends. As shown in Figure 3A, the users go out to work, and the power load is small. As shown in Figure 3B, this type of user consumes less electricity on weekdays and consumes several times more on weekends. They usually have good economic conditions and low DR participation willingness.

(6) Migratory bird type

Migratory bird type means user absence during the part of the studied period. As shown in Figure 3A, during the study period, the power load of this type of users is small. As shown in Figure 3B, the electricity consumption of this type of users from the 18th to 31st is several times of that from the 1st to 17th. Usually, their economic

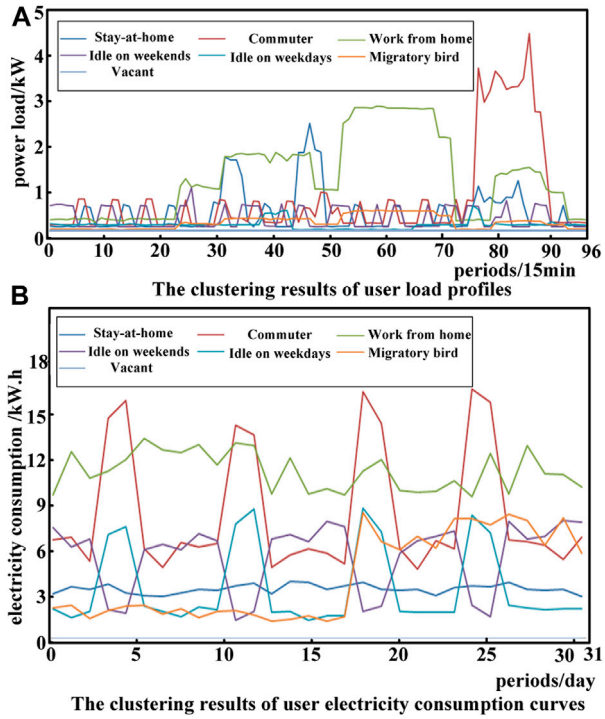

FIGURE 3
(A, B) Typical load profiles and daily electricity consumption curves of RDA users.

conditions are good and their willingness to participate in DR is not high.

(7) Vacant type

As shown in Figures 3A, B, these users have no data. Therefore, they are not considered.

4.2 Classification accuracy of RDA users

In order to ensure the fairness of user classification, experts are invited to classify users based on the typical classification specifications of the Community Housing Industry Association. The results are used as the benchmark to evaluate the classification accuracy. In addition, the proposed method is compared with the fuzzy c-means (FCM) method. Classification accuracy is defined as the degree of overlap with the benchmark result. A total of 500, 1,000, 2000, 3,000, 4,000, and 5,000 users are respectively used to verify the accuracy of the improved k-means clustering method proposed in this paper. The comparison of the results is shown in Figure 4.

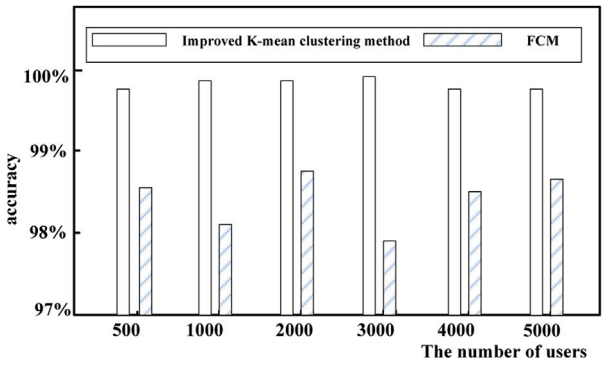

FIGURE 4
Accuracy of the classification result.

As can be seen from Figure 4, the accuracy of the improved k-means clustering method is 99.8%, while the accuracy of the FCM clustering method is 98.4%. This is because FCM determines the category that an RDA user belongs to through the membership function. When users of different types are unbalanced, i.e., the number of users in a certain cluster is much greater than the number of users in other clusters, the probability of new users being misclassified into a larger cluster will increase, resulting in larger errors.

4.3 RDA user grading results

Except for the 42 vacant users, the remaining 6,078 users are graded. The grading results are shown in Table 8.

In order to make the user scoring system operate effectively, the RDA load aggregator would balance the floating price scales to DR users and will use the fine from users in A6–A10 grades to reward users in A1–A4 grades. From Table 8, there are 3,029 users in A1–A4 grades whose DR benchmark price has

TABLE 7 RDA user classification result.

Type	Comment	The number of users	DR sensitivity
b1	Stay-at-home	596	Relatively high
b2	Commuter	2,275	Relatively high
b3	Work from home	862	high
b4	Idle on weekends	1,558	low
b5	Idle on weekdays	413	Relatively low
b6	Migratory bird	374	Very low
b7	Vacant	42	NA

TABLE 8 Grading results of RDA users.

Grade	Score range	The number of users
A1	90 to 100	67
A2	80 to 89	782
A3	70 to 79	1,193
A4	61 to 69	987
A5	60	17
A6	50 to 59	1,275
A7	40 to 49	681
A8	30 to 39	516
A9	20 to 29	479
A10	0 to 19	81

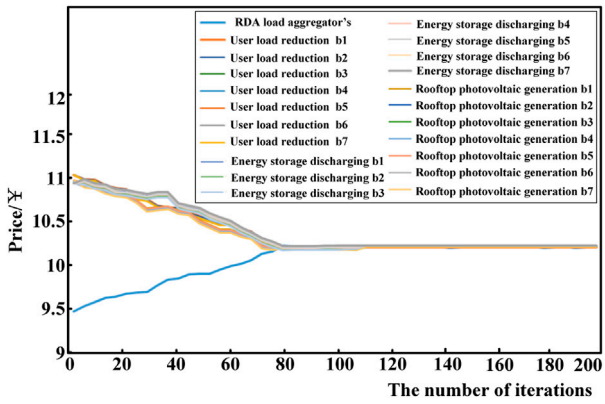

FIGURE 5
RDA demand response pricing game.

been increased and 3,032 users in A6–A10 grades whose DR benchmark price has been decreased. The number of users whose DR benchmark price has been increased is close to that of users whose DR benchmark price has been decreased, ensuring that the scoring system operates effectively. In addition, there are 17 users of A5 grade, whose DR benchmark price remains unchanged.

4.4 RDA demand response game-based pricing

The real-time DR price to the RDA load aggregator is 12 yuan/kWh, and the DR benchmark price is set as 9 yuan/kWh (Tu et al., 2020). On the basis of RDA classification, namely b1–b7 types, RDA users participate in DR load reduction, load reduction, rooftop photovoltaic generation, and energy storage discharging. The RDA aggregator updates the DR compensation price until the Nash equilibrium is reached. The process of the pricing game is shown in Figure 5.

As shown in Figure 5, the RDA load aggregator's initial DR price bidding is 9.5 yuan, and users in categories b1–b7 follow the load aggregator's bidding for load reduction, rooftop photovoltaic generation, and energy storage discharging. The price range is between 10.9 yuan and 11.2 yuan. The load aggregator increases the price based on the price bids of b1–b7 users. This process repeats until the Nash equilibrium is reached after 80 iterations. The price corresponding to the equilibrium is 10.42 yuan/kWh.

With the Nash equilibrium, the final prices to RDA users in categories b1–b7 are adjusted based on the floating price scales according to their grades. Based on the DR base price of 10.42 yuan, the DR prices of different users are shown in Table 9.

4.5 Analysis of the RDA load profile

For simplicity, only the load profile of a transformer distribution area load aggregator is analyzed in this section. Comparisons are carried out with data of 21 June 2021. The method proposed in this paper is compared with the potential game method, the hidden Markov method, and the Monte Carlo method. The RDA load profiles are shown in Figure 6.

As shown in Figure 6, the transformer is overloaded during 9:30 to 10:00. The RDA load aggregator implements the emergency load control strategy to reduce the RDA load within the normal operating range of the distribution transformer. The RDA load aggregator participates in DR from 18:00 to 20:30. As shown in Figure 6, the load with the Monte Carlo method is higher, indicating that the DR effect is the worst. By comparison, the load with the proposed method is the lowest, which shows that it provides the best incentive to users in participating in DR.

4.6 Comparative analysis of RDA load aggregator incomes

The income of the RDA load aggregator in this demonstration residential area on 21 June 2021 is studied and compared with the results for the other three methods. The DR price to the RDA load aggregator from the main power is 12 yuan/kWh. The DR price from the load aggregator to users is 10.42 yuan/kWh. The aggregator's income is equal to the price difference. The comparison results are shown in Table 10.

As shown by the RDA load profile in Figure 6; Table 10, the load analyzed by the Monte Carlo method is obviously higher and the amount of electricity in DR is the least, 7,857 kWh. The load aggregator's income is 9,700 yuan, which is the lowest among the four methods. The load profiles from the potential game and the hidden Markov method are higher than that from the Monte Carlo method. The amounts of electricity in DR are 8,236 kWh and 9,462 kWh. The RDA load aggregator's incomes are 10,200 yuan and 11,700 yuan. The proposed method achieves the lowest load and maximizes the amount of electricity in DR power as 13,027 kWh. The load aggregator's income is

TABLE 9 Adjusted DR prices to RDA users of different types.

Grade	Credit range	Category/DR price bids (yuan)						
		b1	b2	b3	b4	b5	b6	b7
A1	90–100	12.61	12.40	12.71	12.50	12.30	12.71	12.82
A2	80–89	11.57	11.67	11.46	11.67	11.77	11.88	11.57
A3	70–79	10.95	10.97	10.95	10.96	10.98	10.99	10.95
A4	61–69	10.74	10.74	10.75	10.73	10.76	10.77	10.78
A5	60	10.42	10.42	10.42	10.42	10.42	10.42	10.42
A6	50–59	10.12	10.12	10.13	10.14	10.13	10.15	10.12
A7	40–49	9.92	9.91	9.90	9.92	9.93	9.95	9.94
A8	30–39	9.48	9.59	9.69	9.49	9.50	9.51	9.52
A9	20–29	8.87	8.88	8.86	8.87	8.87	8.88	8.86
A10	0–19	8.54	8.65	8.39	8.42	8.37	8.34	8.49

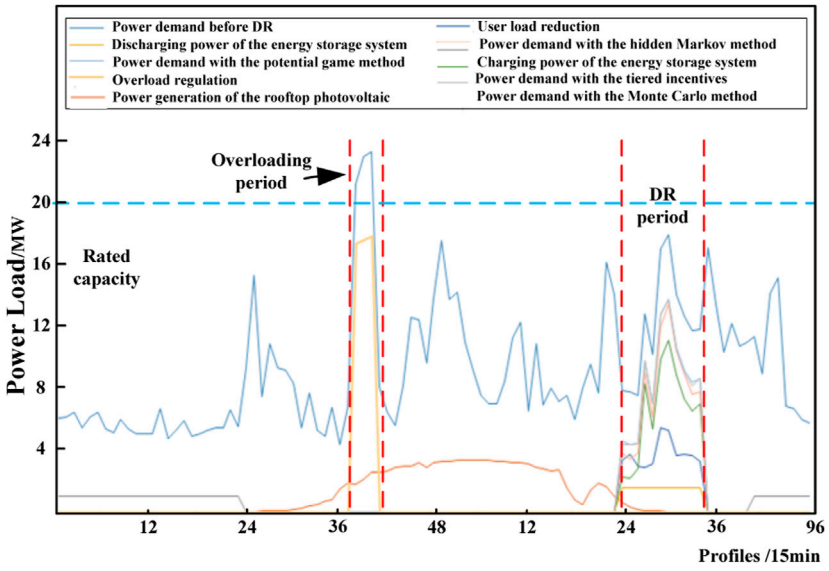

FIGURE 6
Load profile of the regional RDA load aggregator.

TABLE 10 Income comparison results.

Method	Electricity	Income (10^3 yuan)
The proposed method	13,027	2.06
Potential game	8,236	1.02
Hidden Markov method	9,462	1.17
Monte Carlo method	7,857	0.97

20,600 yuan, which is the highest among the four methods. Compared with the potential game, the hidden Markov, and the Monte Carlo methods, the income is, respectively, increased by 101.96%, 76.07%, and 112.37%.

4.7 Comparative analysis of RDA user incomes

Similarly, the smaller the user's load, the greater the amount of electricity in DR; conversely, the larger the user's load, the smaller the amount of electricity in DR. The comparison results of the incomes of RDA users in different grades are shown in Table 11. It can be seen from Figure 5 and Table 11 that the load from the Monte Carlo method is the highest, leading to the lowest income of 81,870 yuan. The loads from the potential game method and the hidden Markov method are higher than that from the Monte Carlo method. The RDA users' incomes are 87,380 yuan and 98,590 yuan. The proposed method gives the lowest load and the highest user income, which is 135,010 yuan. Compared with the potential game,

TABLE 11 Comparison of the incomes of RDA users.

Grade	Number of users	The proposed method		Potential game		Hidden Markov method		Monte Carlo method	
		Electricity (kWh)	Income (10^3 yuan)	Electricity (kWh)	Income (10^3 yuan)	Electricity (kWh)	Income (10^3 yuan)	Electricity (kWh)	Income (10^3 yuan)
A1	67	151	0.189	89	0.094	92	0.096	72	0.075
A2	782	1,507	1.727	997	1.058	1,137	1.185	895	0.933
A3	1,193	2,672	2.951	1,620	1.719	1812	1.888	1727	1.800
A4	987	2017	2.165	1,295	1.374	1,352	1.409	1,308	1.363
A5	17	58	0.060	31	0.033	38	0.040	29	0.030
A6	1,275	2,972	3.004	1,698	1.802	1873	1.952	1,519	1.583
A7	681	1,236	1.224	892	0.946	1,237	1.289	779	0.812
A8	516	1,127	1.057	877	0.930	929	0.968	814	0.848
A9	479	976	0.864	632	0.671	846	0.882	672	0.700
A10	81	311	0.259	105	0.111	146	0.152	42	0.044
Total	6,078	13,027	13.501	8,236	8.738	9,462	9.859	7,857	8.187

the hidden Markov, and the Monte Carlo methods, the income is, respectively, increased by 54.51%, 36.94%, and 64.91%.

5 Conclusion

Focusing on the problem of insufficient demand response incentives for multiple types of RDA users, a demand-side aggregated response method based on tiered incentive price is proposed. The proposed method is to improve the DR benefit of both load aggregators and users in the RDA. By classifying and grading users in the RDA, tiered incentives for users of different grades are provided to increase their enthusiasm for participating in DR. The case study shows a better performance of the proposed method compared to other demand response methods such as the potential game method, the hidden Markov method, and the Monte Carlo method. Specifically, the results demonstrate that the proposed user clustering method has an accuracy of 99.8% in classifying users in a residential distribution area. Compared with the potential game, the hidden Markov method, and the Monte Carlo method, from the results, the income of load aggregators is increased by 101.96%, 76.07%, and 112.37%, respectively, and the income of the users is increased by 54.51%, 36.94%, and 64.91%, respectively. Our future work is to improve the demand response capability of the entire RDA.

Data availability statement

The raw data supporting the conclusion of this article will be made available by the authors, without undue reservation.

Author contributions

DT: methodology, software, supervision, and writing–original draft. QZ: supervision and writing–review and editing. TM: software and writing–review and editing. YO: data curation and writing–review and editing. LW: data curation, software, and writing–review and editing. JT: software and writing–review and editing.

Funding

The author(s) declare that no financial support was received for the research, authorship, and/or publication of this article.

Conflict of interest

Authors DT, QZ, YO, LW, and JT were employed by Aostar Information Technology Co., Ltd.

The remaining author declares that the research was conducted in the absence of any commercial or financial relationships that could be construed as a potential conflict of interest.

Publisher's note

All claims expressed in this article are solely those of the authors and do not necessarily represent those of their affiliated organizations, or those of the publisher, the editors, and the reviewers. Any product that may be evaluated in this article, or claim that may be made by its manufacturer, is not guaranteed or endorsed by the publisher.

References

Avordeh, T. K., Gyamfi, S., and Opoku, A. A. (2022). The role of demand response in residential electricity load reduction using appliance shifting techniques. *Int. J. Energy Sect. Manag.* 16 (4), 605–635. doi:10.1108/ijesm-05-2020-0014

Baek, K., Lee, E., and Kim, J. (2021). Resident behavior detection model for environment responsive demand response. *IEEE Trans. smart grid* 12 (5), 3980–3989. doi:10.1109/tsg.2021.3074955

Chen, L., Xu, Q. S., Yang, Y. B., Gao, H., and Xiong, W. (2022). Community integrated energy system trading: a comprehensive review. *J. Mod. Power Syst. Clean Energy* 10 (6), 1445–1458. doi:10.35833/mpce.2022.000044

Duan, Q. G., Chen, Y. C., Wang, Y., Wu, M. X., Bie, P., and Dong, P. (2021). Trading mechanism and clearing model of incentive demand response in electricity spot market. *Electr. Power Constr.* 42 (6), 145–156. doi:10.12204/j.issn.1000-7229.2021.06.015

Fan, R., Sun, R. J., and Liu, Y. T. (2022). A load restoration amount reduction method considering demand response of air conditioning loads. *Trans. China Electrotech. Soc.* 37 (11), 2869–2877. doi:10.19595/j.cnki.1000-6753.tces.210633

Gharibshah, Z., and Zhu, X. Q. (2022). User response prediction in online advertising. *ACM Comput. Surv.* 54 (3), 1–43. doi:10.1145/3446662

Guo, K. J., Gao, C. W., Lin, G. Y., Lu, S. X., and Feng, X. F. (2020). Optimization strategy of incentive based demand response for electricity retailer in spot market environment. *Automation Electr. Power Syst.* 44 (15), 28–35. doi:10.7500/AEPS20190726002

Hassanniakheibari, M., Hosseini, S. H., and Soleymani, S. (2020). Demand response programs maximum participation aiming to reduce negative effects on distribution networks. *Int. Trans. Electr. Energy Syst.* 30 (8), 1–14. doi:10.1002/2050-7038.12444

Hong, Y., Liu, Y. J., Xu, Q. S., Yin, H. Y., Huang, Y., and Hu, Y. (2020). Hybrid targeted demand response strategy of electric vehicles based on integral system and time-of-use electricity price. *Electr. Power Autom. Equip.* 40 (11), 106–114. doi:10.16081/j.epae.202007017

Huang, C., Huang, J. L., Jia, Y. Q., and Xu, J. (2023). A hybrid Aquila optimizer and its K-means clustering optimization. *Trans. Inst. Meas. Control* 45 (3), 557–572. doi:10.1177/01423312221111607

Huang, K., Hao, S. P., Song, G., Le, J. Y., Wu, Q., and Zhang, X. L. (2020). Layered optimization of AC/DC hybrid microgrid with three-port power electronic transformer. *Electr. Power Autom. Equip.* 40 (3), 37–43. doi:10.16081/j.epae.202003003

Kadadha, M., and Otrok, H. (2021). A blockchain-enabled relay selection for QoS-OLSR in urban VANET: a Stackelberg game model. *Ad hoc Netw.* 117, 102502–102511. doi:10.1016/j.adhoc.2021.102502

Klaucke, F., Hoffmann, C., Hofmann, M., and Tsatsaronis, G. (2020). Impact of the chlorine value chain on the demand response potential of the chloralkali process. *Appl. energy* 276 (15), 115366. doi:10.1016/j.apenergy.2020.115366

Liu, H., Zhao, W., Wen, K. H., He, H. J., Li, S. S., and Huang, S. L. (2022a). Construction scheme and realization of modularized intelligent fusion terminal in low-voltage distribution station areas. *Electr. Meas. Instrum.* 59 (1), 168–175. doi:10.19753/j.issn1001-1390.2022.01.023

Liu, Z. H., Li, Y. M., and Shi, S. D. (2022b). Impulsive noise suppressing method in power line communication system using sparse iterative covariance estimation. *Radio Sci.* 57 (4), 1–8. doi:10.1029/2022rs007424

Liu, Z. Y., Liu, Z. F., Zhao, H. Y., and Wu, Y. (2020). Intelligent socket design based on STM32 and GSM Technology. *Automation Instrum.* 35 (1), 95–99. doi:10.19557/j.cnki.1001-9944.2020.01.021

Pan, Y., Cheng, X. D., Gao, M. Y., Fu, Y., Feng, J., Ahmed, H., et al. (2020). Dual-functional multichannel carbon framework embedded with CoS2 nanoparticles: promoting the phase transformation for high-loading Li-S batteries. *ACS Appl. Mater. interfaces* 12 (29), 32726–32735. doi:10.1021/acsami.0c07875

Preeti, V., Seethalekshmi, K., and Bharti, D. (2022). A cooperative approach of frequency regulation through virtual inertia control and enhancement of low voltage ride-through in DFIG-based wind farm. *J. Mod. Power Syst. Clean Energy* 10 (6), 1519–1530. doi:10.35833/mpce.2021.000092

Qi, B., Zheng, S. L., Sun, Y., Li, B., Tian, S. M., and Shi, K. (2022). A model of incentive-based integrated demand response considering dynamic characteristics and multi-energy coupling effect of demand side. *Proc. CSEE* 42 (5), 1783–1798. doi:10.13334/j.0258-8013.pcsee.202351

Rashidizadeh-kermani, H., Vahedipourdahraie, M., Shafie-khah, M., and Siano, P. (2020). A regret-based stochastic bi-level framework for scheduling of DR aggregator under uncertainties. *IEEE Trans. Smart Grid* 11 (4), 3171–3184. doi:10.1109/tsg.2020.2968963

Ren, H., Lu, H. T., Lu, J. L., and Jin, Z. P. (2020). Analysis of LA demand response characteristics considering cyber physical system coupling and user's response difference. *Power Syst. Technol.* 44 (10), 3927–3936. doi:10.13335/j.1000-3673.pst.2019.1202

Sang, B., Zhang, T., Liu, Y. J., Chen, Y. D., Liu, L. S., and Wang, R. (2020). Theories, energy management system research of multi-microgrid: a review. *Proc. CSEE* 40 (10), 3077–3092. doi:10.13334/j.0258-8013.pcsee.191436

Sheng, H. Z., Wang, C. F., Li, B. W., Liang, J., Yang, M., and Dong, Y. (2021). Multi-timescale active distribution network scheduling considering demand response and user comprehensive satisfaction. *IEEE Trans. Industry Appl.* 57 (3), 1995–2005. doi:10.1109/tia.2021.3057302

striani, A., Y, L., Shafiullah, G. M., and Shahnia, F. (2021). Incentive determination of a demand response program for microgrids. *Appl. energy* 292 (15), 116624. doi:10.1016/j.apenergy.2021.116624

Sun, Y., Hu, Y. J., Zheng, S. L., Li, B., and Qi, B. (2022). Integrated demand response optimization incentive strategy considering users' response characteristics. *Proc. CSEE* 42 (4), 1402–1412. doi:10.13334/j.0258-8013.pcsee.202244

Tan, Z. K., and Zeng, M. (2022). Real-time demand response theory based on load regulation capability model. *South. Power Syst. Technol.* 16 (1), 58–66. doi:10.13648/j.cnki.issn1674-0629.2022.01.006

Torff, B., Kimmons, K., Budris, A., Solosky, E., Maqsood, J., Benincasa, J., et al. (2020). Response, demand, and control: evaluating a three-factor model and measure of teachers' interactional styles. *Microbiol. Mol. Biol. Rev.* 84 (2), 140–149. doi:10.1080/00131725.2020.1702434

Tu, J., Zhou, M., Li, G. Y., and Luan, K. N. (2020). A potential game based distributed optimization strategy for the electricity retailer considering residential demand response. *Proc. CSEE* 40 (2), 400–410. doi:10.13334/j.0258-8013.pcsee.190093

Urban, J. J., Menon, A. K., Tian, Z. T., Jain, A., and Hippalgaonkar, K. (2019). New horizons in thermoelectric materials: correlated electrons, organic transport, machine learning, and more. *J. Appl. Phys.* 125 (18), 1–11. doi:10.1063/1.5092525

Wan, C., and Song, Y. H. (2021). Theories, methodologies and applications of probabilistic forecasting for power systems with renewable energy sources. *Automation Electr. Power Syst.* 45 (1), 2–16. doi:10.7500/AEPS20200811008

Wang, B. B., Xu, P., Wang, X. Y., Zhang, H., and Ning, P. (2022a). Distributionally robust modeling of demand response and its large-scale potential deduction method. *Automation Electr. Power Syst.* 46 (3), 33–41. doi:10.7500/AEPS20210622002

Wang, L., Liu, Y., Li, W. F., Zhang, J., Xu, L. X., and Xin, Z. M. (2022b). Two-Stage power user classification method based on digital feature portraits of power consumption behavior. *Electr. Power Constr.* 43 (2), 70–80. doi:10.12204/j.issn.1000-7229.2022.02.009

Wei, Z. B., Zhang, H. T., Wei, P. Y., Liang, Z., Ma, X. R., and Sun, Z. B. (2021). Two-stage optimal dispatching for microgrid considering dynamic incentive-based demand response. *Power Syst. Prot. Control* 49 (19), 1–10. doi:10.19783/j.cnki.pspc.201605

Xu, H. S., Lu, J. X., Yang, Z. H., Li, J., Lu, J., Jun, et al. (2021). Decision optimization model of incentive demand response based on deep reinforcement learning. *Automation Electr. Power Syst.* 45 (14), 97–103. doi:10.7500/AEPS20200208001

Yang, X. P., Zhang, F. F., Xie, Q., Zhang, M., and Gao, M. H. (2022). Situation orientation method of active distribution network based on incentive demand response. *Acta Energiae Solaris Sin.* 43 (3), 133–140. doi:10.19912/j.0254-0096.tynxb.2020-0587

Zhang, G., Xue, S., Fan, M. H., and Zhang, H. (2021). Theories, design of demand-response market mechanism in accordance with China power market. *Electr. Power Constr.* 42 (4), 132–140. doi:10.12204/j.issn.1000-7229.2021.04.015

Zhang, L. L., Gang, D. U., Jun, W. U., and Ma, Y. J. (2020). Joint production planning, pricing and retailer selection with emission control based on Stackelberg game and nested genetic algorithm. *Expert Syst. Appl.* 161, 1–11. doi:10.1016/j.eswa.2020.113733

Zhao, J. Q., Xia, X., Liu, Z. W., Xu, C. L., Su, D. W., and San, X. (2020). User electricity consumption feature selection and behavioral portrait. *Power Syst. Technol.* 44 (9), 3488–3496. doi:10.13335/j.1000-3673.pst.2019.2138

Zheng, R. N., Li, Z. H., Tang, Y. J., Ni, C. W., Li, G. J., and Han, P. (2022). Incentive demand response model and evaluation considering uncertainty of residential customer participation degree. *Automation Electr. Power Syst.* 46 (8), 154–162. doi:10.7500/AEPS20210404001

Zhong, Z. Q., Cheng, H. S., Cai, H., Zhang, H. H., and Jiang, Y. L. (2021). A coordinated control strategy and implementation of household microgrid based on time-of-use electricity price and demand response. *Mod. Electr. Power* 38 (1), 69–78. doi:10.19725/j.cnki.1007-2322.2020.0101

frontiers | Frontiers in Energy Research

TYPE Correction
PUBLISHED 04 March 2024
DOI 10.3389/fenrg.2024.1389821

OPEN ACCESS

APPROVED BY
Frontiers Editorial Office,
Frontiers Media SA, Switzerland

*CORRESPONDENCE
Donglai Tang,
tangdonglai@sohu.com

RECEIVED 22 February 2024
ACCEPTED 23 February 2024
PUBLISHED 04 March 2024

CITATION
Tang D, Zhang Q, Ma T, Ou Y, Wu L and Tang J (2024), Corrigendum: Aggregated demand-side response in residential distribution areas based on tiered incentive prices.
Front. Energy Res. 12:1389821.
doi: 10.3389/fenrg.2024.1389821

Corrigendum: Aggregated demand-side response in residential distribution areas based on tiered incentive prices

Donglai Tang[1]*, Qiang Zhang[1], Tiefeng Ma[2], Yuan Ou[1], Lei Wu[1] and Jizhong Tang[1]

[1]Aostar Information Technology Co., Ltd, Chengdu, China, [2]School of Statisncs Southwestern University of Finance and Economics, Chengdu, China

KEYWORDS

tiered incentives, residential distribution areas, demand response, leader-follower game, adjustable load

A Corrigendum on
Aggregated demand-side response in residential distribution areas based on tiered incentive prices

by Tang D, Zhang Q, Ma T, Ou Y, Wu L and Tang J (2024). Front. Energy Res. 12:1352356. doi: 10.3389/fenrg.2024.1352356

In the published article, the **Author's name** was incorrectly written as Donglail Tang. The correct spelling is Donglai Tang.

The authors apologize for this error and state that this does not change the scientific conclusions of the article in any way. The original article has been updated.

Publisher's note

All claims expressed in this article are solely those of the authors and do not necessarily represent those of their affiliated organizations, or those of the publisher, the editors and the reviewers. Any product that may be evaluated in this article, or claim that may be made by its manufacturer, is not guaranteed or endorsed by the publisher.

frontiers | Frontiers in Energy Research

TYPE Methods
PUBLISHED 22 February 2024
DOI 10.3389/fenrg.2024.1343309

OPEN ACCESS

EDITED BY
Yaser Qudaih,
Higher Colleges of Technology, United Arab Emirates

REVIEWED BY
Maneesh Kumar,
Indian Institute of Technology Roorkee, India
Mohd Sharizal Alias,
Higher Colleges of Technology, United Arab Emirates

*CORRESPONDENCE
Juhua Hong,
742475603@qq.com

RECEIVED 23 November 2023
ACCEPTED 05 February 2024
PUBLISHED 22 February 2024

CITATION
Hong J, Zhang L, Hu Z, Lin W and Zou Y (2024), A robust system model for the photovoltaic in industrial parks considering photovoltaic uncertainties and low-carbon demand response.
Front. Energy Res. 12:1343309.
doi: 10.3389/fenrg.2024.1343309

A robust system model for the photovoltaic in industrial parks considering photovoltaic uncertainties and low-carbon demand response

Juhua Hong*, Linyao Zhang, Zhenda Hu, Weiwei Lin and Yichao Zou

State Grid Fujian Electric Power Co Ltd., Economic and Technological Research Institute, Fuzhou, China

Against the backdrop of carbon peaking and carbon neutrality initiatives, industrial parks have the potential to mitigate external electricity procurement and reduce carbon emissions by incorporating photovoltaic and energy storage systems. However, the inherent unpredictability in photovoltaic power generation poses notable challenges to the optimal planning of industrial parks. In light of this, the present study proposes a robust planning model for the distribution of photovoltaic and energy storage systems within industrial estates, taking into account uncertainties in photovoltaic output and low-carbon demand response. The primary objective of the model is to minimize the yearly comprehensive cost of the industrial park. It is grounded in the carbon emission flow theory, utilizing dynamic carbon emission factors calculated throughout the year as the pricing basis for real-time electricity rates informed by demand response. Subsequently, historical photovoltaic output data are employed to formulate typical output scenarios and their probability distributions through scenario clustering. These norms and constraints serve to bind the associated uncertainty probabilities. Consequently, a two-stage distribution robust model for the photovoltaic and energy storage system is established, employing a data-driven methodology. The efficacy of the proposed model is substantiated through a case simulation of an industrial park utilizing the CPLEX commercial solver. This approach not only underscores the importance of addressing uncertainties in photovoltaic power generation for industrial park planning but also showcases a practical application of the developed model.

KEYWORDS

photovoltaic uncertainty, low-carbon demand response, two-stage distribution robust, industrial park planning, CPLEX photovoltaic uncertainty, CPLEX

1 Introduction

The total carbon emissions from the electricity industry account for more than 40% of the total carbon emissions in society, making it a pioneer in achieving China's dual-carbon goals. As electricity-intensive areas, industrial estates need to urgently consider how to reduce their carbon emissions (Han et al., 2021).

On one hand, the establishment of a solar-storage power generation system within an industrial park, coupled with the integration of green electricity, presents an opportunity to

mitigate carbon emissions attributable to the consumption of externally procured electrical power. However, the uncertainty of photovoltaic output will have a significant impact on the capacity system of the solar-storage power generation system within the park (Zhi et al., 2017). On the other hand, based on the traditional price–demand response, superimposing electricity prices during peak and off-peak periods and using the TV-viewing angle to determine real-time electricity prices, it is believed that less electricity consumption in the park means eco-friendly environmental protection. However, in reality, because the combination of generating units at each moment is different, the carbon emissions caused by each unit of electricity produced at each moment are different. The carbon emission profile of the power-generating unit is decoupled from the load curve. Consequently, there is a need to institute an eco-friendly demand response framework rooted in a user-centric carbon perspective. This approach is essential for effectively addressing the dual-carbon targets. Therefore, it is of great significance to integrate the system and configuration of solar storage in industrial estates, taking into account the unpredictability associated with photovoltaic systems and the demand response characterized by low carbon emissions.

Currently, the research on photovoltaic uncertainty mainly focuses on three methods: stochastic optimization (Zhu et al., 2021; Li et al, 2022a), robust optimization (Gao et al., 2017; Qiu et al., 2020; Fan et al., 2018), and distributed robust optimization (Chen et al., 2021; He et al., 2019; Ruan et al., 2019; He et al., 2020). Li et al. (2020) used stochastic optimization to optimize the energy storage configuration requirements for various random scenarios, and based on the probability distribution of each typical scenario, the optimal configuration of grid-side energy storage was achieved. Stochastic optimization algorithms mainly use probability to describe the characteristics of uncertain parameters and generate a large amount of discrete data. However, in practical situations, it is not easy to obtain accurate probability distributions. Xue et al. (2022) used robust optimization to constrain the disturbance of photovoltaic output uncertainty using a box uncertainty set and optimize the capacity configuration of solar storage in the park. Robust optimization algorithms are complicated to determine the description of uncertain constraint sets and mainly rely on boundary parameters to express, often leading to either too conservative or aggressive decisions. Yue et al. (2018) used a two-stage distributed robust algorithm to construct an optimization scheduling model driven by data. The worst-case optimal solution was considered, and a column-and-constraint generation (CCG) algorithm was used to solve the problem, improving the acceptance of clean energy by the energy system. The distributed robust optimization algorithm combines the advantages of stochastic and robust optimization algorithms. It does not require accurate probability distribution and can be driven by historical data to find the worst solutions that meet the confidence interval's probability distribution. It can effectively solve problems such as power system and scheduling, ensuring the solution's accuracy and robustness.

Currently, with the proposal of the dual-carbon goal, many scholars are researching how to effectively quantify the carbon emissions of each enterprise in the electricity sector and clarify the carbon emission responsibilities of each link. Zhang et al. (2013) proposed an industrial park carbon emission accounting method that uses the electricity region's carbon emission factor to calculate enterprises' carbon emissions based on their location. This method is convenient for statistics and is simple to calculate. However, the regional carbon emission factor is slow to update, and in the face of more and more new energy generators' access, the accuracy and effectiveness of this regional carbon emission factor are lacking. Zhou et al. (2012) proposed a primary calculation method for the carbon emission flow of the power system based on the connection between carbon emission flow and power flow calculation. Wang et al. (2022) proposed a real-time carbon flow calculation method based on network power decomposition, which overcomes the traditional method's inability to ensure fair carbon flow distribution and effectively solves the problem of quantifying the decarbonization contribution of new energy. Based on the carbon emission flow theory, the carbon flow can be clarified, and it has a certain timeliness. Combining the theory of carbon emission flow with calculating carbon emission factors can more accurately quantify the carbon emissions of various links in the power system (Li et al., 2022a).

In summary, the aim of this paper is to devise a resilient system and arrangement for solar energy storage in industrial complexes, taking into account uncertainties in photo-voltaic systems and responses to eco-friendly demands. First, to tackle the matter of ambiguous carbon emission responsibilities among electricity users during different time intervals, a time-varying dynamic carbon emission coefficient is established, which is built upon the carbon emission flow theory. This dynamic carbon emission factor is then incorporated into the demand response pricing mechanism to achieve a response that aligns with eco-friendly objectives. Second, an optimization objective is formulated for comprehensive cost minimization, encompassing yearly investment, maintenance, electricity purchase, gas procurement, electricity sales revenue, and carbon emission costs. The model for the industrial park's solar energy storage system integrates restrictions like budget constraints, grid transmission power constraints, power balance constraints, energy storage limitations, electricity price restrictions, and demand response constraints.

Historical data are used to obtain typical output scenarios and their probability distributions through scenario clustering to deal with the variability in photovoltaic output. The uncertainty probability is constrained by both the 1-norm and the infinity norm, and a two-stage distribution robust system model is constructed, which is tackled using the CCG algorithm to obtain the optimal system solution. Finally, the model's effectiveness is verified through an industrial park case study.

2 Regional average carbon emission coefficient

Traditional demand response mainly starts from the electricity perspective, using the difference between generation and consumption as the pricing rule, mainly solving the reliability problem caused by the system supply–demand balance. However, in the context of dual-carbon targets, it is necessary to start from the carbon perspective, clarify the direction of carbon emissions based on carbon emission flow theory, and obtain the dynamic carbon emission coefficient at different times. By superimposing the

dynamic carbon emission coefficient on the electricity price, users can be aware of the corresponding carbon emission level of electricity consumption at each time to reduce carbon emissions on the demand side.

Currently, the calculation of carbon emissions caused by the use of electricity is generally obtained using the average within the regional carbon emission coefficient method. The total carbon emissions the user generates throughout the year can be obtained from Equation 1.

$$E_K = \bar{e}_{CO2} \cdot \sum_{t \in Y} Q_{k,t}, \tag{1}$$

where E_k represents the total carbon emissions of user k for the entire year, Y represents a particular year, $Q_{k,t}$ represents the electricity consumption of user k at time t, and $\bar{e}_{CO2}$ represents the average carbon emission coefficient of the region where user k is located. The average carbon emission coefficient of the region can be obtained by the following formula Eq. 2):

$$\bar{e}_{CO2,i} = \frac{E_{Call,i} + \sum_{j \in Z} \left(\bar{e}_{CO2,j} \times Q_{Call,ji} \right)}{Q_{Call,i} + \sum_{j \in Z} Q_{Call,ji}}, \tag{2}$$

where $\bar{e}_{CO2,i}$ and $\bar{e}_{CO2,j}$ represent the average carbon emission factors of the regional power grids i and j, respectively; $E_{Call,i}$, $Q_{Call,i}$, and $Q_{Call,ji}$ represent the CO_2 direct emissions, the total yearly power generation, and the total electricity transmitted from the regional power grid j to i, respectively; represents the set of regional power grids.

The carbon dioxide emissions from power generation within the geographical coverage of the regional power grid i can be obtained by Equation 3.

$$E_{Call,i} = M_{Fall,i} \times \delta_{f,i}, \tag{3}$$

where $M_{Fall,I}$ represents the total amount of fossil fuels used for power generation within the coverage area of the regional power grid i and $\delta_{f,i}$ represents the carbon emission coefficient of fossil fuels.

The regional average carbon emission coefficient has the advantage of simple calculation. However, the errors generated by this method are increasingly expanding under the current context of large-scale integration of new energy.

With the construction of a new type of power system, the proportion of clean energy from different units at different times within each region also varies. For users, carbon emissions generated at different times have significant spatiotemporal differences, and the regional average carbon emission factor cannot sufficiently represent these differences.

3 Time-varying dynamic carbon emission coefficient derived from the carbon emission flow theory across various time periods

Currently, the calculation of carbon emissions in the electricity industry is mainly focused on the power generation side. However, in reality, due to the "generation follows load" characteristic of the power system, electricity consumption on the demand side is the leading cause of carbon emissions. Therefore, carbon emissions generated by the power generation side should be jointly borne by both the supply side and the demand side.

The carbon emission flow theory of the power system can label carbon emissions based on power generation unit information, line flow information, and network loss information, which can effectively clarify the sources and destinations of carbon emissions. In addition, since the theory is based on the time and space characteristics of the flow information for carbon emission traceability and accountability, it can effectively clarify the carbon emissions impact caused by user electricity consumption behavior at different times.

Nonetheless, as the carbon potential derived from the theory is contingent on a singular node, there exists a distinct disparity in carbon potential across different nodes. To adhere to the principle of regional equity, it becomes imperative to compute the average carbon potentials within a specific region. Subsequently, dynamic carbon emission factors are calculated over time and region in accordance with Equation 4.

$$e_{CO2,i,t} = \frac{\sum_{j \in Z} \left(L^{j}_{CO2,i,t} \times \varepsilon^{j}_{CO2,i,t} \right)}{\sum_{j \in Z} L^{j}_{CO2,i,t}}, \tag{4}$$

where $e_{CO2,i,t}$ represents the regional dynamic carbon emission coefficient of region i at time t. $L^{j}_{CO2,i,t}$ is the load at node j at time t, and $\varepsilon^{j}_{CO2,i,t}$ is the carbon potential at node j determined relying on the carbon emission flow theory. Z represents the set of nodes within the regional power grid i.

Utilizing the dynamic carbon emission coefficient specific to the region, the carbon emissions from an individual user at each point in time throughout the year can be determined through the application of the following formula Eq. 5):

$$E^{k}_{CO2,i,t} = e_{CO2,i,t} \times Q_{k,i,t}, \tag{5}$$

where $E^{k}_{CO2,i,t}$ is the carbon emission generated by user k at time t on the ith day and $Q_{k,i,t}$ is the load of user k at time t on the ith day.

4 Formatting the industrial park solar-storage robust system model

4.1 Objective function

This article establishes an objective function with the minimum yearly comprehensive cost of the park, which consists of two parts in total. A part of it is converted into the yearly maintenance and investment costs of the optical storage and power generation equipment. The other part is the yearly cost of purchasing gas, electricity, carbon emissions, and electricity sales revenue, as shown in Equations 6–8.

$$\min F = F_1 + F_2, \tag{6}$$

$$F_1 = F_{\text{yic}} + F_{\text{yr}}, \tag{7}$$

$$F_2 = F_{\text{buye}} + F_{\text{buyg}} - F_{\text{sellein}} + F_{\text{cin}}, \tag{8}$$

where F_1 and F_2 are the yearly investment and maintenance costs, respectively. F_{yic} and F_{yr} are the yearly operating cost and

10.3389/fenrg.2024.1343309

yearly investment cost. F_{buyg}, F_{buye}, F_{cin}, and $F_{sellein}$ are the yearly gas procurement, yearly electricity procurement, yearly approved income generated from the reduction of carbon emissions, and yearly electricity sales income, respectively.

$$F_{\mathrm{yic}} = C_{\mathrm{pv}}E_{\mathrm{pv}}\frac{R_{\mathrm{pv}}\left(1+R_{\mathrm{pv}}\right)^{Y_{\mathrm{pv}}}}{\left(1+R_{\mathrm{pv}}\right)^{Y_{\mathrm{pv}}}-1} + C_{\mathrm{ess}}E_{\mathrm{ess}}\frac{R_{\mathrm{ess}}\left(1+R_{\mathrm{ess}}\right)^{Y_{\mathrm{ess}}}}{\left(1+R_{\mathrm{ess}}\right)^{Y_{\mathrm{ess}}}-1}, \quad (9)$$

$$F_{\mathrm{yc}} = C_{\mathrm{pvr}}E_{\mathrm{pv}}\frac{R_{\mathrm{pv}}\left(1+R_{\mathrm{pv}}\right)^{Y_{\mathrm{pv}}}}{\left(1+R_{\mathrm{pv}}\right)^{Y_{\mathrm{pv}}}-1} + C_{\mathrm{essr}}E_{\mathrm{ess}}\frac{R_{\mathrm{ess}}\left(1+R_{\mathrm{ess}}\right)^{Y_{\mathrm{ess}}}}{\left(1+R_{\mathrm{ess}}\right)^{Y_{\mathrm{ess}}}-1}, \quad (10)$$

$$F_{\mathrm{buye}} = \sum_{s=1}^{N_s} 365 \times P_s \times \sum_{t=1}^{24} P_{s,i,t}^{buye} C_{s,t}^{e} \Delta t, \quad (11)$$

$$F_{\mathrm{buyg}} = \sum_{s=1}^{N_s} 365 \times p_s \times \sum_{t=1}^{24} \left(\partial_2 P_{s,i,t}^{GT} 2 + \partial_1 P_{s,i,t}^{GT} + \partial_0\right) C_{s,t}^{g} \Delta t, \quad (12)$$

$$F_{\mathrm{sellein}} = \sum_{s=1}^{N_s} 365 \times p_s \times \sum_{t=1}^{24} \left(P_{s,i,t}^{selle} C_{s,t}^{se} + P_{s,i,t}^{L} C_{s,t}^{le}\right) \Delta t, \quad (13)$$

$$F_{cin} = \sum_{s=1}^{N_s} 365 \times p_s \times \sum_{t=1}^{24} \left(\left(P_{s,i,t}^{buye} - P_{s,i,t}^{selle}\right)\Delta t\right) \times \varphi_{s,t} \times C_{CO2} \quad (14)$$

where C_{ess} and C_{pv} are the investment costs per unit capacity of energy storage and per unit capacity of photovoltaic investment, respectively. E_{pv} and E_{ess} are the photovoltaic capacity and energy storage capacity, respectively. Rpv, R_{ess}, Y_{pv}, and Y_{ess} are the equivalent yearly investment-related parameters. Ns is a set of all possible scenarios. Ps is the probability that scenario s may occur. $P_{s,i,t}^{buye}$, $P_{s,i,t}^{GT}$, $P_{s,i,t}^{selle}$, and $P_{s,i,t}^{L}$ are the purchased power at time t on day i in scenario s, the generated power of the gas turbine, the power sold to the power grid, and the park load power, respectively. $C_{s,t}^{g}$, $C_{s,t}^{le}$, $C_{s,t}^{se}$, and C_{CO2} are the real-time gas purchase price, real-time electricity selling price for park load, real-time outgoing grid electricity price, and unit carbon trading price at time t under scenario s. $\varphi_{s,t}$ is the carbon emission factor of the regional power grid at time t under scenario s.

Equations 9 and 10 are the calculation formulas for the investment and operating costs, respectively, which are calculated using the yearly equivalent investment cost calculation method.

Equations 11–13 are the yearly electricity procurement, yearly gas procurement, and yearly electricity sales revenue calculated using the scenario probability, respectively. Equation 14 is the carbon emission cost calculated using the scenario probability, which is the product of the difference between purchasing and selling electricity, the price associated with a unit of carbon emissions, and the carbon potential.

4.2 Constraints

The constraints within the model outlined in this article encompass both conventional and eco-friendly considerations. Conventional constraints involve restrictions on investment costs, grid transmission power, power balance, energy storage charging and discharging power, state constraints for energy storage charging, and park load electricity selling prices. The eco-friendly constraints integrate dynamic carbon emission coefficients, utilize carbon emission costs as pricing benchmarks, and incorporate corresponding constraints on electricity prices.

General constraints:

$$C_{ic\_\min} \le C_{\mathrm{pv}}E_{\mathrm{pv}} + C_{\mathrm{ess}}E_{\mathrm{ess}} \le C_{ic\_\max}, \quad (15)$$

$$\begin{cases} P_{\min} \le P_{s,i,t}^{grid} \le P_{\max}, \\ P_{s,i,t}^{grid} = \left|P_{s,i,t}^{buye} - P_{s,i,t}^{selle}\right|, \end{cases} \quad (16)$$

$$P_{s,i,t}^{GT} + P_{s,i,t}^{grid} + P_{s,i,t}^{pv} + P_{s,i,t}^{dis} - P_{s,i,t}^{ch} = P_{s,i,t}^{L}, \quad (17)$$

$$\begin{cases} 0 \le P_{s,i,t}^{ch} \le \beta_{s,i,t}^{ch} P_{ch}^{\max}, \\ 0 \le P_{s,i,t}^{dis} \le \beta_{s,i,t}^{dis} P_{dis}^{\max}, \\ \beta_{s,i,t}^{ch} + \beta_{s,i,t}^{dis} \le 1, \end{cases} \quad (18)$$

$$\begin{cases} E_{s,j,t+1}^{\mathrm{ess}} = E_{s,j,t}^{\mathrm{ess}} + \beta_{s,i,t}^{ch} P_{s,i,t}^{ch} - \beta_{s,i,t}^{dis} P_{s,i,t}^{dis}, \\ 0.1E_{\max} \le E_{s,j,t}^{\mathrm{ess}} \le 0.9E_{\max}, \end{cases} \quad (19)$$

$$\begin{cases} P_{GT}^{\min} \le P_{s,i,t}^{GT} \le P_{GT}^{\max}, \\ P_{s,i,t}^{GT} - P_{s,i,t-1}^{GT} \le R_{GT}^{u}\Delta t, \\ P_{s,i,t-1}^{GT} - P_{s,i,t}^{GT} \le R_{GT}^{d}\Delta t, \end{cases} \quad (20)$$

$$C_{eit}^{\min} < C_{s,t}^{le} \le C_{eit}^{\max}, \quad (21)$$

where $C_{ic\_\min}$, $C_{ic\_\max}$, $C_{eit}^{\min}$, and $C_{eit}^{\max}$ are the minimum investment cost, maximum investment cost, minimum real-time electricity procurement, and maximum real-time electricity purchase price, respectively. $\beta_{s,i,t}^{ch}$, $\beta_{s,i,t}^{dis}$, $E_{s,j,t}^{\mathrm{ess}}$, and $E_{\max}$ are the charging state coefficient, discharge state coefficient, energy storage capacity state, and rated maximum energy storage capacity, respectively. $P_{ch}^{\max}$, $P_{dis}^{\max}$, P_{GT}^{min}, and P_{GT}^{max} are the maximum charging power, maximum discharge power, minimum power of the gas turbine, and maximum power of the gas turbine, respectively.

Equation 15 represents the investment cost constraint. Equation 16 represents the transmission power constraint of the power grid frame. Equation 17 represents the real-time electrical power balance constraint. Equation 18 represents the energy storage state constraint. Equation 19 represents the real-time capacity constraint for energy storage. Equation 20 represents the constraints related to gas turbines. Equation 21 represents the constraints related to electricity prices.

Low-carbon constraints:

$$C_{s,t}^{le} = C_{s,t}^{le,pre} + \varphi_{s,t}C_{CO2}, \quad (22)$$

$$P_{s,i,t}^{L} = P_{s,i,t}^{L,pre}\left[1 + \sum_{t=1}^{24} \frac{\varepsilon_{tt'}\left(C_{s,t}^{le} - C_{s,t}^{le,pre}\right)}{C_{s,t}^{le,pre}}\right], \quad (23)$$

$$\left(1-\underline{\eta}\right) \times P_{s,i,t}^{L,pre} \le P_{s,i,t}^{L} - P_{s,i,t}^{L,pre} \le \left(1+\bar{\eta}\right) \times P_{s,i,t}^{L,pre}, \quad (24)$$

where $C_{s,t}^{le,pre}$ and $C_{s,t}^{le}$ are the real-time reference electricity price and response electricity price at time t under scenario s, respectively. $P_{s,i,t}^{L,pre}$ and $P_{s,i,t}^{L}$ are the reference load power and response load power at time t under scenario s, respectively. $\varepsilon_{tt'}$ is the price elasticity coefficient. $\underline{\eta}$ and $\bar{\eta}$ represent the percentage of load that can be removed and the percentage of load that can be added, respectively. Equation 22 is the pricing rule for electricity prices in response to eco-friendly demands, incorporating carbon emission factors and unit carbon emission prices as the pricing basis. Equation 23 is an equation constraint for calculating the response load using the mutual elasticity coefficient. Equation 24 is the transfer load restriction constraint.

5 Driven distributional robust framework

This article constructs a data-driven, two-stage, distributionally robust system model to address the uncertainty

of photovoltaic power output. The first stage is the investment and maintenance stage, with variables represented by x, including the system capacity sizes of photovoltaics and energy storage. The second stage is the operation stage, intending to minimize the operating cost, given the first-stage plan. The second-stage variables are represented by y_s, including the output of each unit and the charging and discharging status of energy storage in different periods during the simulated operation. The above two-stage distributionally robust system model is expressed in the following matrix form:

$$\min_{x\in X}\left(\boldsymbol{Ax}+\max_{p_s\in\Omega^P}\left(\sum_s^{N_s}p_s\min_{\boldsymbol{y_s}\in\boldsymbol{Y}(\boldsymbol{x},\boldsymbol{\xi_s})}(\boldsymbol{By_s}+\boldsymbol{C\xi_s})\right)\right), \tag{25}$$

$$s.t.\boldsymbol{Dx}\le\boldsymbol{d}, \tag{26}$$

$$\boldsymbol{Ey_s}\le\boldsymbol{e},\forall s, \tag{27}$$

$$\boldsymbol{Fy_s}=\boldsymbol{f},\forall s, \tag{28}$$

$$\boldsymbol{Gx}+\boldsymbol{Hx\xi_s}+\boldsymbol{Jy_s}\le\boldsymbol{g},\forall s, \tag{29}$$

$$\boldsymbol{Ky_s\xi_s}+\boldsymbol{My_s}=\boldsymbol{j},\forall s, \tag{30}$$

where Ω_p represents the set satisfied by P_s and ζ_s represents the unit capacity of photovoltaic output values after scene clustering. In Equation 25, Ax represents the yearly investment and maintenance costs of the photovoltaic-energy storage system F1, and $B_{ys} + C\zeta_s$ represents the yearly operating cost F_2 under the *sth* scenario. Equation 26 represents the investment and operating cost constraints in the first stage, and equations 27 and 28 represent the inequality constraints and equality constraints in the second stage, respectively. Equation 29 represents the inequality constraints between the two-stage variables and the output of photovoltaics and energy storage under discrete scenarios, and Equation 30 represents the equality constraints between the second-stage variables and the demand response.

To ensure that p_s satisfies the true probability distribution, the 1-norm and ∞-norm constraints are added, and the discrete p_s value under the scenario is subject to the following constraint set:

$$\Omega^P=\left\{\{p_s\}\left|\begin{array}{l}p_s\ge0,s=1,\ldots,N_s\\\sum_{s=1}^{N_s}p_s=1\\\sum_{s=1}^{N_s}\left|p_s-p_s^0\right|\le\theta_1\\\max_{1\le s\le N_s}\left|p_s-p_s^0\right|\le\theta_\infty\end{array}\right.\right\}. \tag{31}$$

The variables θ_1 and θ_∞ in the expression, respectively, correspond to the allowed deviation values of the scene probability under the 1-norm and the infinity-norm constraints.

According to ZHAO and GUAN (2016), under distributionally robust system, the scene probability satisfies the confidence constraints.

$$\Pr\left\{\sum_{s=1}^{N_s}\left|p_s-p_s^0\right|\le\theta_1\right\}\ge1-2N_se^{-\frac{2M\theta_1}{N_s}}. \tag{32}$$

$$\Pr\left\{\max_{1\le s\le N_s}\left|p_s-p_s^0\right|\le\theta_1\right\}\ge1-2N_se^{-2M\theta_\infty}. \tag{33}$$

If we want to make the right-hand side of Equations 32 and 33 equal to α_1 and α_∞, respectively, which represent the confidence levels of the probability uncertainty under the 1-norm and infinity-norm constraints, we can follow the following steps:

$$\theta_1=\frac{N_s}{2M}\ln\frac{2N_s}{1-\alpha_1}, \tag{34}$$

$$\theta_\infty=\frac{1}{2N_s}\ln\frac{2N_s}{1-\alpha_\infty}, \tag{35}$$

where the symbol M represents the number of historical data. A transformation is then performed on the absolute value in equations 34 and 35.

Norm constraint:

$$\sum_{s=1}^{N_S}m\le\theta_1, \tag{36}$$

$$\begin{cases}m\ge p_s-p_s^0\\m\ge p_s^0-p_s\end{cases},\forall s, \tag{37}$$

where m is an auxiliary variable.

Infinity-norm constraint:

$$\begin{cases}p_s-p_s^0\le\theta_\infty\\p_s^0-p_s\le\theta_\infty\end{cases},\forall s. \tag{38}$$

TABLE 1 Gas turbine parameters.

∂_1	∂_2	∂_3	P_{GT}^{max}/kW	P_{GT}^{min}/kW
5.635	55*10−3	40*10−6	1,600	400

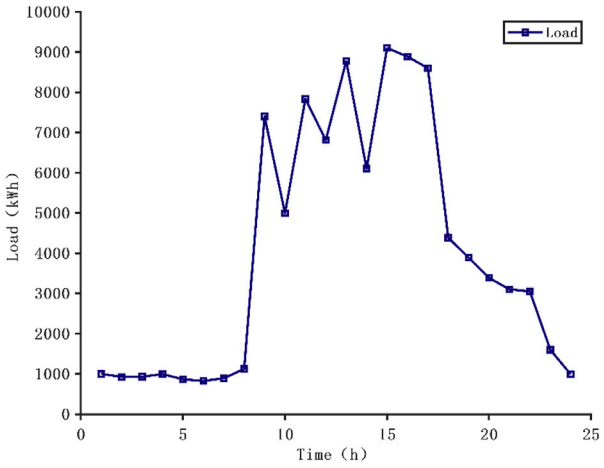

FIGURE 1
Standard daily industrial park electricity demand.

6 Case study

6.1 Configuration of the parameter scenarios

The computational model is resolved utilizing the YALMIP toolbox in MATLAB, along with the commercial solver CPLEX.

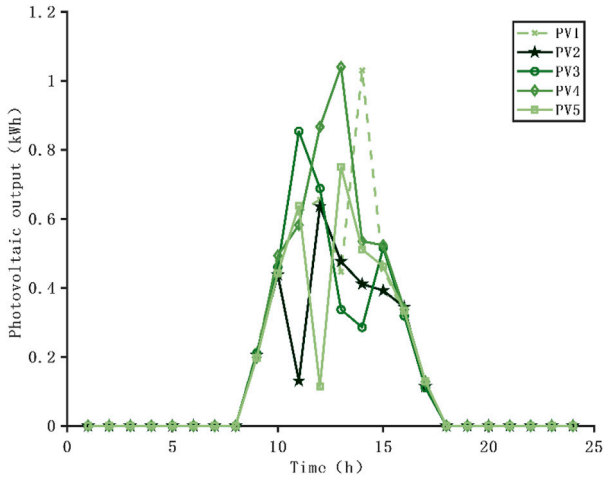

FIGURE 2
Representative photovoltaic scenario post-clustering.

TABLE 2 Electricity purchase price of the park.

Time period	Purchase electricity price (in CNY/kW·h)
Peak period	0.20
Off-peak period	0.63
Valley period	1.05

TABLE 3 Photovoltaic equipment parameters.

Parameter name	Value
Unit capacity price (in CNY/kW)	1,600
Unit capacity yearly operation cost (in CNY/kW·h)	77
Service life (in years)	20
Discount rate	0.05

The CCG algorithm is employed for iterative and staged problem-solving. The industrial park in a southwestern city of China, which includes gas turbine units, is selected as the case study. The relevant parameters of the units are shown in Table 1. The cost of natural gas procured by the park is 0.349 CNY per kilowatt-hour (kWh). Figure 1 illustrates the load curve of the industrial park. In addition, a normal distribution is used to produce errors in the photovoltaic baseline output scenario, with the baseline value as the mean and 0.25 times the baseline value as the variance. Then, 5,000 (K) error scenario data are generated and clustered into five typical scenarios, as shown in Figure 2. The purchasing prices of electricity for the park are shown in Table 2. The grid-connected electricity price for photovoltaics is 0.35 (in CNY/kW·h), and the parameters of the photovoltaic equipment are shown in Table 3. The parameters of the energy storage equipment are shown in Table 4. The dynamic carbon emission factor is calculated according to the method in Li et al. (2022b), and the result is shown in Figure 3. The price elasticity coefficient is selected from DOOSTIZADEH and GHASEMI (2012).

TABLE 4 Parameters related to energy storage.

Parameter name	Value
Unit capacity price (in CNY/kW)	2,000
Unit capacity yearly operation cost (in CNY/kW·h)	5.16
Service life (in years)	10
Discount rate	0.05
Minimum charging power	$0.20E_{max}$
Maximum discharging power	$0.20E_{max}$

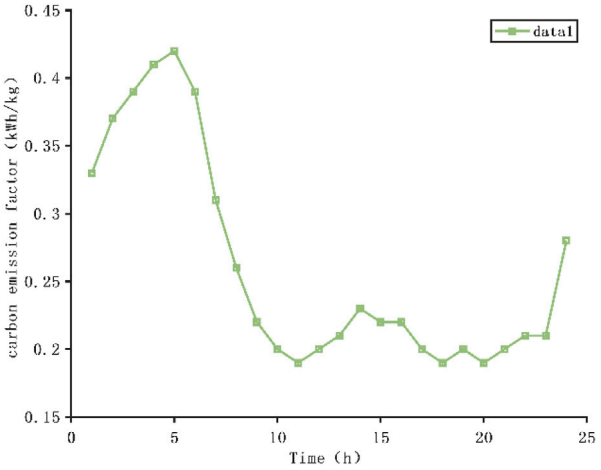

FIGURE 3
Graph depicting the dynamic carbon emission factor over time.

6.2 Figure optimization result analysis

To verify the rationality of the proposed model, this paper conducted a comparative analysis of the following four scenarios:

Scenario 1. A solar-storage power generation system is planned for the park using the random system to consider the photovoltaic uncertainty without considering the eco-friendly demand response.

Scenario 2. A solar-storage power generation system is planned for the park using the distributionally robust system to consider the photovoltaic uncertainty without considering the eco-friendly demand response.

Scenario 3. A solar-storage power generation system is installed in the park using the random system to consider the photovoltaic uncertainty and considering the eco-friendly demand response.

Scenario 4. A solar-storage power generation system is installed in the park using the distributionally robust system to consider the photovoltaic uncertainty and eco-friendly demand response.

10.3389/fenrg.2024.1343309

TABLE 5 Simulation results of each scenario.

Scenario	Investment plan (kW·h)		Various expenses/(10^6 yuan)								
	Photovoltaic capacity	Energy storage capacity	Ratio of energy storage photovoltaic capacity	Investment cost	Power procurement	Gas procurement	Power sales income	Carbon emission cost	Total operating cost	Total carbon emission (10^6kG)
1	7,737	3,810	0.49	2.03	21.61	2.33	25.23	0.25	−1.03	7.23
2	8,090	3,528	0.43	2.00	7.5	0.77	8.62	0.08	1.59	2.46
3	7,918	3,665	0.46	2.00	22.89	2.33	50.05	0.23	−23.06	7.13
4	8,401	3,279	0.39	1.98	7.7	0.76	16.95	0.08	−6.51	2.42

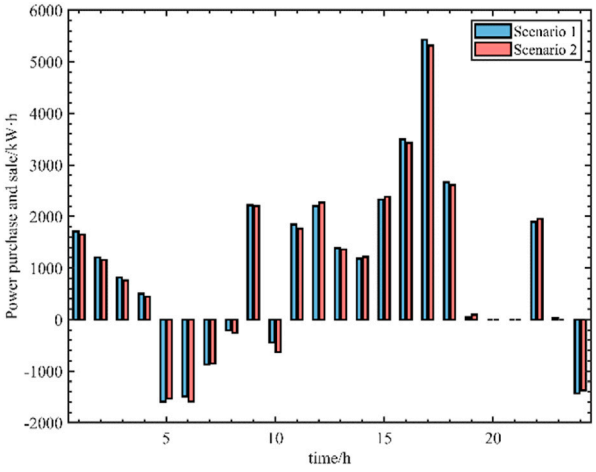

FIGURE 4
Electricity purchase and sale in the park in scenarios 1 and 2.

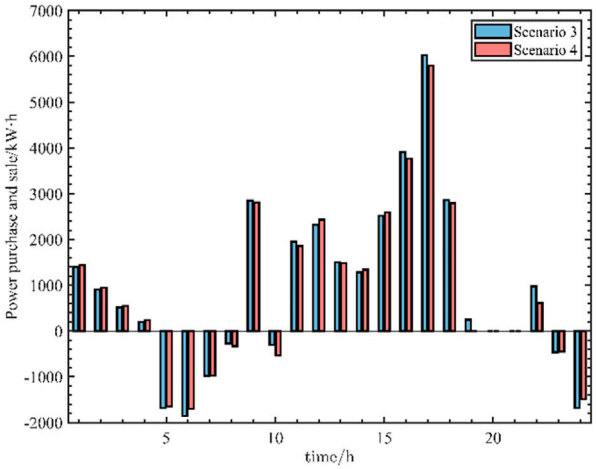

FIGURE 5
Purchase and sale of electricity in the park in scenarios 3 and 4.

The four scenarios were tackled using CPLEX, and the distributionally robust algorithm used the CCG algorithm described in Section 4 for solving. The constraints related to the robustness degree were both set to 0.99. The probability of each scenario in the random system was set to 0.2.

Table 5 outlines the investment scheme, yearly overall operating expenses, yearly investment outlay, yearly maintenance expenditure, yearly electricity procurement costs, yearly gas acquisition costs, yearly revenue from electricity sales, and yearly carbon emission expenses for each scenario.

Figure 4 shows that in scenarios 1 and 2, without considering the demand response, the distributionally robust algorithm purchased less electricity than the random system in each time period. This is because the distributionally robust algorithm has more robustness and plans more photovoltaic capacity to avoid the impact of the photovoltaic output uncertainty on park operation.

Figure 5 shows that in scenarios 3 and 4, when considering the eco-friendly demand response, the distributionally robust algorithm

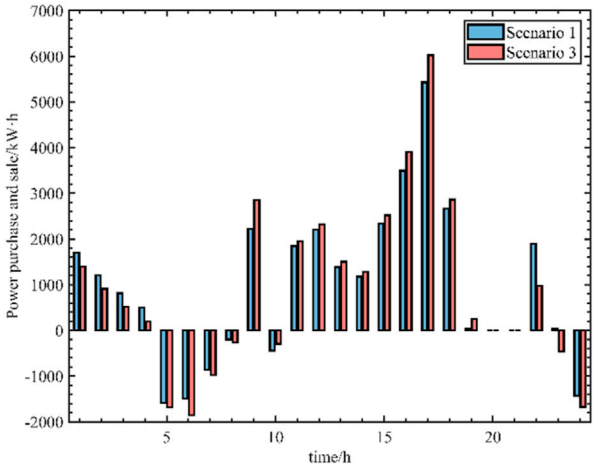

FIGURE 6
Purchase and sale of electricity in the park in scenarios 1 and 3.

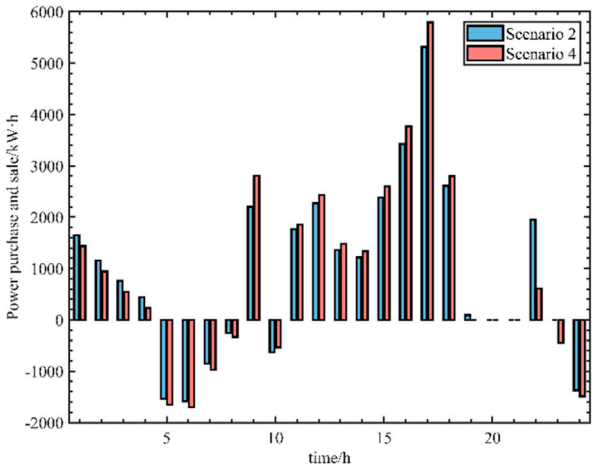

FIGURE 7
Electricity purchase and sale in the park in scenarios 1 and 3.

purchased more electricity than the random system during the high peak period of dynamic carbon emission factors. However, the purchased electricity in other periods was still less than that of the random system. Although the purchased electricity was more significant under high carbon emission factors, the total purchased electricity was still less than the result of the random system. This considers the impact of purchased electricity under high carbon emission factors on park operating costs.In general, it can be observed that the distributionally robust algorithm incurs higher yearly operating costs than the stochastic programming algorithm compared to scenarios 1 and 2 and scenarios 3 and 4. Although its economic efficiency may not be optimal, the lower ratio of energy storage to photovoltaic capacity, compared to stochastic programming, proves more effective in mitigating the influence of photovoltaic uncertainties on park operations. This, in turn, reduces the expenditure on grid electricity purchases and enhances the park's yearly carbon emission reduction with increased robustness.

Based on Figure 6 and Figure 7, considering the eco-friendly demand response, the purchased electricity in scenarios 3 and 4 is higher than that in scenarios 1 and 2 during periods of high-carbon emission factors. However, during periods of low-carbon emission factors, the purchased electricity in scenarios 3 and 4 is lower than that in scenarios 1 and 2. Although the total purchased electricity in scenarios 3 and 4 has increased, the total carbon emissions are lower than those in scenarios 1 and 2. This is because the demand response based on dynamic carbon emission factors reduces the purchased electricity during periods of high carbon emissions.

In general, upon comparing scenarios 1 and 3 and scenarios 2 and 4, it is evident that the utilization of demand response based on the dynamic carbon emission factor pricing rules results in a reduction in the industrial park's yearly carbon emissions compared to traditional time-of-use electricity pricing. This reduction is observed despite an increase in the park's expenditure on purchased electricity. The disparity in peak values between dynamic carbon emission factors and electricity demand, as illustrated in Figure 3, contributes to the overall decrease in total yearly carbon emissions with the heightened electricity cost. This signifies commendable eco-friendly performance.

7 Conclusion

This paper aims to propose a resilient configuration for solar storage systems in industrial estates, taking into consideration uncertainties in photovoltaic generation and incorporating an eco-friendly demand response. It employs a distributed robust algorithm to alleviate the impact of photovoltaic uncertainties on the system through a data-driven approach. Furthermore, it introduces an eco-friendly demand response model based on the carbon emission flow theory, considering dynamic carbon emission factors. The approach is validated through illustrative examples, leading to the following conclusions:

1) The system results under the distributed robust algorithm, compared with the results of the random programming algorithm, show that it can reduce the impact of the photovoltaic uncertainty on the operation of the park, reduce the cost of purchasing electricity from the grid, and thus reduce the yearly carbon emissions of the park. It has better robustness while ensuring a particular economy.
2) Following the implementation of the eco-friendly demand response model grounded in the dynamic carbon emission factor, a comparison with the traditional time-of-use program reveals that the demand response advocated in this paper demonstrates a more pronounced carbon-centric bias. It achieves a reduction in electricity procurement during periods characterized by high carbon emission factors, consequently effectively diminishing the overall yearly carbon emissions of the industrial park.

Data availability statement

The raw data supporting the conclusion of this article will be made available by the authors, without undue reservation.

Author contributions

JH: methodology, resources, writing–original draft, and writing–review and editing. LZ: validation and writing–review and editing. ZH: supervision and writing–review and editing. WL: formal analysis and writing–review and editing. YZ: data curation and writing–review and editing.

Funding

The author(s) declare that no financial support was received for the research, authorship, and/or publication of this article.

Conflict of interest

Authors JH, LZ, ZH, WL, and YZ were employed by State Grid Fujian Electric Power Co Ltd.

Publisher's note

References

Chen, Z., Zhang, X., Wang, X., Peng, L., Wen, W., Liang, W., et al. (2021). Distributed robust optimal configuration method for distributed photovoltaic power stations connected to distribution network. *Power Syst. Prot. Control* 49 (13), 30–42. doi:10.19783/j.cnki.pspc.201082

Doostizadeh, M., and Ghasemi, H. (2012). A day-ahead electricity pricing model based on smart metering and demand-side management. *Energy* 46 (1), 221–230. doi:10.1016/j.energy.2012.08.029

Fan, L., Wang, K., Li, G., Wu, W., and Ge, W. (2018). Robust unit combination considering the time dependence of wind power. *Automation Electr. Power Syst.* 42 (18), 91–97+176. doi:10.7500/AEPS20170917007

Gao, H., Liu, J., Zhenbo, W., and Su, Y. (2017). A hierarchical robust programming model for active distribution network and its solution method. *Chin. J. Electr. Eng.* 37 (05), 1389–1401. doi:10.13334/j.0258-8013.pcsee.152656

Han, X., Li, T., Zhang, D., and Zhou, X. (2021). New problems and key technologies of new power system planning under the dual carbon goal. *High. Volt. Technol.* 47 (09), 3036–3046. doi:10.13336/j.1003-6520.hve.20210809

He, S., Gao, H., Liu, J., Liu, Y., Wang, J., and Xiang, Y. (2019). Distributed robust DG optimal configuration considering demand response flexible adjustment. *Chin. J. Electr. Eng.* 39 (08), 2253–2264+8. doi:10.13334/j.0258-8013.pcsee.181968

He, S., Ruan, H., Gao, H., and Liu, J. (2020). A review of theoretical analysis and application of distributed robust optimization methods in power systems. *Automation Electr. Power Syst.* 44 (14), 179–191. doi:10.7500/AEPS20191022002

Li, W., Zang, C., Ding, L., and Zeng, P. (2022a). Scheduling of combined electric and heating systems based on multi-objective two-stage stochastic programming method. *Inf. Control* 51 (02), 176–187. doi:10.13976/j.cnki.xk.2022.1057

Li, Y., Zhang, N., Du, E., Liu, Y., Xiao, C., and He, D. (2022b). Research and benefit analysis of low-carbon demand response mechanism in power system based on carbon emission flow. *Chin. J. Electr. Eng.* 42 (08), 2830–2842. doi:10.13334/j.0258-8013.pcsee.220308

Li, Z., Yang, H., and Shi, T. (2020). Research on grid-side energy storage configuration method based on stochastic programming theory. *Power Electron. Technol.* 54 (03), 40–43.

Qiu, X., Zhu, Z., Huang, C., Huang, B., Wu, H., and Zhong, S. (2020). Robust optimization of integrated energy system considering wind power output uncertainty. *Smart Power* 48 (05), 1–6+59.

Ruan, H., Gao, H., Liu, J., and Huang, Z. (2019). A robust reactive power optimization model for active distribution network distribution considering DG reactive power support and switch reconfiguration. *Chin. J. Electr. Eng.* 39 (03), 685–695+948. doi:10.13334/j.0258-8013.pcsee.180241

Wang, C., Yi, C., Wen, F., Yuan, T., Chi, C., and Jiang, X. (2022). Improvement and perfection of carbon emission flow theory in power system. *Power Grid Technol.* 46 (05), 1683–1693. doi:10.13335/j.1000-3673.pst.2021.2071

Xue, G., Shan, B., Wang, Ti, Wang, X., Xing, W., and Sun, W. (2022). Robust optimal configuration of light-storage storage in industrial parks considering photovoltaic uncertainty. *J. Syst. Simul.* 1-10. doi:10.16182/j.issn1004731x.joss.21-0601

Yue, S., Liu, J., Gao, H., Gao, Q., Xu, W., and Gou, J. (2018). Two-stage distributed robust coordinated scheduling of electrical energy systems considering wind power uncertainty. *Automation Electr. Power Syst.* 42 (13), 43–50+75. doi:10.7500/AEPS20171218008

Zhang, Y., Wang, X., Yu, F., and Cui, Z. (2013). Carbon emission accounting methods and empirical research in industrial parks. *Ecol. Econ.* (09), 155–157.

Zhao, C., and Guan, Y. (2016). Data-driven stochastic unit commitment for integrating wind generation. *IEEE Trans. Power Syst.* 31 (4), 2587–2596. doi:10.1109/tpwrs.2015.2477311

Zhi, Y., Guo, S., He, X., and Xin, Ai (2017). Two-tier optimal scheduling model for smart industrial parks. *Automation Electr. Power Syst.* 41 (01), 31–38+101. doi:10.7500/AEPS20160103004

Zhou, T., Kang, C., Xu, Q., and Chen, Q. (2012). A preliminary study on the calculation method of carbon emission flow in power system. *Automation Electr. Power Syst.* 36 (11), 44–49. doi:10.3969/j.issn.1000-1026.2012.11.008

Zhu, L., Yin, C., Wang, B., Zhang, Li, Liu, Li, Ye, Y., et al. (2021). Research on stochastic planning of integrated energy stations considering wind/light/load uncertainty. *Power Grid Clean Energy* 37 (05), 96–105. doi:10.3969/j.issn.1674-3814.2021.05.012

frontiers | Frontiers in Energy Research

TYPE Original Research
PUBLISHED 06 March 2024
DOI 10.3389/fenrg.2024.1323800

OPEN ACCESS

EDITED BY
Youbo Liu,
Sichuan University, China

REVIEWED BY
Hongxun Hui,
University of Macau, China
Yushuai Li,
University of Oslo, Norway

*CORRESPONDENCE
Yanyu Yan,
yanyanyu@tju.edu.cn

RECEIVED 18 October 2023
ACCEPTED 14 February 2024
PUBLISHED 06 March 2024

CITATION
Ji X, Liu D, Yan Y, Xiong P, Sun Y and Yang Z (2024), Dynamic planning of edge sensing terminals in distribution network supporting distributed resources observable and controllable.
Front. Energy Res. 12:1323800.
doi: 10.3389/fenrg.2024.1323800

Dynamic planning of edge sensing terminals in distribution network supporting distributed resources observable and controllable

Xiaotong Ji[1], Dan Liu[2], Yanyu Yan[3]*, Ping Xiong[2], Yuce Sun[3] and Zhiduan Yang[3]

[1]State Grid Hubei Electric Power Co. Ltd., Wuhan, China, [2]State Grid Hubei Electric Power Research Institute, Wuhan, China, [3]Key Laboratory of Intelligent Power Grid Ministry of Education, Tianjin University, Tianjin, China

With the advancement of low-carbon distribution networks, the heightened stochasticity introduced by a multitude of renewable energy sources in the power grid has significantly augmented the regulatory challenges faced by the power grid. Dispatching distributed resources emerges as an effective solution to this issue. However, these resources often lack observability and controllability, hindering their participation in power regulation services. To establish a reliable interaction between distributed resources and power grids, the deployment of numerous edge sensing terminals becomes essential, albeit incurring high costs. In light of this, our paper proposes a dynamic network planning method for edge sensing terminals based on node differentiation and resource observability criteria, aiming to facilitate real-time and dependable observation of distributed resources. Initially, the node weight, a metric to gauge the disparity among nodes, is computed, considering communication quality deviation, resource development synergy, and the distribution of distributed resources. Subsequently, an optimal configuration method is introduced, accounting for the terminal's reliability under faults. Lastly, a method for dynamic terminal networking planning is presented, gradually reducing the depth of unobservable resources. An enhanced genetic algorithm is employed to address this challenge. This method was validated using an IEEE 33 node system and a 91 node actual system, demonstrating significant effectiveness in reducing terminal configuration costs.

KEYWORDS

low-carbon grid, edge intelligent sensing terminal, optimal configuration, node weights, genetic algorithm, unobservable depth

1 Introduction

Due to the continuous depletion of traditional energy sources, nations worldwide are actively seeking alternative energy sources. The power system views wind energy, solar energy, and other forms of renewable power generation as the vital means to alleviate strain on conventional resources. With the establishment of low-carbon power grids and the proliferation of diverse loads, a substantial number of distributed photovoltaic systems, electric vehicle charging stations, and flexible controllable loads are interconnected with the power grid. The transformation from a traditional passive power grid to an active one is underway, accompanied by an increasing demand for power control and energy efficiency

management within the distribution network (Fambri et al., 2022; Kong et al., 2022; Nouri et al., 2022; Kong et al., 2023). In the power system, robust sensing of distributed resources in the distribution network can facilitate various services such as dispatching, frequency modulation, demand response, and standby services, thereby enhancing the stability and security of the power system (Ji et al., 2018; Ferreira et al., 2020; Yang et al., 2022). Insufficient sensing may result in control delays, errors, or inadequate fault response, jeopardizing the overall stability of the system. The conventional centralized sensing system encounters challenges such as an extensive array of devices, diverse services, challenging communication environments, limited bandwidth, and certain devices being unmeasurable remotely. Consequently, it falls short of effectively achieving accurate panoramic sensing of distributed resources in the distribution network (Bangjun et al., 2022). The emerging sensing architecture based on edge sensing terminals provides a promising solution to these challenges. However, the characteristics of distributed generation, namely, small capacity, numerous installations, and scattered locations, necessitate the deployment of a considerable number of new edge sensing terminals, incurring high costs. To address these issues, there is an urgent requirement to propose a sensing terminal network planning technology that can efficiently reduce the configuration costs of sensing terminals within the new distributed intelligent sensing system of low-voltage power grids. This technology aims to support the reliable monitoring of distributed resources and facilitate the intelligent and digital transformation of medium- and low-voltage power grids.

Due to the recent emergence of edge sensing terminal products, there has been relatively limited research on their optimized layout both domestically and internationally. However, the principles and model-solving methods for their optimized layout bear similarity to those of other secondary information system terminals in distribution networks, such as feeder terminal units (FTUs) and synchronous phasor measurement units (PMUs). Wang (2019) calculated the probability of node voltage exceeding the limit using the probability model of load and distributed power output, establishing a PMU configuration planning model based on this weight. Li and Lu (2018) combined a state estimation method with a parallel belief propagation algorithm to establish a PMU measurement position optimization model, aiming to minimize the state estimation error of active distribution networks. The improved immune discrete particle swarm optimization algorithm was employed to solve the problem. Xu et al. (2015) employed an improved matrix to design a greedy algorithm with polynomial time computational efficiency, enhancing the power grid's self-healing ability but without due consideration for economic factors. Babu et al. (2020) considered key components and key buses, proposing an optimal terminal configuration algorithm that takes into account the optimal substation and key components. Chen et al. (2019) constructed a switch optimization configuration model, aiming to minimize the sum of user outage loss and switch configuration life cycle cost, constrained by power supply reliability. Liu et al. (2020) proposed a bi-level optimization method for terminal configuration that addressed the significant dimensional differences in multiple indicators within existing configuration models. The upper optimization model determines the installation position of the distribution terminal, while the lower optimization model determines the installation type of the distribution terminal. Kong et al. (2019) suggested the use of the generalized Tellegen's theorem to analyze the economic indicators and robustness of the bus and branch of the power grid, addressing the configuration of measuring points, considering both the entire network and the N-1 situation. From the perspective of real-time identification and localization of fault transmission lines in distribution networks, Ding et al. (2021) determined the minimum number and configuration positions of PMUs with sufficient accuracy to achieve global observability, thereby facilitating network self-healing. Zhao et al. (2019) proposed a linear programming model for distributed state estimation, simultaneously considering PMUs, phasor data concentrator (PDC), and optimal prevention of communication connections, enhancing the state estimation in large-scale active distribution networks. Kong et al. (2024) focused on the impact of flexible resources on power grid frequency regulation and introduced an information physical system planning method considering the multidimensional uncertainty of virtual power plants. This method addresses the optimal solution for coordinating flexible resource pool composition, edge sensing terminal allocation, and communication. However, these studies often treat all nodes equally during configuration, overlooking the differences among individual nodes. When configuring edge terminals, the distribution of distributed resources directly impacts communication quality. Each node in the network holds a distinct status and should not be considered as an equally important factor. Additionally, existing research primarily focuses on one-time planning, falling short of achieving dynamic adaptive network planning.

The characteristics of small capacity, a large number, and scattered installation locations of distributed power supply necessitate the configuration of a considerable number of new edge sensing terminals, incurring high costs. Given the substantial one-time investment, it is often imperative to plan in stages. Numerous studies have addressed the phased planning of secondary information system terminals in the distribution network. Yi et al. (2023) proposed a monitoring criticality evaluation system based on the frequency-coupled impedance model of wind turbines. This system considers differences in importance between the evaluation indexes and probability of occurrence of oscillation conditions. A multistage optimal configuration model for subsynchronous phasor measurement units (SPMUs) is established, taking into account the criticality of node monitoring. The multistage optimal configuration scheme is solved using integer linear programming. Zeng et al. (2021) divided the PMU configuration into two stages. Indicators such as the correlation degree, tightness, and importance of the distribution network are utilized to derive the node centrality index of the distribution network. The first stage configuration is formed by combining the maximum observability under the constraint of the number of configurations. The second stage configuration scheme is formulated by employing multi-objective optimization, considering the minimum number of configurations and the minimum average interval width. Xi et al. (2022) determined critical loads based on the fast voltage stability index to monitor key buses. A phased decision on PMU positions was made using the modified analytic hierarchy process, comprehensively considering various observability indicators to rank the PMU buses. Razavi et al.

(2018) introduced a mathematical linear model of probabilistic multistage PMU configuration that considers changes in network topology caused by long-term expansion during the planning period. Ali et al. (2018) proposed a mathematical linear expansion model of probabilistic multistage PMU configuration, considering the constraints of zero-injection nodes and communication channels. An auxiliary optimization technique, not accounting for the prevalence of each planning stage, ensured obtaining the global optimal solution in a broader and more comprehensive search space. Razavi et al. (2020) explored a multi-level PMU placement model under probabilistic and deterministic frameworks, reflecting a more realistic image of power system observability through the concept of probabilistic observability, thereby providing a more complete search space for optimization problems. Khare et al. (2021) aimed to reduce network vulnerability of the power system to network attacks by using forward dynamic programming to allocate the capital cost of PMUs over time. This approach ensures the critical observability of the grid in the first stage and increases the observability level in subsequent stages. While the above methods are rooted in observability, their different observation objects and criteria hinder direct application to achieve the observability and controllability of distributed resources. Additionally, these methods face challenges in coordinating with the expansion of distributed resources.

While the aforementioned research lays a theoretical foundation for observability, observation reliability, and economy discussed in this study, the terminal configuration of the distribution network primarily centers on the configuration of PMUs, FTUs, and similar elements. The overarching objective is to achieve observability across all nodes of the distribution network, with limited emphasis on edge sensing terminals responsible for sensing distributed resources. This lack of focus on edge sensing terminals can significantly impact the observable model. Furthermore, in practical engineering applications, a single terminal is often tasked with communicating with multiple distributed resources. The numerous challenges posed by these resources, such as their scattered locations, diverse types, substantial differences in data volume, extended communication distances, and random interference in communication links, can result in deviations in communication quality. These deviations, in turn, impede the reliability of data acquisition. In the realm of terminal configuration, it is essential to recognize that each node in the network holds a unique status and should not be treated as an equally important factor. Existing research tends to overlook the variations in communication quality and development potential among individual nodes within the system. It fails to prioritize the reliable observation requirements of high-risk nodes and lacks the capability to effectively cooperate with the expansion of distributed resources.

Therefore, in addressing the aforementioned challenges, this study introduces a distributed intelligent sensing system designed to enhance the observability and controllability of medium- and low-voltage distributed resources. The system aims to overcome issues such as scattered installation positions, random output, and communication congestion within distributed resources, ultimately supporting the comprehensive observability of these resources. Given the current state of research on terminal configuration, distribution system nodes are typically treated as entirely indistinguishable 0-1 variables. To address this limitation, this article takes into account the transformative impact of renewable energy on the distribution system. It considers differences in distributed resource distribution, communication quality disparities induced by the terrain, and the potential for future construction of distributed resources. Recognizing the distinctions between various nodes, a weight model is established to more effectively reflect the rationale behind the configuration. This study proposes a multistage planning method designed to gradually reduce the depth of unobservability. The objective is to guide the dynamic distributed networking of sensing terminals, acknowledging the challenges associated with the inability of a one-time edge sensing terminal configuration to meet the continuous expansion of distributed resources and adhere to funding constraints. The specific contributions of this research are outlined as follows:

1) The introduction of a distributed intelligent sensing system is proposed to tackle the challenges related to data transmission congestion and heightened burden on the main station within an intelligent sensing system encompassing numerous distributed power sources. This system leverages edge sensing terminals for preprocessing and compressing information, thereby enhancing the observability and controllability of resources.
2) In response to the complexities arising from diverse and widely distributed types of distributed resources, which lead to varying communication quality and distribution among nodes in the distribution network, and considering the high cost associated with overlooking resource potential, this research employs indicators such as node degree, resource development synergy, and communication severity as node weights in the optimization process.
3) Addressing the challenge of a high initial investment cost and the incapacity to adapt to the controllable expansion of distributed resources during configuration, a terminal dynamic networking method is proposed. This method aims to systematically reduce the depth of unobservability of resources and attain an optimal configuration sorting of equipment over time.

In Section 2, an intelligent sensing system supporting a multi-service distributed low-voltage power grid is proposed. In Section 3, a one-time configuration optimization method based on node weight is developed. Section 4 develops a multistage optimal configuration method. Section 5 tests the method, and the conclusion is given in Section 6.

2 Low-voltage distributed sensing system of digital power grids

2.1 Distributed smart sensing system

To achieve substantial and controllable support for a vast number of medium- and low-voltage distributed resources, especially following the integration of a high proportion of

distributed generation, enabling efficient interaction with the power grid for participation in services such as dispatching, frequency modulation, and demand response, while addressing the heightened uncertainties introduced by a large volume of distributed generation and the increasing load on the power grid, an intelligent sensing system is proposed. This system is designed to support multi-service distributed low-voltage power grids. Figure 1 illustrates the architecture of the distributed intelligent sensing system for low-voltage power grids comprising four layers: the physical resource layer, terminal sensing layer, communication access layer, and cloud platform layer. This system facilitates the digital transformation of low-voltage power grids, providing robust support for various services such as power equipment condition monitoring and information energy management.

1) Physical resource layer: the low-voltage power grid, following extensive integration of distributed power sources, encompasses diverse distributed source–load–storage resources categorized into three main groups. The power-side resources exhibit coordinated and complementary characteristics, incorporating distributed photovoltaic and wind turbines. The load-side resources possess flexibility, distribution, and adjustability, typically involving terminal loads such as buildings and air conditioners. Energy storage-side resources include electric vehicles and base station energy storage, among others.
2) Terminal sensing layer (user sensing): this layer primarily comprises smart meters, low-voltage data monitoring terminals, intelligent inverters, and environmental sensors. These devices are tasked with collecting, uploading, and receiving superior control commands. They play a crucial role in gathering a diverse set of information indicators to fulfill multi-service requirements.
3) End sensing layer (edge computing side): this layer predominantly consists of wired or wireless edge sensing terminals. The edge computing method is employed to achieve regional autonomy functions, such as the plug-and-play capability of intelligent terminals, local analysis of collected data, and on-site processing of services. Notably, the intelligent edge sensing terminal serves as a crucial data support apparatus for medium- and low-voltage power grids with a high proportion of distributed power access. It is capable of analyzing and processing the received raw data, thereby alleviating the data processing burden on the server or cloud server. The intelligent edge sensing terminal stands as the core component of the sensing system.
4) Local communication layer: this layer is primarily responsible for transmitting the collected data to terminal equipment, employing wired transmission through RS232/RS485. Both wired transmission methods meet the majority of requirements for bandwidth, delay, and reliability. Consequently, buildings and air conditioning systems can leverage existing communication lines, in conjunction with the original wiring of the distribution network, to accomplish information collection. However, for resources like photovoltaic systems, wind turbines, electric vehicles, and others characterized by significant capacity differences, frequent location changes, and diverse types, additional wiring is impractical and wasteful. As a result, wireless communication serves as the primary method. Sensing terminals and monitoring equipment require two-way communication, and high-performance low power consumption (HPLC) + micro-power wireless communication is a suitable choice. This communication method adopts a dual-mode communication approach, enhancing communication coverage and reliability and facilitating automatic integration into a two-channel network. Additionally, long-range radio (LORA) wireless technology presents itself as a viable option for wireless communication due to its low power consumption, robust anti-interference capabilities, and minimal noise.
5) Remote communication layer: this layer manages communication between the terminal equipment and cloud platform, encompassing technologies such as industrial Ethernet, 4G/5G communication, and Ethernet passive optical network (EPON). Public network communication through 4G/5G operators is relatively convenient, yet the internet access rate may be lower (Fang et al., 2020). On the other hand, EPON technology, with its maturity, large capacity, and high security and reliability, proves suitable for scenarios with high reliability requirements, providing support for high bandwidth and low latency (Babaei et al., 2019).
6) Cloud platform layer: this layer encompasses the Internet of Things (IoT) management platform, technology platform, data platform, business platform, and application layer. The IoT management platform facilitates standardized and unified access, authentication, and protocol adaptation for intelligent terminal equipment and edge computing devices. The technology platform serves to provide public technical services. The data platform is responsible for realizing data fusion, storage, and analysis within the IoT system. The business platform is utilized for implementing services such as topology, graphics, and model services. Finally, the application layer integrates hierarchical distributed control, protection, self-healing control, panoramic simulation, and other functionalities to achieve specific business applications.

Through this distributed resource intelligent sensing system, a precise panoramic perception of distributed resources can be achieved, providing ample data support for scheduling distributed resources. The cloud platform layer can more accurately regulate distributed resources. For instance, as distributed resources become more prevalent, congestion issues may arise in the distribution network. Hence, the inherent coupling relationship between various energy carriers can be explored, and renewable energy generation can be optimized through the complementary consumption of electricity, heat, and cold. Leveraging the complementarity of various energy sources can help address distribution network congestion (Hu et al., 2021). The cloud platform layer is also capable of conducting day-ahead and real-time scheduling on a multi-energy system composed of multiple energy entities. By adapting to the distributed execution, asynchronous communication, and independent computing characteristics of the system, event-triggered distributed algorithms (Li et al., 2018) are employed to account for the different time-scale characteristics of electricity and thermal

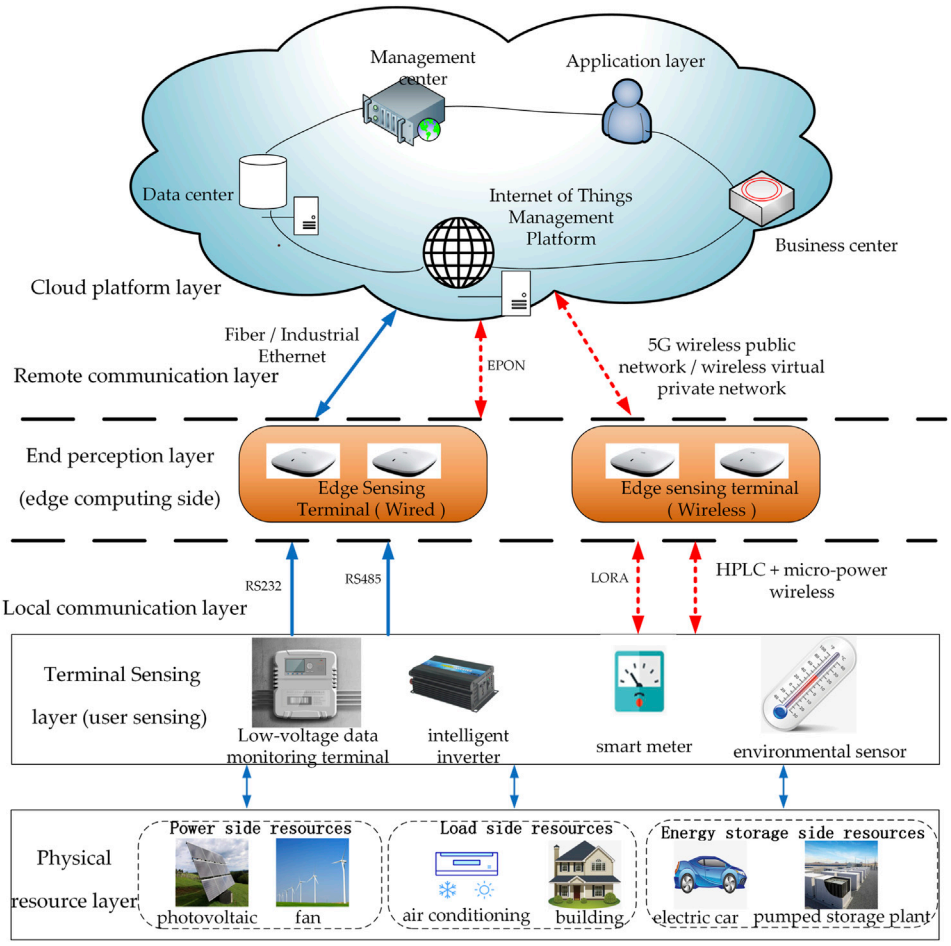

FIGURE 1
Distributed resource intelligent sensing system.

power. This approach achieves the goal of managing smooth real-time load changes and renewable resource fluctuations while considering the reduction of communication costs (Zhang et al., 2021). In specific scenarios, such a system can play a crucial role in scheduling distributed resources. For instance, in isolated islands where the inverse distribution of resources and limited energy transmission are the factors, adaptive energy management can be accomplished through reinforcement learning based on hybrid strategies to govern the energy of island clusters (Yang et al., 2023). Therefore, with a panoramic perception of distributed resources, the regulation of renewable energy can be more precise and effective, facilitating the interconnection and interaction between sources, networks, loads, and storage.

2.2 Distributed resource observability criterion considering edge sensing terminal distribution and fault

Ensuring comprehensive data monitoring is essential for the effective control of diverse distributed resources. When the visibility of distributed resources is optimized, cloud platforms can efficiently manage and regulate a substantial volume of distributed resources. The inherent characteristics of small capacity, large quantity, and dispersed installation locations of distributed energy resources necessitate the configuration of numerous new edge sensing terminals, incurring high costs. Therefore, it becomes imperative to devise an effective method to mitigate the configuration cost of edge sensing terminals. This is essential to support the reliable monitoring of distributed resources, as well as the intelligent and digitized transformation of medium- and low-voltage grids, along with other related technologies.

To achieve efficient and reliable monitoring of distributed resources, optimizing the configuration of edge sensing terminals based on the proposed sensing architecture in this study is crucial. This optimization aims to enhance the controllability and visibility of distributed resources. Consequently, it is imperative to introduce a distributed resource visibility criterion based on the distribution of edge sensing terminals. When optimizing the configuration of measurement devices such as PMUs in the power grid, invisibility depth is commonly employed to describe the sensing capability of the distribution network. Hence, this study also introduces a criterion based on invisibility depth. The invisibility depth of a distributed resource indicates whether it is monitored by edge sensing terminals. This depth is influenced by factors such as the position, quantity, type, and communication conditions of edge

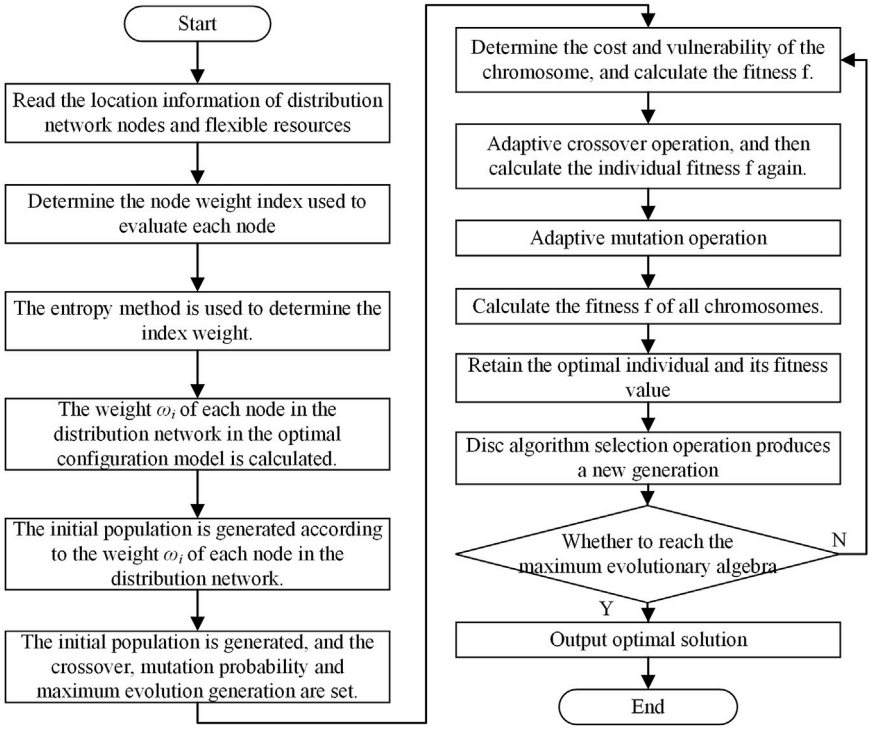

FIGURE 2
Edge sensing terminal optimization configuration solution flow chart.

sensing terminals concerning each distributed resource. This study quantifies the visibility of distributed resources based on their invisibility depth, and the corresponding formula is detailed in Eq. 1. In this study, the observability of distributed resources is gauged by the unobservable depth, as expressed in Eq. 1. The significance of this unobservable depth extends beyond describing the observability of distributed resources; it is also instrumental in analyzing the observability of distributed resources under terminal failure.

$$\eta_s = \frac{\sum_{j=1}^{M} \eta_{sj}}{M} \times 100\%. \tag{1}$$

In the formula, η_{sj} represents the invisibility degree of resource j (Eq. 2); M represents the total number of distributed resources.

$$\eta_{sj} = \begin{cases} 1, & \text{Not subject to edge sensing terminal management, } \sum_{i=1}^{N} Z_{i,j} = 0 \\ 0, & \text{subject to edge sensing terminal management, } \sum_{i=1}^{N} Z_{i,j} = 1 \end{cases}. \tag{2}$$

Edge sensing terminals are susceptible to failures during operation due to their extended operating time, remote communication distances, and high processing demands. When a fault occurs, it can lead to the loss of monitoring and measurement data for connected distributed resources, impeding reliable resource interaction. Consequently, during the configuration of edge sensing terminals, it is essential to ensure that certain visibility requirements are met, even in the event of equipment failure, with the goal of minimizing losses caused by faults.

Considering the relatively low failure rate of edge sensing terminals and the presence of maintenance personnel capable of promptly repairing faults, the likelihood of multiple edge sensing terminals failing simultaneously is exceedingly low. In this model, only the scenario of a single edge sensing terminal failure is considered, corresponding to **N − 1** reliability.

Assuming **X** vector represents the configuration plan of edge sensing terminals (Eq. 3),

$$X = \{x_1, x_2, x_3, \ldots x_n\}. \tag{3}$$

In the equation, x_i represents whether node i is equipped with an edge sensing terminal, with a value of 1 if installed and 0 if otherwise.

Let the number of edge sensing terminals installed be N (Eq. 4).

$$sum(X) = N. \tag{4}$$

If a single edge sensing terminal fails, there are N possible types of failures, and the set of failures can be represented as follows (Eq. 5):

$$\boldsymbol{O} = \left\{X_1', X_2', X_3', \ldots, X_N'\right\}. \tag{5}$$

In the equation, X_i' represents the case where the i-th edge sensing terminal fails, and it is reflected in the X matrix, where the value of x_i changes from 1 to 0 after a failure, as shown in Eq. 6.

$$X_i' = \{x_1, x_2, x_3, \ldots x_i = 0, \ldots x_N\}. \tag{6}$$

When planning the configuration, consider O as the set of faulty edge sensing terminals.

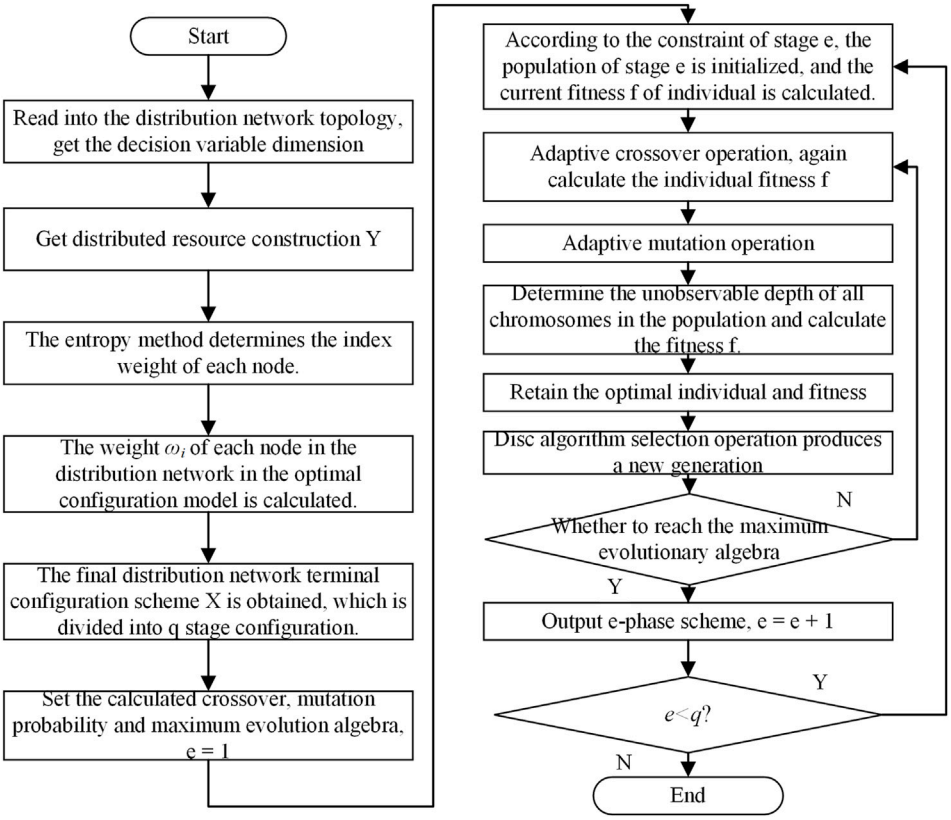

FIGURE 3
Sensing terminal dynamic networking solution flow chart.

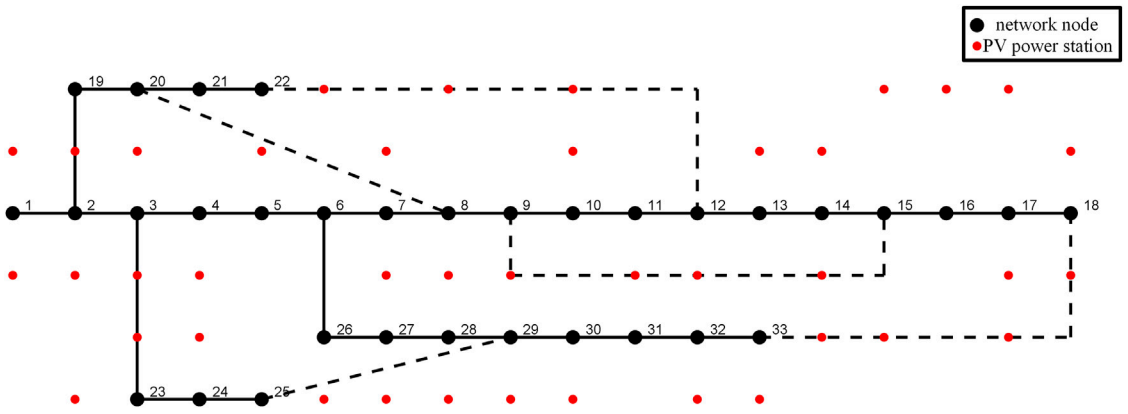

FIGURE 4
IEEE 33 node and photovoltaic power station topology diagram.

Let $Z_{i,j}$ be the connection status between edge sensing terminals and distributed resources when no fault occurs, where 1 report that edge sensing terminal i is connected to the distributed resource j; otherwise, no connection exists. After a fault occurs, the cloud platform layer receives the fault information and feeds it back to each terminal. Each terminal then reallocates and reconnects the distributed resources to maximize coverage, with the connection status updated to $Z'_{i,j}$At this point, the invisibility degree of each distributed resource is updated to $\eta'_{i,s,j}$where i represents the i-th faulty terminal.

However, due to constraints on the number of connections and distances, it cannot be guaranteed that all distributed resources are still observable at this time. The distributed resources that have not established communication with any edge sensing terminal are denoted as U_i and are expressed by Eq. 7.

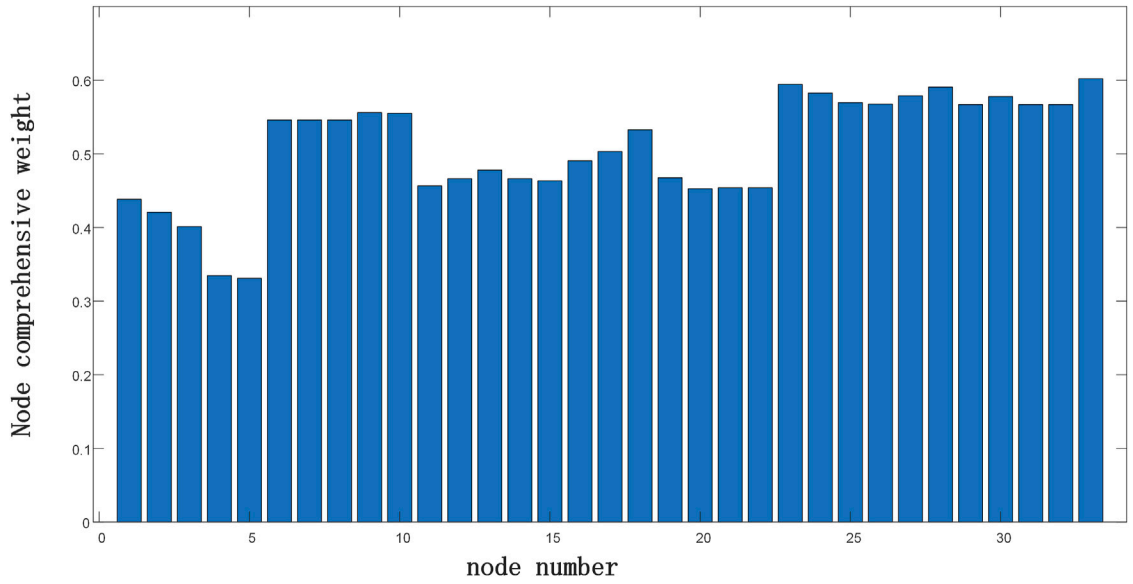

FIGURE 5
Comprehensive weight index of the IEEE 33 node system node.

TABLE 1 Analysis of the influence of node comprehensive weight index.

Optimal allocation model	Number of terminals	Edge sensing terminal configures node location	Cost of the scheme (¥)
Considers the node weight index	13	1, 4, 6, 9, 10, 13, 14, 15, 17, 18, 24, 26, and 30	248409.8
Does not consider the node weight index	13	1, 3, 6, 8, 10, 12, 14, 15, 17, 18, 25, 27, and 30	248409.8

TABLE 2 Optimal configuration results of IEEE 33 node edge sensing terminals with different algorithms.

Optimal configuration methods	Number of terminals	Edge sensing terminal configures node location	Cost (¥)
Proposed algorithm	13	1, 4, 6, 9, 10, 13, 14, 15, 17, 18, 24, 26, and 30	248409.8
Minimum spanning tree algorithm	13	1, 6, 8, 10, 12, 14, 15, 17, 18, 19, 25, 27, and 30	250385.7
0-1 integer programming algorithm	14	4, 6, 9, 10, 12, 14, 15, 17, 18, 19,23, 25, 26, 31, and 32	258349.3

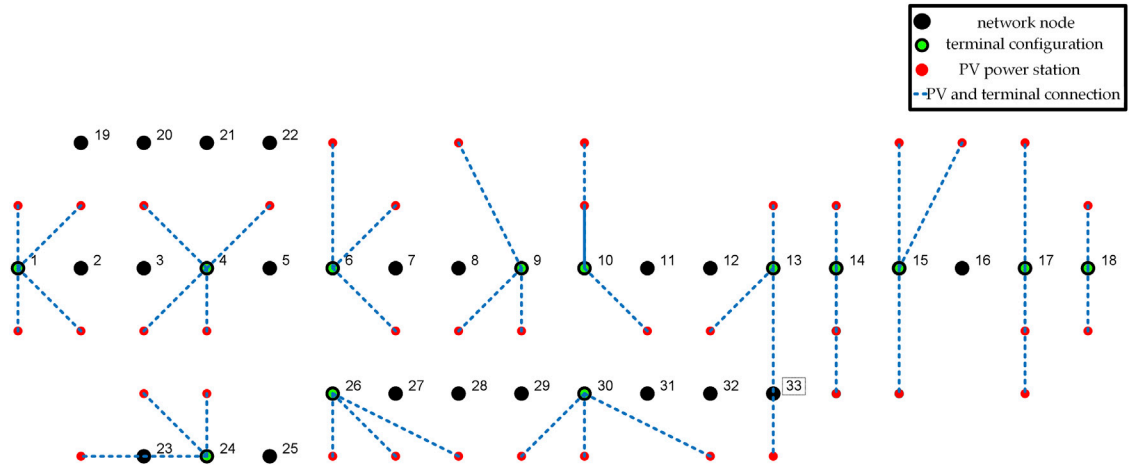

FIGURE 6
IEEE 33-bus system edge sensing terminal configuration scheme.

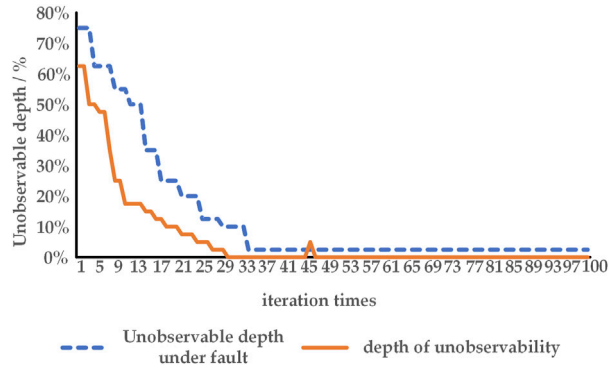

FIGURE 7
Unobservable depth change of the system during the iteration process.

$$U_i = \sum_{j=1}^{M} \eta_{i,sj}^{'} \tag{7}$$

The depth of unobservability during a fault can be represented as follows (Eq. 8):

$$\eta_s^{'} = \frac{\max(U_i)}{M}. \tag{8}$$

3 The optimization method for configuring distribution network edge sensing terminals considering node weights

The second section introduced an intelligent sensing system designed to support multi-business distributed operations in low-voltage power grids. Given the high cost associated with configuring a considerable number of new edge sensing terminals, it becomes imperative to propose a configuration optimization method capable of effectively reducing terminal configuration expenses. The proposed approach begins with the development of a distribution network node weight calculation method based on monitoring distributed resources. These weights serve as crucial parameters in the planning of each node's terminal configuration. Subsequently, the section outlined the establishment of configuration constraints and objective function models for the terminal under both normal operation and fault conditions. To address this optimization problem, an improved genetic algorithm is employed for solution derivation.

3.1 Node weight degree

1) Node degree $d_{i,1}$

In the distribution network, varying installation locations of distributed resources result in distinct levels of node importance. The node degree index serves as an indicator of the installation status of distributed resources around a specific node. For a given node, a higher node degree value implies a greater number of distributed resources installed in its vicinity. While conventional configuration methods are more likely to be applied in such cases, they concurrently increase the terminal failure rate for the node, thereby amplifying the risk associated with uncontrollable resources.

The definition of node degree $d_{i,1}$ is given in Eqs 9, 10.

$$d_{i,1} = \sum_{j=1}^{M} b_{i,j}. \tag{9}$$

$$b_{i,j} = \begin{cases} 1 & R_{i,j} < R_{\max} \\ 0 & R_{i,j} > R_{\max} \end{cases}. \tag{10}$$

In the above equations, $d_{i,1}$ represents the node degree of node i, $R_{i,j}$ represents the distance between node i and resource j, $R_{\max}$ represents the maximum distance between the terminal and distributed resource for communication, and $b_{i,j}$ represents whether resource j is within the $R_{\max}$ range of node i.

2) Resource development synergy $d_{i,2}$

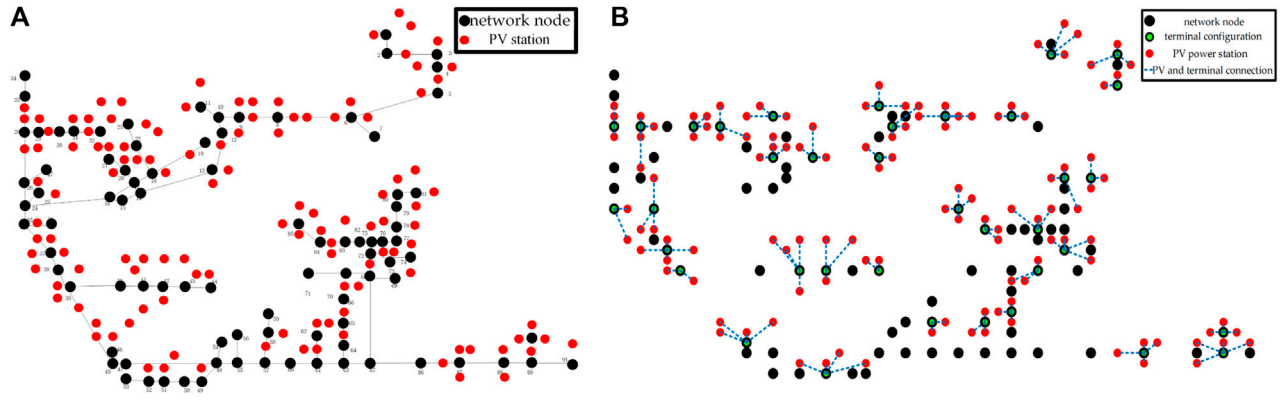

FIGURE 8
Schematic diagram of I loop 408 system. **(A)** Node and photovoltaic location; **(B)** Configuration scheme.

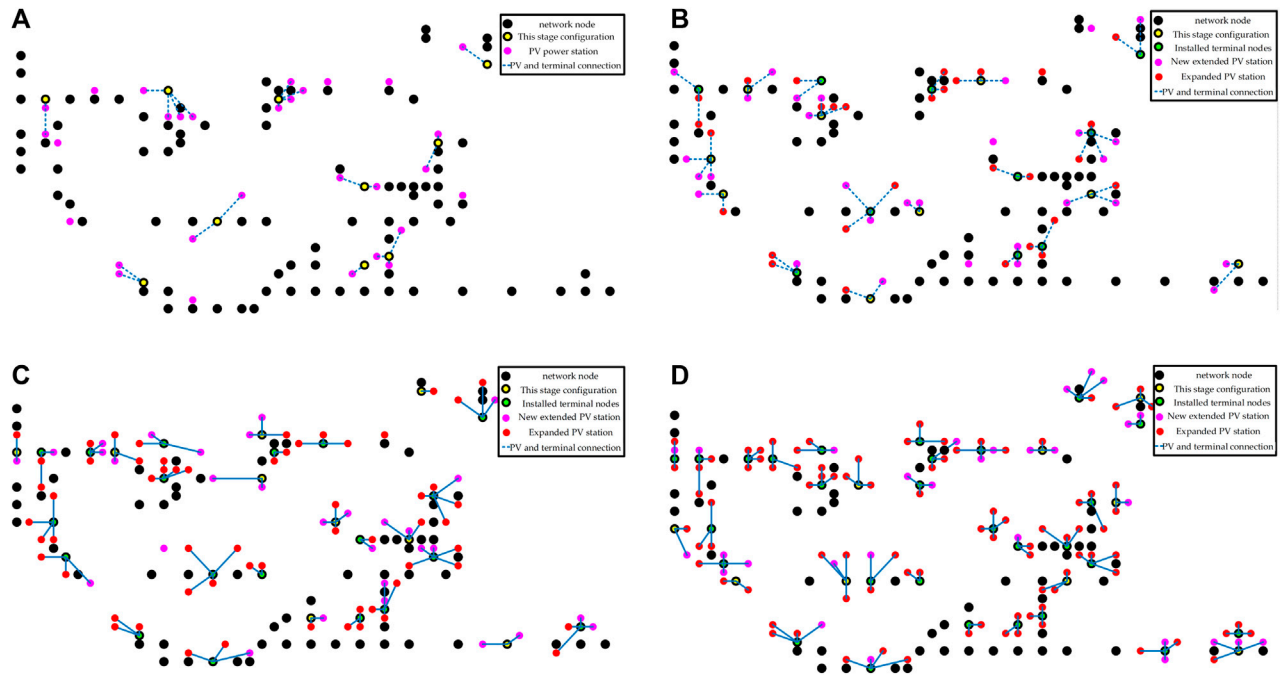

FIGURE 9
Dynamic networking results of 408 system of Guangshui Ten North I loop. **(A)** Results of Phase 1 Planning; **(B)** Results of Phase 2 Planning; **(C)** Results of Phase 3 Planning; **(D)** Results of Phase 4 Planning.

TABLE 3 Networking scheme calculated in this study.

Stage e	Edge sensing terminal
1	5, 12, 23, 29, 42, 46, 62, 65, 80, and 84
2	8, 20, 31, 36, 38, 44, 51, 73, and 90
3	2, 11, 13, 28, 32, 58, 75, 85, and 87
4	3, 6, 18, 35, 39, 41, 68, 81, and 89

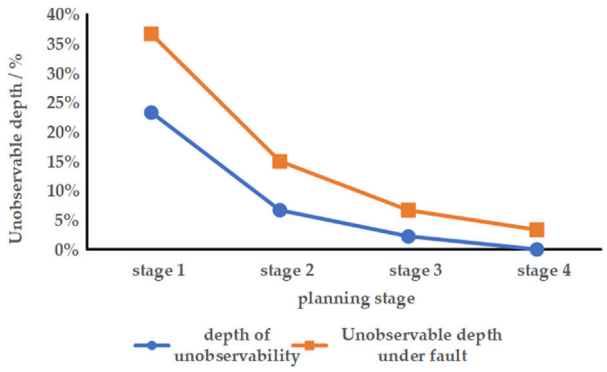

FIGURE 10
Unobservable depth and unobservable depth change under fault.

During terminal configuration, it is crucial to thoroughly assess the potential for the development of distributed resources and integrate future plans into the configuration process. This study focuses on distributed resources, using photovoltaic power plants as an illustrative example. The power generation of photovoltaic power stations is intricately linked to the intensity of solar radiation, with higher radiation intensity corresponding to increased power generation. Consequently, areas with abundant sunlight exhibit a greater likelihood of future photovoltaic power station construction. By strategically configuring edge sensing terminals near these areas, it becomes possible to directly engage with resources following the construction of new photovoltaic power stations in the future, thus obviating the requirement for additional edge sensing terminals.

The initial step involves calculating the global total monthly average solar radiation (G_0) (Duffie and Beckman, 2013). The calculation formula is as follows (Eqs 11, 12):

$$G_0 = \frac{24 \times 3600}{\pi} I_0 f \left(\cos\varphi \cos\delta \cos\omega_s + \frac{\pi}{180} \omega_s \sin\varphi \sin\delta \right). \quad (11)$$

$$\omega_s = \arccos\left(\tan\varphi \tan\delta\right). \quad (12)$$

In the above formulae, G_0 is the global solar radiation, unit J/m^2; I_0 is the solar constant; f is the correction factor for the solar distance; δ is the solar declination angle, unit degrees; ω_s is the sunset angle, unit degrees; and φ is the geographic latitude, unit degrees.

The solar energy received by the object on the inclined surface is given by G_s (Qiao, 2016) (Eqs 13, 14):

$$G_s = 0.774 G_0 \cos\left(\varphi - \gamma_i\right). \quad (13)$$

$$\gamma_i = \frac{23.5\pi}{180 \cos\left(\frac{2\pi}{365 n_d}\right)}. \quad (14)$$

In the above formulae, γ_i is the angle between the solar ray and the equatorial plane; n_d is the number of days.

The underlying assumption in this study posits that the solar panels in a photovoltaic power station consistently maintain a

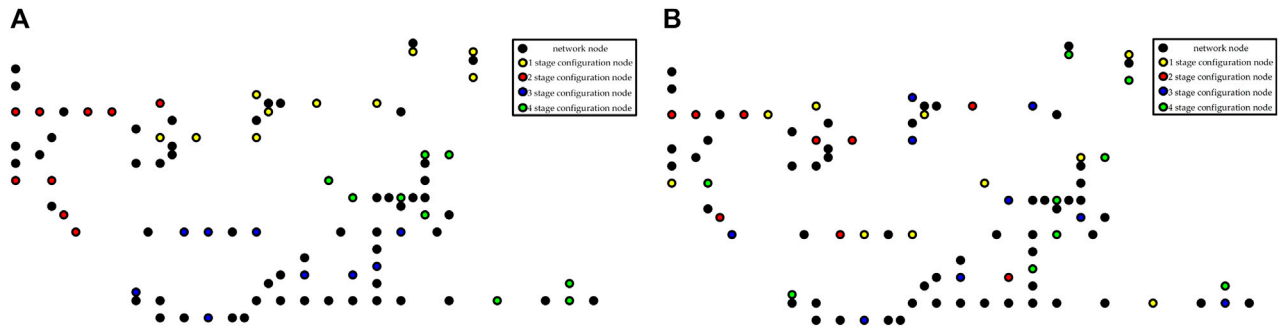

FIGURE 11
The configuration of the other two networking schemes. **(A)** Configuration of networking scheme 1; **(B)** Configuration of networking scheme 2.

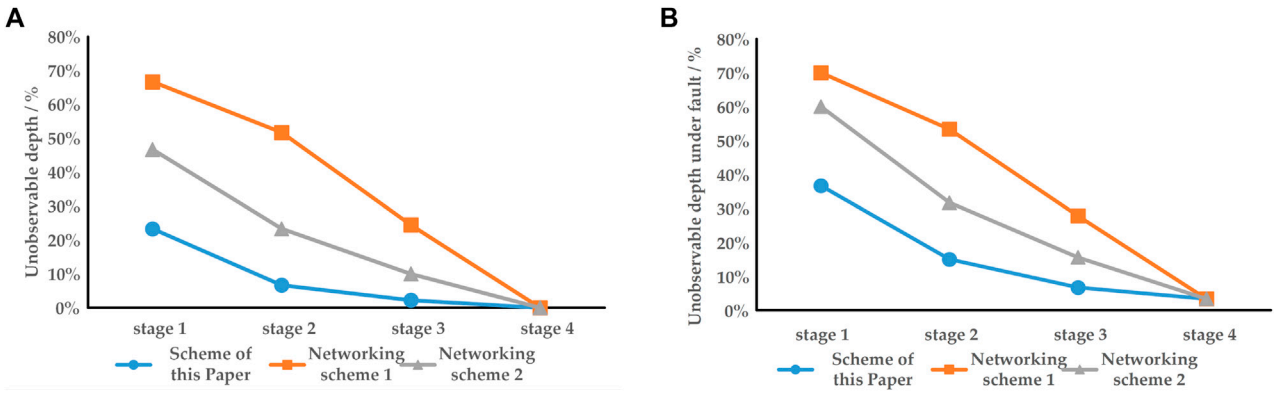

FIGURE 12
Unobservable depth comparison. **(A)** Unobservable depth of three schemes; **(B)** Unobservable depth under three schemes fault.

perpendicular orientation to the Sun's rays. Nodes characterized by higher irradiation intensity signify a greater potential for future installations of new photovoltaic power stations in their vicinity. Consequently, if an edge sensing terminal is deployed at such a node, additional terminals are not required after the construction of new photovoltaic power stations.

Resource development synergy $d_{i,2}$ is defined in Eq. 15

$$d_{i,2} = G_s. \tag{15}$$

3) Badness of communication $d_{i,3}$

The effectiveness of perception can be significantly influenced by the communication quality between edge sensing terminals and distributed resources. However, variations in terrain and distances can introduce differences in communication quality. In practical engineering scenarios, it is advisable to prioritize nodes with minimal communication quality loss when configuring terminals. To predict the wireless transmission quality in urban and surrounding areas, the Okumura model is employed, providing an analytical formula for the median path loss in different terrains (Eq. 16):

$$\begin{aligned} L_p = {} & 69.55 + 26.16LOG_{10}(f_c) - 13.82LOG_{10}(h_b) \\ & + [44.9 - 6.55LOG_{10}(h_b)]LOG_{10}d - a(h_m) \end{aligned}. \tag{16}$$

In the formula, h_b is the height of the base antenna, h_m is the equivalent height of the terminal, and f_c is the carrier frequency in hertz.

Small- and medium-sized towns (Eq. 17):

$$a(h_m) = [(1.1LOG_{10}(f_c) - 0.7)]h_m - [1.56LOG_{10}(f_c) - 0.8]. \tag{17}$$

Metropolis (Eqs 18, 19):

$$a(h_m) = 8.29[LOG_{10}(1.54h_m)]^2 - 1.1 \quad fc \le 200Mhz. \tag{18}$$

$$a(h_m) = 3.2[LOG_{10}(11.75h_m)]^2 - 4.94 \quad fc \ge 400Mhz. \tag{19}$$

Suburbs + correction factor (Eq. 20):

$$L_{ps} = L_{p\ \text{urban area}} - 2 \times [LOG_{10}(f_c/28)]^2 - 5.4. \tag{20}$$

Add correction factor to the open ground (Eq. 21):

$$\begin{aligned} L_{po} = {} & L_{\text{p urban area}} - 4.78 \times [LOG_{10}(f_c)]^2 + 18.33LOG_{10}(f_c) \\ & - 40.94. \end{aligned} \tag{21}$$

In the distribution network area, different terrains will cause differences in communication quality. The communication quality of each node in the maximum working distance communication ($d = R_{\max}$) and is measured by the communication badness $d_{i,3}$ (Eq. 22):

$$d_{i,3} = L_p. \tag{22}$$

Considering the $d_{i,1}$, $d_{i,2}$, and $d_{i,3}$ proposed above, it is necessary to point out that the synergy of resource development $d_{i,2}$ is a positive indicator, while the node degree $d_{i,1}$ and communication badness $d_{i,3}$ are negative indicators.

The three aforementioned indicators are treated as attributes, transforming the problem into a decision scenario with multiple attributes (Yu et al., 2013). Utilizing the entropy method, weights are assigned to the three indicators, assessing their roles and proportions.

Entropy, as an index measuring the disorder state of the system, reflects an increase in the disorder degree and the divergence between the state quantities within the system. Consequently, the entropy value serves to weigh the significance of a single index in the comprehensive node index. The entropy value for index j is defined in Eq. 23

$$\begin{cases} E_j = -\sum_{i=1}^{n} h_{i,j} \ln h_{i,j}, \ (j = 1, 2, \cdots, m) \\ h_{i,j} = d_{i,j} \Big/ \sum_{i=1}^{N} d_{i,j} \end{cases}. \tag{23}$$

In the formulae, n represents the number of distribution network nodes, $h_{i,j}$ represents the proportion of node i in the index j of the system, and m is the number of single indices.

By using entropy to calculate the objective weight of the index, the differences in the degree of the nodes in the system under the index can be revealed, which has a more significant impact on the measurement of the comprehensive index. The weight δ_j of the index j can be defined in Eq. 24

$$\delta_j = \frac{1 - E_j}{m - \sum_{j=1}^{m} E_j} \quad j = 1, 2, \cdots, m. \tag{24}$$

After obtaining the weight, the weight of the node ω_i can be obtained by multiplying the weight of the weight and the index value, which can be used as the basis for optimizing the configuration. Among them, since the synergy of resource development is a positive index, it is necessary to first take the opposite and then solve the weight.

3.2 Objective function

Economic considerations take precedence in the planning problem, with costs comprising that of both investment and operation, as well as maintenance expenses, constituting the life cycle cost. The optimized objective function is formulated as Eq. 25

$$\min C = C_I + C_C + \sum_{i=1}^{n} a x_i \omega_i. \tag{25}$$

In the formula, C_I is the cost of investment, C_C is the operation and maintenance cost, and a is the node weight coefficient.

1) Operation and maintenance cost

The service life of edge sensing terminals is limited. In practical applications, variations in the number of distributed resources and the volume of connected data lead to distinct failure rates and lifetimes of edge sensing terminals (Ge et al., 2021). The operation and maintenance cost is determined by Eq. 26:

$$C_C = u \sum_{i=1}^{N} L_i. \tag{26}$$

In the formula, u represents the cost of a single repair terminal; L_i is the annual average number of repairs for the i-th terminal. The annual average maintenance times L_i can be calculated by Eq. 27.

$$L_i = L_K + \mathrm{ceil}(v p_i n_i). \tag{27}$$

In the formula, L_K is the fixed number of repairs, v is the coefficient related to the number of maintenance, ceil is the integral function, n_i is the number of distributed resources connected to the i-th edge sensing terminal, and p_i is the failure rate of the i-th edge sensing terminal, which is calculated as follows Eq. 28:

$$p_i = \frac{\psi n_i}{n_{\max}}. \tag{28}$$

In the formula, $n_{\max}$ is the maximum number of distributed resources that a single terminal can provide services to and ψ is the fault coefficient.

2) Investment cost

The investment cost C_I encompasses the expenses associated with purchasing and installing the edge sensing terminal. The life cycle investment for equipment of the edge sensing terminal in the medium- and low-voltage power grid is delineated as Eqs 29, 30:

$$C_I = \sum_{i=1}^{N} P A(r, l_i). \tag{29}$$

$$A(r, l_i) = \frac{r(1 + r)^{l_i}}{\left((1 + r)^{l_i} - 1\right)}. \tag{30}$$

In the above formulae, C_I is the investment cost, N is the total number of installation terminals, P is the price of a single terminal, $A(r, l_i)$ is the capital recovery coefficient, and r is the interest rate, l_i is the life of the i-th edge sensing terminal, which is affected by the failure rate. The calculation is as Eqs 31, 32:

$$l_i = l_0 - \omega n_i \sum_{j \in i}^{S} \left(k_j^{1/2} + \sigma\right). \tag{31}$$

$$k_j = \frac{W_j}{W_T}. \tag{32}$$

In the above formulae, l_0 is the maximum life of the terminal, ω and σ are the life coefficients, k_j is the terminal data capacity coefficient,

W_T is the terminal reference capacity, and W_j is the amount of data of the distributed resource j.

3.3 Constraint condition

The optimal configuration model for the terminals is subject to various constraints, outlined as follows:

1) Connection number constraint

The terminal's capacity to connect with distributed resources is limited, and to prevent underutilization, the terminal must cater to at least one distributed resource. This constraint is expressed as Eq. 33:

$$1 \le \sum_{j=1}^{M} Z_{i,j} \le n_{\max}. \tag{33}$$

2) Observability constraint

When all edge sensing terminals are functioning normally, it is required that all distributed resources be fully observable, that is, the unobservable depth is 0. Simultaneously, to prevent redundancy, each distributed resource should only be connected to one terminal. This constraint is expressed as Eqs 34, 35:

$$\sum_{i=1}^{N} Z_{i,j} = 1. \tag{34}$$

$$\eta_s = 0. \tag{35}$$

In the case of an O fault set, the unobservable depth is required to be less than $\eta_{\lim}$, which is expressed as Eq. 36:

$$\eta_s^{'} = \frac{\max(U_i)}{M} < \eta_{\lim}. \tag{36}$$

3) Communication distance constraint

In the intelligent sensing system described in the second section, a bidirectional connection can be established between the edge sensing terminal and the distributed resources through wireless communication. In practical applications, the distance between the edge sensing terminal and the distributed resource should not exceed the optimal communication range. The constraints are as Eq. 37:

$$Z_{i,j} R_{i,j} \le R_{\max}. \tag{37}$$

4) Maximum quantity limit

Due to the spatial constraints of the distribution network, the number of terminals is limited as Eq. 38:

$$N \le N_k. \tag{38}$$

In the formula, N_k is the maximum number of edge sensing terminals installed in a certain area.

5) Maximum quantity limit

In this study, all terminals are configured on nodes, and each node is configured with a maximum of one terminal (Eq. 39).

$$x_{i,b} \le 1 \quad i = 1, 2, 3, \ldots n. \tag{39}$$

In the formula, $x_{i,b}$ is the number of edge sensing terminals installed on node i.

3.4 Configuration process and solution method

Firstly, the index for evaluating the weight of each node is determined, and the comprehensive weight of the index is calculated using the entropy method. Subsequently, the comprehensive node weight of each node is calculated to optimize the terminal configuration. In this study, an improved adaptive genetic algorithm is employed as the solution algorithm. The fitness function for the edge sensing terminal optimization configuration problem is Eq. 40

$$f = -\left(C_I + C_C + \sum_{i=1}^{n} a x_i \omega_i \right). \tag{40}$$

The key steps in the genetic algorithm include selection, crossover, and mutation. In the selection process, the roulette method is employed, favoring the selection of excellent individuals. Let the crossover probability of global search be denoted as P_c, and the mutation probability of local search as P_m. The calculation formulas for crossover probability and genetic probability are as Eq. 41:

$$P_c = \begin{cases} P_{c1} - \dfrac{P_{c1} - P_{c2}}{f_{\max} - f_{av}} \cdot (f_b - f_{av}) & (f_b \ge f_{av}, f_{\max} > f_{av}) \\ P_{c1} & \text{other cases} \end{cases}$$

$$P_m = \begin{cases} P_{m1} - \dfrac{P_{m1} - P_{m2}}{f_{\max} - f_{av}} \cdot (f - f_{av}) & (f \ge f_{av}, f_{\max} > f_{av}) \\ P_{m3} & (f_{\max} = f_{av}) \\ P_{m1} & \text{other cases} \end{cases}. \tag{41}$$

In the formulae, f_b represents the larger fitness value of the two crossover individuals, f_{av} is the average fitness value, $f_{\max}$ is the maximum fitness value of all individuals, P_{c1} and P_{c2} are the upper and lower limits of the crossover probability, respectively, and P_{m1}, P_{m2}, and P_{m3} are the upper, lower, and intermediate values of the mutation probability, respectively.

If the average fitness value is equal to the maximum fitness value, the upper limit is chosen as the crossover probability, and the intermediate value is selected as the mutation probability. Such a choice can maintain a favorable evolutionary trend and simplify the mathematical calculation process. The solution process for the optimal configuration of the edge sensing terminal is illustrated in Figure 2.

4 Dynamic networking method of sensing terminal coordinated with controllable distributed resource expansion plan

The third section discussed the one-time configuration of edge sensing terminals considering node weights. However, it currently lacks the ability to dynamically adapt to changes in the network based on power grid planning, ensuring comprehensive information sensing under evolving conditions. As the integration of renewable energy and load demand rises, the demand for distributed controllable resources increases, leading to a continuous process of resource expansion. In practical engineering applications, more distributed resources are progressively integrated, forming a multistage resource planning selection process, as discussed in Liang and Ma (2021). Due to the characteristics of small capacity, large quantity, and scattered installation locations, newly constructed distributed resources must be gradually incorporated into the observable and controllable range of the power system. Additionally, financial constraints may limit the immediate configuration of edge sensing terminals for perceiving distributed resources, making it more feasible to install new terminals in multiple stages. Considering these aspects, configuring all distributed resources at once to achieve complete observability and controllability is not realistic. Hence, there is a pressing requirement for research on dynamic perception networking technology. The term "dynamic" implies the ability to stagewise configure edge sensing terminals according to plans for expanding distributed resources and the limitations of current terminal configuration funds. This ensures the maximum unobservable depth for each stage, obtaining the optimal ranking of configuration terminals for each stage and gradually expanding the perception of controllable distributed resources.

4.1 Dynamic networking model construction

The power company provides an advance comprehensive plan for the expansion of distributed resources in a specific area and derives the edge sensing terminal configuration scheme based on the planned solution for distributed resources. However, owing to the substantial volume of one-time construction, the expansion of distributed resources and the configuration of edge sensing terminals must be executed in batches according to the plan. Let the state variable indicate whether a specific location in the distributed resource scheme is extended to include sensing (Eq. 42).

$$y_j = \begin{cases} 1, & \text{Distributed resource j has been include in the expansion plan} \\ 0, & \text{Distributed resource j is not included in the expansion plan} \end{cases} \quad y_j \in Y. \tag{42}$$

In the formula, Y represents the construction scheme of all distributed resources.

The state variable V_j is used to indicate whether the distributed resource j is observable (Eq. 43).

$$V_j = \begin{cases} 1, & \text{The unobservable depth of distributed resource j is 0} \\ 0, & \text{else} \end{cases}. \tag{43}$$

In the optimal configuration of the phased edge sensing terminal, it is necessary to minimize the unobservable depth of the distributed resource under the condition of fixed cost. In the case that the distributed resource j has to be included in the expansion, that is, $y_j = 1$, if $V_j = 1$, it indicates that the distributed resource can be observed. Then, $y_j - V_j = 0$. If $y_j - V_j = 1$, it indicates that the distributed resources at j are not monitored.

Assuming that the distributed resource planning is divided into q stages, the objective function of the dynamic networking model of the sensing terminal is Eq. 44

$$\begin{cases} \min \sum_{e=1}^{q} (Y_e - Q_e) \\ S_e = S_{e-1} + X_e \\ X_e = [x_1, x_2, x_3 \ldots\ldots x_N] \\ Q_e = [V_1, V_2, V_3 \ldots\ldots V_m]. \\ V_j = \max\left(Z_{e(i,j)}\right) \\ Y_e = [y_1, y_2, y_3 \ldots\ldots y_m] \\ Z_e = F(S_e, Y_e) \\ e = 1, 2, 3 \ldots q \end{cases} \tag{44}$$

In the formula, S_e is the terminal configuration before the current stage, where the element is defined as the same formula Eq. 44), $S_0 = 0$; X_e is the decision variable phasor of the single-stage configuration edge terminal, which is defined in the same form Eq. 44); Q_e is the observable situation of the distributed resources in the e-th stage, which is composed of V_j. It is determined by the distributed resources and terminal connection Z_e in the e-th stage. If the maximum value of the j-th column of Z_e is 1, then V_j is 1, which means that the resource j is observable. F is the function of calculating the connection condition, and the connection condition Z_e is calculated from the current configuration and photovoltaic construction.

The decision variable x_i is still used to indicate whether node i installs the edge terminal (Eq. 45).

$$x_i = \begin{cases} 1, & \text{Node i installs edge sensing terminal} \\ 0, & \text{Node i does not install edge sensing terminal.} \end{cases} \quad x_i \in X. \tag{45}$$

In the formula, X represents the edge sensing terminal configuration scheme when the power company's distributed resource construction scheme is Y.

The constraints of the model are as follows:

1) Cost constraints

The cost of each stage must not surpass the maximum value (Eqs 46, 47).

$$C_{I,e} = P \times n_e. \tag{46}$$

$$C_{I,e} < C_{\max,e}. \tag{47}$$

In the formulae, $C_{I,e}$ is the direct investment cost in the e-th stage, which is composed of the number of terminals n_e in the e-th stage multiplied by price P of a single terminal; $C_{\max,e}$ is the maximum cost that can be invested in stage e in the optimal allocation. It should be pointed out

that the cost here is different from the cost of the one-time edge sensing terminal configuration. The former is the investment cost of a single investment, and the latter is the annual expenditure cost during the lifetime of the edge sensing terminal, that is, the life cycle cost.

2) State variable constraints

V_j is used to indicate whether the planning point j is connected to the terminal, but the existence of V_j has to be based on $y_j = 1$. When $y_j = 1$, it is meaningful to discuss whether j is observable. The constraint can be expressed as Eq. 48

$$V_j \le y_j. \tag{48}$$

3) Connection number constraint

All edge sensing terminals must provide services for at least one distributed resource (Eq. 49).

$$1 \le \sum_{j=1}^{m_s} Z_{i,j} \le n_{\max}. \tag{49}$$

In the formula, $n_{\max}$ is the maximum number of distributed resources that a single edge sensing terminal can provide services to.

4) The number of monitored constraints

Each distributed resource should be connected by only one edge sensing terminal, and the constraints are expressed as Eqs 50, 51:

$$\sum_{i=1}^{n_s} Z_{i,j} = 1. \tag{50}$$

$$n_s = \sum_{e=1}^{s} n_e. \tag{51}$$

In the formulae, n_s is all edge sensing terminals included in the distribution system up to the current stage; s is the current stage.

5) Communication distance constraint

The distance between the edge sensing terminal and distributed resources should not exceed the ideal range of communication (Eq. 52).

$$Z_{i,j} R_{i,j} \le R_{\max}. \tag{52}$$

6) Maximum quantity limit

Due to the spatial limitations of the distribution network, there are certain constraints on the number of edge sensing terminals (Eq. 53).

$$n_q \le n_k. \tag{53}$$

In the formula, n_k is the maximum number of edge sensing terminals installed at each node of the distribution network and n_q is the total number of terminals in the final planning.

4.2 Configuration process and solution method

In the dynamic networking of edge sensing terminals, the adaptive genetic algorithm is still employed. Initially, the comprehensive weight of each index is calculated based on the final distributed resource expansion plan. Subsequently, the weight index of each node is determined considering the overall weight of the nodes. The final configuration scheme X for edge sensing terminals is then obtained. Following this, iterative solutions using the genetic algorithm are performed according to the distributed resource expansion plan for each stage. The goal is to obtain the edge sensing terminal configuration scheme that minimizes the unobservable depth of distributed resources and establishes connections with them.

When applying the genetic algorithm to address the problem, the fitness function for the edge sensing terminal dynamic networking configuration problem is expressed as Eq. 54

$$f = -\left(\sum_{e=1}^{q} (Y_e - Q_e) \right). \tag{54}$$

The dynamic network configuration of edge sensing terminals is solved using the adaptive genetic algorithm, as illustrated in Figure 3.

5 Case study

5.1 IEEE 33 node system

The optimal configuration method for edge sensing terminals, as proposed, is implemented and validated on the IEEE 33-bus system and the Hubei Guangshui Ten North I loop 408 system using the model and solution approach outlined in this article, with verification performed through the MATLAB software.

The mathematical model parameters are detailed in Supplementary Data SA1, and certain parameters within it are chosen based on Ge et al. (2021). When determining resource development synergy, parameters are selected according to KLEIN (1976). For this study, the typical day parameters from March 16 are used, with the latitude setting for node 1 at 40° north latitude. Due to the small size of the IEEE-33 node system, the nodes are categorized as follows to reflect differences in the weight index of each node: nodes 1–5 and 19–22 are quasi-smooth terrain of large cities, nodes 6–10 and 29–33 are open terrain, nodes 11–18 are suburban terrain, nodes 26–28 are open terrain with the correction factor halved, nodes 23–25 are suburban terrain with the correction factor doubled, and a 0.2 times $a(h_m)$ loss of large cities is introduced at nodes 5, 10, 15, 20, 25, and 30.

The topology of the IEEE 33-bus system and the distribution of photovoltaic power stations are depicted in Figure 4. In the figure, the red points signify the locations of the photovoltaic power stations. While each photovoltaic power station is physically linked to its corresponding node, this connection is not illustrated for simplicity. Supplementary Data SA2 and SA3 provide the positional coordinates of each node and certain photovoltaic power stations, which are measured in kilometers.

The three indices—node degree, resource development synergy, and communication quality—proposed above are collectively

employed to assess the weight index of nodes. Through the entropy method, the objective weights (d1–d3) are determined, yielding comprehensive weight results for the calculated indices: δ1 = 0.4096, δ2 = 0.2933, and δ3 = 0.2971. The weights for each node are presented in Figure 5.

The optimal terminal configuration scheme for the system is computed using the edge sensing terminal optimization configuration method proposed in this study. To assess the impact of node comprehensive weights in the optimization process, a simulation is conducted without considering the node weights. The optimal terminal configuration schemes calculated before and after these two simulations are presented in Table 1. Upon comparison, it is observed that incorporating node comprehensive weight indices does not lead to an increase in the required equipment count, and the cost of the configuration scheme remains the same, albeit with different node weights in the two schemes. Due to the different weights of nodes, the proposed solution in this article is more adaptable and universal and can ensure high reliability, achieving observability and controllability of distributed resources.

To evaluate the effectiveness of the algorithm, the minimum spanning tree algorithm and the 0-1 integer programming method are employed to optimize the edge sensing terminal. The respective configuration schemes are presented in Table 2 for comparison.

The results indicate that the algorithm proposed in this study yields the same number of terminals as the minimum spanning tree algorithm, which is fewer than the number obtained by the 0-1 integer programming algorithm. Moreover, the proposed algorithm minimizes the total cost. Considering the comprehensive weight of nodes, the configuration scheme becomes more feasible and adaptable for the future.

The terminal configuration scheme, taking into account the comprehensive weight of nodes, is illustrated in Figure 6.

In this scheme, a single edge sensing terminal is connected to a maximum of four photovoltaic power stations, and each edge sensing terminal is linked to at least one photovoltaic power station. The distance between the terminal and the photovoltaic power station is within the set R_{max} (4 km), ensuring that the scheme adheres to the constraints and achieves complete observability of the distributed resources.

Throughout the solution process, the unobservable depth progressively diminishes with each iteration, ultimately leading to the comprehensive observability of distributed resources. The unobservable depth during faults also gradually decreases and eventually drops below the predetermined threshold by 5%. The variation of unobservable depth and unobservable depth during faults is shown in Figure 7.

It can be demonstrated that the method proposed in this study accurately accomplishes terminal configuration within the specified target, minimizing both the life cycle cost and node comprehensive weight.

5.2 Hubei Guangshui Ten North I loop 408 system

The terminal dynamic networking model proposed in this study is applied to the actual distribution network system, specifically the Hubei Guangshui Ten North I loop 408 system. The distribution system comprises a total of 91 nodes and 120 photovoltaic power stations. The location of each node and photovoltaic power station are depicted in Figure 8A, with detailed coordinates provided in Supplementary Data SA4 and SA5, which are measured in kilometers. The selection of parameters, aside from the comprehensive weight of nodes, follows the assignments provided in Supplementary Data SA1. After optimization using the method proposed in this study, the final configuration scheme and its connections with resources are illustrated in Figure 8B.

In the edge sensing terminal configuration scheme presented in Figure 9, a total of 37 edge sensing terminals are deployed across 91 nodes. In the simulation of the dynamic networking model, a four-stage planning is set, denoted as $q = 4$. Each stage involves the expansion of 30 photovoltaic power plants, with a maximum investment of ¥600,000 in the first stage and ¥540,000 in subsequent stages.

To validate the effectiveness of the example, MATLAB is utilized to randomly generate the locations of photovoltaic power stations expanded over the four planning stages. The construction planning of photovoltaic power stations for each stage is detailed in Supplementary Data SA6.

In the first stage of planning, edge sensing terminals are configured at nodes 5, 12, 23, 29, 42, 46, 62, 65, 80, and 84. The unobservable depth is 23.3%, and the unobservable depth under fault is 36.67%. At this stage, the number of terminals is small, and the extended photovoltaic power stations are more dispersed, resulting in a higher unobservable depth after a fault. For the second stage, terminals are configured at nodes 8, 20, 31, 36, 38, 44, 51, 73, and 90. The unobservable depth is 6.67%, and the unobservable depth under fault is 15%. In the third stage of planning, terminals are configured at nodes 2, 11, 13, 28, 32, 58, 75, 85, and 87. The unobservable depth is 2.22%, and the unobservable depth under fault is 6.67%. Finally, in the fourth stage, edge sensing terminals are configured at nodes 3, 6, 18, 35, 39, 41, 68, 81, and 89. The unobservable depth is 0, and the unobservable depth under fault is 3.33%.

The comprehensive configuration scheme is presented in Table 3.

The unobservable depth and unobservable depth under fault steadily decrease through the iterative process of the four-stage planning, ultimately achieving complete observability of low-voltage distributed resources. The evolving trend of unobservable depth and unobservable depth under fault is illustrated in Figure 10.

To validate the effectiveness of this method, it is essential to compare it with two other network planning strategies. The first strategy involves arranging nodes sequentially from small to large, denoted as “networking scheme 1.” The second strategy entails a randomly generated network configuration, labeled as “networking scheme 2.” The configurations of these two schemes are illustrated in Figure 11.

The observability of networking scheme 1 and networking scheme 2 at each stage is computed, and the changes in the unobservable depth for all three schemes throughout the networking process are compared. The variations are depicted in Figure 12. By comparing the results, it becomes evident that the model and algorithm introduced in this study exhibit significant advantages in attaining the objective of minimizing the

unobservable depth at each stage. The proposed approach effectively achieves dynamic networking of edge sensing terminals in alignment with the photovoltaic construction process.

6 Conclusion

In this study, a dynamic networking method for monitoring terminals, which takes into account both node weight and unobservable depth while considering node differences, has been proposed to facilitate real-time and dependable monitoring of distributed systems. The key findings of the research are summarized as follows:

1) The proposed one-time configuration planning algorithm successfully achieves the minimum life cycle cost of the terminal while ensuring complete observability of distributed resources and accounting for node differences.
2) The proposed dynamic networking algorithm effectively achieves optimal configuration in phases, progressively reducing the unobservable depth of the system.
3) The comprehensive weight index, considering the differences in nodes, has a negligible impact on the number of monitoring terminals required and does not increase the installation cost.

Nevertheless, the model still has certain limitations that warrant improvement. Future research could consider a broader range of fault types to enhance the evaluation of unobservable depths under faults, moving beyond the current focus on single edge sensing terminal faults. Additionally, the inclusion of various renewable resources, such as the monitoring of wind turbines, could enhance the model's comprehensiveness. Furthermore, considering the diverse data transmission requirements for distributed resource power plants with varying capacities, there is room for optimization to achieve a panoramic perception of distributed resources at the minimum lifecycle cost.

Data availability statement

The original contributions presented in the study are included in the article/Supplementary Material; further inquiries can be directed to the corresponding author.

Author contributions

XJ: data curation, validation, and writing–original draft. DL: investigation, supervision, visualization, and writing–original draft. YY: methodology, validation, writing–original draft, and writing–review and editing. PX: data curation, formal analysis, supervision, and writing–review and editing. YS: validation and writing–review and editing. ZY: supervision and writing–review and editing.

Funding

The author(s) declare that financial support was received for the research, authorship, and/or publication of this article. This research was funded by the Technical Project of State Grid Corporation of China; grant number 5400-202122573A-0-5-SF.

Conflict of interest

Author XJ was employed by State Grid Hubei Electric Power Co. Ltd.

The remaining authors declare that the research was conducted in the absence of any commercial or financial relationships that could be construed as a potential conflict of interest.

Publisher's note

Supplementary material

The Supplementary Material for this article can be found online at: https://www.frontiersin.org/articles/10.3389/fenrg.2024.1323800/full#supplementary-material

References

Ali, Z. M., Razavi, S. E., Javadi, M. S., Gandoman, F. H., and Aleem, S. H. E. A. (2018). Dual enhancement of power system monitoring: improved probabilistic multi-stage PMU placement with an increased search space and mathematical linear expansion to consider zero-injection bus. *Energies* 11 (6), 1429. doi:10.3390/en11061429

Babaei, S., Zhao, C. Y., and Fan, L. (2019). A data-driven model of virtual power plants in day-ahead unit commitment. *IEEE Trans. Power Syst.* 34 (6), 5125–5135. doi:10.1109/tpwrs.2018.2890714

Babu, N. V. P., Babu, P. S., and Sarma, D. S. (2020). Critical elements based optimal PMU placement considering substation coverage. *Int. J. Electr. Eng. Inf.* 12 (3), 418–430. doi:10.15676/ijeei.2020.12.3.2

Bangjun, W., Feng, Z. L., Feng, J., Yu, P., and Cui, L. Y. (2022). Decision making on investments in photovoltaic power generation projects based on renewable portfolio standard: perspective of real option. *Renew. Energy* 189, 1033–1045. doi:10.1016/j.renene.2022.02.112

Chen, R. Z., Chen, H., Yang, S. Y., and Chen, Y. B. (2019). Optimal configuration model of distribution system switch. *Smart Power* 47 (07), 76–83. doi:10.3969/j.issn.1673-7598.2019.07.013

Ding, W., Xu, M., Huang, Y., Zhao, P., and Song, F. (2021). Cyber attacks on PMU placement in a smart grid: characterization and optimization. *Reliab. Eng. Syst. Saf.* 212, 107586. doi:10.1016/j.ress.2021.107586

Duffie, J. A., and Beckman, W. A. (2013). *Solar engineering of thermal processes*. John Wiley and Sons.

Fambri, G., Diaz-Londono, C., Mazza, A., Badami, M., Sihvonen, T., and Weiss, R. (2022). Techno-economic analysis of Power-to-Gas plants in a gas and electricity distribution network system with high renewable energy penetration. *Appl. Energy* 312, 118743. doi:10.1016/j.apenergy.2022.118743

Fang, D. W., Guan, X., Lin, L., Peng, Y., Sun, D., and Hassan, M. M. (2020). Edge intelligence based economic dispatch for virtual power plant in 5G internet of energy. *Comput. Commun.* 151, 42–50. doi:10.1016/j.comcom.2019.12.021

Ferreira, D. M. V. P., Carvalho, P. M. S., and Ferreira, L. A. F. M. (2020). Optimal meter placement in low observability distribution networks with Der. *Electr. Power Syst. Res.* 189, 106707. doi:10.1016/j.epsr.2020.106707

Ge, L. J., Liu, J. H., Yan, J., and Rafiq, M. U. (2021). Improved harris hawks optimization for configuration of PV intelligent edge terminals. *IEEE Trans. Sustain. Comput.* 7 (3), 631–643. doi:10.1109/tsusc.2021.3125016

Hu, J., Liu, X., Shahidehpour, M., and Xia, S. (2021). Optimal operation of energy hubs with large-scale distributed energy resources for distribution network congestion management. *IEEE Trans. Sustain. Energy* 12 (3), 1755–1765. doi:10.1109/tste.2021.3064375

Ji, H. R., Wang, C. S., Li, P., Ding, F., and Wu, J. Z. (2018). Robust operation of soft open points in active distribution networks with high penetration of photovoltaic integration. *IEEE Trans. Sustain. Energy* 10 (1), 280–289. doi:10.1109/tste.2018.2833545

Khare, G., Mohapatra, A., and Singh, S. N. (2021). Strategic PMU placement to alleviate power system vulnerability against cyber attacks. *Energy Convers. Econ.* 2 (4), 212–220. doi:10.1049/enc2.12038

Klein, S. A. (1976). Calculation of monthly average insolation on tilted surfaces. *Sol. energy* 19 (4), 325–329. doi:10.1016/0038-092x(77)90001-9

Kong, X. Y., Liu, C., Wang, C. S., et al. (2022). Demand response potential assessment method based on deep subdomain adaptation network. *Proceeding CSEE* 42 (16), 5786–5797. doi:10.13334/j.0258-8013.pcsee.210903

Kong, X. Y., Ma, Y. Y., Ai, Q., et al. (2023). Review on electricity consumption characteristic modeling and load forecasting for diverse users in new power system. *Automation Electr. Power Syst.* 47 (13), 2–17. doi:10.7500/AEPS20230313005

Kong, X. Y., Sun, Y., Khan, M. A., Zheng, L., Qin, J., and Ji, X. (2024). Cyber-physical system planning for VPPs supporting frequency regulation considering hierarchical control and multidimensional uncertainties. *Appl. Energy* 353, 122104. doi:10.1016/j.apenergy.2023.122104

Kong, X. Y., Wang, Y. T., Yuan, X. X., and Yu, L. (2019). Multi objective for PMU placement in compressed distribution network considering cost and accuracy of state estimation. *Appl. Sci.* 9 (7), 1515. doi:10.3390/app9071515

Li, W. G., and Lu, J. L. (2018). PMU measurement location optimization in active distribution network based on immune discrete PSO algorithm. *Electr. Meas. Instrum.* 55 (21), 14–18+30. doi:10.3969/j.issn.1001-1390.2018.21.003

Li, Y., Zhang, H., Liang, X., and Huang, B. (2018). Event-triggered-based distributed cooperative energy management for multienergy systems. *IEEE Trans. Industrial Inf.* 15 (4), 2008–2022. doi:10.1109/tii.2018.2862436

Liang, H. S., and Ma, J. (2021). Data-driven resource planning for virtual power plant integrating demand response customer selection and storage. *IEEE Trans. Industrial Inf.* 18 (3), 1833–1844. doi:10.1109/tii.2021.3068402

Liu, X. C., Wu, H. C., Li, Y. X., Wang, L., and Wang, C. (2020). A bi-level optimization model of distribution automation terminal configuration. *Power Syst. Prot. Control* 48 (24), 136–144. doi:10.19783/j.cnki.pspc.200170

Nouri, A., Jafarian, M., and Keane, A. (2022). Efficacious models of discrete control devices for convex optimization in distribution systems. *IEEE Trans. Power Syst.* 38 (5), 4682–4696. doi:10.1109/tpwrs.2022.3208751

Qiao, Q. J. (2016). The calculation method of ground objects receiving solar radiation quantity. *Technol. Vis.* (22), 177–178. doi:10.19694/j.cnki.issn2095-2457.2016.22.122

Razavi, S. E., Falaghi, H., Azizivahed, A., Ghavidel, S., Li, L., and Zhang, J. F. (2018). Improved probabilistic multi-stage PMU placement with an increased search space to enhance power system monitoring. *IFAC-PapersOnLine* 51 (28), 262–267. doi:10.1016/j.ifacol.2018.11.712

Razavi, S. E., Falaghi, H., Esmaeel, N. A., Hadidian Moghaddam, M. J., and Gandoman, F. H. (2020). An effective approach for the probabilistic and deterministic multistage PMU placement using cuckoo search: Iran's national power system. *Iran. J. Sci. Technol. Trans. Electr. Eng.* 44, 237–252. doi:10.1007/s40998-019-00236-0

Wang, S. (2019). *Research on multi-objective optimal placement of pmu in smart distribution network considering the accuracy of state estimation. Master Thesis*. Shanghai, China: Shanghai Jiaotong University.

Xi, Y., Yu, L., Jiang, W. H., Chen, B., Zhou, B., Liang, B., et al. (2022). Multi-stage optimal PMU configuration based on revised analytic hierarchy process. *Guangdong Electr. Power* 35 (09), 87–93. doi:10.3969/j.issn.1007-290X.2022.009.010

Xu, Y., Liu, C. C., Schneider, K. P., and Ton, D. (2015). Placement of remote-controlled switches to enhance distribution system restoration capability. *IEEE Trans. Power Syst.* 31 (2), 1139–1150. doi:10.1109/tpwrs.2015.2419616

Yang, F., Ling, Z. N., Zhang, Y. H., He, X., Ai, Q., and Qiu, R. (2022). Event detection, localization, and classification based on semi-supervised learning in power grids. *IEEE Trans. Power Syst.* 38 (5), 4080–4094. doi:10.1109/tpwrs.2022.3209343

Yang, L., Li, X., Sun, M., and Sun, C. (2023). Hybrid policy-based reinforcement learning of adaptive energy management for the Energy transmis-sion-constrained island group. *IEEE Trans. Industrial Inf.* 19, 10751–10762. doi:10.1109/tii.2023.3241682

Yi, S. J., Xiang, S., Su, P., Wang, Y., and Song, Z. H. (2023). A multi-stage optimal configuration method for SPMU of subsynchronous oscillation monitoring system under high proportion of wind power. *Mod. Electr. Power* 40 (01), 18–26. doi:10.19725/j.cnki.1007-2322.2021.0239

Yu, H., Liu, Z., and Li, Y. J. (2013). Key nodes in complex networks identified by multi-attribute decision-making method. *ActaPhysica Sin.* 62 (02), 1–9. doi:10.7498/aps.62.020204

Zeng, S. Q., Wu, J. K., Li, X., Wang, R. D., and Zhang, H. Y. (2021). Multi-stage optimal configuration of PMU considering changes in distribution network topology. *Guangdong Electr. Power* 34 (09), 51–59. doi:10.3969/j.issn.1007-290X.2021.009.007

Zhang, N., Sun, Q., Yang, L., and Li, Y. (2021). Event-triggered distributed hybrid control scheme for the integrated energy system. *IEEE Trans. Industrial Inf.* 18 (2), 835–846. doi:10.1109/tii.2021.3075718

Zhao, Z., Yu, H., Li, P., Kong, X., Wu, J., et al. (2019). Optimal placement of PMUs and communication links for distributed state estimation in distribution net-works. *Appl. energy* 256, 113963. doi:10.1016/j.apenergy.2019.113963

frontiers | Frontiers in Energy Research

TYPE Original Research
PUBLISHED 01 May 2024
DOI 10.3389/fenrg.2024.1352385

OPEN ACCESS

EDITED BY
Yaser Qudaih,
Higher Colleges of Technology, United Arab Emirates

REVIEWED BY
Mansoor Janjua,
Higher Colleges of Technology, United Arab Emirates
Gaber Magdy,
Aswan University, Egypt

*CORRESPONDENCE
Gu Tingyun,
gutingyun@126.com

RECEIVED 08 December 2023
ACCEPTED 27 March 2024
PUBLISHED 01 May 2024

CITATION
Tingyun G, Houyi Z, Bowen L, Junyi M, Qiang F, Yutao X and Qihui F (2024), Virtual inertia control to active support of the variable-speed wind turbine in variable frequency limit time. *Front. Energy Res.* 12:1352385. doi: 10.3389/fenrg.2024.1352385

Virtual inertia control to active support of the variable-speed wind turbine in variable frequency limit time

Gu Tingyun*, Zhang Houyi, Li Bowen, Mao Junyi, Fan Qiang, Xu Yutao and Feng Qihui

Electric Power Research Institute of Guizhou Power Grid Co., Ltd., Guiyang, Guizhou, China

Constraining the virtual inertia of variable-speed wind turbines within the variable frequency limit time will be the key to improving the wind power's reliability in actively supporting the system frequency. First, this paper analyzes the controllable characteristics and evaluation methods of the virtual inertia of the wind turbine. Second, it quantifies the variable frequency limit time of the grid with high-proportion wind power and considers the wind turbine speed and power margin to restrict the virtual inertia of the wind turbine during the period of frequency drop or increase to provide reliable inertia support to ensure the safety of the system frequency. On this basis, the inertia demand under the frequency safety of the system was analyzed, and the virtual inertia control strategy of the variable-speed wind turbine in the variable frequency limit time was proposed using the speed tracking performance of the wind turbine. Finally, the grid with a high-proportion wind power simulation system is built to verify that the variable-speed wind turbine can reliably satisfy the inertia demand of system frequency modulation under the proposed control strategy and significantly improve its active support performance to the power grid.

KEYWORDS

wind power generation, virtual inertia, frequency support, rotor speed tracking, power grid

1 Introduction

Improving the grid-connected support capability of wind turbines has become a key technology for enabling high-proportion wind power consumption and achieving the "30·60 carbon target." Under maximum power tracking control, large-scale random and intermittent wind power is injected into the power grid, and the synchronous generator is unable to ensure the safe operation of the system due to the reduction of the installed proportion (Fernández-Guillamón et al., 2019; Mensou et al., 2020; Zhu et al., 2021). At present, the frequency active support control of variable-speed wind turbines has attracted much attention.

Variable-speed wind turbines can actively participate in the frequency adjustment of the power grid by adding virtual inertia and primary frequency controllers based on power tracking control (Yuan et al., 2017; Ochoa and Martinez, 2018; Yuan et al., 2018). In the early stage of frequency change, if the wind turbine does not have an inertial response, it will lead to a significant increase in the frequency change rate, and a large frequency drop or increase will seriously threaten the safety of system operation (Sun et al., 2010; Tielens and

Hertem, 2016; Das et al., 2020). In order to solve the problem of low inertia in wind turbines, Fu et al. (2017) and Qi et al. (2022) defined the virtual inertia of wind turbines. Different from the constant inherent inertia of the synchronous generator, the virtual moment of inertia through additional control not only depends on the inherent inertia, initial speed, and control parameters of the wind turbine but is also closely related to the change in the system frequency, resulting in its complex and changeable characteristics while also renders it more flexible and controllable. Mauricio et al. (2009); Gautam et al. (2011); and Li et al. (2016) proposed a virtual inertia control strategy for wind turbines and used the differential link df/dt to simulate the rotor motion characteristics of synchronous generators. On this basis, ULLAH et al. (2008); Makrini et al. (2017) further added a speed recovery module to ensure the speed recovery of the wind turbine after the inertial response, avoiding the secondary frequency drop caused by excessive inertial support during system recovery. Effective inertia support can avoid large and rapid changes in frequency, and allowing for sufficient adjustment time for subsequent primary frequency modulation. In order to reduce the static deviation of the system frequency after primary frequency modulation, the same active frequency droop control as the synchronous generator was introduced into the active power control of the wind turbine. Ramtharan et al. (2007) and Zertek et al. (2012) proposed a deloading control method for wind turbines and simulated the primary frequency modulation characteristics of synchronous generators through variable pitch control. Almeida and Lopes (2007) and Zhang et al. (2012) used the overspeed control of the wind turbine to complete the deloading operation of the wind turbine and cooperated with the virtual inertia to improve the frequency modulation performance of the wind turbine. In theory, the power electronic converter gives the wind turbine flexible power control performance. However, the characteristics of virtual frequency modulation are affected by many factors, and its engineering practicability still requires to be explored.

The performance evaluation of the virtual inertia and primary frequency modulation of the wind turbine is generally difficult to solve (Wu and Infield, 2014; Zhu et al., 2018). Among them, the additional primary frequency control is relatively simple. When the load-shedding reserve capacity is sufficient, the wind turbine can have the same power distribution capability as the synchronous generator using the active power frequency droop characteristics (Vidyanandan and Senroy, 2013; Xiao et al., 2017). However, it is difficult to evaluate the virtual inertia of the wind turbine, which requires discussion at present. Because the initial wind speed determines the kinetic energy reserve of the wind turbine and the wind turbine speed will be affected by power tracking control, additional inertia control, and system frequency characteristics at the same time, the virtual inertia is always in dynamic change, which is not only complicated in quantification but also has operating risk. Ma et al. (2017); Zhu et al. (2017); and Ying et al. (2018) analyzed that although the introduction of virtual inertia can reduce the frequency change rate, it has the risk of aggravating the system power oscillation. Shi et al. (2011) and Lucas et al. (2019) used the small disturbance analysis method to prove that the virtual inertia of the wind turbine would lead to the right shift of the characteristic root and weaken the stability of the system. Reasonable quantification of virtual inertia can not only provide a basis for accurately predicting the effect of frequency active support but also be the key to evaluating the operation risk of additional control. Wen and Lin (2021) and Wang et al. (2022) proposed quantitative requirements for virtual inertia to ensure the frequency security of the grid through constraints such as frequency change rate and minimum value. However, the expected virtual inertia support is not only a prerequisite but also an urgent problem to be solved. Although the source of virtual inertia has been extended to various renewed energy sources and loads, the nonlinear time-varying characteristics make it difficult to quantify the inertia, and a reasonable time scale is urgently needed to constrain the multi-source inertia to complete the evaluation (Wen and Lin, 2021). In summary, the wind power frequency active support technology is not mature at present, and the promotion and application still lack the quantification and control methods of virtual inertia.

In order to improve the reliability of wind turbine frequency active support control according to the system frequency safety requirements, this paper proposes a quantitative method and control strategy of virtual inertia using the inertia support time and wind turbine operation characteristics constraints. First, based on the definition of virtual inertia of the wind turbine, the frequency characteristics of the wind power grid-connected system and the problems of inertia evaluation are analyzed. Second, the frequency conversion extreme time is calculated, and the wind turbine speed and power margin are considered to constrain and quantify the wind turbine virtual inertia. Third, according to the virtual inertia demand and quantitative index, the virtual inertia control strategy of the variable-speed wind turbine in the extreme time of frequency conversion is proposed by speed tracking control. Finally, a simulation system with high-proportion wind power is built to verify the improvement effect of the proposed evaluation method and control strategy on the reliability of wind turbine frequency active support.

The remainder of this paper is organized as follows: Section 2 presents the virtual inertia evaluation method for wind turbines. Section 3 presents the calculation method of frequency conversion extreme time for the system with high-proportion wind power. Section 4 presents the virtual inertia constraint and evaluation of wind turbines. Section 5 presents the virtual inertia demand and control of wind turbines. Section 6 presents the numerical results and demonstrates the effectiveness of the proposed method. Section 7 concludes the paper and presents future work.

2 Virtual inertia evaluation of the wind turbine

2.1 Wind turbine frequency active support characteristics

After the system with a high proportion of wind power encounters an active power disturbance, the system frequency support should be completed by the synchronous generator set and wind turbine. In order to improve the utilization rate of wind energy, wind farms usually do not use the deloading operation mode to reserve for primary frequency regulation. In this mode, the virtual inertial response will be the frequency active support function that wind power urgently needs. In the wind power grid-connected

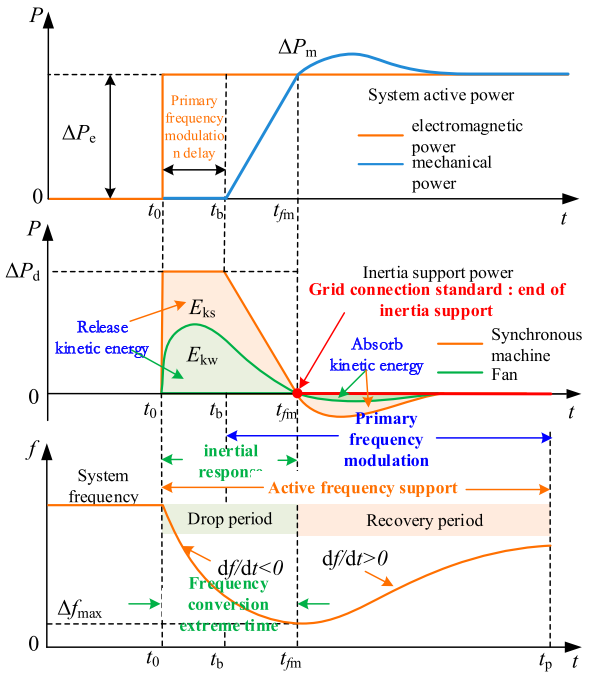

FIGURE 1
Power support of generators and dynamic response of system frequency.

system, the synchronous generator and the wind turbine should jointly complete the inertial support, and the primary frequency modulation function is borne by the synchronous generator and the energy storage.

Taking a short-term frequency drop as an example, the dynamic response of wind turbines and synchronous generators participating in frequency adjustment is shown in Figure 1. In this figure, t_0 is the frequency drop time, t_b is the primary frequency modulation action time, t_{fm} is the time when the frequency drops to the lowest value, and t_p is the end time of the primary frequency modulation.

At time t_0, the load suddenly increases ΔP_d, and the system frequency drops sharply. The synchronous generator set and wind turbine need to respond quickly to the frequency change, and the system power demand is compensated by the fast active power support, that is, $\Delta P_e = \Delta P_d$.

At the t_0~t_{fm} stage, after the wind turbine starts the inertia support control, it will share the unbalanced power borne by the synchronous generator, thereby slowing down the system frequency drop speed. The common virtual inertia control of wind turbines adopts a differential link, and the power response is defined as Eq. (1):

$$\Delta P_w = -K_I \times \mathrm{d}f/\mathrm{d}t, \tag{1}$$

where ΔP_w is the wind turbine inertial support power and K_I is the differential control coefficient.

As shown in Figure 1, during a frequency drop ($\mathrm{d}f/\mathrm{d}t$ <0), the power response of the virtual inertia controller is ΔP_w >0. At this stage, the synchronous generator and the wind turbine jointly maintain the inertia support power and satisfy the load demand ΔP_d. The wind turbine reduces the kinetic energy demand of the synchronous generator by releasing the kinetic energy.

At the t_{fm} ~ t_p stage, during frequency recovery ($\mathrm{d}f/\mathrm{d}t$ >0), the power response of the virtual inertia controller is ΔP_w <0. At this stage, the wind turbine absorbs power from the system under virtual inertia control, and the wind turbine changes from releasing kinetic energy to absorbing kinetic energy, which increases the primary frequency regulation burden of the synchronous generator and slows down the frequency recovery speed.

Considering that the virtual inertia has the problem of grid-connected security, at present, GB/T19963.1–2021 “wind farm access power system technical regulations” have stipulated that the wind turbine is required to have the inertia support function after being connected to the system, but the additional controller must satisfy the following conditions: $\Delta f \times \mathrm{d}f/\mathrm{d}t$ >0. The wind turbine should set the time t_{fm} as the end time of the virtual inertia control to satisfy the grid-connected requirements.

It is worth noting that it is necessary to detect the frequency signal at the grid-connected point of the wind turbine when determining the end t_{fm} of the inertial support. The differential signal has high-frequency noise in the field test. Combined with the actual test situation, it is difficult to determine whether $\Delta f \times \mathrm{d}f/\mathrm{d}t$ is greater than zero. In addition, at the end of the moment of inertia support, the wind turbine has released kinetic energy, resulting in a decrease in speed. After restoring to the maximum power tracking control, the output power of the wind turbine will still be lower than the initial level before the frequency drop. This is because the wind turbine speed has dropped. Therefore, even if the inertial control can be terminated in time, the wind turbine will still absorb the power, accelerate the rotor, store kinetic energy, and complete the maximum power tracking target; however, this will not be conducive to frequency recovery during primary frequency modulation.

It can be seen from Figure 1 that during the active frequency support period, the virtual inertia control of the wind turbine cannot continuously provide effective active power support for the system. Combined with the inertia start-up conditions specified in the grid-connected standard, this paper defines the effective time of the inertia response as the frequency conversion extreme time t_{fm}; that is, after the system is disturbed, the frequency drops or increases from the initial value to the maximum frequency deviation.

Before adopting virtual inertia control, if the wind turbine can predict the extreme time of frequency conversion, it not only ensures the safe removal of the additional control and effectively avoids the misoperation caused by the large monitoring error of the frequency differential signal but also helps solve the problem of quantitative evaluation of virtual inertia, and then it provides a more reliable calculation method for the inertia demand under the system frequency safety.

2.2 Virtual inertia evaluation based on frequency conversion extremum time

The inertia of the wind power grid-connected system is composed of the inherent inertia of the synchronous generator and the virtual inertia of the wind turbine. The inertia time constant of the synchronous generator depends on the mechanical characteristics of the rotor, which can be expressed as Eq. (2) (Zhu et al., 2021)

$$H_g = \frac{E_{kg}}{S_g} = \frac{J_g \omega_e^2}{2p_g^2 S_g}, \tag{2}$$

where J_g is the mechanical moment of inertia of the synchronous generator; ω_e is the synchronous speed; p_g is the number of rotor poles; E_{kg} is the rotor kinetic energy stored at the rated speed of the synchronous generator; and S_g is the rated capacity of the synchronous generator.

Referring to the definition of the inertia time constant of a synchronous generator, the virtual inertia time constant H_{vir} of a variable-speed wind turbine can be expressed as (Qi et al., 2022)

$$H_{vir} = \frac{J_{vir}\omega_e{}^2}{2p_w^2 S_w} = \frac{\Delta\omega_r}{\Delta\omega_e}\frac{\omega_{r0}}{\omega_e}H_w, \tag{3}$$

where H_w is the inherent inertia time constant of the wind turbine; $\Delta\omega_r$ is the change in the wind turbine speed; ω_{r0} is the initial speed of the wind turbine before the inertial response; $\Delta\omega_e$ is the synchronous speed variation; p_w is the number of wind turbine poles; S_w is the rated capacity of the wind turbine; and J_{vir} is the virtual moment of inertia of the wind turbine, which can be expressed as

$$J_{vir} = \frac{\Delta\omega_r}{\Delta\omega_e}\frac{\omega_{r0}}{\omega_e}J_w, \tag{4}$$

where J_w is the inherent moment of inertia of the wind turbine.

According to the definition of the virtual inertia of the wind turbine in (3) and (4), it can be seen that if $\Delta\omega_r/\Delta\omega_e >>1$, the virtual inertia will be much larger than the inherent inertia of the wind turbine and even has better inertial support ability than the synchronous generator set. However, in practical control, H_{vir} is determined by ω_{r0}, H_w, and $\Delta\omega_r/\Delta\omega_e$, where ω_{r0} depends on the real-time wind speed, which can be expressed as Eq. (5)

$$\omega_{r0} = \begin{cases} \frac{\lambda_{opt} v}{R}, v_{min} < v < v_{max}, \\ \omega_{max}, v > v_{max} \end{cases} \tag{5}$$

where λ_{opt} is the optimal tip speed ratio; v is the real-time wind speed; R is the radius of the wind wheel; ω_{max} is the maximum speed allowed for the stable operation of the wind turbine; v_{min} is the cut-in wind speed; and v_{max} is the maximum wind speed before the pitch control starts.

In the control process, it is necessary to comprehensively consider the dynamic changes in the inherent inertia H_w, wind speed, additional power, and system frequency of the wind turbine to obtain the effect of $\Delta\omega_r >> \Delta\omega_e$. Due to the coupling problem of multiple variables, the virtual inertia of the wind turbine can be much higher than the inherent inertia in theory, but the dynamic changes in the control process will make it difficult to predict its support performance and seriously weaken its application value.

In the current virtual inertia evaluation method, due to the real-time fluctuation of wind turbine speed and system angular frequency, $\Delta\omega_r/\Delta\omega_e$ needs to be monitored in real-time. In the absence of time-scale constraints, the virtual inertia of the wind turbine will be an uncertain parameter. If reliable inertia reserves cannot be obtained, it will be impossible to predict the drop or increase in the amplitude of frequency after disturbance, which makes the key problem of frequency security early warning difficult to solve.

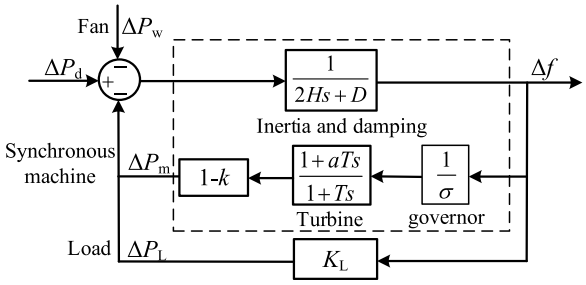

FIGURE 2
System frequency response aggregation model.

To solve this problem, a time scale must be introduced to constrain the virtual inertia. In this paper, the extreme time of frequency conversion is taken as the effective time of inertia response of the wind turbine. In the range of $t_0 \sim t_{fm}$, if $\Delta\omega_e$ is equal to the unit value of Δf_{max}, then H_{vir} can be expressed as

$$H_{vir} = \begin{cases} \frac{\Delta\omega_r H_w}{\Delta f_{max}\omega_e} \times \frac{\lambda_{opt} v}{R}, v_{min} < v < v_{max} \\ \frac{\Delta\omega_r H_w}{\Delta f_{max}\omega_e} \times \omega_{max}, v > v_{max}. \end{cases} \tag{6}$$

According to (6), $\Delta\omega_r$ determines the size of H_{vir} when other parameters are known. At this time, the virtual inertia of the wind turbine can be quantitatively evaluated according to the speed variation in the frequency conversion extreme time. Therefore, the key to evaluating the virtual inertia of the wind turbine is to calculate the extreme value time of the system frequency conversion and obtain the speed change after the inertia response of the wind turbine.

3 Frequency conversion extreme time of system with high-proportion wind power

3.1 Frequency conversion extreme time calculation

Considering the limitation of the inherent inertia of the wind turbine on the speed, as well as the real-time changes in the wind turbine speed and system frequency, not only the potential of virtual inertia control remains unclear, but there are also still many problems in quantitative evaluation. In order to solve this problem, this paper will use the frequency conversion extreme time and the wind turbine operating state to constrain the virtual inertia for quantitative evaluation. Among them, the calculation process of the system frequency conversion extreme time as a key parameter is as follows.

In the system with high-proportion wind power, the aggregation model structure of the synchronous generator set and wind turbine is shown in Figure 2. The model includes the synchronous generator, wind turbine, and load frequency response module. The parameter design of each module is shown in Table 1.

TABLE 1 System frequency response model parameters and value range.

Model parameter	Value range
System inertia time constant H	4~10 s
System damping coefficient D	0~1
System load regulation coefficient K_L	0~2
Synchronous machine adjustment coefficient σ	0.03–0.05
Turbine equivalent inertia time constant T	6~10 s
Turbine characteristic coefficient a	0<a<1
Wind power penetration k	\

According to Figure 2, the system frequency response equation can be expressed as

$$2H\frac{\mathrm{d}\Delta f}{\mathrm{d}t} + D\Delta f = -\Delta P_m - \Delta P_w - \Delta P_L + \Delta P_d, \tag{7}$$

where ΔP_m is the synchronous generator power response signal; ΔP_w is the wind turbine power response signal; ΔP_L is the load power response signal; and H is the system inertia time constant. Among them, ΔP_m depends on the synchronous generator adjustment coefficient and turbine parameters, which can be expressed as

$$\Delta P_m = \frac{1-k}{\sigma} \times \frac{1+aTs}{1+Ts}\Delta f, \tag{8}$$

where ΔP_L depends on the load regulation coefficient, equal to $K_L \times \Delta f$, and H depends on the system capacity and wind power penetration, which can be expressed as

$$H = H_g\frac{S_g}{S_B} = H_g(1-k), \tag{9}$$

where k is the wind power penetration and S_B is the rated capacity of the system.

The system frequency variation can be calculated using (7) and expressed as

$$\Delta f(s) = \frac{1+Ts}{2HT(s^2+2b\xi s+b^2)}[\Delta P_d(s) - \Delta P_w(s)]. \tag{10}$$

The inverse Laplace transform is applied to (10), and the system frequency response $\Delta f(t)$ is

$$\Delta f(t) = (\Delta P_d - \Delta P_w) \times G(t) = (\Delta P_d - \Delta P_w) \times \left\{\frac{\sigma}{(D+K_L)\sigma + 1 - k}\left[1 + \alpha e^{-b\xi t}\sin(wt+\varphi)\right]\right\}. \tag{11}$$

In (11), each parameter is expressed as

$$b = \sqrt{\frac{(D+K_L)\sigma+1-k}{2H\sigma T}},\ \alpha = \sqrt{\frac{1-2b\xi T+b^2T^2}{1-\xi^2}},$$
$$\xi = \frac{(D+K_L)\sigma T + 2H\sigma + aT}{2[(D+K_L)\sigma+1-k]/b},\ w = b\sqrt{1-\xi^2}, \text{and} \tag{12}$$
$$\varphi = \arctan\left(\frac{wT}{1-b\xi T}\right) - \arctan\left(\frac{\sqrt{1-\xi^2}}{-\xi}\right).$$

TABLE 2 Parameter values and calculation results of frequency expression.

Parameter value		
H = 5 s	σ = 0.04	D = 0
T = 8 s	a = 0.3	K_L = 1
k = 0% computation		
b = 0.570	w = 0.299	ξ = 0.855
α = 7.218	φ = −8.34°	t_{fm} = 2.305 s
k = 20% computation		
b = 0.573	w = 0.279	ξ = 0.873
α = 7.668	φ = −7.492°	t_{fm} = 2.298 s
k = 40% computation		
b = 0.577	w = 0.249	ξ = 0.902
α = 8.671	φ = −6.619°	t_{fm} = 2.295 s

Without considering the power response of the wind turbine, $\Delta P_w = 0$ is taken, and ΔP_d is regarded as a step disturbance. At this time, the derivative of (11) is obtained, and the extreme time of frequency conversion of the system can be expressed as

$$t_{fm} = \frac{1}{w}\arctan\left(\frac{wT}{b\xi T - 1}\right). \tag{13}$$

According to (11)–(13), the extreme time of frequency conversion is not only related to the inertia of conventional synchronous generators but also affected by wind power penetration and wind turbine power response. Among them, conventional synchronous generators can take typical parameter settings. The following section further discusses the influence of wind turbine-related parameters on the frequency conversion extreme time.

3.2 Influencing factors of frequency conversion extreme time

3.2.1 Wind power penetration

From (8) and (9), it can be seen that under the influence of wind power penetration, the system inertia time constant becomes H_g (1-k), and the adjustment coefficient becomes σ/(1-k); that is, wind power penetration will reduce the system inertia time constant. However, at the same time, the system adjustment coefficient is equivalently increased. When the two parameters change at the same time, the influence of the two on the frequency conversion extreme time has an offset effect. Therefore, the influence of wind power penetration on the frequency conversion extreme time is not significant. In order to verify this conclusion, the typical data in Table 1 are substituted into (12) and (13) to calculate the intermediate variables and the frequency conversion extreme time, as shown in Table 2.

The calculation results in Table 2 are brought into (11), and the power disturbance ΔP_d = 0.05 pu is taken to obtain the frequency

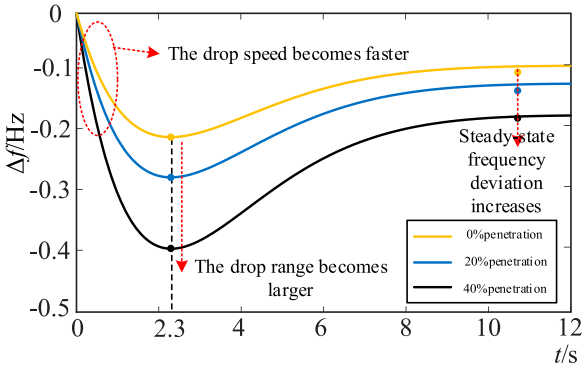

FIGURE 3
System frequency response curves under different wind power penetration.

response under different wind power penetration rates, as shown in Figure 3.

It can be seen from Figure 3 that the wind power penetration rate will affect the system frequency change rate, the maximum frequency deviation, and the steady-state frequency deviation after primary frequency regulation, but it has little effect on the frequency conversion extreme time. According to the calculation results in Table 2, 2.3 s is used as the typical value for system frequency conversion extreme time in this paper.

3.2.2 Additional inertial response

In the extreme time of frequency conversion, when the inertia support potential of the wind turbine is stimulated to the maximum extent, the power response of the wind turbine can be regarded as a step change, and the power reference value will jump from the maximum power tracking control signal to the rated power or the minimum power output in a short time. Under this condition, the limit power support signal of the wind turbine can be expressed as

$$\Delta P_w = \begin{cases} P_n - P_{opt} & \Delta P_d > 0 \\ P_{opt} - P_{min} & \Delta P_d < 0 \end{cases}, \tag{14}$$

where P_n is the rated power of the wind turbine; P_{min} is the power corresponding to the minimum speed of the stable operation of the wind turbine; and P_{opt} is the active output power of the wind turbine under MPPT control, which can be expressed as

$$P_{opt} = \begin{cases} k_{opt}\omega_r^3 & \omega_0 < \omega_r < \omega_{max} \\ P_n & \omega_r > \omega_{max}, \end{cases} \tag{15}$$

where k_{opt} is the maximum power tracking coefficient and ω_0 is the cut-in speed.

When ΔP_w is equivalent to a step signal, its effect is equivalent to the equivalent reduction of ΔP_d, and it does not affect the parameters in $G(t)$. Therefore, the power response of the wind turbine only affects the increase and decrease in the speed of frequency and the frequency deviation extremum and does not affect the frequency conversion extremum time.

In summary, when evaluating the inertia of the wind turbine in the extreme time of frequency conversion, the calculation results of (13) can be regarded as the action time of the virtual inertia of the wind turbine. At this time, the wind turbine speed variation can be calculated by the wind turbine running state constraint, and then the virtual inertia of the wind turbine can be estimated.

4 Virtual inertia constraint and evaluation of wind turbines

4.1 Wind turbine operating state constraints

The virtual inertia of the wind turbine depends on its kinetic energy reserve and is closely related to its initial speed ω_{r0}. In addition, the initial active power P_{we0} of the wind turbine determines the adjustment range of the power support ΔP_w, which in turn affects the kinetic energy release or absorption capacity of the wind turbine.

4.1.1 Kinetic energy reserve constraint

The wind turbine energy reserve depends on the allowable value of the speed change during the frequency conversion extreme period. When the disturbance power $\Delta P_d > 0$, the system has a power shortage, and the wind turbine needs to release the rotor kinetic energy; when $\Delta P_d < 0$, the system has a power surplus, and the wind turbine needs to absorb energy and store it as rotor kinetic energy. Therefore, the kinetic energy reserve constraint of wind turbines can be expressed as Eq. (16)

$$\Delta E_{kw} \le \Delta E_{kwmax} = \begin{cases} \frac{1}{2}J_w\left(\omega_{r0}^2 - \omega_{min}^2\right) & \Delta P_d > 0 \\ \frac{1}{2}J_w\left(\omega_{r0}^2 - \omega_{max}^2\right) & \Delta P_d < 0, \end{cases} \tag{16}$$

where ΔE_{kwmax} is the wind turbine energy reserve; ω_{r0} is the wind turbine speed at the beginning of the inertial response; ω_{min} and ω_{max} are the allowable minimum and maximum speeds for the stable operation of the wind turbine, respectively, usually 0.7 pu and 1.2 pu (Fu et al., 2017). Under the constraint of kinetic energy reserve, the variation range of $\Delta\omega_r$ in the frequency conversion extreme time is expressed as

$$\Delta\omega_r \le \Delta\omega_{rmax1} = \begin{cases} \omega_{r0} - \omega_{min} & \Delta P_d > 0 \\ \omega_{max} - \omega_{r0} & \Delta P_d < 0, \end{cases} \tag{17}$$

where $\Delta\omega_{rmax1}$ is the maximum speed variation under the constraint of kinetic energy reserve.

4.1.2 Wind turbine power constraint

In order to ensure the safe operation of the wind turbine, the support power provided by the virtual inertia control is not allowed to exceed the limit. According to (14) and (15), the wind turbine power constraint is

$$\Delta P_w \le \Delta P_{wmax} = \begin{cases} P_n - k_{opt}\omega_{r0}^3 & \Delta P_d < 0 \\ k_{opt}\omega_{min}^3 - k_{opt}\omega_{r0}^3 & \Delta P_d > 0. \end{cases} \tag{18}$$

In the process of the inertial response, the rotor motion equation of the wind turbine can be expressed as

$$2H_w\omega_r\frac{d\omega_r}{dt} = P_{wm} - P_{we} = -\Delta P_w, \tag{19}$$

where P_{we} is the electromagnetic power output by the wind turbine and P_{wm} is the mechanical power captured by the wind turbine, $P_{wm} = k_{opt}\omega_{r0}^3$.

Combining (18) and (19), under the constraint of the rated power of the wind turbine, the variation range of $\Delta\omega_r$ in the extreme time of frequency conversion is

$$\Delta\omega_r \le \Delta\omega_{rmax2} = \begin{cases} \omega_{r0} - \sqrt{\frac{k_{opt}\omega_{r0}^3 - P_n}{H_w} t_{fm} + \omega_{r0}^2} & \Delta P_d > 0 \\ -\omega_{r0} + \sqrt{\frac{k_{opt}\left(\omega_{r0}^3 - \omega_{min}^3\right)}{H_w} t_{fm} + \omega_{r0}^2} & \Delta P_d < 0, \end{cases} \quad (20)$$

where $\Delta\omega_{rmax2}$ is the maximum speed variation under the wind turbine power constraint.

It can be seen from (20) that the size of $\Delta\omega_{rmax2}$ is determined using H_w, k_{opt}, ω_{r0}, and other parameters. When the capacity and type of the wind turbine are determined, H_w and k_{opt} can be obtained, and $\Delta\omega_{rmax2}$ only depends on $\Delta\omega_{rmax2}$.

In order to satisfy the kinetic energy reserve constraint and the wind turbine power constraint at the same time, according to (17) and (20), the maximum speed variation of the wind turbine $\Delta\omega_{rmax}$ can be expressed as Eq. (21)

$$\Delta\omega_{rmax} = \min\{\Delta\omega_{rmax1}, \Delta\omega_{rmax2}\}. \quad (21)$$

Taking the typical parameters of a 2 MW doubly fed wind turbine as an example, take H_w = 4 s, k_{opt} = 1/1.23, ω_{min} = 0.7 pu, ω_{max} = 1.2 pu, and t_{fm} = 2.3 s. According to (17), (20), and (21), $\Delta\omega_{rmax}$ corresponding to different initial speeds of the wind turbine under kinetic energy reserve constraints and power constraints is obtained as follows.

According to Figure 4, when ΔP_d >0, the wind turbine needs to release the kinetic energy of the rotor. When the initial speed of the wind turbine is small, the kinetic energy reserve of the wind turbine is small, but the inertial support power available is large. At this time, $\Delta\omega_{rmax}$ is determined using the kinetic energy reserve constraint; when the initial speed of the wind turbine is large, its kinetic energy reserve is large, but the available inertial support power is small. At this time, $\Delta\omega_{rmax}$ is determined using the wind turbine power constraint. When the initial speed of the wind turbine is 0.905 pu, $\Delta\omega_{rmax1} = \Delta\omega_{rmax2}$, and $\Delta\omega_{rmax}$ reaches the maximum of 0.205 pu at this initial speed. When ΔP_d <0, when the wind turbine needs to absorb energy, the relationship between $\Delta\omega_{rmax}$ and speed constraint is completely opposite to that when ΔP_d <0. When the initial speed of the wind turbine is small, $\Delta\omega_{rmax}$ depends on the power constraint of the wind turbine. When the initial speed is large, $\Delta\omega_{rmax}$ depends on the kinetic energy reserve constraint. When the initial speed is 1.07 pu, $\Delta\omega_{rmax}$ reaches the maximum of 0.13 pu.

In summary, in the extreme time of frequency conversion, under the constraint of the wind turbine's operating state, when ΔP_d > 0, the range of rotational speed variation provided is 0–0.205 pu; when ΔP_d <0, the range of rotational speed variation is 0–0.13 pu.

4.2 Virtual inertia evaluation of the wind turbine

According to (6), the virtual inertia time constant of the wind turbine also depends on Δf_{max}. Since the lower limit of power system frequency security is 48 Hz, the frequency deviation extremum of the system should be limited within this range after the inertial response of the wind turbine. Since the wind turbine has a fast power response capability, it can be set within the frequency safety range to complete the predetermined virtual inertia support. Therefore, Δf_{max} = 2 Hz is used to conservatively estimate the virtual inertia of the wind turbine.

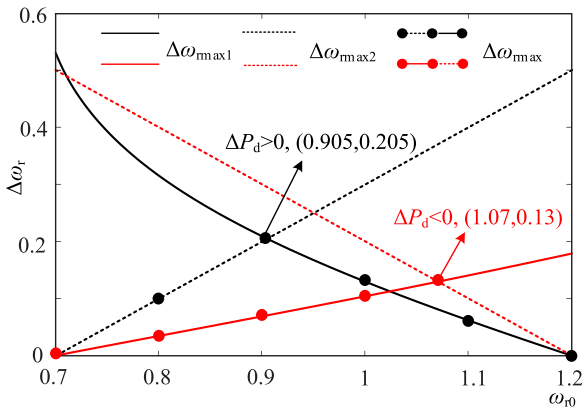

FIGURE 4
Evaluation results of the maximum speed variation of the wind turbine.

According to the evaluation results of Section 4.1 $\Delta\omega_{rmax}$, the range of the virtual inertia time constant of the wind turbine during the frequency conversion extreme time is as follows.

In the diagram, $H_{virmax1}$ and $H_{virmax2}$ are the maximum inertia time constants of the wind turbine under rotor kinetic energy constraint and power constraint, respectively. When the above two constraints are satisfied simultaneously, H_{virmax} can be expressed as Eq. (22)

$$H_{virmax} = \min\{H_{vir\ max1}, H_{vir\ max2}\}. \quad (22)$$

It can be seen from Figure 5 that when ΔP_d > 0 and the speed of the rotor kinetic energy released by the wind turbine decreases, H_{virmax} depends on the rotor kinetic energy constraint at low speeds, and H_{virmax} depends on the wind turbine power constraint at high speeds. The H_{virmax} range is 0–18.61 s; when ΔP_d<0, when the wind turbine absorbs energy and the speed increases, H_{virmax} depends on the wind turbine power constraint at low speed, and H_{virmax} depends on the rotor kinetic energy constraint at high speed. The H_{virmax} range is 0–13.85 s.

However, Δf_{max} in the actual response process of the system is related to the disturbance power. When the disturbance power is small, Δf_{max} will be less than 2 Hz, and H_{virmax} of the wind turbine will be greater than the evaluation result, which can ensure that the wind turbine has a credible inertial support capability.

According to the above analysis, the wind turbine can show strong inertial support performance in a short time by changing the rotational speed through additional control. In theory, the wind turbine can cope with large power disturbances and has frequency support potential. In the actual control process, a large change in the speed in a short time will bring about problems such as power overshoot, increased mechanical load, and difficulty in speed recovery. Therefore, the wind turbine should perform an inertial

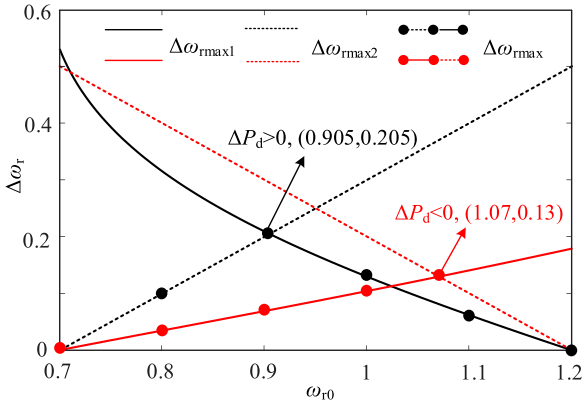

FIGURE 5
Evaluation results of the maximum virtual inertia of the wind turbine.

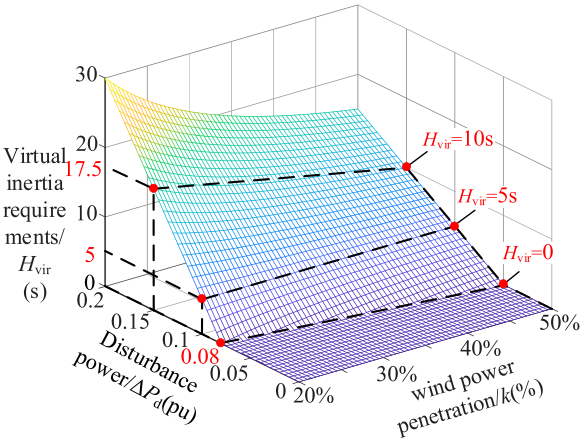

FIGURE 6
Wind turbine virtual inertia demand assessment results.

response under the premise of considering the system's inertia demand.

5 Virtual inertia demand and control of wind turbines

5.1 Virtual inertia requirements

The inertia of the wind power high-proportion system is significantly reduced, and the virtual inertia of the wind turbine should be set according to the system frequency safety requirements. At present, foreign research has put forward relevant standards for microgrid island operation, requiring that the system frequency change rate (df/dt) is not higher than ±0.5 Hz/s (Wang et al., 2022). The maximum frequency change rate of the system occurs at the initial stage of the power disturbance. The primary frequency modulation has not yet acted, and the unbalanced power of the rotor side of the synchronous machine is the largest. At this time, the system frequency change rate can be expressed as Eq. (23)

$$\left.\frac{df}{dt}\right|_{max} = \frac{\Delta P_d}{2H}. \tag{23}$$

According to the above formula, when the frequency change rate constraint is determined, the system inertia requirement can be expressed as

$$H \geq H_{min} = \Delta P_d \Big/ 2\left.\frac{df}{dt}\right|_{max}, \tag{24}$$

where H_{min} is the minimum inertia requirement of the system.

When the wind turbine provides virtual inertia, the inertia time constant of the system with a high proportion of wind power can be further expressed using (9) as

$$H = H_g\frac{S_g}{S_B} + H_{vir}\frac{S_w}{S_B} = H_g(1-k) + H_{vir}k. \tag{25}$$

Combining (24) and (25), the inertia demand of the wind turbine is expressed as

$$H_{vir} = \Delta P_d \Big/ \left(2k \times \left.\frac{df}{dt}\right|_{max}\right) - \frac{H_g(1-k)}{k}. \tag{26}$$

Taking H_g = 5s and $(df/dt)_{max}$ = ±0.5 Hz/s, the virtual inertia requirement of the wind turbine is calculated using the brought-in (26), as shown in Figure 6.

It can be seen from Figure 6 that the demand of system frequency security for the virtual inertia for the wind turbine mainly depends on disturbance power and wind power penetration. When the disturbance power is small and the wind power penetration rate is low, only the synchronous machine inertia H_g can meet the system inertia demand. When the permeability is lower than 20%, the inertia of the synchronous machine can cope with more than 8% of the disturbance. However, with the increase in wind power penetration, the ability of the system to cope with power disturbances is gradually weakened. When the wind power penetration reaches 50%, the system can cope with disturbances of less than 5%, which is not enough to cope with typical faults. At this time, the wind turbine should provide the necessary inertial support according to the system requirements. The inertia demand of the system increases with the increase in power disturbance. Under the same power disturbance, the virtual inertia demand of the wind turbine can be calculated according to the wind power penetration rate. When ΔP_d = 0.15 pu, the system inertia requirement is 7.5 s. When k = 20%, the wind turbine needs to provide 17.5 s of virtual inertia to make the total inertia of the system reach 7.5 s. When k = 50%, the wind turbine needs to provide 10 s of virtual inertia to make the total inertia of the system reach 7.5 s.

5.2 Virtual inertia control strategy

Combined with the system frequency safety requirements, the wind turbine can use its speed tracking performance to complete the virtual inertial support within the frequency conversion extreme time. The structure of the wind turbine virtual inertia controller proposed in this paper is shown in Figure 7, which consists of two modules: virtual inertia control and virtual inertia evaluation. Among them, the virtual inertia evaluation module has two

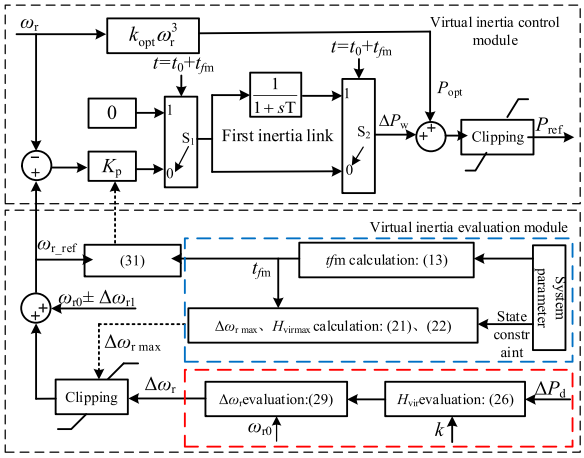

FIGURE 7
Wind turbine virtual inertia controller structure.

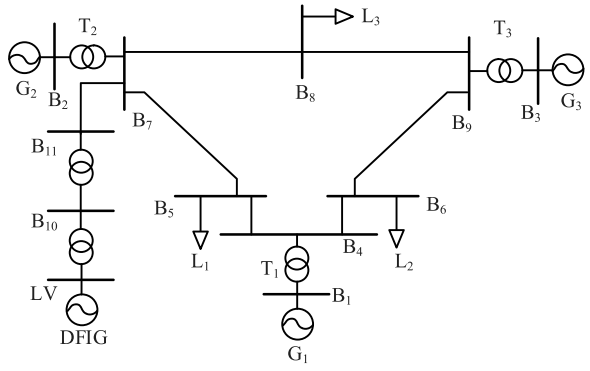

FIGURE 8
Simulation model of the wind power high permeability system.

evaluation functions: the maximum inertia of the wind turbine and the system inertia demand.

In the wind turbine virtual inertia evaluation module, the maximum speed variation and maximum inertia are evaluated according to the operating state and frequency conversion extreme time constraint, which are used as the limiting conditions of the wind turbine inertia demand and speed variation demand evaluation results. For the evaluation of the wind turbine's virtual inertia demand, according to (26), disturbance power and wind power permeability can be introduced to calculate the wind turbine's inertia demand. According to the evaluation results of the wind turbine's inertia demand, the wind turbine's speed demand can be calculated. The specific analysis is as follows:

The real-time equivalent inertia time constant H_{vir} in the process of wind turbine inertia response can be expressed as

$$H_{vir} = \frac{\Delta P_w(t)}{2\mathrm{d}f/\mathrm{d}t}. \tag{27}$$

In the extreme time of frequency conversion, both sides of (27) are integrated at the same time to obtain

$$\int_0^{t_{fm}} \Delta P_w(t)\mathrm{d}t = 2H_{vir}\Delta f_{max}, \tag{28}$$

where Δf_{max} is the frequency deviation value corresponding to t_{fm}, which can be calculated according to (11) under the assumption that the system inertia meets the demand. According to the calculation results, the simultaneous formulas (19) and (28) are solved, and the rotational speed variation that meets the inertia demand of the wind turbine can be expressed as

$$\Delta\omega_r = \begin{cases} \omega_{r0} - \sqrt{\dfrac{2H_{vir}\Delta f_{max}}{H_w} + \omega_{r0}^2} & \Delta P_d > 0 \\ -\omega_{r0} + \sqrt{\dfrac{2H_{vir}\Delta f_{max}}{H_w} + \omega_{r0}^2} & \Delta P_d < 0. \end{cases} \tag{29}$$

According to the above formula, the required speed variation $\Delta\omega_r$ of the wind turbine at different initial speeds can be obtained by introducing the operating state parameters and inertia requirements of the wind turbine. Then, within t_{fm} time, wind turbine corresponding speed can be calculated as $\omega_{r1} = \Delta\omega_r + \omega_{r0}$.

The wind turbine virtual inertia control module generates additional power signals through speed tracking control to make the wind turbine track the reference speed in real-time, and the reference speed ω_{r_ref} is set according to ω_{r1}. First, in order to ensure that the wind turbine speed can change from ω_{r0} to ω_{r1} within t_{fm}, the speed-tracking control principle based on the wind turbine rotor motion equation is designed as follows:

$$\int_0^t K_p(\omega_{r\_ref} - \omega_r)\mathrm{d}t = \int_{\omega_{r0}}^{\omega_{r1}} 2H_w\omega_r\mathrm{d}\omega_r, \tag{30}$$

where K_p is the speed-tracking controller parameter.

According to (30), the value of K_p in t_{fm} can be calculated as

$$K_p = \begin{cases} \dfrac{2H_w}{t_{fm}}\left[\omega_{r\_ref} \times \ln\dfrac{\omega_{r0} - \omega_{r\_ref}}{\omega_{r1} - \omega_{r\_ref}} + \Delta\omega_r\right] & \Delta P_d > 0 \\ \dfrac{2H_w}{t_{fm}}\left[\omega_{r\_ref} \times \ln\dfrac{\omega_{r\_ref} - \omega_{r0}}{\omega_{r\_ref} - \omega_{r1}} - \Delta\omega_r\right] & \Delta P_d < 0, \end{cases} \tag{31}$$

where $\omega_{r\_ref} = \omega_{r1} \pm \Delta\omega_{r1}$ and $\Delta\omega_{r1}$ is the speed change margin.

According to (31), the value of K_p can be calculated to realize the change in the wind turbine speed from ω_{r0} to ω_{r1} in t_{fm} to realize the quantitative control of the wind turbine speed.

Second, in order to ensure the smooth exit of the inertial support power of the wind turbine after the t_{fm} moment, the first-order inertial link is introduced, as shown in Figure 7. When the wind turbine speed changes to ω_{r1} at $t_0 + t_{fm}$, the switches S_1 and S_2 switch from 0 to 1, and the speed tracking control exits through the first-order inertia link. Under the above control, the wind turbine inertial support power signal can be expressed as

$$\Delta P_w = \begin{cases} K_p \times (\omega_{r\_ref} - \omega_r), t_0 < t < t_0 + t_{fm} \\ K_p \times (\omega_{r\_ref} - \omega_{r1}) \times e^{-\frac{1}{T}t}, t > t_0 + t_{fm}, \end{cases} \tag{32}$$

where T is the first-order inertial link time parameter, taking 5 s.

Under the control of (32), the inertial support power of the wind turbine is the largest at the initial moment of disturbance, which can effectively suppress the frequency change rate. After the frequency reaches the extreme point, the rotational speed changes to the

TABLE 3 System parameters.

Parameters of the wind turbine	Numerical value	Parameters of the wind turbine	Numerical value
Rated voltage/kV	0.69	Frequency bias coefficient	0.04
Rated power/kVA	2,222	Rated frequency/Hz	50
Inherent inertia/s	4	Inherent inertia/s	5
Wind speed/m/s	8		

TABLE 4 Parameter setting of simulation example 1

System parameter	Numerical value	Calculation	Numerical value
Installed gross capacity/MW	1,500	Wind power penetration k	20%
Total load/MW	900	Power disturbance ΔP_d	0.06 pu
Wind turbine capacity/MW	300	System inertia requirements H	3 s
Load mutation amount/MW	90	Wind turbine inertia demand H_{vir}	0

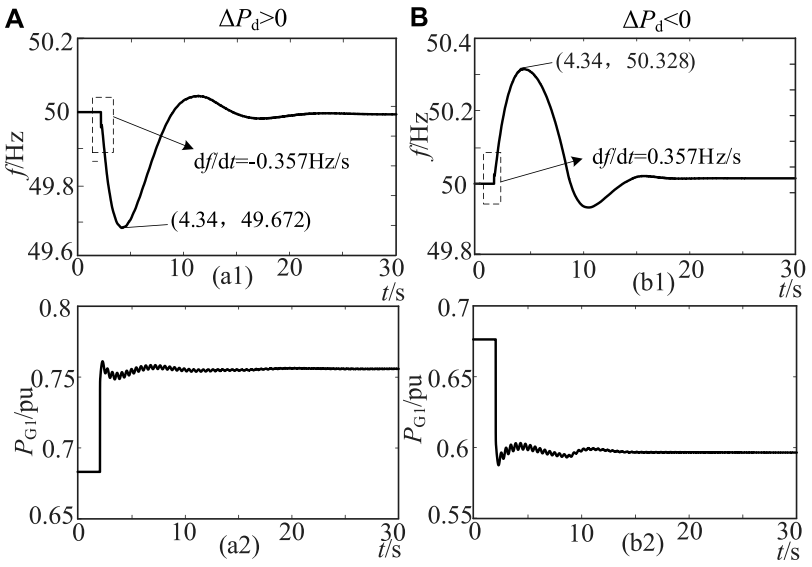

FIGURE 9
(a1): The change curve of frequency with time $\Delta P_d > 0$. **(a2)**: The change curve of PG with time $\Delta P_d > 0$. **(b1)**:The change curve of frequency with time $\Delta P_d < 0$. **(b2)**:The change curve of PG with time $\Delta P_d < 0$.

TABLE 5 Calculation results of simulation examples.

Parameter	Simulation result	Calculation result	Deviation (%)
Frequency conversion extreme time/s	2.34	2.3	1.74
Maximum frequency change rate/Hz/s	0.357	0.375	4.7
Maximum frequency deviation/Hz	0.328	0.318	3.14

According to Table 5, when the system generator governor is set to a typical parameter, the error between the simulation and calculation results of the system frequency conversion extreme time, the maximum frequency change rate, and the maximum frequency deviation is within 5%. The simulation results verify the accuracy of the calculation and analysis results of the system frequency response model.

TABLE 6 Parameter setting of simulation example 2.

System parameter	Numerical value	Calculation parameter	Numerical value
Installed gross capacity/MW	1,500	Wind power penetration k	20%
Total load/MW	900	Power disturbance ΔP_d	0.12 pu
Wind turbine capacity/MW	300	System inertia requirements H	6s
Load mutation amount/MW	180	Wind inertia demand H_{vir}	10 s

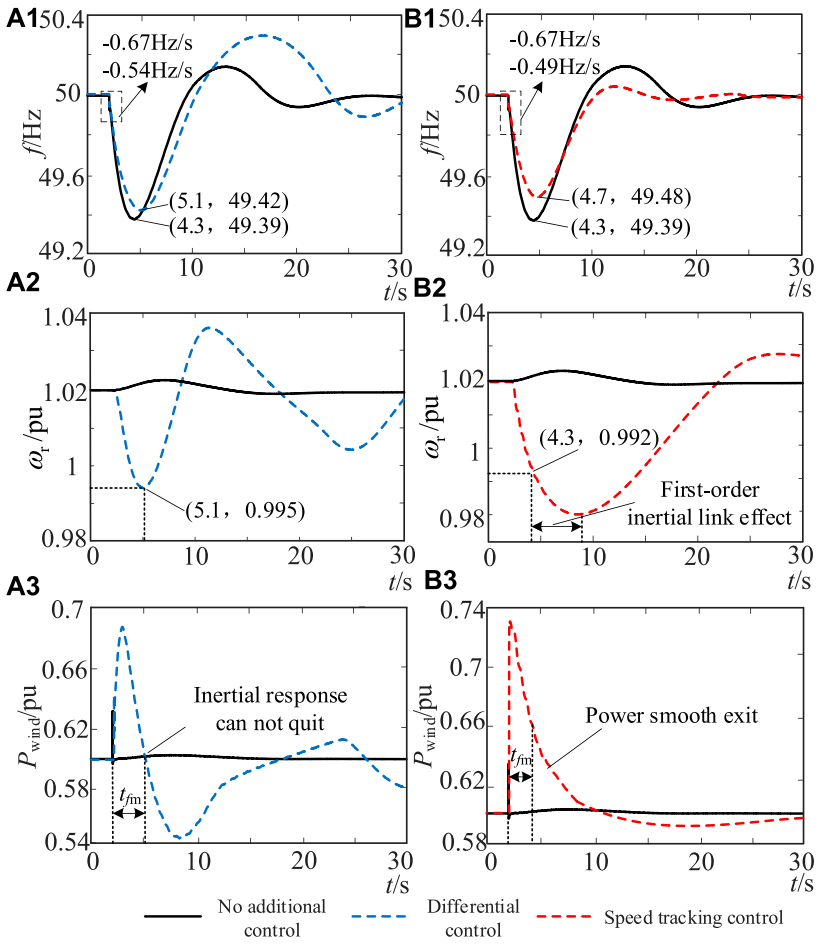

FIGURE 10
(A1):The first case using differential control. **(A2)**:The second case using differential control. **(A3)**:The third case using differential control. **(B1)**:The first case using speed tracking control. **(B2)**:The second case using speed tracking control. **(B3)**:The third case using speed tracking control.

demand evaluation value ωr1, and the smooth exit of the inertial support power is realized under the action of the first-order inertial link.

6 Simulation verification

6.1 Simulation system

In order to verify the effectiveness of the virtual inertia evaluation and control method of the wind turbine proposed in this paper, the IEEE-9 bus system (None, 2015) with high-proportion wind power shown in Figure 8 is built using DIgSILENT/PowerFactory simulation software. The test system includes three thermal power plants (G1, G2, and G3) and a wind farm (DFIG), which can change the wind power penetration by adjusting the capacity of thermal power units and wind turbines. Assuming that the wind speed remains unchanged at 8 m/s, the main parameters of the system are shown in Table 3. The load mutation occurs when t_0 = 2.0 s.

6.2 Frequency conversion extreme time verification

In order to verify the correctness of the frequency conversion extreme time theory calculation, the test system adopts the following

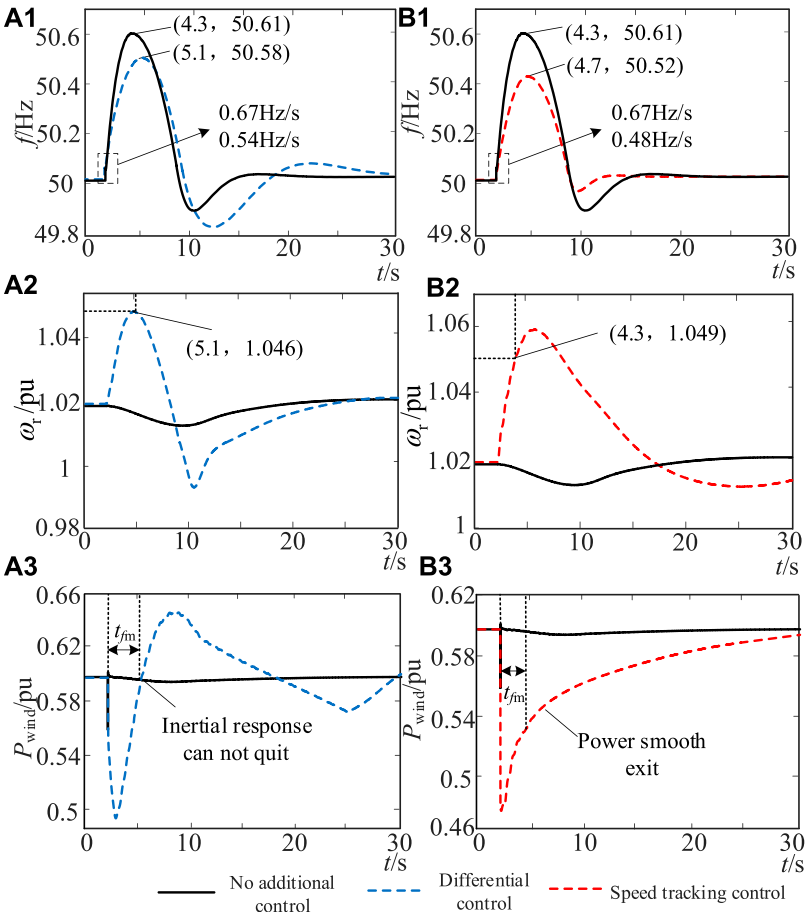

FIGURE 11
(A1):The first case using differential control. **(A2)**:The second case using differential control. **(A3)**:The third case using differential control. **(B1)**:The first case using speed tracking control. **(B2)**:The second case using speed tracking control. **(B3)**:The third case using speed tracking control.

TABLE 7 Parameter setting of simulation example 3.

System parameter	Numerical value	Calculation parameter	Numerical value
Installed gross capacity/MW	1,500	Wind power penetration k	30%
Total load/MW	900	Power disturbance ΔP_d	0.3 pu
Wind turbine capacity/MW	450	System inertia requirements H	15 s
Load mutation amount/MW	450	Wind inertia demand H_{vir}	50 s

parameter settings to analyze the frequency response characteristics after disturbance.

As shown in Table 4, in example 1, the wind power penetration rate in the test system is $k = 20\%$. At the period of 2.0 s, the power disturbance is encountered, and the variation is $\Delta P_d = 0.06$ pu. According to Figure 6, the inherent inertia of the synchronous machine can meet the system frequency safety requirements, and the wind turbine is not required to provide virtual inertia. When the wind turbine is not controlled by virtual inertia, the dynamic response of system frequency and synchronous machine power is shown in Figure 9.

As shown in Figure 9, the synchronous machine responds to frequency changes by increasing/decreasing power when the load changes suddenly. The simulation results of Figure 9 are compared with the theoretical calculation results, as shown in Table 5.

6.3 Frequency modulation effect comparison of virtual inertia control

In order to verify the frequency modulation effect of the virtual inertia control strategy proposed in this paper, the power disturbance is increased and compared with the commonly used differential control. The system parameters in example 2 are set as Table 6:

In example 2, the load disturbance variation increases to 180 MW. The test system uses formula (26) to analyze the frequency safety, and the demand for the virtual inertia of the wind turbine is 10 s. In order to meet the needs of inertial support, the wind turbine adopts the following two control strategies for comparison: 1) when differential control is adopted, K_I is 20 to meet

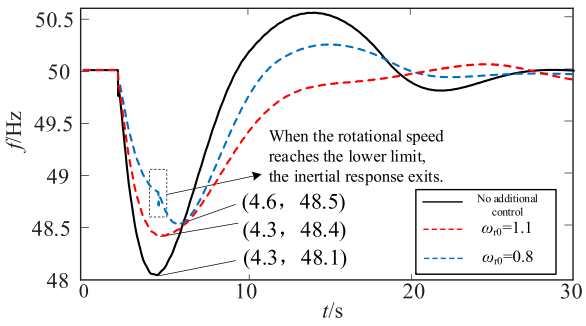

FIGURE 12
Frequency response when $\Delta P_d > 0$.

the inertia demand; 2) when the proposed control is adopted, speed tracking is used. According to the formula (27), when $\Delta P_d > 0$ and $\Delta P_d < 0$, the required speed changes in the wind turbine are 0.03 pu and 0.029 pu, respectively, and the K_p values obtained using formula (30) are 3.2 and 3.3, respectively. Under the two control strategies, the dynamic response of the system is shown in Figures 10, 11.

As shown in Figure 10, without additional control, the wind turbine hardly responds to frequency changes. The maximum frequency drop amplitude of the system Δf_{max} is −0.61 Hz, and the maximum frequency change rate $(df/dt)_{max}$ is −0.67 Hz/s, which has exceeded the allowable value of frequency safety.

When the differential control is adopted, the speed change in the wind turbine is 0.025 pu within the frequency conversion extreme time t_{fm}, and the maximum frequency change rate $(df/dt)_{max}$ and the drop amplitude Δf_{max} of the system are reduced to −0.54 Hz/s and −0.58 Hz, respectively, but still do not meet the maximum frequency change rate constraint. The H_{vir} value of the wind turbine in t_{fm} is 8.79 s, which does not meet the inertia demand of the wind turbine under this example. In addition, since the differential control cannot exit at t_{fm}, the overshoot occurs during the frequency recovery process, which is not conducive to frequency security and stability.

When the control strategy proposed in this paper is adopted, the wind turbine speed variation is 0.028 pu, the system frequency change rate $(df/dt)_{max}$ and the drop amplitude Δf_{max} are reduced to −0.49 Hz/s and −0.52 Hz, respectively, and H_{vir} of the wind turbine within t_{fm} is 10.98 s, which meets the system's demand for virtual inertia. According to Figure 10(b1)~(b3), the smooth exit of the inertial support power of the wind turbine can be realized in the speed tracking control, which reduces the overshoot in the system frequency recovery process. In addition, under the action of the first-order inertial link, the inertial support power of the wind turbine is reduced to 0 after experiencing delay, and the speed begins to recover later, which avoids the wind turbine absorbing power in the frequency recovery stage and is conducive to system frequency recovery. The frequency modulation effect is better than the traditional differential control.

Similarly, when ΔPd <0, the wind turbine speed variation under differential control is 0.026 pu, the system frequency change rate $(df/dt)_{max}$ and the drop amplitude Δf_{max} are reduced to 0.54 Hz/s and 0.58 Hz, respectively. The H_{vir} value of the wind turbine within t_{fm} is 9.14 s, which does not meet the inertia demand of the wind turbine under this example; under the control strategy proposed in this paper, the wind turbine speed variation is 0.029 pu, and the system frequency change rate $(df/dt)_{max}$ and the drop amplitude Δf_{max} are reduced to 0.48 Hz/s and 0.52 Hz, respectively. The H_{vir} value of the wind turbine within t_{fm} is 11.37 s, which meets the system's demand for virtual inertia.

In summary, in both cases of $\Delta P_d > 0$ and $\Delta P_d < 0$, the proposed control can make the wind turbine show a virtual inertia that meets the system requirements within t_{fm} by tracking the speed and can achieve a smooth exit of the inertial support power after t_{fm}, avoiding frequency overshoot. The test results show that compared with the current

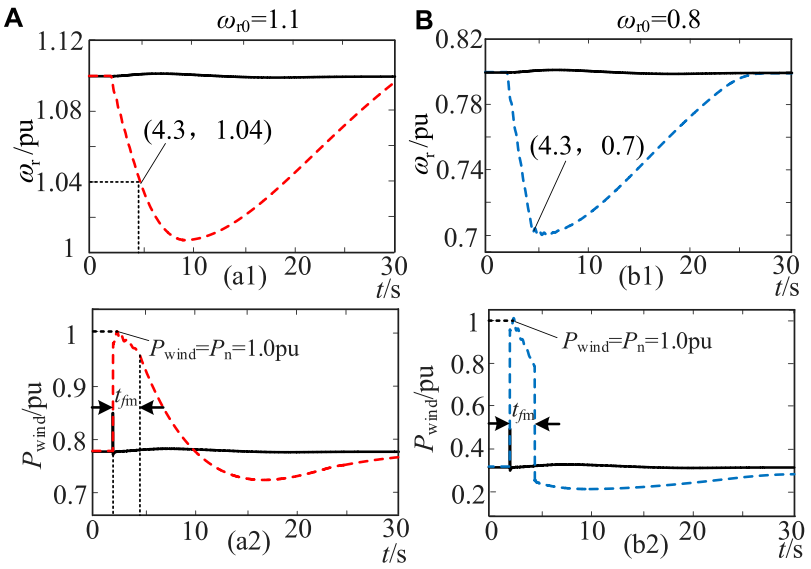

FIGURE 13
(a1):The first case when it is w_{ro}=1.1. **(a2)**:The second case when it is w_{ro}=1.1. **(b1)**:The first case when it is w_{ro}=0.8. **(b2)**:The second case when it is w_{ro}=0.8.

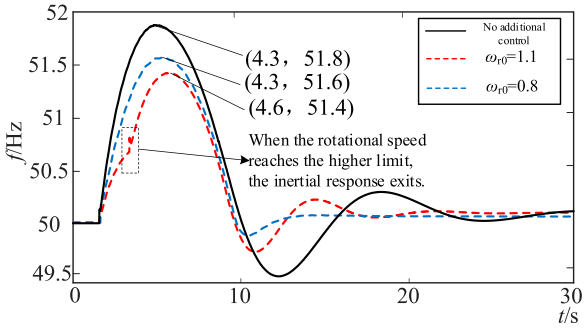

FIGURE 14
Frequency response when $\Delta P_d < 0$.

differential control, the inertial support proposed in this paper aims to meet the inertia requirements of the system and combines the virtual inertia constraint of the wind turbine to complete the design of control parameters, which is more conducive to the reliability of the wind turbine to improve frequency support.

6.4 Evaluation and verification of the maximum inertia of the wind turbine

In order to further test the maximum inertia performance of the wind turbine under the operating state constraints, we will further increase the power disturbance and improve the wind power penetration rate; the system parameters in example 3 are set as Table 7:

In example 3, the wind power penetration rate is increased to 30%, and the disturbance variation reaches 450 MW. In order to ensure that the system frequency change rate meets the constraints, the test system's inertia requirement is set to 15 s, and the virtual inertia requirement of the wind turbine is set to 50 s. In this case, the inertia demand of the system is far greater than the maximum virtual inertia that the wind turbine can provide, so the wind turbine should provide the maximum inertia support according to the initial operating state during the frequency conversion extreme time. By changing the wind speed, the initial speed of the wind turbine is set to 0.8 pu and 1.1 pu, and the dynamic response of the system frequency, wind turbine speed, and power output is obtained when $\Delta P_d > 0$ and $\Delta P_d < 0$, as shown in Figures 12–15.

When the initial speed of the wind turbine is 1.1 pu, the theoretical analysis of Figures 4, 5 shows that the maximum speed change in the wind turbine in t_{fm} is 0.062 pu and the maximum inertia is 7.44 s. As shown in Figure 13, when $\Delta P_d > 0$, although the kinetic energy of the rotor that the wind turbine can release is large, due to the power constraint, the speed change in the wind turbine during the frequency conversion extreme time is only 0.06 pu, which can increase the maximum frequency deviation by 0.3 Hz. The maximum inertia H_{vir} = 7.56 s, allows for the smooth exit of wind turbine inertial support after the frequency conversion extreme moment, under the action of the first-order inertial link.

When the initial speed of the wind turbine is ω_{r0} = 0.8 pu, the maximum speed change in the wind turbine in t_{fm} is 0.1 pu and the maximum inertia is 8 s. As shown in Figure 13, due to the constraint of the rotor kinetic energy reserve, the inertia response of the wind turbine immediately exits after the speed of the wind turbine drops to the minimum value of 0.7 pu at the extreme time of frequency conversion, which will cause a secondary drop in frequency. However, due to the large inertial support power available at this speed, the maximum frequency deviation can be increased by 0.4 Hz, and the maximum inertia of the wind turbine during the extreme time of frequency conversion is H_{vir} = 10 s.

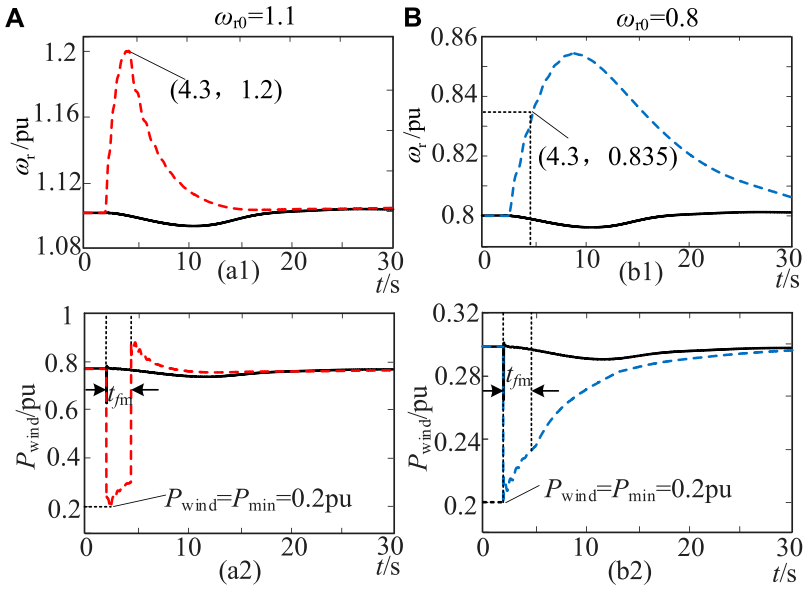

FIGURE 15
(a1):The first case when it is w_{ro}=1.1. **(a2)**:The second case when it is w_{ro}=1.1. **(b1)**:The first case when it is w_{ro}=0.8. **(b2)**:The second case when it is w_{ro}=0.8.

Similarly, when ΔP_d <0, it can be seen from Figures 4, 5 that the theoretical values of the maximum speed change in the wind turbine within t_{fm} are 0.1 pu and 0.034 pu at the initial speeds of 1.1 pu and 0.8 pu, respectively. The maximum inertia is 12 s and 2.75 s, respectively.

According to the test results in Figures 14, 15, when ω_{r0} = 1.1 pu, due to the constraint of the rotor kinetic energy reserve, the inertia response of the wind turbine increases to 1.2 pu and the frequency continues to increase. However, due to the large inertial support power provided by the wind turbine, the maximum frequency deviation can be reduced by 0.4 Hz, and the maximum inertia H_{vir} = 13.75 s. When ω_{r0} = 0.8 pu, due to the small inertial support power provided by the wind turbine, the speed change in the wind turbine is 0.035 pu in the extreme time of frequency conversion, which can reduce the maximum frequency deviation by 0.2 Hz, and the maximum inertia H_{vir} = 3.5 s.

In summary, when the wind turbine needs to provide the maximum inertia support in the face of large disturbances, for the two cases of $\Delta P_d > 0$ and $\Delta P_d < 0$, the maximum speed variation of the wind turbine within t_{fm} under the constraint of the operating state is basically consistent with the theoretical analysis results in this paper. Since Δf_{max} is lower than 2 Hz under this disturbance, the maximum inertia of the wind turbine is slightly larger than the conservative evaluation result at Δf_{max} = 2 Hz, as shown in Figure 5. The simulation test results verify the accuracy of the maximum inertia evaluation analysis method of the wind turbine proposed in this paper.

7 Conclusion

In order to solve the problem of evaluation and control of the virtual inertia of the wind turbine, this paper proposes the constraint and control method of the virtual inertia in the extreme time of frequency conversion, which is beneficial to improving the frequency active support performance of the wind turbine. The following conclusions are obtained through theoretical analysis and simulation verification:

1) The virtual inertia obtained by the rapid adjustment of the active power of the wind turbine is closely related to many factors, such as frequency change and its own operating state. The dynamic change in virtual inertia in the process of frequency support will greatly increase the difficulty of system frequency safety warning, and it is impossible to accurately predict the control effect.
2) In this paper, the frequency response model of the wind power grid-connected system is established, and the calculated frequency conversion extreme time is introduced into the virtual inertia evaluation. Combined with the wind turbine speed and power output state, the virtual inertia constraint is completed, which can provide more reliable inertia support data for the wind turbine frequency response.
3) Within the allowable range of the system frequency change rate, this paper evaluates the inertia requirements of the system and proposes a virtual inertia control method within the frequency conversion extreme time using the wind turbine speed tracking control performance. The test results show that the proposed control meets the support requirements of the system frequency more reliably and avoids the secondary fluctuation of frequency caused by inertia overshoot.

Data availability statement

The original contributions presented in the study are included in the article/Supplementary Material; further inquiries can be directed to the corresponding author.

Author contributions

GT: conceptualization, validation, and writing–original draft. ZH: data curation and writing–review and editing. LB: methodology and writing–original draft. MJ: project administration and writing–review and editing. FaQ: formal analysis and writing–review and editing. XY: resources and writing–review and editing. FeQ: investigation and writing–original draft.

Funding

The author(s) declare that no financial support was received for the research, authorship, and/or publication of this article.

Conflict of interest

Authors GT, ZH, LB, MJ, FaQ, XY, and FeQ were employed by Electric Power Research Institute of Guizhou Power Grid Co., Ltd.

Publisher's note

All claims expressed in this article are solely those of the authors and do not necessarily represent those of their affiliated organizations, or those of the publisher, the editors, and the reviewers. Any product that may be evaluated in this article, or claim that may be made by its manufacturer, is not guaranteed or endorsed by the publisher.

References

Almeida, R. G., and Lopes, J. A. P. (2007). Participation of doubly fed induction wind generators in system frequency regulation. *IEEE Trans. Power Syst.* 22 (3), 944–950. doi:10.1109/tpwrs.2007.901096

Das, K., Guo, F., Nuño, E., and A. Cutululis, N. (2020). Frequency stability of power system with large share of wind power under storm conditions. *J. Mod. Power Syst. Clean Energy* 8 (2), 219–228. doi:10.35833/mpce.2018.000433

Fernández-Guillamón, A., Gómez-Lázaro, E., Muljadi, E., and Molina-García, Á. (2019). Power systems with high renewable energy sources: a review of inertia and frequency control strategies over time. *Renew. Sustain. Energy Rev.* 115, 109369. doi:10.1016/j.rser.2019.109369

Fu, Y., Zhang, X., Hei, Y., and Wang, H. (2017). Active participation of variable speed wind turbine in inertial and primary frequency regulations. *Electr. Power Syst. Res.* 147, 174–184. doi:10.1016/j.epsr.2017.03.001

Gautam, D., Goel, L., Ayyanar, R., Vittal, V., and Harbour, T. (2011). Control strategy to mitigate the impact of reduced inertia due to doubly fed induction generators on large power systems. *IEEE Trans. Power Syst.* 26 (1), 214–224. doi:10.1109/tpwrs.2010.2051690

Li, P., Hu, W., and Rui, H. (2016). "The integrated control strategy for primary frequency control of DFIGs based on virtual inertia and pitch control[C]," in Innovative Smart Grid Technologies-ASIA, IEEE, Melbourne, Australia, 28 November - 1 December 2016.

Lucas, E., Campos-Gaona, D., and Anaya-Lara, O. (2019). Assessing the impact of DFIG synthetic inertia provision on power system small-signal stability. *Energies* 12 (18), 3440. doi:10.3390/en12183440

Ma, J., Qiu, Y., Li, Y., Zhang, W., Song, Z., and Thorp, J. S. (2017). Research on the impact of DFIG virtual inertia control on power system small-signal stability considering the phase-locked loop:. *IEEE Trans. Power Syst.* 32 (3), 2094–2105. doi:10.1109/tpwrs.2016.2594781

Makrini, A. E., Karkri, Y. E., Boukhriss, Y., et al. (2017). LVRT control strategy of DFIG based wind turbines combining passive and active protection. *Int. J. Renew. Energy Res.* 7 (3), 1258–1269.

Mauricio, J. M., Marano, A., Expósito, A. G., and Martinez Ramos, J. (2009). Frequency regulation contribution through variable-speed wind energy conversion systems. *IEEE Trans. Power Syst.* 24 (1), 173–180. doi:10.1109/tpwrs.2008.2009398

Mensou, S., Essadki, A., Nasser, T., and Bououlid Idrissi, B. (2020). A direct power control of a DFIG based WECS during symmetrical voltage dips. *Prot. Control Mod. Power Syst.* 5 (1), 5–47. doi:10.1186/s41601-019-0148-y

None (2015). Definition and classification of power system stability IEEE/CIGRE joint task force on stability terms and definitions. *Gold. Res. Thoughts* 4 (3), 1387–1401.

Ochoa, D., and Martinez, S. (2018). Frequency dependent strategy for mitigating wind power fluctuations of a doubly-fed induction generator wind turbine based on virtual inertia control and blade pitch angle regulation. *Renew. Energy* 128 (PT.A), 108–124. doi:10.1016/j.renene.2018.05.047

Qi, X., Madonski, R., Huang, C., and Ke, Y. (2022). Tracking-differentiator-based dynamic virtual inertial control of offshore wind power plant for frequency regulation. *Int. J. Electr. power energy Syst.* 141, 108150. doi:10.1016/j.ijepes.2022.108150

Ramtharan, G., Ekanayake, J. B., and Jenkins, N. (2007). Frequency support from doubly fed induction generator wind turbines. *IET Renew Power Gener* 1 (1), 3–9. doi:10.1049/iet-rpg:20060019

Shi, L. B., Wang, C., Yao, L. Z., and Ni, Y. X. (2011). Analysis of impact of grid-connected wind power on small signal stability. *Wind Energy* 14 (4), 517–537. doi:10.1002/we.440

Sun, Y., Wang, L., and Li, G. (2010). "A review on analysis and control of small signal stability of power systems with large scale integration of wind power," in International Conference on Power System Technology, IEEE, Zhejiang, Hangzhou, China, 24-28 October 2010.

Tielens, P., and Hertem, D. V. (2016). The relevance of inertia in power systems. *Renew. Sustain. Energy Rev.* 55, 999–1009. doi:10.1016/j.rser.2015.11.016

Ullah, N. R., Thiringer, T., and Karlsson, D. (2008). Temporary primary frequency control support by variable speed wind turbines— potential and applications. *IEEE Trans. Power Syst.* 23 (2), 601–612. doi:10.1109/tpwrs.2008.920076

Vidyanandan, K. V., and Senroy, N. (2013). Primary frequency regulation by deloaded wind turbines using variable droop. *IEEE Trans. Power Syst.* 28 (2), 837–846. doi:10.1109/tpwrs.2012.2208233

Wang, B., Sun, H., and Wenfeng, L. (2022). Minimum inertia estimation of power system considering dynamic frequency constraints. *Proc. CSEE* 42 (1), 114–127.

Wen, Y., and Lin, X. (2021). Minimum inertia requirement assessment of microgrids in islanded and grid-connected modes. *Proc. CSEE* 41 (6), 2040–2053.

Wu, L., and Infield, D. (2014). Power system frequency management challenges-a new approach to assessing the potential of wind capacity to aid system frequency stability. *IET Renew. Power Gener.* 8 (7), 733–739. doi:10.1049/iet-rpg.2013.0424

Xiao, W., Gao, W., Scholbrock, A., Muljadi, E., Gevorgian, V., Wang, J., et al. (2017). Evaluation of different inertial control methods for variable-speed wind turbines simulated by fatigue, aerodynamic, structures and turbulence (FAST). *IET Renew. Power Gener.* 11 (12), 1534–1544. doi:10.1049/iet-rpg.2017.0123

Ying, J., Yuan, X. M., Hu, J. B., and He, W. (2018). Impact of inertia control of DFIG-based WT on electromechanical oscillation damping of SG. *IEEE Trans. Power Syst.* 33 (3), 3450–3459. doi:10.1109/tpwrs.2018.2801283

Yuan, F., Wang, Y., and Zhang, X. (2017). Integrated wind turbine controller with virtual inertia and primary frequency responses for grid dynamic frequency support. *IET Renew. Power Gener.* 11 (8), 1129–1137. doi:10.1049/iet-rpg.2016.0465

Yuan, T., Wang, J., Guan, Y., Liu, Z., Song, X., Che, Y., et al. (2018). Virtual inertia adaptive control of a doubly fed induction generator (DFIG) wind power system with hydrogen energy storage. *Energies* 11 (4), 904. doi:10.3390/en11040904

Zertek, A., Verbic, G., and Pantos, M. (2012). Optimised control approach for frequency-control contribution of variable speed wind turbines. *IET Renew. Power Gener.* 6 (1), 17–23. doi:10.1049/iet-rpg.2010.0233

Zhang, Z. S., Sun, Y. Z., Lin, J., and Li, G. J. (2012). Coordinated frequency regulation by doubly fed induction generator-based wind power plants. *IET Renew Power Generation* 6 (1), 38–47. doi:10.1049/iet-rpg.2010.0208

Zhu, X., Chen, Y., Zhang, X., et al. (2017). Impact of wind turbine on power oscillation characteristic in region network and integrated control strategy. *Electr. Meas. Instrum.* 54 (1), 33–38.

Zhu, X. H., Xie, Y., and Zhu, H. (2018). Review on power system frequency regulation with high wind power permeability. *Energy Power Eng.* 10 (8), 366–382. doi:10.4236/epe.2018.108023

Zhu, Y., Liu, S., and Wang, W. (2021). Comprehensive coordinated control strategy of PMSG-based wind turbine for system inertia support. *IET Renew. Power Gener.* 15 (9), 1915–1926. doi:10.1049/rpg2.12115

Frontiers in
Energy Research

Advances and innovation in sustainable, reliable and affordable energy

Explores sustainable and environmental developments in energy. It focuses on technological advances supporting Sustainable Development Goal 7: access to affordable, reliable, sustainable and modern energy for all.

Discover the latest Research Topics

See more →

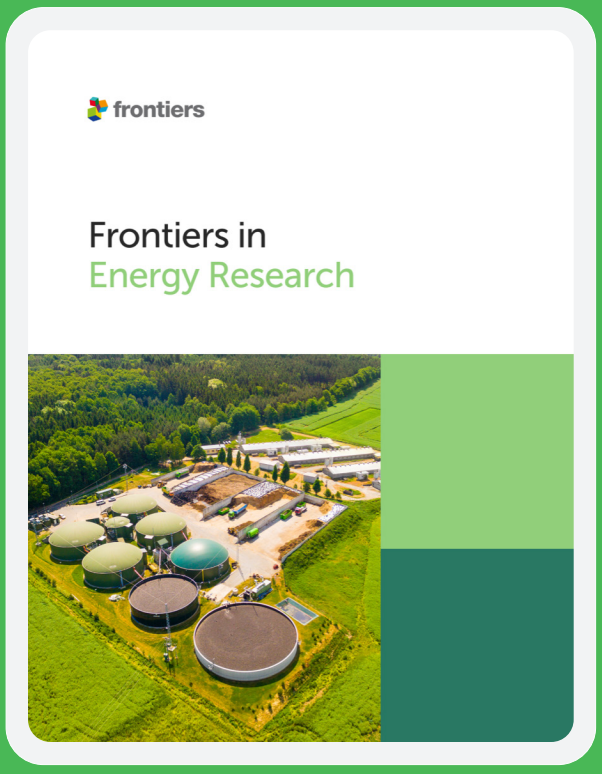

Frontiers

Avenue du Tribunal-Fédéral 34
1005 Lausanne, Switzerland
frontiersin.org

Contact us

+41 (0)21 510 17 00
frontiersin.org/about/contact